Modélisation et simulation de la co-électrolyse du H2O et du CO2 à haute température dans les carbonates fondus

Dayan Monzer

PSL UNIVERSITÉ PARIS

THÈSE DE DOCTORAT

DE L'UNIVERSITÉ PSL

Préparée à l'École Nationale Supérieure des Mines de Paris

Modélisation et simulation de la co-électrolyse du H_2O et du CO_2 à haute température dans les carbonates fondus

Modeling and Simulation of High-temperature H_2O and CO_2 co-electrolysis in Molten Carbonates

Soutenue par

Dayan MONZER

Le 14 septembre 2023

École doctorale n°621

Ingénierie des Systèmes, Matériaux, Mécanique, Energétique

Spécialité

Energétique et Génie des Procédés

Composition du jury :

Michel CASSIR Professeur des Universités Chimie ParisTech - IRCP	*Président*
Yann BULTEL Professeur des Universités Grenoble INP - Ense3	*Rapporteur*
Mohamed MACHMOUM Professeur des Universités Université de Nantes - IREENA	*Rapporteur*
Annabelle BRISSE Docteure Hynamics	*Examinatrice*
Anne-Cécile ROGER-CHARBONNIERE Professeure des Universités Université de Strasbourg - ICPEES	*Examinatrice*
Chakib BOUALLOU Professeur MINES Paris	*Directeur de thèse*

MINES PARIS | PSL

Acknowledgements

At the very outset of the report, I would like to thank all the people whose assistance was a milestone in completing this thesis.

Firstly, I would like to express my sincere gratitude and appreciation to my director, **Prof. Chakib BOUALLOU**, for the trust he has bestowed upon me by proposing and supervising this doctoral work and for his continuous encouragement, support, and unwavering belief in my abilities throughout this Ph.D. journey.

I am also immensely grateful to the members of my thesis committee. Firstly, I extend my gratitude to **Prof. Michel CASSIR** for agreeing to lead my Examination Board. Additionally, I would like to express my thanks to **Prof. Yann BULTEL**, **Prof. Mohamed MACHMOUM**, **Dr. Annabelle BRISSE**, **Prof. Anne-Cécile ROGER-CHARBONNIERE**, for their insightful feedback, constructive criticism, and valuable suggestions that have significantly improved the quality of my research work.

I would like to extend my heartfelt gratitude to **Dr. Rodrigo RIVERA TINOCO**, whose continuous support throughout the initial year of my thesis motivated me to approach each day with a focused mind. I am immensely thankful to him for being there during times of uncertainty and self-doubt, and for offering consistent encouragement and support even after his departure from the lab.

I sincerely thank **Prof. Michel CASSIR**, **Ersan GURBUZ**, and **Haitam MESKINE** from the Chimie ParisTech for their collaboration and support in the experimental research as a part of the ANR MCEC project. Their expertise in the domain of the practical approach has helped me validate my model and develop part of the dynamic-state work.

I would also like to offer a profound thanks to **Prof. Assaad ZOUGHAIB** for having helped me with the thermal integration of the processes. I also thank **Maëlle THALLER** and **Salomé GOBBI** for their valuable contributions to a specific section of this thesis, specifically, the CO_2 capture and desulfurization simulation discussed in Chapter 3. Their dedicated work during their 3-month research internship significantly enriched this aspect of the study. Additionally, I extend my thanks to **Erick REYES RODRIGUEZ** for his substantial input in integrating renewable energy sources with the Power-to-Gas system during his 2-month master's internship. His work was helpful in gathering and processing real-world data from renewable energy farms in France, which was essential for this research.

I would like to acknowledge the financial support from the French National Research Agency (ANR) for this research project, the MCEC project of the reference ANR-17-CE05-0025, which has allowed me to gather crucial data.

My sincere appreciation also goes to my colleagues at the Center of Energy Efficiency of Systems (CES) for their collaboration, insightful discussions, and willingness to share their expertise, which has significantly enriched my work and helped me overcome various challenges. Their support has been instrumental in shaping the outcome of this project.

I am indebted to my loving family members and my supportive and caring fiancé. Their unconditional love, unwavering faith, and support have been the pillars of strength that kept me going. Their understanding and sacrifices have allowed me to pursue my dreams with determination and focus.

Thank you all for your invaluable contributions, support, and belief in my abilities. Your presence in my life has been truly transformative, and I am forever grateful.

Contents

List of Figures

List of Tables

Nomenclature

Abbreviations

ACM	Aspen Custom Modeler
AEL	Alkaline Electrolyzer [*Électrolyseur alcaline*]
BoP	Balance of Plant
CAPEX	Capital Expenses [*Coûts d'investissement*]
CCS	Carbon Capture and Storage [*Captage et stockage du carbone*]
DOE	Department of Energy
EOR	Enhanced Oil Recovery
FCE	FuelCell Energy
FGD	Flue-Gas Desulphurization
GC	Gas Chromatography
HTE	High-Temperature Electrolysis
HX	Heat Exchanger [*Échangeur de chaleur*]
IGCC	Integrated Gasification-Combined Cycle
LNG	Liquified Natural Gas
MCEC	Molten Carbonate Electrolysis Cell [*Électrolyseur à carbonates fondus*]
MCFC	Molten Carbonate Fuel Cell [*Pile à combustible à carbonates fondus*]
MEA	Monoethanolamine
NG	Natural Gas [*Gaz naturel*]
NGCC	Natural Gas-fired Combined Cycle
Ni	Nickel
NiO	Nickel Oxide
OPEX	Operating Expenses [*Coûts d'exploitation*]

P2G	Power-to-Gas
PC	Pulverized Coal
PEM	Proton Exchange Membrane [*Électrolyseur à membrane échangeuse de protons*]
PV	Photovoltaic [*Photovoltaïque*]
RWGS	Reverse Water Gas Shift [*Réaction inverse du gaz à l'eau*]
SCR	Selective Catalytic Reduction
SNG	Substitute Natural Gas [*Substitut de gaz naturel*]
SOEC	Solid Oxide Electrolysis Cell [*Électrolyseur à oxyde solide*]
VRES	Variable Renewable Energy Sources [*Sources d'énergie renouvelables variables*]
WGS	Water Gas Shift [*Réaction du gaz à l'eau*]

Greek letters

η	Efficiency	
ρ	Density	[kg/m^3]

Latin letters

$\dot{m}$	Mass flow rate	[kg/h]
$\dot{n}$ or F	Molar flow rate	[kmol/h]
A	Surface Area	[cm^2 or m^2]
C	Cost	[€]
C_p	Heat capacity	[kJ/(mol · K)]
F	Faraday's Constant	[C/mol]
G	Free Energy	[kJ/mol]
H	Enthalpy	[kJ/mol]
j	Current density	[A/cm^2]
m	Mass	[kg]
P	Pressure	[bar]
Q	Heat flow	[kW]
S	Entropy	[kJ/(mol · K)]
T	Temperature	[°C or K]
U	Potential	[V]
V	Volume	[m^3]

W	Power	[kW]
Y	Molar fraction	

Subscripts

act	Activation
av	Average
$conc$	Concentration
e	Electrons
el	Electrolysis
eq	Equilibrium
f	Final
fe	Fuel electrode side
$limit$	Limiting
oe	Oxygen electrode side
ohm	Ohmic
$prod$	Produced
R	Reaction
r	Reactor
rev	Reversible
tn	Thermo-neutral
w	Wall

Variables

ASR	Area Specific Resistance [*Résistance surfacique spécifique*]	[$\Omega \cdot cm^2$]
LHV	Lower Heating Value [*Pouvoir calorifique inférieur*]	[J/kg]

General Introduction

The issue of global warming has become a pressing concern, and countries worldwide must take action to reduce their carbon footprint. According to the 2021 Emissions Gas Report by the United Nations, achieving the targets set out in the 2015 Paris Agreement and limiting global temperature increase to 1.5 °C requires a 50% reduction in global emissions [1]. However, the power sector is considered the most significant contributor to global CO_2 emissions, accounting for nearly 40% of the total, primarily due to the burning of fossil fuels [2]. As a result, many countries have emphasized the importance of transitioning to a decarbonized energy mix by integrating non-polluting energy sources, such as Variable Renewable Energy Sources (VRES) like solar and wind energy. In recent years, these technologies have played a significant role in the electricity mix, with solar and wind power generation increasing by an average of 32% and 15.5% per year, respectively, between 2011 and 2021 [3]. However, their intermittent nature limits their widespread integration, as they must match load demand and electric power supply profiles.

Another crucial approach for achieving an eco-friendly future is capturing, sequestering, and reusing CO_2, which could introduce a new energy paradigm. CO_2 capture and valorization is gaining momentum as a global priority due to the urgent need for environmental conservation. This approach is widely considered effective and efficient in achieving clean energy. However, with only 10 $GtCO_2$ of the 38 Gt of CO_2 emitted annually being suitable for storage, complementary pathways for captured CO_2 must be considered, such as CO_2 valorization. Using CO_2 as a valuable source of chemicals and fuels can significantly impact the world's future by reducing carbon emissions and promoting a low-carbon future.

With the renewable energy massive integration challenges and the need for energy storage, the Power-to-Gas (P2G) system is a promising technology for energy storage and CO_2 conversion into valuable fuels. It also plays a crucial role in the energy transition toward a sustainable future. P2G systems can help to integrate renewable energy sources into the energy mix by converting excess electricity through electrolysis into hydrogen or methane, which can be stored and transported in existing gas infrastructure. These products can be used as fuel for power generation, heating, and transportation, thereby reducing carbon emissions and increasing the energy system's flexibility. Therefore, the P2G system can serve as a critical enabler for the energy transition, supporting the decarbonization of the energy sector and helping to achieve climate goals.

The P2G system now incorporates low-temperature electrolysis cells such as alkaline or proton membrane electrolyzers, which have gained popularity due to their technological maturity and low capital investment. In contrast, high-temperature electrolysis has been found in studies to reduce electrical demand but increase thermal requirements [4]. Consequently, there is growing interest in exploring

high-temperature electrolysis using solid-oxide electrolyzers. Within this domain of interest, molten carbonate electrolysis cells (MCEC) have emerged as a promising system for Power-to-Gas applications, branching off from the molten carbonate fuel cell (MCFC) technology. This technology has drawn significant attention due to the advanced development stage of MCFC technology, which encompasses all fuel cell technologies [5]. Furthermore, MCFC have demonstrated remarkable capacity at the multi-megawatt scale. Thus, the choice of MCFC is supported by its maturity, success, and ability to capture CO_2 while generating power. Indeed, there is still substantial interest in evaluating the potential of this technology for CO_2 valorization and energy storage applications.

This thesis is conducted as part of ANR project MCEC (CoMprehension and Optimization of high temperature CO_2 Electrolysis in Carbonates) in collaboration with IRCP (Chimie ParisTech), ENS, CEMHTI, and ISTO. The project's objective was to understand the behavior of CO_2 in molten carbonates through theoretical and experimental approaches. This included conducting electrochemical tests on the cathode side, exploring different electrodes, conditions, and mechanistic pathways, and studying single MCEC cells with CO_2 electrolysis and co-electrolysis with water. By obtaining proper data and considering existing MCFC installations, the project sought to develop a comprehensive view of the application, including balance of plant simulation, comparison with competing devices, and economic analysis. This thesis aims to investigate the technical and economic potential of the molten carbonate electrolysis cell, which operates in the reversible mode of the molten carbonate fuel cell, for the valorization of CO_2 and energy storage. For this objective, the innovative technology is examined for its ability to produce syngas through the co-electrolysis of H_2O and CO_2 within the cell. This produced gas is then directed towards a methanation process, where it is converted into substitute natural gas (SNG), that can be integrated into the existing natural gas grid. Throughout the research, detailed attention is given to developing and optimizing the entire process, encompassing all the unitary operations required to create an energy-efficient process that delivers substitute natural gas, meeting the specified requirements.

The manuscript is structured into five parts. Firstly, in Chapter 1, we will begin with exploring the motivation behind the current research focus on Power-to-Gas systems. Subsequently, in Chapter 2, we will present the model setup for the principal equipment, namely the molten carbonate electrolysis cell (MCEC). The model development contains two scenarios: H_2O electrolysis and co-electrolysis of H_2O and CO_2. Afterward, we will integrate the MCEC model with the balance of plant (BoP) equipment to simulate the complete Power-to-Gas process in Chapter 3. In this part, this process will be evaluated and optimized by studying process efficiency, providing insights into the feasibility of energy efficiency in the proposed process. To examine the dynamic behavior of the Power-to-Gas system, Chapter 4 will focus on analyzing the dynamic response of its main components, including the MCEC electrolyzer and the methanation reactor. Furthermore, a real case study will be conducted to investigate the integration of the system with intermittent renewable energy sources and to analyze how the system responds to variations in input power. Finally, moving on to Chapter 5, an economic assessment of the process will be carried out to evaluate its feasibility within the current context. This assessment will involve identifying the cost drivers that impact the production cost of methane and determining the necessary lifespan of MCEC technologies, manufacturing costs and other relevant factors that may make CO_2 valorization and energy storage by this pathway economically competitive.

Introduction générale

La question du réchauffement climatique est devenue une préoccupation urgente et les pays du monde entier doivent agir pour réduire leur empreinte carbone. Selon le rapport sur les gaz à effet de serre de 2021 des Nations Unies, pour atteindre les objectifs fixés par l'Accord de Paris de 2015 et limiter l'augmentation de la température mondiale à 1,5 °C, une réduction de 50% des émissions mondiales est nécessaire [1]. Cependant, le secteur de l'énergie est considéré comme le plus grand contributeur aux émissions mondiales de CO_2 représentant près de 40% du total, principalement en raison de la combustion de combustibles fossiles [2]. Par conséquent, de nombreux pays ont souligné l'importance d'aller vers un mix énergétique décarboné en intégrant des sources d'énergie non polluantes, telles que les sources d'énergie renouvelables variables (VRES) comme l'énergie solaire ou l'éolienne. Ces technologies ont joué un rôle important dans le mix électrique ces dernières années, avec une augmentation moyenne annuelle de la production d'énergie solaire et éolienne de 32% et 15,5% respectivement entre 2011 et 2021 [3]. Cependant, leur nature intermittente limite leur intégration généralisée, car elles doivent correspondre à la fois à la demande de charge et aux profils d'approvisionnement en électricité.

Une autre approche cruciale pour atteindre un avenir écologique consiste à capter, séquestrer et réutiliser le CO_2, ce qui pourrait introduire un nouveau paradigme énergétique. La captage et la valorisation du CO_2 gagnent en importance en tant que priorité mondiale en raison de la nécessité urgente de protéger l'environnement. Cette approche est largement considérée comme efficace et efficiente pour parvenir à une énergie propre. Toutefois, avec seulement 10 Gt de CO_2 potentiellement stockés sur les 38 Gt de CO_2 émis annuellement, des voies complémentaires pour le CO_2 capté doivent être envisagées, elles concernent essentiellement la valorisation du CO_2. L'utilisation du CO_2 comme source de valeur de produits chimiques ou de carburants peut avoir un impact positif significatif sur l'avenir du monde en réduisant les émissions de carbone et en promouvant un futur bas-carbone.

Avec les défis massifs d'intégration des énergies renouvelables et la nécessité de stocker l'énergie, le système Power-to-Gas (P2G) est une technologie prometteuse pour le stockage d'énergie et la conversion du CO_2 en carburants. Il joue également un rôle crucial dans la transition énergétique vers un futur écologique. Les systèmes P2G peuvent aider à intégrer les sources d'énergie renouvelable dans le mix énergétique en convertissant l'électricité excédentaire par électrolyse en hydrogène ou en méthane, qui peuvent être stockés et transportés dans l'infrastructure existante de gaz. Ces produits peuvent être utilisés comme carburants pour la production d'électricité, le chauffage et le transport, réduisant ainsi les émissions de carbone et augmentant la flexibilité du système énergétique. Par conséquent, le système P2G peut servir d'élément critique pour la transition énergétique, soutenant la décarbonisation du secteur de l'énergie et aidant à atteindre les objectifs climatiques.

Le système P2G intègre désormais des cellules d'électrolyse à basse température telles que des électrolyseurs alcalins ou à membrane échangeuse de proton, qui ont gagné en popularité en raison de leur maturité technologique et de leur faible investissement en capital. En revanche, l'électrolyse à haute température a été mise en évidence dans des études comme réduisant la demande électrique tout en augmentant les besoins thermiques [4]. Par conséquent, il existe un intérêt croissant pour l'exploration de l'électrolyse à haute température utilisant des électrolyseurs à oxyde solide. Dans ce domaine d'intérêt, les cellules d'électrolyse à carbonates fondus (MCEC) ont émergé comme un système prometteur pour les applications de Power-to-Gas, s'inspirant de la technologie des piles à combustible à carbonates fondus (MCFC). Cette technologie a suscité une attention considérable en raison du stade avancé de développement de la technologie MCFC, qui englobe toutes les technologies des piles à combustible [5]. De plus, MCFC a démontré une capacité remarquable à l'échelle du multimegawatt. Ainsi, le choix du MCFC est justifié par sa maturité, son succès et sa potentialité à capter le CO_2 tout en générant de l'électricité. En effet, il existe un intérêt substantiel à évaluer le potentiel de cette technologie pour la valorisation du CO_2 et le stockage d'énergie.

Cette thèse est réalisée dans le cadre du projet ANR MCEC (Compréhension et optimisation de l'électrolyse du CO_2 à haute température dans les carbonates) en collaboration avec l'IRCP (Chimie ParisTech), l'ENS, le CEMHTI et l'ISTO. L'objectif du projet était de comprendre le comportement du CO_2 dans les carbonates fondus par des approches théoriques et expérimentales. Cela comprenait la réalisation de tests électrochimiques du côté cathode, l'exploration de différents électrodes, conditions et voies mécanistiques, ainsi que l'étude de cellules individuelles MCEC avec électrolyse du CO_2 et co-électrolyse avec de l'eau. En obtenant des données appropriées et en tenant compte des installations MCFC existantes, le projet visait à développer une vision globale de l'application, y compris la simulation des équipements de l'usine, la comparaison avec des dispositifs concurrents, et l'analyse économique. Le but de cette thèse est d'étudier le potentiel technique et économique de la cellule d'électrolyse à carbonates fondus, qui fonctionne en mode réversible de la pile à combustible à carbonates fondus, pour la valorisation du CO_2 et le stockage d'énergie. Dans cette optique, la technologie innovante est examinée pour sa potentialité à produire du gaz de synthèse par co-électrolyse de H_2O et de CO_2 au sein de la cellule. Ce gaz produit est ensuite dirigé vers un procédé de méthanation, où il est converti en substitut de gaz naturel (SNG) pouvant être intégré au réseau de gaz naturel existant. Tout au long de la recherche, une attention particulière est accordée à la mise au point et à l'optimisation de l'ensemble du procédé, englobant toutes les opérations unitaires requises pour créer un procédé énergétiquement efficace qui fournit du substitut de gaz naturel répondant aux exigences spécifiées.

Le manuscrit est structuré en cinq parties. Tout d'abord, dans le Chapitre 1, nous commencerons par explorer les motivations actuelles portant sur la recherche concernant les systèmes P2G. Ensuite, dans le Chapitre 2, nous présenterons la description du modèle pour l'équipement principal, à savoir la cellule d'électrolyse à carbonates fondus (MCEC). Le développement du modèle comprend deux scénarios : l'électrolyse de H_2O et la co-électrolyse de H_2O et de CO_2. Ensuite, nous coupellerons le modèle MCEC avec les équipements auxiliaires dans le but de simuler l'ensemble du procédé P2G dans le Chapitre 3. Dans cette partie, ce procédé sera évalué et optimisé en étudiant son efficacité, offrant ainsi un aperçu de la faisabilité de l'efficacité énergétique dans le procédé proposé. Afin d'examiner le comportement dynamique du système P2G, le Chapitre 4 se concentrera sur l'analyse de la réponse dynamique de

ses principaux composants, notamment l'électrolyseur MCEC et le réacteur de méthanation. De plus, une étude de cas réelle sera menée pour étudier l'intégration du système avec des sources d'énergie renouvelable intermittentes et analyser la réponse du système aux variations de puissance d'entrée. Enfin, dans le Chapitre 5, une évaluation économique du procédé sera réalisée afin d'évaluer sa faisabilité dans le contexte actuel. Cette évaluation consistera à identifier les facteurs économiques qui influencent le coût de production du méthane et à déterminer la durée de vie nécessaire des technologies MCEC, ainsi que les coûts de fabrication et d'autres facteurs pertinents qui pourraient rendre la valorisation du CO_2 et le stockage d'énergie par cette voie économiquement compétitive.

Chapter 1

State of the Art

Objective

First, in Section 1, the general situation on which this study is based will be discussed, highlighting the challenges of climate change and global warming, and detailing the measures being taken to address them, including the transition to renewable energies. After that, Section 2 will explore the obstacles to the energy transition and potential solutions. Finally, among the available solutions, the Power-to-Gas system is chosen for study, and it will be thoroughly discussed in Section 3, clearly showing the positioning of the thesis.

Table of Contents

1 General Context:

1.1 Climate Change and Global Warming Issue

Global warming has been all over the media since the 20th century. It was first raised by U.S. Scientist Wallace Broecker in 1975 to refer to the continuous increase in the average temperature of the Earth's climate system. Throughout the severe research and studies on the cause and the effects of global warming, human activities have shown a massive influence on its growth that, in turn, results in climate change. Human activities are the source of greenhouse gas emissions, by which carbon dioxide and methane contribute to over 90% of the impact. These activities involve all means of transportation, industries, and power plants with conventional fossil fuels energy sources. The combustion of fossil fuels emits carbon dioxide into the atmosphere. It was confirmed that carbon dioxide, released from fossil fuels and industrial applications, is considered the principal promoter of global warming [6]. Although there are various manners for the absorption of CO_2 by nature, a large amount of CO_2 still enters the atmosphere, thus influencing the Earth's temperature. Consequently, the Intergovernmental Panel on Climate Change (IPCC) collaborates with other organizations to fight climate change.

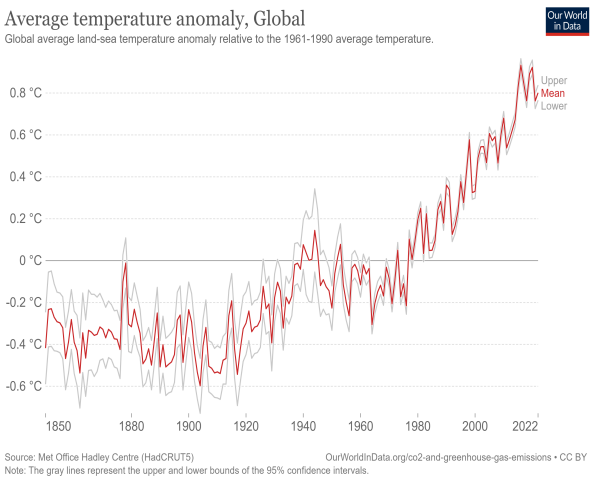

Figure 1.1: Global average temperature rise from 1850 till 2022, reprinted from [7].

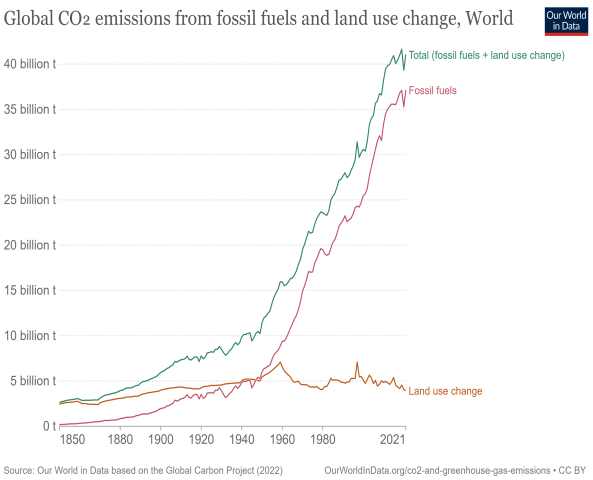

Figure 1.2: Global CO_2 emissions for the years between 1990-2022, reprinted from [8].

Since the pre-industrial period, the global surface temperature has increased dramatically in the past few decades to approximately 0.7 °C higher than the 1961-1990 baseline, as depicted in Figure 1.1. The severe rise in global temperature goes back to the massive growth in CO_2 emissions resulting from the large dependency of fossil fuels in energy, mobility, and industrial sectors. The CO_2 equivalent attained a value of around 40 gigatonnes in 2022, as presented in Figure 1.2, where fossil fuels contribute to around 93% of the total CO_2 emissions.

The COVID-19 epidemic that invades the world has confirmed the significant impact of energy, mobility, and industrial sectors on CO_2 emissions. During this epidemic, government policies substantially affected global energy consumption patterns. The imposed measures gradually increased, beginning with isolating symptomatic persons and progressing to prohibiting mass gatherings, impelling mandatory school closures and house confinement, and even closing international borders. The population lockdown

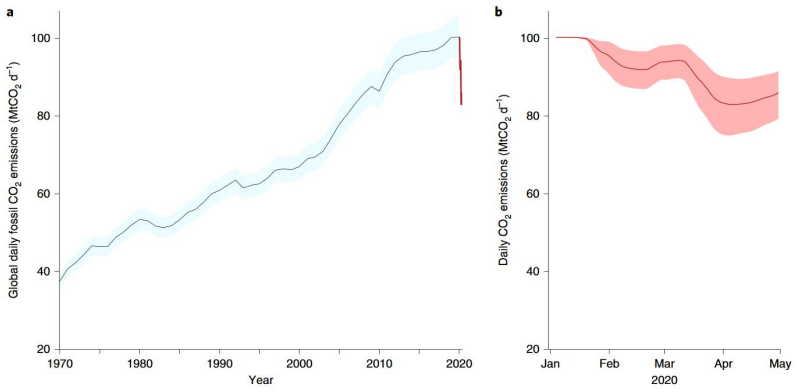

Figure 1.3: Global daily fossil CO_2 emissions ($MtCO_2$ d^{-1}). **(a)** Annual mean daily emissions in 1970–2019 (black line); the red line shows the daily emissions up to the end of April 2020 estimated here. **(b)** Daily CO_2 emissions in 2020 (red line, as in **(a)**), reprinted from [9].

drastically changed energy use, affecting the CO_2 emissions. In this context, Le Quéré et al. (2020) [9] studied the impact of confinement on the global and sector-specific CO_2 emissions. Their study showed that the global daily CO_2 emissions decreased by 17% by early April 2020, as illustrated in Figure 1.3. It can also be noticed that the daily CO_2 emissions in early April 2020 are close to the 2006 level.

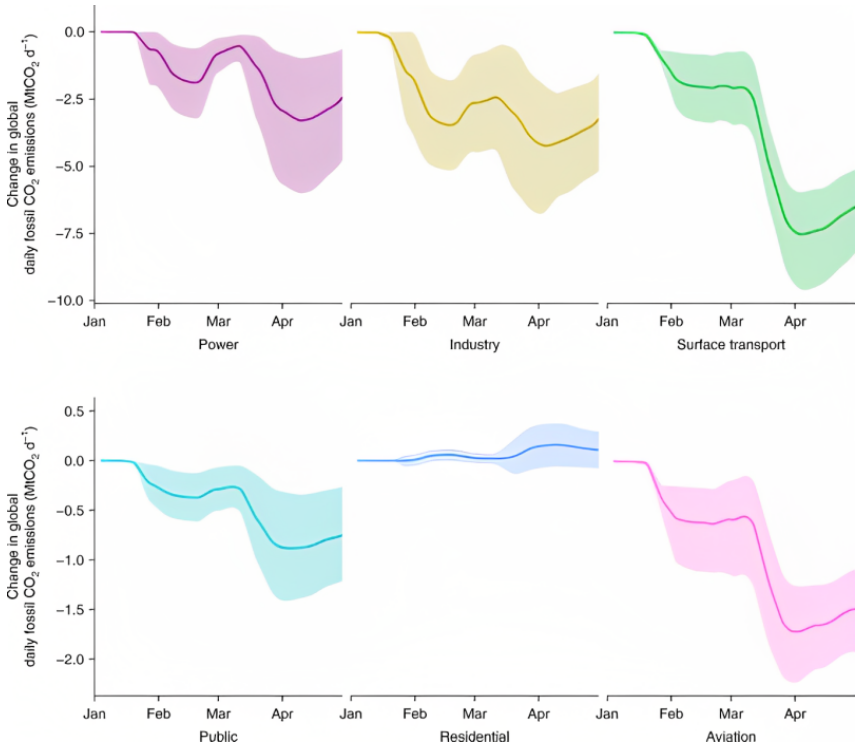

Figure 1.4: Daily fossil CO_2 emissions by sector ($MtCO_2$ d^{-1}) during lockdown, adopted from [9].

The study on the change in daily fossil CO_2 emissions by sector, presented in Figure 1.4, revealed that the surface transport emissions dropped by 36% by 7 April 2020, accounting for the most influential contribution to total emissions change (-43%). Emissions in the electricity sector declined by 7.4% and in

the industries sector by 19%. In absolute terms, surface transportation, electricity, and industry emissions were the most affected, accounting for 86% of the overall reduction in world emissions. CO_2 emissions in the aviation industry decreased by 60%, and by 21% in the public sector. The residential sector increased world emissions by 2.8% [9].

In this regard, a worldwide concern towards the objectives of reducing energy consumption, maximizing energy efficiency, switching to alternative fuels, increasing renewable energy share, and reaching a zero CO_2, were stated in the agreements, Rio in 1992, Kyoto in 1997, and Paris Agreement in 2015. The Paris Agreement contains an ambitious goal to limit the global temperature rise to 1.5 °C [10]. The 1.5 °C Scenario presented in the 2021 World Energy Transitions Outlook [11] proposes six technical pathways for an energy transition compatible with achieving the Paris climate objective of 1.5 °C. Pursuing these six technical pathways aggressively would lead to massive emission reductions between today and 2050, thereby opening the way for a net-zero carbon world by mid-century. These pathways are illustrated in Figure 1.5. They include **1.** renewable electricity generation sources and direct use of renewable heat and biomass, **2.** energy conservation and efficiency measures related to reduced demand and efficiency improvements, **3.** electrification of end-use sectors such as transportation and heating applications, **4.** hydrogen gas and its derivatives, **5.** carbon capture, and storage (CCS) from fossil fuel-based and other emitting processes, primarily in industry, and **6.** bioenergy coupled with carbon capture and storage (BECCS) and other carbon removal measures.

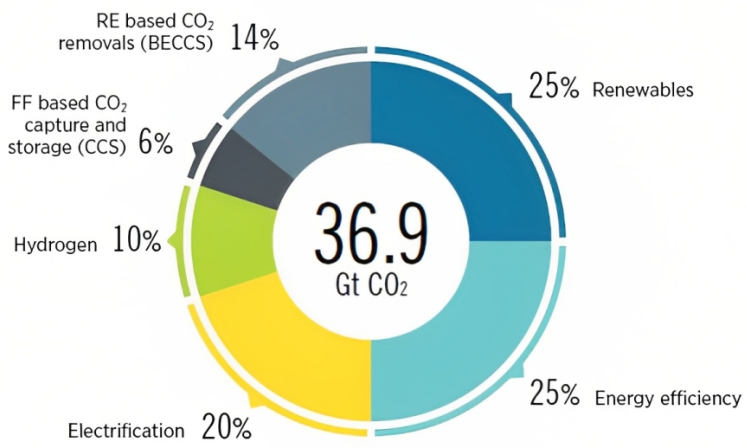

Figure 1.5: Six technological approaches for reducing emissions by 2050, adopted from [12]. *CCS = carbon capture and storage; BECCS = bioenergy with carbon capture and storage; RE = renewables; FF = fossil fuel; GtCO2 = gigatonnes of carbon dioxide.*

1.2 Energy Transition into Renewables

The first technological approach to climate neutrality by 2050 is transitioning from fossil-based energy sources, including oil, natural gas, and coal, to low-carbon energy sources, like variable renewable energy sources (VRES). These innovative energy sources play a dual role in reducing fossil fuel dependency and providing clean and efficient energy. Several countries have insisted on the importance of the energy transition process in decarbonizing the energy mix by integrating non-contaminant energy sources.

In Europe, the European Union has committed to reducing net emissions by at least 55% by 2030 [13]. This target could be reached by raising the share of renewable energy since energy production and consumption contribute to more than 75% of the EU's total greenhouse gas emissions. For this reason, the European Commission revised the Renewable Energy Directive in May 2022 and proposed increasing the renewable energy share's target from 32% in 2018 to 45% by 2030 [13]. From 2011 to 2021, Europe's wind and solar power generation increased by 10.7% and 11.6% annually, respectively [3]. More specifically, as a member of the European Union, France is currently working on boosting the share of renewable energy in the energy mix, even though the French energy mix is highly reliant on nuclear energy with zero carbon emissions. Figures 1.6a and 1.6b displays the distribution of energy produced and the installed power in France in 2021. In terms of installed power, renewable energy contributes to 38%, comparable with installed nuclear power of 39%. However, when it comes to energy produced, nuclear energy dominates with a share of approximately 69%, followed by renewables at 23.64%. The largest share of renewable energy installation in France is formed of hydropower.

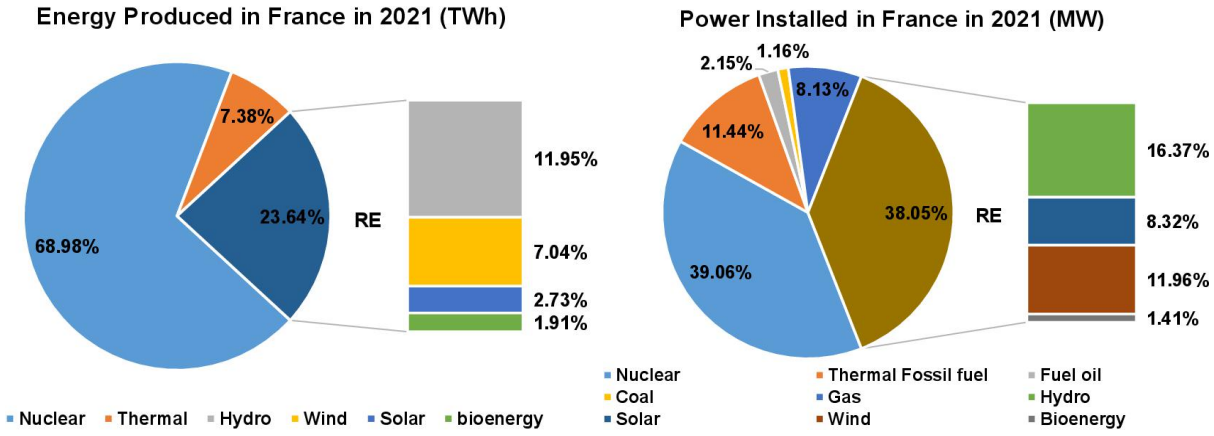

Figure 1.6: Distribution of the energy production in France in 2021 (TWh) **(a)** and power installed in France in 2021 (MW) **(b)**, extracted from RTE database [14].

The primary global increase in the implementation of renewable energy has dramatically decreased the Levelized Cost of Electricity (LCOE) of these sources. For instance, according to the International Renewable Energy Agency (IRENA) [11], the LCOE of solar PV decreased by 85% between 2010 and 2020 (from 0.381 to 0.057 $/kWh), and that of concentrating solar power reduced by 68% (from 0.34 to 0.108 $/kWh). Additionally, from 2010 to 2020, the LCOE of offshore wind energy fell by 42% (from 0.162 to 0.084 $/kWh). The precipitous decline in LCOE encourages investing in integrating renewable energy sources. However, the massive integration of these sources for electricity generation poses some problems related to the difficulty in balancing electricity production with the demand and the transmission and distribution of electricity responsible for managing the national electricity network. This issue is because renewable energy sources, primarily wind and solar, depend highly on meteorological conditions, making them uncontrollable for fulfilling energy demands. Therefore, to solve this problem, massive energy storage and a transmission and distribution network are required to address the challenges of renewable energy.

2 Renewable Energy Storage Techniques

Balancing fluctuating electrical power production and consumption requires management to facilitate renewable energy integration. This management may be accomplished by utilizing an energy storage system to store excess energy produced during low-demand periods and reuse it during shortages and high-demand periods. Currently, there are different storage technologies; however, each technology has distinct characteristics and can be used depending on the need. Energy storage systems (ESS) transform electric energy into mechanical, thermal, electrochemical, chemical, and electromagnetic forms [15].

Mechanical energy storage (MES) is based on storing electric energy as potential energy using pumped storage hydroelectric (PSH), kinetic energy in flywheels, or compressed air energy storage (CAES) (Figure 1.7). A pumped storage hydroelectric (PSH) system is a large-scale energy storage system. It stores the excess power by pumping water from a lower to an upper reservoir during low-demand periods. When electricity is needed, water flows from the upper reservoir through a turbine into the lower reservoir, generating electricity [16]. A flywheel is an electromechanical system that operates as a motor, where the rotor (flywheel) accelerates to a very high speed and maintains the energy in the system as rotational energy. This stored energy is discharged when the flywheel slows down. Compressed air energy storage (CAES) is based on the conventional gas turbine cycle. In this cycle, the air is compressed and stored under pressure in an underground cavern. During high power demand, the compressed air is removed from the cavern, heated, and then expanded through high and low-pressure turbines connected to electrical generators to transform the kinetic energy produced by the compressed air or gas into electrical energy.

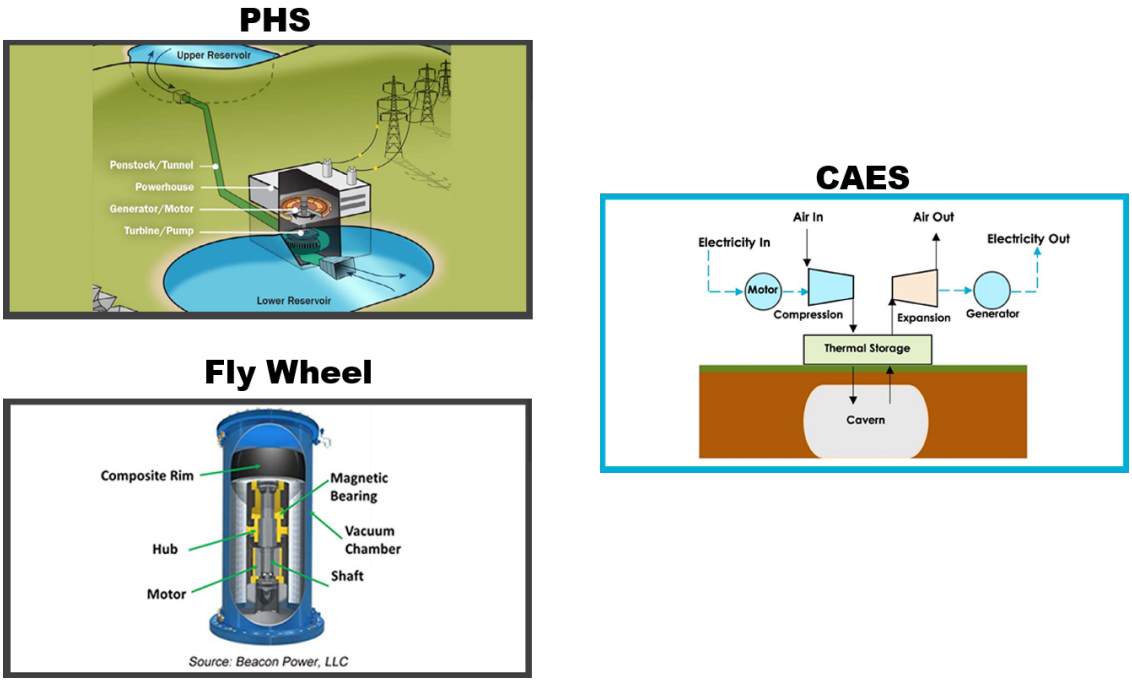

Figure 1.7: Schematic representation of the mechanical energy storage systems.

Thermal energy storage (TES) systems stock electrical energy in the form of thermal energy by heating or cooling a storage medium. The stored energy can later be utilized for heating and cooling applications and power generation via steam turbines. The TES systems include sensible heat, latent heat, or thermochemical storage (Figure 1.8) [17]. Sensible heat is used to store energy by changing the temperature of the material. Concrete, cast ceramics, and molten salts are the most commonly used materials for sensible heat storage. Latent heat storage occurs due to the phase change of a material. Phase change materials (PCMs), which are classed as organic PCMs and inorganic PCMs, store latent heat generated by the material's phase change in storage media. Finally, thermochemical heat storage applies the process of a reversible reaction in which heat is stored during the endothermic reaction path and released during the exothermic one. During the storage stage, thermal energy is applied to dissociate the reactant into products of an endothermic reaction. The products are stored separately to avoid the reversible process of the reaction. When energy is required, the stored products are mixed, which will react to form the initial reactants, thus releasing the stored thermal energy since the reversible reaction is exothermic. Another thermal energy storage is considered, which is the pumped heat electrical storage (PHES). The working principle of this process is to convert electricity into heat using a large-scale heat pump. The heat pump is powered by electricity, which transfers heat from the cold to the hot store. Then, the heat pump operation is reversed to become a heat engine to recover the energy. The engine extracts heat from the hot store, transports waste heat to the cold store, and generates mechanical work that runs an electrical generator, thus producing electricity [15].

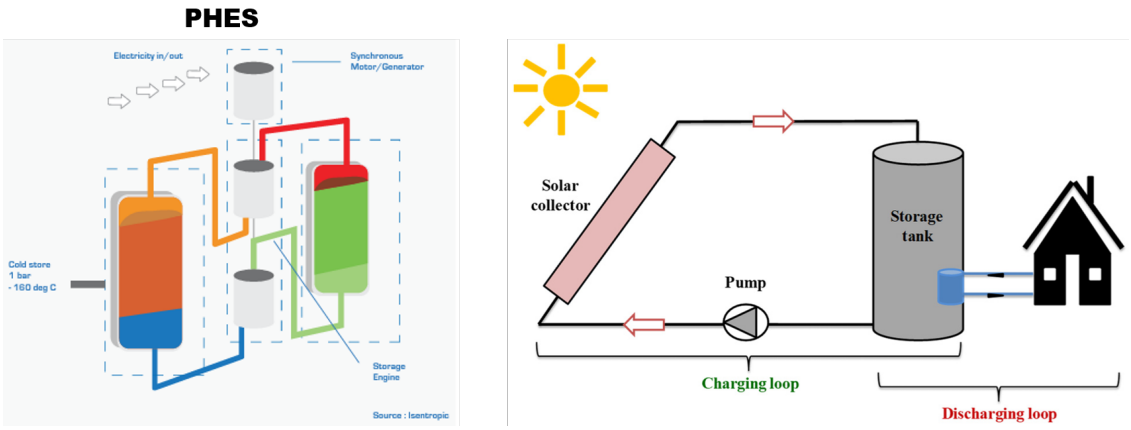

Figure 1.8: Schematic representation of the thermal energy storage systems.

Electrochemical energy storage occurs either in rechargeable batteries (Pb-A, Na-S, Li-ion, Ni-Cd) or flow batteries (vanadium redox, FeCr, and Zn-Br) [18]. Batteries are the most used technology for energy storage. The battery stores electricity as electrochemical energy. The device consists of multiple cells connected in series or parallel to achieve the desired storage capacity. Different types of batteries are currently used in energy storage applications, and they include Lead Acid batteries (Pb-A), Sodium Sulfur (Na-S) batteries, Lithium-ion (Li-ion) batteries, and Nickel-Cadmium (Ni-Cd) batteries. Flow batteries store energy in an electrochemical cell containing two aqueous solutions (electrolytes) through reversible electrochemical reactions. Electrolytes can store energy by oxidizing one and reducing the other. Three types of flow batteries are commercially available, which are Vanadium Redox Battery (VRB), Zinc Bromine Battery (ZBB), and Polysulfide Bromide Battery (PSB).

Electromagnetic energy storage includes superconducting magnetic energy storage (SMES) and super-capacitor energy storage system (SCESS). SMES system stores energy in the form of direct current electricity through the passage of a current via a superconductor, which stores this energy in the form of a direct current magnetic field, as presented in Figure 1.9. The current conductor operates at cryogenic temperatures, transforming into a superconductor. Super-capacitor energy storage system is composed of electrochemical cells, which contain two conducting electrodes, an electrolyte, and a porous membrane like batteries; however, no redox reactions occur in the cells. Therefore, the capacitors can store the energy as an electric field.

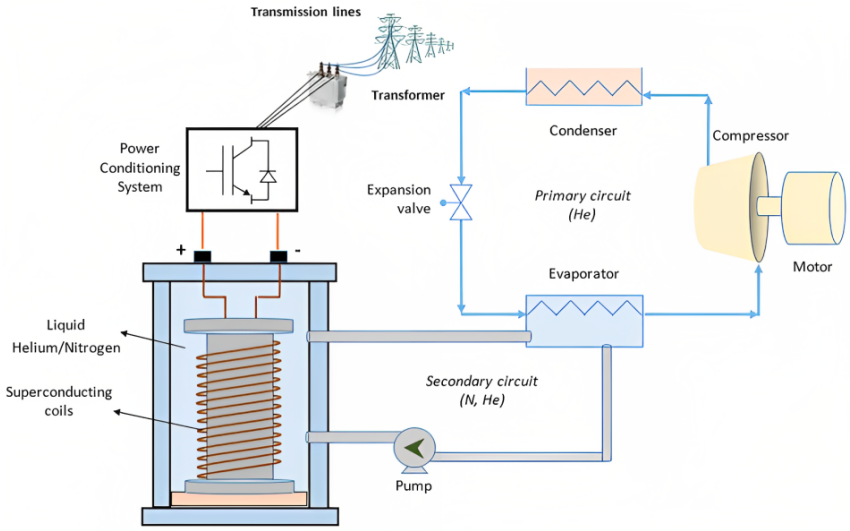

Figure 1.9: Schematic representation of a SMES energy storage systems, reprinted from [19].

Chemical energy storage corresponds to the storage of electrical energy in the form of chemical energy. It is known as a "Power-to-Gas" system, where electrical power produces chemical compounds. These compounds are stored and reused later to generate energy when needed. Several chemical compounds are considered for energy storage applications, such as hydrogen gas, methane, methanol, and hydrocarbons. Among these compounds, hydrogen gas production from electricity is the quickest route for chemical energy storage. It is produced via water electrolysis. Other chemical compounds can be formed from hydrogen gas and a carbon source, such as CO and CO_2.

The choice of storage device relies on the capacity and the storage duration needed. Depending on the technology, energy can be stored for either a short or a long time. Figure 1.10 depicts the placement of the different EES technologies regarding their capacity and storage period. Short-term storage technologies that can store energy for a short time (less than 1 second to a few minutes) are inductors (SMES), super capacitors, and flywheels. These technologies have high efficiency above 90%; however, they are limited in storage capacity and period [15]. Midterm storage technologies correspond to a storage duration ranging from hours up to 1 week and include batteries, pumped hydro storage, and compressed air. Batteries are the most used technology for renewable energy storage, with an efficiency of 80% and a capacity of 85 kWh for Li-ion and 40 MWh for Pb-A. Whereas, pumped hydro storage and compressed air have lower efficiency than batteries, with 56% for pumped hydro and 42% for compressed air, but they have a higher capacity between 3 and 5 GWh [15]. Finally, long-term storage technologies belong

to chemical storage techniques, Power-to-hydrogen, or Power-to-Gas systems, with a capacity of several TWh, a storage period from days up to a year, and an efficiency of 40% for hydrogen gas and 36% for synthetic methane [15]. Hence, for a massive insertion of VRES, it is necessary to use a high-capacity and long-term storage technology. The only technologies with these qualities are those in the top right corner of Figure 1.10, namely synthetic methane, hydrogen gas, compressed air, and pumped hydro storage.

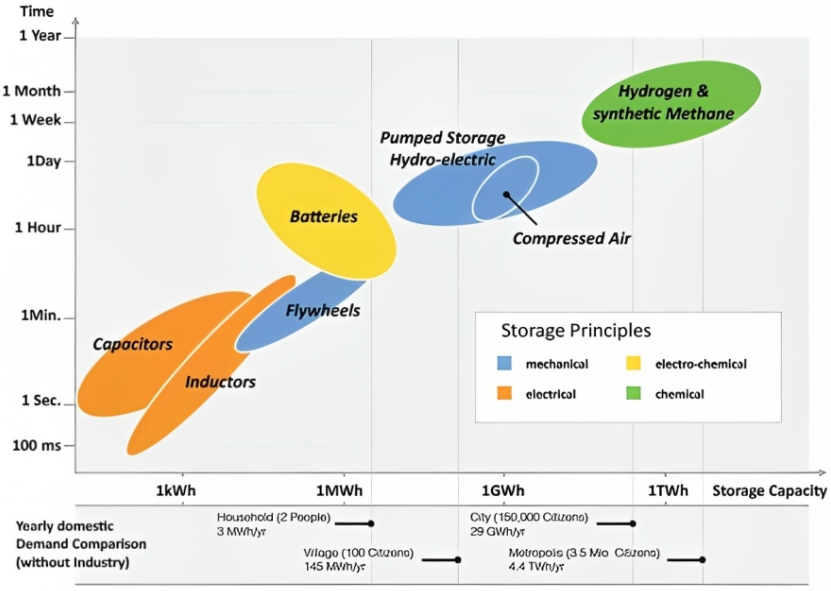

Figure 1.10: The storage capacity and period of the energy storage systems, reprinted from [15].

EES technology maturity levels range from research and development to demonstration and deployment to commercialization. The maturity of the technology is essential in selecting an energy storage system because the more mature the technology is, the more cost-effective it is. Today's most mature technology is pumped hydro energy storage (PHES) and lead-acid batteries. The pumped hydro system is a well-established technology that contributes to the most significant energy storage share of around 90%, with a total installed capacity of 172.5 GW [20]; however, its expansion is restricted by geographical and environmental constraints. Batteries come in the second position with an installed capacity of 14.1 GW [20]. Although lead acid batteries are more mature than lithium-ion batteries, lithium-ion batteries are more widely used in energy storage, with 13.1 GW installed capacity out of 14.1 GW, due to the significant advance of the cost turning point of these batteries in 2020 [20]. Compressed air energy storage, on the other hand, is still at the demonstration project scale despite being a developed technology due to its low round-trip efficiency, which requires further improvement. Furthermore, NaS batteries, flywheels, and liquid air energy storage are commercially available in demonstration projects, not on a large scale. Other technologies are in the research and development stage: thermal storage (sensible/latent heat), hydrogen gas, and synthetic methane (Power-to-Gas system). However, chemical storage systems, such as hydrogen or synthetic methane gas, are rapidly evolving due to their ability to integrate with several sectors, including industrial processes, power generation systems (fuel cells and power plants), and transportation, thereby replacing fossil fuels. Therefore, the subsequent research will focus on and explore the chemical storage system known as the Power-to-Gas system.

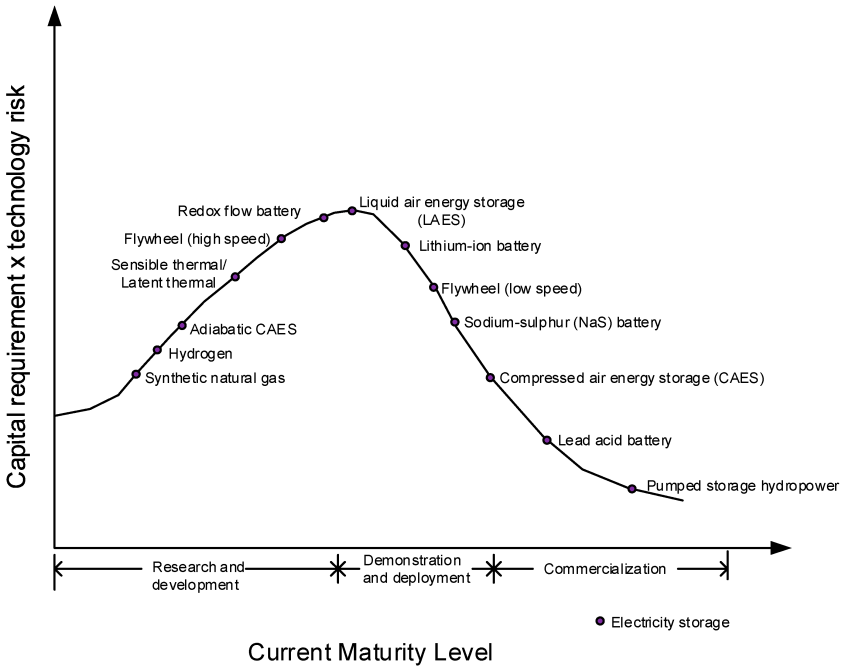

Figure 1.11: The technological maturity of different energy storage systems, reprinted from [20].

3 Chemical Storage System: Power-to-Gas System

Power-to-Gas (P2G) technology has recently been heavily debated as an energy storage system with the vision to integrate future energy systems. The notion of the Power-to-Gas system was first established in Japan by Hashimoto et al. (1999) [21], who proposed a CO_2 recycling strategy. This strategy uses electricity generated by solar cells in deserts to electrolyze seawater and produce H_2, which is subsequently used to synthesize methane from CO_2 and H_2. Afterward, this concept expanded with the growth of renewable energy sources to connect the electricity grid to the gas grid by converting the surplus of renewable power into a gas compatible with the gas grid through a two-step process. First, H_2 is produced by water electrolysis, then converted in the presence of external CO or CO_2 source to CH_4 via methanation, as illustrated in Figure 1.12. The system can be a one-step process, producing only hydrogen gas (H_2), and is known as a Power-to-H_2 system, where H_2 can be used as a chemical product for industrial process, or as a fuel for mobility, or directly injected into the gas grid. On the other hand, the Power-to-SNG system is the classical route of the Power-to-Gas that produces substitute natural gas (SNG), which can be used in various applications. For example, substitute natural gas (CH_4) is used directly in combined heat power (CHP) systems to generate electricity and heat for household applications or injected into the gas network.

Power-to-SNG system is more favorable than the Power-to-H_2 system due to the problems associated with the hydrogen gas storage and the applied constraints for injecting H_2 in the gas grid. H_2 storage is the leading technical problem with the hydrogen gas economy as it requires either high pressures to be stored as compressed gas or low temperatures for H_2 liquefaction, thus consuming so much energy. For instance, the energy consumed for the liquefaction process is about one-third of the combustion energy of H_2 [21]. Besides, H_2 has a low energy storage per volume (2.5 times less than natural gas), implying that

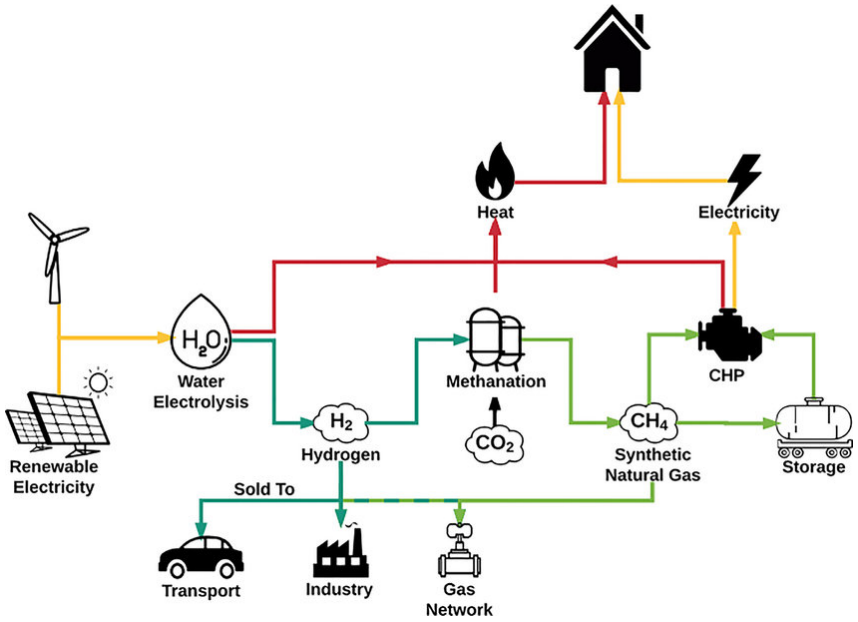

Figure 1.12: Schematic representation of the Power-to-Gas system [22].

it necessitates a storage space. Furthermore, the natural gas grid imposes a blending limit of single-digit percentage, of 6% in France [23] and 2% in Germany [24], which limits the amount of H_2 to be injected. On the contrary, methane (CH_4) is simpler to compress, store, and transport and is well-established thanks to existing natural gas infrastructure. Hence, Power-to-SNG is the most considerable method for rapid response to the energy storage problem while simultaneously reducing fossil fuel dependency by replacing natural gas derived from fossil fuels with a more sustainable energy source. In the following sections, the principal processes of this system will be introduced. First, the water electrolysis process for hydrogen gas production will be discussed, including the different electrolysis unit technologies. Second, we will dig into the methanation process responsible for the methane synthesis from the hydrogen gas produced by electrolysis and an external CO_2 source from carbon capture units. This section will also present the different methanation reactors and processes. Finally, a review of the Power-to-Gas projects that are either installed or ongoing will be stated.

3.1 Water Electrolysis Process

Water Electrolysis is the breaking up of a water molecule into hydrogen and oxygen molecules using an electric source. During the process, two partial redox reactions occur at the electrolyzer's electrodes, the cathode (-) and the anode (+). At the cathode side, the reduction reaction takes place where electrons are collected, whereas the oxidation reaction happens at the anode side, leading to a loss of electrons. When a voltage is applied, the cathode produces hydrogen gas, and the anode produces oxygen. The charge equalization between the two partial reactions occurs in the form of ion conduction through an electrolyte, which is an electrically conductive substance. Electrolyzers usually comprise multiple interconnected electrolysis cells, thus forming a stack. Currently, there are different types of electrolyzers. The electrolysis can be conducted at low or high temperatures. This subchapter will review and compare electrolyzer technologies regarding technical and economic specifications.

3.1.1 Low-Temperature Water Electrolysis

Low-temperature electrolysis occurs in two primary electrolyzers: Alkaline electrolyzers (AEL) and Proton Exchange Membrane electrolyzers (PEM).

3.1.1.1 Alkaline Electrolyzer (AEL)

The alkaline electrolyzer is the most mature technology since the early 20th century. By 1902, 400 industrial electrolyzers had been installed, primarily used to produce hydrogen gas for synthesizing ammonia fertilizers using low-cost hydropower [25], where the most significant water electrolysis plant with a H_2 capacity of 10,000 Nm^3/h was first put into operation in 1939. After that, in 1948, the first commercial pressurized electrolyzer was developed by Zdansky/Lonza [26]. However, between the 1970s and the 1980s, the installed large-scale plants of AEL electrolyzers were decommissioned with the discovery of cheap fossil fuels, which were highly applied for hydrogen gas production by steam reforming [26]. Nevertheless, over the last ten years, the interest in H_2 production by AEL electrolyzers has returned, intending to provide clean energy to counteract climate change.

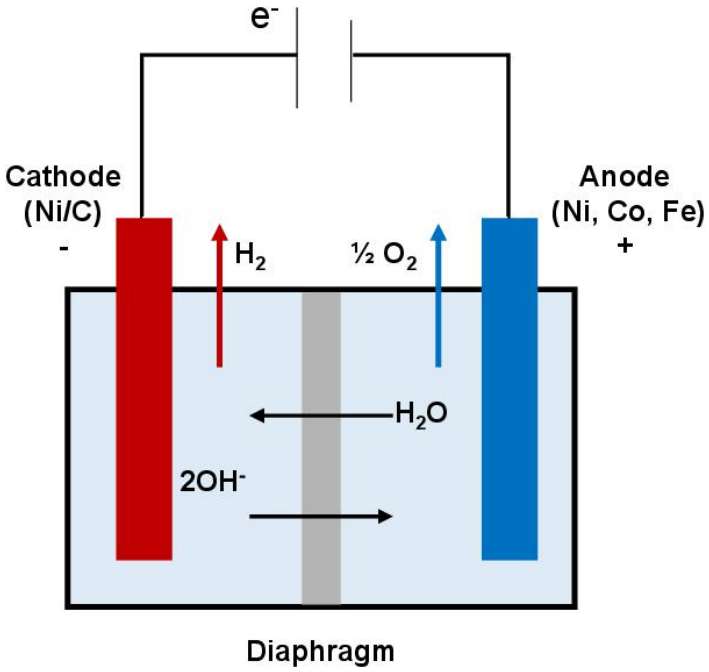

Figure 1.13: Schematic diagram of the Alkaline Electrolyzer.

Alkaline Electrolyzers operate at a temperature range of 60-90 °C and pressures up to 30 bar [27]. Each electrolysis cell inside the electrolyzer stack comprises two electrodes separated by a diaphragm that conducts hydroxide ion (OH^-) through a KOH solution, as illustrated in Figure 1.13. The role of the diaphragm is to ensure the separation of oxygen and hydrogen gases and prevent their mixing inside the cell. This technology has several advantages, including long-term stability, usage of non-noble metal catalysts, and a low relative cost. Despite these benefits, it also has some drawbacks represented by a limited current density below 400 mA/cm^2, gas crossover due to the ineffectiveness of the diaphragm, low operating pressure, and low energy efficiency [28, 29].

3.1.1.2 Proton Exchange Membrane (PEM) Electrolyzer

The PEM electrolyzer is another low-temperature electrolyzer developed in 1966 as an alternative to overcome the issues of alkaline water electrolysis [30]. The electrolyzer operates at temperatures between 30 and 80 °C [31], and pressures ranging from 30 to 40 bar, where some systems have been demonstrated to operate at several hundred bars [32].

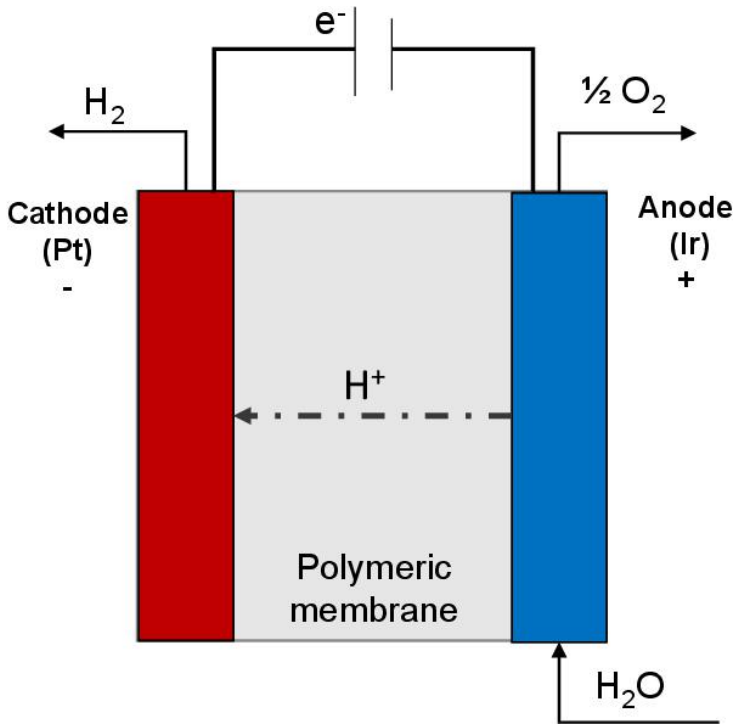

Figure 1.14: Schematic diagram of the Proton Membrane Electrolyzer.

The PEM electrolysis cell consists of two electrodes separated by a polymer electrolyte membrane, as shown in Figure 1.14. The anode electrode is coated with a platinum metal catalyst, while the cathode electrode is covered with iridium oxide. The employment of an expensive platinum catalyst is due to its high stability and high acidic conditions that satisfy the requirements of the PEM system. This catalyst selection explains the high investment cost of the PEM technology. The key benefits of this technology are its compact design, high current density > 2 A/cm^2, high efficiency, high operating pressure, fast dynamic response, and ability to produce pure oxygen as a by-product [28]. On the other hand, the main disadvantages of the PEM electrolyzers are the high equipment cost, low durability, and acidic corrosive environment [28].

Both low-temperature electrolyzers are proven technologies in the MW range for commercial use. The leading manufacturers of these electrolyzers are summarized in Table 1.1. In practice, alkaline electrolysis is a more cost-efficient technology than PEM electrolysis, which suffers from significantly high CAPEX and OPEX. Today, an AEL electrolyzer costs 270 €/kW for a minimum of 1 MW stack and between 500 and 1,000 €/kW for a minimum of 10 MW stack [33]. However, the PEM electrolyzer is 40-50% more expensive than AEL, with a cost of 400 €/kW for a minimum of 1 MW stack and of 700-1,400 €/kW for a minimum of 10 MW stack [33].

Type of Electrolyzer	Manufacturer	Location	Generic name	H_2 Capacity (Nm^3/h)	Energy Consumption (kWh/Nm^3)	Reference
AEL	Nel.	Norway	A3380	2,400-3,880	3.8-4.4	[34]
	Cummins	Canada	HyStat-100-10	100	5-5.4	[35]
	John Cockerill	Belgium	DQ-500	500	4-4.3	[36]
	McPhy	France	MeLyzer800-30	100-800	4.5	[37]
	Sunfire	Germany	HyLink	2,230	4.7	[38]
	GreenHydrogen	Denmark	HyProvide A-90	90	4.3	[39]
PEM	Nel.	Norway	M5000	5,000	4.5	[40]
	Cummins	Canada	HyLyzer-4-30	4,000	4.3	[41]
	Siemens	Germany	Silyzer 300	100-2,000	N/A	[42]
	Proton onsite	USA	M400	417	N/A	[43]
	ITM Power	UK	HGASXMX	110-1,900	N/A	[44]
	Plug Power	USA	GenFuel 5 MW	1,000-2,000	5.2	[45]
	Elogen	France	ELYTE 260	260	4.9	[46]

Table 1.1: Summary of the global leading manufacturers of the low-temperature electrolyzer and their specifications.

3.1.2 High-Temperature Steam Electrolysis

High-temperature steam electrolysis is another promising technology for Power-to-Gas systems. They have the advantage of low electrical voltage compared to low-temperature processes. Furthermore, from a kinetic point of view, the high temperature reduces cell overpotential by promoting electrode activity, which lowers the energy losses [47]. This feature could be converted into a significant advantage if the need for thermal energy for steam generation is freely available from waste heat and if the technologies show higher lifespans than today's systems. A performance comparison between low and high temperature electrolyzers is depicted in Figure 1.15, revealing a high efficiency of a high-temperature electrolyzer, the solid oxide electrolysis cell (SOEC), compared to low-temperature ones (AEL and PEM).

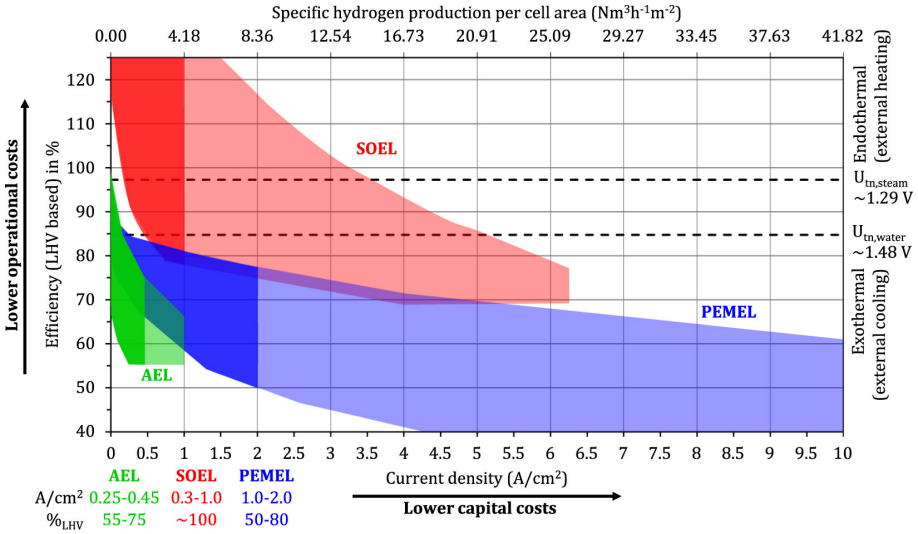

Figure 1.15: Representation of the performance of low-temperature (AEL and PEM) and high-temperature (SOEC) electrolyzers, reprinted from [48].

High-temperature electrolysis (HTE) technology was under development several years ago, but the effort has concentrated on SOEC. However, a novel technology called molten carbonate electrolysis cell (MCEC) is being studied, representing the reverse operation of the commercial molten carbonate fuel cell (MCFC). Exploring MCEC is significant due to MCFC's proven effectiveness in clean energy generation and carbon capture [49]. MCFC is also well-advanced. Thus, studying MCEC's reverse operation for hydrogen production is of great interest. This study will focus on MCEC as an electrolyzer in the Power-to-SNG system, evaluating its technical and economic feasibility.

3.1.2.1 Solid Oxide Electrolyzer (SOEC)

The first project on SOEC was developed in Germany in 1980. Within eight years later, the development of this technology reached an advanced status where a single cell operated for a long-term test [50]. A solid oxide electrolysis cell is formed of two electrodes separated by an oxide ion (O^{2-}) conducting electrolyte, as presented in Figure 1.16. The materials used for SOEC are Yttria-stabilized zirconia (YSZ) for the electrolyte, Ni-YSZ for the anode electrode catalyst, and LSM (lanthanum strontium manganite)-YSZ for the cathode electrode catalyst. Since the electrolytes have a limited ionic conductivity at lower temperatures, the cell is operated at a very high temperature of 800-1,000 °C [51].

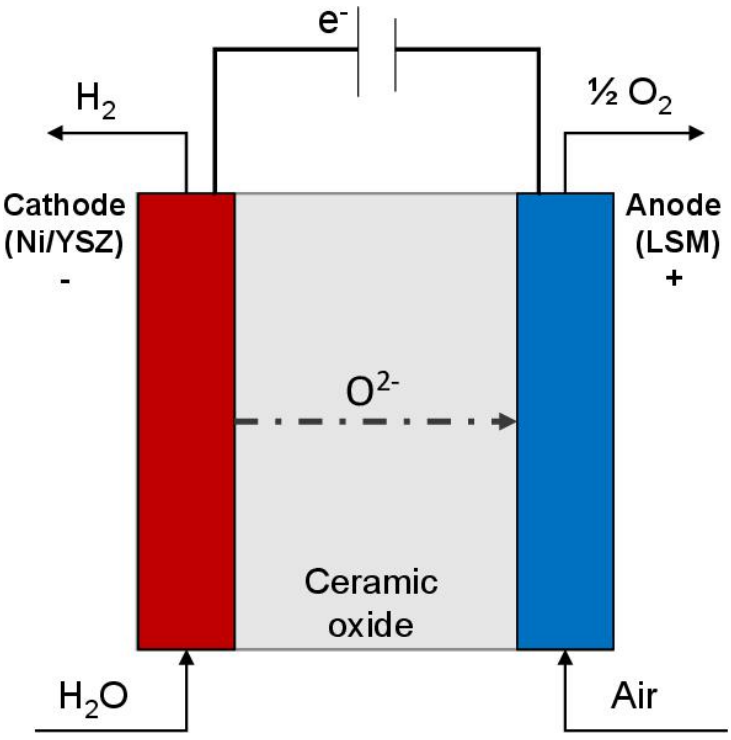

Figure 1.16: Schematic diagram of the Solid Oxide Electrolyzer.

With the development of renewable energy capacity in the 21st century, this technology has regained attention as an efficient solution to balance renewable energy fluctuation and energy supply-demand. Several studies were carried out to study the feasibility of SOEC electrolyzers in the Power-to-Gas process. At the SOEC performance level, it was found that the potential losses of the cell can be reduced with the decrease in the current densities and the increase in the cell's temperature [52]. In 2009, a research program was established at the Idaho National Laboratory (INL) to tackle the issues associated with

the industrial scaling up of the solid oxide electrolyzer technology for efficient production of hydrogen gas from high-temperature steam [53]. Within this program, the performance of a large-scale SOEC electrolyzer was evaluated, revealing that the overall production efficiencies could reach 50% for HTE with an outlet temperature above 850 °C [54]. Later, Petipas et al. (2013) [55] studied a pressured high-temperature SOEC-based system, which exhibited a 91% efficiency influenced by the power load. In 2007 [56], the entire efficiency of the water electrolysis was expected to be improved by high-pressure or low-temperature operation. The latter was confirmed by research work performed years later by Wendel et al. (2016) [57], which revealed that higher efficiencies could be achieved either with pressurized systems operating at a high temperature or with non-pressurized systems running at low temperatures.

Over the past four decades, high-temperature steam electrolysis via the solid oxide electrolyzer technology has reached an advanced level concerning the electrolyte composition and electrode materials [58]. However, this technology mainly functions at high temperatures, which leads to various challenges in terms of (a) cell degradation, (b) longer start-up duration, (c) mechanical instability due to thermal stress, (d) loss of gas tightness (electrolyte/sealant failure) [59].

These electrolyzers have been commercialized since 2021. Some manufacturers have launched SOEC into the market, such as Sunfire in Germany [60], HALDOR TOPSOE in Denmark [61], and Fuelcell Energy in the USA [62]. The Sunfire SOEC stack (Hylink) can produce 750 Nm^3/h H_2 with an energy consumption of 3.6 kWh/Nm^3. The TOPSPE stack design of 100 MW has a H_2 production capacity of 32,000 Nm^3/h and an energy consumption of 3.1 kWh/Nm^3. In addition, the SOEC stack of Fuelcell Energy generates 600 kg/day H_2 while consuming 39.4 kWh/kg electricity with heat input and 43.8 kWh/kg without heat input.

3.1.2.2 Molten Carbonate Electrolyzer (MCEC)

This electrolyzer emerged from the molten carbonate fuel cell technology as a novel system for Power-to-Gas application. This technology gained extreme interest due to the high development stage of MCFC technology, which has already been commercialized and implemented in South Korea, the USA, and Europe [63]. The molten carbonate electrolyzer is constructed of two electrodes and an ion-conductive electrolyte that conducts the carbonate ions (CO_3^{2-}), as illustrated in Figure 2.5. The cathode electrode is coated by Nickel-based alloy with chromium and aluminum composition between 2-10% to reduce sintering and mechanical issues [64]. The anode electrode is composed of NiO catalyst with lithium [58]. The electrolyte consists of a eutectic mixture of lithium and potassium carbonates $(Li/K)_2CO_3$ or lithium and sodium carbonate $(Li/Na)_2CO_3$ or a ternary mixture of $(Li/K/Na)_2CO_3$. Since the carbonate salt mixture is liquid at the operating temperature, a porous $\gamma-LiAlO_2$ matrix retains the electrolyte. This highly conductive electrolyte induces the passage of carbonate ions from the cathode to the anode without intermixing the fuel and oxidant gases [58]. MCEC electrolyzer operates at a high temperature of 600-700 °C since unitary and secondary eutectic molten salts require high temperature above 600 °C to be melted [65].

Since MCEC is a new concept under research, few studies have been executed to determine the best conditions for the cell to perform better and propose a scale-up strategy. The first study on the molten carbonate electrolyzer was reported by Hu et al. (2014) [58] that aimed to study the feasibility and the durability of using the MCFC for electrolysis. The results revealed that the cell performs better in the

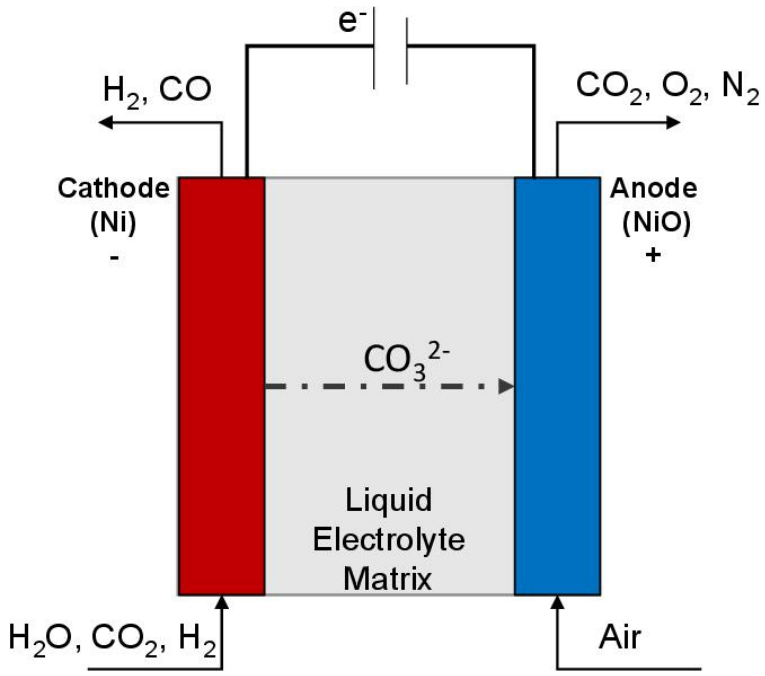

Figure 1.17: Schematic diagram of the Molten Carbonate Electrolyzer.

electrolysis mode than the fuel cell mode due to the lower polarization losses at the NiO electrode, even though the Ni electrode exhibits high polarization losses in the electrolysis mode. Later, the authors investigated the kinetics of cathodic porous Ni electrode for hydrogen gas production [66] and anodic NiO electrode for CO_2 and O_2 production [67] in a molten carbonate electrolyzer. Their study demonstrated that high CO_2 content enhances the Ni electrode for hydrogen gas production, and its polarization losses diminish as the concentration of H_2O and H_2 in the inlet fuel gases increases [66]. Conversely, NiO electrode performance is improved with increasing O_2 content; however, the inlet CO_2 impact highly relies on the cell's operating temperature [67].

Nevertheless, the principal role of an electrolyzer is to produce hydrogen gas, so it is essential to supply the cell with a low amount of or even no hydrogen gas. Therefore, Hu et al. (2016a) [68] examined the performance operation of the Ni electrode with four different hydrogen lean gases. Their results revealed that the Ni electrode exhibits high polarization loss at low hydrogen gas content, except for equal H_2O and CO_2 inlet compositions with a low H_2 content. Furthermore, regarding the MCEC durability, Hu et al. (2016b) [69] evaluated its performance and durability during a long-term test using coin-type cells of small geometrical area (3 cm^2) and showed that it is viable to operate a molten carbonate electrolyzer based on the conventional MCFC components, at least at lab-scale.

Hu et al. work raises more interest in studying the MCEC electrolyzer in Power-to-Gas systems. Thus, Reyes-Belmonte et al. (2017) [70] developed an electrochemical and thermodynamic model for molten carbonate electrolyzer to investigate the effect of the working operating conditions (current density, steam temperature, conversion ratio, and others) on its performance. Furthermore, they were the first to propose and simulate a scale-up design for MCEC using Aspen Hysys software. The results revealed that higher conversion rates and lower energy density currents with an intermediate cell temperature range (400-500 °C) and high feeding temperature would be desired to reduce the electrolyzer's electrical power

consumption. Subsequently, Lucas Mastropasqua et al. (2018) [71] proposed and simulated a new plant concept based on the molten carbonate electrolyzer using Aspen Plus software. The advantage of their system is its capability for long-term electrochemical storage and substitute natural gas production.

Afterward, Barelli et al. (2021) [5] assessed a system for hydrogen gas production based on molten carbonate electrolysis. The electrolyzer produces syngas in their system, which is then sent to a sorption-enhanced shift reactor system to convert CO into CO_2 and separate it from H_2. Their system proved a H_2 production of 0.074 Nl/(h·cm^2) at a power density of 0.213 W/cm^2 for an energy consumption of 3.4 kWh/Nm^3 H_2. Besides, Ferrario et al. (2021) [72] conducted an experimental-simulative technique to investigate the integration of a system based on a MCEC unit under varied operating circumstances in a steam-reforming process of an Italian oil refinery. The results revealed a specific energy consumption for H_2 production of 3.24 kWh/Nm^3H_2 for a 1 MW system. With the increased studies on the scale-up system of molten carbonate electrolyzer, it was necessary to verify the cell's durability at a larger geometrical area than 3 cm^2. For this reason, Frangini et al. (2021) [73] investigated the alternated fuel cell/electrolysis cell operation of a single cell of 81 cm^2 active area assembled with MCFC materials at 650 °C for about 400 h. Their experimental testing reported rapid cell degradation when the cell works in reverse mode after an initial operation as a fuel cell for 650 h. Furthermore, it was discovered that the electrolyte evaporation caused this degradation since an enhanced performance was obtained after the electrolyte refilling process. Later on, Audasso et al. (2022) [74] examined the 100 cm^2 cell's performance under different operating conditions at only electrolysis mode and revealed that MCEC can operate at different conditions and proved a long term of operation for about 1,000 h when the electrolyte is periodically supplied to replenish the consumed amount. In addition to that, Koomson and Lee (2022) [75] have recently studied and compared the gas phase transport effects of a 100 cm^2 molten carbonate cell in both fuel cell (FC) and electrolysis cell (EC) modes. Their results showed that EC mode exhibits lower total voltage loss than FC mode due to the lower gas phase mass transport resistance obtained in EC mode. These findings are analogous to those reported in research conducted by Hu et al. [58] at a 3 cm^2 scale of the molten carbonate electrolyzer.

Although MCFC is now available at a large scale of multimegawatts, its reverse operation as electrolyzer is restricted to lab-scale research, with the biggest studied electrolyzer having a surface area of 100 cm^2. This technology has proven excellent performance in the electrolysis process. Nevertheless, further research is required to enhance the cell's stability and alleviate the degradation issues related to electrolyte evaporation so that the current MCFC module scale can operate in the electrolysis mode.

3.1.3 Comparison of the Different Electrolyzer Technologies

Low-temperature electrolyzer technologies (AEL and PEM) are the most established and commercially available. Furthermore, a high-temperature electrolyzer, notably represented by SOEC, is approaching commercialization. Table 1.2 summarizes the technical and economical specifications of the three known electrolyzers. Nonetheless, MCEC, as a new technology under investigation, lacks technical and economic specifications. Thus, a review of the experimental and simulation works conducted on MCEC was performed to collect a possible range of specifications, which are summarized in Table 1.3.

	Low-temperature		High-temperature
	AEL	**PEM**	**SOEC**
Nominal current density	0.2-0.8 A/cm^2	1-2 A/cm^2	0.3-1 A/cm^2
Voltage range (limits)	1.4-3 V	1.4-2.5 V	1-1.5 V
Operating temperature	70-90 °C	50-80 °C	700 - 850 °C
Cell pressure	< 30 bar	< 30 bar	1 bar
Load range	15%-100%	5%-120%	30%-125%
H_2 purity	99.9%-99.9998%	99.9%-99.9999%	99.90%
Voltage efficiency (LHV)	50%-68%	50%-68%	75%-85%
Electrical effficiency (Stack)	47-66 kWh/kg H_2	47-66 kWh/kg H_2	30-50 kWh/kg H_2
Electrical effficiency (System)	50-78 kWh/kg H_2	50-83 kWh/kg H_2	40-50 kWh/kg H_2
Lifetime (Stack)	60,000 h	50,000-80,0000 h	< 20,000 h
Stack unit size	1 MW	1 MW	5 kW
Electrode area	10,000-30,000 cm^2	1,500 cm^2	200 cm^2
Cold start (to nominal load)	< 50 minutes	< 20 minutes	> 600 minutes
Capital cost (Stack) minimum 1 MW	270 $/kW	400 $/kW	> 2,000 $/kW
Capital cost (System) minimum 10 MW	500-1,000 $/kW	700-1,400 $/kW	N/A

Table 1.2: State-of-the-art on the specifications of the different electrolyzers, [33].

MCEC	Reyes et al. (2017) [70]	Mastropasqua et al. (2018) [71]	Barelli et al. (2020) [5]	Ferrario et al. (2021)[72]	Frangini et al. (2021) [73]	Audasso et al. (2022) [74]
Current density (A/cm^2)	0.0073-0.014	0.353	0.15	0.15	0.15	0.15
Voltage (V)	1.34-1.6	1.31	1.422	-	-	1.14-1.15
Power density (W/cm^2)	-	-	0.213	0.204	-	-
Power consumption (kW)	593-726	1,250.02	-	1,000	-	-
Temperature (°C)	539-550	650	650	650	650	625-675
H_2 production rate	400 kg/day	-	0.074 Nl/(h·cm^2)	0.086 Nl/(h·cm^2)	-	-
Energy consumption (kWh/kg)	-	-	37.7	36	-	-
Electrode area (cm^2)	0.2	-	-	1,000	81	100
Cell operation duration	-	-	-	-	1,000 h	1,000 h

Table 1.3: State-of-the-art on the specifications of the MCEC electrolyzer.

The electrolyzers are in charge of transforming renewable energy into fuel gas, either hydrogen gas or syngas. For completing the Power-to-SNG system, hydrogen gas is fed into a reactor with a CO_2 feed, where CO_2 hydrogenation reaction occurs to produce methane. Thus, the methane synthesis process will be explored in the following section, including the different reactor types used and the state-of-the-art methanation processes.

3.2 Methanation Process

In 1902, Sabatier and Senderens came up with a process called Methanation. This process is catalytic based on the thermochemical hydrogenation of a carbon source, carbon monoxide CO or carbon dioxide CO_2 into methane CH_4 [76]. There are two possible catalytic methanation processes: CO methanation (Eq. 1.1) and CO_2 methanation (Eq. 1.2). These two reactions are connected to the reverse water-gas shift (RWGS) reaction (Eq. 1.3), which represents an intermediate reaction.

$$CO + 3\,H_2 \longleftrightarrow CH_4 + H_2O \qquad \Delta_R H^0 = -205.9\,\mathrm{kJ \cdot mol^{-1}} \tag{1.1}$$

$$CO_2 + 4\,H_2 \longleftrightarrow CH_4 + 2\,H_2O \qquad \Delta_R H^0 = -164.8\,\mathrm{kJ \cdot mol^{-1}} \tag{1.2}$$

$$CO_2 + H_2 \longleftrightarrow CO + H_2O \qquad \Delta_R H^0 = 41\,\mathrm{kJ \cdot mol^{-1}} \tag{1.3}$$

For the CO_2 molecule to be reactive, the energy of the carbon-oxygen bond must decrease. This objective is achieved by using a catalyst. These catalysts are generally constituted of a metallic active phase, the place of the reaction, which is dispersed on porous or non-porous support of oxide nature like alumina (Al_2O_3), silica (SiO_2), or ceria (CeO_2). Transition metals of group VIII, such as Ru, Rh, Pd, Pt, Co, Fe, Mn, W, or Ni, are used as the active phase of the catalyst [77]. Nickel (Ni) is the most widely used among these metal catalysts due to its lower cost.

Moreover, the Boudourard reaction (Eq. 1.4) and the reaction in Eq. 1.5 can also occur in the methanation reactor, resulting in carbon deposition, which has been shown to deactivate the catalyst [78].

$$2\,CO \longleftrightarrow C_{(s)} + CO_2 \qquad \Delta_R H^0 = -172\,\mathrm{kJ \cdot mol^{-1}} \tag{1.4}$$

$$CO_2 + 2\,H_2 \longleftrightarrow C_{(s)} + 2\,H_2O \qquad \Delta_R H^0 = -90\,\mathrm{kJ \cdot mol^{-1}} \tag{1.5}$$

Therefore, Gao et al. (2012) [78] use the Gibbs free energy minimization approach to conduct a complete thermodynamic investigation of processes occurring in the methanation of carbon oxides (CO and CO_2) and investigated the impact of temperature, pressure, the ratio of y_{H_2}/y_{CO} (and y_{H_2}/y_{CO_2}), and the addition of other compounds (H_2O, O_2, CH_4, and C_2H_4) in the feed gas (syngas) on the conversion of CO and CO_2, CH_4 selectivity and yield, as well as carbon deposition. Based on their study, it was found that the selection of appropriate thermodynamic conditions and input gas composition can avoid this phenomenon [78]. These conditions that favor the methanation reactions are a low temperature, high pressure, and a large ratio of y_{H_2}/y_{CO}, precisely > 3, and of y_{H_2}/y_{CO_2} > 4. Besides, the addition of steam into the feed gas could alleviate the carbon deposition to a large extent. Schmider et al. 2021 [79] also studied the detailed thermodynamic reaction mechanism of CO and CO_2 methanation over Ni-catalyst. Their study provided the equilibrium position of a stoichiometric feed for CO (y_{H_2}/y_{CO}= 3) and CO_2 (y_{H_2}/y_{CO_2}= 4) as a function of temperature and pressure, as illustrated in Figure 1.18. Another mole-fraction ratio is considered when both CO and CO_2 methanation reactions are occurring, which is $(y_{H_2}\text{-}y_{CO_2})/(y_{CO_2}+y_{CO})$ of around 3 [80]. This ratio will be considered in this thesis work rather than y_{H_2}/y_{CO} ratio due to the presence of both CO and CO_2 in the inlet feed for methane synthesis.

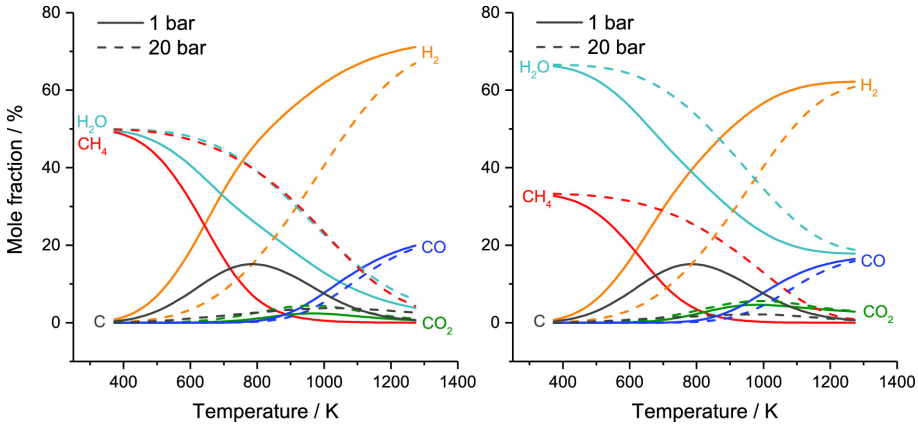

Figure 1.18: Equilibrium position as a function of temperature and pressure for CO (left) and CO_2 (right) at their stoichiometric feed, [79].

The CO and CO_2 methanation reactions are strongly exothermic. Consequently, the enormous heat released must be removed to avoid thermal degradation of the catalyst and the reactor wall damage. For this reason, two approaches can be carried out in the methanation process. The methanation reactors can be operated either in adiabatic or isothermal mode. For adiabatic reactors, no heat is drawn out from the reactor, and the heat generated is evacuated by the outlet feed gases. In this mode, the temperature dramatically increases along the reaction, which alters the reaction rate. Therefore, the adiabatic process comprises a series of reactors with an inter-stage cooling step. However, in the isothermal mode, the reactor operates at a constant temperature; thus, it is equipped with a cooling fluid to remove the excess heat generated by the reaction and keep it isothermal. There are currently several catalytic reactor technologies, adiabatic and isothermal. Thus, Section 3.2.1 will be dedicated to presenting these technologies. Afterward, the state-of-the-art methanation processes will be discussed in Sections 3.2.2 and 3.2.3.

3.2.1 Different Catalytic Reactor Technologies

The methanation process is conducted using different types of catalytic reactor technologies. They can be classified into four categories: fixed-bed, fluidized-bed, slurry-bed, and structured reactors.

3.2.1.1 Fixed-bed reactors

This reactor type is the main reactor for large-scale chemical synthesis and is widely used in research and industrial-commercial applications. The fixed-bed reactor is divided into two types: adiabatic and multi-tubular reactor [81], illustrated in Figure 1.19. The adiabatic reactor is a two-phase reactor, compromising the solid catalyst and the fluid. The catalyst is arranged in a packed bed through which the reactant gases flow uniformly. The adiabatic reactor is commonly used when only one main reaction pathway exists. On the other hand, multi-tubular fixed-bed reactors are selected for multiple reactions to enhance product selectivity and separation. It is mainly composed of a cylindrical tube packed with either catalyst pellets or powder. A reactant fluid enters the tube, following the path of a heat carrier, which allows for controlling the different temperature profiles around the fixed tubular catalysts [81]. The heat carrier is usually pressurized water circulated in the cooling tubes. The water evaporates, which

allows the evacuation of the reaction heat. The reactor temperature is efficiently controlled by adjusting the steam pressure in a feed water boiler.

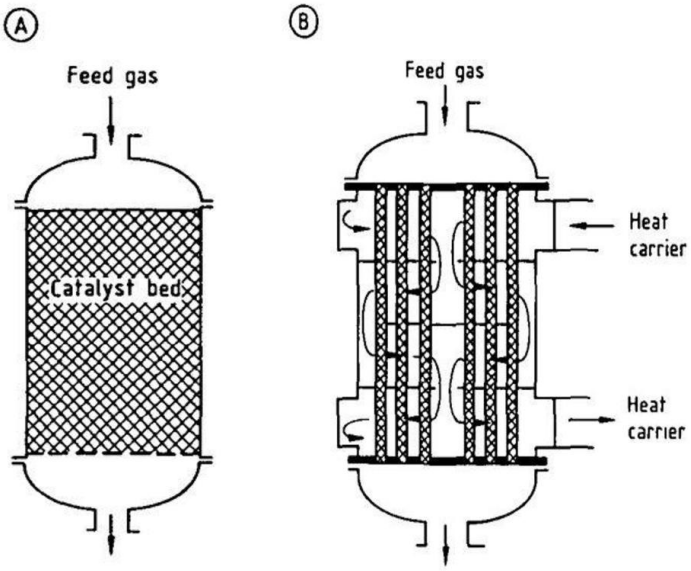

Figure 1.19: Schema of the adiabatic fixed-bed reactor **(A)** and the multi-tubular fixed-bed reactor **(B)**, reprinted from [81].

The advantages of fixed-bed reactors are based on the high reaction rate and low mechanical stress on catalysts. Furthermore, they are characterized by simple catalyst handling and a simple dimensioning and scale-up [82]. Therefore, they can be used for a wide range of operations. Nevertheless, this reactor has numerous limitations, including a high thermal load on the catalyst and the difficulty of heat removal and temperature gradient management [82]. Multiple reactors in series are required to accomplish the desired conversion. Besides, several compressors for recycling flow and heat exchangers for inter-stage cooling are required to regulate the temperature within the reactor. These requirements necessitate a significant investment in capital and operational costs.

3.2.1.2 Fluidized-bed reactors

They are multiphase catalytic reactors used for many industrial applications. In the fluidized-bed reactor, a high-velocity fluid (gas or liquid) flows through the granular solid catalyst to suspend the solid and force it to act as a fluid, as depicted in Figure 1.20. Therefore, it has unique advantages regarding heat and mass rates and particle mixing. The catalyst particles' uniform mixing and high heat capacity allow almost isothermal operation and avoid hot temperature spots.

In the process design, a single reactor is often adequate to achieve the needed conversion for injection into the natural gas system. Nevertheless, some drawbacks are associated with this reactor type, such as high mechanical stress of the particles and reactor walls due to the catalyst fluidization, thus resulting in catalyst loss and a shorter reactor lifespan [84].

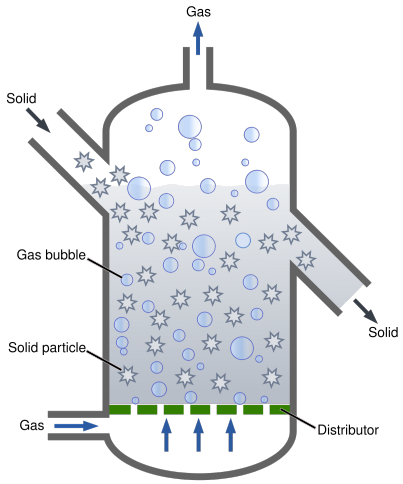

Figure 1.20: Representative diagram of the fluidized-bed reactor, reprinted from [83].

3.2.1.3 Slurry-bed reactors

This technology is known as a three-phrase reactor due to the presence of three phases (liquid, solid, and gas) in the reactor. Figure 1.21 presents the design diagram of a three-phase reactor. It is similar to the fluidized-bed reactor, where the gas flows through a reactor containing solid catalyst particles suspended in a fluid. The main difference between the two types is that the catalyst is suspended in a liquid in the slurry-bed reactor, whereas in the fluidized-bed reactor, the suspending fluid is the reacting gas itself [85].

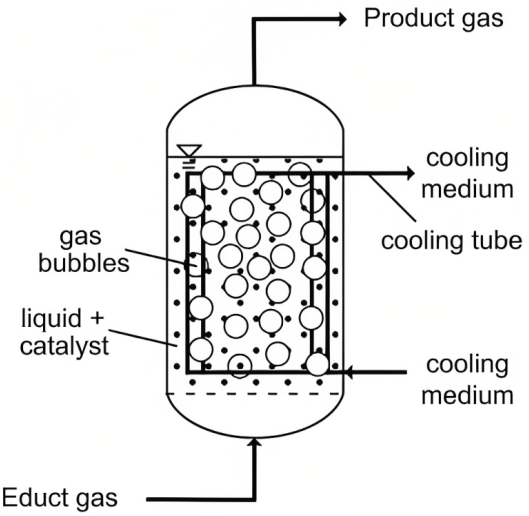

Figure 1.21: Schematic design of the slurry-bed reactor, reprinted from [86].

In the slurry-bed reactor, the liquid fluid is designated to have a high heat capacity to control the reactor temperature effectively [84]. Therefore, the reactor can operate under isothermal conditions and at high load variations [82]. Apart from its advantage in effective heat removal, this reactor is less sensitive to fluctuating feed streams, and the catalyst is less subjected to abrasion than the fluidized bed. However, the slurry-bed reactor encounters some limitations concerning the liquid-side mass transfer, the possible back mixing, and the evaporation and decomposition of heat transfer liquid [82].

3.2.1.4 Structured reactors

The structured reactor is a relatively brand-new reactor technology for methanation. This design reactor concept intends to address the main drawbacks of adiabatic fixed-bed reactors related to the temperature hot spots and pressure drops [87].

Honeycomb technology is a type of structured reactor and has long been under investigation. The reactor consists of a tube filled with a metallic honeycomb-like body as a carrier system for the methanation catalyst. The honeycomb-like body combines corrugated and plain metal sheets, which are jointly coiled up, as illustrated in Figure 1.22. The honeycomb design ensures a high radial heat transfer when the support material is well-chosen, a lower abrasion of the catalyst, and a lower pressure drop. However, the cooling design is still to be improved. For this aim, Biegger et al. (2018) [88] developed a ceramic-supported honeycomb reactor that can handle a flexible operation for Power-to-Gas applications. The ceramic material is selected as a heat storage medium since it has a low thermal expansion and conduction and high thermal shock resistance. Thus, the heat of the reaction is stored in the ceramic carrier. This reactor concept is designed with three beds and up to four compartments per stage. The compartments' operation is adjustable with the load supply, which means that all compartments are equally utilized at 100% load, and fewer chambers are used with the load drops. Hence, these compartments have the advantage of allowing flexible operation of the reactions. Besides, the stored heat in each compartment in the ceramic carrier facilitates the start-up process.

Figure 1.22: Honeycomb cylindrical reactor in the Falkenhagen plant under Store&Go project, reprinted from [89]. Image: ©Institute of Technology (KIT)

Another type of structured reactor is micro-channel technology. It is built around the concept of a plate heat exchanger. The reactor comprises micro-channels in the longitudinal and axial directions. The channels in the longitudinal direction of the reactor are coated with a catalyst and represent the reactive zone where the reaction occurs. The axial channels are water-filled coolant channels interconnecting the reactive channels to evacuate the reaction heat and cool the reactor. This design enables efficient heat removal, resulting in a homogeneous temperature profile, an isothermal operation, and an easy temperature control [90]. Furthermore, this technology is a very compact reactor design and proves a high catalyst activity, high conversion rates, and low residence times [91].

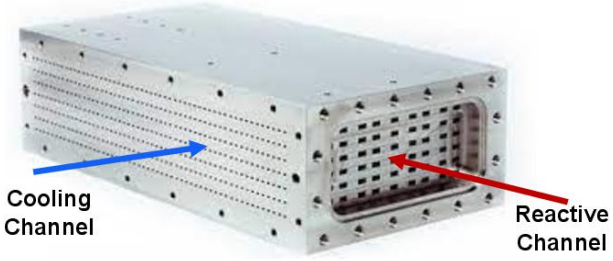

Figure 1.23: Micro-channel reactor developed by ATMOSTAT, reprinted from [92].

This reactor technology was first demonstrated by ETOGAS, which has extensive expertise in Power-to-Gas technology. The industrial manufacturing of micro-channel reactors is also performed by a French company, ATMOSTAT, which participated in several well-known European research projects, such as STORE&GO and JUPITER1000. The reactor design illustrated in Figure 1.23 corresponds to the one developed by ATMOSTAT. Since micro-channel reactors are newly developed technology, they have high manufacturing costs and the cost reduction through increasing mass production seems limited. Another drawback of this technology is that the catalyst is irreplaceable once deactivated, meaning that the entire reactor must be replaced [90].

To sum up, the fixed-bed reactor is the most mature technology. It is classified into two types: an adiabatic fixed-bed reactor used for the adiabatic process and a multi-tubular fixed-bed reactor employed for the isothermal process. However, this technology suffers from high thermal load and weak temperature gradient management. This problem is overcome in the fluidized bed reactor, ensuring an isothermal operation while avoiding hot temperature spots. Nevertheless, it is subjected to high mechanical stress due to the catalyst fluidization, leading to a catalyst loss and a shorter reactor lifespan. Another technology called slurry-bed or three-phase reactor, emerged to surmount the issues of the fluidized-bed reactor. This reactor can operate under isothermal and high load variation conditions. Nonetheless, it encounters some problems regarding the liquid-side mass transfer, the back mixing, and the evaporation and decomposition of heat-transfer liquid. Finally, the recent technology is the structured reactors developed to overcome other technologies' problems. This reactor type is considered a promising technology for a Power-to-Gas system since it can handle flexible loads and manage temperature gradients.

3.2.2 Adiabatic Methanation Process

The adiabatic methanation process is based on a series of fixed-bed reactors with intermediate cooling. It is a well-established and commercially available process. The large-scale methanation technologies were commissioned during the first oil crisis in 1973, raising the interest in coal-to-SNG processes [93]. The most commonly used commercial methanation processes are LURGI and TREMP processes.

3.2.2.1 Lurgi Process

The Lurgi process, developed in Germany to produce SNG from coal, was one of the first commercialized SNG production processes in the 1930s. The methanation unit comprises two adiabatic fixed bed reactors, separated by heat exchangers to cool the gases from the first reactor and recover the heat produced by the reaction, as depicted in Figure 1.24. For this process, a syngas feed is designed to provide

a near stoichiometric ratio of hydrogen gas to carbon oxides (CO_2, CO) according to the methanation reactions. Since the methanation is exothermal and the reactors used are adiabatic, the reaction heat results in a significant temperature increase in the reactor. Thus, a recycle flow is required to control the temperature gradient in the first methanation reactor, where almost 90% of the gas is recycled to limit the temperature to 450 °C [77]. However, the recycling step imposes an energy penalty due to the energy consumed by the flow compression. Besides, the carbon monoxide is almost entirely converted at the second reactor outlet, unlike the CO_2, which remains at a very high concentration [77]. Therefore, the gas produced by this process is incompatible with injection into a gas network. A purification step is, thus, necessary, which entails a higher installation cost.

Lurgi and SASOL designed and built the first pilot plant in Sasolburg (South Africa). Another pilot plant was then constructed by Lurgi and El Paso Natural Gas Corporation in Schwechat (Austria) [94]. These pilot plants were constructed using two adiabatic fixed bed reactors with a recycling stream from the first reactor's product. On the contrary, the world's first large-scale coal-to-SNG plant, installed at Great Plains Synfuels plant in 1984 in North Dakota, USA, was based on three adiabatic fixed bed reactors with a recycled gas from the second reactor product [95].

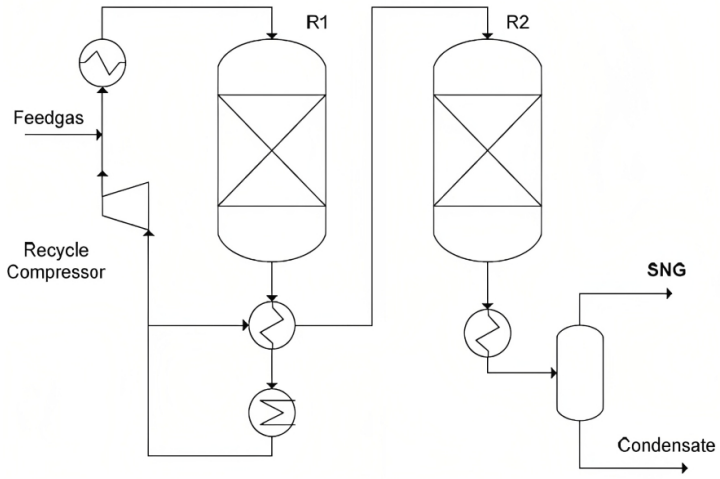

Figure 1.24: Lurgi methanation process with two adiabatic fixed bed reactors, reprinted from [94].

3.2.2.2 TREMP™ Process

The TREMP™ process was invented by the Danish Company "Haldor Topsoe" in the 1970-1980s as part of the "NFE Nuclear long-distance energy transportation" project in Denmark and Germany. This company is the principal actor in this domain, with the most methanation plants installed worldwide. The term "TREMP™" stands for Topsoe Recycle Energy-efficient Methanation Process [96]. The first project of TREMP technology (ADAM I) originated in the year 1978, which was conducted within the ADAM and EVA research project at the Kernforschungsanlage Jülich [97].

This technology is established on the unique Topsoe MCR methanation catalyst family, which has high and stable activity over a wide temperature range of 250 to 700 °C. The process is similar to Lurgi methanation but consists of a series of 3 to 4 adiabatic fixed-bed reactors with intermediate cooling stages instead of two reactors. The number of reactors and the process configuration depend on the product

application. The process scheme is presented in Figure 3.4. Similar to the Lurgi process, the temperature rise in the first reactor is limited by gas recycling. Because of the high energy cost of recycling, Topsoe's catalysts are developed to handle high temperatures. Therefore, Topsoe TREMP™ technology can reach a higher temperature at the outlet of the first reactor between 600 and 700 °C, compared to the Lurgi process. The high temperature of the outlet gas is then used to produce superheated high-pressure steam from the heat released while cooling the exit gas [96]. Furthermore, using a higher temperature also reduces the recycling rate downstream of the first reactor by about 70% for a temperature of 600 °C and minimizes energy consumption. The TREMP™ process is currently used in coal gasification and biomass plants, such as the Quinghua plant in China, which has been producing 1.4 billion Nm^3 of SNG per year from coal since 2013 [98]. Recently, this technology was installed in the GoBioGas facility in Gothenburg (Sweden) [84]. Haldor Topsøe is also involved in a Power-to-Gas project in Denmark, aiming to produce 10 Nm^3/h from CO_2 from a methanation process.

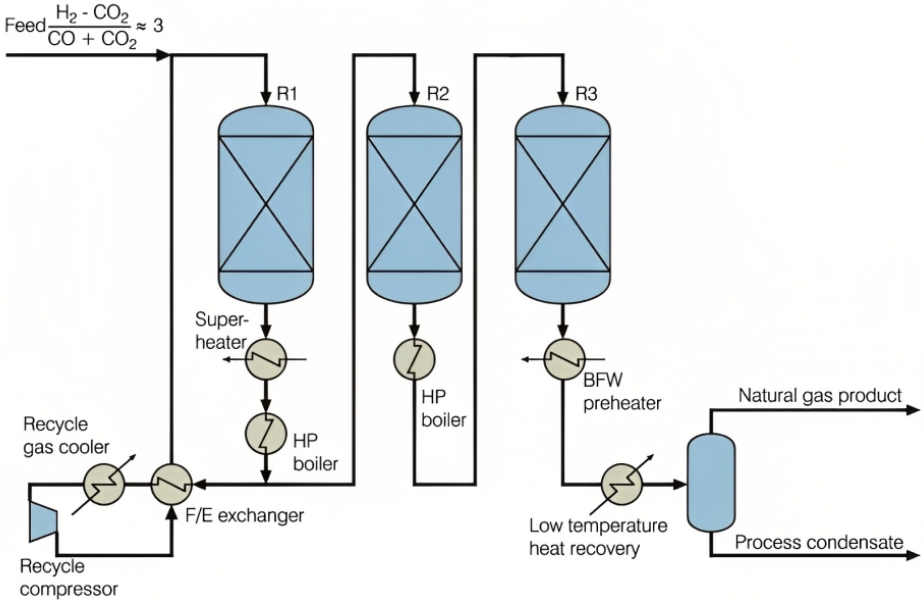

Figure 1.25: Topsoe TREMP™ methanation technology, reprinted from [96].

Nevertheless, although the adiabatic process is well-established, it is incompatible with P2G applications. Power-to-Gas systems are employed at small scales with intermittent operation related to renewable energy fluctuation, for which adiabatic reactors are ineffective due to thermal management issues [99]. Rönsch et al. [100] have already demonstrated that the most advanced reactors used in commercial CO methanation plants, which are adiabatic fixed-bed reactors with interstage cooling and gas recirculation, exhibit thermal runaway issues when operated under transient conditions. In this context, isothermal reactors, in which a cooling fluid directly cools the reactor, are typically favored. Therefore, Section 3.2.3 will be devoted to reviewing and introducing the isothermal methanation process.

3.2.3 Isothermal Methanation Process

This process is based on a reactor structure that uses an external heat carrier as a coolant fluid to extract the heat generated by the methanation reaction. The first isothermal reactor concept is the cooled fixed-bed

reactor. Several cooled reactor designs were developed in some demonstration projects throughout the 1970s and 1980s; however, in the end, they were either abandoned or shifted to other applications rather than methanation. The Linde isothermal reactor, invented by the Linde corporation in the 1970s, is one of the designs examined in the methanation process.

3.2.3.1 Linde Process

This process invented by Linde AG employs two fixed-bed reactors, the first being an adiabatic and the other an exchanger-reactor, allowing a quasi-isothermal operation, as shown in Figure 1.26. The isothermal reactor incorporates several cooling tubes directly embedded in the fixed bed. The Linde methanation process allows the reactants to be distributed across both types of reactors. It even transfers gases from the isothermal reactor to the adiabatic reactor to enhance syngas conversion [94]. Furthermore, the steam produced in the isothermal reactor's cooling circuit is superheated at the adiabatic reactor's outlet. The produced steam may subsequently be mixed with the reagents to improve temperature control and reduce the formation of carbon deposits [94].

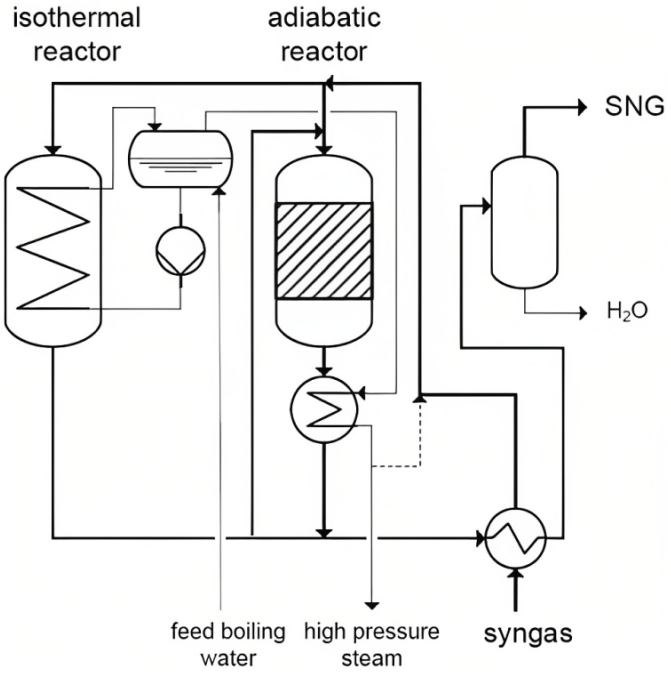

Figure 1.26: Process flow diagram of the Linde methanation process, reprinted from [101].

The isothermal reactor allows a good conversion of the reactants in a single stage. In contrast to the processes with adiabatic fixed beds, which require several reactors separated by heat exchangers, this reactor maintains the temperature sufficiently low, thus extracting the conversion limitation imposed by the thermodynamic equilibrium. It also enables the co-production of SNG and steam in a single unit. However, the difficulties of thermal management of the reaction necessitate a complex reactor design to minimize thermal stress in the catalytic bed and achieve quasi-isothermal operation. This technology was never commercialized for methanation processes; nonetheless, the Linde isothermal reactors are employed today to produce methanol.

3.3 Power-to-Gas Status and Projects

The Power-to-Gas system is currently being installed in pilot scales. AEL and PEM electrolyzers are the most dominant in the Power-to-Gas market due to their maturity and cost-effectiveness. Nevertheless, some projects consider using SOEC in their process, but this technology is currently limited to small-scale development and is only used for hydrogen gas production. In this context, various Power-to-X projects have been installed worldwide. Thema et al. (2019) [102], who examined the existing Power-to-Gas: hydrogen gas and methane projects globally, found that there have been 153 P2G projects completed and planned in 22 countries since 1988. As of 2019, only 56 hydrogen gas and 38 methanation projects were in operation. Over 45% of the existing projects feed or plan to feed gas into the grid or reconvert it into power or heat, even though most of these projects are under 1 MW pilot or demonstration projects.

Among these projects, Europe comprises about 134 projects, with only 54 projects based on synthetic methane production. Germany is the most advanced in the field with many large-scale projects, reported to be 64 projects installed so far. We can mention the world's first industrial-scale Power-to-Gas plant, installed in Wertle, Germany (Figure 1.27), which was constructed as part of Audi's "Audi e-Gas" research project [103]. An AEL electrolyzer converts the electrical regenerative power of 6 MW_{el} from a wind farm into hydrogen gas, which is then converted into synthetic methane after a reaction with CO_2 feed from a biogas plant installed near the site. This Audi e-gas is intended to power motor vehicles. This installation has operated since June 2013, producing 1,000 tonnes of gas annually. Furthermore, the Energiepark Mainz project is another largest demonstrator in the world, with a power of 6 MW_{el} supplied to a PEM electrolyzer to produce hydrogen gas [104]. There is also the WindGas Falkenhagen project, with a power of 2 MW_{el}, which has been active since 2013 [105].

Figure 1.27: The Audi e-gas Power-to-Gas plant in Wertle, Germany, reprinted from [106].

France, too, is following the overall trend and is currently in the deployment phase of pre-industrial projects. On this basis, about 15 P2G projects have been launched since 2012, where three pilot demonstrators are in operation, and ten are programmed. The first French demonstrator is the MYRTE project, which started operation in early 2012. It intends to construct an experimental platform consisting of a field of photovoltaic collectors (560 kW), an electrolyzer, a gas storage system (hydrogen and oxygen), and a fuel cell (100 kW) connected to the island's electricity grid to reduce peak demand. Following this, the GRHYD project was launched in 2014 and was officially inaugurated on 11 June 2018. ENGIE leads this demonstrator in partnership with GRDF, CEA, Areva H2Gen, and Ademe. It aims to produce hydrogen gas from the electricity grid and inject it into the local gas network.

Still, on the subject of demonstrators, we can mention another project developed by GRTgaz, the so-called Jupiter1000, located in Fos-sur-Mer (Figure 1.28). It is the first industrial demonstrator to use "Power to Gas" technology for synthetic methane production in France. The project was initiated in 2016 with a funding round consisting of RTE, CEA, McPhy, Khimod, and Leroux & Lotz. The installation is based on two electrolyzer types, AEL and PEM, of 500 kW each, giving a total of 1 MW_{el} power rating [107]. This installation produces 200 m^3/h of hydrogen gas, which is then converted into 25 m^3/h synthetic methane. The electrolyzer is supplied by wind energy produced by a wind park of 4 wind turbines with a total capacity of 10 MW, producing 280,000 MWh. The construction began in 2017, starting with the electrolyzers' installation for producing hydrogen gas, which was injected for the first time into the gas grid in 2020. Then, in early 2022, the CO_2 piping was delivered from a carbon capture plant from a nearby industry to be combined with hydrogen gas, leading to the first methane production in mid-2022 [108].

Figure 1.28: The Jupiter1000 Power-to-Gas plant in Fos-sur-Mer, France, reprinted from [109].

Recently, a new project, named MethyCentre, has been carried out by Storengy and its partners in the Centre-Val de Loire region near the Céré-la-Ronde underground gas storage site. It is dedicated to installing a 250 kW PEM electrolyzer and a methanation unit. The unit can potentially produce 50 kg per day of hydrogen gas. This gas will be reacted with CO_2 originating from biogas to synthesize methane gas. The MethyCentre project work began in June 2021 and was commissioned in 2023. It

comprises three installations: a 250 kW electrolyzer supplied by Elogen, a bio-methanation plant for biomethane production and CO_2 supply, and a methanation and gas separation unit supplied by Khimod and Prodeval. The final synthetic methane produced is injected into the network operated by GRDF. In addition to the abovementioned projects, France has about 9 P2G projects planned for the upcoming years [110]. This initiative to massively deploy Power-to-Gas technology arose in response to the gas shortage caused by the Ukraine war. Gas is France's second-most commonly used grid energy and is currently imported. However, the Russian decision to cut off the gas supply to European countries, mainly France, prompted the French government to develop an alternative to satisfy the demands. One alternative is the Power-to-Gas technology, which generates substitute natural gas from renewable sources. Ultimately, with the expansion of renewable gas sources, France might become gas self-sufficient by 2050.

4 Conclusion

This chapter explores the interest in the eco-friendly Power-to-Gas (P2G) system for addressing environmental and energy challenges. It can reduce carbon emissions by promoting renewable energy sources as clean alternatives to fossil fuels. The P2G system solves renewable energy's intermittency issues by storing excess electrical energy for later use. To achieve zero carbon emissions, carbon capture technologies must be employed in industrial sectors, and the captured CO_2 can be combined with hydrogen produced through water electrolysis in this system to produce valuable fuels.

The P2G system can be a single-stage Power-to-H_2 system or a two-stage Power-to-SNG system, with the latter being more favorable due to the challenges of hydrogen storage and injection into the gas grid. While there has been extensive research on low-temperature electrolysis in the Power-to-Gas system, limited research has been conducted on high-temperature electrolysis, mainly using molten carbonate electrolysis cells (MCEC). The existing literature has mainly concentrated on experimental-scale research for MCEC electrolysis. However, further investigation is needed to understand the technical and dynamic aspects of MCEC electrolysis on a large scale, particularly in the context of the Power-to-SNG system. The methanation process, corresponding to the second stage of the Power-to-SNG system, can be carried out adiabatically or isothermally. Isothermal reactors that utilize a cooling fluid are preferred in Power-to-Gas applications due to the intermittent operation and small scale of these systems.

Current research lacks comprehensive studies on the electrochemical reaction in MCEC under industrial operating conditions and its relationship with the methanation reaction. Furthermore, since the MCEC requires CO_2, it raises the question of the possibility of electrolyzing CO_2 with H_2O to produce syngas (H_2 and CO). This aspect is extensively examined and discussed in Chapter 2. Then, the overall Power-to-SNG system is evaluated technically and economically using the MCEC electrolyzer. Moreover, previous studies have not adequately addressed the dynamic behavior of MCEC when coupled with intermittent renewable energy sources. Therefore, it is important to investigate and understand the dynamic response of MCEC in such scenarios to ensure effective integration with these energy sources.

Résumé: État de l'art

Dans un premier temps, la situation générale qui sert de base à cette étude sera abordée, mettant en évidence les défis liés aux changements climatiques et au réchauffement mondial, et décrivant en détail les mesures prises pour y faire face, notamment la transition vers les énergies renouvelables. Ensuite, les obstacles de la transition énergétique et les solutions potentielles sont présentées. Enfin, parmi les solutions disponibles, le système Power-to-Gas est choisi pour être étudié, et le système est examiné en détail en montrant clairement le positionnement de la thèse.

Contexte génerale

Le terme « réchauffement climatique », a été introduit en 1975 par Wallace Broecker pour désigner l'augmentation continue de la température moyenne de la Terre. Le principal contributeur à ce réchauffement est le dioxyde de carbone (CO_2) émis par les combustibles fossiles et l'industrie [6]. Bien qu'il existe divers mécanismes naturels d'absorption du CO_2, une grande quantité continue de pénétrer dans l'atmosphère, influençant ainsi la température terrestre. Par conséquent, le Groupe d'experts intergouvernemental sur l'évolution du climat « Intergovernmental Panel on Climate Change (IPCC) » collabore avec d'autres organisations pour lutter contre le changement climatique. Les températures de surface mondiales ont considérablement augmenté au cours des dernières décennies, atteignant environ 0,7 °C de plus que notre référence de 1961-1990, comme le montre la Figure 1.29. Cette hausse est due aux émissions massives de CO_2 résultant de la forte dépendance aux combustibles fossiles dans les secteurs de l'énergie, de la mobilité et de l'industrie. En 2022, les émissions de CO_2 étaient d'environ 40 gigatonnes, comme le montre la Figure 1.30, dont 93% provenaient des combustibles fossiles.

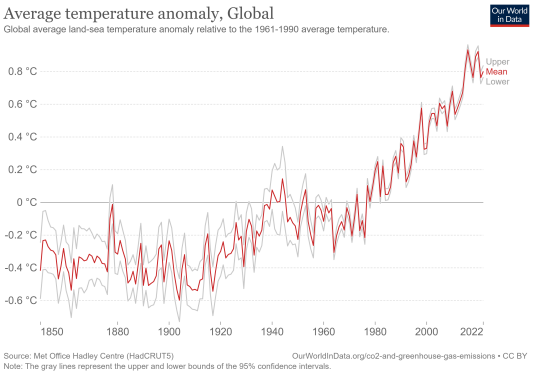

Figure 1.29: Augmentation de la température moyenne mondiale de 1850 à 2022, reproduite de [7].

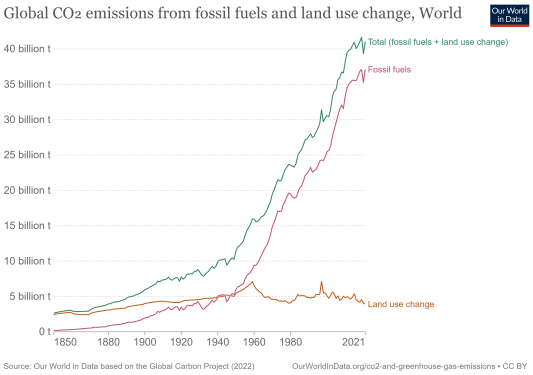

Figure 1.30: Émissions mondiales de CO_2 pour les années 1990-2022, reproduite de [8].

Une préoccupation mondiale envers les objectifs de réduction de la consommation d'énergie, de maximisation de l'efficacité énergétique, de transition vers des combustibles alternatifs, d'augmentation de la part des énergies renouvelables et d'atteinte d'une émission de CO_2 nulle, a été exprimée dans les accords suivants : Rio en 1992, Kyoto en 1997 et Paris en 2015. L'accord de Paris vise spécifiquement à limiter l'augmentation de la température mondiale à 1,5 °C [10]. Le scénario 1,5 °C présenté dans le

« 2021 World Energy Transitions Outlook » [11] propose six voies techniques pour atteindre cet objectif climatique. Ces voies sont illustrées dans la Figure 1.31.

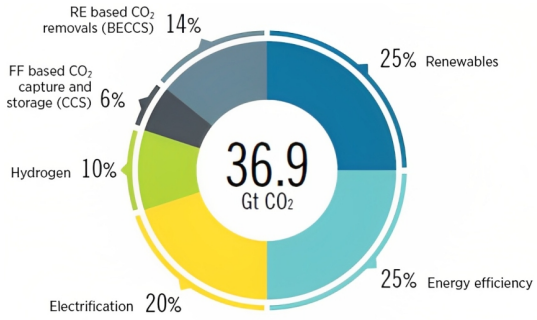

Figure 1.31: Six approches technologiques pour réduire les émissions d'ici 2050, adoptées à partir de [12]. *CCS = captage et stockage du carbone; BECCS = bioénergie avec CCS ; RE = renewables; FF = fossil fuel "combustible fossile"; Gt CO2 = gigatonnes de dioxyde de carbone*.

La neutralité climatique d'ici 2050 implique de remplacer les énergies fossiles par des sources à faible émission de carbone, comme les sources d'énergie renouvelable variable (VRES). Ces sources d'énergie réduisent la dépendance aux combustibles fossiles et fournissent une énergie propre et efficace. La production mondiale d'énergie solaire et éolienne a augmenté [3], et l'Union européenne s'engage à augmenter la part des énergies renouvelables. En France, le mix énergétique est dominé par l'énergie nucléaire, mais les énergies renouvelables sont en croissance. En 2021, les énergies renouvelables représentaient 38% de la puissance installée, comparable à l'énergie nucléaire (39%) [14]. Toutefois, l'énergie nucléaire représente environ 69% de l'énergie produite, tandis que les énergies renouvelables représentent 23,64%. L'hydraulique est la plus grande source d'énergie renouvelable en France. Le coût de l'électricité des énergies renouvelables a diminué, favorisant leur intégration. Cependant, l'intégration massive de ces sources pose des défis en termes de conciliation de l'offre et de la demande, et de gestion du réseau. En effet, les sources d'énergie renouvelable, principalement l'énergie éolienne et solaire, sont fortement dépendantes des conditions météorologiques, ce qui les rend incontrôlables pour répondre aux besoins énergétiques. Par conséquent, pour résoudre ce problème, un stockage massif d'énergie ainsi qu'un réseau de transmission et de distribution sont nécessaires pour relever les défis des énergies renouvelables.

Pour augmenter l'intégration des VRES, il est nécessaire d'utiliser des systèmes de stockage d'énergie (SSE). Différentes technologies de stockage existent, chacune ayant des caractéristiques distinctes et une durée de stockage spécifique. Selon la technologie utilisée, l'énergie peut être stockée pendant une courte ou une longue durée (Figure 1.32). Les technologies à court terme (inducteurs, supercondensateurs, volants d'inertie) permettent de stocker l'énergie pendant une courte période avec un rendement élevé (> 90%), mais ont une capacité et durée limitées [15]. Les technologies à moyen terme (batteries, stockage par pompage-turbinage, air comprimé) offrent une durée de stockage de quelques heures à une semaine. Les batteries sont largement utilisées, avec un rendement de 80% et une capacité allant jusqu'à 85 kWh pour les batteries Li-ion [15]. Les technologies à long terme (stockage chimique, Power-to-hydrogen, Power-to-Gas) ont une capacité élevée de plusieurs TWh et une durée de stockage allant de quelques jours à un an. Elles ont un rendement de 40% pour l'hydrogène et de 36% pour le gaz de méthane,

mais peuvent stocker de grandes quantités d'énergie [15]. Pour une intégration massive des VRES, il est nécessaire d'utiliser des technologies de stockage à long terme et à haute capacité, telles que le méthane de synthèse, l'hydrogène, l'air comprimé et le stockage par pompage-turbinage.

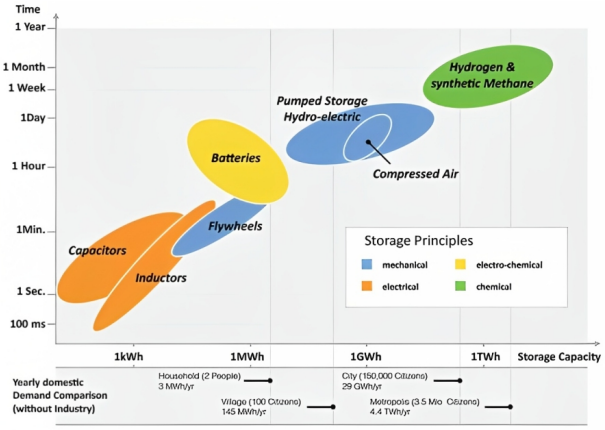

Figure 1.32: La capacité de stockage et la durée des systèmes de stockage de l'énergie, reproduite de [15].

Système de stockage de produits chimiques : système de Power-to-Gas

La technologie Power-to-Gas (P2G) est un système de stockage d'énergie qui intéresse les futurs systèmes énergétiques. Le concept du système Power-to-Gas a été proposé au Japon par Hashimoto et al. (1999) [21], qui utilise l'électricité générée par des cellules solaires dans les déserts pour électrolyser l'eau de mer et produire de l'H_2, qui est ensuite utilisé pour synthétiser du méthane à partir du CO_2 et de l'H_2. Ce concept s'est développé pour relier les réseaux d'électricité et de gaz, permettant la conversion de l'excédent d'énergie renouvelable en gaz compatible avec le réseau de gaz grâce à un procédé en deux étapes, comme illustré dans la Figure 1.33. Le système P2G peut prendre différentes formes. Le système Power-to-H_2 produit uniquement de l'hydrogène gaz (H_2), qui peut être utilisé dans diverses applications industrielles, comme carburant ou injecté dans le réseau de gaz. D'autre part, le système Power-to-SNG produit du substitut de gaz naturel (SNG), utilisé pour la production d'électricité et de chaleur domestiques ou injecté dans le réseau de gaz.

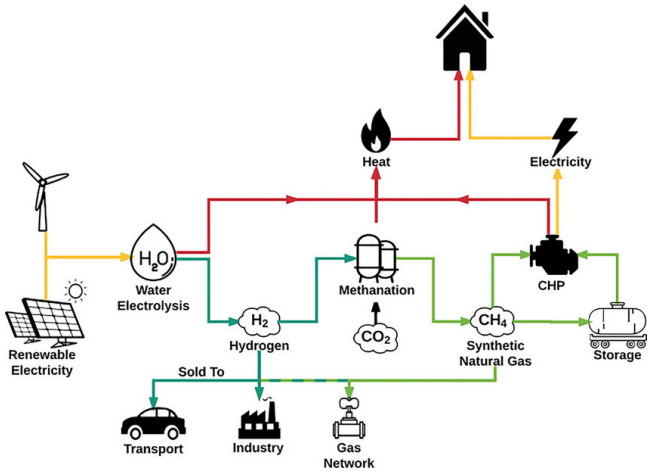

Figure 1.33: Représentation schématique du système Power-to-Gas [22].

Le système Power-to-SNG est préférable au système Power-to-H_2 en raison des problèmes de stockage de l'hydrogène gaz et des restrictions liées à son injection dans le réseau de gaz. L'hydrogène gaz nécessite des conditions de stockage spécifiques, telles que des hautes pressions ou des basses températures, ce qui consomme beaucoup d'énergie. De plus, sa capacité de stockage d'énergie par volume est faible par rapport au gaz naturel. En outre, les limites d'injection d'hydrogène dans le réseau de gaz naturel sont assez strictes, telles que 6% en France [23] et de 2% en Allemagne [24], ce qui limite la quantité de H_2 pouvant être injectée. En revanche, le méthane est plus facile à comprimer, stocker, transporter et utiliser grâce à l'infrastructure existante du gaz naturel. Le système Power-to-SNG offre donc une solution plus pratique pour résoudre rapidement les problèmes de stockage de l'énergie tout en réduisant la dépendance à l'égard des combustibles fossiles en remplaçant le gaz naturel dérivé des combustibles fossiles par une source d'énergie plus durable. Les étapes clés de ce système comprennent l'électrolyse de l'eau pour produire de l'hydrogène gaz, suivie de la méthanation où l'hydrogène est combiné avec du CO_2 provenant du captage du carbone.

Procédé d'électrolyse de l'eau

L'électrolyse de l'eau est le procédé de dissociation d'une molécule d'eau en molécules d'hydrogène et d'oxygène à l'aide d'une source électrique. Deux réactions d'oxydoréduction partielles se produisent aux électrodes de l'électrolyseur, la cathode (-) et l'anode (+), où l'hydrogène est produit du côté de la cathode et l'oxygène du côté de l'anode. L'égalisation de la charge entre les deux réactions partielles se fait sous forme de conduction ionique à travers un électrolyte, qui est une substance conductrice de l'électricité. Les électrolyseurs sont composés de plusieurs cellules d'électrolyse interconnectées, formant ainsi ce que l'on appelle des piles.

Le concept de Power-to-Gas a été étudié en utilisant différents types de cellules d'électrolyse. L'électrolyse peut être réalisée à basse température en utilisant des électrolyseurs alcalins (AEL) ou à membrane échangeuse de protons (PEM), ou à haute température en utilisant des électrolyseurs à oxyde solide (SOEC) ou des électrolyseurs à carbonates fondus (MCEC). Les installations pilotes actuelles du système Power-to-Gas se basent principalement sur l'électrolyse à basse température, mais la recherche récente se concentre sur l'électrolyse à haute température pour ce type de système.

Électrolyseurs à basse température

Deux principaux types de cellules d'électrolyse sont utilisés pour l'électrolyse à basse température : les électrolyseurs alcalins (AEL) et les électrolyseurs à membrane échangeuse de protons (PEM).

Les **electrolyseurs alcaline (AEL)** sont composés de deux électrodes séparées par un diaphragme qui conduit les ions hydroxyde (OH^-) à travers une solution de KOH, comme illustré dans la Figure 1.34. Ils fonctionnent à une température inférieure à 100 °C et à une pression atmosphérique. Ils présentent plusieurs avantages, tels qu'une stabilité à long terme, l'utilisation de catalyseurs métalliques non nobles et un coût relativement faible. Cependant, ils ont des inconvénients tels qu'une densité de courant limitée, une migration de gaz, une faible pression de fonctionnement et une faible efficacité énergétique [28, 29].

Les **électrolyseurs à membrane échangeuse de protons (PEM)** ont été développés en 1966 pour surmonter les problèmes de l'électrolyse alcaline [30]. Cet électrolyseur est composé de deux électrodes séparées par une membrane d'électrolyte polymère, comme indiqué dans la Figure 1.35, avec l'électrode

d'anode revêtue d'un catalyseur métallique de platine et l'électrode de cathode recouverte d'oxyde d'iridium. La technologie PEM présente une conception compacte, une densité de courant élevée, une grande efficacité, une haute pression de fonctionnement, une réponse dynamique rapide et la capacité de produire de l'oxygène pur comme sous-produit. Les principaux inconvénients des électrolyseurs PEM sont le coût élevé de l'équipement, la faible durabilité et l'environnement corrosif acide [28].

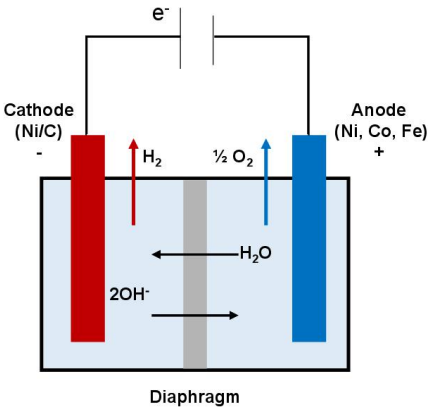

Figure 1.34: Schéma d'une cellule d'électrolyse alcaline (AEL).

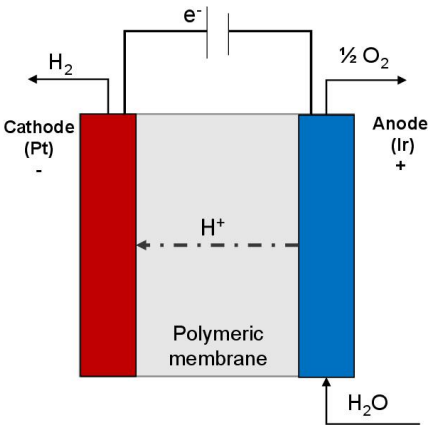

Figure 1.35: Schéma d'une cellule d'électrolyse à membrane échangeuse de protons (PEM).

Les deux types d'électrolyseurs à basse température sont des technologies éprouvées dans la plage des mégawatts pour une utilisation commerciale. L'électrolyseur alcaline est une technologie plus rentable que l'électrolyseur PEM, qui souffre de coûts d'investissement (CAPEX) et de fonctionnement (OPEX) significativement élevés. Un électrolyseur AEL coûte environ 270 €/kW pour une pile minimale de 1 MW, et entre 500 et 1000 €/kW pour une pile minimale de 10 MW [33]. Cependant, l'électrolyseur PEM est de 40 à 50% plus cher que l'électrolyseur AEL, avec un coût d'environ 400 €/kW pour une pile minimale de 1 MW et de 700 à 1400 €/kW pour une pile minimale de 10 MW [33].

Électrolyseurs à haute température

L'électrolyseur à vapeur à haute température est une autre technologie prometteuse pour les systèmes Power-to-Gas. Il offre une faible tension électrique par rapport aux procédés à basse température, réduisant ainsi les pertes d'énergie. De plus, la haute température favorise l'activité des électrodes, réduisant la surtension de la cellule [47]. Ceci peut être avantageux si le besoin en énergie thermique pour la génération de vapeur est disponible à partir de la chaleur résiduelle et si la durée de vie de cette technologie est supérieure à celle des systèmes actuels. Une comparaison des performances entre les électrolyseurs à basse et haute température a révélé un rendement élevé d'un électrolyseur à haute température, par rapport aux électrolyseurs à basse température (AEL et PEM).

L'électrolyse à haute température est en développement depuis plusieurs années, mais les efforts se sont concentrés sur les électrolyseurs à oxyde solide (SOEC). Cependant, une nouvelle technologie appelée électrolyseur à carbonates fondus (MCEC) est actuellement étudiée, ce qui représente l'opération inverse de la pile à combustible à carbonates fondus (MCFC) commerciale. Les MCFC ont connu un succès massif dans la production d'électricité et de chaleur et peuvent être utilisées comme système de

captage du carbone. Cette thèse se concentrera sur l'évaluation technique et économique du MCEC dans le contexte du système Power-to-SNG.

Une **cellule d'électrolyse à oxyde solide (SOEC)** est composée de deux électrodes séparées par un électrolyte conducteur d'ions oxyde (O^{2-}), comme présenté dans la Figure 1.36. Les matériaux utilisés pour les SOEC sont la zircone stabilisée à l'yttria (YSZ) pour l'électrolyte, le Ni-YSZ pour le catalyseur de l'électrode anodique, et le LSM (manganite de lanthane et strontium)-YSZ pour le catalyseur de l'électrode cathodique. Étant donné que les électrolytes ont une conductivité ionique limitée à des températures plus basses, la cellule fonctionne à une température très élevée de 800 à 1000 °C [51].

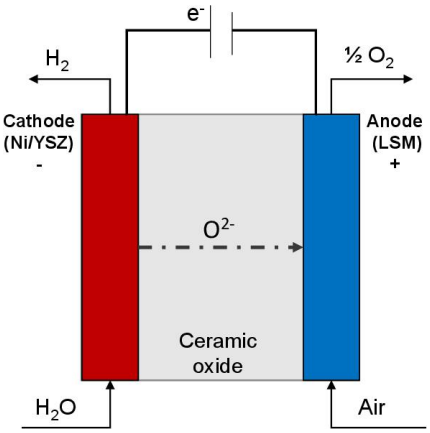

Figure 1.36: Schéma d'un électrolyseur à oxyde solide (SOEC).

Avec le développement croissant des énergies renouvelables au 21^{e} siècle, l'électrolyseur SOEC est devenu une solution efficace pour équilibrer les fluctuations de ces sources et répondre à la demande d'énergie. Plusieurs études ont été menées pour étudier la faisabilité des électrolyseurs SOEC dans le procédé Power-to-Gas. Au niveau des performances des SOEC, il a été constaté que les pertes potentielles de la cellule peuvent être réduites en diminuant les densités de courant et en augmentant la température de la cellule [52]. En 2009, un programme de recherche a été lancé au Laboratoire national de l'Idaho (INL) pour développer l'électrolyseur SOEC à grande échelle et produire efficacement de l'hydrogène gazeux à partir de vapeur à haute température [53]. Les résultats ont montré que les rendements de production pouvaient atteindre 50% pour une technologie à haute température avec une température de sortie supérieure à 850 °C [54]. Une étude ultérieure menée par Petipas et al. (2013) [55] a montré un rendement de 91% pour un système SOEC à haute température sous pression, influencé par la charge de puissance. Des recherches ont également montré que des rendements plus élevés pouvaient être obtenus avec des systèmes pressurisés fonctionnant à une température élevée, ou avec des systèmes non pressurisés fonctionnant à basse température [56, 57].

Au cours des quatre dernières décennies, l'électrolyse à haute température utilisant l'électrolyseur à oxyde solide a connu des avancées significatives en termes de composition de l'électrolyte et les matériaux d'électrodes [58]. Cependant, cette technologie fonctionne principalement à des températures élevées, ce qui pose divers défis, notamment (a) la dégradation de la cellule, (b) une durée de démarrage plus longue, (c) une instabilité mécanique due au stress thermique, (d) perte d'étanchéité des gaz (défaillance de l'électrolyte/joint d'étanchéité) [59].

Ces électrolyseurs ont été commercialisés depuis 2021. Certains fabricants ont lancé la pile SOEC

sur le marché, tels que Sunfire en Allemagne [60], HALDOR TOPSOE au Danemark [61] et FuelCell Energy aux États-Unis [62]. La pile SOEC Sunfire (Hylink) peut produire 750 Nm^3/h de H_2 avec une consommation d'énergie de 3,6 kWh/Nm^3. La conception de la pile TOPSPE d'une capacité de 100 MW permet de produire 32000Nm^3/h de H_2 avec une consommation d'énergie de 3,1 kWh/Nm^3. De plus, la pile SOEC de FuelCell Energy génère 600 kg/jour de H_2 tout en consommant 39,4 kWh/kg d'électricité avec apport de chaleur et 43,8 kWh/kg sans apport de chaleur.

La **cellule d'électrolyse à base de carbonates fondus (MCEC)** fonctionne à une température élevée de 600 à 700 °C. Elle est composée de deux électrodes et d'un électrolyte conducteur d'ions carbonate (CO_3^{2-}), comme illustré dans la Figure 1.37. L'électrode d'anode est revêtue d'un alliage à base de nickel avec une composition de chrome et d'aluminium entre 2 et 10% pour réduire le frittage et les problèmes mécaniques [64]. Quant à l'électrode de cathode, elle est composée d'un catalyseur de NiO avec du lithium [58]. L'électrolyte est constitué d'un mélange eutectique de carbonates de lithium et de potassium $(Li/K)_2CO_3$ ou de carbonates de lithium et de sodium $(Li/Na)_2CO_3$, ou d'un mélange ternaire de $(Li/K/Na)_2CO_3$. Étant donné que le mélange de sels de carbonate est liquide à la température de fonctionnement, une matrice poreuse de $\gamma-LiAlO_2$ retient l'électrolyte. Cet électrolyte est hautement conducteur, ce qui permet le passage des ions carbonate de la cathode vers l'anode sans mélange des gaz combustible et oxydant [58].

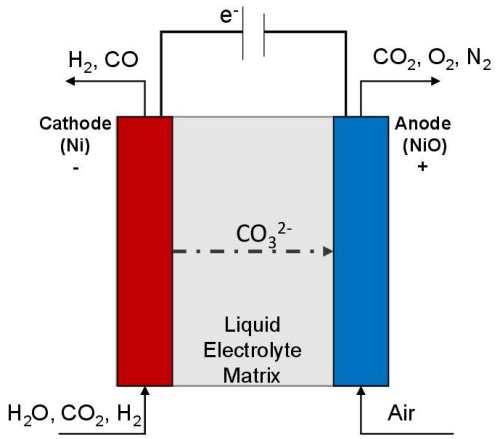

Figure 1.37: Schéma de l'électrolyseur de carbonates fondus (MCEC).

La technologie des piles à combustible à carbonates fondus (MCFC) a inspiré le développement de l'électrolyseur à carbonates fondus (MCEC) pour l'application Power-to-Gas. Les MCFC, déjà commercialisées en Corée du Sud, aux États-Unis et en Europe [63], ont contribué à l'intérêt croissant pour le MCEC. Les recherches sur l'électrolyseur MCEC sont encore limitées, mais des études ont exploré ses performances et proposé des stratégies d'expansion. Hu et al. (2014) [58] ont étudié la faisabilité et la durabilité de l'utilisation des MCFC pour l'électrolyse. Ils ont constaté que la cellule fonctionne mieux en mode électrolyse qu'en mode pile à combustible, avec des pertes de polarisation plus faibles au niveau de l'électrode de NiO, même si l'électrode de Ni présente des pertes de polarisation élevées. Des études ultérieures ont examiné la cinétique des électrodes cathodique (Ni) et anodique (NiO) [66, 67]. En fait, le rôle principal d'un électrolyseur est de produire du gaz hydrogène, il est donc essentiel de fournir à la cellule une faible quantité, voire aucune quantité de gaz hydrogène. Par conséquent, Hu

et al. (2016a) [68] ont examiné le fonctionnement de l'électrode de Ni avec différents gaz appauvris en hydrogène, montrant des pertes de polarisation élevées en présence d'une faible teneur en gaz hydrogène. La durabilité du MCEC a également été évaluée lors d'un test à long terme par Hu et al. (2016b) [69], qui ont montré qu'il est possible de faire fonctionner un électrolyseur à carbonates fondus basé sur les composants conventionnels des MCFC, du moins à l'échelle du laboratoire.

Pour optimiser les performances du MCEC, des études se sont concentrées sur les conditions de fonctionnement et les conceptions d'échelle. Ainsi, Reyes-Belmonte et al. (2017) [70] ont développé des modèles électrochimiques et thermodynamiques pour étudier l'effet de divers paramètres de fonctionnement sur les performances du MCEC. De plus, ils ont été les premiers à proposer et à simuler une conception d'échelle pour le MCEC, révélant des taux de conversion plus élevés et des courants de densité d'énergie plus faibles avec une plage de température de cellule intermédiaire (400-500 °C) et des exigences élevées de température d'alimentation pour réduire la consommation d'énergie électrique de l'électrolyseur. Par la suite, Lucas Mastropasqua et al. (2018) [71] ont proposé et simulé un nouveau concept de centrale basé sur l'électrolyseur à carbonates fondus. Les résultats ont démontré la viabilité du MCEC pour le stockage électrochimique à long terme et la production de substitut de gaz naturel (SNG).

Cependant, des défis tels que la durabilité et l'évaporation de l'électrolyte doivent être résolus pour permettre une mise en œuvre à plus grande échelle du MCEC. Des tests expérimentaux sur des zones géométriques plus grandes, menés par Frangini et al. (2021) [73], ont révélé des problèmes de dégradation de la cellule, qui peuvent être atténués par le remplissage de l'électrolyte. Le rechargement périodique de l'électrolyte a permis de prolonger le temps de fonctionnement du MCEC, comme l'ont obtenu Audasso et al. (2022) [74]. Des études ont également examiné les effets de transport en phase gazeuse par Koomson et Lee (2022) [75], mettant en évidence une perte de tension plus faible en mode électrolyse par rapport au mode pile à combustible.

La réversibilité de l'opération MCFC en tant qu'électrolyseur est encore limitée à la recherche à l'échelle du laboratoire, et des recherches supplémentaires sont nécessaires pour améliorer la stabilité des cellules et résoudre les problèmes de dégradation afin de permettre un fonctionnement en mode électrolyse à plus grande échelle.

Procédé de méthanation

En 1902, Sabatier et Senderens ont développé un procédé de méthanation basé sur la catalyse pour convertir le monoxyde de carbone (CO) ou le dioxyde de carbone (CO_2) en méthane (CH_4) par hydrogénation thermo-chimique [76]. Il existe deux procédés catalytiques de méthanation : la méthanation du CO (Eq. 1.1) et la méthanation du CO_2 (Eq. 1.2), qui sont liées à la réaction inverse du gaz à l'eau (RWGS) (Eq. 1.3) représentant une réaction intermédiaire.

$$CO + 3\,H_2 \longleftrightarrow CH_4 + H_2O \qquad \Delta_R H^0 = -205.9\,\mathrm{kJ \cdot mol^{-1}} \tag{1.1}$$

$$CO_2 + 4\,H_2 \longleftrightarrow CH_4 + 2\,H_2O \qquad \Delta_R H^0 = -164.8\,\mathrm{kJ \cdot mol^{-1}} \tag{1.2}$$

$$CO_2 + H_2 \longleftrightarrow CO + H_2O \qquad \Delta_R H^0 = 41\,\mathrm{kJ \cdot mol^{-1}} \tag{1.3}$$

La réaction de Boudouard (Eq. 1.4) et une autre réaction (Eq. 1.5) peuvent se produire dans le réacteur de méthanation, entraînant un dépôt de carbone qui désactive le catalyseur [78].

$$2\,CO \longleftrightarrow C_{(s)} + CO_2 \qquad \Delta_R H^0 = -172\,\mathrm{kJ}\cdot\mathrm{mol}^{-1} \tag{1.4}$$

$$CO_2 + 2\,H_2 \longleftrightarrow C_{(s)} + 2\,H_2O \qquad \Delta_R H^0 = -90\,\mathrm{kJ}\cdot\mathrm{mol}^{-1} \tag{1.5}$$

Les conditions favorables aux réactions de méthanation sont une basse température, une haute pression et des ratios élevés de y_{H_2}/y_{CO}(> 3) et de y_{H_2}/y_{CO_2} (> 4). Cependant, pour la synthèse du méthane en présence à la fois de CO et de CO_2 dans le gaz d'alimentation initial, un ratio $(y_{H_2}\text{-}y_{CO_2})/(y_{CO_2}+y_{CO})$ d'environ 3 est nécessaire [80].

Les réactions de méthanation du CO et du CO_2 sont fortement exothermiques, nécessitant l'élimination de chaleur pour protéger le catalyseur et le réacteur. Les procédés de méthanation peuvent être adiabatiques ou isothermes, utilisant différents types de réacteurs catalytiques : lit fixe, lit fluidisé, lit de suspension et réacteurs structurés. Les réacteurs à lit fixe sont les plus matures et peut être classé en deux types : un réacteur à lit fixe adiabatique utilisé pour les procédés adiabatiques et un réacteur à lit fixe multitubulaire utilisé pour les procédés isothermes. Cependant, cette technologie présente des problèmes de charge thermique élevée et d'une gestion faible du gradient de température. Le réacteur à lit fluidisé assure un fonctionnement isotherme, mais présente des contraintes mécaniques et une durée de vie réduite. Le réacteur à lit de suspension résout ces enjeux, permettant un fonctionnement isotherme avec des variations de charge élevées, mais rencontre des difficultés liées au transfert de masse et au mélange. Les réacteurs structurés sont une technologie prometteuse qui surmonte ces problèmes et peut gérer des charges flexibles et les gradients de température, les rendant attrayants pour les systèmes P2G.

Procédé de méthanation adiabatique

Le procédé de méthanation adiabatique utilise une série de réacteurs à lit fixe avec un refroidissement intermédiaire. C'est une méthode bien établie et largement disponible commercialement. Les procédés LURGI et TREMP sont les plus couramment utilisés à grande échelle pour la méthanation.

Le **procédé Lurgi** dans la Figure 1.38, développé dans les années 1930, utilisait réacteurs à lit fixe adiabatiques, séparés par des échangeurs de chaleur pour refroidir les gaz provenant du premier réacteur et récupérer la chaleur produite par la réaction. Un flux de recyclage était nécessaire pour contrôler la température. Cependant, cette étape de recyclage entraînait une pénalité énergétique et le gaz produit nécessitait une purification coûteuse. Le **procédé TREMP™** (Figure 1.39) développé par Haldor Topsoe est utilisé dans la gazéification du charbon et les installations de biomasse. Il utilise 3 à 4 réacteurs à lit fixe adiabatiques avec des étapes de refroidissement intermédiaires, permettant une flexibilité d'application. Cette technologie atteint des températures de sortie plus élevées que le procédé Lurgi, ce qui permet de produire un vapeur surchauffé à haute pression et de minimiser la consommation d'énergie.

Cependant, le procédé adiabatique n'est pas adapté aux applications Power-to-Gas en raison de problèmes de gestion thermique [99]. Les réacteurs adiabatiques à lit fixe avec refroidissement inter-étapes et recirculation de gaz, considérés comme les plus avancés pour la méthanation commerciale du CO, rencontrent des problèmes de surchauffe thermique lors d'une utilisation en conditions transitoires [100]. Par conséquent, les réacteurs isothermes, qui utilisent un fluide de refroidissement directement dans le

réacteur, sont généralement privilégiés pour les applications Power-to-Gas.

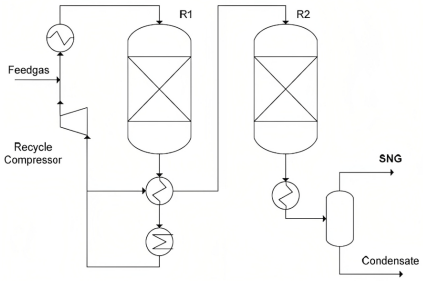

Figure 1.38: Procédé de méthanation de Lurgi avec deux réacteurs adiabatiques à lit fixe, reproduite de [94].

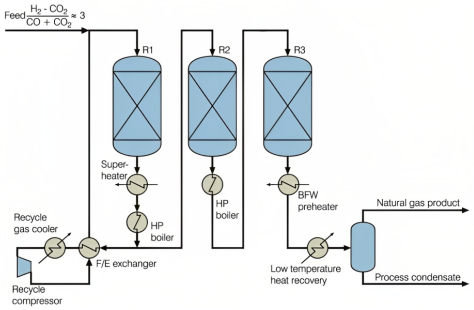

Figure 1.39: Technologie de méthanation Topsoe TREMP™, reproduite de [96].

Procédé de méthanation isotherme

Le procédé isotherme utilise un réacteur à lit fixe refroidi avec un agent de transfert de chaleur externe pour extraire la chaleur de la réaction de méthanation. Le **procédé isotherme Linde** est un exemple de cette technologie, qui utilise deux réacteurs à lit fixe : un réacteur adiabatique et un réacteur-échangeur pour un fonctionnement quasi-isotherme, comme illustré dans la Figure 1.40. Les tubes de refroidissement intégrés dans le lit fixe facilitent le transfert de chaleur et permettent une conversion élevée en une seule étape, offrant la co-production de SNG et de vapeur [94]. Bien que cette technologie ne soit pas utilisée commercialement pour la méthanation, elle est appliquée dans la production de méthanol avec les réacteurs isothermes Linde.

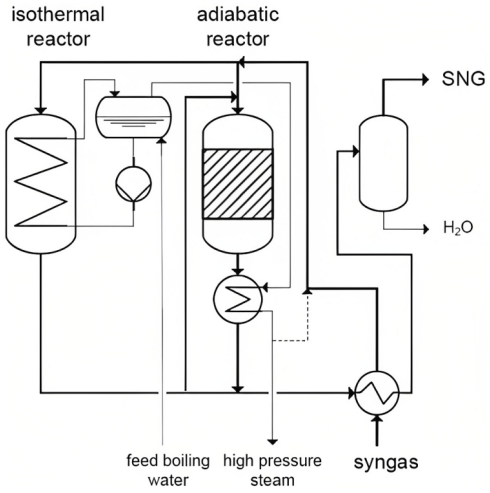

Figure 1.40: Schéma du procédé de méthanation de Linde, reproduite de [101].

Statut et projets de Power-to-Gas

Le système Power-to-Gas gagne du terrain avec des installations à l'échelle pilote. Les électrolyseurs AEL et PEM dominent le marché en raison de leur maturité et de leur rentabilité. Bien que certains projets explorent la technologie SOEC, elle reste limitée au développement à petite échelle pour la production d'hydrogène gaz. Dans le monde, il y a eu 153 projets Power-to-Gas dans 22 pays depuis 1988, avec

des projets opérationnels de production d'hydrogène gaz (56 projets) et de méthanation (38 projets) en 2019 [102]. En France, environ 15 projets Power-to-Gas ont été lancés depuis 2012, avec plusieurs démonstrateurs pilotes en fonctionnement et d'autres prévus, dont certains visent à atteindre l'autosuffisance en gaz d'ici 2050.

Conclusion

Ce chapitre explore l'intérêt du système Power-to-Gas (P2G) respectueux de l'environnement pour relever les défis environnementaux et énergétiques. Il a le potentiel de réduire les émissions de carbone en promouvant les sources d'énergie renouvelable comme des alternatives propres aux combustibles fossiles. Le système P2G résout les problèmes d'intermittence des sources d'énergie renouvelable en stockant l'excès d'énergie électrique pour une utilisation ultérieure. Pour atteindre une neutralité carbone, il est nécessaire de mettre en place des technologies de captage du carbone dans les secteurs industriels, et le CO_2 capté peut être combiné à l'hydrogène produit par électrolyse de l'eau dans ce système pour produire des combustibles de valeur.

Le système P2G peut être soit un système Power-to-H_2 à un seul étage, soit un système Power-to-SNG à deux étages, ce dernier étant plus favorable en raison des défis liés au stockage de l'hydrogène et à son injection dans le réseau de gaz. Bien qu'il y ait eu de nombreuses recherches sur l'électrolyse à basse température dans le système P2G, peu de recherches ont été menées sur l'électrolyse à haute température, principalement en utilisant des cellules d'électrolyse à carbonates fondus (MCEC). La littérature existante se concentre surtout sur la recherche à l'échelle expérimentale pour l'électrolyseur MCEC. Cependant, des investigations supplémentaires sont nécessaires pour comprendre les aspects techniques et dynamiques de l'électrolyseur MCEC à grande échelle, en particulier dans le contexte du système Power-to-SNG. Le procédé de méthanation, qui est la deuxième étape du système Power-to-SNG, peut être réalisé de manière adiabatique ou isotherme. Les réacteurs isothermes qui utilisent un fluide de refroidissement sont préférés dans les applications Power-to-Gas en raison du fonctionnement intermittent de ces systèmes.

Les recherches actuelles manquent d'études approfondies sur la réaction électrochimique dans les MCEC dans des conditions de fonctionnement industrielles et de sa relation avec la réaction de méthanation. De plus, étant donné que les MCEC nécessitent du CO_2, cela soulève la question de la possibilité d'électrolyser le CO_2 avec H_2O pour produire du gaz de synthèse (mélange de H_2 et CO). Cet aspect est examiné en détail et discuté dans le chapitre 2. Ensuite, le système Power-to-SNG dans son ensemble est évalué sur le plan technique et économique en utilisant l'électrolyseur MCEC. De plus, les études précédentes n'ont pas suffisamment abordé le comportement dynamique des MCEC lorsqu'ils sont couplés à des sources d'énergie renouvelable intermittentes. Il est donc important d'étudier et de comprendre la réponse dynamique des MCEC dans de tels scénarios afin d'assurer une intégration efficace avec ces sources d'énergie.

Chapter 2

Modelling of the Electrolysis and co-electrolysis of H_2O and CO_2 in Molten Carbonate Electrolysis Cell

Objective

This chapter aims to present the model basis of H_2O electrolysis and co-electrolysis in a molten carbonate electrolyzer and evaluate the model by validating it with experimental work. In addition, a parametric study will be carried out to understand the key parameters for improving cell performance and syngas (mixture of H_2 & CO) production.

Table of Contents

1 Literature Review on co-electrolysis

The effort has recently focused on carbon dioxide capture and utilization applications and renewable energies to reduce CO_2 emissions. Thus, this target raises the concern about utilizing CO_2 in high-temperature electrolyzers through the co-electrolysis of CO_2 and H_2O to produce syngas (H_2 and CO). The co-electrolysis of CO_2 and H_2O was first studied by Stoots et al. (2008) using a solid oxide electrolyzer. Stoots et al. (2008) [111] deduced that CO is chemically produced via RWGS, and there is no electrolysis of CO_2. However, Ebbesen et al. (2009) [112] later studied the ASR's variation between H_2O electrolysis and CO_2 electrolysis. This study demonstrated that CO_2 and H_2O undergo reduction reaction in a Ni/YSZ-based SOEC to produce H_2 and CO. Besides, the authors stated that the CO is also produced via RWGS in parallel with the electrochemical reactions. Later, Ni Meng (2012) [113, 114] presented a 2D model to study the co-electrolysis of CO_2/H_2O in the SOEC for syngas production and assess the contribution of the RWGS reaction to CO production. As a result, it was found that the reversible water gas shift reaction significantly alters the H_2O/CO_2 electrolysis, where its contribution depends on the operating temperature and the inlet gas composition. Also, the study showed that the CO is produced by RWGS reaction at a low operating potential; however, it is consumed via water gas shift (WGS) reaction at a high operating potential.

Carbon monoxide (CO) production within the cell via CO_2 electrolysis or RWGS has become a promising approach in the Power-to-Gas process. Redissi and Bouallou (2013) [115] have considered the co-electrolysis of H_2O and CO_2 in the solid oxide electrolyzer when examining the overall Power-to-Gas process. This process reveals an efficiency of 62.3%, lower than the system producing only hydrogen gas. On the other hand, Hanaa et al. (2018) [116] evaluated the overall performance of the P2G system based on SOEC, showing a 67.1% process efficiency. However, in their simulation, CO is chemically produced and not electrochemically. Wang et al. (2019) [80] investigated the design of co-electrolysis in SOEC electrolyzer for Power-to-SNG system and examined the role of CO_2 in co-electrolysis. They showed that the electrochemical reaction of co-electrolysis is mainly H_2O splitting, while CO_2 is converted via RWGS reaction. Indeed, the concept of co-electrolysis in SOEC still needs to be clarified.

On the contrary, molten carbonate electrolyzer is now under the scope of interest in the renewable energy storage and CO_2 valorization fields through the co-electrolysis of CO_2 and H_2O in the electrolysis cell. Furthermore, this type of electrolyzer is recommended for CO_2 transformation since carbon dioxide is highly soluble in the molten carbonate, which is the electrolyte of the MCEC [117]. The ability of its carbonate electrolyte to trap large amounts of CO_2 raises the possibility of reducing carbon dioxide within it to generate syngas (H_2 & CO) via a co-electrolysis process. The co-electrolysis of CO_2 and H_2O in molten carbonate electrolyzers is being investigated to demonstrate the molten carbonates' capacity to electrolyze CO_2 into CO.

For this technology, the electrochemical conversion of CO_2 into CO in the reversible operation of the molten carbonate fuel cell set-up, which is a molten carbonate electrolyzer, and the Ni and NiO as electrodes' catalysts, still needs to be apprehended. Some studies examined the electrochemical conversion of CO_2 into CO in the MCEC. For example, Lorenz and Janz in 1970 [118] investigated the electrolysis mechanism of molten carbonates in an electrolysis cell. Their study demonstrated the presence of CO on the cathodic discharge side of the cell. Peelen et al. (1998) [119] studied the electrochemical reduction

of CO_2 into CO on a gold flag electrode in 62/38 mol% Li/K carbonate mixture in the temperature range 575–700 °C. Also, Kaplan et al. (2010, 2012) [120, 121] reported the conversion of CO_2 to CO by using a cell with a molten electrolyte mixture of lithium carbonate and lithium oxide at 850-900 °C. The electrodes were graphite (anode) and titanium (cathode), not conventional MCFC electrodes (Ni-based materials), and the working temperature was much higher than that of the MCFC system. All these studies proved the electrochemical conversion of CO_2 using flag electrodes instead of the conventional MCFC electrodes.

In addition to that, Chery et al. (2014) [122] conducted thermodynamic calculations and experimental measurements on the reduction of CO_2 into CO on a gold flag or planar disk electrode with Li/K and Li/Na carbonate eutectic at temperatures from 575 °C to 650 °C. Later on, Chery et al. (2015) [117] reviewed different types of electrolytes with different operating temperatures to determine the best electrolyte and operating conditions for CO_2 reduction. They found that CO_2 reduction to CO/C depends on various parameters like temperature, the partial pressure of both CO_2 and CO, and the medium of the electrolyte, whether it is oxo-acidic or oxo-basic. For CO production, a high temperature, an oxoacidic domain, a high CO_2 and low CO partial pressures. After that, Ji et al. (2019) [123] investigated the impact of the electrolyte composition on the H_2O/CO_2 co-electrolysis for H_2 and CH_4 production. They obtained a high yield of 63.34% CH_4 and 35.81% H_2 in an electrolyte composition of $Li_{0.85}Na_{0.61}K_{0.54}$+0.15 $Ca(OH)_2$ at 575 °C. Recently, Meskine et al. (2020) [124] have verified the electrochemical production of CO through CO_2 electrolysis using conventional MCFC electrode materials with a limited maximum cell potential of 1.4 V to avoid the production of C instead of CO in the cell. However, despite all the research that has confirmed the CO_2 electrolysis inside the MCEC, no model has considered CO_2 electrolysis.

All models have assumed that CO is only generated chemically via the reverse water gas shift. Mastropasqua et al. (2018) [71] simulated the reversible operation of the molten carbonate fuel cell by developing a model that took into account the chemical production of CO inside the cell. Later, Perez-Trujillo et al. (2018) [125] worked on finding the best-fit model that can express the potential losses of the electrolysis cell by comparing five different models. These models were used to determine the voltage losses in the MCFC. Along with this work, the authors studied experimentally the performance of MCEC and the effect of temperature, electrode flow ratio, and the composition of the component entering the fuel and oxygen electrodes on the overpotential losses of the cell. Finally, the validated model, which considers all overpotential losses, was used by Perez-Trujillo et al. (2020) [126] to calculate the overpotentials of the MCEC accompanied by equations to improve the prediction of the limiting current densities where the fuel supply has become insufficient. Their model considers the electrochemical conversion of water into hydrogen gas and the chemical conversion of CO_2 into CO.

Moreover, Barelli et al. (2021) [5] investigated the cell's performance using a numerical model that assumes CO generation by reverse water gas shift. Also, Ferrario et al. (2021) [72] developed the mass balance of their MCEC model system based on the electrochemical reaction for hydrogen gas generation and the chemical reaction for CO generation. This work aims to develop a model to cover both H_2O and CO_2 co-electrolysis for syngas production in the MCEC and further compare it with a developed model based on the state-of-the-art scenario, which signifies H_2 production from water electrolysis and CO production chemically from CO_2.

2 Electrolysis: Fundamentals

2.1 Thermodynamics

Water Electrolysis is splitting water into hydrogen and oxygen gases using electricity. This reaction takes place in a device known as an electrolyzer. Electrolyzers, like fuel cells, are made up of an anode and a cathode separated by an electrolyte. Different electrolyzers work differently according to the various electrolyte materials used and the ionic species they conduct. The water electrolysis process depends on the electrolyzer's operating temperature, which takes place according to Eqs. 2.1 and 2.2. $\Delta_R H^\circ$ stands for the standard enthalpy of reaction (in kJ·mol^{-1}).

$$H_2O_{(l)} \longrightarrow H_{2(g)} + \frac{1}{2} O_{2(g)} \qquad \Delta_R H^\circ = 286\,\mathrm{kJ \cdot mol^{-1}} \tag{2.1}$$

$$H_2O_{(g)} \longrightarrow H_{2(g)} + \frac{1}{2} O_{2(g)} \qquad \Delta_R H^\circ = 242\,\mathrm{kJ \cdot mol^{-1}} \tag{2.2}$$

The enthalpy of the reaction is calculated based on the first law of thermodynamics. It is formulated as the sum of the Gibbs free energy $\Delta_R G$ (in kJ·mol^{-1}) and the reaction heat composed of the product of the temperature T (in K) and the reaction entropy $\Delta_R S$ (in kJ·mol^{-1}·K^{-1}), according to Eq. 2.3.

$$\Delta_R H = \Delta_R G + T \cdot \Delta_R S \tag{2.3}$$

Thermodynamic principles determine the minimum energy needed for water splitting in the electrolysis process. The free Gibbs energy represents the electrical energy required for dissociation. The amount $T \cdot \Delta_R S$ defines the thermal energy form; it is derived from the environment at temperature T to meet the total enthalpy requirement. Therefore, temperature T is a critical parameter in water electrolysis because T is needed to meet $T \cdot \Delta_R S$. The influence of the temperature on water electrolysis is presented in Figure 2.1. The diagram is divided into two parts, separated by the discontinuity linked

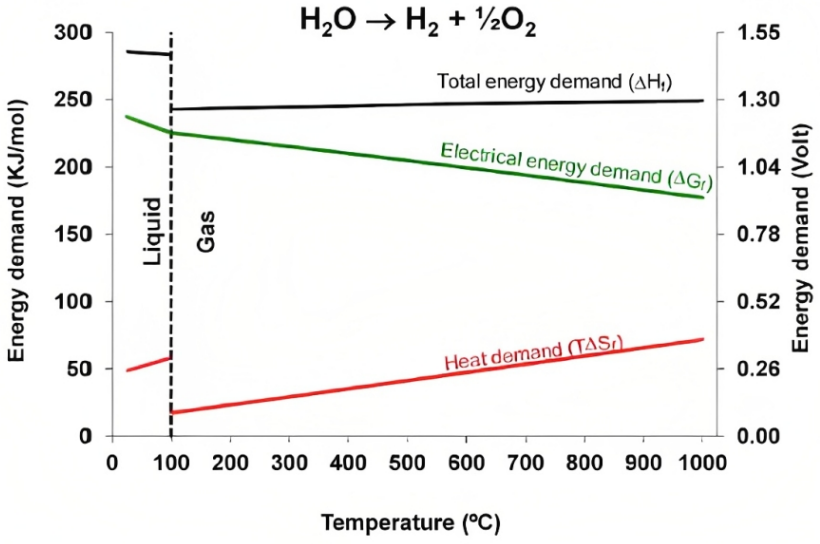

Figure 2.1: Thermodynamics for H_2O electrolysis at atmospheric pressure, reprinted from [127].

to the water evaporation. The left part corresponds to the liquid water electrolysis, and the right to the steam electrolysis. From this diagram, several observations can be extracted. First, the heat demand significantly decreases from liquid to gas state, thus decreasing the total energy demand. This decrease is due to eliminating the water vaporization enthalpy (44 kJ·mol^{-1} at 298 K). Second, in the gaseous phase, as temperature increases, the electrical energy demand decreases while the heat demand increases.

CO_2 Electrolysis occurs to split carbon dioxide into carbon monoxide and oxygen, according to Eq. 2.4. Like water electrolysis, it follows the same thermodynamic principles, where the temperature's impact on its energy demand is presented in Figure 2.2. Electrolysis of CO_2 requires an extensive heat supply with increased temperature, as shown in Figure 2.2. At high temperatures, the heat demand represents a significant part of the total energy demand.

$$CO_{2(g)} \longrightarrow CO_{(g)} + \frac{1}{2} O_{2(g)} \tag{2.4}$$

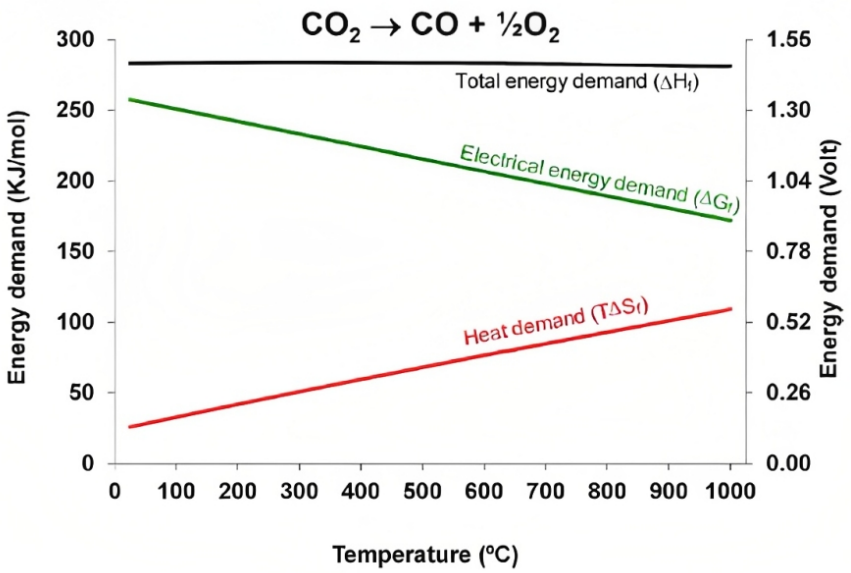

Figure 2.2: Thermodynamics for CO_2 electrolysis at atmospheric pressure, reprinted from [127].

In both H_2O and CO_2 electrolysis, thermodynamic studies have shown the advantage of high-temperature electrolysis over low-temperature. The high temperature facilitates the electrolysis process. The cell exhibits lower electrical potentials, indicating enhanced ionic conductivity, low electrical resistance, and improved electrolysis efficiency. In summary, temperature is a crucial factor in electrolysis, and increasing it enhances the efficiency by substantially decreasing the potential required to generate the same quantity of hydrogen gas.

2.2 Operation of the Electrolysis Cell

2.2.1 Reversible Potential

The reversible potential is the minimum potential required for electrolysis to proceed. In the ideal case, it corresponds to the operating potential of the cell. This potential is related to the standard free energy of formation (ΔG_f°), determined by Eq. 2.5.

$$U^{\circ}_{rev} = \frac{\Delta G^{\circ}_{f}}{nF} \tag{2.5}$$

The standard free energy of formation of water H_2O is $\Delta G^{\circ}_{f,H_2O}$ = 229.8 kJ·mol^{-1} and that of CO_2 is $\Delta G^{\circ}_{f,CO_2}$ = −250.1 kJ·mol^{-1}, at standard conditions [127]. Thus, using Eq. 2.5, the standard reversible potential can be determined to be 1.23 V for H_2O electrolysis and 1.33 V for CO_2 electrolysis. At any pressure and temperature, Nernst potential describes the reversible potential, which links the standard potential (U°_{rev}) and the reversible potential (U_{rev}) at different partial pressures of reactions and products [127]. The reversible potential (U_{rev}) is represented by Eq. 2.6.

$$U_{Nernst} = U_{rev} = \frac{\Delta G^{\circ}_{f}}{nF} - \frac{RT}{nF} lnQ \tag{2.6}$$

In this equation, Q is the reaction coefficient and equals 1 for all reactants and products at standard conditions. For H_2O electrolysis, the reaction coefficient $Q = p_{H_2O}/(p_{H_2} + p_{O_2}^{1/2})$, where p_i corresponds to the partial pressure of the species i. Whereas, for the CO_2 electrolysis, it is $Q = p_{CO_2}/(p_{CO} + p_{O_2}^{1/2})$.

2.2.2 Cell Potential

The cell potential is the potential at which the cell operates. In the ideal case, the cell potential is the reversible potential (U_{rev}). However, in the real-case operation, the potential required for operating an electrolysis cell is significantly higher than the theoretical reversible voltage U_{rev} due to the losses resulting from the gas diffusion and transportation, charge transfer, and the resistance of the electrolyte and the electrodes. These losses are called **"overpotentials"** and can be categorized into three types: activation, ohmic, and concentration overpotentials.

Activation overpotentials are associated with the activation energies of hydrogen and oxygen gas formation reactions on electrode surfaces. They are determined based on the Butler-Volmer equation that depends on the materials used [114]. Ohmic overpotentials are the sum of the electrical resistances of various components, such as electrodes, current collectors, and transport resistances caused by gas bubbles, ionic transfer in the electrolyte, and membrane resistivity [127]. From Ohm's law, ohmic overpotentials can be calculated as a function of temperature [114]. The concentration losses are due to the mass diffusion limitations of the reactants from the bulk phase into the reaction phase (the electrodes) at high currents and are calculated from Fick's law [114]. Figure 2.3 presents the polarization curve of an alkaline electrolyzer at different temperatures. This diagram illustrates that activation overpotentials emerge at low current densities, ohmic overpotentials at moderate levels, and concentration overpotentials at high current densities. The polarization curve also shows that at high operating temperatures, overpotential losses diminish, which confirms the thermodynamic approach, stating that higher temperature leads to lower electrical energy.

Consequently, the cell potential (U_{cell}) is a sum of the reversible potential (U_{rev}) and the overpotential losses, as presented in Eq. 2.7.

$$U_{cell} = U_{rev} + \eta_{act} + \eta_{ohmic} + \eta_{conc} \tag{2.7}$$

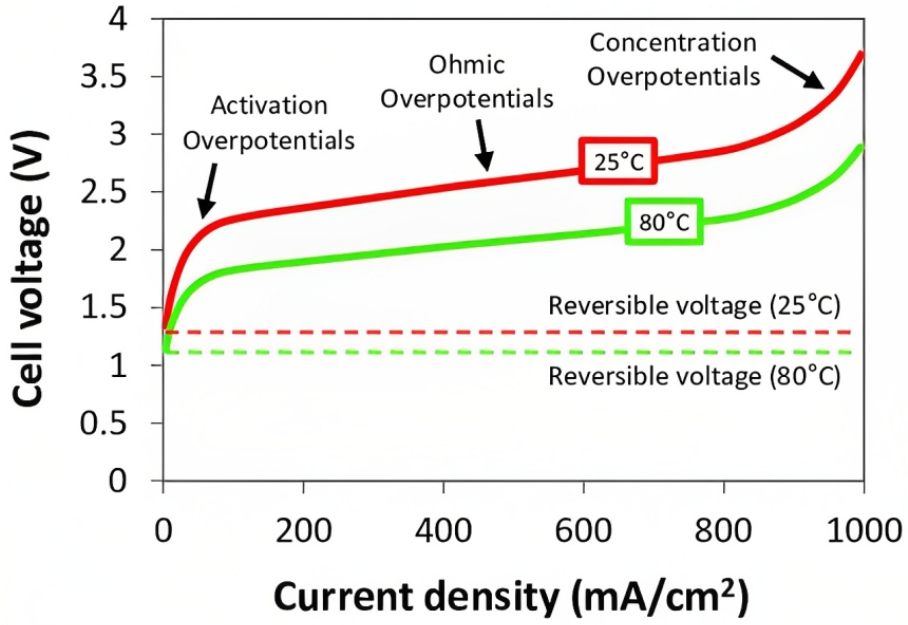

Figure 2.3: Schematic representation of a polarization curve of an alkaline electrolyzer at different temperatures, representing the voltage losses with current density, reprinted from [128].

2.2.3 Area Specific Resistance

The Area Specific Resistance (ASR) depicts the stack's performance and incorporates all loss mechanisms, such as ohmic, activation, and concentration overpotentials. It represents the slope of the V-I curve, illustrated in Figure 2.3, and is measured in $\Omega \cdot cm^2$. Therefore, the cell potential (U_{cell}) equation can be written in a linear form as follows:

$$U_{cell} = U_{rev} + j \cdot ASR \tag{2.8}$$

The term $j \cdot ASR$ replaces the sum of the overpotentials in Eq. 2.7, where j is the current density in A/cm^2, and ASR is usually defined as a function of temperature [129].

2.2.4 Faraday's Law of Electrolysis

Faraday's laws of electrolysis are quantitative laws used in chemistry to quantify the magnitudes of electrolytic effects. The first law states that the amount of chemical change induced by a current at an electrode-electrolyte interface is proportional to the amount of electricity used. In contrast, the second law dictates that the amounts of chemical change generated by the same amount of electricity in different substances are proportional to their equivalent weights. The equivalent weight of a material in an electrolytic reaction is the formula weight in grams associated with a unit gain or loss of electrons [130]. Therefore, a Faraday constant (F) is designated to represent the amount of electricity that will produce a chemical change in one equivalent weight unit. It corresponds to a value of 9.648×10^4 coulombs of electricity.

$$\begin{aligned} H_2O + 2\,e^- &\longrightarrow H_2 + O^{2-} \\ O^{2-} &\longrightarrow \frac{1}{2}\,O_2 + 2\,e^- \end{aligned} \tag{2.9}$$

According to the H_2O electrolysis redox reactions in Eq. 2.9, two moles of electrons are required to produce one mole of hydrogen gas (H_2). Therefore, for an applied amount of electricity, it is required to determine the amount of H_2 produced. Since Faraday's constant represents the amount of electricity in Coulombs (A·s) per one equivalent weight unit, the amount of H_2 produced $\dot{n}_{H_2}$ by water electrolysis is determined by Eq. 2.10. Where j is the current density in A/cm^2, A is the active surface area in cm^2, n_e is the mole of electrons required per mole of hydrogen gas produced, and F is Faraday's constant in Coulombs per mol (C/mol). According to Eq. 2.9, n_e equals 2 moles of electrons per one mole of hydrogen gas.

$$\dot{n}_{H_2} = \frac{j \cdot A}{n_e \cdot F} \tag{2.10}$$

2.2.5 Cell Operating Mode

In thermodynamics, the system can absorb or reject heat. Therefore, it can operate in an endothermal state, which means it needs heat, or in an exothermal state, where it releases heat. In the electrolysis cell, the parameter that determines the operation state of the cell is the thermo-neutral potential (U_{tn}) . It is the voltage at which the electrolysis reactions' thermal requirements balance the cell's thermal generation. The generated heat is due to the cell's losses and equal to the amount needed for the electrolysis, which is η_{ohm}+η_{act}+η_{conc}= $T \cdot \Delta_R S$ [131]. In this case, the applied electrical potential is the thermo-neutral potential (U_{tn}), expressed in Eq. 2.11 as a function of the electrolysis total energy ($\Delta H_{T_{cell},R}$) at the cell's temperature (T_{cell}).

$$U_{tn} = \frac{\Delta H_{T_{cell},R}}{n_e F} \tag{2.11}$$

At standard conditions (298 K and 1 bar), the thermo-neutral potential is 1.481 V.

Figure 2.4 illustrates the cell's operating mode. As mentioned in Section 2.2.1, water electrolysis is impossible below the reversible potential. When the cell potential is lower than the U_{tn}, the cell consumes heat, meaning that it is in an endothermic state; thus, the gas outlet temperature will be lower than the inlet temperature. On the contrary, when the cell potential exceeds the U_{tn}, the cell reaches an exothermic state where it generates heat, causing an increase in outlet stream temperature.

2.2.6 Cell Efficiency

The cell efficiency (η_{cell}) is expressed as the ratio of the energy content of the hydrogen gas produced to the electrical power applied to the cell. The energy content of hydrogen gas is represented by its lower (LHV) and higher (HHV) heating value, which corresponds to the enthalpy of formation difference between the reactants and the products (ΔH_R) . Therefore, the cell efficiency is determined using Eq. 2.12, [133].

$$\eta_{cell} = \frac{\dot{n}_{H_2} \cdot LHV}{W_{el}} = \frac{(j \cdot A)/(n_e \cdot F) \cdot \Delta H_R}{U_{cell} \cdot j \cdot A} = \frac{\Delta H_R/(n_e \cdot F)}{U_{cell}} = \frac{U_{tn}}{U_{cell}} \tag{2.12}$$

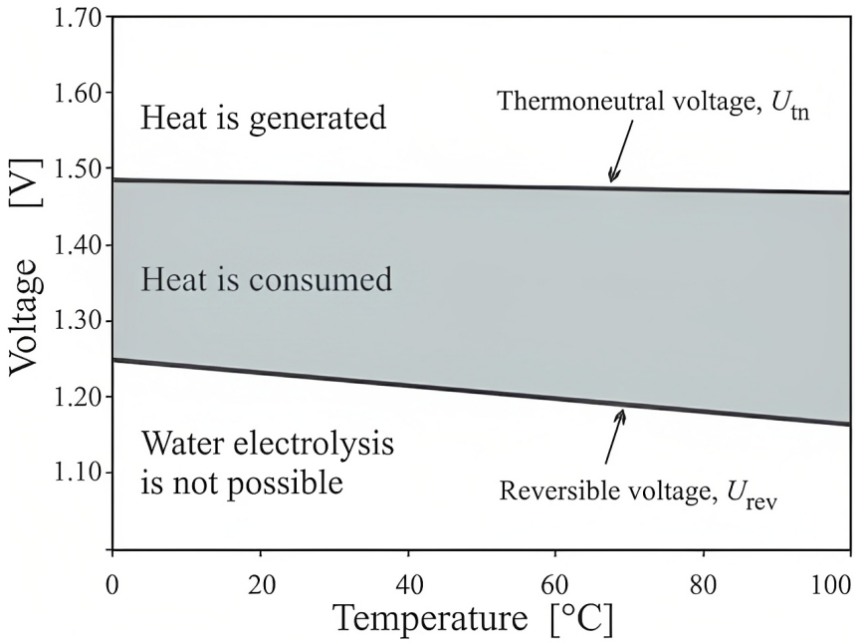

Figure 2.4: Schematic representation of the operating mode of the electrolysis cell between the reversible and the thermo-neutral potential, reprinted from [132].

3 Model Development

This section presents an electrochemical model for the molten carbonate electrolyzer, based on electrochemical knowledge and material and energy balances, built within the Aspen Custom Modeler (ACM) software. This model was applied to two different scenarios. The first model corresponding to Scenario I is composed of the electrolysis of H_2O, which is the source of H_2 production, and the chemical reaction "RWGS", which is the source of CO production. Whereas, in the second model corresponding to Scenario II, the H_2O and CO_2 co-electrolysis was considered to produce H_2 and CO in parallel with the chemical reaction "RWGS". The purpose of both models is to determine the outlet temperature and the cell's potential, taking into account the overpotential losses.

3.1 Material Balance

The electrochemical reactions involved in the molten carbonate electrolysis cell are the reduction of H_2O with the help of CO_2 at the cathode electrode side and the oxidation of the carbonate ions (CO_3^{2-}) at the anode electrode side, as presented in Eqs. 2.13 and 2.14, respectively. CO_2 inlet at the cathode side is essential for producing carbonate ions, thus preventing cell degradation caused by carbonate-based electrolyte loss. According to the study of Bove et al. (2021) [134], it was reported that a low CO_2 cathode feed could substantially affect the electrochemistry of the cell.

$$H_2O + CO_2 + 2\,e^- \longrightarrow H_2 + CO_3^{2-} \tag{2.13}$$

$$CO_3^{2-} \longrightarrow \frac{1}{2}\,O_2 + CO_2 + 2\,e^- \tag{2.14}$$

Many studies were carried out on the possibility of the electrochemical conversion of CO_2 into CO, as presented previously in the literature, through the following reaction in Eq. 2.15:

$$2\,CO_2 + 2\,e^- \longrightarrow CO + CO_3^{2-} \tag{2.15}$$

Moreover, carbon monoxide can be chemically produced via reverse water gas shift "RWGS" in Eq. 2.16.

$$CO_2 + H_2 \longrightarrow CO + H_2O \tag{2.16}$$

Figure 2.5 illustrates the operation of the molten carbonate electrolyzer between the fuel and the oxygen electrode to produce H_2 and CO at the fuel electrode and CO_2 and O_2 at the oxygen one.

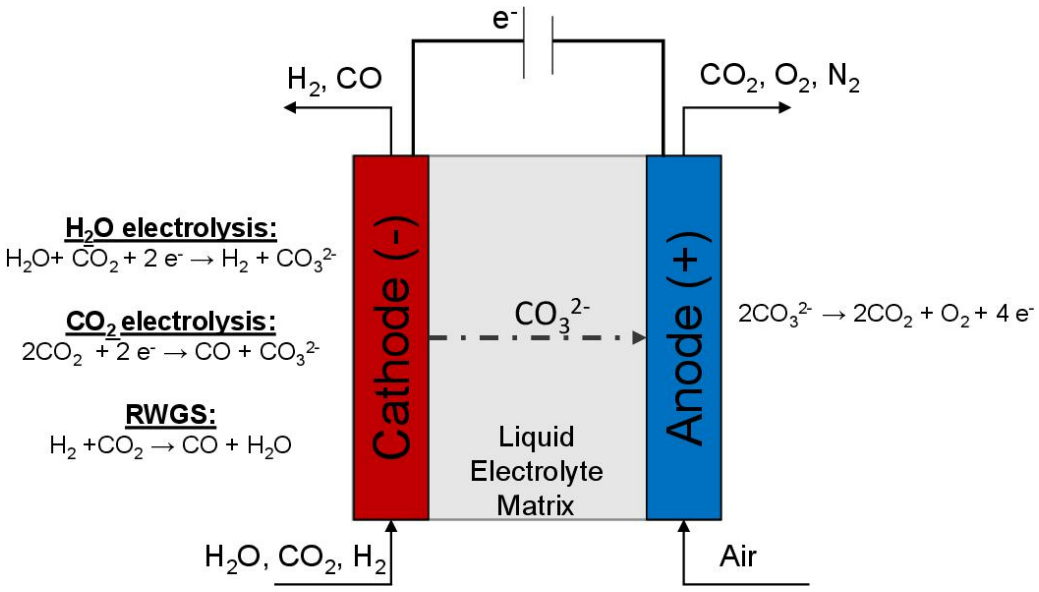

Figure 2.5: Schema of the operation mode of the MCEC.

3.1.1 H_2O electrolysis: Scenario I

For this scenario, the global electrochemical reaction between both electrodes is represented in Eq. 2.17. This reaction is in charge of producing hydrogen gas. The carbon monoxide is produced via the RWGS reaction (Eq. 2.16).

$$H_2O + CO_{2\,\text{(fuel–electrode)}} \longrightarrow H_2 + CO_{2\,\text{(oxygen–electrode)}} + \frac{1}{2}\,O_2 \tag{2.17}$$

The material balance is performed at the exit of the fuel and oxygen electrodes, aiming to determine the mole quantity of species formed from the reactions presented in Eqs. 2.16 and 2.17, which are involved in this case. Then, based on the mole transfer inside the cell presented in Figure 2.6, the material balance is determined, described in detail in Table 2.1, where $\dot{n}_{H_2}$ refers to the mole transferred by H_2O electrolysis and $\dot{n}_{CO}$ to the mole transferred by the RWGS chemical reaction.

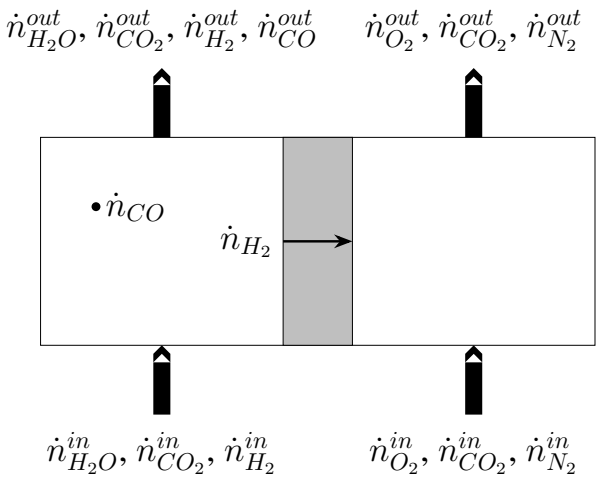

Figure 2.6: Schematic representation of the mole transfer in the molten carbonate electrolyzer for Scenario I.

Fuel Electrode (Cathode)	$\dot{n}^{out}_{H_2O} = \dot{n}^{in}_{H_2O} - \dot{n}_{H_2} + \dot{n}_{CO}$ $\dot{n}^{out}_{CO_2} = \dot{n}^{in}_{CO_2} - \dot{n}_{H_2} - \dot{n}_{CO}$ $\dot{n}^{out}_{H_2} = \dot{n}^{in}_{H_2} + \dot{n}_{H_2} - \dot{n}_{CO}$ $\dot{n}^{out}_{CO} = \dot{n}^{in}_{CO} + \dot{n}_{CO}$
Oxygen Electrode (Anode)	$\dot{n}^{out}_{CO_2} = \dot{n}^{in}_{CO_2} + \dot{n}_{H_2}$ $\dot{n}^{out}_{O_2} = \dot{n}^{in}_{O_2} + 0.5 \times \dot{n}_{H_2}$ $\dot{n}^{out}_{N_2} = \dot{n}^{in}_{N_2}$

Table 2.1: Material balance at both electrodes for Scenario I.

This balance requires the amount of the H_2O reacted electrochemically to produce H_2 ($\dot{n}_{H_2}$) at the fuel electrode and the amount of CO_2 and O_2 formed at the oxygen electrode. This amount is calculated by Faraday's Law, according to Eq. 2.10. It is worth noting that steam electrolysis cannot occur in a molten carbonate electrolyte without the presence of CO_2, as shown in Eq. 2.13. Therefore, the amount of CO_2 consumed to be transformed electrochemically into carbonate ions CO_3^{2-} is equal to that of the reacted H_2O ($\dot{n}_{H_2}$).

The amount of CO_2 reacted chemically to produce CO ($\dot{n}_{CO}$) is determined from the equilibrium constant of the RWGS reaction ($K_{eq,\ RWGS}$). The equilibrium constant can be calculated using Eq. 2.18. Therefore, the amount $\dot{n}_{CO}$ can be calculated according to Eq. 2.19 since the equilibrium constant of the reaction corresponds to the product partial pressures' ratio to that of the reactants at the equilibrium state.

$$\Delta G^{\circ} = -RT \ln K_{eq} \tag{2.18}$$

$$K_{eq,\ RWGS} = \frac{P_{CO} \cdot P_{H_2O}}{P_{CO_2} \cdot P_{H_2}} \tag{2.19}$$

The free energy required to determine the equilibrium constant K_{eq} is calculated using data and equations from the NIST Webbook [135]. The free energy equation as a function of x equivalent to the temperature T in Kelvin K divided by 1,000 as reported in NIST Webbook [135], is shown in Eq. 2.20. In addition, the equation coefficients are presented in Table A.1 of Appendix A.

$$\Delta G^{\circ} = A + Bx \ln x + Cx + Dx^2 + Ex^3 + Fx^4 + G/x \tag{2.20}$$

3.1.2 Co-electrolysis: Scenario II

In this case, material balance is performed while considering the additional reaction that was not taken into account in Scenario I, which is the CO_2 electrolysis in Eq. 2.15. Consequently, the new material balance is based on the global electrochemical reaction in Eq. 2.18 and the chemical reaction in Eq. 2.16.

$$H_2O + 3\,CO_{2\ \text{(fuel–electrode)}} \longrightarrow H_2 + CO + 2\,CO_{2\ \text{(oxygen–electrode)}} + O_2 \tag{2.21}$$

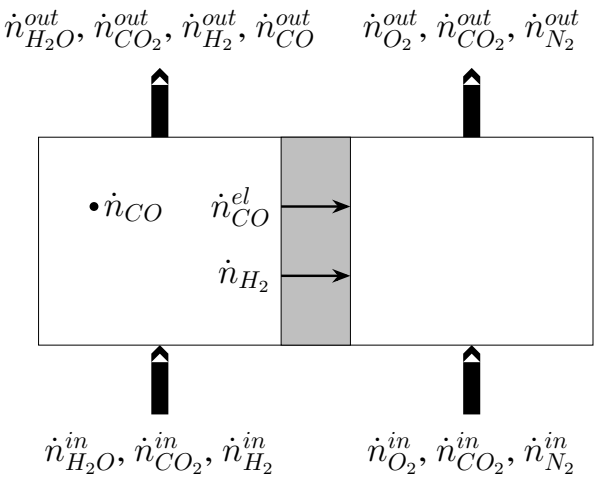

Figure 2.7: Schematic representation of the mole transfer in the molten carbonate electrolyzer for Scenario II.

Figure 2.7 presents the mole transfer inside the cell during co-electrolysis. It includes the moles transferred by the H_2O electrolysis ($\dot{n}_{H_2}$), the CO_2 electrolysis ($\dot{n}^{el}_{CO}$), and the RWGS chemical reaction ($\dot{n}_{CO}$). According to this mole transfer, the detailed material balance is conducted and presented in Table 2.2.

In this balance, the new variable $\dot{n}^{el}_{CO}$ is the amount of CO_2 consumed by the CO_2 electrolysis (Eq. 2.15). In the model of H_2O electrolysis, the applied current is utilized to produce H_2. However, for the co-electrolysis model with two electrolysis reactions, it is assumed that the global current density is split between H_2O and CO_2 electrolysis using: Eqs. 2.22 and 2.23 [136]. While this assumption serves

Fuel Electrode (Cathode)	$\dot{n}^{out}_{H_2O} = \dot{n}^{in}_{H_2O} - \dot{n}_{H_2} + \dot{n}_{CO}$ $\dot{n}^{out}_{CO_2} = \dot{n}^{in}_{CO_2} - \dot{n}_{H_2} - 2 \times \dot{n}^{el}_{CO} - \dot{n}_{CO}$ $\dot{n}^{out}_{H_2} = \dot{n}^{in}_{H_2} + \dot{n}_{H_2} - \dot{n}_{CO}$ $\dot{n}^{out}_{CO} = \dot{n}^{in}_{CO} + \dot{n}^{el}_{CO} + \dot{n}_{CO}$
Oxygen Electrode (Anode)	$\dot{n}^{out}_{CO_2} = \dot{n}^{in}_{CO_2} + \dot{n}_{H_2} + \dot{n}^{el}_{CO}$ $\dot{n}^{out}_{O_2} = \dot{n}^{in}_{O_2} + 0.5 \times \dot{n}_{H_2} + 0.5 \times \dot{n}^{el}_{CO}$ $\dot{n}^{out}_{N_2} = \dot{n}^{in}_{N_2}$

Table 2.2: Material Balance at both electrodes for Scenario II.

as an initial and fundamental approach to investigate co-electrolysis reactions, it's imperative to adopt a more comprehensive and intricate method to describe the co-electrolysis process within the MCEC electrolyzer accurately.

$$j_{H_2O} = \beta \cdot j \tag{2.22}$$

$$j_{CO_2} = (1 - \beta) \cdot j \tag{2.23}$$

The parameter β refers to the distribution of the active electrode sites between both H_2O and CO_2 electrolysis reactions [136]. It is defined as the ratio of inlet H_2O (Y^{in}_{H2O}) and CO_2 (Y^{in}_{CO2}) at the electrode interface (Eq. 2.24).

$$\beta = \frac{Y^{in}_{H2O}}{Y^{in}_{H2O} + Y^{in}_{CO2}} \tag{2.24}$$

Based on the current split assumption, $\dot{n}_{H_2}$ and $\dot{n}^{el}_{CO}$ can be calculated by applying Faraday's Law, according to the Eqs. 2.25 and 2.26, respectively.

$$\dot{n}_{H_2} = \frac{\beta \cdot j \cdot S}{n_e \cdot F} \tag{2.25}$$

$$\dot{n}^{el}_{CO} = \frac{(1 - \beta) \cdot j \cdot S}{n_e \cdot F} \tag{2.26}$$

According to the stoichiometric coefficient of the co-electrolysis reaction in Eq. 2.21, carbon dioxide CO_2 is the limiting reactant, meaning it is the first to be consumed. At these conditions, the reactions are ceased due to reactant blockage at the electrode surface, and the corresponding current density is called "limiting current density" [137]. Figure 2.8 illustrates the polarization curve, indicating the cell potential state at three essential current densities. The limiting current density is calculated using Eq. 2.27.

$$j_{limit} = \frac{-(2 \cdot F \cdot \dot{n}^{in}_{CO_2})}{((2-\beta) \cdot S \cdot 3.6 \times 10^4)} \tag{2.27}$$

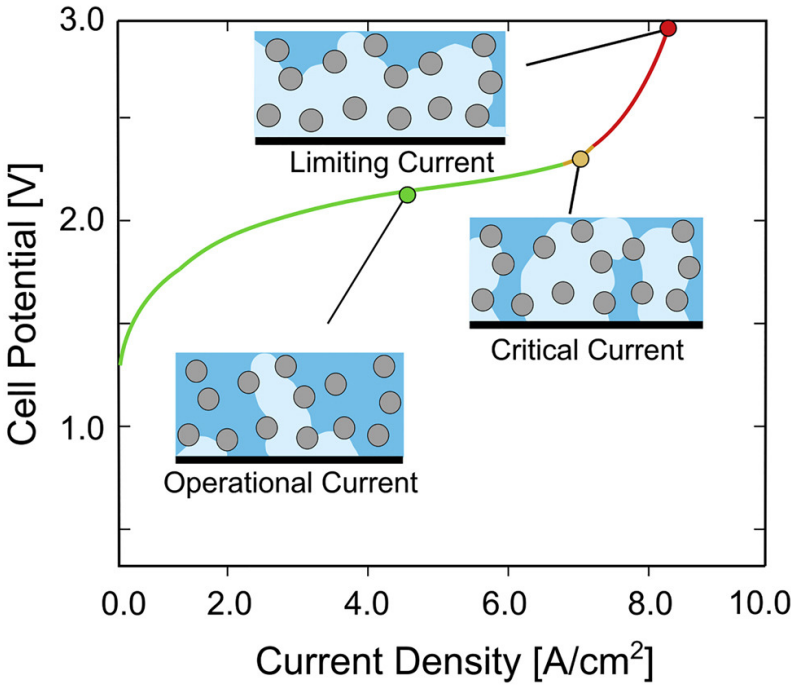

Figure 2.8: Schematic illustration of the three essential current densities in the electrolysis operation, reprinted from [137].

If the limiting state is reached, the material balance is carried out based on the value of β. If β > 0.5, there is more H_2O than CO_2 in the inlet gas feed. In this case, it is assumed that the H_2O electrolysis is prioritized over the CO_2 electrolysis. Thus, CO_2 is first consumed by the reaction in Eq. 2.13 and then by the CO_2 electrolysis. On the other hand, a value of β < 0.5 corresponds to the reverse case, where more CO_2 enters the cell than H_2O. Therefore, CO_2 electrolysis occurs first, followed by H_2O electrolysis.

3.2 Electrochemical Model

The electrochemical model is performed to determine the cell potential and power. The cell potential (U_{cell}) in Eq. 2.28 is an essential parameter in the electrochemical process. It is a function of the operating conditions, temperature, gas composition, flow rate, and current density (j). It consists of three terms: a reversible potential U_{rev}, which depends on both temperature and partial pressures of the gas, and a term named Area Specific Resistance (ASR), representing the overpotential losses of the cell, as stated in Section 2.2.3.

$$U_{cell} = U_{rev} + j \cdot ASR(T) \tag{2.28}$$

The reversible potential U_{rev} is composed of the standard reversible potential U°_{rev} (Eq. 2.5) and a second term as a function of the partial pressure of gases in the cell. The standard reversible potential U°_{rev} is a function of the free energy ΔG° of the electrolysis reaction, which depends on the temperature. Therefore, U°_{rev} changes from Scenario I of H_2O electrolysis to Scenario II of co-electrolysis.

For Scenario I, the standard reversible potential $U^{\circ}_{rev,\,I}$ is determined using Eq. 2.29, where the free energy $\Delta G^{\circ}_{H_2O}$ refers to the H_2O electrolysis reaction in Eq. 2.17. The free energy $\Delta G^{\circ}_{H_2O}$ is derived using Eq. 2.20. However, for Scenario II, the standard reversible potential $U^{\circ}_{rev,\,II}$ in Eq. 2.30 depends on two free energies: $\Delta G^{\circ}_{H_2O}$ applying the reaction in Eq. 2.17 and $\Delta G^{\circ}_{CO_2}$ using the global reaction of Eq. 2.14 and Eq. 2.15. The free energy equation's coefficients for H_2O electrolysis and CO_2 electrolysis are illustrated in Tables A.2 and A.3 of Appendix A, respectively.

$$U^{\circ}_{rev,\,I} = \frac{\Delta G^{\circ}_{H_2O}}{n_e F} \tag{2.29}$$

$$U^{\circ}_{rev,\,II} = \frac{\Delta G^{\circ}_{H_2O} + \Delta G^{\circ}_{CO_2}}{n_e F} \tag{2.30}$$

Concerning the term of U_{rev}, it also changes between the two scenarios similarly to U°_{rev}. For Scenario I, the U_{rev} is represented in Eq. 2.31, and, for Scenario II, in Eq. 2.32.

$$U_{rev,I} = U^{\circ}_{rev,I} - \frac{RT_{cell}}{n_e F} \ln\left(\frac{P_{H_2O}}{P_{H_2} \cdot P_{O_2}^{1/2}} \cdot \frac{P_{CO_2,\,fe}}{P_{CO_2,\,oe}} \cdot (P^{\circ})^{1/2}\right) \tag{2.31}$$

$$U_{rev,II} = U^{\circ}_{rev,II} - \frac{RT_{cell}}{n_e F} \ln\left(\frac{P_{H_2O}}{P_{H_2} \cdot P_{CO} P_{O_2}} \cdot \frac{P^3_{CO_2,\,fe}}{P^2_{CO_2,\,oe}} \cdot P^{\circ}\right) \tag{2.32}$$

The overpotential equations (η_{act}, η_{ohm}, η_{conc}) require detailed experimental data that is unavailable in this work. Consequently, a grey-box model, derived from experimental data performed on a solid oxide electrolysis cell by Fu et al. (2010) [129], is adapted to this work because it provides accurate results. Besides, this exponential form model was used by several authors with different coefficients based on their experimental data ([54], [55], and [138]). Therefore, the overpotential losses, in this work, are calculated by the ASR equation below (Eq. 2.33).

$$ASR(T_{cell}) = \phi_0 \cdot exp\left(\frac{4900}{T_{cell}} - 5.95\right) + \varepsilon \tag{2.33}$$

In this work, the ASR exponential term multiplied by a coefficient ϕ_0 equal to 1 $\Omega{\cdot}cm^2$ is considered and corrected by a factor ε ($\Omega{\cdot}cm^2$), which symbolizes the adjustment related to the difference in electrode-based catalyst and cell materials between the SOEC and MCEC. The correction factor ε is calculated based on the current density versus cell potential graph in Figure 2.9, supplied from the experimental work performed at the Chimie ParisTech [124], as part of the ANR project.

The experimental graph in Figure 2.9 is composed of four curves, where the thin curves correspond to the current-voltage profile, and the thick ones represent the cell power trend with the current density at the start-up of the cell (the red one), and after 1630 operating hours (the green one). In our case, the model is performed at the steady state; therefore, the experimental data is extracted from the thin red curve. This curve generates a linear regression equation of the form $y = ax + b$. The slope value "a" represents the ASR value. Accordingly, the factor ε is calculated by a simple subtraction phenomenon between the value a and the first term of the ASR equation ($\phi_0 \cdot exp\left(\frac{4900}{T_{cell}}\right)$) value, adapted from Fu et al. (2012) [129].

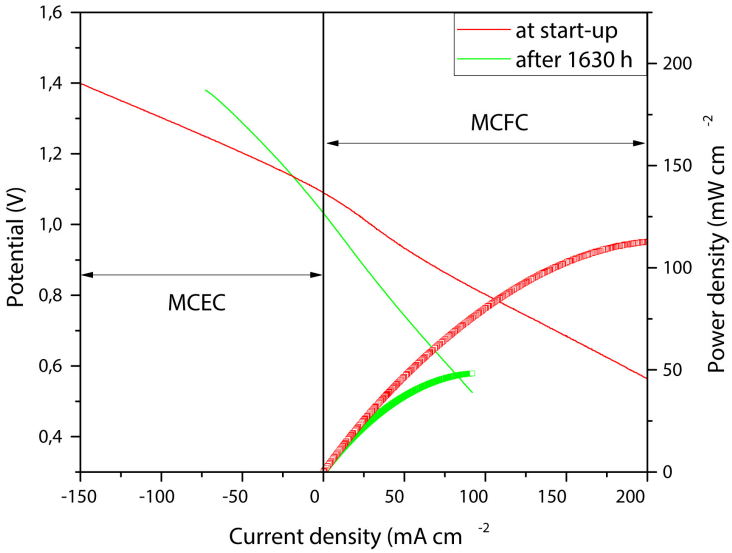

Figure 2.9: Cell potential versus current density curve supplied from the experimental data [124].

3.3 Energy Balance

An energy balance is essential to complete the model, enabling the calculation of the cell's outlet temperature on both sides. In the context of water electrolysis in an electrolyzer, the energy balance is determined by referencing Eq. 2.34 from the literature [55, 139]. This balance considers the thermal contribution of the reaction's enthalpy and the cell's power consumption.

$$\dot{Q}_{in} + \dot{W}_{el,\ MCEC} - \dot{n}_{H2,\ prod} \cdot \Delta H_r = \dot{Q}_{out} \tag{2.34}$$

Based on the first law of thermodynamics and Eq. 2.34, the energy transfer within the MCEC open system is applied, taking into consideration the thermal enthalpy associated with all reactions involved, denoted as $\dot{Q}_{reaction}$, as illustrated in Figure 2.10. This demonstration allows for generating the energy balance in Eq. 2.35.

Figure 2.10: Schematic representation of the energy transfer of the MCEC open system.

$$\dot{Q}_{in} + \dot{W}_{el,\ MCEC} + \dot{Q}_{reaction} = \dot{Q}_{out} \tag{2.35}$$

The input energy in the MCEC system is the gas inlet heat flow ($\dot{Q}_{in}$), and the outlet energy is the gas outlet heat flow ($\dot{Q}_{out}$). They are determined by Eq. 2.36, where k corresponds to in and out. The equation corresponds to the sum of the molar flow rate of each gas ($\dot{n}_i^k$) multiplied by its heat capacity (C_p^i) and the temperature (T_k). The heat capacity C_p^i in kJ/(mol·K) is calculated using data from NIST Webbook [135] at the average temperature T_{av} between the inlet and the outlet temperature of the cell.

$$Q_k = \sum_i \dot{n}_k^i \cdot C_p^i \cdot T_k \tag{2.36}$$

$\dot{W}_{el,MCEC}$ in kW is the electric power consumed by the cell and is determined by multiplying the cell's potential (U_{cell}) by the current density (j), the cell's active surface area (A), and the number of cells in the MCEC system (N_{cells}), as presented in Eq. 2.37.

$$\dot{W}_{el,\ MCEC} = N_{cells} \cdot U_{cell} \cdot j \cdot A \tag{2.37}$$

Finally, $\dot{Q}_{reaction}$ represents the heat of reactions occurring in the cell. This term varies from Scenario I to Scenario II because of the different reactions between the scenarios. For Scenario I, the $\dot{Q}_{reaction}$ is determined using two reactions: the H_2O electrolysis and the RWGS reaction, as shown in Eq. 2.38. The heat required for H_2O electrolysis depends on the amount of H_2 produced ($\dot{n}_{H_2,\ produced}$), and the reaction's heat enthalpy of formation (ΔH_{H_2O}). In contrast, for Scenario II, the H_2O and the CO_2 electrolysis and the RWGS reaction are involved in the $\dot{Q}_{reaction}$, as presented in Eq. 2.39. In this case, the CO_2 electrolysis's heat of reaction is a function of the amount of CO produced by CO_2 electrolysis ($\dot{n}^{el}_{CO,\ produced}$) and the heat enthalpy of formation (ΔH_{CO_2}). For the RWGS reaction, the reaction's heat is determined by the amount of CO produced ($\dot{n}^{RWGS}_{CO,\ produced}$) and RWGS heat enthalpy of formation (ΔH_{RWGS}).

$$\dot{Q}_{reaction} = -\dot{n}_{H_2,\ produced} \cdot \Delta H_{H_2O} - \dot{n}^{RWGS}_{CO,\ produced} \cdot \Delta H_{RWGS} \tag{2.38}$$

$$\begin{aligned} \dot{Q}_{reaction} = &- \dot{n}_{H_2,\ produced} \cdot \Delta H_{H_2O} - \dot{n}^{el}_{CO,\ produced} \cdot \Delta H_{CO_2} \\ &- \dot{n}^{RWGS}_{CO,\ produced} \cdot \Delta H_{RWGS} \end{aligned} \tag{2.39}$$

4 Results of the Model: Validation and Discussion

After setting up the model, it was validated by comparing it with the results obtained from experimental work. Following this, the effect of current density on the voltage, power, output composition, and output temperature of the cell flux was investigated. Besides, a sensitivity analysis was conducted to study the optimal operating conditions required for high cell performance and productivity. In this part, the experimental work is firstly presented in Section 4.1. Then, Section 4.2 is dedicated to illustrating the model validation results, and Section 4.3 provides a comparison of the model results for both scenarios: Scenario I (H_2O electrolysis) and Scenario II (H_2O and CO_2 co-electrolysis). Finally, Section 4.4 presents the outcomes of the parametric study conducted to investigate the impact of the inlet composition of the cell on the cell potential and the syngas production.

4.1 Experimental Work

This work was carried out in collaboration with the ANR project partner, the Chimie ParisTech, during Ersan Gürbüz's Ph.D. studies [140]. In this work, the MCFC/MCEC cell was implemented on a complete test bench coupled to a gas chromatography (GC) apparatus. The cell, developed by Fiaxell, includes current collectors (gold grids), the electrodes (Ni-based fuel electrode and NiO oxygen electrode, with a diameter of 2 cm and approximately 0.05 cm thickness, provided by the Korea Institute of Science and Technology), the matrix ($\gamma-LiAlO_2$, with a diameter of 3.6 cm and approximately 0.05 cm thickness) and the electrolyte sheet (Li-K or Li-Na, with a diameter of 3.6 cm and approximately 1.5 mm total

thickness). This stack assembly was then compressed between two alumina tubes terminated with metal plates. Each alumina tube allows gas inlet, gas outlet, and temperature control via a thermocouple. Figure 2.11 provides a photograph of the complete experimental bench.

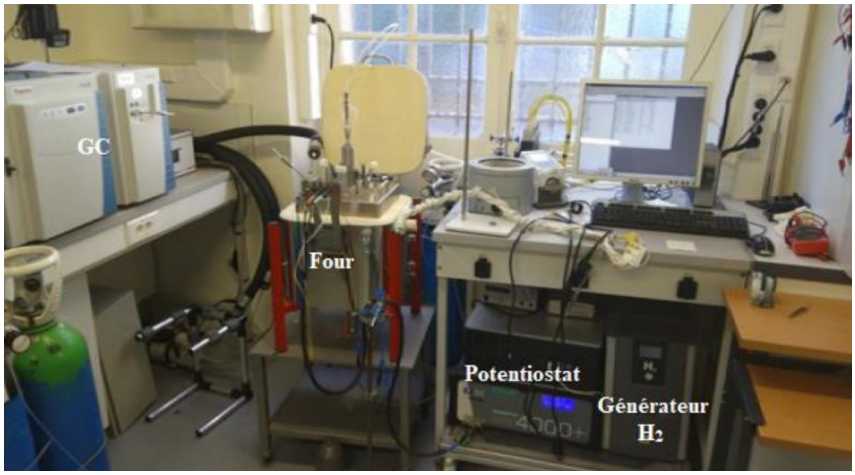

Figure 2.11: MCFC/MCEC test rig with GC, reprinted from [140].

A gas inlet circuit equipped with 6 mass flow controllers (BROOKS 5800 Series), computer-controlled via an RS485 protocol, is located upstream of the cell. CO_2, O_2, and N_2 are directly supplied from gas cylinders (Air Liquide), while hydrogen gas is obtained from an HK-250-EU LNI-Swissgas generator, and water is obtained by bubbling through a temperature-controlled flask. The coupling with GC has been specifically developed for this application, with a gas evacuation system that enables the investigation of both inlet and outlet gases on the H_2 or O_2 side. A schematic of the coupled assembly can be found in Figure 2.12.

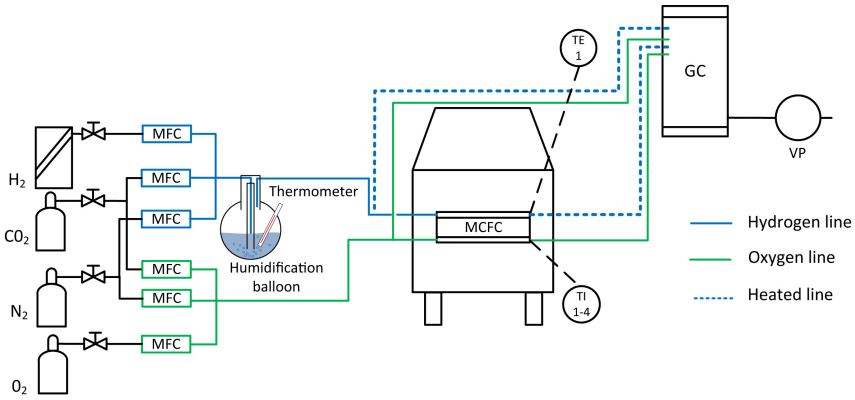

Figure 2.12: Gas and water supply scheme of complete cell testing system, reprinted from [124].

The GC used is a Trace 1310 device from Thermo Fisher Scientific, specifically adapted to the MCFC/MCEC application, as schematized in Figure 2.13. The GC comprises two columns (RESTEK) within an auxiliary Trace 1310 furnace at a temperature of 90 °C and two bypass valves labeled V1 and V2 (VICI) in the diagram. This instrument is computer-controlled using Chromeleon 7.2.8 software, which controls the multiport valve and programs the position of V1 and V2. Once the sampling command is initiated for the selected position (1, 2, 3, or 4), the vacuum pump removes all unwanted material between

the multiport valve and V1, eliminating them from the analysis system. Then, the sample is taken, and V1 simultaneously changes position to send the sample to column 1. This column separates H_2, CO_2, CH_4, and H_2O from the mixture of N_2, O_2, and CO. The first column cannot thoroughly examine the remaining three gases at 90 °C. Therefore, they are sent to the second column, which can easily perform this task and separate N_2, O_2, and CO.

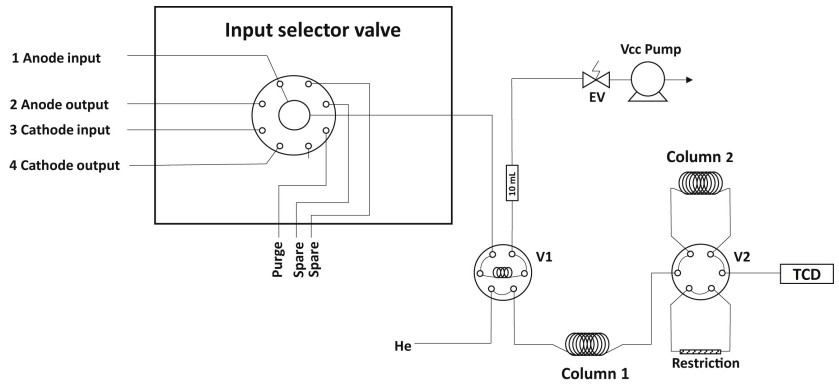

Figure 2.13: Scheme of Gas Chromatograph configuration-Experiment, reprinted from [140].

Once the MCFC/MCEC cell is assembled, it is subjected to pre-treatment due to the vaporization and combustion of organic solvents and polymers in the matrix and electrolyte. At the end of the pre-treatment, the system is stabilized in the study atmosphere, and measurements are performed. The single cell operates at 650 °C and atmospheric pressure, with the standard atmospheres. The standard atmosphere is $H_2/CO_2/H_2O$ (64/16/20%) at the fuel electrode (Ni cathode) and $O_2/CO_2/N_2$ (15/30/55%) at the oxygen electrode (NiO anode) in MCEC mode, and the reverse concerning the electrodes in MCFC mode. The total flow rates are 150 mL/min on each side.

4.2 Model Results

This study used the operating conditions of a single cell with laboratory module dimensions. The electrode's inlet compositions are that of the standard experimental conditions. The electrode's surface-active area is 3.14 cm^2. The input current density has been set to -150 mA/cm^2. This section presents the results of Scenario I, corresponding to the H_2O electrolysis.

4.2.1 Cell Potential and Power

The polarization curve depicts the cell's voltage output for a specific current density. Figure 2.14 presents the polarization curve generated by the model for the MCEC/MCFC cell in electrolysis and fuel cell modes and the one obtained experimentally. The negative current densities correspond to the electrolysis mode, and the positive ones correspond to the fuel cell mode. During electrolysis mode, the cell potential increases with the current density. This observation justifies the overpotential losses' impact on the cell potential. Since electrolysis requires electrical input, overpotential losses increase electrical demand to compensate for these losses, causing a higher cell potential.

The results showed a satisfactory agreement with the experimental ones, with an average error of around 2.6% (Figure 2.9). Besides, the model was validated by the experimental results of Perez et al.

[126] at different inlet compositions. The results are consistent, with an average error of 1% for 50/25/25% $H_2O/CO_2/H_2$ inlet gas mixture composition and a 4% for 25/50/25% $H_2O/CO_2/H_2$ composition.

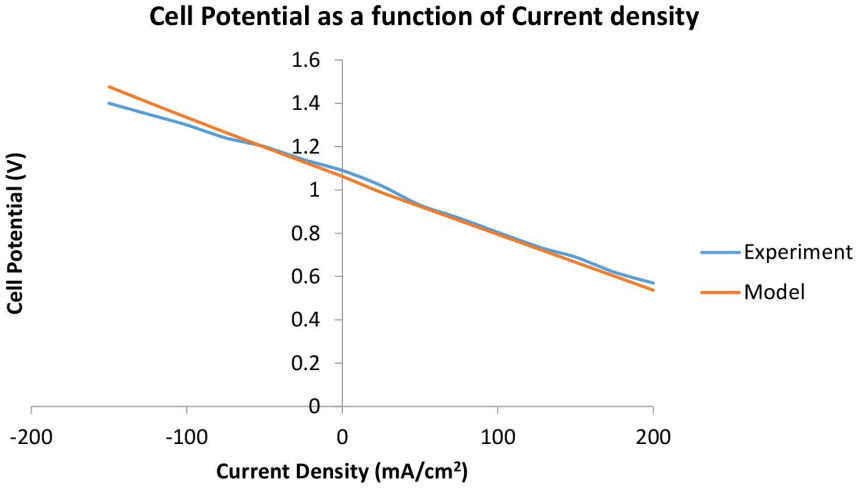

Figure 2.14: Comparison of model results with those determined experimentally: electrolyzer mode (left) and fuel cell mode (right).

The electrical power and the cell's potential are crucial parameters in studying its performance. Thus, the effect of the current density on the cell power was also examined, and the results are presented in Figure 2.15. In this manner, better comprehension could be achieved regarding the operating current density and the number of cells required to store a specific amount of renewable energy. In the graph, the negative power values during electrolysis represent power consumption, whereas positive values reflect power generation in fuel cell mode. In the electrolysis mode, the power consumption increases as the current density increases. Similarly, the power generation increases with the current density in the fuel cell mode.

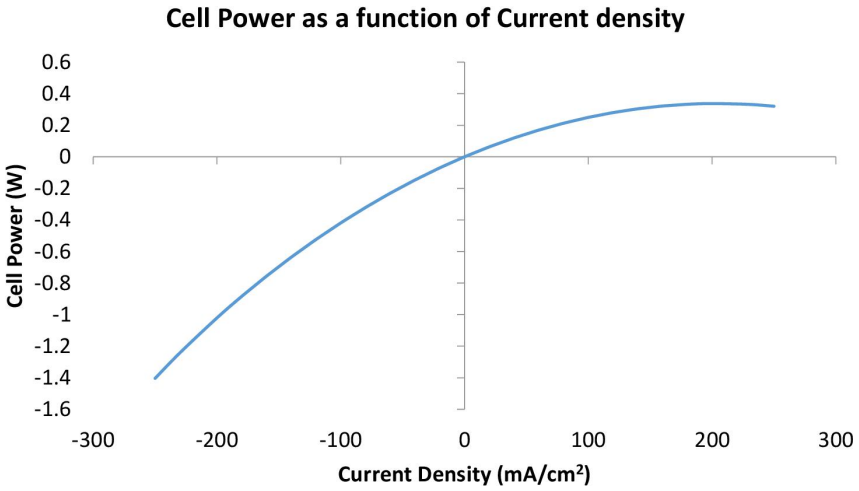

Figure 2.15: Electrical power of the cell as a function of the current density in electrolysis and fuel modes.

4.2.2 Cell's Outlet Gas Temperature

The energy balance aims to calculate the outlet temperature of the cell. The effect of the cell operation on the outlet temperature is crucial since the MCEC working temperature is already high, at 650 °C. Therefore, the temperature is a critical parameter for avoiding mechanical instability and electrolyte loss through evaporation inside the cell. Figure 2.16 illustrates the cell's outlet temperature as a function of cell potential.

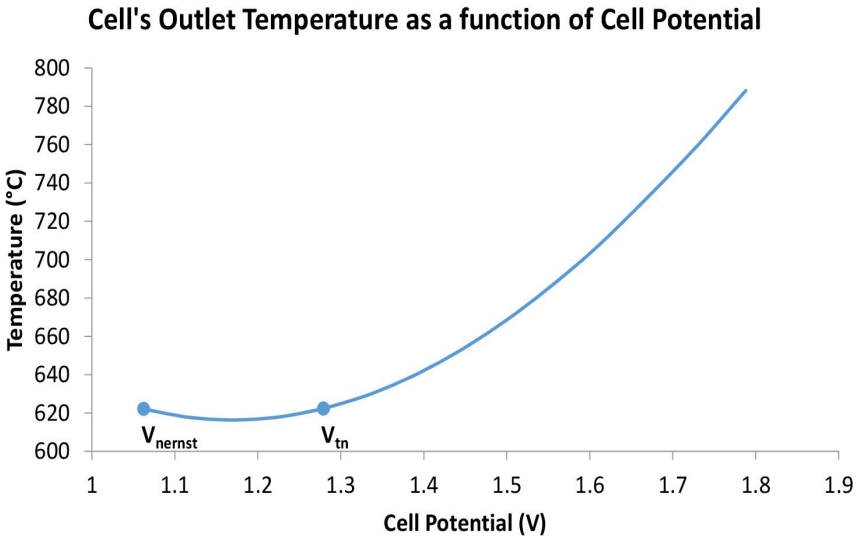

Figure 2.16: Effect of the cell potential on the outlet temperature of the cell streams during electrolysis mode.

The graph shows that the outlet temperature slightly declines with the increase in the cell potential to reach a minimum and then increases progressively, which agrees with the state-of-the-art [141]. The outlet temperature remains below the cell temperature during the operation between the Nernst and the thermo-neutral voltage. This result is due to the theoretical fact that the heat produced by electric heating is smaller than the heat required by the reaction, implying that the cell is in an endothermic state. When the electrolyzer's operation surpasses the thermo-neutral voltage, the outlet temperature increases since the heat produced by the electrical heating is higher than the heat required by the reaction, leading to an exothermic operation of the cell.

4.2.3 Cell's Outlet Gas Flow rates

The fuel electrode outlet stream comprises the products, CO, and H_2, and the remaining reactants, CO_2, and H_2O. At the same time, the oxygen electrode outlet stream contains CO_2, O_2, and N_2. Their outlet flow rates vary with current density and from electrolysis to fuel cell mode operations, as shown in Figures 2.17 and 2.18. This variation is linked to Faraday's Law, which determines the amount of H_2 produced during electrolysis or consumed during fuel cell mode.

In the electrolysis cell mode, the flow rate of H_2 at the fuel electrode increases with the current density, while that of H_2O and CO_2 decrease (Figure 2.17). At the oxygen electrode, the flow rates of O_2 and CO_2 increase when the current density increases (Figure 2.18). These outcomes confirm the operation mode

of the MCEC, based on the schema presented in Figure 2.5. On the other hand, the situation is reversed for the fuel cell mode.

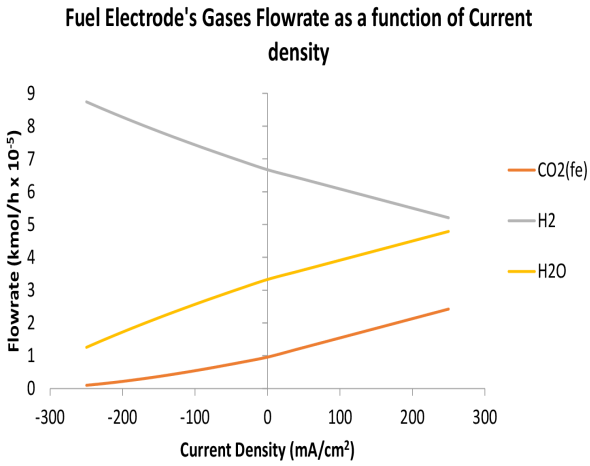

Figure 2.17: The effect of the current density on the H_2O, H_2, and CO_2 outlet molar flow rates at the fuel electrode during both electrolysis (left) and fuel cell (right) modes.

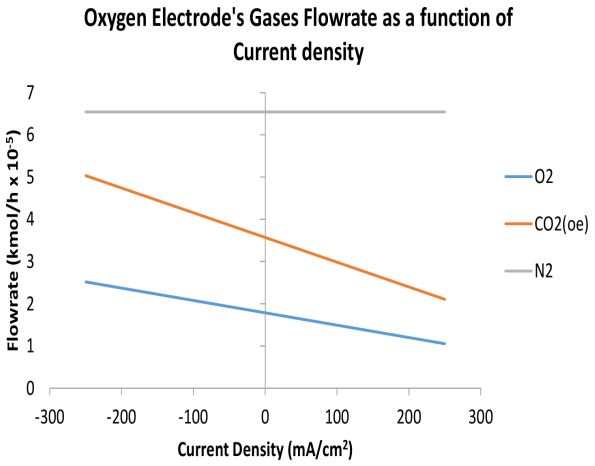

Figure 2.18: The effect of the current density on the O_2, CO_2, and N_2 outlet molar flow rates at the oxygen electrode during both electrolysis (left) and fuel cell (right) modes.

Concerning the outlet flow rate of CO, Figure 2.19 shows that it decreases with the increase in the current density. This result can be explained according to the dominance between the RWGS and electrochemical reactions. As the current density increases, the electrochemical reaction predominates the RWGS chemical reaction, causing a decrease in CO produced by the RWGS reaction since H_2O electrolysis rather than RWGS consumes carbon dioxide.

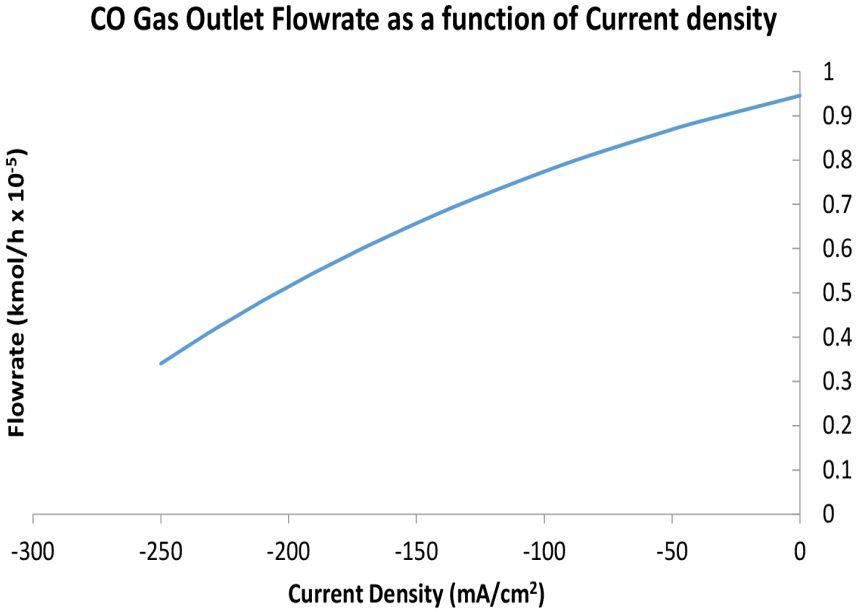

Figure 2.19: CO molar flow rate variation in the outlet stream of the fuel electrode with the current density during the electrolysis cell operation.

4.3 Comparison of two Models

The main conceptual difference between the two scenarios is the CO_2 electrolysis inside the cell. The presence of CO_2 electrolysis has changed its material and energy balance and the electrochemical model. In this work, an analysis was performed for Scenario II to investigate the impact of the current density on the cell potential, the cell's outlet composition, and the stream outlet temperature. The outcomes of this investigation were further compared with that of Scenario I.

	H_2O electrolysis	CO_2 electrolysis	RWGS
Scenario I	✓	✘	✓
Scenario II	✓	✓	✓

Table 2.3: The conditions of the two different scenarios.

4.3.1 The Trend of Outlet Gases Flow rates with the Current Density

The outlet flow rate of the gases, mainly H_2O, CO_2, H_2, and CO, change with the current density, as illustrated in Figure 2.20 for Scenario I and Figure 2.21 for Scenario II. Both graphs demonstrate that the outlet H_2 flow rate (gray line) increases while that of H_2O (yellow line) decreases, indicating that water is involved in hydrogen gas production. However, at high current densities, the outlet CO_2 flow rate (orange line) and the outlet CO flow rate (blue line) differ from Scenarios I to Scenario II. The intervention of CO_2 electrolysis can typically explain this difference.

In Scenario I, CO and CO_2 flow rates decrease with the increase in the current density. On the other hand, in Scenario II, the outlet CO flow rate (blue line) also declines with the increase in current density, with the same trend as that in Figure 2.20. However, at a specific current density of -200 mA/cm^2, which is the optimum point, the curve's trend change where the CO flow rate increases with the current density to become stable at the end. Parallel to this, the outlet CO_2 flow rate, represented by the orange line, decreases and then rapidly starts to fall at a current density of -200 mA/cm^2 to reach zero at the end.

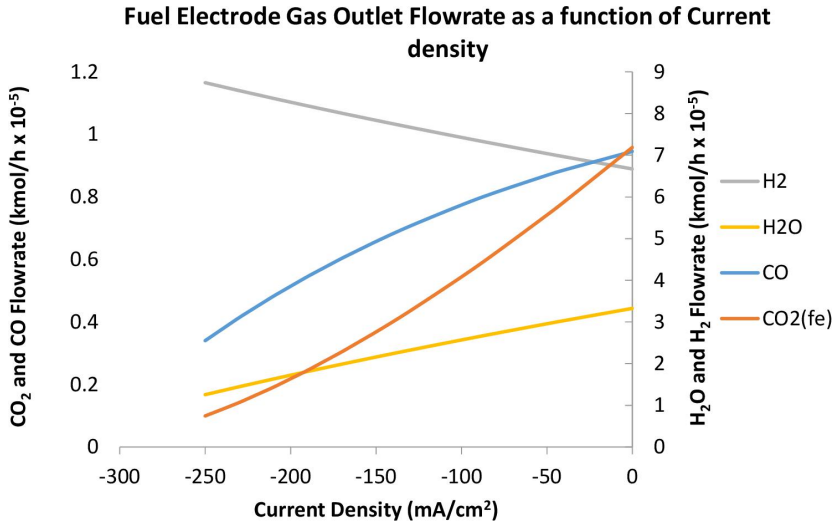

Figure 2.20: The variation of the outlet gas flowrate (kmol/h) with the current density (mA/cm^2) in Scenario I (H_2O electrolysis).

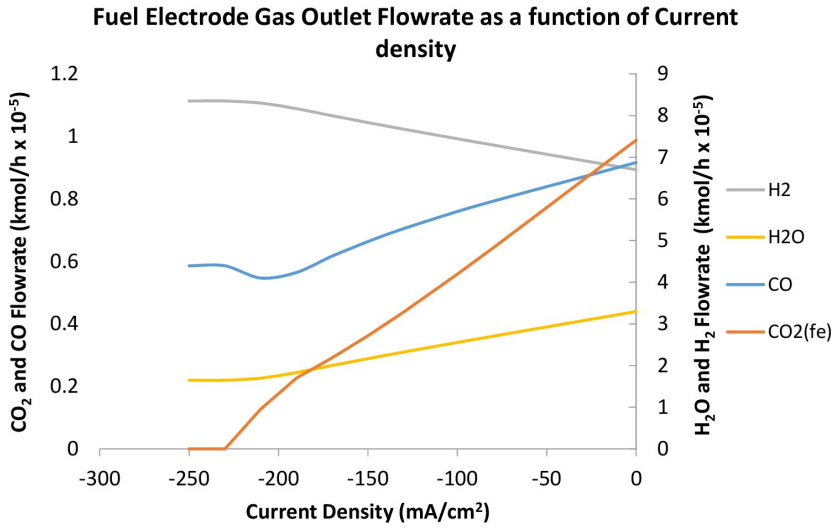

Figure 2.21: The variation of the outlet gas flowrate (kmol/h) with the current density (mA/cm^2) in Scenario II (co-electrolysis).

This divergence in these curves is better explained in Figure 2.22, which illustrates how the outlet CO flow rate trend is linked to the evolution of the CO_2 electrolysis and RWGS reactions. This curve enables to derive two distinct origins that define the cause of the variance. The first origin is related to the condition in which the RWGS equilibrium is not attained, indicating that the RWGS reaction is not taking place inside the cell. For example, Figure 2.22 reveals that at a current density of -200 mA/cm^2, the mole of CO generated by RWGS is zero, implying that RWGS does not occur. At this point, the CO_2 electrolysis process yields CO solely. This situation leads to a divergent increase in the outlet CO trend, which follows the increasing trend of CO_2 electrolysis. The second origin is the point at which the limiting current density is achieved, and all CO_2 is consumed. In Figure 2.21, the CO_2 flow rate curve shows that after a given current density (-230 mA/cm^2), the outlet CO_2 flowrate reaches zero, meaning that the CO_2 has been entirely consumed. At this point, the cell operates at the limiting current density of -230 mA/cm^2

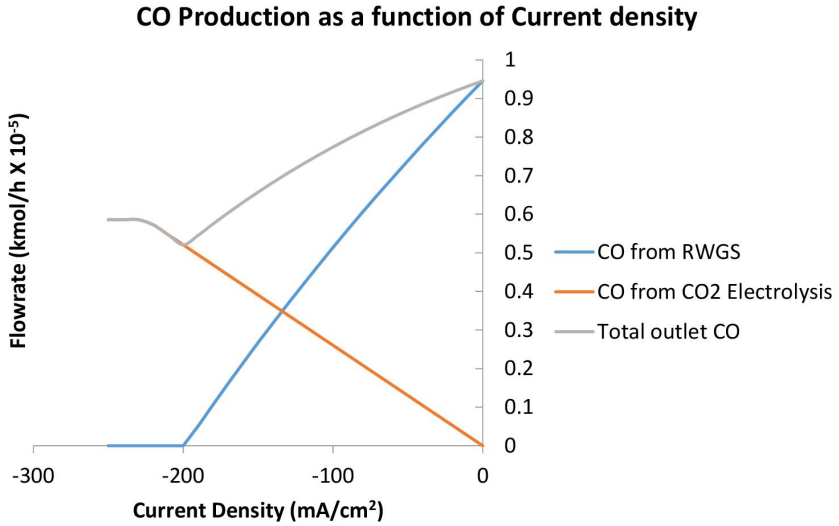

Figure 2.22: The flow rate of the outlet CO (gray curve), the CO produced by RWGS (blue curve), and the CO produced by CO_2 electrolysis (orange curve) as a function of the current density (mA/cm^2).

and cannot work at a current density above this. As a result, the curve becomes steady. This restriction is applied to the model to avoid exceeding the limiting current density. Therefore, it is assumed that if the operating current density is more than the calculated limiting current density, the model will use the limiting one.

4.3.2 Sensitivity Analysis on CO Composition: Limiting Current Density

To better evaluate the co-electrolysis of H_2O and CO_2, a sensitivity study was performed on the deviation point of the CO outlet composition with the change in the inlet gas of the cell. Recycling a portion of the fuel electrode's outlet gas back to the cell is necessary for thermal management and maintaining electrode stability by having a quantity of H_2 in the inlet feed stream [68]. This recycled stream contains CO, in addition to H_2, H_2O, and CO_2. For this reason, it is essential to understand how the inlet CO affects the point where the outlet CO composition deviates, presented in Figure 2.22. This study evaluated three cases of the fuel electrode's inlet gas compositions, shown in detail in Table 2.4.

	H_2O	CO_2	H_2	CO
Case I	52%	40%	8%	0%
Case II	52%	40%	7.14%	0.86%
Case III	52%	40%	6%	2%

Table 2.4: Cell's inlet gas compositions of the three studied cases.

From this study, it could be highlighted the evolution of the total CO outlet composition, illustrated in Figure 2.23, and the CO flow rate produced from RWGS, represented in Figure 2.24. These results provided insight into the deviation's changing point, as explained in Figure 2.22. Furthermore, from Figure 2.23, it can be revealed that the curve deviates at lower current densities with the increase in the inlet CO composition. For example, in Case I, where there is no inlet CO to the cell, the curve has an optimum point at a current density of -120 mA/cm^2 and reaches a steady state at a limiting current density of -150 mA/cm^2. On the contrary, in Case III, where the inlet gas contains 2% CO, the curve's optimum was obtained at a current density of -20 mA/cm^2 and the limiting current density of -110 mA/cm^2.

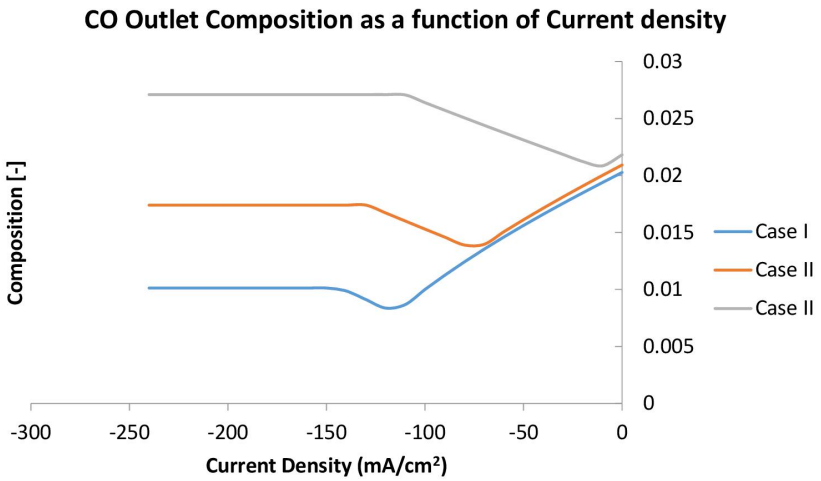

Figure 2.23: The CO outlet molar composition variation with the current density in the three cases.

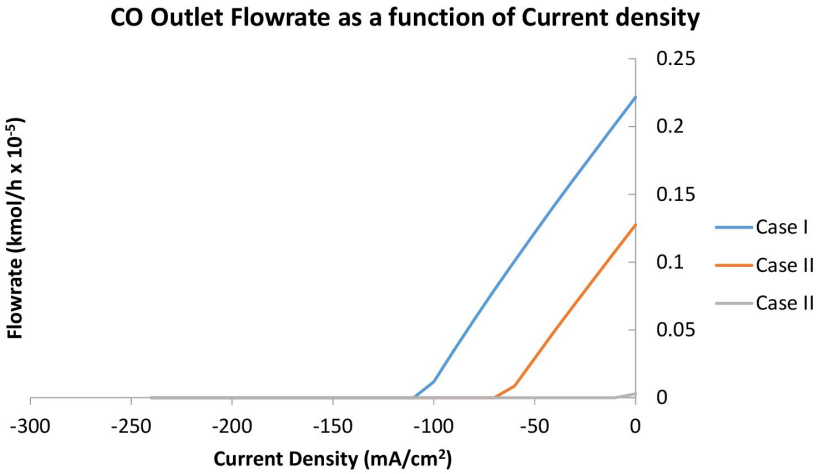

Figure 2.24: The variation of the CO flow rate produced from RWGS with the current density in the three cases.

As previously stated, the optimum point reveals that the RWGS reaction is not occurring at the electrode's interface. This observation is affirmed by examining the CO flow rate produced by RWGS in Figure 2.24, where at the optimum point in Figure 2.23, the CO flow rate becomes zero. After this point, the CO outlet composition increases due to the CO_2 electrolysis to CO. Furthermore, it could be noticed that the gap between the optimum point and the steady state one is broader in Case III at 2% CO inlet composition compared to other cases, which means that the CO production electrochemically is enhanced at a lower current density with the increase in CO inlet composition. However, this analysis could be altered if the equilibrium shift of RWGS is reversed after the optimum point, which could cause CO consumption by WGS reaction. Finally, based on this model's study, it could be revealed that the inlet gas composition alters the deviation in the CO and CO_2 outlet compositions due to the change in the RWGS equilibrium and the limiting current density in the function of these compositions.

4.3.3 The Trend of Cell Potential and Temperature with the Current Density

Apart from the material balance results, the cell potential and gas outlet temperature evolution were examined for the two scenarios. Since there is a link between the cell potential and the outlet gases within the Nernst equation, it is expected to be affected similarly to the gas composition in Scenario II. The cell potential evolution with the current density is comparable between Scenarios I and II till reaching the point of deviation explained previously. As shown in Figure 2.25, this circumstance results in a sharp increase in cell potential once the limiting current density is approaching since the low CO_2 reacting agent caused higher concentration losses, thus higher overpotentials.

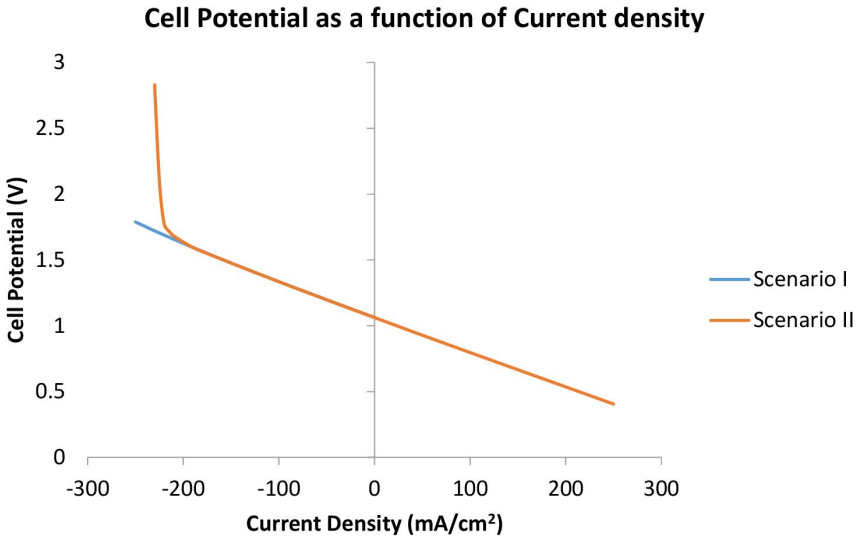

Figure 2.25: The variation of the cell potential with the current density (mA/cm^2) in electrolysis mode and fuel cell mode for both scenarios.

On the other hand, the outlet gas temperature is also influenced by its composition when applying the energy balance. So, by comparing the results of Scenario I in Figure 2.26 with that of Scenario II in Figure 2.27, it can be noticed that the temperature is similar till reaching the breakeven point of a current density of -190 mA/cm^2. However, the curve trend slightly deviates to higher temperatures in Scenario II after this point, then sharply increases from 850 °C (-225 mA/cm^2) to 1060 °C (-250 mA/cm^2) when approaching the limiting current density, as depicted in Figure 2.27. This observation can be seen when comparing the cell potential and the temperature levels between both Scenarios. For example, at -225 mA/cm^2, the temperature is 850 °C, and the cell potential is 2.1 V in Scenario II. However, this point refers to a temperature of around 750 °C and a cell potential of 1.7 V in Scenario I.

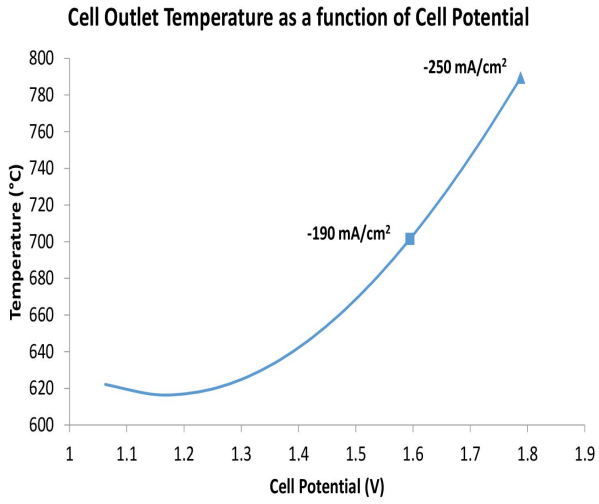

Figure 2.26: The temperature of the outlet gases as a function of the cell potential (V) for Scenario I (electrolysis).

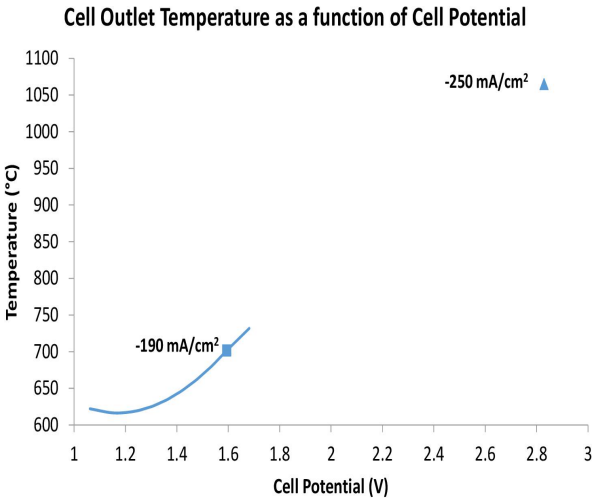

Figure 2.27: The temperature of the outlet gases as a function of the cell potential (V) for Scenario II (co-electrolysis).

The cell potential and temperature outcomes at the state of the limiting current density were also obtained by A. Szczęśniak et al. (2020) [142] in their analysis of the effects of various malfunctions on the performance of the molten carbonate fuel cell. They reported that at low feed gas flow rates, one of the malfunctions observed was a drop in cell voltage and a considerable rise in cell temperature in fuel cell mode. However, in the electrolysis mode, it can be figured out that this malfunction will cause a sharp increase in cell potential and temperature. In conclusion, these findings revealed the importance of considering the CO_2 electrolysis in the cell since it affects its operating conditions, thus causing its damage if no precautions are taken.

Generally, both models are comparative to some extent, just before the point of divergence caused by the co-electrolysis state. Two aspects could explain this similarity. The first is that both models have the exact total applied current density. However, this current was solely used for H_2O electrolysis in Scenario I, whereas in Scenario II, it was divided between H_2O and CO_2 co-electrolysis. The second is the equilibrium balance of the reverse water gas shift reaction with the CO_2 electrolysis reaction, which yielded a similar gas composition at the beginning in both models. These findings were obtained by Ersan Gürbüz (2021) [140], as part of the ANR project, using a thermodynamic simulation with a current density ranging from 0 to -200 mA/cm^2. Their findings concluded that H_2O electrolysis and H_2O and CO_2 co-electrolysis produce the same outlet results. Besides, the outlet CO composition represented by the black curve in Figure 2.22 is analogous to the percentages obtained by the work of Ersan Gürbüz at the Chimie ParisTech, a partner of the ANR project [140].

4.4 Sensitivity Analysis at Model Scale

In this section, a sensitivity analysis was conducted to study the effect of H_2O, H_2, and CO_2 molar compositions in the inlet cell stream on the outlet H_2 and CO produced. Since the outlet stream of the cell contains H_2 and CO, the intermediate species for the methanation process, the H_2/CO ratio must be above a value of 3 for the methanation reaction to occur. Consequently, this study can provide an overview of the optimal inlet composition required to achieve the target ratio.

For this investigation, two approaches were considered to understand the variability in the outlet molar composition of both H_2 and CO, the cell potential, and its electrical power consumption. Firstly, the effect of H_2 inlet molar fraction was studied. Following this, an equivalent study was performed by varying the molar compositions of H_2O and CO_2. This study was conducted at a current density of -150 mA/cm^2. The two scenarios do not reveal any difference at this value according to the results presented in Section 4.3. Therefore, this sensitivity analysis corresponds to both scenarios I and II.

4.4.1 Effect of H_2 Inlet Molar Composition

The presence of H_2 in the inlet stream of an electrolysis cell is controversial. The electrolysis process requires water to produce hydrogen gas. On the other hand, having a quantity of H_2 in the inlet feed stream is necessary for electrode stability [68]. Consequently, a parametric study was carried out to investigate the effect of the inlet H_2 on the cell potential and the syngas outlet composition at a constant current density of -150 mA/cm^2. It is worth noting that the H_2O and CO_2 molar composition are equally modified, according to the H_2 molar composition. For example, at a 40% H_2 inlet composition, the inlet

composition of H_2O and CO_2 is 30%.

Figure 2.28 depicts the impact of inlet H_2 composition on the cell potential. The result revealed that the cell potential increases with the hydrogen gas inlet composition. This change in cell potential is related to the effect of H_2 concentration on the Nernst cell potential. High inlet H_2 is required for fuel cell operation to generate more power by increasing the cell potential. In contrast, less power consumption is the best option for electrolysis, so the inlet feed must contain low H_2 content.

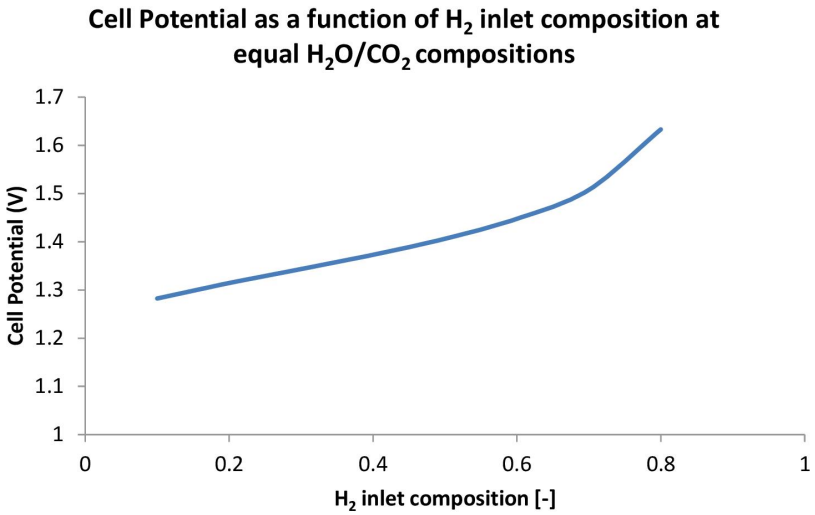

Figure 2.28: Effect of the inlet H_2 molar composition on the cell potential.

On the other hand, H_2 inlet composition significantly affects the amount of CO and H_2 produced, as presented in Figure 2.29. H_2 is produced by H_2O electrolysis (Eq. 2.13) and consumed by the RWGS (Eq. 2.16), where it reacts with CO_2 to produce CO. This state explains the significant impact of the inlet H_2 on the syngas outlet composition. From Figure 2.29, it can be noticed that the blue curve, which represents the trend of the H_2 produced, fluctuates between positive and negative values. The negative value of the H_2 produced by electrolysis means that the H_2 consumption by RWGS is favored over its production by the electrochemical reaction. The reason for this alternative trend of the H_2 produced curve is the equilibrium shift of the RWGS, which is affected by the change in the concentration of reactants (H_2 and CO_2). These results demonstrated that the H_2 production deteriorates while the CO production increases when the inlet H_2 composition increases till reaching a value of 45%. When the inlet H_2 composition increases above 45%, the H_2 production is enhanced, and that of CO decreases. Thus, for H_2 production, two critical limits of inlet H_2 composition must be remarked, below 25% or above 60%. The enhancement of the H_2 production by electrolysis at high inlet H_2 composition over its consumption by RWGS to produce CO is owed to the low CO_2 concentration in the inlet feed that is a complement reactant to H_2 for the RWGS reaction. Based on these outcomes, it can be deduced that the choice of the inlet H_2 composition is critical regarding syngas production. H_2 inlet composition must be $< 25\%$ or $> 60\%$. Since the role of the process is to produce H_2, it seems logical to have a low H_2 composition in the inlet gas. However, it was reported that a deficient H_2 composition of 1% causes a mass-transfer limitation at the Ni-electrode, leading to a high mass-transfer overpotential [68]. Thus, a H_2 lower bounder of 10% was assumed for our study.

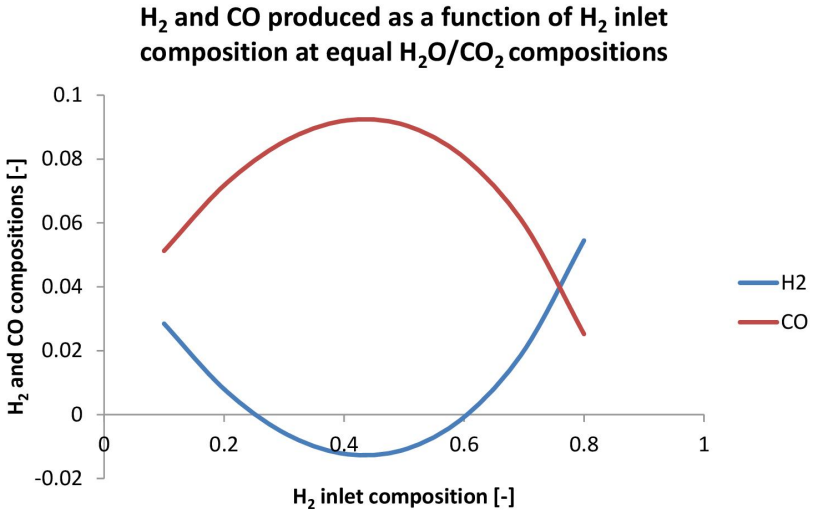

Figure 2.29: Effect of the inlet H_2 molar composition on the H_2 and CO produced in the cell.

4.4.2 Effect of H_2O and CO_2 Inlet Molar Compositions

The molar compositions of both H_2O and CO_2 also impact the cell potential and the amount of H_2 and CO produced. In this analysis, the H_2 composition is fixed at a specific value of 20%, while H_2O and CO_2 compositions are reciprocally varied to have a unitary total composition. For example, a 10% inlet H_2O composition correlates to 70% inlet CO_2 composition, implying that as inlet H_2O composition increases, the inlet CO_2 composition decreases. The effect of H_2O inlet composition on the cell potential is illustrated in Figure 2.30. The cell potential increases with the increase in the H_2O inlet composition and decreases when the CO_2 composition increases.

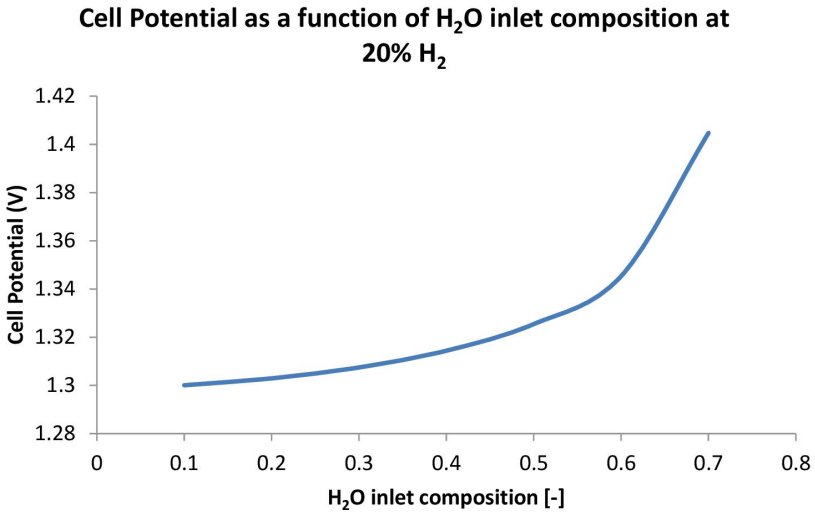

Figure 2.30: Effect of the inlet H_2O and CO_2 molar composition on the cell potential with 20% H_2 inlet composition.

The molar composition of H_2 and CO produced were also investigated according to the H_2O and CO_2 inlet molar composition. As expected, the production of H_2 boosts with the increase in H_2O content and the decrease of CO_2 content, while CO production is enhanced with high CO_2 and low H_2O content, as shown in Figures 2.31 and 2.32. However, it can be noticed that the H_2 produced composition is negative at H_2O inlet composition below 40% and CO_2 inlet composition above 40%, assuming 20% H_2 inlet composition. This outcome revealed that the H_2O to CO_2 ratio must be above 1 to promote H_2 production.

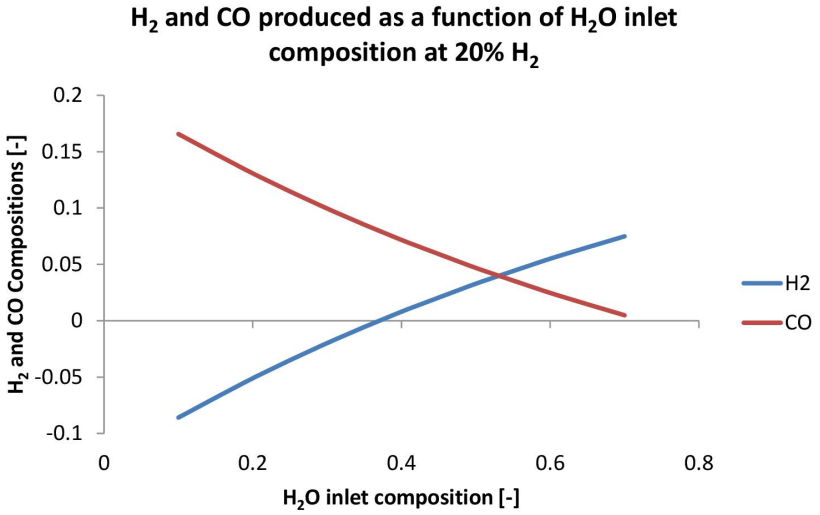

Figure 2.31: Effect of the inlet H_2O molar composition on the H_2 and CO produced in the cell.

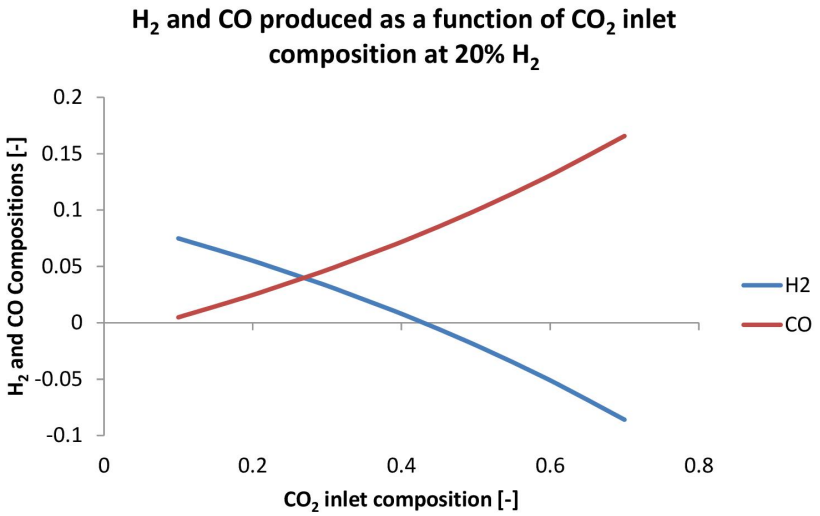

Figure 2.32: Effect of the inlet CO_2 molar composition on the H_2 and CO produced in the cell.

The state of negative value for H_2 produced was obtained at a certain H_2 inlet composition. Therefore, the impact of changing the fixed value of the inlet H_2 molar composition with different complementary H_2O and CO_2 inlet composition on the H_2 produced was examined. The outcomes are illustrated in Figure 2.33, where each curve corresponds to a specific H_2 inlet composition. The results revealed that

the H_2 produced composition is always negative at low H_2O and high CO_2 inlet composition. Therefore, it can be deduced that the H_2 is consumed in the cell when the ratio of H_2O/CO_2 is less than 1. The involved reactions, electrolysis and RWGS, can explain this incompatible variation in the cell. More H_2O favors the electrolysis over the RWGS, which leads to more production of H_2. On the contrary, the rise of CO_2 content in the inlet feed makes the RWGS more thermodynamically favorable by which CO_2 and H_2 are consumed to produce CO.

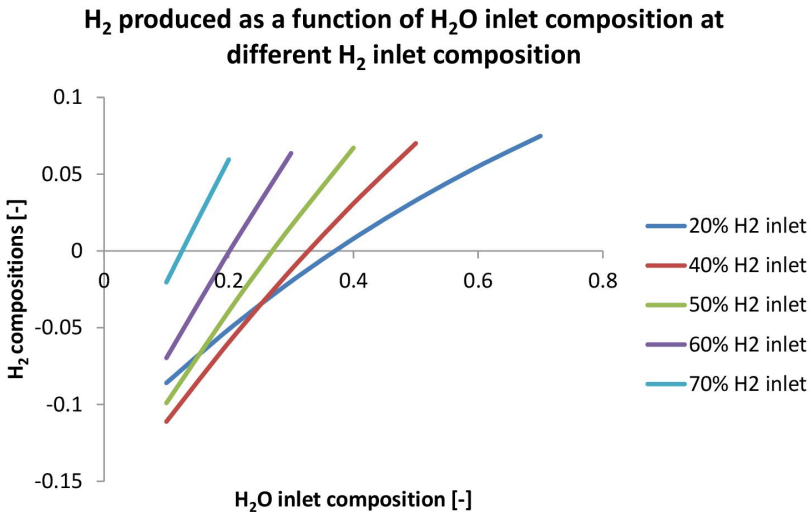

Figure 2.33: Effect of the inlet H_2O composition on H_2 produced in the cell at different H_2 inlet compositions.

This sensitivity analysis highlighted the relevant conditions required for the inlet composition to produce synthetic gas that must follow a specific ratio to produce synthetic methane. Despite these extracted conditions on the inlet composition, this analysis remains limited in choosing the perfect composition for the full process simulation.

5 Conclusion

This chapter presented a one-dimensional steady-state model for the molten carbonate electrolysis cell based on mass and energy balances and electrochemical approaches. It was applied to two scenarios, Scenario I corresponding to the H_2O electrolysis and Scenario II to the co-electrolysis of H_2O and CO_2. The model's outcomes followed a linear path, with an acceptable average error of 2.6%. The V-I curve generated from the model showed a satisfactory result compared with the experimental one, with an average error of 1% for an inlet gas mixture composition of 50/25/25% $H_2O/CO_2/H_2$ and 4% for 25/50/25% $H_2O/CO_2/H_2$ compositions. The outlet temperature varies according to the exothermic or endothermic state of the process, and the outlet composition of the cell's exit streams depends on the operation mode of the cell between the electrolysis cell and the fuel cell mode of operation.

The results obtained from the co-electrolysis model aligned well with the H_2O electrolysis model within a specific range of current density. However, a critical point was observed where the co-electrolysis model's outcomes deviated, primarily due to changes in the RWGS equilibrium and the attainment of

the limiting current density. The deviation point was influenced by variations in the cell's input gas composition, which could be reached at lower or higher current densities depending on the composition. Upon reaching the limiting current density, the cell's voltage and temperature increased by approximately 65% and 40%, respectively, compared to the case of H_2O electrolysis alone. A sensitivity analysis was also conducted to explore further the impact of inlet stream composition on cell performance and the required H_2 and CO ratio for methane synthesis. The three components studied (H_2O, CO_2, and H_2) had conflicting effects on cell performance and syngas production. An optimal feed composition was determined, where the ratio of H_2O to CO_2 should be greater than 1, and the H_2 content should be at least 25% or greater than 60%. This study highlights the importance of considering co-electrolysis as a possibility for safe cell operation.

Résumé: Modélisation de l'électrolyse et de la co-électrolyse du H_2O et CO_2 dans les carbonates fondus

Ce chapitre vise à présenter les bases du modèle pour l'électrolyse de l'eau en H_2 et la co-électrolyse de l'eau et du CO_2 dans un électrolyseur à carbonates fondus, et à évaluer ce modèle en le validant par comparaison avec des travaux expérimentaux. De plus, une étude paramétrique sera réalisée afin de comprendre les paramètres clés qui permettent d'améliorer les performances de la cellule et la production de gaz de synthèse (mélange de H_2 et CO).

État de l'art: co-électrolyse

La récente attention portée à la réduction des émissions de CO_2 a entraîné des efforts dans le domaine du captage et de l'utilisation du dioxyde de carbone et des sources d'énergie renouvelables. Une des approches consiste en la co-électrolyse de CO_2 et de H_2O dans des électrolyseurs à haute température pour produire du gaz de synthèse. Des études préliminaires menées par Stoots et al. (2008) [111] en utilisant un électrolyseur à oxyde solide ont indiqué que le CO est produit chimiquement par la réaction inverse du gaz à l'eau, plutôt que par l'électrolyse du CO_2. Cependant, des recherches ultérieures menées par Ebbesen et al. (2009) [112] ont démontré que le CO_2 et le H_2O peuvent subir des réactions de réduction dans un électrolyseur à oxyde solide pour produire du H_2 et du CO, et que le CO est également produit par la réaction inverse du gaz à l'eau (RWGS).

En revanche, la co-électrolyse du CO_2 et du H_2O dans les électrolyseurs à carbonates fondus (MCEC) suscite un intérêt croissant en tant que moyen de stockage de l'énergie renouvelable et de l'utilisation du CO_2. Les carbonates fondus ont une grande capacité à capter le CO_2 et peuvent générer du gaz de synthèse par co-électrolyse. Des études antérieures ont examiné la conversion électrochimique du CO_2 en CO dans les MCEC. Lorenz et Janz (1970) [118], Peelen et al. (1998) [119] et Kaplan et al. (2010, 2012) [120, 121] ont examiné la conversion du CO_2 en CO en utilisant différents matériaux d'électrode et des compositions d'électrolyte. Meskine et al. (2020) [124] ont vérifié la production électrochimique de CO par électrolyse du CO_2 en utilisant des matériaux d'électrode conventionnels pour les MCEC. Cependant, aucune étude de modèle MCEC n'a pris en compte l'électrolyse du CO_2. Tous les modèles présentés dans la littérature ont supposé que le monoxyde de carbone (CO) était uniquement généré chimiquement par la réaction inverse du gaz avec l'eau. Ce travail vise à développer un modèle couvrant à la fois la co-électrolyse de H_2O et de CO_2 pour la production de gaz de synthèse dans les MCEC et à le comparer avec un modèle développé basé sur l'état de l'art portant sur la production de H_2 par l'électrolyse de l'eau et la production de CO chimiquement à partir de CO_2.

Dévelopment du modèle

Un modèle électrochimique pour l'électrolyseur à carbonates fondus, basé sur les connaissances électrochimiques, ainsi que sur les bilans de matière et d'énergie, est intégré dans le logiciel « Aspen Custom Modeler (ACM) ». Ce modèle a été appliqué à deux scénarios différents. Le premier modèle correspondant au scénario I est composé de l'électrolyse de H_2O, qui est la source de production de H_2, et de la réaction chimique RWGS, qui est la source de production de CO. Alors que, dans le deuxième

modèle correspondant au scénario II, la co-électrolyse de H_2O et de CO_2 a été prise en compte pour produire du H_2 et du CO en parallèle avec la réaction chimique RWGS. L'objectif des deux modèles est de déterminer la température de sortie de la cellule d'électrolyse à carbonates fondus et le potentiel de la cellule, en tenant compte des pertes de surtension.

Le bilan matière implique les réactions électrochimiques et chimiques qui se produisent dans la cellule d'électrolyse à carbonates fondus pour chaque scénario. L'électrolyse de H_2O se déroule selon les équations 2.13 et 2.14, tandis que l'électrolyse de CO_2 suit l'équation 2.15. Par ailleurs, la réaction chimique RWGS se produit conformément à l'équation 2.16.

$$H_2O + CO_2 + 2\,e^- \longrightarrow H_2 + CO_3^{2-} \tag{2.13}$$

$$CO_3^{2-} \longrightarrow \frac{1}{2}\,O_2 + CO_2 + 2\,e^- \tag{2.14}$$

$$2\,CO_2 + 2\,e^- \longrightarrow CO + CO_3^{2-} \tag{2.15}$$

$$CO_2 + H_2 \longrightarrow CO + H_2O \tag{2.16}$$

Pour ce bilan matière, la quantité de H_2 produite électrochimiquement ($\dot{n}_{H_2}$) dans le scénario I est déterminée en utilisant la loi de Faraday avec l'équation 2.10. Dans le deuxième modèle correspondant au scénario II, l'électrolyse de H_2 et de CO_2 sont prises en compte en supposant que le courant total est réparti entre les deux électrolyses en utilisant un paramètre β, qui fait référence à la répartition des sites actifs de l'électrode entre les deux réactions d'électrolyse, et est défini comme le rapport de la composition d'entrée en H_2O et CO_2 à l'interface de l'électrode [136]. Ainsi, dans ce scénario, la quantité de H_2 et de CO produite électrochimiquement ($\dot{n}^{el}_{CO}$) est déterminée par l'équation 2.10 en remplaçant la densité de courant j par celle correspondante pour chaque réaction, avec $\beta \cdot j$ pour l'électrolyse de H_2O et $(1-\beta)\cdot j$ pour l'électrolyse de CO_2. D'autre part, la quantité de CO produite chimiquement ($\dot{n}_{CO}$) est déterminée à partir de la constante d'équilibre de la réaction RWGS ($K_{eq,\ RWGS}$).

$$\dot{n}_{H_2} = \frac{j \cdot A}{n_e \cdot F} \tag{2.10}$$

Le modèle électrochimique est utilisé pour déterminer le potentiel de la cellule et la puissance. Le potentiel de la cellule est calculé selon l'équation 2.28, en fonction du potentiel réversible U_{rev}, de la densité de courant j et du terme de surtension ASR (Résistance surfacique spécifique). Le potentiel réversible U_{rev} est déterminé en fonction du scénario (voir Eq. 2.31 pour le scénario I et Eq. 2.32 pour le scénario II). Le terme ASR est fixe pour les deux scénarios et est calculé selon l'équation 2.33.

$$U_{cell} = U_{rev} + j \cdot ASR(T) \tag{2.28}$$

$$U_{rev,I} = U^{\circ}_{rev,I} - \frac{RT_{cell}}{n_e F} \ln\left(\frac{P_{H_2O}}{P_{H_2}.P_{O_2}^{1/2}} \cdot \frac{P_{CO_2,\,fe}}{P_{CO_2,\,oe}} \cdot (P^{\circ})^{1/2}\right) \tag{2.31}$$

$$U_{rev,II} = U^{\circ}_{rev,II} - \frac{RT_{cell}}{n_e F} \ln\left(\frac{P_{H_2O}}{P_{H_2}.P_{CO}P_{O_2}} \cdot \frac{P^3_{CO_2,\,fe}}{P^2_{CO_2,\,oe}} \cdot P^{\circ}\right) \tag{2.32}$$

$$ASR(T_{cell}) = \phi_0 \cdot exp\left(\frac{4900}{T_{cell}} - 5.95\right) + \varepsilon \tag{2.33}$$

Le bilan d'énergie du système MCEC permet de calculer la température de sortie de la cellule des deux côtés: l'anode et la cathode. Le bilan d'énergie est établi pour les scénarios selon l'équation 2.34.

$$\dot{Q}_{in} + \dot{W}_{el,\ MCEC} + \dot{Q}_{reaction} = \dot{Q}_{out} \tag{2.34}$$

Résultats du modèle: Validation et discussion

Validation du modèle

Après la mise en place du modèle, sa validation par comparaison avec les résultats de travaux expérimentaux a été réalisée et avant d'étudier l'effet de la densité de courant sur la tension, la puissance, la composition à la sortie et la température de sortie du flux de la cellule. Cette étude a utilisé les conditions de fonctionnement d'une seule cellule avec des dimensions de module de laboratoire. Les compositions d'entrée des électrodes correspondent aux conditions expérimentales standards, soit 64/20/16% de H_2/H_2O/CO_2 côté cathode, et 30/15/55% de CO_2/O_2/N_2 côté anode. La surface active des électrodes est de 3,14 cm^2. La densité de courant d'entrée a été fixée à -150 mA/cm^2. Cette section présente les résultats correspondant au Scénario I (l'électrolyse de H_2O).

Tout d'abord, la courbe de polarisation, qui représente la tension de sortie de la cellule pour une densité de courant spécifique, générée par le modèle pour la cellule MCEC/MCFC en modes électrolyse et pile à combustible, est présentée dans la Figure 2.34 et comparée à celle obtenue expérimentalement. Les résultats ont montré un accord satisfaisant avec les résultats expérimentaux, avec une erreur moyenne d'environ 2,6%. De plus, le modèle a été validé par comparaison aux résultats expérimentaux de Perez et al. [126] pour différentes compositions d'entrée. Les résultats sont concordants, avec une erreur moyenne de 1% pour une composition de mélange de gaz d'entrée de 50/25/25% H_2O/CO_2/H_2 et de 4% pour une composition de 25/50/25% H_2O/CO_2/H_2.

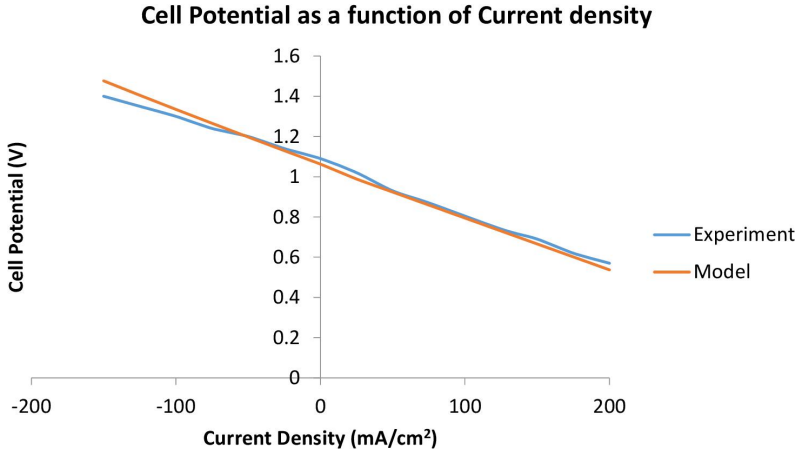

Figure 2.34: Comparaison des résultats fournis par le modèle avec ceux déterminées expérimentalement : mode électrolyseur (à gauche) et mode pile à combustible (à droite).

Ensuite, l'effet de la densité de courant sur la puissance de la cellule a été examiné, car la puissance électrique de la cellule et son potentiel sont des paramètres cruciaux pour étudier ses performances. Les

résultats sont présentés dans la Figure 2.35. Dans le mode électrolyseur, la consommation d'énergie augmente à mesure que la densité de courant augmente. De même, la production d'énergie augmente avec la densité de courant en mode pile à combustible.

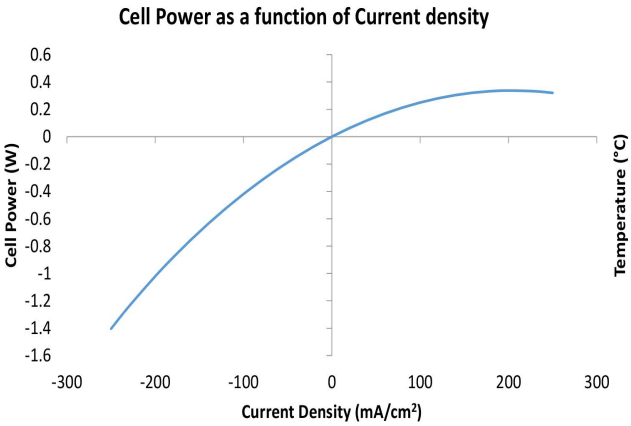

Figure 2.35: Puissance électrique de la cellule en fonction de la densité de courant pour les modes électrolyseur et pile à combustible.

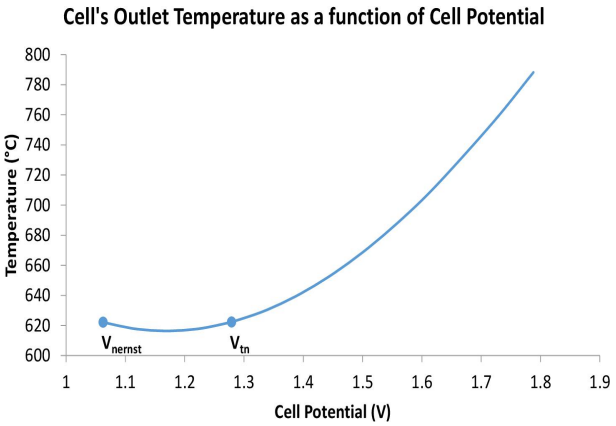

Figure 2.36: Effet du potentiel de la cellule sur la température de sortie des flux de la cellule pendant le mode d'électrolyse.

De plus, l'effet du fonctionnement de la cellule sur la température de sortie est crucial, étant donné que la température de fonctionnement du MCEC est déjà élevée, à 650 °C. Par conséquent, la température est un paramètre critique pour éviter les instabilités mécaniques et la perte d'électrolyte par évaporation à l'intérieur de la cellule. La Figure 2.36 donne la température de sortie de la cellule en fonction du potentiel de la cellule. Le graphique montre que la température de sortie diminue avec l'augmentation du potentiel de la cellule pour atteindre un minimum, puis augmente progressivement, ce qui est conforme à l'état de l'art [141]. La température de sortie reste inférieure à la température de la cellule pendant le fonctionnement entre la tension de Nernst et la tension thermo-neutre. Ce résultat est dû au fait théorique que la chaleur produite par le chauffage électrique est inférieure à la chaleur requise par la réaction, ce qui implique que la cellule est dans un état endothermique. Lorsque le fonctionnement de l'électrolyseur surpasse la tension thermo-neutre, la température de sortie augmente car la chaleur produite par le chauffage électrique est supérieure à la chaleur requise par la réaction, ce qui entraîne un fonctionnement exothermique de la cellule.

Comparaison des deux modèles

Dans cette étude, une analyse a été réalisée pour le Scénario II afin d'étudier l'impact de la densité de courant sur le potentiel de la cellule, la composition de la sortie de la cellule et la température de sortie du flux de la cellule. Les résultats de cette investigation ont ensuite été comparés à ceux du Scénario I.

Tout d'abord, le débit des gaz à la sortie, principalement H_2O, CO_2, H_2 et CO, change en fonction de la densité de courant, comme illustré dans la Figure 2.37 pour le Scénario I et dans la Figure 2.38 pour le Scénario II. Les deux graphiques montrent que le débit de l'H_2 en sortie (ligne grise) augmente tandis que celle du H_2O en sortie (ligne jaune) diminue, ce qui indique que l'eau est impliquée dans la production d'hydrogène gaz. Cependant, à des densités de courant élevées, le débit de CO_2 en sortie (ligne orange) et le débit de CO en sortie (ligne bleue) diffèrent entre le Scénario I et le Scénario II.

L'intervention de l'électrolyse du CO_2 peut généralement expliquer cette différence. Dans le Scénario I, les débits de CO et de CO_2 diminuent avec l'augmentation de la densité de courant. En revanche, dans le Scénario II, le débit de CO en sortie (ligne bleue) diminue avec l'augmentation de la densité de courant, suivant la même tendance que celle de la Figure 2.37. Cependant, à une densité de courant spécifique de -200 mA/cm^2, qui correspond au point optimal, la courbe change et le débit de CO augmente avec la densité de courant pour devenir stable à la fin. Parallèlement à cela, le débit de CO_2 en sortie, représentée par la ligne solide bleue, diminue considérablement, puis commence rapidement à baisser à une densité de courant de -200 mA/cm^2 pour atteindre zéro à la fin.

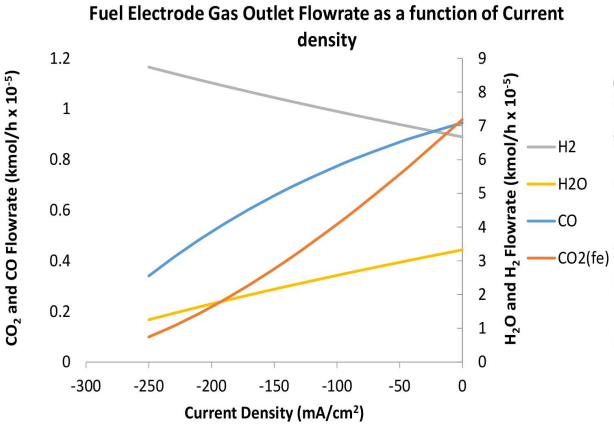

Figure 2.37: La variation du débit des gaz en sortie (kmol/h) en fonction de la densité de courant (mA/cm^2) dans le Scénario I (électrolyse de H_2O).

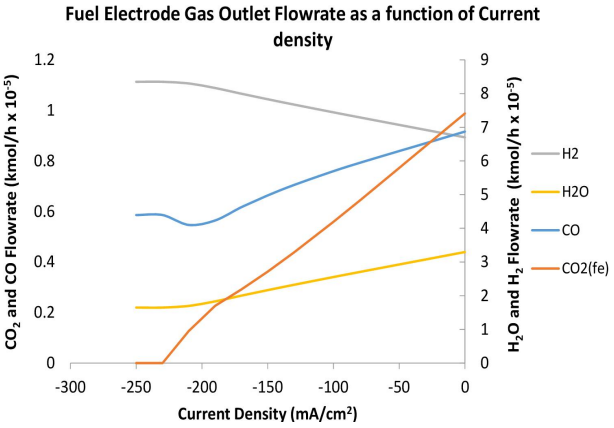

Figure 2.38: La variation du débit des gaz en sortie (kmol/h) en fonction de la densité de courant (mA/cm^2) dans le Scénario II (co-électrolyse).

Cette divergence dans ces courbes est mieux expliquée dans la Figure 2.39, qui illustre comment la tendance du débit de CO en sortie est liée à l'évolution des procédés d'électrolyse du CO_2 et de RWGS. Cette courbe peut être utilisée pour expliquer deux origines distinctes qui définissent la cause de la variation. La première origine est liée à la condition dans laquelle l'équilibre de RWGS n'est pas atteint, ce qui indique que la réaction RWGS ne se produit pas à l'intérieur de la cellule. Par exemple, la Figure 2.39 révèle qu'à une densité de courant de -200 mA/cm^2, la quantité de CO générée par RWGS est nulle, ce qui signifie que la réaction RWGS ne se produit pas. À ce stade, le procédé d'électrolyse du CO_2 ne produit que du CO. Cette situation entraîne une augmentation divergente de la tendance de sortie du CO, qui suit la tendance croissante de l'électrolyse du CO_2. La deuxième origine est le point où la densité de courant limite est atteinte et où tout le CO_2 est consommé. Dans la Figure 2.38, la courbe du débit de CO_2 montre qu'après une certaine densité de courant (-230 mA/cm^2), le débit de CO_2 en sortie devient nulle, ce qui signifie que le CO_2 a été entièrement consommé. À ce stade, la cellule fonctionne à la densité de courant limite de -230 mA/cm^2, et elle ne peut pas fonctionner à une densité de courant supérieure à celle-ci.

Ensuite, une étude de sensibilité a été réalisée sur le point de déviation de la composition du gaz de sortie en CO par rapport à celle du gaz d'entrée de la cellule. Le recyclage d'une partie du gaz de sortie de l'électrode de combustible « fuel electrode » vers la cellule est nécessaire pour la gestion thermique et le maintien de la stabilité de l'électrode en ayant une quantité de H_2 dans le flux d'alimentation d'entrée

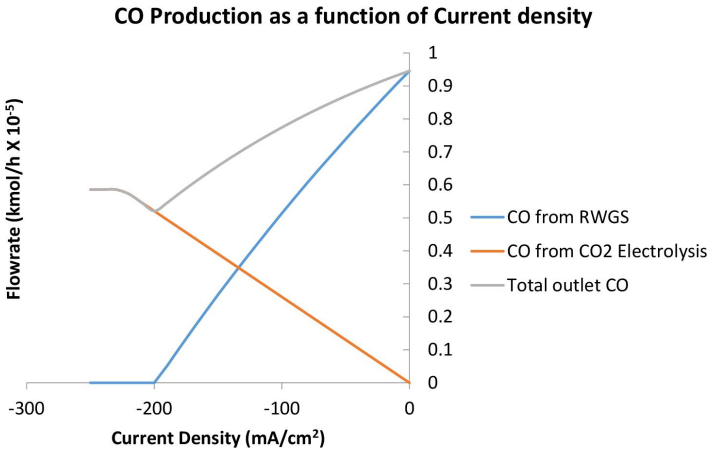

Figure 2.39: Le débit du CO de sortie (courbe grise), du CO produit par RWGS (courbe bleue) et du CO produit par électrolyse CO_2 (courbe orange) en fonction de la densité de courant (mA/cm^2).

[68]. Ce flux recyclé contient du CO, en plus de H_2, H_2O et CO_2. Pour cette raison, il est essentiel de comprendre comment le CO d'entrée affecte le point où la composition en CO de sortie présente une déviation, comme illustré dans la Figure 2.39. L'étude a révélé que la composition du gaz d'entrée modifie l'emplacement de ce point pour les compositions du gaz de sortie en CO et CO_2 en raison des changements d'équilibre de la réaction de conversion du CO et de la densité de courant limite en fonction de ces compositions.

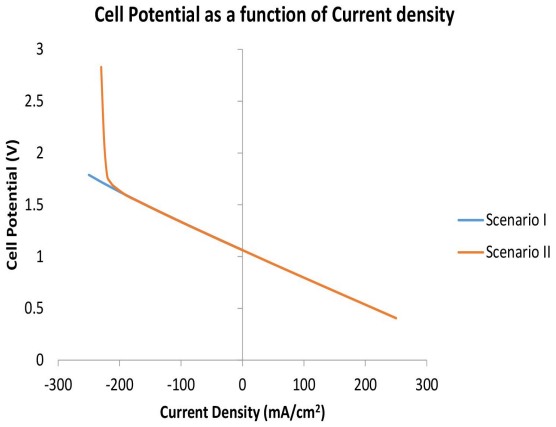

Figure 2.40: La variation du potentiel de la cellule en fonction de la densité de courant (mA/cm^2) en mode électrolyse et en mode pile à combustible pour les deux scénarios.

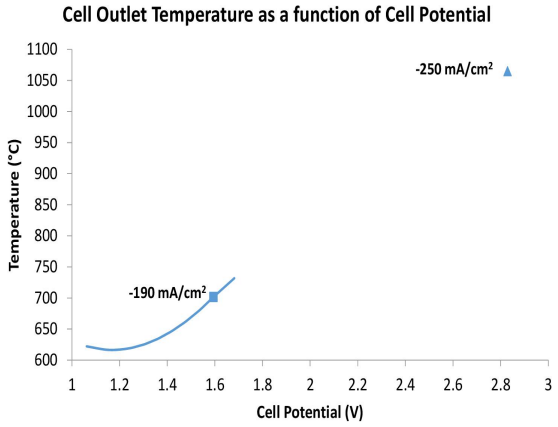

Figure 2.41: La température des gaz de sortie en fonction du potentiel de la cellule (V) dans le cas du scénario II (co-électrolyse).

En outre, l'évolution du potentiel de la cellule et de la température de sortie du gaz a été examinée pour les deux scénarios. L'évolution du potentiel de la cellule en fonction de la densité de courant est comparable entre les scénarios I et II jusqu'à l'atteinte du point de déviation expliqué précédemment. Comme le montre Figure 2.40, cette circonstance entraîne une forte augmentation de la tension de la cellule à l'approche de la densité de courant limite, car le faible réactif CO_2 entraîne des pertes de concentration plus élevées, et donc des surtensions plus élevées. De plus, la température de sortie du gaz augmente brusquement de 850 °C (-225 mA/cm^2) à 1060 °C (-250 mA/cm^2) avec la tension de la

cellule lorsqu'on approche la densité de courant limite, comme illustré dans la Figure 2.41. Les résultats relatifs à la tension de la cellule et à la température à l'état de la densité de courant limite ont également été obtenus par Szczęśniak et al. (2020) [142] dans leur analyse des effets de divers dysfonctionnements sur les performances de la pile à combustible à carbonates fondus. Ils ont signalé qu'un faible débit de gaz d'alimentation, l'un des dysfonctionnements observés est la diminution de la tension de la cellule et une augmentation considérable de sa température en mode pile à combustible. Toutefois, en mode électrolyse, il est possible de comprendre que ce dysfonctionnement entraînera une forte augmentation de la tension et de la température de la cellule.

De manière générale, les deux modèles sont comparables dans une certaine mesure, juste avant le point de divergence causé par l'état de co-électrolyse. Deux aspects peuvent expliquer cette similarité. Le premier est que les deux modèles ont la même densité de courant totale appliquée. Cependant, ce courant était utilisé uniquement pour l'électrolyse du H_2O dans le scénario I, tandis que dans le scénario II, il était réparti entre l'électrolyse du H_2O et du CO_2. Le second aspect est l'équilibre entre la réaction inverse du gaz à l'eau avec la réaction d'électrolyse du CO_2, ce qui a conduit à une composition du gaz similaire au début dans les deux modèles. Ces résultats ont été obtenus par Ersan Gürbüz (2021) [140], dans le cadre du projet ANR, en utilisant une simulation thermodynamique avec une densité de courant allant de 0 à -200 mA/cm^2. Ils ont conclu que l'électrolyse de H_2O et la co-électrolyse de H_2O et de CO_2 produisent les mêmes résultats à la sortie. De plus, la composition en CO en sortie représentée par la courbe noire dans la Figure 2.39 est analogue aux pourcentages obtenus par les travaux réalisés par Ersan Gürbüz à Chimie ParisTech, partenaire de l'ANR projet [140].

Analyse de sensibilité à l'échelle du modèle

Dans cette section, une analyse de sensibilité a été réalisée pour étudier l'effet des compositions molaires en H_2O, H_2 et CO_2 dans le flux d'entrée de la cellule sur les quantités de H_2 et de CO produites en sortie. Étant donné que le flux de sortie de la cellule contient du H_2 et du CO, qui sont les espèces intermédiaires du procédé de méthanation, le rapport H_2/CO doit être supérieur à une valeur de 3 pour que la réaction de méthanation ait lieu. Par conséquent, cette étude peut fournir un aperçu de la composition d'entrée optimale nécessaire pour atteindre le rapport cible.

Pour cette étude, deux approches différentes ont été envisagées afin de comprendre la variabilité de la composition molaire en sortie de H_2 et de CO, de la tension de la cellule et, et de sa consommation d'énergie électrique. Tout d'abord, l'effet de la fraction molaire d'entrée de H_2 a été étudié. Ensuite, une étude équivalente a été réalisée en faisant varier les compositions molaires de H_2O et CO_2. Cette étude a été menée à une densité de courant de -150 mA/cm^2. À cette valeur, les deux scénarios ne présentent aucune différence selon les résultats obtenus par l'étude comparative. Par conséquent, cette analyse de sensibilité correspond aux scénarios I et II.

Les résultats de l'étude ont révélé que la tension de la cellule augmente avec la composition d'entrée en hydrogène. Une teneur élevée en H_2 à l'entrée est nécessaire pour le fonctionnement de la pile à combustible afin de générer plus de puissance en augmentant la tension de la cellule. En revanche, une consommation d'énergie plus faible est préférable pour l'électrolyse, il est donc nécessaire que l'alimentation d'entrée contienne une faible teneur en H_2. Les compositions molaires de H_2O et de CO_2 ont également un impact sur la tension de la cellule. Celle-ci augmente avec l'augmentation de

la composition d'entrée en H_2O et diminue avec l'augmentation de la composition en CO_2.

D'autre part, la composition d'entrée en H_2 a un impact significatif sur la quantité de CO et de H_2 produite. Les résultats ont révélé que la production de H_2 se détériore tandis que la production de CO augmente lorsque la composition d'entrée en H_2 augmente jusqu'à atteindre une valeur de 45%. Lorsque la composition d'entrée en H_2 dépasse 45%, la production de H_2 augmente et celle de CO diminue. Cependant, pour la production de H_2, deux limites critiques de la composition d'entrée en H_2 doivent être mentionnées, en dessous de 25% ou au-dessus de 60%. L'amélioration de la production de H_2 par l'électrolyse à une composition d'entrée en H_2 élevée par rapport à sa consommation par la réaction de RWGS pour produire du CO est due à la faible concentration de CO_2 dans l'alimentation d'entrée, qui est un réactif complémentaire à H_2 pour la réaction de RWGS. Sur la base de ces résultats, on peut en déduire que le choix de la composition d'entrée en H_2 est critique en ce qui concerne la production de gaz de synthèse. Étant donné que le rôle du procédé est de produire du H_2, il semble logique d'avoir une faible composition en H_2 dans le gaz d'entrée. Cependant, une composition déficiente en H_2 de 1% entraîne une limitation du transfert de masse au niveau de l'électrode de Ni, conduisant à une surtension élevée de transfert de masse [68]. Ainsi, une limite inférieure de la composition en H_2 de 10% a été retenu pour notre étude.

Les compositions molaires de H_2 et de CO produites ont été étudiées en fonction de la composition molaire d'entrée en H_2O et en CO_2. Comme prévu, la production de H_2 augmente avec l'augmentation de la teneur en H_2O et la diminution de la teneur en CO_2, tandis que la production de CO est améliorée avec une teneur élevée en CO_2 et une faible teneur en H_2O. Cependant, il est à noter que la composition du H_2 produit est négative pour une composition d'entrée en H_2O inférieure à 40% et une composition d'entrée en CO_2 supérieure à 40%, en supposant une composition d'entrée en H_2 de 20%. Ce résultat révèle que le rapport H_2O/CO_2 doit être supérieur à 1 pour favoriser la production de H_2.

Conclusion

Ce chapitre présente un modèle unidimensionnel de la cellule d'électrolyse à base de carbonates fondus, basé sur des bilans de matière et d'énergie ainsi que sur des approches électrochimiques. Il a été appliqué à deux scénarios, le Scénario I correspondant à l'électrolyse de H_2O et le Scénario II à la co-électrolyse de H_2O et CO_2. Les résultats du modèle suivent une trajectoire linéaire, avec une erreur moyenne acceptable de 2,6%. La courbe V-I générée par le modèle montre un résultat satisfaisant par rapport à l'expérimentation, avec une erreur moyenne de 1% pour une composition de mélange gazeux d'entrée de 50/25/25% $H_2O/CO_2/H_2$ et de 4% pour les compositions de 25/50/25% $H_2O/CO_2/H_2$. La température de sortie varie en fonction de l'état exothermique ou endothermique du procédé, et la composition de sortie des flux de sortie de la cellule dépend de son mode de fonctionnement entre le mode électrolyseur et le mode pile à combustible.

Les résultats obtenus à partir du modèle de co-électrolyse concordaient bien avec le modèle d'électrolyse de H_2O dans une plage spécifique de densité de courant. Cependant, un point critique a été observé où les résultats du modèle de co-électrolyse divergeaient, principalement en raison des changements dans l'équilibre de la réaction RWGS et de l'atteinte de la densité de courant limite. Le point de divergence était influencé par les variations de la composition du gaz d'entrée de la cellule, pouvant être atteint à des densités de courant plus faibles ou plus élevées en fonction de la composition.

Lorsque la densité de courant limite était atteinte, la tension de la cellule augmentait d'environ 65% et la température de 40% par rapport au cas de l'électrolyse de H_2O seule. Une analyse de sensibilité a été réalisée pour explorer davantage l'impact de la composition du flux d'entrée sur les performances de la cellule et le rapport H_2 et CO requis pour la synthèse du méthane. Les trois composants étudiés (H_2O, CO_2 et H_2) avaient des effets contradictoires sur les performances de la cellule et la production du gaz de synthèse. Une composition optimale du flux d'alimentation a été déterminée, où le rapport H_2O/CO_2 doit être supérieur à 1 et la teneur en H_2 doit être d'au moins 25% ou supérieure à 60%. Cette étude met en évidence l'importance de considérer la co-électrolyse comme une possibilité pour un fonctionnement sûr de la cellule.

Chapter 3

Power-to-Gas System Simulation

Objective

This chapter aims to evaluate the MCEC of the Power-to-SNG system through a complete simulation carried out in Aspen Plus software. The simulation covers a 1 MW scale MCEC module with the necessary balance of plant (BoP) equipment. The primary objective of the process is to convert H_2O and CO_2 into synthetic gas (H_2 and CO) and then into synthetic methane. A rigorous sensitivity analysis was then performed using VBA Excel to determine the optimal operating conditions of the process. Finally, a pinch study was carried out, seeking to minimize energy consumption by incorporating heat integration.

Table of Contents

1 Simulation of the Power-to-SNG Process

The Power-to-SNG system was simulated in this work using Aspen Plus software. It consists, as mentioned previously, of two principal processes: Electrolysis and Methanation. This process requires firstly H_2O and CO_2 feed for the electrolysis to occur in the MCEC electrolyzer, as illustrated in the schematic representation in Figure 3.1. After that, the syngas produced by co-electrolysis was treated to be then sent into a methanation reactor to produce synthetic methane. Therefore, this section is divided into four sections related to the simulation process, where Section 1.2 describes the electrolysis process, Section 1.3 presents the treatment process of syngas for methane synthesis, Section 1.4 covers the methanation process, and Section 1.5 presents the carbon capture process for the CO_2 source.

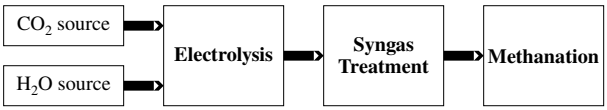

Figure 3.1: Schematic representation of the Power-to-SNG system based on molten carbonate electrolyzer.

1.1 General Assumptions

An MCEC model was applied for a single cell and implemented in the Aspen Plus software for the process simulation. At the scale-up of the MCEC unit, several cells are assembled and separated by a bipolar plate to form a "stack".

In this process simulation, some assumptions were applied to the MCEC stack model, which are:

- The presented MCEC module of 1 MW power consumption consists of 4 stacks of 375 cells each, with a cell electrode active area of 8460 cm^2, based on the industrial surface area of the MCFC cell of 9000 cm^2 with 6% inactive area, produced by the FuelCell Energy manufacturer [143], where the scale-up of the model was performed by determining the number of cells required for the stack to consume 1 MW electric power.
- The CO_2 electrolysis was considered in this process simulation.
- The possible reactions that may occur within the bipolar plates were not considered.
- The methanation reaction inside the cell was not considered in this study because the cell's inlet conditions don't meet the ones required to promote methane production.

1.2 Electrolysis Process

The *Electrolysis Process* includes the MCEC stack and all additional components that provide the desired operating condition. The primary responsibilities of this subsystem are vaporizing the water and the CO_2 feed mixture at the cathode side, heating the inlet streams of the cell to its target operating temperature, which is 650 °C, and producing syngas within the MCEC stack.

At the system's startup, water coming from the supply network, at ambient temperature and atmospheric pressure, is pumped to a pressure of 1.133 bar to compensate for the pressure drop throughout

the process, as shown on the left-bottom side of Figure 3.2. In parallel, a stored CO_2, at ambient temperature and 50 bar, is expanded via a valve to a pressure of 1.203 bar. In this simulation, a pure CO_2 is considered; nevertheless, the CO_2 is usually supplied from the capture process, meaning it is not entirely pure. Thus, the CO_2 capture and purification process is examined and simulated separately, which will be presented in Section 1.5. Following the choice of pure CO_2, its conditions are chosen based on the fact that CO_2 is transported, stored, and handled at two conditions, either ambient temperature and pressure of 45-65 bar or temperatures between -35 °C and -15 °C and pressure of 12–25 bars [144]. The outlet temperature of the valve is below 0 °C, around -40 °C, so it is reheated to reach a temperature of 11.8 °C. This outlet temperature is set based on the available duty that can be recovered from the system.

Afterward, the CO_2 stream is split into two flow fractions to supply both sides of the cell since an inlet flow is needed to sweep out the produced CO_2 and O_2 at the anode electrode side. Besides, this flow fraction of CO_2 at the anode electrode side also serves as a cooling utility required to cool down the leaving products before purification.

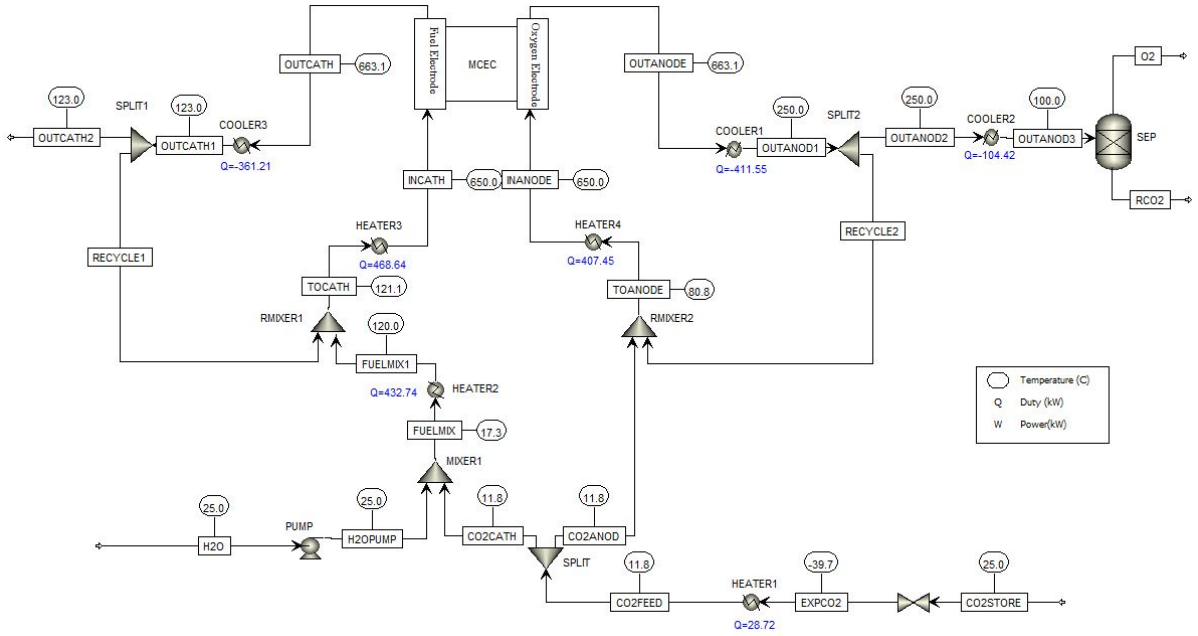

Figure 3.2: The steady-state MCEC electrolysis process system in Aspen Plus.

The electrolysis process operates in two closed loops, which are only connected based on the phenomenon occurring at the MCEC stack level. The first loop, called the oxygen loop (Anode side), presented on the right side of Figure 3.2, is supplied by the stream CO2ANOD and the recycled stream from the outlet stream of the cell OUTANODE, named RECYCLE2. This mixture stream will be heated by HEATER 4 to 650 °C, corresponding to the cell's operating temperature. Afterward, the outlet stream OUTANODE is further cooled to meet the separation conditions. This stream contains CO_2 and O_2 that can be separated to take advantage of selling oxygen and recycling CO_2 into the process.

Regarding the second loop on the cathode side (Fuel electrode side), the "CO2CATH" stream is mixed with water exiting the pump. Then, the mixture stream is vaporized using a heater (HEATER2) since the MCEC operates at a high temperature, requiring an inlet H_2O steam. After that, the vaporized stream is mixed with the recycled stream (RECYCLE1) from the cell, which will be heated via HEATER3 to

reach the target temperature of 650 °C. Finally, the cell's outlet stream at the cathode side (OUTCATH) is cooled down, where the unrecycled fraction (OUTCATH2) will pass into the second process, the Syngas Purification and Post-treatment.

1.3 Syngas Purification and Post-treatment Process

The purification and the post-treatment subsystem in Figure 3.3 is in charge of removing water from syngas (H_2, CO, and CO_2), compressing and heating the syngas to reach the conditions required for promoting methane synthesis. The process is initiated by cooling down the OUTCATH2 stream to condense the contained water and separate it from the rest to be further stored and reused. Next, two drums are added to remove the condensed water, with an inter-stage cooling (COOLER5) to promote water condensation and separation.

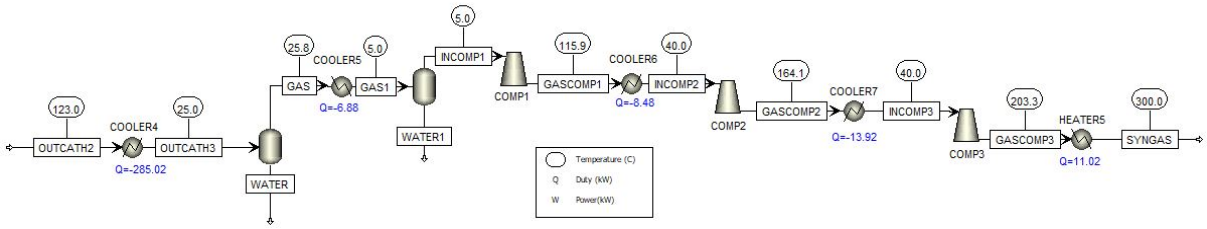

Figure 3.3: The process of syngas purification and pre-treatment for methanation.

Subsequently, rich syngas exiting the water removal drum (INCOMP1) enters a new procedure to be prepared for methanation. Firstly, it is compressed by three consecutive compressors with pressure ratios of 2.5 to attain the operating pressure of methanation, which is chosen to be 20 bars. The compressors are accompanied by intercoolers (COOLER6 and COOLER7) to remove the heat generated by compression, thus lessening the compression work and avoiding mechanical damage. Finally, the syngas stream (GASCOMP3) composed of H_2, CO, and CO_2 passes through a heater (HEATER5) to increase its temperature to 300 °C, a temperature recommended for the methanation's catalyst to be active. As a result, the syngas stream (SYNGAS) is now ready to be sent to the methanation process.

1.4 Methanation Process

This section covers the simulation of two methanation processes. The well-known TREMP process, where methanation occurs under adiabatic conditions, was first simulated. Secondly, an isothermal process was simulated using a reactor that operates at a constant temperature. Both simulations are presented; nevertheless, the complete Power-to-SNG simulation will be based on the isothermal methanation process because of its suitability for systems connected to a fluctuating renewable energy source.

1.4.1 Adiabetic TREMP Process

The process known as adiabatic TREMP, introduced in Chapter 1, involves utilizing a sequence of fixed-bed reactors that typically ranges from 3 to 4 and includes an intercooler system. Following this configuration, the current implementation of the TREMP process employs four adiabatic reactors, as illustrated in Figure 3.4.

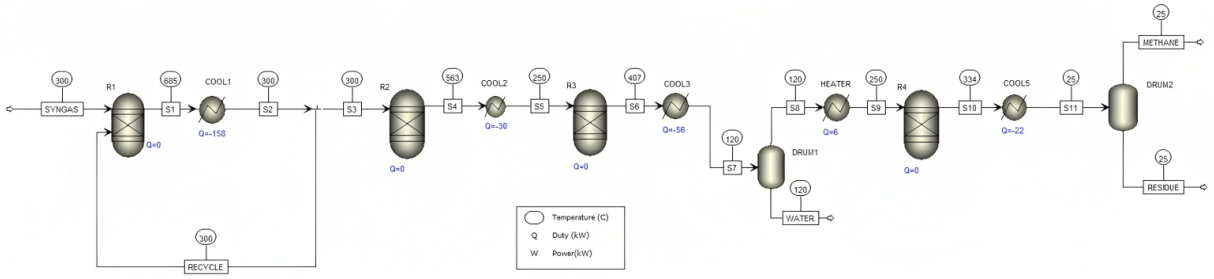

Figure 3.4: Process flow diagram for the TREMP methanation process at steady-state.

In this process, the syngas stream (SYNGAS) is introduced into the first reactor (R1) at a temperature of 300 °C. The reaction occurs in each of the four adiabatic reactors where the temperature increases until thermodynamic equilibrium is reached (points S1, S4, S6 and S10, in Figure 3.5). The stream S1 exits reactor R1 at 685 °C. To prevent the temperature from exceeding 700 °C, since CO_2 and CO methanations are highly exothermic, a recycle stream (RECYCLE) is used to cool down the reactor. Thus, 75% of the cooled outlet stream is recycled back to the first reactor. Next, the stream (S3) undergoes methanation in reactors R2 and R3, with an intercooler in between to enhance the process. However, before entering the fourth reactor (R4), excess water produced in the process must be removed to promote syngas conversion and methane yield. Therefore, the outlet stream (S6) from reactor R3 is cooled by COOL3 to 120 °C and passed through a drum to remove water. The drum's vapor stream (S8) is then heated to 250 °C for the fourth methanation step. Finally, the resulting methane gas stream (S10) is cooled to 25 °C to remove excess water and obtain a rich methane stream (METHANE). The chemical and thermodynamic properties of each stream of this process are summarized in Table B.3 in Appendix B.

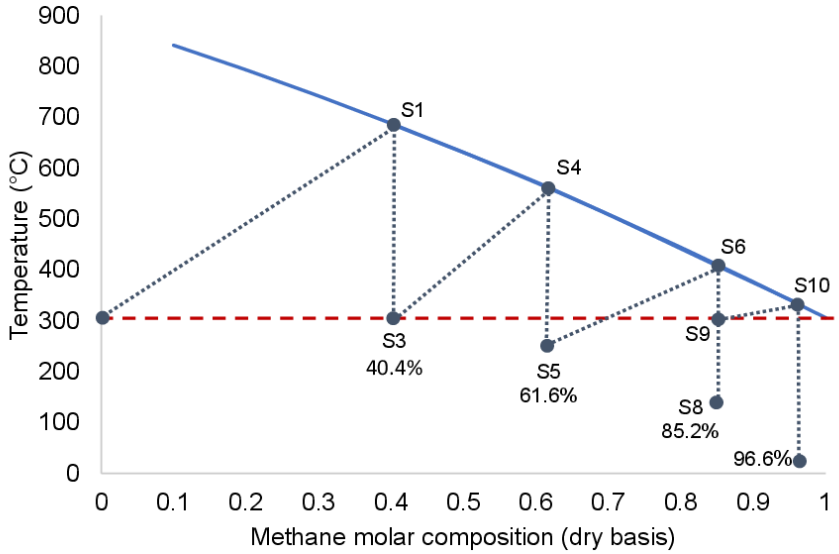

Figure 3.5: Equilibrium curve of adiabatic reactors of methanation, temperature as a function of molar composition of methane on dry basis.

1.4.2 Isothermal Process

In this process, the syngas stream (SYNGAS) is directed into an isothermal reactor for methane synthesis. First, an equilibrium reactor is used, where the temperature is fixed at 300 °C to ensure the isothermal condition. Once the methane product is formed, it exits the reactor at the same temperature and is cooled down to ambient temperature by COOLER8, as shown in Figure 3.6. This step is vital as it facilitates the separation of water and other impurities from the produced methane, allowing it to meet the required specifications for its final use. The resulting methane product can be transported to consumers or directly injected into the natural gas grid. However, injecting the synthetic product into the natural gas grid must meet specific requirements, which may vary from country to country. For instance, the NG network in France has particular specifications, which include a CO_2 concentration of less than 2.5%, CO concentration of less than 2%, H_2 concentration of less than 6%, and a Wobbe index range between 49.1 and 56.52 MJ/Nm^3 [23]. Therefore, achieving the NG specifications requires careful selection of the operating conditions for the system.

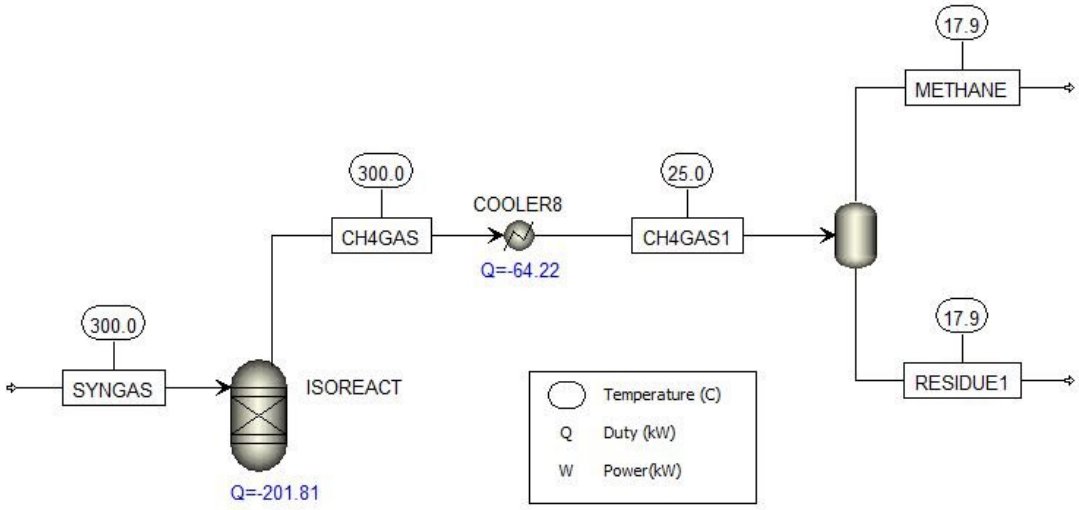

Figure 3.6: Process flow diagram for the isothermal methanation process at steady-state.

1.5 CO_2 Source from Carbon Capture Process

MCEC electrolyzer requires CO_2 as a feed to produce and store clean electricity. Furthermore, carbon capture and storage (CCS) has proven an incredible pace in mitigating global warming changes by limiting CO_2 emission through capturing CO_2 and storing or re-using it. Therefore, using this cell type is relevant to valorize the CO_2 captured from flue gases. Indeed, by using CO_2 as a reagent, this cell allows electricity production when used in fuel cell mode and produces, when used in electrolysis mode (MCEC), synthesis gases, which allow the storage of electricity produced by renewable energy.

Focusing on the CO_2 source for the Power-to-Gas system, it is necessary to have an overview of the different types of carbon capture technologies to select the appropriate CO_2 capture process to be simulated and used as a CO_2 feed supply for the MCEC.

1.5.1 Different Types of CO_2 Capture Techniques

Technologies to capture CO_2 from the significant plants responsible for the high CO_2 emissions include post- combustion, oxy-combustion, and pre-combustion. For all carbon capture technologies, the captured CO_2 requires separation technologies to separate it from H_2 in pre-combustion, N_2 in post-combustion, and H_2O in oxy- combustion. The mature separation processes that can be applied to capture CO_2 are chemical and physical absorption, solid adsorption, membrane technology, and cryogenic distillation. In addition, novel separation concepts are being investigated, like chemical looping combustion, calcium looping technology, clathrate hydrate process, and molten carbonate fuel cells.

The literature contains extensive research studies focusing on the technologies for capturing CO_2, including their recent advancements and the challenges involved in their commercialization. Pires et al. (2011) [145] consulted the developments carried on the carbon capture and storage (CCS) methodologies between the periods 2006 and 2011. Later, Mondal et al. (2012) [146] tackled the progress in CO_2 capture and presented the various new emerging technologies such as chemical looping combustion, integrated gasification combined cycle, facilitated transport membrane, hydrate-based separation, calcium looping, etc. Leung et al. (2014) [147] reviewed the various features, including the CO_2 capture, separation, storage, and utilization with giving more attention to the leaking and the life cycle assessment of the CO_2 capture process. Recently, Sifat et al. (2019) [148] re-highlighted the different methods and the further updates of CO_2 capture and separation. Besides, they conducted a comparison of the novel technology of oxy-combustion (Allam Cycle) and the chemical looping combustion with the traditional post-combustion and pre-combustion carbon capture techniques, which have shown to have the potential to be the leading technologies in the future. Osman et al. (2020) [149] provided a profound and detailed review of the current status of the three major technologies with the advances in carbon capture storage and utilization. To date, carbon capture technologies are being evolved both potentially and commercially. The main obstacle in deploying CCS technologies is their enormous cost, which increases the electricity price. The current cost of capturing CO_2 is estimated to be 60 \$/tCO_2; the research is ongoing to reach a cost of around 20 \$/tCO_2 [150].

1.5.1.1 Pre-combustion

The idea of this system is to de-carbonize the fuel before it is burned. For doing this, the fuel is transformed into syngas through steam reforming or partial oxidation for liquid or gas fuel and gasification for solid fuels. Then, water vapor is introduced into this gas, which will react and convert CO into CO_2 via a water-gas shift reaction, with additional hydrogen production. The product gas stream composition, produced by the catalytic WGS, has been reported to be 72.5-73% H_2 and 20-23% CO_2 [151]. Therefore, at this stage, CO_2 can be captured and separated from H_2 using a low-cost physical solvent such as Rectisol and Selexol. While hydrogen, used alone, produces energy without emitting CO_2, it can be an energy source for supercritical boilers and gas turbines or be used in the integrated gasification-combined cycle (IGCC) power plants [152]. A schematic representation of the entire process of the Pre-combustion carbon capture system is illustrated in Figure 3.7.

Pre-combustion CO_2 capture is highly efficient and requires less energy consumption for CO_2 separation than post-combustion since it can occur at high pressure (2-7 MPa) in the absence of combustion pollutants SO_x and NO_x, resulting in 90-95% of CO_2 capture [150, 153]. On the contrary, high

energy demand is needed for air separation, reforming, or gasification processes [150]. A new technology, which involves integrating WGS and CO_2 separation, has proven the reduction in this energy penalty. This technique is called Sorption Enhanced Water Gas Shift (SEWGS) technology. It works according to the Le Chatelier principle, where CO reduction is enhanced by removing the CO_2 product [150].

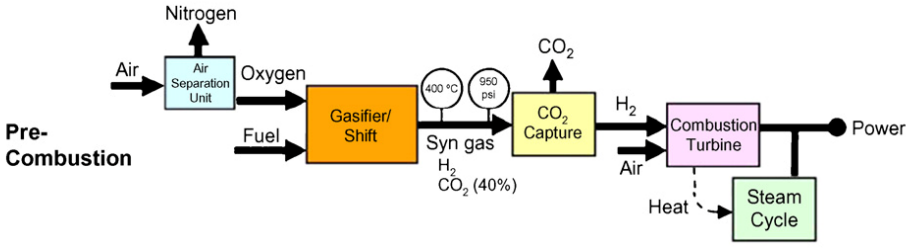

Figure 3.7: Schematic diagram of the pre-combustion carbon capture process, reprinted from [154].

Current research on pre-combustion carbon capture put its effort into applying this technique in integrated gasification combined cycle (IGCC) power plants. Today, the available pre-combustion carbon capture technologies typically use physical or chemical absorption processes. However, it will cost around 60 \$/tonne of CO_2 captured from the exhaust of an IGCC power plant. Hence, the target of DOE's research efforts is to reach a cost of 30 \$/tonne of CO_2 [155]. In line with this target, research activities focused on developing new separation technologies for H_2 and CO_2, such as advanced solvents, sorbents, and membranes.

1.5.1.2 Oxy-combustion

In a conventional combustion scheme, the air is supplied as an oxidizer. This process generated large volumes of smoke, in which the CO_2 is much diluted. On the other hand, oxy-combustion involves burning fossil energy with pure oxygen; the fumes generated essentially contain CO_2 and water in the form of vapor, which is easy to separate by water condensation. Therefore, the preliminary step consisted of separating the oxygen from the other air constituents, mainly nitrogen, as depicted in Figure 3.8. Cryogenic distillation is the only proven air separation process, where O_2 and N_2 are separated by condensation. Although this technique is well-known, it is an energy-intensive process for air separation and has a high capital cost [149]. These factors limit the commercialization of the oxy-combustion process.

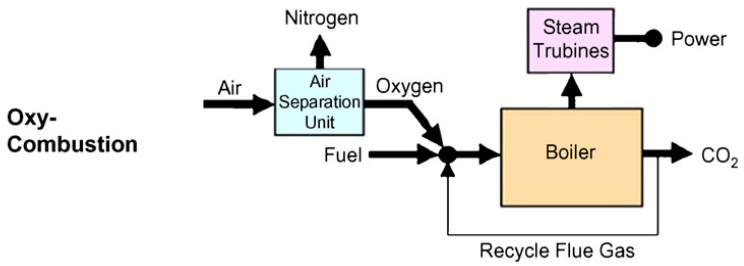

Figure 3.8: Schematic diagram of the oxy-combustion carbon capture process, reprinted from [154].

In general, the nitrogen of air in conventional combustion plays a significant role in moderating the flame temperature. Unfortunately, the absence of N_2 in the combustor of oxy-fuel combustion increases the flame temperature. Therefore, combustion flue gas is recycled, or steam is injected into the combustor to regulate this temperature within the limit.

This technology may be the most energy-efficient method for CO_2 capture if a low-energy intensive air separation process can be demonstrated. Lately, oxygen-transport membranes were developed, known as the Mixed Ionic–Electronic Conducting membrane (MIEC), to resolve the problem associated with the energy need for cryogenic air separation [156]. Furthermore, it can be employed in current and new power plants using various fuels.

1.5.1.3 Post-combustion

Post-combustion is a CO_2 capture method applied after the fuel combustion process. The exhaust flue gases are released from a carbon-fired power plant at a temperature of 50-200 °C, and pressure below 1.5 bar [152]. They mainly contain CO_2, H_2O, N_2, and other impurities (NO_x, SO_x, and others) that vary according to the types of fuel used. Before CO_2 capture, NO_x and SO_x have to be removed from the exhaust gases through de-nitrification and desulfurization along with dust removal and cooling because these impurities have a critical impact on the CO_2 separation process [157]. After that, the diluted CO_2 in the flue gas is separated from N_2. The post-combustion carbon capture process is presented in block diagram form in Figure 3.9.

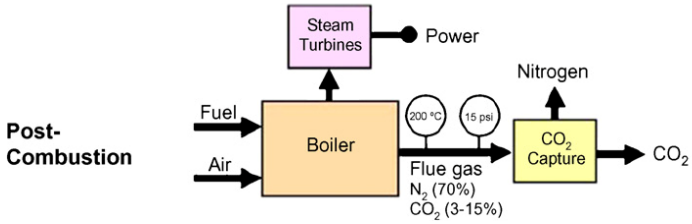

Figure 3.9: Schematic diagram of the post-combustion carbon capture process, reprinted from [154].

Post-combustion technology has proven high maturity in full-scale commercial plant applications and is the most preferred for retrofitting. Besides, its implementation is feasible technically and economically. It typically works on the principle of chemical solvent absorption using Monoethanolamine (MEA) solvent, which is the most widely studied as an amine-based solvent for absorbing CO_2. However, it has some disadvantages, such as the high energy penalty linked to the regeneration of the solvent, sensitivity to thermal and chemical degradation, and it is also found to be corrosive, toxic, and volatile [158].

Aside from the solvent degradation issue, post-combustion capture encounters the biggest challenge in separating the relatively low concentration of CO_2 from the excessive amount of nitrogen in the flue gas. This dilemma limits the options for CO_2 separation; for instance, the gas separation membrane is inefficient. Therefore, the R&D efforts are centralized on developing advanced solvent, sorbent, and membrane systems and novel concepts such as calcium looping systems to afford technologies with reduced cost and energy penalties compared to currently available technologies.

1.5.2 Impurities in the Captured CO_2 and their Impact on MCFC/MCEC

Although carbon capture technologies can potentially separate CO_2 from the other gases, they cannot guarantee 100% pure CO_2. This weakness can cause some impurities to be released with the CO_2 stream. The potential impurities are NO_x, SO_x, H_2S, and possibly others that can vary depending on the fuel source used and the carbon capture methodology applied. The fuel sources used in power plants and industries are hard coal, lignite, oil, and natural gas.

The impurities may be mainly produced due to three unfavorable conditions: fuel oxidation, excess oxidant/air entrance, and process fluids [159]. Porter et al. (2015) [159] have summarized in Figure 3.10 the different impurities that may be present in CO_2 based on these conditions. Fuel oxidation, partial or complete oxidation, can result in the formation of different impurities. For instance, partial oxidation products of coal and biomass are carbon monoxide (CO) and hydrogen sulfide (H_2S). In contrast, coal and biomass's standard complete oxidation products are water, SO_x, NO_x, and halogens [159]. In addition, excess oxidant products are considered inactive species. Process fluids are used for CO_2 separation, like monoethanolamine and selexol, which may be present in the captured CO_2.

Coal/biomass oxidation products	
Complete	**Partial**
H_2O, SO_x, NO_x, HCl, HF	CO, H_2S, COS, NH_3, HCN
Volatiles	**Biomass alkali metals**
H_2, CH_4, C_2H_6, C_3+	KCl, NaCl, K_2SO_4, KOH, etc.
Trace metals	**Particulates**
Hg ($HgCl_2$), Pb, Se, As, etc.	Ash, PAH/soot
Oxidant/air ingress	**Process fluids**
O_2, N_2, Ar	Glycol, MEA, Selexol, NH_3, etc.

Figure 3.10: Classes of CO_2 impurities, reprinted from [159].

Several studies have been conducted to identify the different impurities in the captured CO_2 and evaluate their impact on CO_2 compression, transport, and storage. The following section presents the impurities from different carbon capture technologies, with the maximum limits required for CO_2 transport and storage.

1.5.2.1 Post-combustion CO_2 Capture Stream Impurities

For the post-combustion capture process, chemical absorption via amine scrubbing is the most commercially installed process. In such a process, the flue gas obtained from combustion will undergo a pre-treatment step for NO_x and SO_x removal before carbon capture. This preliminary step is essential since the amine compounds are sensitive to acid gases and potential oxidants. For instance, the MEA-based CO_2 absorption process imposes a limit for the SO_2 level below 10 ppmv before CO_2 capture unit [160]. This target is met by integrating Flue-Gas Desulphurization (FGD) system for sulfur removal and Selective Catalytic Reduction (SCR) system for NO_x removal with power plants equipped with CO_2 capture unit.

Despite these purification processes, these impurities must be entirely removed, meaning that the captured CO_2 is not 100% pure. The study of Lee et al. (2009) [160] observed this issue. The authors' case study showed that the separated CO_2 stream after FGD, SCR, and MEA absorption still contains

impurities that range between 34 and 135 ppm for SO_2, 21 and 302 ppm for SO_3, 7 and 35 ppm for NO_x, 2 and 44 ppm for HCl, and 2 to 27 ppm for Hg.

Post Combustion MEA-based Absorption						
Components	**(2005) [161]**	**(2011) [162]**	**(2013) [163]**	**(2015) [159]**	**(2017) [164]**	**Summary**
CO_2	99.8%	99.8-99.93%	92-97%	99.6-99.8%	99.8%	92-99.93%
H_2O	0.14%	100-600 ppm	2.8-7.3%	100-640 ppm	-	0.01-7.3%
Ar	0.021%	-	10-25 ppm	11-210 ppm	100 ppm	10-210 ppmv
N_2	0.021%	0.045-0.09%	0.02-0.13%	0.045-0.29%	2,000 ppm	0.021-0.2%
O_2	0.003%	0.015-0.03%	0.001-0.03%	35-150 ppm	200 ppm	0.001-0.03%
SO_2	0.001%	10-20 ppm	0.001%	0-67.1 ppm	10 ppm	10-20 ppmv*
SO_3	-	-	-	-	-	-
NO	10 ppmv	10 ppm	-	3.8-20 ppm	50 ppm	1.5-50 ppm
CO	-	10-20 ppm	-	1.2-10 ppm	10 ppm	10-20 ppm
NH_3	-	-	-	-	1 ppm	1 ppm
Amine	-	-	-	-	1 ppm	1 ppm

Table 3.1: Composition of CO_2 product of post-combustion MEA-based absorption process (* *SO_2 range excludes the range presented by Porter et al. (2015) [159] since most of the references presented a common SO_2 range of 10-20 ppmv*).

Later, Abbas et al. (2013) [163] evaluated the CO_2 stream specifications and impurities from the conventional MEA-based absorption capture process from Siemens coal-fired and natural gas-fired combined cycle (NGCC) power plant sources. The level of impurities was selected based on three main applications of the captured CO_2, where the required level for H_2S is < (10-50) ppmv, and for SO_x is < 50 ppmv [163].

Table 3.1 presents the CO_2 stream composition of the MEA-based absorption post-combustion carbon capture process from various study sources from 2005 to 2017. From these different sources, it can be deduced that the CO_2 stream after the MEA-based absorption process will contain 10-20 ppm SO_2, 1.5-50 ppm NO, 10-20 ppm CO, 1 ppm NH_3, and 1 ppm amines. This range of impurities can be confirmed or be further treated based on the final use recommended limits.

1.5.2.2 Pre-combustion CO_2 Capture Stream Impurities

A separation process follows pre-combustion carbon capture to separate CO_2 from H_2 and other impurities, mainly H_2S. Physical absorption is the most likely process to be adopted for CO_2 separation at this stage. This process uses two physical solvents, which are Selexol and Rectisol. In addition to the physical absorption, the new technology, called Sorption Enhanced Water Gas Shift (SEWGS), is also implemented. This technology involves the integration of WGS and CO_2 separation to promote the CO reduction into CO_2 and then remove the CO_2 product.

Based on several studies, the final CO_2 gas composition is reported in Table 3.2. The contaminants present in CO_2 gas from pre-combustion are mainly H_2S, CO, and Ar. Among the three CO_2 separations, it turned out that the physical absorption using Rectisol as a solvent can be a preferable separation technique. This process produces a product CO_2 stream with the lowest impurity concentration of 0.2-20 ppm H_2S, 150 ppm Ar, and 400 ppm CO.

Pre Combustion				
Components	**Selexol**		**Rectisol**	**SEWG**
	(2011) [13]	(2017) [164]	(2007) [165]	(2012) [166]
CO_2	98.1-99.7%	98.2%	95-98.5%	> 99%
H_2O	376 ppm	-	0.1-10 ppm	500 ppm
Ar	178 ppm	500 ppm	150 ppm	< 1%
N_2	195 ppm	6,000 ppm	< 1%	< 1%
CO	100-1,300 ppm	400 ppm	400 ppm	< 1%
H_2S	2-1700 ppm	100 ppm	0.2-20 ppm	< 200 ppm
H_2	1.5%	1%	20 ppm	< 1%
CH_4	112 ppm	1,000 ppm	100 ppm	< 1%
CH_3OH	-	-	20-200 ppm	-

Table 3.2: Composition of CO_2 product of various pre-combustion separation processes.

1.5.2.3 Oxy-combustion CO_2 Capture Stream Impurities

The oxy-combustion process for carbon capture is a process by which fuel combustion occurs in a pure oxygen environment. The oxy-fuel flue gases will be subjected to further treatment for CO_2 purification. The treatment includes SO_x and NO_x removal through FGD and SCR units and water removal. This step is essential to avoid corrosion problems since water is the primary source of corrosion, especially in the presence of CO_2 and other acid gases (H_2S, SO_x, and NO_x). Water condensation is the well-established process for water removal in the oxy-fuel CO_2 capture.

Oxy Combustion								
Components	**Dry raw flue gas (Water Removal)**		**Desulphurized flue gas (Sulfur Removal)**		**CO_2 Treatment by Double Flashing**		**CO_2 Treatment by Distillation**	
	NG	PC	NG	PC	NG	PC	NG	PC
CO_2	88%	74.8%	88.1%	75%	96.4%	96.7%	99.3%	99.3%
H_2O	0.1%	0.1%	0.2%	0.2%	-	-	-	-
Ar	5.7%	2.3%	5.7%	2.3%	2%	0.4%	0.5%	0.1%
N_2	3.8%	16.6%	3.7%	16.4%	0.8%	1.6%	440 ppm	0.2%
O_2	2.2%	6%	2.2%	6%	0.8%	1.2%	0.2%	0.4%
SO_2	130 ppm	702 ppm	30 ppm	25 ppm	34 ppm	36 ppm	25 ppm	37 ppm
NO	150 ppm	708 ppm	148 ppm	703 ppm	53 ppm	150 ppm	10 ppm	32 ppm
NO_2	1 ppm	1 ppm	1 ppm	1 ppm	1 ppm	1 ppm	1 ppm	1 ppm

Table 3.3: The CO_2 product composition from different technologies of oxy-combustion carbon capture process, NG: Natural Gas and PC: Pulverized Coal, [167].

Table 3.3 provides detailed feedback on the range of impurities in the CO_2 stream from natural gas and pulverized coal-fired power plants. It includes the dehumidified raw flue gas composition, the desulphurized treated CO_2 stream, the treated CO_2 stream with double flashing, and the treated CO_2 stream with distillation. Double flashing occurs after water and sulfur removal units by which two flash separators are consecutively used to remove O_2, N_2, and Ar from the oxy-fuel gas. The distillation process is a separation process based on the boiling points of the gases. The dry desulphurized flue gas enters the distillation column, and the condensed CO_2 rich stream is then collected at the bottom.

As shown in Table 3.3, CO_2 treatment by distillation for natural gas (NG) and pulverized coal (PC) flue gases provides the lowest impurity concentrations compared to other treatment techniques. However, the

distillation process consumes excessive energy for refrigeration. Therefore, treatment technology choice has to be balanced between the CO_2 quality specifications for final use and the energy utility cost.

1.5.2.4 Recommended CO_2 Quality for Transport and Storage

The CO_2 stream from the captured process has to be transported from the process plant to the storage field. The transportation occurs via a carbon steel pipeline. The pipeline may be subjected to corrosion and deterioration due to impurities in the CO_2 stream. The impact of the impurities on the CO_2 transport and storage needs to be better examined. However, some CO_2 quality recommendation limits were proposed based on health, safety and technical measures.

The National Energy Technology Laboratory (NETL) [168] provided a report that offers the recommended limits for carbon dioxide quality for transportation, utilization, and storage. Table 3.4 summarizes the specific requirements of the CO_2 quality for CO_2 transport in carbon steel pipeline, CO_2 use in enhanced oil recovery (EOR), and CO_2 sequestration in Saline reservoirs.

Components	**Units**	**Carbon Steel Pipeline**		**Enhanced Oil Recovery (EOR)**		**Saline Reservoir Sequestration**	
		Conceptual Design	Range in Literature	Conceptual Design	Range in Literature	Conceptual Design	Range in Literature
CO_2	vol%	95	90-99.8	95	90-99.8	95	99.8
H_2O	ppm	300	20-650	300	20-650	300	20-650
N_2	vol%	4	0.01-7	1	0.01-2	4	0.01-7
O_2	vol%	4	0.01-4	0.01	0.001-1.3	4	0.01-4
Ar	vol%	4	0.01-4	1	0.01-1	4	0.01-4
CH_4	vol%	4	0.01-4	1	0.01-2	4	0.01-4
H_2	vol%	4	0.01-4	1	0.01-1	4	0.01-4
CO	ppm	35	10-5,000	35	10-5,000	35	10-5,000
H_2S	ppm	100	20-13,000	100	20-13,000	100	20-13,000
SO_2	ppm	100	10-50,000	100	10-50,000	100	10-50,000
NO_x	ppm	100	20-2,500	100	20-2,500	100	20-2,500
NH_3	ppm	50	0-50	50	0-50	50	0-50
COS	ppm	trace	trace	5	0-50	50	0-50

Table 3.4: The recommended limits for CO_2 quality for transportation in pipelines, utilization in EOR, and storage in saline reservoirs, [168].

The limits are chosen based on technical and safety criteria. The technical part involves impurity concentration constraints to minimize the risk of ductile fracture of pipelines and minimize the compression work by reducing the amount of non-condensable gases (O_2, N_2, Ar, H_2). The safety criteria concern the constraints on the concentrations of sulfur compounds (H_2S, SO_x, COS), ammonia (NH_3), nitrous oxides (NO_x), and carbon monoxide CO. These compounds are toxic to health in case of carbon dioxide leakage. Another constraint is imposed on the oxygen concentration if CO_2 is used for EOR since oxygen can react with hydrocarbons. Therefore, the O_2 concentration must be reduced to avoid the reaction with hydrocarbons and the growth of aerobic bacteria.

1.5.2.5 Effect of impurities on the Molten Carbonate Fuel cell

Carbon dioxide is a crucial compound for molten carbonate fuel cell operation. For this reason, MCFC seems a promising technique for carbon capture during fuel cell mode operation and for re-using the captured CO_2 during electrolysis mode operation. In both cases, particular attention should be given to the impacts of the impurities in the anode and cathode feed on the molten carbonate fuel cell components and performance. The cathode (fuel electrode) feed gases can be a diversity of fuels. These fuels may contain some impurities that may cause cell degradation. The anode (oxygen electrode) feed gases are mainly CO_2 contained gases, either the flue gases for carbon capture or the captured CO_2 for re-use. These gases may generate an additional risk of cell degradation due to the impurities that remain in the flue gases.

The impurities impacting the performance of the MCFC are sulfur, selenium, chlorine, and fluorine [169]. The degree of influence of these impurities can vary depending on the partial pressure of the other species in the feed gas (like hydrogen, carbon dioxide, and water), the current operating density of the cell, the temperature, and the fuel utilization [170].

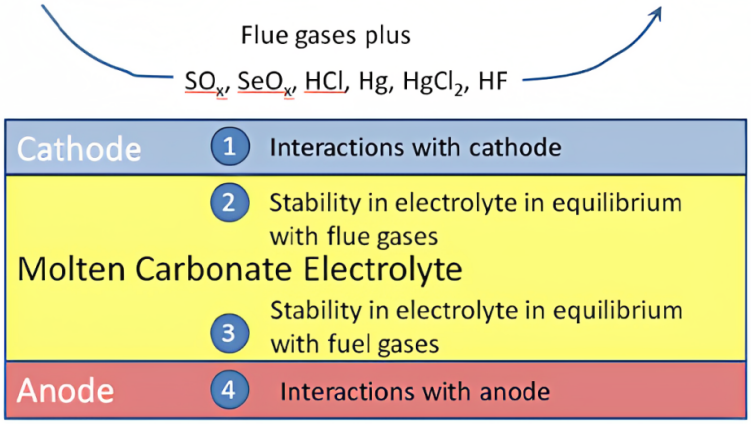

Figure 3.11: Schema of the interaction between the impurities and the MCFC components, reprinted from [169].

The impurities can interact with the electrode catalysts, causing their degradation, and with the cell's electrolyte, leading to the loss of carbonate electrolyte. The impurity interactions can be divided into three sections: the direct reaction with the cathode, the interaction with the molten carbonate electrolyte, and the reactions that would permit the passage of the impurity to the anode.

Sulfur compounds are present in all flue gases under several forms, such as SO_2, SO_3, or H_2S. The possible reactions at the electrode side are presented in the Eqs. 3.1 to 3.3. The formation of nickel sulfide ($Ni_xS_{y(s)}$), as presented in Eq. 3.1, at the Ni electrode blocks the catalyst sites, inhibits the oxidation reaction rate and reduces the active surface area. Nickel sulfide can be produced via electrochemical or chemical reactions, depending on the ratio H_2/H_2S. However, the chemical production of nickel sulfide can be thermodynamically prohibited at low H_2S concentration and normal operating conditions of MCFC, as reported in [171], [172]. For the electrochemical reaction, the production of nickel sulfide is favored when the electrode potential reaches the standard potentials of formation, which are -0.756 V for NiS and -0.829 V for Ni_3S_2 [171]. In the fuel cell mode, nickel sulfide may be electrochemically formed if the cell

potential reaches the standard formation potential. On the contrary, there is no concrete evidence of the formation of nickel sulfide at the Ni-electrode when the cell operates in the electrolysis mode. Besides, the critical H_2S concentration required for the nickel sulfide formation, particularly Ni_3S_2, is approximately 1,000 ppm at 650 °C [169]. For the formation of $NiSO_{4(s)}$ (Eq. 3.2) at the electrode, it was reported that it would occur if more than 500 ppm of $SO_{x(g)}$ is present in the feed gas [169].

$$xNi_{(s)} + yH_2S_{(g)} \longrightarrow Ni_xS_{y(s)} + yH_{2(g)} \tag{3.1}$$

$$NiO_{(s)} + SO_{3(g)} \longrightarrow NiSO_{4(s)} \tag{3.2}$$

$$SO_x + \frac{1}{2}O_2 + 2\,e^- \longrightarrow SO^{2-}_{(x+1)} \tag{3.3}$$

Not only does sulfur interact with the electrode's catalyst, but it is also potentially favorable to displace the molten carbon electrolyte via the reactions presented in Eqs. 3.4 to 3.6. The produced sulfide (S^{2-}) or sulfate (SO_4^{2-}) ions will replace the carbonate ions of the electrolyte, thus reducing the active charge carriers of the electrochemical mechanism. It was also pointed out that the cell performance deteriorates, even though the ion conductivity remains unchanged, which is attributed to replacing carbonate ions with an equivalent number of sulfur-based anions [171].

$$H_2S_{(g)} + M_2CO_{3(l)} \longrightarrow M_2S + H_2O_{(g)} + CO_{2(g)} \tag{3.4}$$

$$H_2S_{(g)} + M_2CO_{3(l)} + 3\,H_2O_{(g)} \longrightarrow M_2SO_{4(l)} + CO_2 + 4\,H_2 \tag{3.5}$$

$$M_2CO_{3(l)} + SO_{3(g)} \longrightarrow M_2SO_{4(l)} + CO_{2(g)} \tag{3.6}$$

$$M_2CO_{3(l)} + SO_{2(g)} + \frac{1}{2}O_{2(g)} \longrightarrow M_2SO_{4(l)} + CO_{2(g)} \tag{3.7}$$

The other impurities are likely present in the flue gas; however, their presence can affect cell performance. Selenium, found in the form of SeO_2 in flue gases, was stated to not react with nickel oxide in the cathode. A possible interaction between the SeO_2 and the carbonate electrolyte might occur, leading to the displacement of carbonate salts. However, M_2SeO_x species formed from the interaction are unstable and are intended to decompose to form H_2Se. The latter will pass into the other electrode side; however, no interaction is expected with the nickel catalyst. Chlorine (HCl) and fluorine (HF) in the flue gas would not react with Ni or NiO catalysts. However, both impurities are thermodynamically favored to replace carbonates in molten salt electrolytes. Mercury can be present in flue gases under the form of Hg without other impurities or under the form of $HgCl_2$ in the presence of HCl. Mercury is not expected to react with either NiO or Ni catalyst nor interact with the molten salt electrolyte [169].

Marine OA (2014) [169] conducted experimental and modeling studies to estimate the effect of the impurities on the cell's performance. The experimental testing involved the addition of different concentrations of specific impurities, which are 0.4 to 40 ppm sulfur, 0.2 to 100 ppm chlorine, and 250 ppb mercury, with the feed gas. The testing outcomes showed that a sulfur concentration of 1 ppm or less has a minor impact on the cell performance of < 1-2%. Besides, cell performance is not affected

with 0.2 ppm of HCl present in flue gas; however, rapid cell degradation occurs after a steady operation of 100–400 hours with 5-100 ppm chlorine concentration. The reason for cell degradation at high chlorine concentrations is the volatility of chlorides that causes them to be released from the electrolyte, leading to substantial electrolyte loss, cell degradation, and failure. The presence of mercury (Hg or HgCl) at a concentration of 250 ppb was reported to have no impact on cell performance.

Based on this study, it can be concluded that MCFC/MCEC is highly sensitive to impurities. This constraint implies the necessity to purify the feed stream to reach the tolerance limit. Hence, it is essential to consider a purification process for the captured CO_2 to complete the Power-to-Gas system.

Impurity	Concentration limit
Total Sulfur (H_2S, SO_x)	< 1 ppm
Chlorine	0.2 ppm
Fluorine	N/A
Mercury	250 ppb
Selenium	N/A

Table 3.5: Impurity concentration limit for the MCFC/MCEC feed.

1.5.3 CO_2 Capture and Purification Process Simulation

Given that Germany is still a significant user of coal, ranking seventh worldwide with the most coal-fired power plants in operation in 2021, it seemed interesting to consider a method for capturing CO_2 from such power plants. Therefore, this section is dedicated to presenting the simulation of a complete process for capturing CO_2 and purifying it to fulfill impurity constraints for use in the MCEC cell.

1.5.3.1 Flue Gas Composition

To begin, as the primary goal of the research is to simulate the whole purification and capture process as close to reality as possible, the actual composition of the feeding flue gas must be found. However, since the most significant impacts are related to CO_2 and impurity concentration, finding a complete composition that compromises the precise concentration of impurities was impossible. Therefore, the volumetric percentages for most components, such as CO_2 and all impurities, were selected from Lee et al. (2009) [160] experiments, classic concentrations of O_2 and H_2O were taken from various literature sources, such as Song et al. (2004) [173] and Di Giulio et al. (2012) [172], and N_2 was used as a balance since it is an inert gas.

Given the selected flue gas composition, it will only be necessary to desulfurize the smoke from the thermal power plant since the other impurities fulfill the tolerance limit presented in Table 3.5. Given this purpose, it is necessary to find an appropriate desulfurization mode. A thorough literature review by Li et al. (2022) [174] led to the selection of two desulphurization methods, which had already been implemented on Aspen Plus software: cryogenic desulfurization and desulfurization using limestone. However, none of these simulations were focused on reducing the sulfur concentration to 1 ppm, nor were they combined with a CO_2 capture system. As a result, for the method of capturing CO_2 from the flue gas, it was decided to investigate a chemical absorption method using MEA as a solvent. This process, however, is sensitive to sulfur with a tolerance limit of 10 ppm. So, it seemed appropriate to perform the

desulfurization to 1 ppm before capturing CO_2 for its final use in the MCEC cell. Several models of the MEA capture process have already been set up using Aspen Plus [175]. However, in all of these models, it was assumed that the incoming gas was sulfur-free.

Parameters	**Value**
Inlet Flue Gas Parameters	
Temperature (°C)	52
Pressure (MPa)	0.1
Volumetric flow rate (m^3/h)	2.55×10^6
Process Parameters	
MEA inlet mass fraction	0.3
Lean MEA purge loss (%)	15
$CaCO_3$ inlet mass fraction	0.0007

Flue gas composition	**Value (vol%)**
CO_2	12
SO_2	0.3
SO_3	0.006
NO_2	0.004
HCl	0.01
H_2O	10
O_2	5
N_2	72.68

Table 3.6: Inlet flue gas conditions, and simulation parameters.

1.5.3.2 Desulfurization Process

Li et al. (2022) [174] provided a state-of-the-art on the desulfurization processes. They highlighted that wet desulfurization is the most efficient among dry, wet, and semi-dry desulfurization. In addition, Gutiérrez Ortiz et al. (2006) [176] argued that desulfurization using limestone is the most suitable for the current study's purpose due to its low installation cost. Figure 3.12 shows the wet limestone desulfurization process scheme. The flue gas desulfurization happens in the absorber tower, where the slurry – a calcium carbonate ($CaCO_3$) mixture – reacts with the SO_x and removes it by chemical absorption. Finally, a filter is added after the absorber tower to remove the precipitated gypsum and recycle the liquid outlet through a loop. To reach the goal of 1 ppm sulfur at the outlet, an optimal calcium carbonate to sulfur ratio needed to be found. A sensitivity analysis on Aspen Plus demonstrated that the more slurry entering, the more efficient the desulfurization. However, the economic analysis module revealed that the most costly component of this process is the raw material ($CaCO_3$) contained in this slurry, leading to the selection of the lowest mass flow, allowing it to reach the objective of 1 ppm.

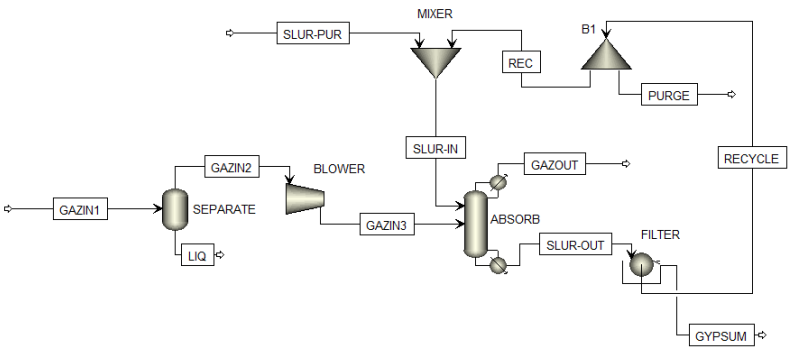

Figure 3.12: Aspen Plus implementation of limestone desulfurization.

In addition, recent research led by Zhang et al. (2021) [177] has focused on using a new process: cryogenic desulfurization. Their study's results demonstrated that this process, which is based on the liquefaction of sulfur in the flue gas, provides a desulfurization efficiency of 73.2% at a low temperature of -45 °C and pressure of 0.5 MPa, where this efficiency can reach 90.2% with a pressure increase to 2.5 MPa. Based on this study, the cryogenic process was adapted and modified to desulfurize the flue gas to a target of 1 ppm. However, CO_2 liquefies with sulfur at high pressures based on phase diagram data, which are the condition cases addressed by Zhang et al. (2021) [177]. As a result, the process's working pressure has been reduced to 0.1-0.2 MPa to avoid CO_2 liquefaction with sulfur. The standard cryogenic desulfurization process was studied at low pressure, and then, an optimized process was proposed and studied. The latter consists of an additional pre-reactor that is added to shift SO_2 into SO_3, since SO_3 has a higher boiling point than that of SO_2, as illustrated in Figure 3.13.

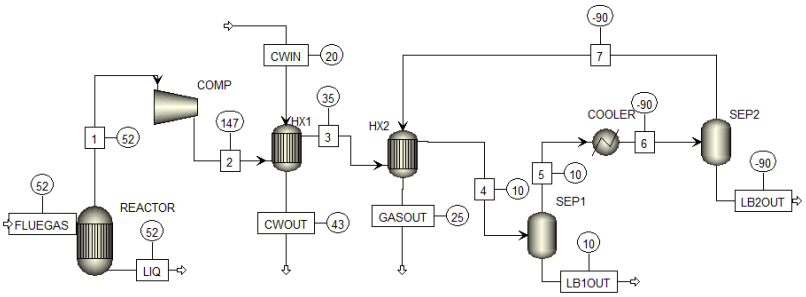

Figure 3.13: Aspen Plus implementation of cryogenic desulfurization.

The current process operates by cooling the gas stream to remove excess water before the temperature further drops and freezes the water, potentially blocking the pipes. To achieve this, two successive heat exchangers are used to lower the temperature to 10 °C and separate the water from the gas stream. The outlet vapor stream from the separator (SEP1) is then further cooled to -90 °C, where the sulfur is separated from the rest of the flue gas. Finally, the vapor stream from the separator (SEP2) is reheated by the inlet feed using the second-stage heat exchanger to reach a higher temperature required for the CO_2 capture, which is selected to be 25 °C in this work.

1.5.3.3 CO_2 Capture Process

The post-combustion carbon capture process using chemical absorption technology was chosen for this study due to its compatibility with existing thermal power plants. There has been much research into the chemical capture of CO_2 by chemical absorption using different solvents. The most mature solvent for this process is monoethanolamine (MEA), but other solvents were also studied and revealed an exciting performance. For example, Molina and Bouallou (2015) [178] have studied the CO_2 absorption using ammonia solvent that has proved the possibility of capturing CO_2 with an efficiency of 90%. Regardless of the solvents investigated, this work focuses on simulating the reference MEA-based CO_2 capture process. Such a process has already been modeled on Aspen Plus [179] to achieve a CO_2 rate of 85% in outgoing flows. However, these studies did not consider the presence of sulfur traces in the gas. In this study, two processes are considered: a standard MEA capture process (Figure 3.14a) and another process considering the heat recovery from the process (Figure 3.14b) where two heat exchangers (HeatX1 and HeatX2) are added in the recycling loop to replace the cooler in Figure 3.14a.

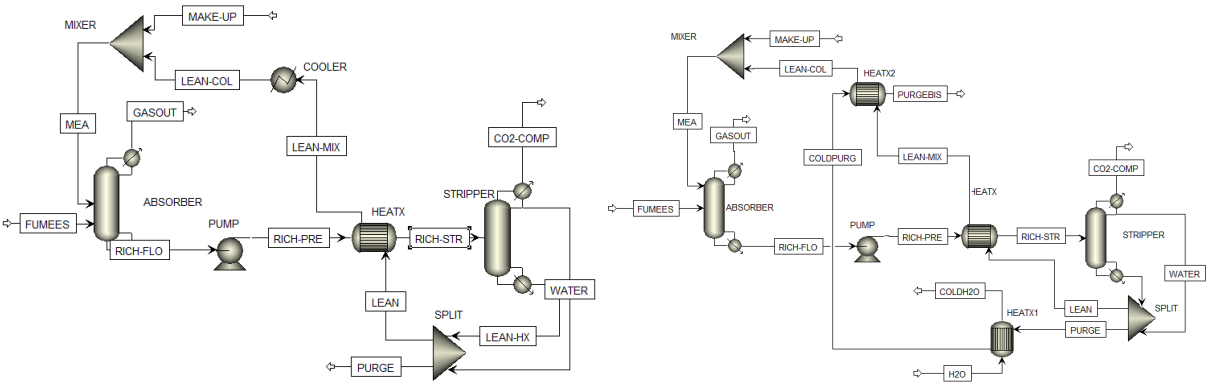

(a) (b)

Figure 3.14: Aspen Plus implementation of carbon capture without heat exchangers (**a**) and with heat exchangers (**b**).

1.5.3.4 Results

Five different simulations were conducted using Aspen Plus software: the flue gas desulfurization using the wet limestone process at 0.11 MPa, the cryogenic desulfurization in two different processes at 0.2 MPa, and two different CO_2 capture processes of the flow from the optimized cryogenic desulfurization with a reactor. The flue gas composition at each stage of the two desulfurization processes is shown in Table 3.7.

Chemical Species	**Entering Flue Gas Mass Fraction**	**Outgoing Flue Gas Mass Fraction (wet limestone)**	**Outgoing Flue Gas Mass Fraction (cryogenic)**	
			Without reactor	With reactor
CO_2	0.1610	0.164	0.1609	0.1644
SO_2	0.0067	1.32×10^{-24}	0.0023	1.35×10^{-13}
SO_3	0.00019	0.269×10^{-6}	0.0126×10^{-6}	0.77×10^{-6}
NO_2	9.385×10^{-5}	3.238×10^{-7}	1.52×10^{-6}	2.03×10^{-6}
HCl	0.00011	0.000126	0.000135	0.000135
H_2O	0.163	0.077	9.99×10^{-18}	1.3×10^{-17}
O_2	0.05	0.053	0.061	0.06
N_2	0.619	0.704	0.776	0.776

Table 3.7: Flue gas composition at various stages of the wet limestone and the cryogenic desulfurization processes.

The limestone desulfurization process could meet the sulfur tolerance threshold of 1 ppm. However, using the standard cryogenic technique without a reactor could not achieve a sulfur level of 1 ppm, with the SO_2 outlet mass fraction being 230 ppm. Increasing the pressure to 3 MPa improved the desulfurization process but resulted in a significant loss of CO_2 with sulfur in liquid form. Therefore, the standard cryogenic technique was ineffective for reaching 1 ppm sulfur. However, adding a pre-reactor improved the cryogenic desulfurization process, as shown in Table 3.7, where the sulfur mass fraction in the outgoing flue gas is below 1 ppm. As a result, the wet limestone process achieved almost 100% yield of both SO_2 and SO_3 removal, while the standard cryogenic technique without a reactor yielded 72% SO_2 and almost 100% SO_3 removal. The optimized cryogenic process with a reactor achieved almost

100% yield of SO_2 and SO_3 removal, making it comparable with conventional wet limestone processes. However, further studies are needed to reduce or avoid the 31% CO_2 loss obtained in the optimized cryogenic process.

Both simulations for MEA successfully achieved their objectives. The first objective was to capture a significant portion of CO_2 from the flue gas and release carbon-free fumes into the atmosphere, while the second was to concentrate the CO_2 to produce an outlet flow with high purity for use as feed for the cell. The post-limestone MEA process obtained a CO_2 capture yield of 94.5% and 94.7% without and with recovery heat exchangers (HeatX), respectively. The post-cryogenic MEA process achieved a CO_2 capture yield of 94.8% for both processes. In addition, the optimized process with recovery heat exchangers for the post-limestone MEA process resulted in a decrease of 20% in reboiler duty, while for the post-cryogenic MEA process, the decrease is 36%.

2 Process Efficiency

The system's performance was investigated by evaluating the overall efficiency. The efficiency of the MCEC system η_{MCEC} (Eq. 3.8) is defined by the ratio of heating power contained in produced methane and the total consumption of the system, which is composed of the power consumed by the stack $\dot{W}_{el,\ MCEC}$ and the consumption of the balance of plant (BoP) equipment $\dot{W}_{el,\ BoP}$, including pumps, compressors, etc…

$$\eta_{MCEC} = \frac{\dot{m}_{CH_4,\ prod} \times LHV}{\dot{W}_{el,\ MCEC} + \dot{W}_{el,\ BoP}} \tag{3.8}$$

It was crucial to determine the most effective operating conditions to evaluate the system's overall efficiency. This involved conducting an optimizing sensitivity analysis, which will be detailed in the subsequent section.

3 Process Optimization

The co-electrolysis process posed a series of restrictions due to the limiting current density. As mentioned previously, the limiting current density changes with the inlet composition of the cell. As a consequence, the outlet gas compositions are altered. Since the target of the process is to produce a methane gas that meets the requirements of the natural gas network, the operating conditions of the process have to be carefully selected. For this purpose, a profound sensitivity analysis was performed by developing an Excel VBA code linked to the Aspen Plus simulation.

The sensitivity analysis compromises the key variables, the outputs, and the constraints on the outcomes. The key variables are the cell's inlet temperature, operating pressure, the H_2O and CO_2 inlet flow rates, and the current density. The margin of change of critical variables was fixed based on several constraints and parameters. First, the cell's inlet temperature was varied between 500 °C and 750 °C to ensure the full coverage of the melting point temperature of all the molten carbonate mixtures of the electrolyte. Second, the cell's operating pressure range was fixed between 1.013 bar and 6 bar since, based on the thermodynamic approach, the cell voltage increases with pressure, which is not

recommended. Third, the water and CO_2 inlet flow rates were chosen to vary between 5 and 15 kmol/h. This range was chosen arbitrarily because the most crucial factor is the composition ratio of H_2O and CO_2 at the fuel electrode side, which is also influenced by the split fraction of CO_2 flow between both electrodes and the recycling ratio of the fuel electrode's outflow to its inlet. Finally, the current density was varied between -40 and -160 mA/cm^2, where a limit of -160 mA/cm^2 was imposed due to the observed rise in cell potential with increasing current density. This increase could lead to carbon formation at voltages exceeding 1.4 V, as reported in Meskine et al. (2020) [124]. It must be noted that these margins were applied on a simulation where the MCEC consists of 213 cells. The outputs are those related to the performance of the electrolysis and methanation processes. They include the cell's voltage, outlet temperature, the total electrical energy consumed by the cell per methane gas produced (E_{elec}/m_{CH4}), and the final methane composition (Y^f_{CH4}).

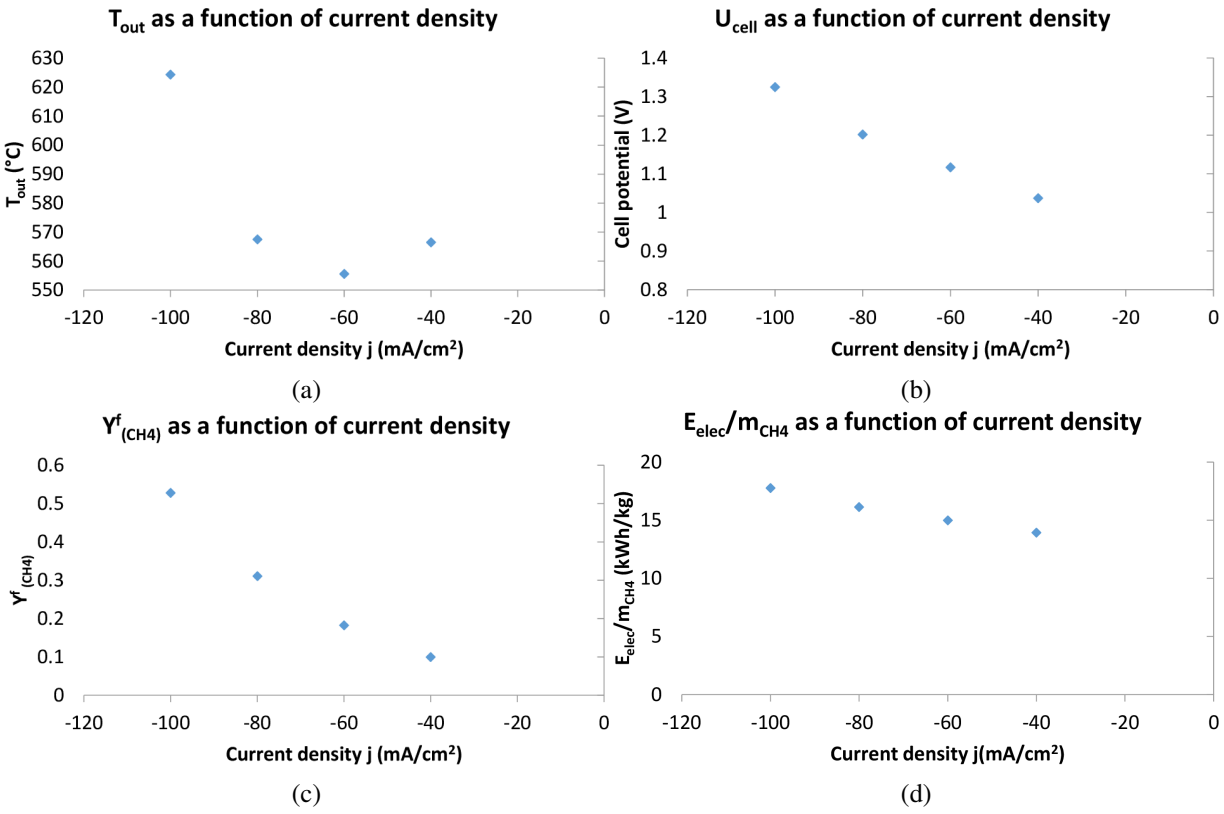

Figure 3.15: Impact of current density j (mA/cm^2) on the gas outlet temperature **(a)**, the cell's voltage **(b)**, the final methane composition **(c)**, and the consumed energy per mass-produced CH_4 **(d)**.

Before selecting the optimal inputs, it was essential to understand the impact of each input parameter on the outlet one. First, starting with the current density, its impact on the cell's outlet temperature, voltage, outlet methane composition, and the cell's energy per methane gas produced is presented in Figure 3.15. This study was conducted at a fixed value of inlet temperature of 650 °C, the pressure of 1.013 bar, inlet H_2O and CO_2 flow rate of 5 kmol/h and 7 kmol/h, respectively, a CO_2 split fraction of 0.5, and recycling ratio of 0.2. From Figure 3.15a, it can be seen that the temperature decreases with the increase negatively in current density to reach an optimum at -60 mA/cm^2, then increases progressively with the current density. At the fixed parameters' conditions, the cell operates in the endothermic state;

however, this state changes when changing the rest of the parameters. As expected, the cell's voltage (Figure 3.15b) increases with the current density. Since the system is a Power-to-Gas process, it is essential to look at the outlet methane composition (Y^{f}_{CH4}), depicted in Figure 3.15c. The results showed that the current density affects the outlet methane composition, which increases with the current density. Finally, the outcomes of the electrical energy required per mass-produced CH_4, presented in Figure 3.15d, give a premier vision of the process efficiency. From these results, it can be deduced that this ratio slightly increases with the current density, implying that the process efficiency may be lowered somewhat.

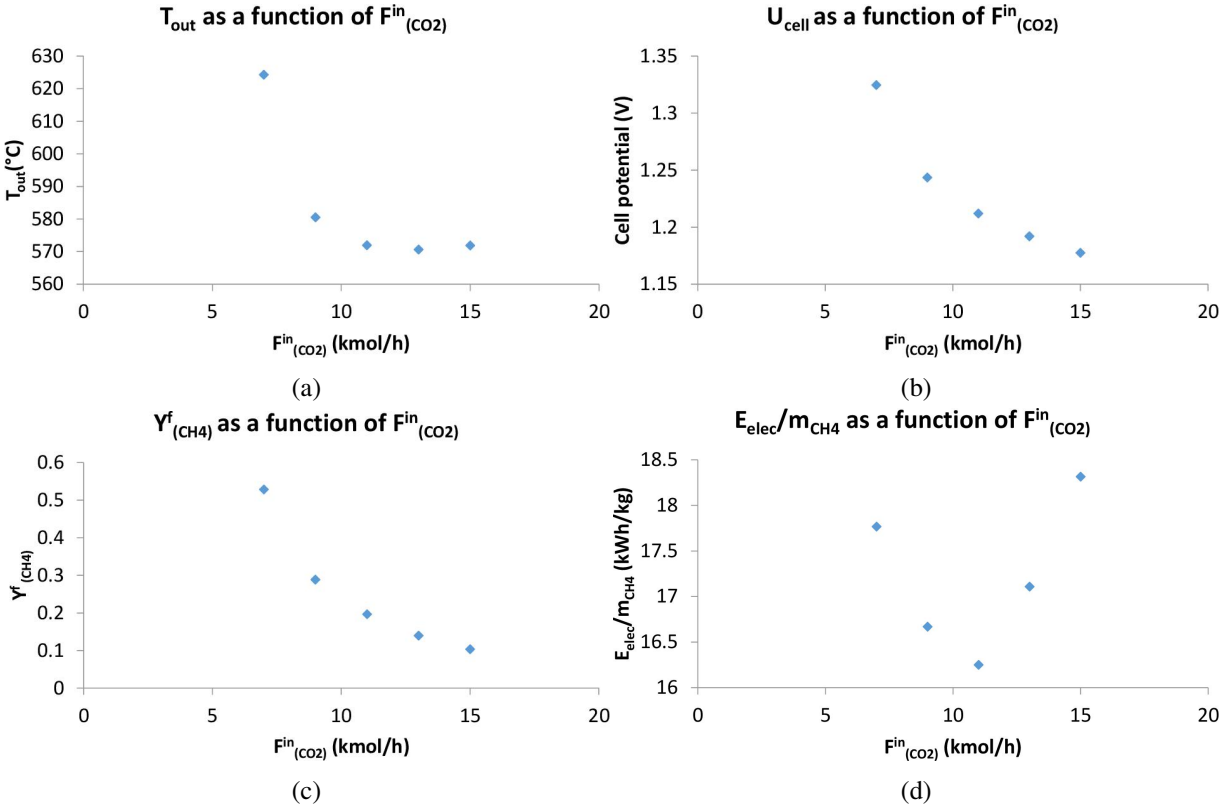

Figure 3.16: Impact of inlet CO_2 flow rate on the gas outlet temperature **(a)**, the cell's voltage **(b)**, the final methane composition **(c)**, and the consumed energy per mass-produced CH_4 **(d)**.

Second, the effect of the inlet CO_2 flow rate on the previously mentioned outcome parameters was evaluated and is illustrated in Figure 3.16. In this case, the fixed input conditions were selected with the current density of -100 mA/cm^2. The other values are similar to the previous case, where the variable parameter is the inlet CO_2 flow rate. The results presented here start with a CO_2 flow rate of 7 kmol/h, not 5 kmol/h since some errors were generated during the simulation, causing some limitations to be added to the VBA code excel to skip the input values that produce these problems. In Figure 3.16a, the cell's outlet temperature decreases rapidly when the CO_2 flow rate increases from 7 to 9 kmol/h, then it gradually decreases to become stable at higher flow rates. Furthermore, the cell voltage is reversibly affected by the increase in CO_2 flow rate, resulting in a decrease as the flow rate increases (Figure 3.16b). This finding is considered a good point from the cell's performance perspective. On the contrary, the produced methane composition is diminished with the increase of CO_2 flow rate. The obtained result can be well explained by the fact that there would be an excess CO_2 in the syngas entering the methanation

process. This circumstance will cause the syngas ratio to shift from its optimal, thus leading to a possible generation of carbon deposit in the methanation reactor [78]. On the other hand, the electrical energy per kg of CH_4 produced decreases with CO_2 flow rate till reaching an optimum with 11 kmol/h CO_2 flow rate, then re-increases. From this outcome, it can be deduced that the CO_2 flow rate choice is a compromise between the final CH_4 composition and the electrical energy consumed by the electrolyzer, an essential parameter for process efficiency.

Third, similar to CO_2, the H_2O flow rate impact on the chosen outcome parameters was also examined, and the results are depicted in Figure 3.17. Here, the CO_2 inlet flow rate was set at 7 kmol/h, and that of H_2O was varied. The first parameter is the cell's outlet temperature in Figure 3.17a, where the outcomes demonstrate a rapid temperature drop between 5 and 7 kmol/h of H_2O. After that, it gradually increases as the H_2O flow rate increases. However, it remains below the temperature obtained at 5 kmol/h. The high temperature at 5 kmol/h is related to the low gas flow into the cell, leading to an increase in temperature based on the thermodynamics principle. In addition, the increase in H_2O flow rate positively impacts cell voltage (Figure 3.17b), resulting in its decrease. The same is observed for the outlet methane composition in Figure 3.17c, which increases linearly when more H_2O enters the cell. Finally, the process efficiency is enhanced with the increase in H_2O flow rate, which can be seen by the decrease in the electrical energy consumed per kg of CH_4 produced in Figure 3.17d.

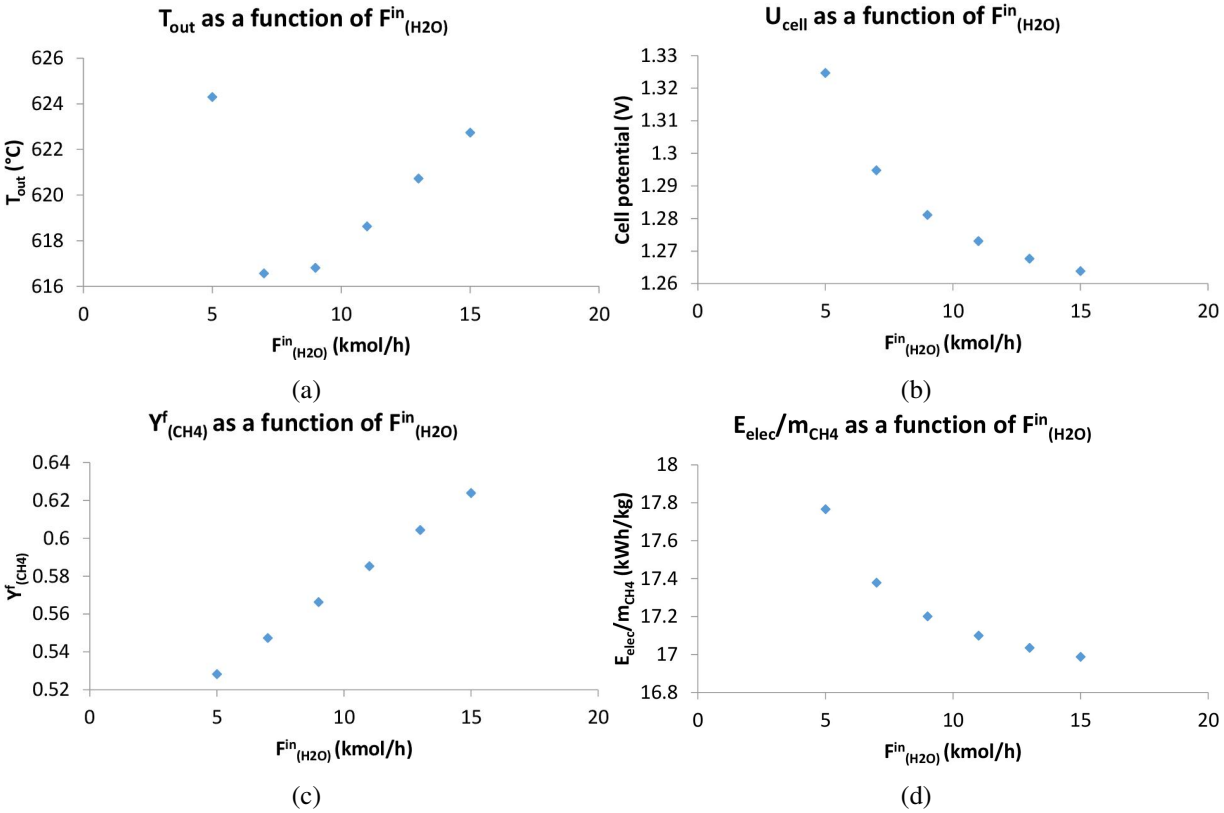

Figure 3.17: Impact of inlet H_2O flow rate on the gas outlet temperature **(a)**, the cell's voltage **(b)**, the final methane composition **(c)**, and the consumed energy per mass-produced CH_4 **(d)**.

In addition to the H_2O and CO_2 flow rate variation, the CO_2 split fraction between the electrodes ($r_{CO2split}$) and the recycling ratio ($R_{outcathode}$) of the fuel electrode's outflow to its inlet were also studied,

since these four parameters determine the cell's inlet composition. The study's outcomes are presented in Figure 3.18, where the x-axis presents the recycling ratios studied, and the legend shows the different CO_2 split fractions. For more comprehension, increasing the CO_2 split fractions signifies that more CO_2 enters the fuel electrode where co-electrolysis occurs, indicating that it follows the same concept as increasing the CO_2 flow rate. Likewise, the recycling ratio increase implies that additional H_2O, CO_2 enters the fuel electrode. Therefore, by analyzing Figure 3.18a, it is apparent that the temperature increases with the recycling ratio regardless of the CO_2 split fraction, except for a split fraction of 0.5, where the temperature declines with the recycling ratio. From the CO_2 split fraction side, the temperature decreases when the fraction increases, mainly above 0.6, regardless of the recycling ratio. However, it cannot be similarly reported for the 0.4 and 0.5 fractions. Even though the temperature at the 0.5 CO_2 split fraction drops with the recycling rate, it stays higher than the temperature at the 0.4 fraction when the recycling ratio is less than 0.4. After that, both CO_2 fractions 0.4 and 0.5 show the same temperature at 0.4 recycling ratio, and then they reverse directions, with 0.4 CO_2 fractions providing a higher temperature than 0.5.

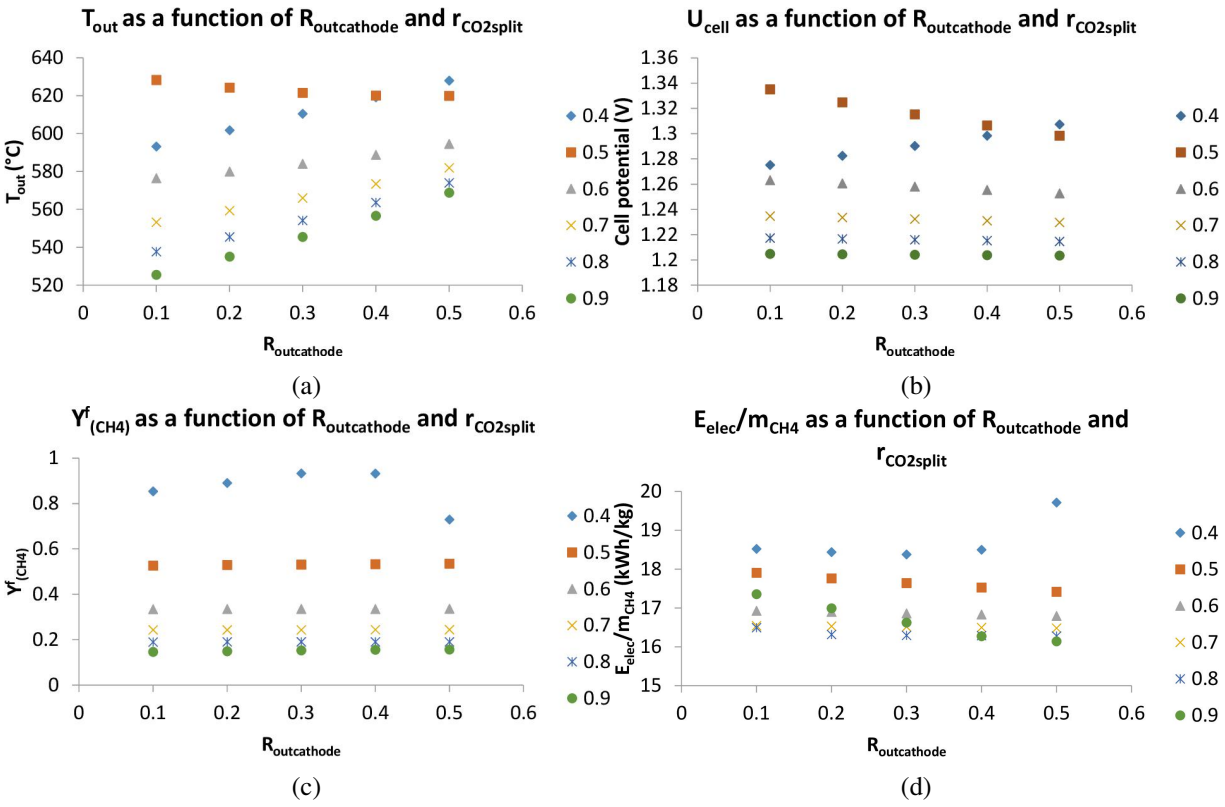

Figure 3.18: Impact of the CO_2 split fraction ($r_{CO2split}$) and the recycle ratio ($R_{outcathode}$) on the gas outlet temperature **(a)**, the cell's voltage **(b)**, the final methane composition **(c)**, and the consumed energy per mass-produced CH_4 **(d)**.

Regarding the cell potential in Figure 3.18b, the outcome fluctuation at 0.4 and 0.5 CO_2 fractions can be similarly observed. When the CO_2 fraction exceeds 0.5, the cell potential decreases as the split fraction increases at any fixed recycling ratio. Moreover, at a specific split fraction above 0.5, the cell potential remains relatively constant with the variation of the recycling ratio. On the contrary, it cannot be stated similarly for split fractions 0.4 and 0.5 because the cell voltage increases with the recycling ratio at 0.4

split fractions and decreases at 0.5 split fractions. The results of the methane composition in Figure 3.18c and the electrical energy per kilogram of CH_4 produced in Figure 3.18d differ somehow from the previous ones. At all recycle ratios studied, the methane composition decreases as the CO_2 split fraction increases. It does not, however, vary with the recycling ratio, except for a split fraction of 0.4, where it increases until reaching a recycling ratio of 0.4, then drops when the recycling ratio is 0.5. On the other hand, the electrical energy per kg of CH_4 produced decreases while increasing the recycling ratio and the CO_2 split fraction above 0.4; whereas, for 0.4 split fractions, it stays constant with the recycling ratio till a value of 0.4, and then rapidly increases at a recycling ratio of 0.5. Because there are various factors to consider, explaining this fluctuation is complicated. However, it can be deduced that the deficient composition of CO_2 in the feed significantly influences the outlet gas temperature and, consequently, the cell temperature, potential, and power.

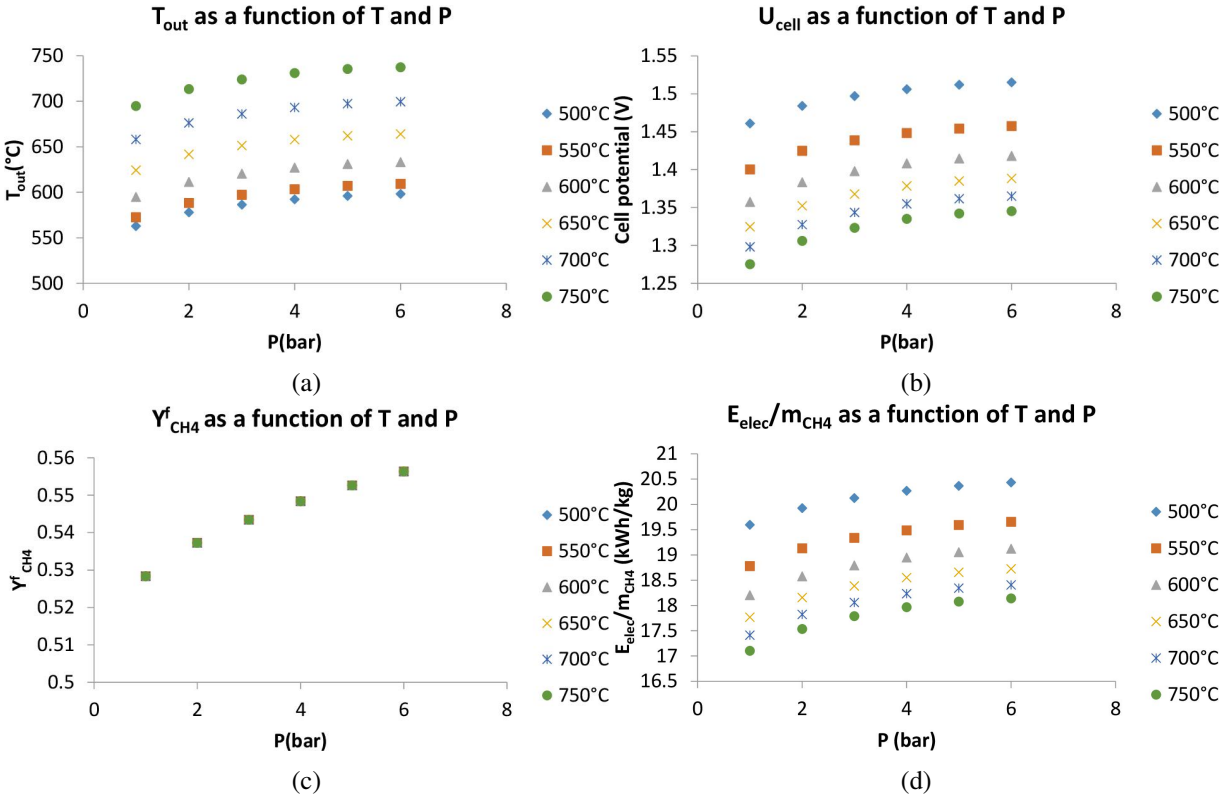

Figure 3.19: Impact of inlet gas temperature and pressure on the gas outlet temperature **(a)**, the cell's voltage **(b)**, the final methane composition **(c)**, and the consumed energy per mass-produced CH_4 **(d)**.

Finally, the impact of the inlet gas temperature and pressure was assessed to cover all possible factors impacting the Power-to-Gas system's efficiency. Figure 3.19 depicts the variation of the outlet gas temperature, cell's voltage, energy per kg of CH_4 produced, and the methane composition as a function of the temperature and pressure. To study these factors, the model required adjusting the thermodynamic parameters' equations, like enthalpy, entropy, and heat capacity, to include their variation with temperature and pressure. The equations as a function of temperature are taken from NIST Webbook [135]; however, that of pressure are generated through profound calculations of data extracted from Aspen Properties, presented in detail in Appendix A.

Looking at the results, Figure 3.19a reveals that the outlet gas temperature increases with the increase in the inlet temperature and pressure. The same is applicable for the cell potential in Figure 3.19b, signifying that the inlet gas temperature and pressure have the same influence on the outlet gas temperature and the cell voltage. As viewed in Figure 3.19c, the methane composition is affected only by the inlet pressure, as it increases with the pressure. Two reasons can explain this observation. The first reason is that, at the cell's fixed conditions selected here, the RWGS reaction is not occurring, as described in Figures 2.23 and 2.24. Thus, based on thermodynamics and chemical principles, temperature and pressure do not impact the outlet composition. This case explains the obtained constant value of methane composition with the temperature change. The second reason is related to the change of methane composition with pressure, which, based on the first reason, must not change. This change is due to the effect of pressure on the water separation from the syngas before methanation, where water separation is enhanced with the pressure increase. Therefore, the final syngas contains less water, which favors methane production, according to Le Chatelier's principle, so the methane composition increases with pressure. When the cell voltage and methane composition findings are combined, the outcomes of the electrical energy per kg of CH_4 produced may be predicted. The ratio of electrical energy to CH_4 mass-produced changes proportionally with cell voltage. It does, however, vary irreversibly with the amount of methane produced. As a result, while methane production is unaffected by the cell's inlet temperature and the cell voltage decreases when increasing the temperature, the electrical energy per kg of CH_4 produced must also decrease with the increase in temperature, as shown in Figure 3.19d. However, for the inlet pressure, the electrical energy ratio per kg of CH_4 produced is determined by the more significant influence between the cell potential and methane production, which both increase with pressure. According to the study findings, increasing the pressure results in higher electrical energy per the mass of CH_4 produced. In conclusion, temperature and pressure significantly impact the cell's performance and the Power-to-Gas system's efficiency.

Due to the massive number of outcomes obtained by the sensitivity study, it was relevant to put some constraints. These constraints targeted the cell's voltage, outlet temperature, and the final composition of the methane gas. The cell's voltage limit was chosen to be 1.4 V since it was reported, in [124], the formation of carbon solid in the cell at a voltage of 1.4 V. The outlet's temperature of the cell was restricted to above the cell's inlet temperature, referring to an exothermic operation of the cell to benefit from the high temperature of the outlet gases for heating the inlet ones. After applying these two limitations, the remaining set of outputs was inspected regarding the final composition of methane gas. At this stage, three cases were discovered: methane gas rich in H_2, methane gas rich in CO_2, and methane gas with H_2 and CO_2 composition meeting the specifications of the natural gas grid. The first case was neglected since it is impossible to separate H_2 from CH_4. For the second case, a separation process is needed to purify the methane gas from the excess CO_2, which poses extra expenses. Therefore, it seemed the most appropriate to choose the inputs for having a methane gas composition that meets the requirements of the gas grid. This choice led to minimizing the scope of inputs.

For the selection of the best final input conditions, it was necessary to test each input category in the process and calculate the process efficiency (η_{MCEC}) using Eq. 3.8. This final step allowed us to choose the operating conditions for the process simulation as follows: 650 °C, 1 atm, and a current density of -60 mA/cm^2. The inlet flow rates selected were scaled up from a system of 213 cells to a 1 MW system

with 1,428 cells using the "Rule of three" method. The final flow rates are 31.5 kmol/h of H_2O, and 56.69 kmol/h of total inlet CO_2, with 17 kmol/h of CO_2 supplied to the fuel electrode. Besides, half of the outlet fuel electrode gas was selected to be recycled to supply H_2 and CO, as well as additional amounts of H_2O and CO_2 to the inlet mixture of the cell's fuel electrode. However, only 20% of the outlet oxygen electrode was recycled. Therefore, these inputs corresponded to a cell inlet gas composition of 63% H_2O, 21% CO_2, 12% H_2, and 0.4% CO at the fuel electrode side, and 97% CO_2 and 3% O_2 at the oxygen electrode side.

4 Pinch Study

Combining the process modification and the pinch study enabled us to manage the process's energy efficiency improvement by acting on the energy recovery and reuse possibilities. In this section, the pinch analysis was performed using a code developed in Python software by Rupu YANG [180, 181] during his Ph.D. thesis. This pinch analysis generates the process streams' hot and cold composite curves and the grand composite curve, presented in Figures 3.20a and 3.20b, respectively. These curves aim to determine the minimum utility requirements of the system. The results revealed that the minimum heating utility required is zero kW, which is the upper gap between the red and blue curve in Figure 3.20a, and the minimum cooling one is 115 kW, represented by the lower gap between the curves.

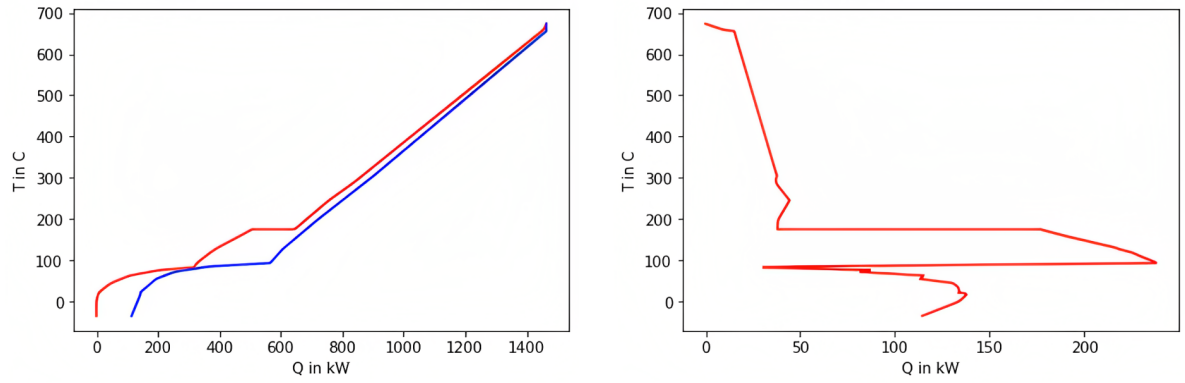

(a) (b)

Figure 3.20: The process streams' hot (red) and cold (blue) composite curves **(a)** and grand composite curve **(b)** obtained by the python code.

According to the Pinch study's outcomes, the process does not require any external heating source, which would result in a process efficiency of 70.6%. In this scope, the heat exchanger network of the process, which enables achieving the maximum possible efficiency of 70.6%, was determined using the Python model. This code studies the different heating and cooling requirements, proposes a series of heat exchanger network configurations, and selects the most flexible and cost-effective one.

Consequently, the model's results were applied to the process simulation to integrate the heat exchanger network, which allowed the recovery of the heat released in the system. The system's overall performance for this process compared to the initial state, where there is no heat recovery from the system, was evaluated. The results, displayed in Figure 3.21, revealed a significant improvement with a 36% increase in the efficiency from the initial case (Case 0) to the optimized case (Case 1). The final efficiency

of the new optimized process configuration is 68.7%, which is lower by 2% than the maximum efficiency of 70.6% that could be reached. The new design configuration is detailed in Section 5.

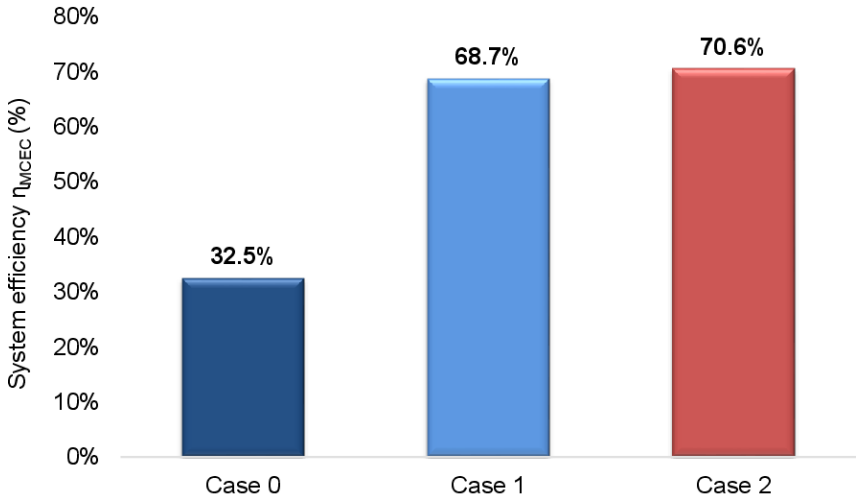

Figure 3.21: The overall system's efficiency evolution.

5 Optimized Process Overview and Description

5.1 Process Overview

The updated complete process was constructed and simulated after selecting the optimal operating conditions and optimizing the process's heat integration. Figure 3.22 illustrates the overall Power-to-SNG process with the heat integration network. In this figure, the solid lines represent the flow streams, while the dashed lines refer to the energy streams, where the blue ones correspond to the heat released and the red ones for the heat supplied. The steam generation block refers to the process where the waste heat from the system (blue dashed lines) is transferred through a series of heat exchangers into the cell's inlet feed (red dashed line), thus replacing Heater2 duty in Figure 3.2. These heat exchangers utilize the maximum heat available from the system, represented by Q1, Q2, Q3, and Q4. Q1 is the heat released during the methanation process that is recovered by generating steam. Q2 and Q4 are the cooling duties of the product streams of the cell from the cooler (COOLER2 and COOLER4) in Figure 3.2. Q3 is the heat of water condensation in the methane reactor product released by COOLER8 in Figure 3.6. This process will be demonstrated in Section 5.2.

Furthermore, in the syngas purification and treatment part shown in Figure 3.3, a heat Q is recovered from the cooler (COOLER5) located between the two consecutive water removal drums and from the inter-stage coolers (COOLER6 and COOLER7) located between the three consecutive compressors. This heat is then used to warm up the expanded CO_2 stream (EXPCO2) in Figure 3.2. Additionally, the stream INCATH is heated to the target temperature of 650 °C via a heat exchanger, which uses the outlet stream OUTANODE as a heating utility (Q") and an additional heater. Finally, stream INANODE is heated by the heat released (Q') by OUTCATH when it is cooled down.

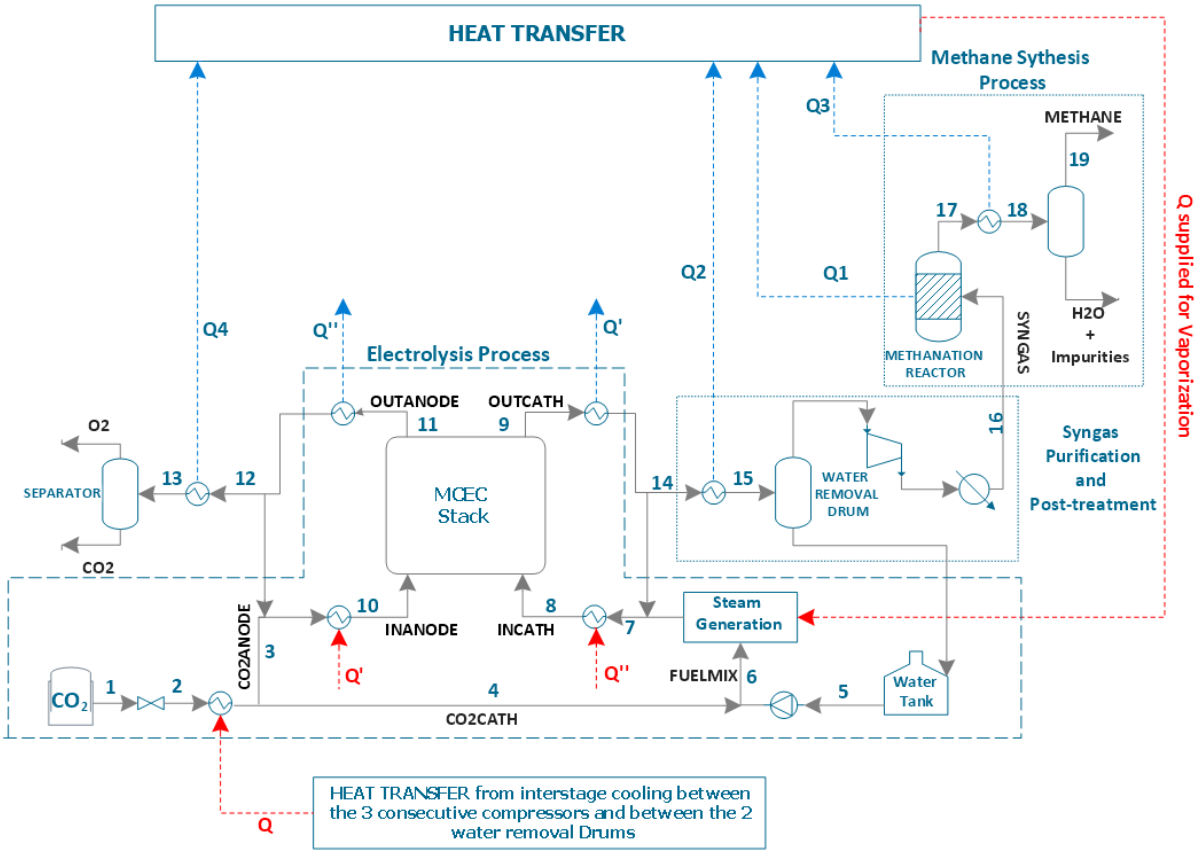

Figure 3.22: General configuration of the Power-to-SNG system using MCEC electrolyzer.

In this simulation, a pressure drop of 2% was considered inside the heat exchangers. However, the heat exchangers responsible for heating the cell's inlet feed (INCATH and INANODE) to the target temperature (650 °C) were assumed to be ideal with no pressure drop. This assumption was based on the fact that the recycle streams in the system will affect the heat exchangers' inlet streams, resulting in zero pressure in the system. It was assumed that the cell's electrode could compensate for the pressure drop within this loop.

The main thermochemical properties of the main streams depicted in Figure 3.22 are reported in Tables B.1, B.2 and B.4 in Appendix B. The operating conditions involved in the simulation were determined from the optimization analysis presented in Section 3. These operating conditions are summarized in Table 3.8.

In the simulated 1 MW power-to-SNG system, 1.3 t/day synthetic methane is produced, composed of 94.44% CH_4, 3.15% H_2, 2.2% CO_2, 0.2% H_2O, and traces of CO, and having a Wobbe Index of 50.92 MJ/Nm^3 (at 0 °C and 1 atm standard conditions). Based on these properties, it can be inferred that the produced methane strongly satisfies the French natural gas grid requirements. Therefore, it can be injected directly without requiring additional purification processes.

Parameters	Value
Number of Cells	1,428 cells
Total System Power	1 MW
Cell's Current Density	-60 mA/cm^2
Cell's Temperature	650 °C
Cell's Pressure	1 atm
Fuel Electrode Composition	mol%
H_2O	63%
CO_2	21%
H_2	12%
CO	4%
Oxygen Electrode Composition	mol%
CO_2	97%
O_2	3%

Table 3.8: Operating conditions of the 1 MW Power-to-SNG process simulation.

5.2 Steam Generation Process

The mixture stream (H_2O and CO_2) passes through 5 heat exchangers (HX4, HX5, HX6, HX7, HX8) with different heat sources to obtain a vapor state stream, as shown in Figure 3.23. The steam generation process utilizes the most available heat sources in the system.

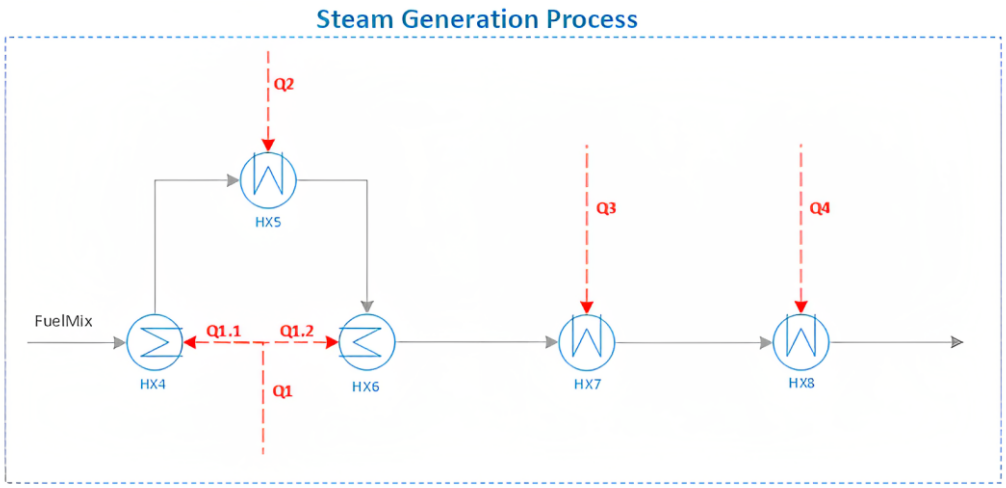

Figure 3.23: Steam Generation subsystem within the full MCEC process system.

Starting with the complementary heat exchangers HX4 and HX6, presented on the left side, in Figure 3.23:

- The liquid mixture receives the heat source from steam, which is first condensed in HX6 (heat duty Q1.2) and then further cooled in HX4 (heat duty Q1.1).
- This steam is generated by the absorbed heat Q1 from the methane synthesis reactor to keep it in an isothermal state

The feed mixture (FUELMIX) utilizes the heat remaining in the cooling water (Q1.1) through the heat exchanger HX4 and then passes into the second heat exchanger HX5. This heat exchanger, HX5, transfers the heat (Q2) between the liquid mixture and the separated stream of the outlet cathode gas (OUTCATH2 in Figure 3.2) after recycling. After that, the partially vaporized feed is supplied with additional heat (Q1.2) through heat exchanger HX6, which uses the steam from the methane reactor, and two other heat exchangers, HX7 and HX8. The heat exchanger HX7 transfers the heat (Q3), the heat of condensation of the water in the methane product stream exiting the reactor (CH4GAS in Figure 3.6). Finally, heat is provided by the heat exchanger HX8 to complete the final vaporizing phase and increase the feed temperature further. This heat (Q4), transferred by heat exchanger HX8, is supplied from the separated outlet stream of the oxygen electrode (OUTANOD2 in Figure 3.2) into the feed liquid stream. By these five series heat exchangers, the feed stream is completely vaporized.

5.3 Process Outcomes

The principle results of the process are summarized in Table 3.9. Compared to the studies available in the literature, the current proposed process yields more compelling results. For example, Mastropasqua et al. (2018) [71] simulated the Power-to-SNG process based on a MCEC electrolyzer that operates at a current density of -353 mA/cm^2 for a power load of 1,250 kW and a cell voltage of 1.31 V. The full process system produces about 2 tonnes per day CH_4 and has an efficiency of 60.4%. In contrast, Barelli et al. (2021) [5] simulated a MCEC system that produces hydrogen at a current density of 150 mA/cm^2 at a power density load of 0.213 W/cm^2 and cell voltage 1.42 V. The hydrogen capacity is 0.074 Nl/(h·cm^2). By comparing our process with this latter simulation process, the process produces a hydrogen capacity of 0.068 Nl/(h·cm^2) at a current density of -60 mA/cm^2, a power density of 0.083 W/cm^2 and a cell voltage of 1.38V.

Parameters	**Value**
Power Density	0.082 W/cm^2 per cell
Cell Voltage	1.38 V
Number of Cells	1,428 cells
Total System Power	1 MW
Methane Produced	1.29 t/day
Methane Composition	94.44% CH_4, 3.15% H_2, 2.2% CO_2, 0.2% H_2O, and traces of CO
Methane Wobbe Index	50.92 MJ/Nm^3 (at 0 °C and 1 atm standard conditions)
Process Efficiency	68.7%

Table 3.9: Principle results of the Power-to-Gas process simulation.

6 Conclusion

In this chapter, a steady-state simulation was performed using Aspen Plus software to study the Power-to-SNG process. First, the co-electrolysis model of MCEC was utilized to produce syngas from co-electrolysis and transform it into synthetic methane. Additionally, a CO_2 capture based on MEA chemical absorption was simulated, taking into account the CO_2 desulfurization process before injection into the MCEC electrolyzer, which is highly sensitive to sulfur. The process was then optimized by conducting a profound sensitivity analysis to select optimal operating conditions. Furthermore, a pinch analysis study was carried out to improve the overall performance of the process by using waste heat to supply the duty required for vaporizing and heating the inlet water of the cell, as well as heating the cell's inlet streams to the target temperature of 650 °C. Therefore, applying the heat recovery integration and the optimal conditions on the process resulted in an optimized process with an overall energy efficiency of 68.7% and a methane production rate of 1.3 t/day, ready for injection into the natural gas network.

Résumé: Simulation du système de Power-to-Gas

Simulation du procédé de Power-to-SNG

Le système Power-to-SNG a été étudié en utilisant le logiciel Aspen Plus. Il se compose, comme mentionné précédemment, de deux procédés principaux : l'électrolyse et la méthanation. Ce procédé nécessite tout d'abord une alimentation en H_2O et en CO_2 pour que l'électrolyse puisse se produire dans l'électrolyseur MCEC, comme illustré dans la représentation schématique de la Figure 3.24. Ensuite, le gaz de synthèse produit par la co-électrolyse a été traité avant d'être envoyé dans un réacteur de méthanation pour produire du méthane de synthèse.

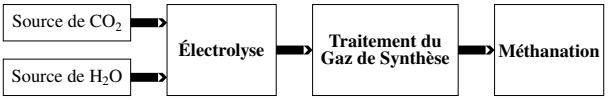

Figure 3.24: Représentation schématique du système Power-to-SNG basé sur un électrolyseur à carbonates fondus.

Les hypothèses générales

Un modèle MCEC a été appliqué à une seule cellule et implémenté dans le logiciel Aspen Plus pour la simulation du procédé. Pour le module MCEC, plusieurs cellules sont assemblées et séparées par une plaque bipolaire pour former une « pile ».

Dans cette simulation du procédé, certaines hypothèses ont été appliquées au modèle de pile MCEC, qui sont les suivantes :

- Le module MCEC présenté de 1 MW, était composé de 4 piles de 375 cellules chacune, avec une surface active d'électrode de cellule de 8460 cm^2, basée sur la surface industrielle de la cellule MCFC de 9000 cm^2 avec une zone inactive de 6%, produite par les fabricants de piles à combustible [143]. L'échelle du modèle a été réalisée en déterminant le nombre de cellules nécessaires pour que la pile consomme 1 MW d'énergie électrique.
- L'électrolyse du CO_2 a été prise en compte dans cette simulation du procédé.
- Les réactions possibles qui peuvent se produire au sein des plaques bipolaires n'ont pas été prises en compte.
- La réaction de méthanation à l'intérieur de la cellule n'a pas été prise en compte dans cette étude car les conditions d'entrée de la cellule ne sont pas conformes à celles requises pour favoriser la production de méthane.

Optimisation du procédé

Après avoir sélectionné les équipements nécessaires au système Power-to-SNG et précisé leurs spécifications pour compléter les électrolyseurs MCEC, une analyse de sensibilité des paramètres d'entrée a été réalisée pour retenir les conditions optimales permettant de produire un gaz de méthane de qualité

satisfaisant les exigences du réseau de gaz naturel et d'obtenir le rendement maximal du procédé. Le rendement du système η_{MCEC} (Eq. 4.3) est défini par le rapport de la puissance de chauffage contenue dans le méthane produit et de la consommation totale du système, qui est composée de la puissance consommée par la pile $\dot{W}_{el,\ MCEC}$ et de la consommation des équipements de l'installation des équipements des usines (BoP) $\dot{W}_{el,\ BoP}$, comprenant les pompes, les compresseurs, etc.

$$\eta_{MCEC} = \frac{\dot{m}_{CH_4,\ prod} \times LHV}{\dot{W}_{el,\ MCEC} + \dot{W}_{el,\ BoP}} \tag{4.3}$$

Ensuite, l'analyse du pincement a été réalisée à l'aide d'un code développé dans le logiciel Python par Rupu YANG [180, 181] lors de sa thèse de doctorat. À partir de cette analyse du pincement, les courbes composites chaudes et froides des flux du procédé ainsi que la courbe composite globale ont été obtenues, comme présenté respectivement dans la Figure 3.25a et la Figure 3.25b. Ces courbes ont pour objectif de déterminer les besoins minimums en utilités du système. Les résultats ont révélé que l'utilité de chauffage minimale requise est nul kW, ce qui correspond à l'écart supérieur entre la courbe rouge et la courbe bleue dans la Figure 3.25a, et l'utilité de refroidissement minimale est de 115 kW, représentée par l'écart inférieur entre les courbes.

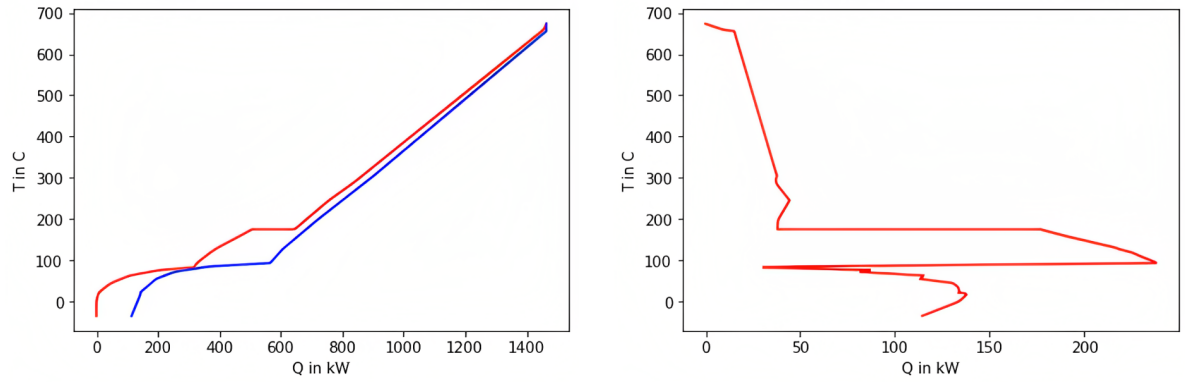

(a) (b)

Figure 3.25: Courbes composites chaudes (rouge) et froides (bleu) des flux de traitement **(a)** et courbe composite globale **(b)** obtenues par le code python.

Selon les résultats de l'étude de pincement, le procédé ne nécessite aucune source de chaleur externe, ce qui se traduit par un rendement du procédé de 70,6%. Dans ce cadre, le réseau d'échangeurs de chaleur du procédé, permettant d'atteindre le rendement maximal possible de 70,6%, a été déterminé en utilisant le modèle Python. Ce code étudie les différents besoins en chauffage et en refroidissement, propose une série de configurations de réseau d'échangeurs de chaleur et sélectionne la plus flexible et la plus rentable.

Aperçu du procédé

Après avoir sélectionné les conditions de fonctionnement optimisées et optimisé l'intégration thermique du procédé, le procédé complet mis à jour a été construit et simulé. La Figure 3.26 présente l'ensemble du procédé Power-to-SNG avec le réseau d'intégration thermique. Il est composé de 3 sous-systèmes principaux :

1. Le ***procédé d'électrolyse*** comprend la pile MCEC et tous les composants supplémentaires qui assurent les conditions de fonctionnement souhaitées. Les principales fonctionnalités de ce sous-système sont les suivantes :
   - Vaporiser le mélange d'eau et de CO_2 du côté de la cathode pour générer un flux entièrement vaporisé en utilisant la chaleur résiduelle du système (bloc de génération de vapeur "Steam generation")
   - Chauffer les flux d'entrée de la cellule jusqu'à sa température de fonctionnement cible, qui est de 650 °C.
   - Produire du gaz de synthèse au sein de la pile MCEC.
2. Le sous-système de ***purification et post-traitement du gaz de synthèse***, qui permet de :
   - Séparer l'eau du gaz de synthèse.
   - Comprimer et chauffer le gaz de synthèse pour atteindre les conditions requises pour favoriser la synthèse du méthane.
3. Le ***procédé de synthèse du méthane***, qui permet de :
   - Transformer le gaz de synthèse en méthane à l'intérieur du réacteur.
   - Purifier le méthane afin de répondre aux spécifications requises pour l'injecter dans le réseau de gaz naturel.

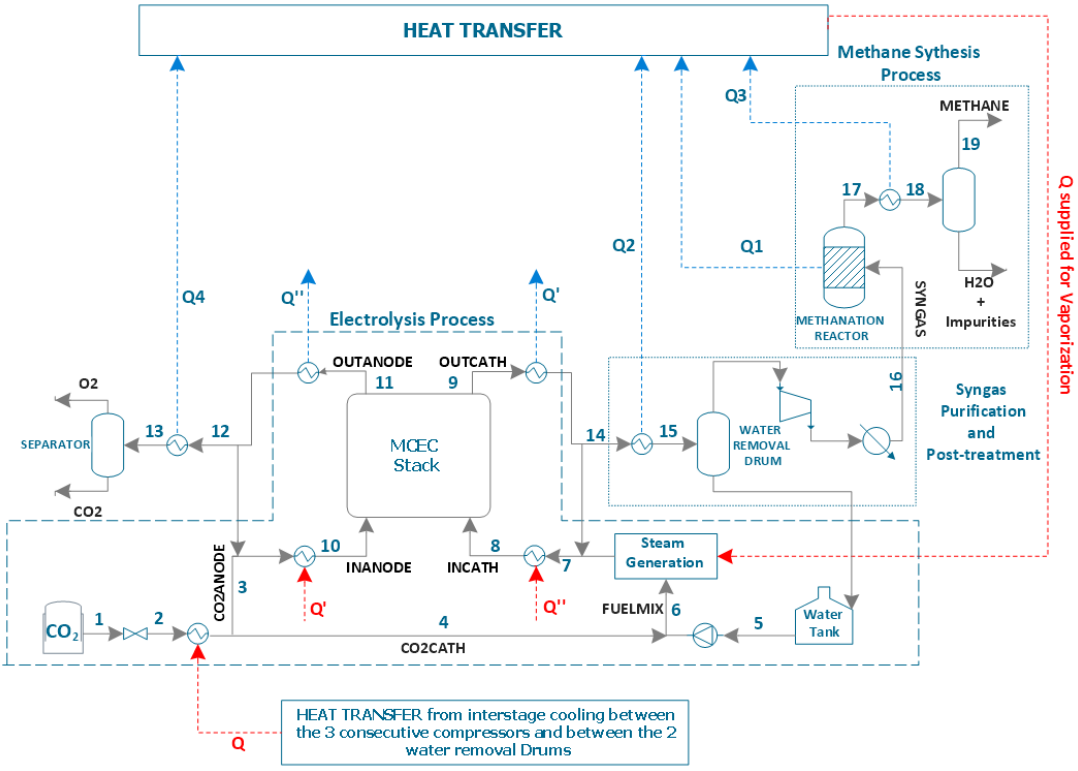

Figure 3.26: Configuration générale du système Power-to-SNG utilisant l'électrolyseur MCEC.

Dans la Figure 3.26, les lignes solides représentent les flux de matière, tandis que les lignes en pointillés font référence aux flux d'énergie, où les lignes en pointillés bleues correspondent à la chaleur libérée et les lignes en pointillés rouges à la chaleur fournie. Le bloc de génération de vapeur fait référence au procédé où la chaleur perdue du système (lignes en pointillés bleues) est transférée à travers une série d'échangeurs de chaleur vers l'alimentation d'entrée de la cellule (ligne en pointillés rouges). Ces échangeurs de chaleur utilisent la chaleur maximale disponible du système, représentée par Q1, Q2, Q3 et Q4. Q1 est la chaleur libérée lors du procédé de méthanation qui est récupérée en produisant de la vapeur. Q2 et Q4 sont les charges de refroidissement des flux de produits de la cellule. Q3 est la chaleur de condensation de l'eau dans le produit du réacteur à méthane. Ce procédé sera démontré dans la Figure 3.27.

De plus, dans la partie de purification et de traitement du gaz de synthèse, une quantité de chaleur Q est récupérée à partir du refroidisseur situé entre les deux tambours d'élimination de l'eau consécutifs et des refroidisseurs inter-étages situés entre les trois compresseurs consécutifs. Cette chaleur est ensuite utilisée pour réchauffer le flux de CO_2 en expansion (flux 2) dans la Figure 3.26. De plus, le flux INCATH est chauffé jusqu'à la température cible de 650 °C via un échangeur de chaleur, qui utilise le flux de sortie OUTANODE comme source de chaleur (Q") et un dispositif de chauffage supplémentaire. Enfin, le flux INANODE est chauffé par la chaleur libérée (Q') par OUTCATH lorsqu'il se refroidit.

Dans cette simulation, une baisse de pression de 2% a été considérée uniquement à l'intérieur des échangeurs de chaleur. Cependant, les échangeurs de chaleur permettant de chauffer l'alimentation de la cellule (INCATH et INANODE) à la température cible de 650 °C ont été supposés idéaux, sans baisse de pression. Cette hypothèse repose sur le fait que les flux de recyclage dans le système vont influencer les flux d'entrée des échangeurs de chaleur, ce qui entraîne une pression nulle dans le système. Il a été supposé que l'électrode de la cellule pouvait compenser la chute de pression à l'intérieur de cette boucle.

Les principales propriétés thermochimiques des flux principaux représentés dans la Figure 3.26 sont rapportées dans les tableaux B.1, B.2 et B.4 de l'annexe B. Les conditions de fonctionnement utilisées dans la simulation ont été déterminées à partir de l'analyse d'optimisation présentée dans la Section 3. Ces conditions de fonctionnement sont résumées dans le tableau 3.10.

Paramètres	**Valeur**
Nombre de cellules	1428 cellules
Puissance totale du système	1 MW
Densité de courant de la cellule	-60 mA/cm^2
Température de la cellule	650 °C
Pression de la cellule	1 atm
Composition de l'électrode de combustible (Fuel electrode)	mol%
H_2O	63%
CO_2	21%
H_2	12%
CO	4%
Composition de l'électrode d'oxygène (Oxygen electrode)	mol%
CO_2	97%
O_2	3%

Table 3.10: Conditions de fonctionnement de la simulation du procédé Power-to-SNG de 1 MW.

Procédé de génération de vapeur

Le mélange de vapeur (H_2O et CO_2) passe à travers cinq échangeurs de chaleur (HX4, HX5, HX6, HX7, HX8) avec différentes sources de chaleur pour obtenir un flux à l'état de vapeur, comme indiqué dans la Figure 3.27. Le procédé de génération de vapeur utilise les sources de chaleur les plus disponibles dans le système.

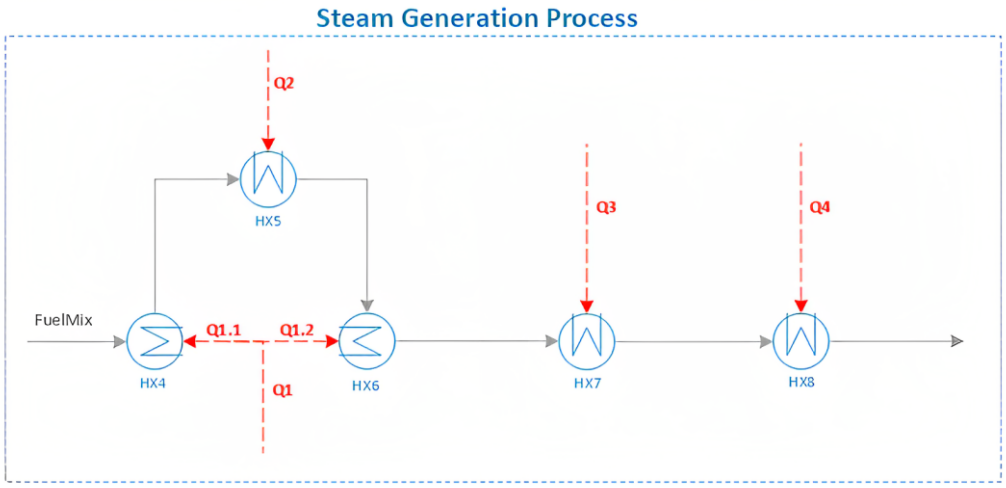

Figure 3.27: Sous-système de production de vapeur au sein du système complet du MCEC.

En commençant par les échangeurs de chaleur complémentaires HX4 et HX6, présentés du côté gauche dans la Figure 3.27:

- Le mélange liquide reçoit la source de chaleur provenant de la vapeur, qui est d'abord condensée dans HX6 (besoin thermique Q1.2) puis refroidie davantage dans HX4 (besoin thermique Q1.1).
- Cette vapeur est générée par la chaleur absorbée Q1 provenant du réacteur de synthèse de méthane, afin de maintenir ce dernier dans un état isotherme.

Le flux d'alimentation (FUELMIX) utilise la chaleur restante dans l'eau de refroidissement (Q1.1) à travers l'échangeur de chaleur HX4, puis passe dans le deuxième échangeur de chaleur HX5 qui transfère la chaleur (Q2) entre le mélange liquide (H_2O and CO_2) et le flux séparé du gaz de cathode de sortie (Flux 14 dans la Figure 3.26) après recyclage. Ensuite, le mélange partiellement vaporisé est alimenté en chaleur supplémentaire (Q1.2) à travers l'échangeur de chaleur HX6, qui utilise la vapeur provenant du réacteur de méthane, ainsi que deux autres échangeurs de chaleur, HX7 et HX8. L'échangeur de chaleur HX7 transfère la chaleur (Q3), la chaleur de condensation de l'eau dans le flux produit de méthane sortant du réacteur (Flux 17 dans la Figure 3.26). Enfin, la chaleur est fournie par l'échangeur de chaleur HX8 pour compléter la phase de vaporisation finale et augmenter davantage la température de l'alimentation. Cette chaleur (Q4), transférée par l'échangeur de chaleur HX8, est fournie à partir du flux séparé de sortie de l'électrode d'oxygène (Flux 12 dans la Figure 3.26) dans le flux liquide d'alimentation. Grâce à ces cinq échangeurs de chaleur en série, le flux d'alimentation est complètement vaporisé.

Résultats du procédé

Les principaux résultats du procédé sont résumés dans le tableau 3.11. Comparé aux études existantes, notre procédé présente des résultats plus intéressants. À titre d'exemple, Mastropasqua et al. (2018) [71] ont simulé un procédé Power-to-SNG basé sur un électrolyseur MCEC fonctionnant à une densité de courant de -353 mA/cm^2 pour une charge de puissance de 1250 kW et une tension de cellule de 1,31 V. Leur système produit environ 2 tonnes de CH_4 par jour avec un rendement de 60.4%. En revanche, Barelli et al. (2021) [5] ont étudié un système MCEC qui produit de l'hydrogène à une densité de courant de 150 mA/cm^2 pour une charge de densité de puissance de 0,213

Paramètres	Valeur
Densité de puissance	0,082 W/cm^2 par cellule
Tension de la cellule	1,38 V
Nombre de cellules	1428 cellules
Puissance totale du système	1 MW
Méthane produit	1.29 t/jour
Composition du méthane	94,44% CH_4, 3,15% H_2, 2,2% CO_2, 0,2% H_2O, et des traces de CO
Indice de Wobbe du méthane	50,92 MJ/Nm^3 (à 0 °C et 1 atm condition standards)
Rendement du procédé	68,7%

Table 3.11: Principaux résultats de la simulation du procédé Power-to-Gas.

Source de CO_2 à partir du procédé de captage du carbone : simulation

L'électrolyseur MCEC nécessite du CO_2 comme alimentation pour son fonctionnement afin de produire et de stocker de l'électricité propre. Ainsi, les flux d'alimentation de la cellule doivent être inspectés pour détecter toute impureté, car les MCFC/MCEC sont très sensibles au soufre. Étant donné que le CO_2 utilisé comme alimentation pour la cellule est capté à partir des gaz de combustion qui contiennent des impuretés telles que les SO_x, les NO_x et autres, il est nécessaire de le purifier afin d'atteindre la limite de tolérance des MCFC, qui reste encore assez floue pour le moment. En effet, bien que le soufre ait été reconnu comme l'impureté la plus nocive dans les gaz de combustion pour les MCFC [172], les conditions de fonctionnement telles que la température ou la pression semblent susceptibles de modifier l'influence du soufre sur la dégradation de la cellule et la limite de tolérance de la cellule.

Composition des gaz de combustion

Étant donné que l'Allemagne est toujours un utilisateur important du charbon, se classant septième au monde sur la liste des pays ayant le plus de centrales au charbon en fonctionnement en 2021, il semblait intéressant de considérer une méthode de captage du CO_2 à partir de ces centrales. Pour commencer, puisque l'objectif principal de la recherche est d'étudier tout le procédé de purification et de captage aussi fidèlement que possible par rapport à la réalité, il est nécessaire de connaître la composition réelle des gaz de combustion utilisés comme alimentation. Cependant, étant donné que les impacts les plus importants sont liés au CO_2 et à la concentration des impuretés, il était impossible de trouver une composition complète qui ne compromettrait pas la précision de la concentration des impuretés. Par conséquent, les pourcentages volumétriques pour la plupart des composants, tels que le CO_2 et toutes les impuretés,

ont été sélectionnés à partir des expériences de Lee et al. (2009) [160], les concentrations classiques de O_2 et H_2O ont été prises à partir de différentes sources de littérature, telles que Song et al. (2004) [173] et Di Giulio et al. (2012) [172], et le N_2 a été utilisé pour équilibrer la composition puisqu'il s'agit d'un gaz inerte.

Paramètres	Valeur
Paramètres des gaz de combustion à l'entrée	
Température (°C)	52
Pression (MPa)	0,1
Débit volumétrique (m^3/h)	$2{,}55\times10^6$
Paramètres du procédé	
Fraction massique à l'entrée de la MEA	0,3
Perte de purge de l'MEA pauvre (%)	15
Fraction massique à l'entrée de la $CaCO_3$	0,0007

Composition des gaz de combustion	Valeur (vol%)
CO_2	12
SO_2	0,3
SO_3	0,006
NO_2	0,004
HCl	0,01
H_2O	10
O_2	5
N_2	72,68

Table 3.12: Conditions d'entrée des gaz de combustion et paramètres de simulation.

Limites et tolérance pour les impuretés

En ce qui concerne la composition choisie pour simuler les gaz de combustion d'une centrale au charbon, il est important d'examiner l'impact que différentes impuretés ont sur la cellule, afin d'établir une limite à respecter grâce à une purification préalable des gaz. Étant donné que les cellules MCEC et MCFC ont la même composition chimique, mais simplement un fonctionnement électrochimique différent, il sera approprié d'examiner l'impact des différentes espèces sur l'une de ces deux cellules, qui sera la MCFC. Di Giulio et al. (2012) [172] confirment que le soufre est l'impureté la plus dangereuse pour la MCFC. Ils ont étudié l'interaction du soufre avec la cellule et ont démontré que des concentrations aussi faibles que 1 ppm de H_2S pouvaient entraîner une dégradation significative de la cellule. Milewski et Lewandowski (2012) [182] ont poursuivi ces recherches en étudiant l'impact du soufre à des concentrations plus élevées, jusqu'à 680 ppm. Leurs résultats ont montré que même à des concentrations inférieures à 100 ppm, une baisse de tension de 2% était observée après 48 heures de fonctionnement. Ces concentrations endommageraient donc rapidement la cellule, réduisant sa durée de vie. Marina (2014) [169] a étendu ces études en incluant d'autres impuretés telles que le mercure, le chlore, le fluor et le sélénium. Les résultats ont indiqué que des concentrations de soufre allant jusqu'à 1 ppm n'entraînaient que des pertes de performance négligeables. Cependant, le chlore était susceptible de provoquer une détérioration de la cellule en déplaçant les carbonates de l'électrolyte. Des concentrations supérieures à 0,1 ppm de HCl(g) entraîneraient une perte d'électrolyte de 5% pendant le fonctionnement de la cellule. Par conséquent, une désulfuration des fumées de la centrale thermique est nécessaire compte tenu de la composition mentionnée précédemment.

Procédé de désulfuration

Li et al. (2022) [174] ont réalisé un état de l'art sur les procédés de désulfuration. Ils ont souligné que parmi les procédés de désulfuration à sec, humide et semi-sec, la désulfuration humide est la plus efficace. De plus, Gutiérrez Ortiz et al. (2006) [176] soutiennent que la désulfuration utilisant le calcaire est la plus adaptée aux besoins de l'étude actuelle en raison de son faible coût d'installation. La Figure 3.28 présente un schéma du procédé de désulfuration humide au calcaire. La désulfuration des gaz de combustion se

déroule dans la tour d'absorption où la boue — un mélange de carbonates de calcium ($CaCO_3$)— réagit avec les SO_x et les élimine par absorption chimique. Enfin, un filtre est ajouté après la tour d'absorption pour éliminer le gypse précipité et recycler le liquide de sortie à travers une boucle. Afin d'atteindre l'objectif de 1 ppm de soufre à la sortie, il était nécessaire de trouver un rapport optimal entre le carbonate de calcium et le soufre. Une analyse de sensibilité réalisée avec Aspen Plus a démontré que plus de boue entrant dans le procédé, plus la désulfuration est efficace. Cependant, le module d'analyse économique a révélé que le composant le plus coûteux de ce procédé est la matière première ($CaCO_3$) contenue dans cette boue, ce qui a conduit à la sélection du débit massique le plus bas, permettant ainsi d'atteindre l'objectif de 1 ppm.

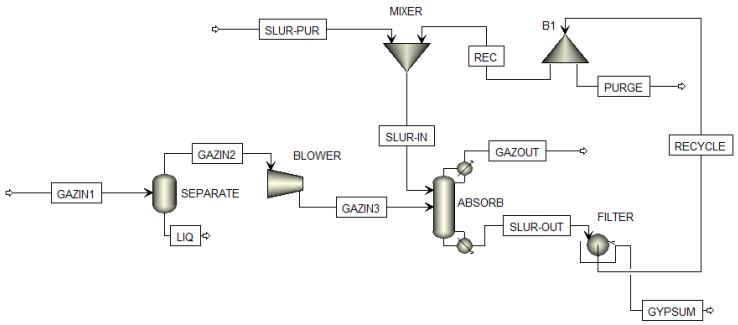

Figure 3.28: Mise en œuvre d'Aspen Plus pour la désulfuration du calcaire.

Des recherches récentes menées par Zhang et al. (2021) [177] se sont concentrées sur la désulfuration cryogénique. Leur simulation, basée sur la liquéfaction du soufre dans les gaz de combustion, a montré un rendement de désulfuration de 73,2% à -45 °C et 0,5 MPa, pouvant atteindre 90,2% à 2,5 MPa. Sur la base de cette étude, le procédé cryogénique a été adapté pour atteindre une concentration de soufre cible de 1 ppm. Cependant, le CO_2 se liquéfie avec le soufre à haute pression [177], ce qui a nécessité une réduction de la pression de fonctionnement à 0,1-0,2 MPa. Le procédé standard de désulfuration cryogénique a été étudié à basse pression, et un procédé optimisé a été proposé, incluant un pré-réacteur pour convertir le SO_2 en SO_3, car le SO_3 a un point d'ébullition plus élevé que celui du SO_2, comme illustré dans la Figure 3.29.

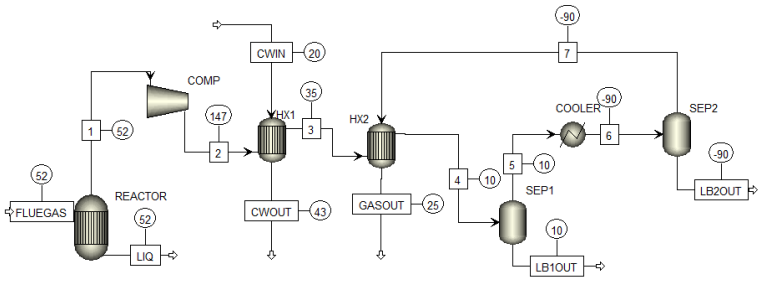

Figure 3.29: Mise en œuvre de la désulfuration cryogénique par Aspen Plus.

Le procédé actuel fonctionne en refroidissant le flux de gaz pour éliminer l'excès d'eau avant que la température ne baisse plus et ne fassent geler l'eau, bloquant potentiellement les tuyaux. Pour cela, deux échangeurs de chaleur successifs sont utilisés pour abaisser la température à 10 °C et séparer l'eau du

flux de gaz. Le flux de vapeur de sortie du séparateur (SEP1) est ensuite refroidi davantage à -90 °C, où le soufre est séparé du reste du gaz de combustion. Enfin, le flux de vapeur du séparateur (SEP2) est réchauffé par l'alimentation d'entrée à l'aide du deuxième échangeur de chaleur pour atteindre les températures supérieures requises pour le captage du CO_2, qui est fixée à 25 °C dans cette étude.

Procédé de captage de CO_2

Le captage du CO_2 peut prendre plusieurs formes, du captage en pré-combustion au captage en post-combustion. L'avantage du captage en post-combustion est qu'il serait compatible avec les centrales thermiques existantes. De nombreuses recherches ont été menées sur le captage du CO_2 par absorption chimique à l'aide de différents solvants. Le solvant le plus mature pour ce procédé est la monoéthanolamine (MEA), mais d'autres solvants ont également été étudiés et ont révélé des performances intéressantes. Indépendamment des solvants étudiés, ce travail se concentre sur la simulation du procédé de captage du CO_2 de référence utilisant la MEA. Un tel procédé a déjà été modélisé à l'aide du logiciel Aspen Plus [179] pour atteindre un taux de captage de CO_2 de 85% dans les flux sortants. Cependant, ces études n'ont pas pris en compte la présence de traces de soufre dans le gaz. Dans cette étude, deux procédés sont considérés : un procédé de captage utilisant la MEA standard (Figure 3.30a) et un autre procédé prenant en compte la récupération de chaleur du procédé (Figure 3.30b) où deux échangeurs de chaleur (HeatX1 et HeatX2) sont ajoutés dans la boucle de recyclage pour remplacer le refroidisseur dans Figure 3.30a.

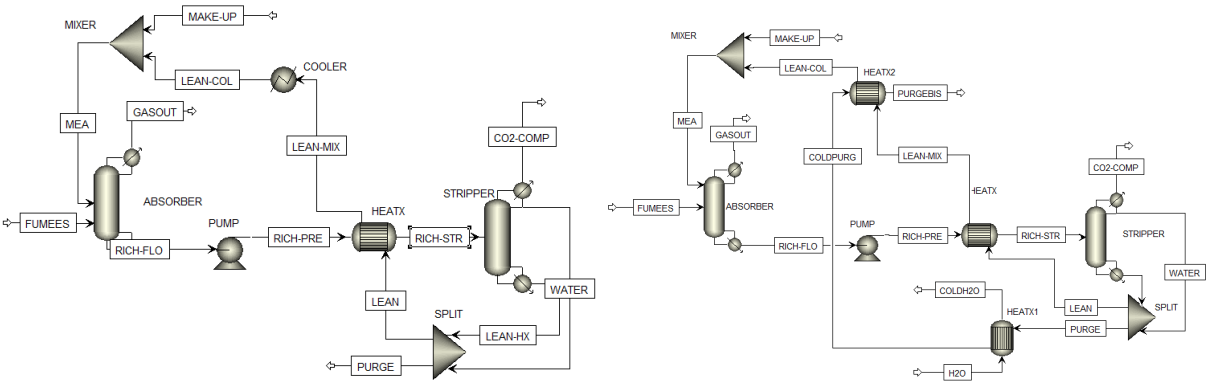

(a) (b)

Figure 3.30: Mise en œuvre par Aspen Plus du captage du CO_2 sans échangeurs de chaleur (**a**) et avec échangeurs de chaleur (**b**).

Résultats

Cinq simulations différentes ont été réalisées en utlisant Aspen Plus : désulfuration des gaz de combustion à l'aide du procédé de calcaire humide à 0,11 MPa, désulfuration cryogénique selon deux procédés différents à 0,2 MPa, et deux captages de CO_2 différents selon le flux provenant de la désulfuration cryogénique optimisée avec réacteur. La composition des gaz de combustion à chaque étape des deux procédés de désulfuration est présentée dans le tableau 3.7.

Le procédé de désulfuration par calcaire humide a réussi à atteindre un seuil de soufre tolérable de 1 ppm. En revanche, la technique cryogénique standard sans réacteur n'a pas pu atteindre ce niveau, avec une sortie de SO_2 à une fraction massique de 230 ppm. L'augmentation de la pression à 3 MPa a amélioré le procédé de désulfuration, mais a entraîné une perte significative de CO_2 liquide avec le soufre. Par conséquent, la technique cryogénique standard s'est révélée inefficace pour la désulfuration à un seuil de soufre de 1 ppm. Cependant, l'ajout d'un pré-réacteur a amélioré le procédé de désulfuration cryogénique, permettant une fraction massique de soufre inférieure à 1 ppm dans les gaz de combustion en sortie. Le procédé de calcaire humide a atteint un rendement de près de 100% pour le SO_2 et le SO_3, tandis que la technique cryogénique standard sans réacteur a obtenu un rendement de 72% pour le SO_2 et près de 100% pour le SO_3. Le procédé cryogénique optimisé avec réacteur a atteint un rendement de près de 100% pour l'élimination du SO_2 et du SO_3, ce qui le rend compétitif par rapport aux procédés classiques de calcaire humide. Toutefois, des études supplémentaires sont nécessaires pour réduire ou éviter la perte de CO_2 de 31% observée dans le procédé cryogénique optimisé.

Les simulations la MEA ont atteint avec succès leurs objectifs. Le premier objectif était de captager une partie significative du CO_2 des gaz de combustion et de libérer des fumées sans carbone dans l'atmosphère, tandis que le second était de concentrer le CO_2 pour produire un flux de sortie de haute pureté utilisable comme alimentation pour la pile à combustible. Le procédé MEA post-limestone a obtenu un rendement de captage de CO_2 de 94,5% sans échangeurs de chaleur de récupération (HeatX) et 94,7% avec HeatX. Le procédé MEA post-cryogénique a atteint un rendement de captage de CO_2 de 94,8% pour les deux procédés. De plus, l'utilisation d'échangeurs de chaleur de récupération dans le procédé MEA post-limestone a réduit la charge de rebouilleur de 20%, tandis que dans le procédé MEA post-cryogénique, la réduction était de 36%.

Conclusion

Dans ce chapitre, une simulation en régime permanent a été réalisée avec Aspen Plus pour étudier le procédé de Power-to-SNG. Tout d'abord, le modèle de co-électrolyse du MCEC a été utilisé pour produire du gaz de synthèse par co-électrolyse et le transformer en méthane de synthèse. De plus, un captage de CO_2 basé sur l'absorption chimique au MEA a été simulée, en tenant compte du procédé de désulfuration du CO_2 avant l'injection dans l'électrolyseur MCEC pour éviter les problèmes liés au soufre. Le procédé a été optimisé par une analyse de sensibilité approfondie pour sélectionner les conditions de fonctionnement optimales. Ensuite, une étude d'analyse du pincement a été réalisée pour améliorer les performances globales du procédé en utilisant la chaleur résiduelle pour la vaporisation et le chauffage de l'eau d'alimentation de la cellule, ainsi que le chauffage des flux d'entrée à la température cible de 650 °C. Ainsi, l'intégration de la récupération de chaleur et l'application des conditions optimales sur le procédé ont permis d'obtenir un procédé optimisé avec un rendement énergétique global de 68,7% et une production de méthane de 1,3 t/jour, prêt à être injecté dans le réseau de gaz naturel.

Chapter 4

Dynamic Simulation

Objective

This chapter examines the dynamic operation of the various stages of the Power-to-SNG process. A dynamic model was developed in "Aspen Custom Modeler (ACM)" software to study cell degradation and its response to unexpected changes. The methanation unit was simulated in dynamic mode, and the cold start-up procedures of each unit were discussed. Finally, the response of the Power-to-SNG system to variable renewable energy sources such as wind and solar was examined.

Table of Contents

1 Literature Review on Dynamic Modeling

1.1 Review of MCEC Dynamic Modeling

The dynamic process is an essential step for monitoring and controlling the development and operation of a process, from the heat-up to start-up and controlling strategy in case of unexpected changes. Therefore, it is crucial to study the dynamic operation of the process. Since MCEC is a recent technology, no literature preview has addressed its dynamic behavior. However, the dynamic behavior was studied for the MCFC technology, which was first commercialized in 2005. For instance, Sasaki et al. (1988) [183] examined the dynamic characteristics of a 10 kW-MCFC stack using both experimental and theoretical approaches. The experimental study investigated the outlet gas pressure, total cell current, stack voltage, and temperature response with an applied step load. The results revealed that stack temperature is easily controlled by the cathode gas recycle flow, whereas pressure is susceptible to load changes.

Later, W. He (1998) [184] studied the dynamic performance of MCFC by developing a model to calculate the load-following capability of the system under various step changes and determine the potential operational problems of the components in these load-following modes. Their investigation demonstrated that the system output power responds quickly to a current step change and slowly to a gas-flow change. Besides, the fuel cell pressure difference was found to be within the safety constraints of the system. Furthermore, Lukas et al. (1999, 2001) [185, 186] developed a nonlinear explicit mathematical dynamic model of an internal reforming MCFC stack. This model aimed to obtain a realistic interpretation of the load variation response on the fuel cell stack and defined the transient limitations and control requirements. The study was conducted by operating the MCFC plant at its rated power and then applying a sudden 10% step-up increase in power demand. This step change showed a quick change in the anode gas composition, increased outlet gas pressures, and a fast drop in the stack voltage. Subsequently, Kang et al. (2001) [187] built dynamic models for two types of kW-scale MCFC based on experimental data to study the stack response to a unit step-change of the manipulated variables, which include the current load and the fuel and oxidation utilization.

Continuing the exploration of the dynamic aspect of the MCFC stack, several other researchers have also investigated this area. Heidrechtet et al. (2002) [188] conducted a dynamic simulation of a MCFC cell response to a load disturbance by introducing a dynamic mathematical model that yields the dynamics of the mole fractions, molar flow, temperatures in anodic and cathodic gas phases, solid temperatures, cell voltage, and the current density distribution. Fermeglia et al. (2004) [189] performed a steady and dynamic state modeling and simulation of a 500 kW MCFC power system. They aimed to determine the interaction between the different devices composing the process through a steady-state simulation and evaluate the quantitative response of the system to several disturbances through a dynamic simulation. Moreover, Bittanti et al. (2005) [190] developed a mathematical model of the MCFC stack to indicate its dynamic characteristics for future coupling with gas turbines to achieve higher total efficiency. A year later, Brouwer et al. (2006) [191] created a detailed dynamic model incorporating the geometric resolution of MCFC to forecast the dynamic variations of voltage, current, and temperature with the load demand change. In addition, Yang et al. (2007) [192] studied the dynamic behavior of a MCFC by developing a nonlinear fuzzy model that can handle multi-inputs and multi-outputs. Besides, Bittanti et al. (2007) [193] built up a complete dynamic model of a MCFC to understand the stack behavior in different possible

operating conditions and different time scales.

In addition, Liu et al. (2009) [194] developed a one-dimensional MCFC model considering the local flow properties, heat transfer, and chemical and electrochemical phenomena. Later, Ovrum et al. (2011) [195] modeled and validated a MCFC unit installed onboard a merchant vessel for marine applications. The study developed a 3-dimensional dynamic model based on detailed thermodynamic, heat transfer, and electrochemical reaction phenomena to investigate the cell's performance under real operating conditions. Furthermore, Kim et al. (2013) [196] studied the distribution of the MCFC process variables over the cell surface and along the stacking direction using a detailed dynamic cross-flow MCFC model. Afterward, Law et al. (2015) [197] conducted a study to examine the dynamic thermal response/temperature gradients of a MCFC under an unexpected sudden shut-down, using a mathematical model based on the mass and energy properties and chemical and electrochemical reactions of the MCFC process. Finally, Szczęśniak et al. (2020) [142] performed a dynamic study on a 1 kW MCFC to examine its response to emergency fuel cell malfunctions. The model simulates some malfunctions with 5.66% damaged cells in the stack and investigates the response of the stack's performance. Furthermore, the study investigated several emergency operation scenarios, such as sudden loss of electric load, fuel, and oxidant supply.

Looking at the literature, the dynamic models of MCFC were based on the principle of the dynamic response to manipulated variables. Most variables were related to load power demand changes, flow rate changes, and cell malfunctions. Likewise, the dynamic models for other high-temperature electrolyzer types like SOEC. For example, Luo et al. (2015) [198] investigated the dynamic response of a SOEC with load change, with inlet gas composition and flow rate change, with inlet temperature change. Besides, Chen et al. (2019) [199] proposed a system that combines reversible solid oxide cells with the CO_2 methanation process, called ReSOC-MS, to store grid electricity at a scale of MW class. A dynamic model was created and supervised by a dynamic control strategy that considers the system and grid state to test the system's ability to stabilize the grid. In their study, two scenarios of surplus and shortage of electricity were simulated by assuming two-stepping electricity conditions, each lasting 5,000 seconds and represented by the stepping grid state variable. Recently, Sun et al. (2022) [200] developed a multi-physics model of a SOEC to explore its dynamic characteristics while being powered by a photovoltaic power supply for co-electrolysis of H_2O and CO_2. The model examines the dynamic responses of critical performance metrics such as the current density, average temperature of the SOEC, H_2O/CO_2 conversion rate, and output H_2/CO ratio over an entire day.

On the contrary, no dynamic models have been established to investigate the dynamic characteristics of the MCEC electrolyzer. However, Frangini et al. (2021) [73] conducted a distinctive experimental study to assess the feasibility of using a conventional molten carbonate fuel cell as an alternative fuel cell/electrolysis cell. They examined the degradation of the cell during 1200 hours of operation in both modes.

1.2 Review of Methanation Dynamic Modeling

Dynamic modeling of the methanation process is essential because it allows us to understand how the system will behave under different conditions and to optimize the process for maximum efficiency and stability. By developing mathematical models to describe reaction kinetics, we can simulate the system's behavior and predict how it will react to changes in temperature, pressure, flow rates, and other parameters. During the last decade, the dynamic modeling of the different methanation reactor types has been widely present in the literature. Different researchers have focused on developing the kinetics of the CO and CO_2 methanation.

For example, Li et al. (2013) [201] used the Aspen Dynamics Tool to conduct non-linear and linear dynamic simulations of a low-temperature isothermal methanation reactor with mass and heat recycling. They discovered that changes in the inlet temperature and CO mole fraction caused a temperature shift and hot spot position within the catalyst bed. A change of ±10 °C in the inlet temperature has an inverse effect on the reaction rate and heat released from the reactor, leading to a longer thermal response time and slower establishment of a steady state due to the thermal inertia of the catalytic bed. On the other hand, changes in the stoichiometric ratio of the reactants at the inlet had a more rapid effect on the temperature profiles within the reactor, with a 33% change in CO fraction causing a 21 °C temperature increase near the reactor inlet. In addition, Er-rbib and Bouallou (2014) modeled and simulated the CO methanation process for renewable electricity storage. Their model involved multistage adiabatic fixed reactors with a recycle loop in the first reactor, and it focused on the kinetic aspects of the CO methanation and the RWGS reactions.

Later on, in 2017, Ducamp et al. [202] proposed a heterogeneous model of a cooled fixed-bed reactor for CO_2 methanation on an industrial Ni/$\gamma-Al_2O_3$ catalyst. The model was based on two-dimensional momentum, mass, and heat transfer, as well as kinetic parameters, and it was evaluated at various temperature and pressure conditions. The results showed a significant radial temperature gradient and CH_4 production in the reactor. Based on this observation, the authors suggested ways to intensify mass and heat transfer, such as reducing the diffusion lengths in the reacting channels, decreasing the catalyst size to increase reaction efficiency, and reducing the cooling channel size. These conditions can be achieved using a modular plate milli-structured reactor-exchanger design.

After that, Try et al. (2018) [203] used a multidimensional heterogeneous model to simulate the dynamic behavior of a multi-tubular fixed-bed heat exchanger reactor under transient changes in inlet gas temperatures, cooling temperatures, gas inlet flow rate, and outlet pressure. The simulation showed that sudden temperature changes can lead to wrong-way behaviors, while gradual temperature changes can mitigate or eliminate such behavior. This phenomenon is primarily due to the bed's high thermal inertia, which slows heat transfer. Changes to the reactor's feed profile can also cause locally generated hot spots to move through the bed via convection. The extent of this phenomenon is influenced by the velocity, composition, and temperature of the feed gas.

The methanation process is being investigated for potential coupling with renewable hydrogen production units. Therefore, it is crucial to consider the interaction between the reaction section and other process units when determining the optimal operating conditions. Sibai et al. (2015) [204] highlighted this need in their study. In response, Giglio et al. (2018) [205] focused on combining high-temperature steam electrolysis via solid oxide cells and carbon dioxide methanation to produce substitute natural gas

suitable for direct injection into the natural gas distribution grid using a Power-to-Gas process. They employed a plug flow reactor model with intrinsic kinetics from the literature for methane synthesis in a series of multitube fixed-bed reactors cooled by evaporating water as a coolant with a high heat transfer coefficient. In addition, the methanation section was optimized to maintain the catalytic bed temperature and reduce the catalyst load.

In a subsequent study, Giglio et al. (2021) [206] investigated the dynamic performance of a cooled fixed-bed methanation reactor in a Power-to-Gas system for two scenarios: start-up from hot standby mode and partial load. The study revealed that the methanation system achieved the desired methane content after approximately 130 seconds when started up from hot standby, and the temperature gradually stabilized at a new steady state under partial load. The authors also proposed a strategy that involves adjusting CO_2 staging to enhance the system's rangeability and prevent hot spots from forming in the catalytic bed. This strategy allows a fraction of carbon dioxide to bypass both the first and second reactors, as shown in Figure 4.1, and the methanation unit was found to operate safely within a range of 45% to 100% of the nominal load with this adjustment.

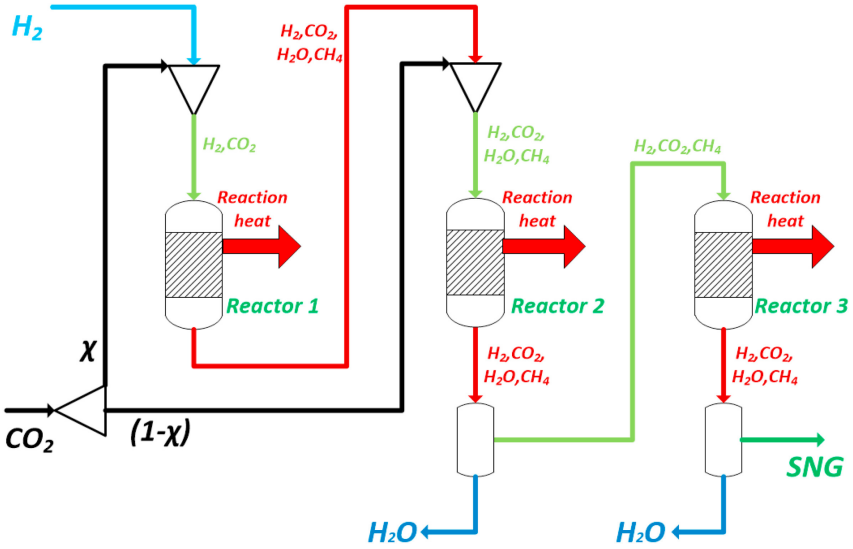

Figure 4.1: Methanation unit configuration, reprinted from [206].

Recently, Aubin et al. (2023) [207] proposed an innovative methanation reactor design that converts H_2 and CO_2 to methane and produces steam required by solid oxide electrolyzers. The concentric shell-and -tube reactor consists of a center tube filled with pellets and an outer shell holding the cooling liquid. The study includes theoretical and experimental assessments of the reactor's capabilities and an understanding of its dynamic performance under different operating conditions. The reactor model was validated with experimental data and could be used for hardware-in-the-loop and real-time optimization simulations. The outcomes revealed that direct evaporation of water in the reactor increased system efficiency, but a damping system would be required for transient operation and flexibility. Furthermore, the hot spot location changes along the reactor length as the reactant gas flow rates and cooling system pressure vary. Low flow rates produce a rigid temperature profile with a hot spot close to the reactor's inlet, while higher flow rates require increased cooling water pressure to keep the hot spot location at the reactor's inlet and achieve a higher conversion rate.

2 Dynamic Modeling of MCEC

The dynamic modeling of the MCEC electrolyzer covers three aspects. First, a dynamic model was developed in ACM software by transforming the material and energy balances into a dynamic state. Then, the electrochemical model was modified to examine the MCEC operation while considering the degradation over time. Next, another dynamic study was conducted by applying the concept of dynamic response to unexpected changes. Lastly, the heating up process of the MCEC electrolyzer was evaluated, and the best procedure was selected.

2.1 Development of the Dynamic Model of MCEC Electrolyzer

2.1.1 Material Balance

The components involved in the cell are represented by a vector : **comp** = $\begin{pmatrix} H_2O \\ CO_2 \\ H_2 \\ CO \\ O_2 \\ N_2 \end{pmatrix}$

The material balance is described as follows: Eq. 4.1 for the cathode side and Eq. 4.2 for the anode side.

$$\frac{d\dot{n}_{c,i}^{out}}{dt} = \dot{n}_{c,i}^{in} - \dot{n}_{c,i}^{out} + R_{c,i} \tag{4.1}$$

$$\frac{d\dot{n}_{a,i}^{out}}{dt} = \dot{n}_{a,i}^{in} - \dot{n}_{a,i}^{out} + R_{a,i} \tag{4.2}$$

$R_{c,i}$ and $R_{a,i}$ are represented by vectors, including the cathode and anode total rate of production or consumption of the component i within the vector **comp**. Therefore, these vectors are represented as follows:

$$R_c = \begin{pmatrix} -\dot{n}_{H_2} + \dot{n}_{CO} \\ -\dot{n}_{H_2} - 2\dot{n}_{CO}^{el} - \dot{n}_{CO} \\ \dot{n}_{H_2} - \dot{n}_{CO} \\ \dot{n}_{CO} + \dot{n}_{CO}^{el} \\ 0 \\ 0 \end{pmatrix} \qquad R_a = \begin{pmatrix} 0 \\ \dot{n}_{H_2} + \dot{n}_{CO}^{el} \\ 0 \\ 0 \\ \frac{1}{2}(\dot{n}_{H_2} + \dot{n}_{CO}^{el}) \\ 0 \end{pmatrix}$$

2.1.2 Energy Balance

The energy balance of the cell was adjusted to include the rate of accumulation of total energy of the solid stack mass, represented by the term $\rho^s V^s C_p^s \frac{dT^{out}}{dt}$, as shown in Eq. 4.3.

$$\rho^s V^s C_p^s \frac{dT^{out}}{dt} = \dot{Q}_{in} - \dot{Q}_{out} + \dot{W}_{el,\ MCEC} + \dot{Q}_{reaction} \tag{4.3}$$

2.2 Degradation Model in the MCEC

Cell degradation primarily affects the materials of the electrodes and the electrolyte, which in turn impacts the electrochemical behavior of the cell. To account for this, the electrochemical model was adjusted to incorporate degradation coefficients, as shown in Eq. 4.4. The change in U_{nernst} with time is due to the material degradation of the cell. U_{nernst} is not purely the electromotive force of the cell, which is theoretically constant, but the actual voltage observed depends on the status of the cell. Thus, cell degradation results in mechanical instability, where the cells are not compacted well together. This instability can affect the surface contact interaction with the electrodes and inter-connector, leading to blockage of the contact surface due to material degradation.

$$U_{cell} = \gamma U_{nernst} + j \cdot \delta \cdot ASR \tag{4.4}$$

In this equation, γ represents the electrode degradation coefficient, while δ denotes the coefficient for electrolyte loss and current collector corrosion. These coefficients are derived from experimental data obtained by Meskine et al. (2020) [124] (presented in Figure 2.9) and are based on the study conducted by Frangini et al. (2021) [73]. They are determined over time using Eqs. 4.5 and 4.6.

$$\gamma = \exp(\alpha_1 \cdot \Delta t) \qquad \alpha_1 = -3.36 \times 10^{-5}\,\mathrm{h}^{-1} \tag{4.5}$$

$$\delta = \exp(\alpha_2 \cdot \Delta t) \qquad \alpha_2 = -4.39 \times 10^{-4}\,\mathrm{h}^{-1} \tag{4.6}$$

Since the electrodes' materials deteriorate with time during the electrolysis operation of the conventional MCFC stack [73], it was crucial to consider the active electrode area change with time in the model. To this end, an expression for the area change was included in the model, as depicted in Eqs. 4.7 and 4.8. This expression determines the change in the area $A_{t=0}$ at time $t = 0$ over time, taking into account the degradation rate (d_A) per 1,000 h, which is included in the coefficient (φ) derived from experimental results [124].

$$A = A_{(t=0)} \exp(\varphi \cdot \Delta t) \tag{4.7}$$

$$\varphi = 0.0011 \times \frac{d_A}{100} - (1 \times 10^{-6}) \quad \mathrm{h}^{-1} \tag{4.8}$$

The dynamic MCEC model was validated by applying these equations to experimental conditions (Section 2.2.1) before being applied to scale-up conditions (Section 2.2.2). The conditions used for this study are presented in Table 4.1. Besides, three degradation rate (d_A) values were studied: 1%, 5%, and 10% per 1,000 h of operation. According to Petipas et al. (2013) [208] study on the transient operation of the SOEC, it was found that the cell's active area decreases by 5% during a 505 h operation. This finding allowed us to study the 10% degradation per 1,000 h, given that the SOEC and MCEC electrolyzers operate at high temperature. This degradation rate was viewed as the worst case. Therefore, a lower value was examined to represent the scenarios corresponding to the cell's state.

			Fuel electrode gas composition				Oxygen electrode gas composition		
	A (cm^2)	j (mA/cm^2)	H_2O	CO_2	H_2	CO	O_2	CO_2	N_2
Experimental	3.14	-75	20%	12%	64%	-	15%	30%	55%
Scale-up	8460	-60	63%	21%	12%	4%	3%	97%	-

Table 4.1: Dynamic Model Conditions.

2.2.1 Model Validation at Experimental Scale Conditions

This study section aims to validate the model by examining the experimental conditions during a transient operation of 1630 hours while considering the cell's degradation over time. To accomplish this, the V-I curve in Figure 2.9, obtained after 1,630 hours of cell operation, was used as the available experimental data. The model validation involved studying the cell potential over time at a constant current density of -75 mA/cm^2. The results obtained for the three degradation rates are presented in Figure 4.2.

Based on the experimental data, the cell potential at 1,630 hours is 1.39 V for a current density of -75 mA/cm^2. Comparing this value with the model's outcomes at the three degradation rates showed a comparable result, with a difference of approximately -1%. Additionally, the degradation rate was observed to not significantly affect the cell potential trend over time. This result can be explained by the fact that the cell potential model was developed as a function of the fixed current density used in this study. Another explanation could be related to the relatively small surface area (3.14 cm^2) of the cell, making its change between the three cases insignificant.

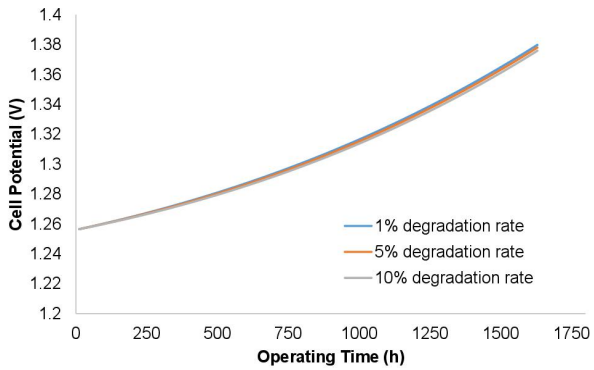

Figure 4.2: Cell potential (V) over time at various degradation rates at experimental conditions.

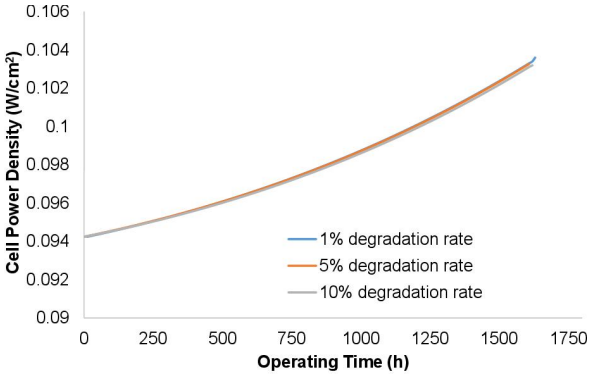

Figure 4.3: Cell power density (W/cm^2) over time at various degradation rates at experimental conditions.

Furthermore, it was found that the cell power density increases with time, indicating that the cell consumes more electrical power as time progresses, as depicted in Figure 4.3. This behavior is attributed to the negative impact of the degradation issue on the cell. Moreover, the cell power density trend remains unchanged for the three different degradation rates, similar to the cell potential result.

2.2.2 Results at Scale-up Conditions

This case study analyzed the scale-up conditions regarding the degradation rate during the transient operation, corresponding to the industrial scale process of 1 MW MCEC module. Various parameters affected by this degradation were explored, including the outlet flow rates of H_2 and CO, the cell current, power, potential, and temperature. In this case, the current density is fixed.

First, it is crucial to monitor the change in the active surface area over time at different degradation rates (Figure 4.4) to evaluate the impact of electrode degradation on the cell's performance. As expected, the surface area decreases with time, and the degradation rate determines the rate of decrease. This reduction in the active surface area directly impacts the applied current, as shown in Figure 4.5.

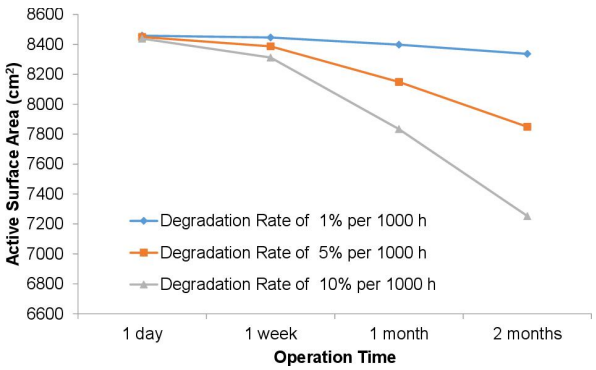

Figure 4.4: Active surface area A (cm^2) over time at various degradation rates.

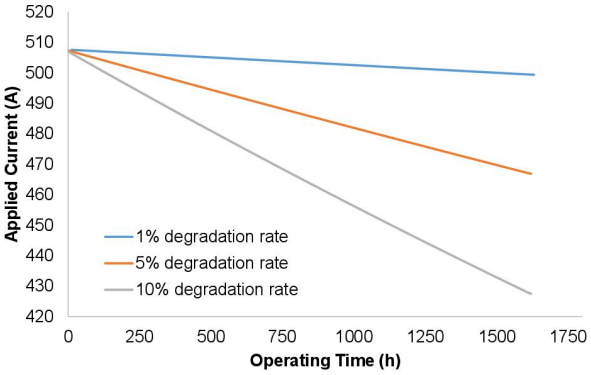

Figure 4.5: Cell current (A) over time at various degradation rates.

The cell potential and power density describe the cell's performance. Thus, these parameters were analyzed with the degradation rate, and the results are depicted Figures 4.6 and 4.7. In contrast to the experimental conditions case, the cell potential trend with time varies with the degradation rate. At a degradation rate of 1%, the cell potential and power density increase over time. However, at degradation rates of 5% and 10%, they decrease. Although they eventually start to increase after a certain period, they remain below their initial level. This could be related to the significant impact of the degradation rate on the syngas partial pressure that is directly linked to the Nernst potential (U_{nernst}).

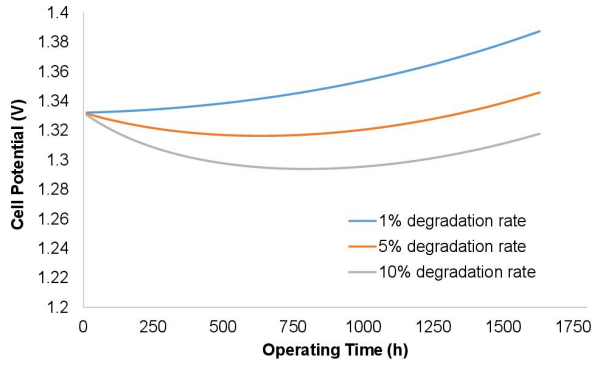

Figure 4.6: Cell potential (V) over time at various degradation rates at scale-up conditions.

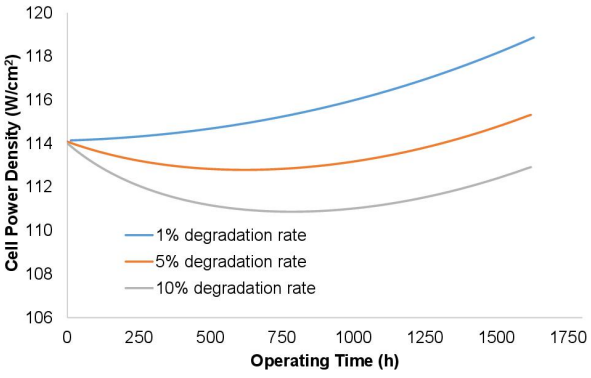

Figure 4.7: Cell power density (W/cm^2) over time at various degradation rates at scale-up conditions.

The decline in cell potential and power density over time under high degradation is better clarified by analyzing the syngas production. Figures 4.8 and 4.9 present the outlet flow rates of H_2 and CO over time at three different degradation rates. The degradation rate significantly affects syngas production over time. The degradation reduces the electrode's active surface area, thereby decreasing the hydrogen produced by electrolysis. This decline occurs while maintaining a constant current density, meaning that the production rate is directly proportional to the surface area, as Faraday's law describes. Moreover, the effect of electrode degradation on the H_2 outlet flow rate increases with the degradation rate. For instance, at a degradation rate of 1%, the H_2 outlet flow rate decreases by 0.8%. At a 5% degradation rate, the decrease is even more significant, with a reduction of 4%. Finally, at the highest degradation rate of 10%, the H_2 outlet flow rate decreases by 7.9%.

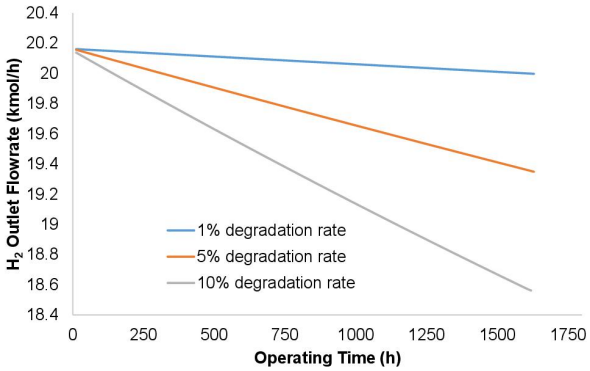

Figure 4.8: H_2 outlet flowrate (kmol/h) over time at various degradation rates.

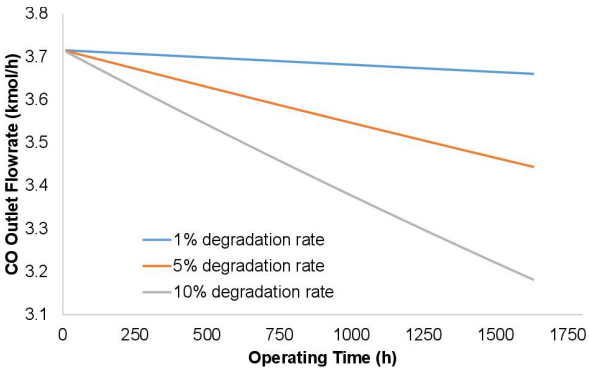

Figure 4.9: CO outlet flowrate (kmol/h) over time at various degradation rates.

Furthermore, the CO outlet flow rate decreases over time, and the decline is more noticeable at higher degradation rates. Specifically, a decrease of 1.5% is observed at a 1% degradation rate, 7.2% at a 5% degradation rate, and 14.3% at a 10% degradation rate. This observation demonstrated that electrode degradation has a more pronounced effect on the H_2 and CO outlet flow rates at higher degradation rates, thus explaining the trend in cell potential. In addition, changes in the composition of H_2 and CO can significantly impact methane synthesis, which requires a specific ratio of H_2, CO_2, and CO for efficient CH_4 yield and to avoid carbon deposition produced by undesired reactions.

Additionally, it is essential to investigate the effect of degradation on cell temperature over time, as it is a crucial parameter in cell operation. The cell can operate at an endothermal or exothermal state, depending on the conditions. However, the endothermal state cools down the outlet gas and even the cell, and it may reach a state where it is necessary to heat the cell to compensate for the heat consumed. In Figure 4.10, cell outlet temperature trends with time are similar to those observed for cell potential and power density. This outcome is because the system's energy balance is related to the gas composition, which is affected by degradation. These findings further reinforce the significant impact of syngas composition variation on cell potential and power with the degradation rate.

However, when the total applied current remains constant, the current density will increase as the surface area decreases. While this doesn't affect the syngas production rate due to the constant current, it significantly affects the cell's performance. The cell potential will rise due to the increased current density, directly linked to the reduced surface area. This clearly illustrates the negative impact of degradation

on the cell's performance. Furthermore, cell degradation has economic implications for the system. It reduces the cell's lifespan, necessitating more frequent cell replacements. This, in turn, leads to higher capital expenses, which can affect the overall cost-effectiveness of the system.

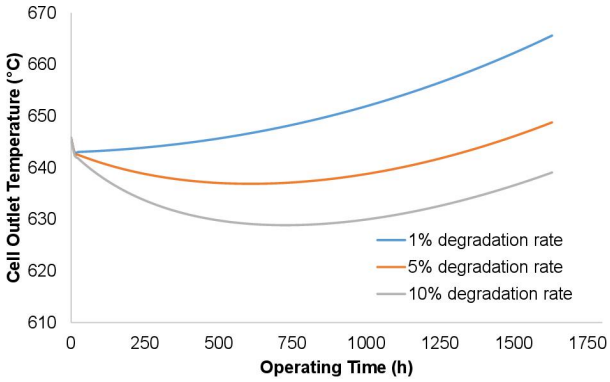

Figure 4.10: Cell's outlet temperature over time at various degradation rates.

2.2.3 Comparison between Experimental Scale and Scale-up in terms of Degradation Impact

Cell degradation has a significant concern for small-scale and large-scale cells. For this reason, it seemed interesting to look at the cell's performance at both scales. Therefore, this study examined critical parameters, such as cell potential and temperature, at a 1% degradation rate. Except for the surface area, the experimental conditions are used for the scale-up conditions. The results, presented in Figures 4.11 and 4.12, showed that the cell potential and outlet temperature increased over time for both scales. However, at the same inlet conditions, the potential and temperature were higher in the large-scale cells compared to the small-scale ones. These findings highlight the importance of addressing degradation issues in larger-scale cells.

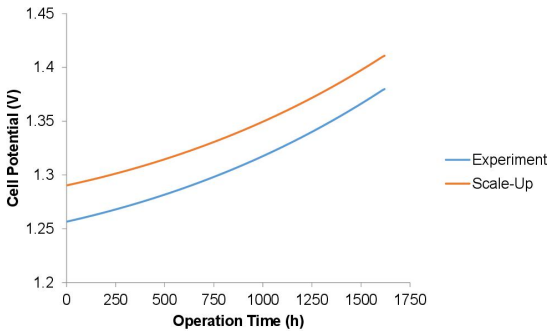

Figure 4.11: Cell potential variation with time at experimental and scale-up scales.

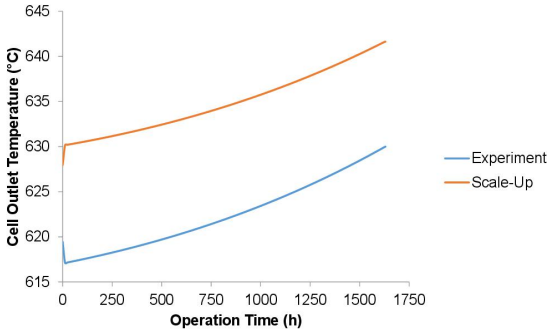

Figure 4.12: Cell outlet temperature variation with time at experimental and scale-up scales.

2.3 Dynamic Response

This section focuses on analyzing the dynamic response of the MCEC electrolyzer to changes in power load, flow rate, and the number of operating cells on the cell's electrical power, voltage, gas composition, and temperature.

2.3.1 Dynamic Response to Load Change

A load change refers to a variation in the input current achieved by applying a ramp up and down of the current. Figure 4.13 displays the response of the cell potential to a load change, indicating that it changes proportionally with the load change. When the load increases, the cell potential also increases; when the load decreases, the cell potential decreases. This trend is also observed in the cell power, as shown in Figure 4.14. It can also be noticed that the cell potential and power progressively ramp up/down with the load change during a specific period to reach its stable state.

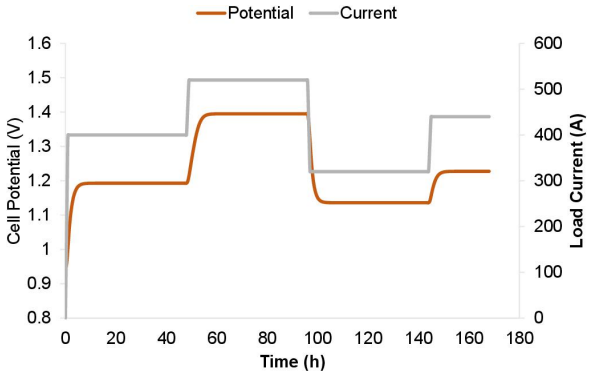

Figure 4.13: Cell potential's response to the load change.

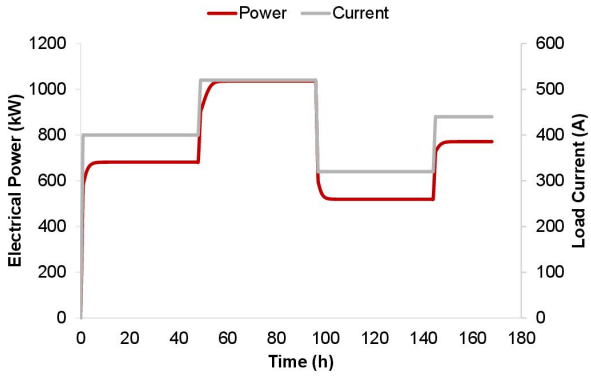

Figure 4.14: Cell power's response to the load change.

The cell's outlet temperature trend also responds proportionally to the load change, as shown in Figure 4.15. In addition, the load change significantly impacts the cell's thermal state, which fluctuates between the endothermal and exothermal states depending on the applied load.

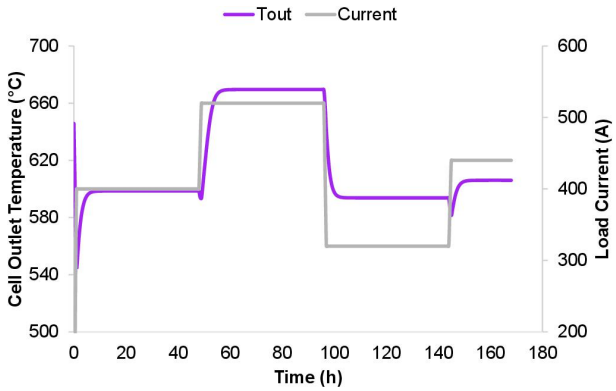

Figure 4.15: Cell outlet temperature (Tout) response to the load change.

Lastly, the outlet flow rates of reactants (H_2O and CO_2) and products (H_2 and CO) were analyzed to observe their response to load changes. As the load change corresponds to the current change, it is expected that the co-electrolysis process lessens with a decrease in load and boosts with load ramp-up. This expectation is demonstrated by Figures 4.16 and 4.17, which respectively show the outlet flow rates of H_2O and CO_2, and H_2 and CO in response to load changes. Both the H_2O and CO_2 outlet flow rates decrease with load ramp-up, as they are consumed to produce H_2 and CO, which in turn display an increase in their outlet flow rates. Nonetheless, the opposite scenario is observed when the load decreases. This

change in the syngas production can impact its ratio for methane synthesis, which will be addressed in detail in Section 4.

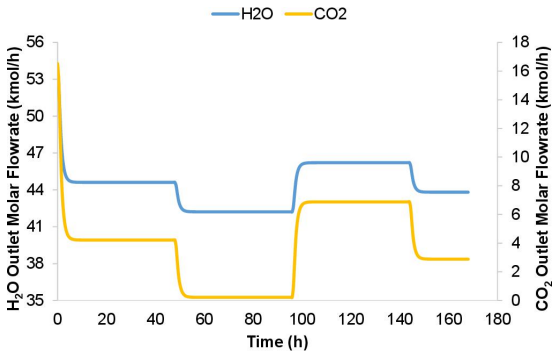

Figure 4.16: H_2O and CO_2 outlet flow rates response to the load change.

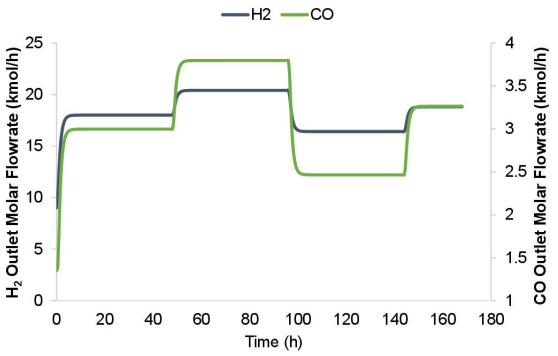

Figure 4.17: H_2 and CO outlet flow rates response to the load change.

2.3.2 Dynamic Response to Inlet Flow Rate Change

Another factor that can lead to unexpected changes is the alteration in the inlet gas flow rates of the fuel (cathode side) and oxygen (anode side) electrodes (Fin_{fe} and Fin_{oe}), which was examined in this study by varying both flow rates proportionally and reversely. The response of the cell potential to these changes is illustrated in Figure 4.18 where it is observed that the potential decreases when both flow rates increase and vice versa. However, in the last two ramp steps, the cell potential decreases with an increase in the fuel electrode's inlet gas flow rate and a decrease in the oxygen electrode's inlet gas flow rate.

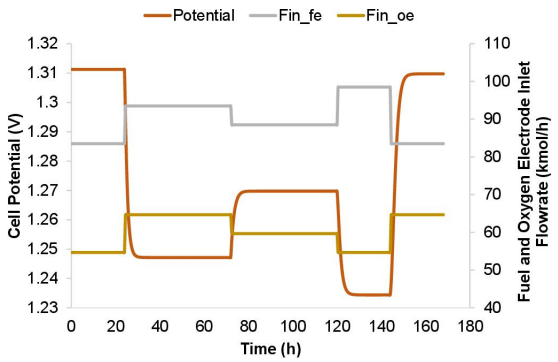

Figure 4.18: Cell potential response to the inlet gas flow rate change.

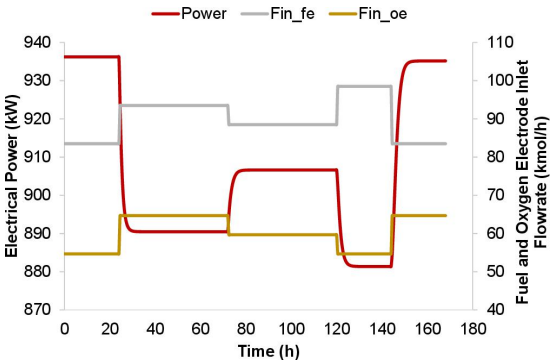

Figure 4.19: Cell power response to the inlet gas flow rate change.

Conversely, when the fuel electrode's inlet gas flow rate decreases and that of the oxygen electrode increases, the cell potential increases. Furthermore, it is worth noting that the cell potential returns to its initial value of 1.31 V when the fuel electrode's inlet gas flow rate is restored to its initial value, even though that of the oxygen electrode differs from its initial value. The cell power, shown in Figure 4.19, exhibits a similar response to changes in flow rates as the cell potential. Thus, it can be inferred that only the fuel electrode's inlet gas flow rate impacts the cell's potential and power.

The change in the flow rates, as illustrated in Figure 4.20, also affects the cell outlet temperature. Similar to the conclusion drawn about the significant impact of the fuel electrode's inlet gas flow rate on

cell potential and power, it is also observed in the cell outlet temperature. Moreover, a similar response is noticed, where the temperature decreases with an increase in the fuel electrode's inlet gas flow rate and vice versa. However, when the gas flow rate of the fuel electrode increases, the temperature initially shows a rapid rise followed by a subsequent decrease. Contrarily, a sudden drop is noticed initially when the flow rate decreases, which is then followed by a consequent increase.

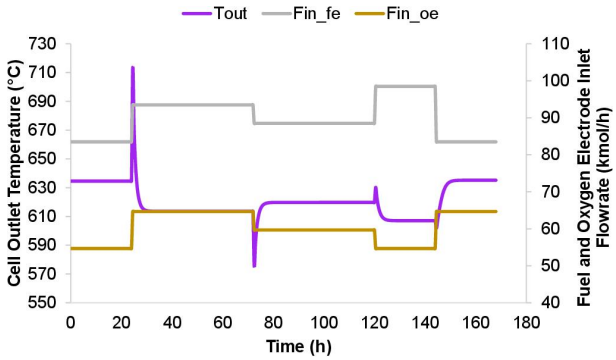

Figure 4.20: Cell outlet temperature (Tout) response to the inlet gas flow rate change.

The fuel electrode's inlet consists of H_2O, CO_2, H_2, and CO. Since the current is fixed, no changes are expected in the electrochemical reactions. However, the chemical reaction RWGS could be affected. Under the scaling-up conditions, the reaction is not attaining equilibrium, indicating that it is not occurring as per the model. Consequently, modifying the total gas flow rate entering the fuel electrode causes a comparable change in the outlet flow rates of H_2O, CO_2, H_2, and CO. Therefore, the outlet flow rates of these components were not analyzed in this study.

2.3.3 Dynamic Response to Number of Cells Change

The third parameter under study is the number of cells, given that the scale-up 1 MW-module consists of 1,428 cells. This parameter is essential to be considered, as the overall performance of the stack depends on the number of cells it comprises. Furthermore, over time, the cells may start to degrade, thus reducing the total number of functional cells in the stack. Szczęśniak et al. (2020) [142] examined this aspect in a 1 kW MCFC stack. Therefore, in this study, a cell deactivation rate of 0.1% per 1,000 hours, equivalent to two cells malfunctioning, was assumed and analyzed. It is important to highlight that this study assumed that the cells are connected in parallel, without considering their actual influence on the overall stack. It is evident that there is a limit to the number of cells that can be operational while ensuring the continued functioning of the entire stack.

For better comprehension, the function of the stack model will be explained. The developed MCEC model is based on a single cell, and a stack comprises a particular number of cells (Ncells), as depicted in Figure 4.21. This function implies that, at a constant current, there is a constant production of H_2 and CO in each cell. However, with a reduction in the number of cells due to degradation, the inlet flow per cell will change, and consequently, the outlet flow will also be affected. This state means that the stack's performance will be affected by the number of cells and their state of degradation, highlighting the importance of this parameter in the study of MCFC stacks.

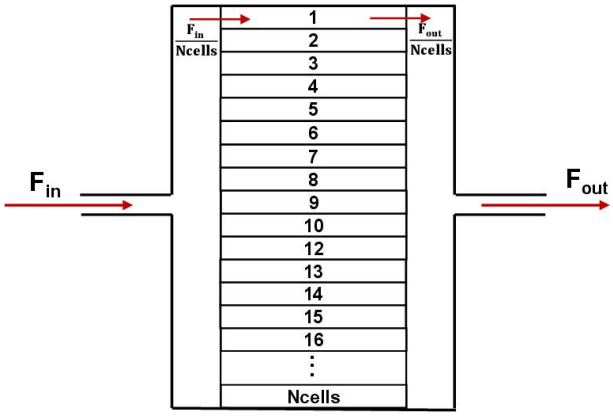

Figure 4.21: A representation of the MCEC stack's structure.

Therefore, the cell potential and power were monitored to analyze this aspect, and the results are displayed in Figures 4.22 and 4.23. They diminish with the decrease in the number of cells. This finding can be explained by the fact that the Nernst potential, affected by the gases, decreases with the reduction of the number of cells. Looking at the U_{cell} equation, which is a function of U_{nernst} and $j \cdot ASR$, it can be noticed that it depends on U_{nernst} in this case, given that the current density (j) is fixed and ASR is a function of cell temperature.

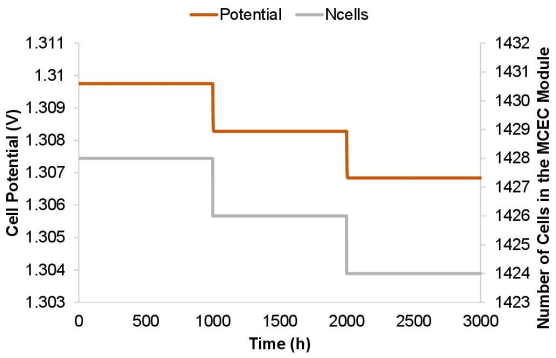

Figure 4.22: Cell potential response to the number of cells change.

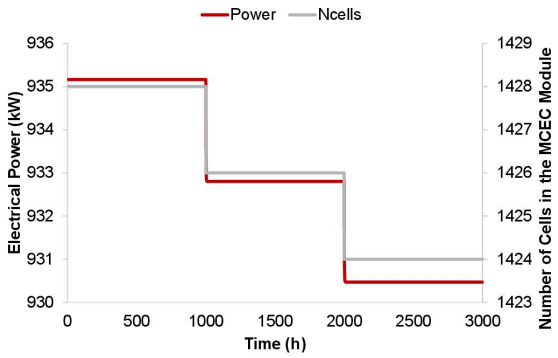

Figure 4.23: Cell power response to the number of cells change.

Furthermore, the reduction in the number of cells affects the H_2O, CO_2, H_2, and CO outlet flow rates of the stack. As shown in Figure 4.24, the outlet flow rates of H_2O and CO_2 increase with the increase in cell malfunctioning, expressed by a decrease in the number of cells in operation. This observation is due to the increased flow rate entering each cell and the constant production of H_2 and CO. For example, when the number of cells is reduced by two after 1,000 h, the total flow rate is divided into 1,426 cells instead of 1,428. This case means that the cell's inlet gas flow rate will increase and, thereby, its outlet flow rate. In Eq. 4.9, a more precise understanding can be acquired as $F_{production}$ and $F_{in}(reactants)$ remain constant, and the number of cells decreases. Therefore, the term $F_{production} \times Ncells$ decreases, leading to a higher outlet flow rate of the reactants (H_2O and CO_2).

$$F_{out}(reactants) = F_{in}(reactants) - F_{production} \times Ncells \tag{4.9}$$

On the other hand, as illustrated in Figure 4.25, the outlet flow rates of the products (H_2 and CO) drop with the decrease in the number of operating cells. A similar explanation can be clarified, based on the Eq. 4.10, where the term $F_{production} \times Ncells$, representing the production rate per stack, is reduced over time with the decrease in the number of cells.

$$F_{out}(products) = F_{in}(products) + F_{production} \times Ncells \tag{4.10}$$

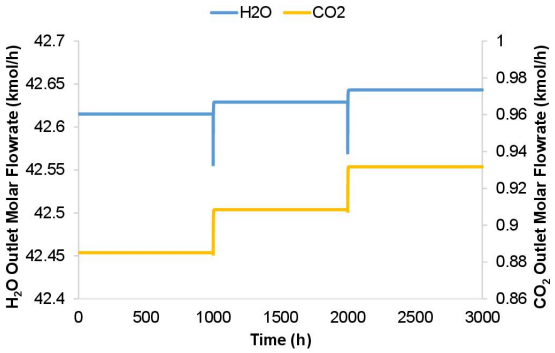

Figure 4.24: H_2O and CO_2 outlet flow rates response to the number of cells change.

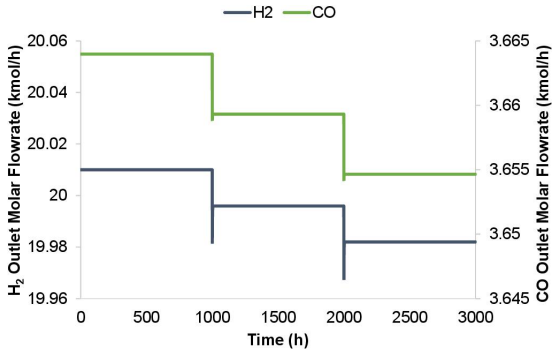

Figure 4.25: H_2 and CO outlet flow rates response to the number of cells change.

Besides, as the number of operating cells is reduced, the cell outlet temperature decreases, as shown in Figure 4.26. This outcome is caused by the drop in the cell potential and power, which leads to a cooling effect on the cell. As a result, the outlet gases exit at a lower temperature.

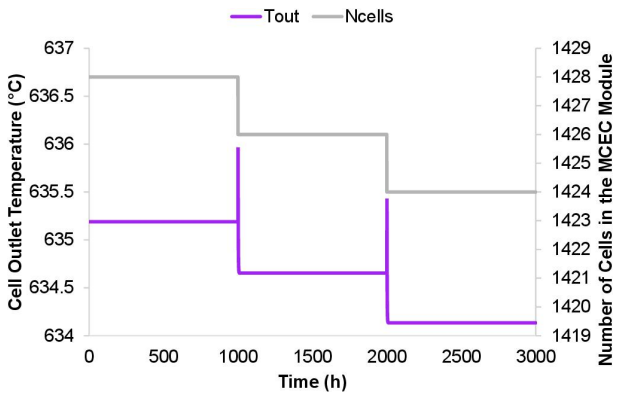

Figure 4.26: Cell outlet temperature (Tout) response to the number of cells' change.

This overall analysis highlighted that fewer operating cells reduce the total H_2 and CO production, causing a decrease in the cell potential and power. However, to maintain the same production level in the presence of malfunctioning cells, the applied current must be increased to enhance the production, thus increasing cell potential and power.

2.4 Cold Start-up of the MCEC Electrolyzer

The heat-up of the MCEC stack is similar to that of MCFC, so two different heat-up scenarios were collected. Scenario A is presented in detail in Table 4.2, based on the MCFC heat-up patent [209].

Another heating scenario was applied by Zhou et al. (2006) [210], explained in Table 4.3.

Temperature (°C)	**Time (h)**	**Heating rate (°C/h)**
25 → 150	2	62
150 → 300	30	5
300 → HOLD	35	0
300 → 500	40	5
500 → 600	20	5
600→ 650	10	5
Total	137 h (≈ 5 days)	

Table 4.2: MCFC heating up scenario (A) [209].

Temperature (°C)	**Time (h)**	**Average Time (h)**
20→108	6-12	9
108→HOLD	6-12	9
108→210	32-42	37
210→HOLD	14-24	19
210→315	44-54	49
315→HOLD	25-35	29
315→375	32-42	37
375→HOLD	25-35	29
375→420	34-44	39
420→450	8-18	13
450→HOLD	2-6	4
450→530	12-20	16
530→600	7-13	10
600→650	4-9	6
Total	194 h (8 days) - 289 h (12 days)	

Table 4.3: MCFC heat up scenario (B) [210].

The two scenarios provide different steps of heating and duration. However, it was essential to select one of the heating processes; thus, an energy consumption analysis was conducted to determine the more energy-efficient heating-up method. The energy analysis involved evaluating the energy consumed by the stack for heating up and compensating for the heat losses during the hold-up period. Heat losses occur due to the transfer of heat between the stack and the environment, which is influenced by the temperature difference. There are three types of heat transfer: conduction, convection, and radiation.

- **Thermal conduction** corresponds to a transfer of heat from one point to another in a material through collisions between particles. Heat naturally diffuses from hotter (more agitated) regions to

colder (less agitated) regions. This mode of heat transfer can only occur in a continuous material medium.

- **Thermal convection** is the heat transfer between the wall and a moving fluid in contact with the boundary of a solid medium. It can occur through a combination of mechanisms. These mechanisms include heat transfer by conduction at the wall-fluid interface, diffusion of heat through the fluid, and transport of energy due to the movement of the fluid.
- **Thermal radiation** is a mode of heat transfer through the emission of electromagnetic waves or photons, without needing any material support.

In this case, the MCEC stack can experience two types of heat transfer: conduction and convection. The amount of these heat transfers Q can be calculated using Eq. 4.11, where U represents the overall heat transfer coefficient, A is the heat transfer area, and ΔT is the temperature difference between the solid and the environment. The overall heat transfer coefficient U can be calculated by taking the inverse of the sum of the conduction resistance R_{cond} and the convection resistance R_{conv} (Eq. 4.12). These resistances are determined based on the solid geometry and other parameters.

$$Q = U \cdot A \cdot \Delta T \tag{4.11}$$

$$U = \frac{1}{R_{cond} + R_{conv}} \quad \mathrm{W}/(\mathrm{m}^2 \cdot \mathrm{K}) \tag{4.12}$$

Therefore, determining the amount of heat transferred requires knowledge of stack geometry. Two different geometries exist for the MCFC module: cylindrical and rectangular manifolds, each containing four stacks with a capacity of 250 kW, as illustrated in Figures 4.27 and 4.28. The MCFC cell has a length of 150 cm, a width of 60 cm [143], and a thickness of 0.635 cm [211] in both module geometries.

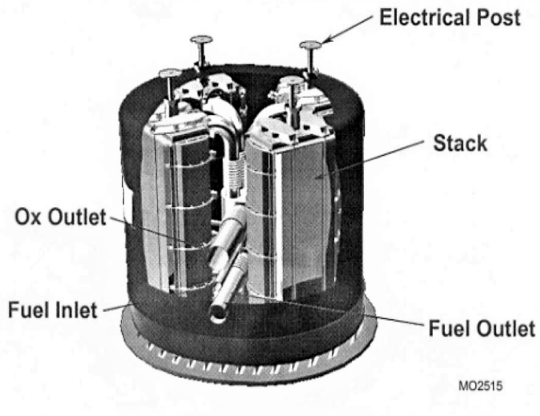

Figure 4.27: Structure of a cylindrical form module, reprinted from [143].

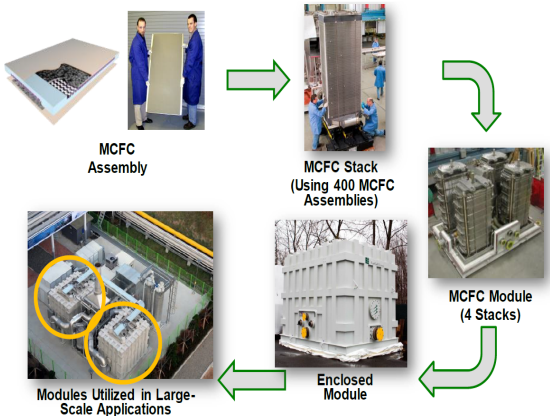

Figure 4.28: Structure of a rectangular form module, reprinted from [211].

2.4.1 Cylindrical Module

The cylindrical module manifold has a diameter of 430 cm and a height of 260 cm [143]. The outer shell of the cylinder is made of carbon steel [143], and the inner shell is composed of insulation made of

ceramic fiber [212].

The conductive resistance of the cylinder is determined by Eq. 4.13, where $r_\circ$ and r_i are the outer and inner radius, respectively, and k is thermal conductivity, which varies depending on the material and the temperature.

$$R_{cond} = \frac{r_\circ ln\left(\frac{r_\circ}{r_i}\right)}{k} \tag{4.13}$$

To account for the two shells constituting different materials, it was essential to determine the conductive resistance for both the inner shell ($R_{cond,ceramic}$) and the outer shell ($R_{cond,carbon}$), as depicted in Figure 4.29. The first step involved obtaining the thermal conductivity k of each material as a function of temperature. For carbon steel, the handbook of heat transfer [213] was used to collect the data, while for ceramic insulation, information from [214, 215] was applied. Next, to calculate the inner and outer radii, it was crucial to determine the thickness of each shell. According to the API 650 Standards [216], the minimum thickness of a carbon steel shell is 5 mm for a diameter less than 15 m. The ceramic insulation is commercially available in three standard thicknesses: 13 mm, 25 mm, and 50 mm [214].

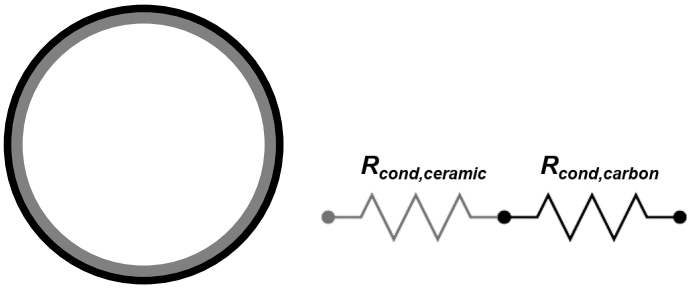

Figure 4.29: Schematic representation of the thermal conductive resistance of the cylindrical module.

As no information has been provided regarding the thickness of the insulation and outer enclosure of the module, a sensitivity analysis was performed on the thickness of the outer and inner shells. In particular, the thickness of the carbon outer shell has been varied from 5 mm to 20 mm. Meanwhile, three thicknesses were selected for analysis for the ceramic insulation inner shell, namely 13 mm, 25 mm, and 50 mm.

The study revealed that the conductive resistance R_{cond} increases significantly with an increase in the thickness of the inner shell (insulation), as illustrated in Figure 4.30. Consequently, the heat loss Q_{loss} decreases, as shown in Figure 4.31. However, the thickness of the cylinder's outer shell does not impact the resistance R_{cond}, as it remains constant with the change in thickness. Based on this finding, a thickness of 20 mm (2 cm) was chosen for the cylinder's outer shell. Since the resistance increases with an increase in the insulation thickness of the inner shell, a thicker insulation layer is better for minimizing heat loss. Given that the standard thickness of ceramic fiber insulation is 25 mm, the energy analysis will be evaluated using 25 mm and 50 mm insulation thicknesses. Therefore, the conductive resistance will be calculated for the energy analysis based on Eq. 4.14.

$$R_{cond} = R_{cond,ceramic}(\text{at } e_i = 25 \text{ and } 50 \text{ mm}) + R_{cond,carbon}(\text{at } e_o = 20 \text{ mm}) \tag{4.14}$$

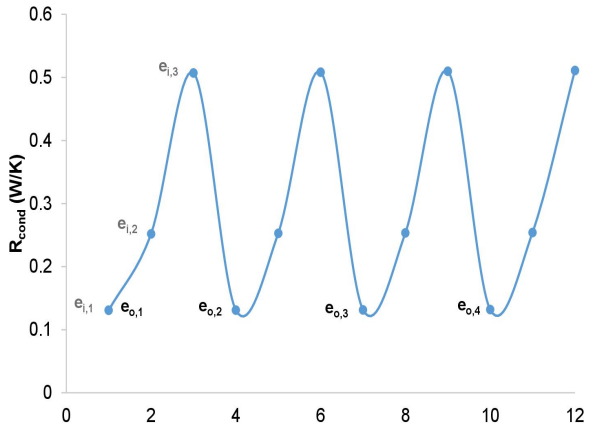

Figure 4.30: Total conductive resistance as a function of the outer shell thickness (e_o) and inner shell thickness (e_i).

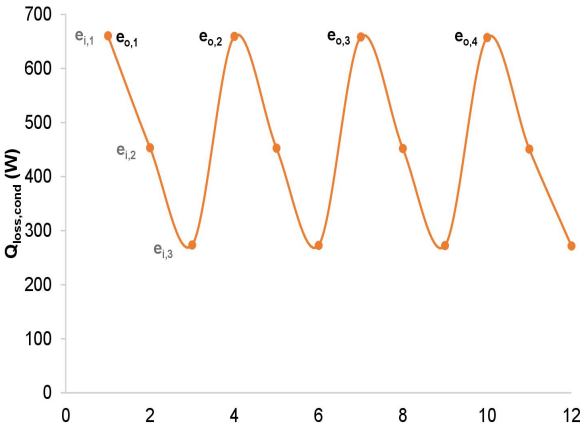

Figure 4.31: Heat loss by conduction as a function of the outer shell thickness (e_o) and inner shell thickness (e_i).

The convection resistance R_{conv} is determined using Eq. 4.15.

$$R_{conv} = \frac{1}{h_{air}} \tag{4.15}$$

For this equation, the air heat transfer coefficient h_{air} must be determined. It is calculated from Nusselt number, based on Eq. 4.16.

$$Nu = \frac{hL}{k} \tag{4.16}$$

However, to calculate the Nusselt number, an appropriate equation must be selected based on the geometry. Therefore, the vertical cylinder is treated as a vertical plate since the boundary layer thickness is much less than the cylinder diameter, and Eq. 4.17 is satisfied.

$$\frac{D}{L} \geq \frac{35}{Gr^{1/4}} \tag{4.17}$$

In this equation, D and L correspond to the diameter and length of the cylinder, respectively. Gr is Grashof number, determined by Eq. 4.18, where g is the gravitational acceleration in m²/s, β is the coefficient of volume expansion in 1/K (equals to 1/T for ideal gases), T_s and T_∞ are the temperatures of the surface and the fluid sufficiently far from the surface, respectively, L is the characteristic length of the cylinder, and υ is the kinematic viscosity of the fluid in m²/s.

$$Gr = \frac{g\beta(T_s - T_\infty)L^3}{\upsilon^2} \tag{4.18}$$

Consequently, the Nusselt number for the vertical plate is calculated using *Churchill-Chu* correlation in Eq. 4.19 that is applicable for the entire range of R_a [217].

$$Nu = \left(0.825 + \frac{0.387Ra_L^{1/6}}{[1 + (0.492/Pr)^{9/16}]^{8/27}}\right)^2 \tag{4.19}$$

The energy consumption was evaluated for Scenarios A and B at two different insulation (inner shell) thicknesses. Scenario A utilizes an initial high heating rate with only one stand-by hold-up, while

Scenario B operates at a low heating rate with five stand-by hold-ups. Figure 4.32 illustrates the energy consumption in MWh of a cylindrical MCEC module by applying both scenarios at two different insulation thicknesses. The results indicated that Scenario B consumes 75% more energy than Scenario A when the insulation thickness is 25 mm and 54% more when the thickness is 50 mm. Regardless of the insulation thickness, Scenario A remained the most energy-efficient. However, the energy consumption of this process decreases even further with an insulation thickness of 50 mm.

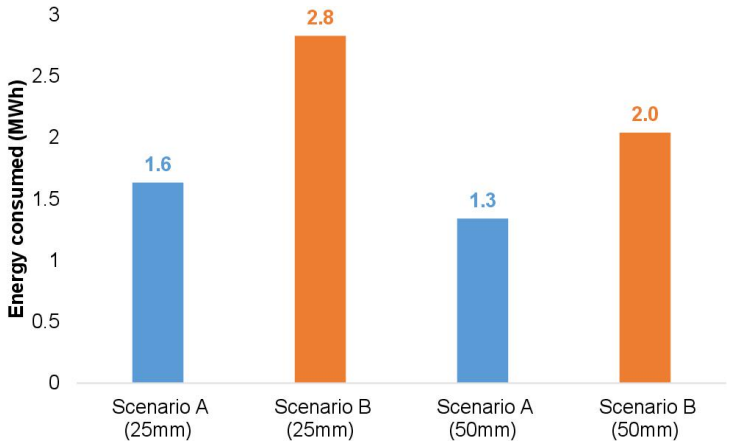

Figure 4.32: Energy consumption for heating the MCEC cylindrical module.

2.4.2 Rectangular Module

The rectangular manifold has dimensions of 6 m in length, 4 m in width, and height [211]. The rectangular geometry is treated as four vertical plates. Therefore, the conductive resistance of each vertical plate is determined using Eq. 4.20, where e represents the wall thickness of the plate.

$$R_{cond} = \frac{e}{k} \tag{4.20}$$

Similar to the cylindrical module, the conductive resistance of the rectangular manifold consists of the conductive resistance of the ceramic material $R_{cond,ceramic}$ and the carbon material conductive resistance $R_{cond,carbon}$, as illustrated in Figure 4.33. The thickness of the ceramic shell corresponds to that of the insulation, which was studied at 25 and 50 mm. Meanwhile, the outer carbon shell has a thickness of 20 mm.

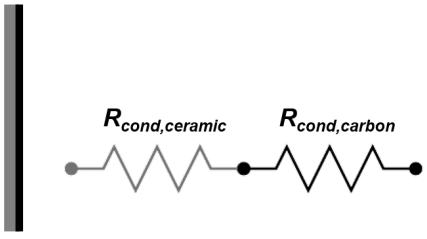

Figure 4.33: Schematic representation of the thermal conductive resistance of the rectangular module.

The convection resistance of the rectangular module is computed using the same methodology as that of the cylindrical module, with the only difference being the dimensions used. The energy consumption

for the heating processes of the rectangular module is illustrated in Figure 4.34. In this case, Scenario A is less energy-consuming than Scenario B. However, the energy consumption for the rectangular module is higher than that of the cylindrical module. Therefore, the cylindrical shape of the module enclosure was found to be more suitable for minimizing heat loss and energy consumption.

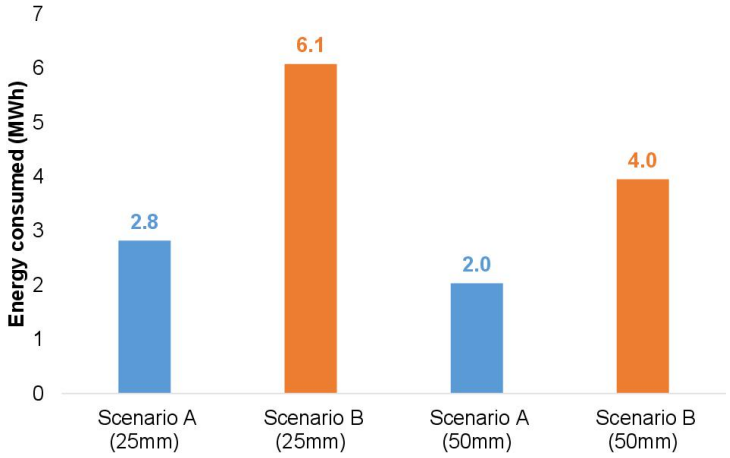

Figure 4.34: Energy consumption for heating the MCEC rectangular module.

The above energy analysis indicated that scenario A is the most energy-efficient when implemented in a cylindrical module design. The heating process is conducted gradually, and it takes approximately five days. This step is critical as it allows for the vaporization and combustion of solvents and organic polymers in the matrix and electrolyte. The patent's procedure [209] states that the cell is first heated in the presence of an oxygen-containing gas, such as air, to 300 °C to eliminate the organic binder from the electrolyte matrix and electrolyte carbonate tapes. This step lasts for 32 hours, after which the cell is held on standby at 300 °C for 35 hours to maintain stability. Subsequently, the heating process continues in the presence of an inert gas with a small hydrogen gas composition, gradually increasing the temperature to 650 °C. Injecting hydrogen gas during heating to high temperatures provides a reducing atmosphere that prevents the oxidation of the metallic cathode material and chemically reduces any undesirable oxides formed when the cathode is exposed to an oxidizing atmosphere. This procedure was applied to the MCEC electrolyzer model, and the cell's temperature response to the heating process with time is illustrated in Figure 4.35.

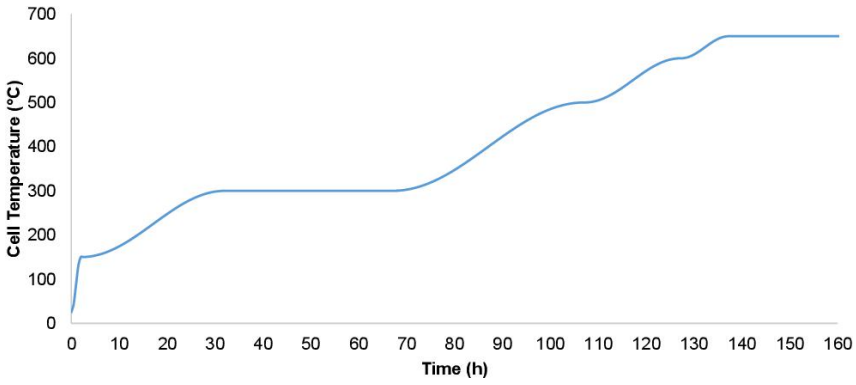

Figure 4.35: Cell temperature variation with time during the cold start-up process.

3 Dynamic Modeling of the Methanation Unit

This section is dedicated to modeling the dynamic phenomena characterizing the operation of fixed-bed methanation reactors. The study mainly aims to identify the reactor's behavior under transient conditions. First, the dynamic model of the reactor was developed by involving the kinetics of the reactions that might take place in the reactor. This dynamic study ignored the catalyst degradation over time, focusing primarily on its operational aspects. Finally, the cold start-up procedure of the reactor was evaluated in terms of energy consumption and time required to heat it.

3.1 Development of the Dynamic Model of the Methanation Reactor

The methanation reactor was modeled as "*Plug Flow Reactor – PFR*" in Aspen Plus software. This model assumed that mass and heat transfer in the axial direction are uniform, simplifying the modeling to one dimension. In addition, the kinetic expressions of the reactions in the reactor are incorporated by applying kinetic laws, which have been obtained through experimental validation. The methanation kinetic model was then validated using industrial data.

3.1.1 Kinetics of the Reactions

The reactions involved in the methanation reactor are CO_2 methanation (Eq. 4.21), RWGS (Eq. 4.22), and CO methanation (Eq. 4.23).

$$H_2 + 4\,CO_2 \longleftrightarrow CH_4 + 2\,H_2O \tag{4.21}$$

$$H_2 + CO_2 \longleftrightarrow CO + H_2O \tag{4.22}$$

$$H_2 + 3\,CO \longleftrightarrow CH_4 + H_2O \tag{4.23}$$

The model used in this study relies on the kinetic law recently developed by Champon et al. (2019) [218] for a commercial catalyst in a fixed-bed reactor. The kinetic expressions are based on the semi-empirical LHHW (Langmuir-Hinshelwood-Hougen-Watson) formulation and are integrated into Aspen Plus to represent the CO and CO_2 conversion rates. The rate of the CO_2 methanation reaction is denoted as $r_{CO_2,\,meth}$ and is calculated by Eq. 4.24, while the rate of the RWGS reaction is designated as r_{RWGS} and determined by Eq. 4.25. Finally, the CO methanation reaction rate is denoted as $r_{CO,\,meth}$ and is computed by Eq. 4.26.

$$r_{CO_2,\,meth} = \frac{k_{CO_2,\,meth} K_{H_2} K_{CO_2} p_{H_2} p_{CO_2} \left(1 - \frac{p_{CH_4} p_{H_2O}^2}{p_{H_2}^4 p_{CO_2} K_{eq,\,CO_2,\,meth}}\right)}{(1 + K_{CO_2} p_{CO_2} + K_{H_2} p_{H_2} + K_{H_2O} p_{H_2O} + K_{CO} p_{CO})^2} \tag{4.24}$$

$$r_{RWGS} = \frac{k_{RWGS} K_{CO_2} p_{CO_2} \left(1 - \frac{p_{CO} p_{H_2O}}{p_{H_2} p_{CO_2} K_{eq,\,RWGS}}\right)}{(1 + K_{CO_2} p_{CO_2} + K_{H_2} p_{H_2} + K_{H_2O} p_{H_2O} + K_{CO} p_{CO})} \tag{4.25}$$

$$r_{CO,\,meth} = \frac{k_{CO,\,meth} K_{H_2} K_{CO} p_{H_2} p_{CO} \left(1 - \frac{p_{CH_4} p_{H_2O}}{p_{H_2} p_{CO_2} K_{eq,\,CO,\,meth}}\right)}{(1 + K_{CO_2} p_{CO_2} + K_{H_2} p_{H_2} + K_{H_2O} p_{H_2O} + K_{CO} p_{CO})^2} \tag{4.26}$$

These kinetic expressions involve several terms. The first is the kinetic rate constant k_i, which represents the rate at which the reaction occurs. The second term corresponds to the driving force of the reactants and products, denoted by the remaining part of the numerator apart from the kinetic factor, k_i. Finally, the third term involves the adsorption of gases on the catalyst, represented in the denominator. All of these terms are included in the expressions for $r_{CO_2,\,meth}$ for the CO_2 methanation, r_{RWGS} for the RWGS, and $r_{CO,\,meth}$ for the CO methanation, as described earlier.

The Arrhenius equation in Eq. 4.27 calculates the kinetic rate k_i. The pre-exponential factor k_i° and activation energy $E_{a,i}$ are specific to each reaction i and listed in Table 4.4. This equation depends on the temperature T of the reactor, and R represents the gas constant.

$$k_i = k_i^\circ \exp\left(\frac{-E_{a,i}}{RT}\right) \tag{4.27}$$

	i	CO_2, meth	RWGS	CO, meth
Kinetic Constants	$E_{a,i}$ (kJ · mol^{-1})	110	97.1	97.3
	k_i° (mol · min^{-1} · g^{-1})	1.14 × 10^{8}	1.78 × 10^{6}	2.23 × 10^{8}

Table 4.4: Kinetic coefficients of the reactions, taken from [218].

The adsorption constant K_i is a function of temperature and follows the Van Hoff equation given in Eq. 4.28. The adsorption coefficient K_j° and heat Q_j are provided in Table 4.5 for each species j.

$$K_j = K_j^\circ \exp\left(\frac{Q_j}{RT}\right) \tag{4.28}$$

	j	CO	H_2O	CO_2	H_2
Adsorption Constants	Q_j (kJ · mol^{-1})	40.6	14.5	9.72	52
	K_j° (bar^{-1})	2.39 × 10^{-3}	6.09 × 10^{-1}	1.07	5.2 × 10^{-5}

Table 4.5: Adsorption coefficients of the species, taken from [218].

The equilibrium constant $K_{eq,i}$ of each reaction i is calculated according to Eq. 4.29. The coefficients are provided by Khorsand et al. (2007) [219], where the equilibrium coefficient $K_{eq,i}^\circ$ and the free energy ΔG_i are adjusted to be applied for the CO_2 and CO methanation reactions, and the RWGS reactions at the same unit conditions of k_i and K_j. The newly generated coefficients are presented in Table 4.6.

$$K_{eq,i} = K_{eq,i}^\circ \exp\left(\frac{-\Delta G_i}{RT}\right) \tag{4.29}$$

	i	CO_2, meth	RWGS	CO, meth
Equilibrium Constants	$K_{eq,i}^\circ$ (bar^2)	7.12 × 10^{14}	1.72 × 10^{-2}	1.22 × 10^{13}
	$\Delta_i G/R$ (K)	31,230	-4,400	26,830

Table 4.6: Equilibrium coefficients of the reactions.

3.1.2 Model Validation

After setting up the PFR model of the methanation reactor in Aspen Plus, the kinetics were validated by industrial data presented in [219]. They include the design of the methanation reactor in Table 4.7 and the input feed specifications in Table 4.8. The reactor operates in an adiabatic state at these conditions.

Dimensions	
Reactor length	4.8 m
Inside diameter	2.686 m
The Catalyst Pellet	
Shape	spherical particles
Diameter	0.00494-0.00476 m
Porosity	0.625
Tortuosity factor	2.74
Bulk density	1,014 kg/m^3
Catalyst length	0.0010583 m
Mean pore radius	8,000 A°

Table 4.7: Methanation reactor design, taken from [219].

Feed Input Specifications	
Temperature	586.3 K
Pressure	2,074.75 kPa
Species	**Flow rate (kmol/h)**
CO	20.5
CO_2	3.4
H_2	4,186.7
CH_4	26.1
H_2O	58
Inert	16.6

Table 4.8: Reactor's input feed specifications, taken from [219].

The simulation of the methanation process was carried out for this industrial data, and the results of the output stream are presented in Table 4.9. The outcomes confirm the industry's data, indicating the kinetics' validity for the three reactions involved.

Species	**Flow rate (kmol/h)**	
	Simulation	**Industrial [219]**
CO	0	0
CO_2	2.54×10^{-8}	0
H_2	4,111.6	4,111.5
CH_4	50.0	50.1
H_2O	85.3	85.3
Inert	16.6	16.6

Table 4.9: Simulation results and industrial data of the reactor's output stream.

Once the kinetic expressions were validated, they were applied to our process conditions. First, sizing the reactor was necessary to meet the operating conditions of our specific process. For an industrial scale, multi-tubular reactors appear to provide a suitable solution for the methanation process.

For reactor design, a study conducted by Giglio et al. (2018) [205] on a cooled fixed bed reactor was utilized to determine the dimensions of the reactor. A cooled fixed-bed reactor was considered since the methanation process was operated under an isothermal condition. However, during the early stages of operation, when the reactant concentration is high, there is an initial temperature rise in the fixed bed despite cooling. Therefore, to prevent channeling phenomena within the catalytic bed and regulate the maximum temperature, the ratio between the tube diameter containing the fixed bed and the catalyst

particle was assumed to be at least 10, as recommended by Giglio et al. (2018) [205]. In addition, this limit provides more flexibility for the reactor operation with variable loads. Consequently, 15 tubes, each with a length of 1.35 m and a diameter of 60 mm, are selected for the reactor design [205].

The total catalyst mass m_c in the reactor tubes was set to be 39.9 kg [205] and to calculate the void fraction of the solid bed (ε) required for simulation, Eq. 4.30 was used. The void fraction ε is the volume fraction not occupied by the catalyst. The reactor volume (V_r) was calculated by multiplying tube volume by the number of tubes in the reactor. The catalyst mass density (ρ_c) was assumed to be 1,270 kg/m^3 [203]. Consequently, a bed void fraction of 0.45 was obtained for the given parameters. The specifications for the methanation reactor design are summarized in Table 4.10.

$$m_c = \rho_c \cdot V_r \cdot (1 - \varepsilon) \tag{4.30}$$

Dimensions	
Number of tubes	15
Tube length	1.35 m
Tube diameter	60 mm
Catalyst bed properties	
Catalyst particle diameter	5 mm
Catalyst loading	39.9 kg
Catalyst density	1,270 kg/m^3
Bed void fraction	0.45

Table 4.10: Methanation reactor sizing specifications under the current conditions.

The reactor design parameters were then incorporated into the Aspen Plus simulation. Figure 4.36 illustrates the methanation process. At start-up, the reactor is supplied with syngas at a temperature of 300 °C and pressure of 20 bar. The feed has a flow rate of 13.7463 kmol/h and is composed of a mixture of 74.22% H_2, 24.04% CO, 0.89% CO_2, and 0.84% H_2O.

In a PFR reactor, the reactants undergo chemical reactions as they flow through the reactor from one end to another. Therefore, the residence time is a crucial factor that needs to be determined, as it represents the total time the gases spend within the reactor volume. This parameter is expressed in hours and is calculated as the ratio of the reactor volume to the gas flow rate entering the reactor. The residence time determines how long the reactants must react with each other. A longer residence time may allow for more complete reactions, but it may also result in undesirable side reactions or degradation of the reactants. Therefore, the residence time must be carefully controlled to achieve the desired reaction outcome. Figure 4.37 demonstrates the residence time of gases moving through the reactor. Longer residence time is observed as the gases move further through the reactor. Thus, along the reactor's length, a residence time of approximately 0.0015 h is needed to achieve a 97% conversion. Furthermore, the molar composition of the outlet gases along the length of the reactor is given in Figure 4.38, with methane production increasing significantly in the initial 0.2 meters of the reactor, followed by a gradual increase along the length until it stabilizes towards the end of the reactor.

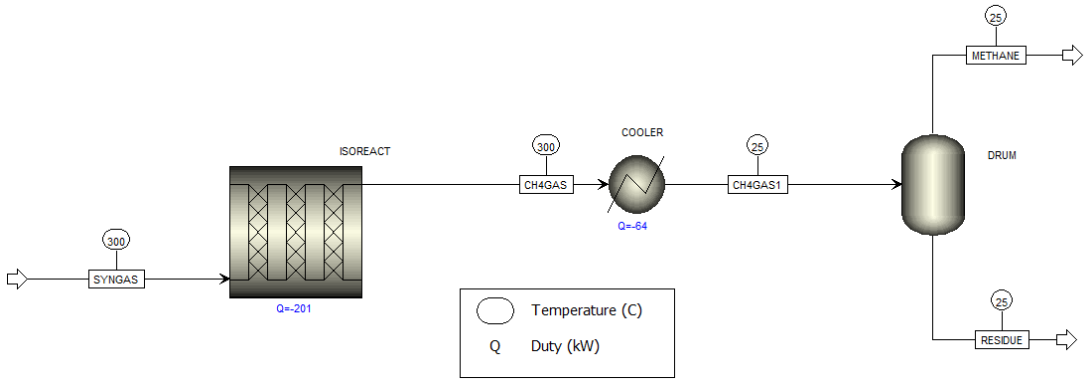

Figure 4.36: Methanation process using "Plug Flow Reactor PFR" model.

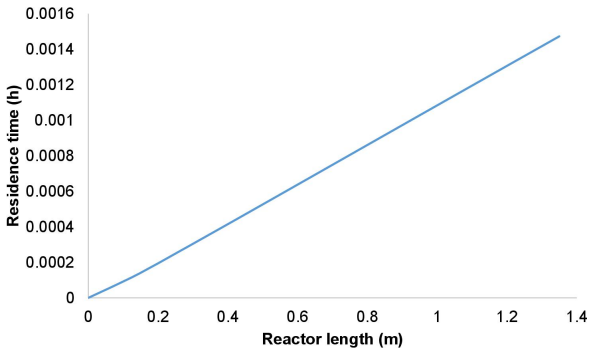

Figure 4.37: The residence time as a function of the reactor's length.

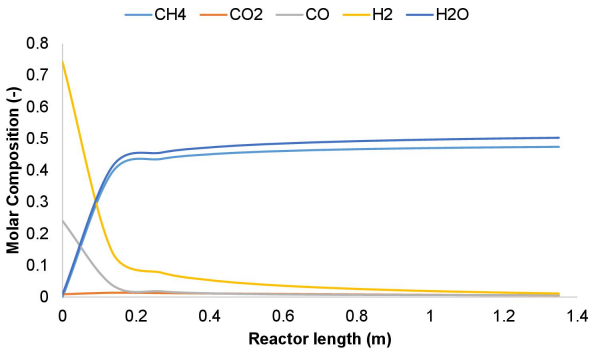

Figure 4.38: Outlet gases compositions as a function of the reactor's length.

In conclusion, the reactor design allowed for a 97% conversion of the reactants, resulting in a methane product with a composition of 95.36% CH_4, 1% CO_2, 1.26% CO, 2.2% H_2, and 0.18% H_2O. The Wobbe index of the methane product is 51.52 MJ/m^3. The reactor produced methane at a rate of 53.389 kg/h, equivalent to 1.28 tonnes per day. When considering the kinetics of the reaction, the methane quality meets the requirements of the natural gas grid even more effectively. However, the dynamic response of the methanation reactor, particularly concerning changes in the syngas ratio, is linked to the operation of the electrolyzer, which is affected by variations in power load. This aspect is addressed in Section 4, where the coupling of the P2G system with intermittent renewable power was studied.

3.2 Cold Start-up of the Methanation Reactor

The reactor must be heated before injecting the reactant gases to activate the nickel catalyst and initiate the reaction. Aubin et al. [207] explained this heat-up process, which involves external heating of the reactor using a silicon mat and internal heating using a mixture of N_2 and H_2 to preserve the catalyst. The reactant gases can be injected once the reactor temperature reaches 280 °C.

The heating time of the reactor varies depending on its design and material. In this case, the reactor was constructed as a multi-tubular reactor, utilizing austenitic stainless steel material. Therefore, to calculate the heating time, it was necessary to determine the energy and power required for heating, which can be achieved using Eq. 4.31.

$$\rho_w V_r C_{p,\,w} \frac{dT}{dt} = k_w A_r \Delta T \tag{4.31}$$

The wall density of the reactor, ρ_w, and its heat capacity, $C_{p,\,w}$, were obtained from [220]. The heat transfer coefficient of the wall, k_w, was obtained from [221]. The reactor volume and lateral surface area are denoted by V_r and A_r, respectively. Based on the design specifications presented in Table 4.10, the energy consumed by the reactor is calculated to be 19.5 kWh, and the power consumed is approximately 126 kW. Thus, the heating time required for the reactor is approximately 10 minutes.

4 Coupling Power-to-SNG System with Renewable Energies

This section examines the feasibility of connecting the Power-to-SNG system based on a MCEC electrolyzer to a variable renewable energy source (VRES), specifically wind or solar energy. To achieve this, obtaining reliable data on VRES energy production was necessary. Therefore, actual wind and solar plants in France are considered to simulate a realistic scenario. The country installed 60 TW of VRES capacity in 2021, including hydro, wind, solar, and bioenergy, contributing to 38% of the total share of electricity and energy production [14]. The System Advisor Modeler (SAM) software, created by the US-based National Renewable Energy Laboratory (NREL) [222], was used to obtain the data for this work. They cover two months: February represents the winter period, and August represents the summer period.

4.1 Wind Power

Wind power is a renewable energy source that converts the wind's kinetic energy into electricity through wind turbines. Wind turbines require wind speeds of at least 10 km/h to operate, and in the case of strong winds, they must be shut down for safety reasons. Therefore, wind turbines are typically installed in areas with wind speeds above 20 km/h.

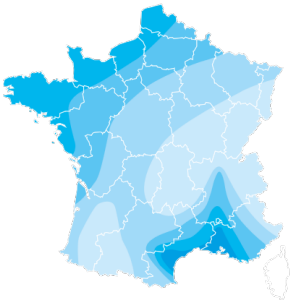

	WIND SPEED (km/h)				
	Zone 1	Zone 2	Zone 3	Zone 4	Zone 5
Bocages denses, bois, banlieues	< 12,6	12,6 - 16,2	16,2 - 18	18 - 21,6	> 21,6
Rase campagne, obstacles épars	< 12,6	16,2 - 19,8	19,8 - 23,4	23,4 - 27	> 27
Prairies plates, quelques buissons	< 18	18 - 21,6	21,6 - 25,2	25,2 - 30,6	> 30,6
Lacs, mer	< 19,8	19,8 - 25,2	25,2 - 28,8	28,8 - 32,4	> 32,4
Crêtes, collines	< 25,2	25,2 - 30,6	30,6 - 36	36 - 41,4	> 41,4

*50 meters above ground depending on topography

Figure 4.39: Wind speed distribution in France for different topographic zones. Picture taken from ADEME [3].

Wind power has experienced significant growth globally, and France has substantial potential for wind energy, as shown in Figure 4.39, with wind capacities distributed throughout the country. This advantage has made France the fourth-largest market for wind power in Europe, after Germany, Spain,

and the United Kingdom, with significant growth in recent years. In 2021, France had an installed wind energy capacity of 18.88 GW, generating 36.8 TWh of electricity, accounting for 7.8% of the total national energy production. Nearly 60% of the wind-generated electricity production came from three regions: Grand-Est (7.67 TWh), Hauts-de-France (8.95 TWh), and Occitanie (3.75 TWh) [223].

4.1.1 Wind Energy Data

For the wind energy case, a farm in Saint-Martin-de-Crau, a commune in the Bouches-du-Rhône department in the Provence-Alpes-Côte d'Azur region (43.623, 4.765), was chosen. This wind farm comprises nine Enercon E48/800 wind turbines, each with a nominal power of 800 kW, resulting in a total nominal power of 7.2 MW. The wind turbines have a diameter of 48 meters and a rotor height of 50 meters [224].

SAM's databases are limited to regions in North America, so it was necessary to obtain meteorological data from other sources for this analysis. In this case, the data were sourced from the LFMI (07647) meteorological station, located 16.88 kilometers from the wind farm (43.523, 4.922), and were collected at an elevation of 24 meters. However, some data processing was required to prepare the data for use in SAM. Additionally, there may be periods when data was missing, which can be addressed with a Matlab code. Therefore, a code was developed to simplify the data processing and fill in any missing values with the average of the last reported values.

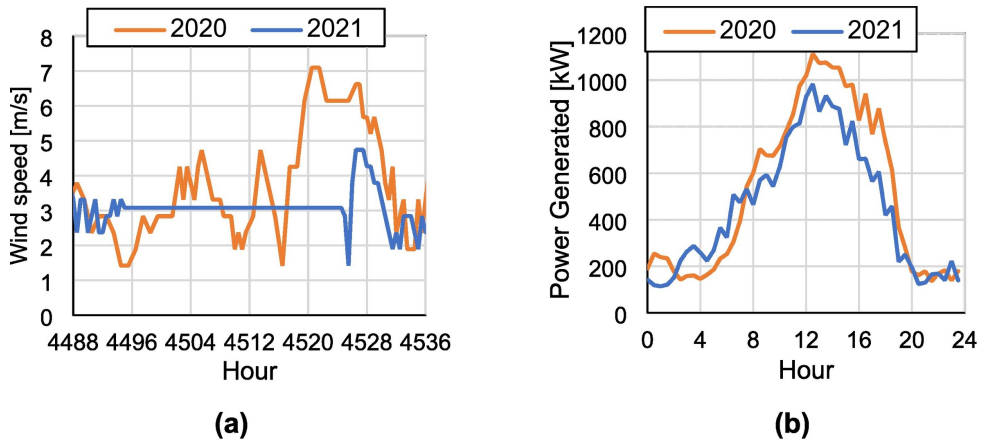

Figure 4.40: **(a)** Wind speed profile for the 7 and 8 July. **(b)** Average daily power profile generated during July.

Using SAM, the period with inadequate data in 2021 was compared to 2020 values to confirm the assumption of taking average values where data was missing. Figure 4.40a shows the wind speed profile from July 7th to July 8th. In the 2021 curve, where no data was reported, an average value was taken and is depicted as a straight line. Considering the constant value, the energy produced during this period was estimated to be 5,359 kWh, which is quite different from the 18,441 kWh generated in 2020. This finding demonstrated that this assumption does not accurately reflect the behavior of daily energy production. However, when the total amount of energy produced over the month was analyzed, a difference of only 14% was found, which is insignificant given the variable nature of wind energy.

To summarize, relying on average values to fill in missing data is not always reliable. Nonetheless, the average monthly energy production remains relatively unchangeable. To illustrate, Figure 4.40b displays July's average daily power profile, calculated using SAM data from both years. This assumption was used to estimate the monthly energy production of the wind farm, as shown in Figure 4.41, using the SAM software.

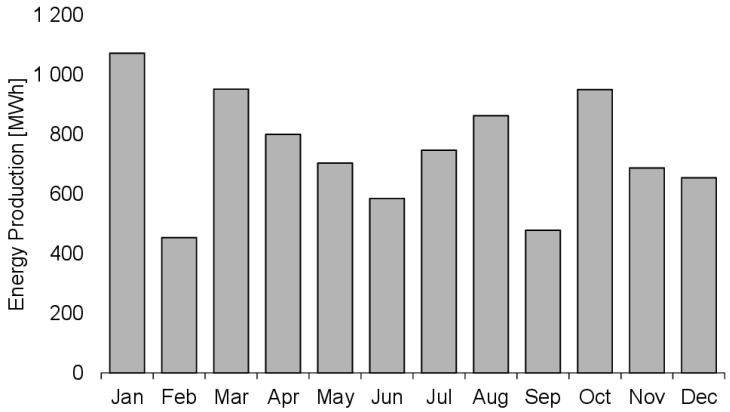

Figure 4.41: Monthly energy production in MWh by the wind farm.

4.1.2 Case Study

After collecting the data, examining the connection of renewable energy sources with the Power-to-Gas process was necessary. The electrolyzer requires a gradual heat-up process that takes an average of five days. This process involves significant energy consumption because the cell must be heated up to melt the electrolyte before start-up operation, and the streams must reach an operating temperature of 650 °C. Therefore, turning the electrolyzer on and off is not entirely practical. One option is to put it in standby mode, which involves keeping the electrolyzer at operating temperature and ready to turn on when electricity is available. However, the standby mode requires an external heating source to maintain the cell operating temperature at 650 °C, thus keeping the molten carbonate electrolyte in a liquid state and avoiding solidification when the cell is cooled down. In addition, this standby state consumes around 42 kW of power, as presented in Section 2.4, leading to additional operating expenses. In this section, seasonal storage using wind energy will be studied, addressing two important questions:

- Question 1: what is the optimal modular electrolyzer configuration system to be implemented, given wind farm production in southern France?
- Question 2: how does the MCEC electrolyzer respond to the intermittent input power regarding the syngas production and its impact on the methanation process for methane synthesis and the process efficiency?

4.1.2.1 Operation at Nominal Power with Electricity Support

A fixed 1 MW output for each module was assumed. When wind energy production is less than the sum of the module outputs, external electricity grid support is used to make up for the shortfall. The second assumption is that storage will only occur during high wind energy production periods, with the electrolyzer running in standby mode during low production periods. A Matlab code has been developed to identify these high wind energy production periods. The code looks for periods of continuous power supply within a defined power range, indicating when storing energy in the electrolyzer is feasible.

Table 4.11 presents the findings obtained by considering the abovementioned assumptions. The methane production values are based on Aspen simulation results for modules operating at their nominal power of 1 MW, and a production coefficient of 53.38 kg per operating hour per module has been considered. The table shows that the total methane production significantly increases from one to two modules, but the increase becomes negligible when more than two modules are proposed. Methane production decreases from five modules, indicating more wind energy is needed to distribute it equally among five or six modules. Therefore, from a performance perspective, the most accurate number of modules is between one and two. It should be noted that an increase in the number of modules installed after two modules means more electric consumption with the same methane production and, therefore, less efficiency.

Number of modules	Total yearly hours of operation	Total yearly hours in stand-by mode	Total energy supplied from the grid [MWh]	Total energy supplied from the wind [MWh]	Total yearly methane production [kg]
1	2,034	6,462	196.96	1,837	109,475.98
2	1,926	6,570	712	3,139.95	207,326.20
3	1,284	7,212	679.65	3,172.35	207,326.20
4	1,104	7,392	833.56	3,582.44	237,682.37
5	528	7,968	153.07	2,486.93	142,092.72
6	318	8,178	106.69	1,801.31	102,694.28

Table 4.11: Results considering using a different number of modules coupled to a wind source over the year.

Now that it had been concluded that the optimal modular system lies between 1 and 2 modules, the next step was determining the best modular configuration between them. This will be achieved by calculating each modular system's final methane production cost and selecting the one with the lowest price. An economic datasheet that quantifies the economic aspect of the system's entire life cycle was created and used to calculate the methane production cost (See Chapter 5). In addition, the electricity cost and operating hours per year were considered in the datasheet, with an electricity grid cost of 174 €/MWh and an onshore wind energy cost of 36 €/MWh taken from the IRENA report [225]. Based on these costs, a methane cost of 13.032 €/kg and 14.074 €/kg was found for one and two modules, respectively. The results indicated that adding a module increases methane production significantly but does not make up for the investment cost of the second module. Consequently, it has been determined that a single module of 1 MW is the optimal choice for coupling with VRES.

4.1.2.2 Operation in Dynamic Mode (100% Wind Energy)

In this part, the system was subjected to some flexibility to investigate the impact of wind energy variability on its performance. The storage periods for this analysis are shown in orange in Figure 4.42, which was generated using Matlab code. However, the data was manually adjusted to extend the storage periods in cases where the gap between consecutive periods is short. Although the orange line appears to follow the same pattern throughout, some differences appear during specific periods.

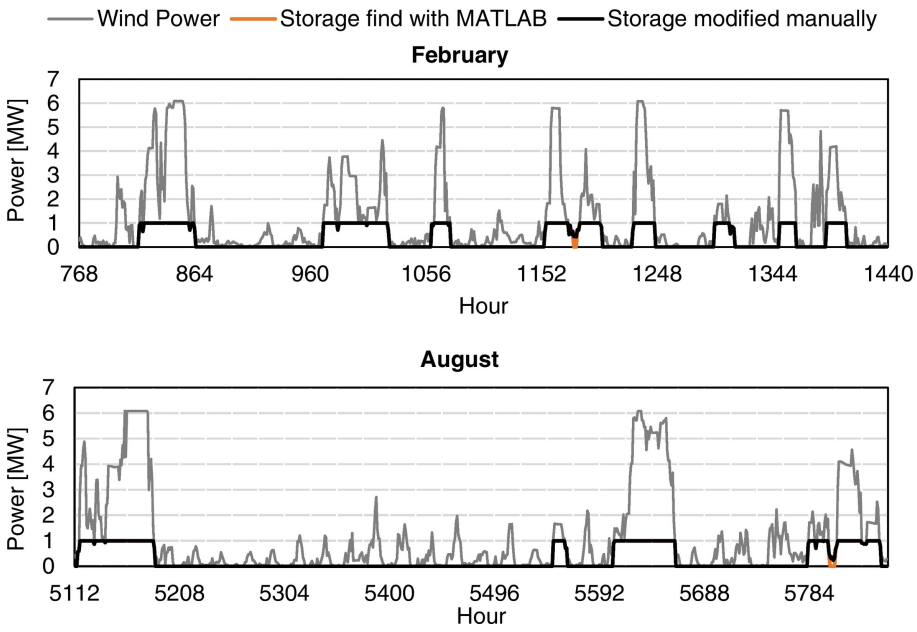

Figure 4.42: Storage periods found considering one module for February and August, respectively.

This data was then integrated into the Aspen Plus model to analyze the dynamic behavior. Following the suggestion of Olivier et al. (2017) [226], a control strategy was applied to determine the system's operational parameters while accounting for a variable load. The electrical power consumed by the electrolyzer was determined based on the current density (j [A/cm^2]) until the difference between this power and the power supplied by the wind source reaches zero, as shown in Figure 4.43.

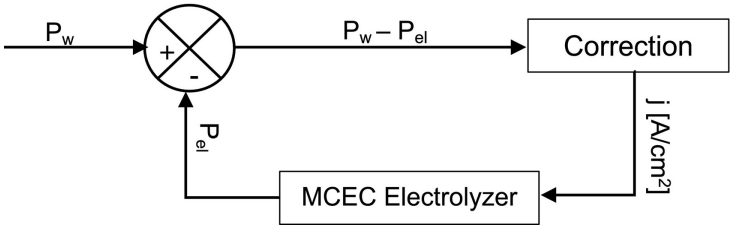

Figure 4.43: Control strategy, to determine the value of the operation current density j, based on wind power P_w and power consumed by the electrolyzer P_{el}.

The two main results that quantify the overall process's performance are depicted in Figure 4.44, which shows the methane production flow rate and the efficiency of the overall process, respectively. When analyzing both parameters, it can be noticed that they exhibit the same tendency regarding the power supply, shown in Figure 4.42. This observation indicated that the power supply directly impacts

the system's performance.

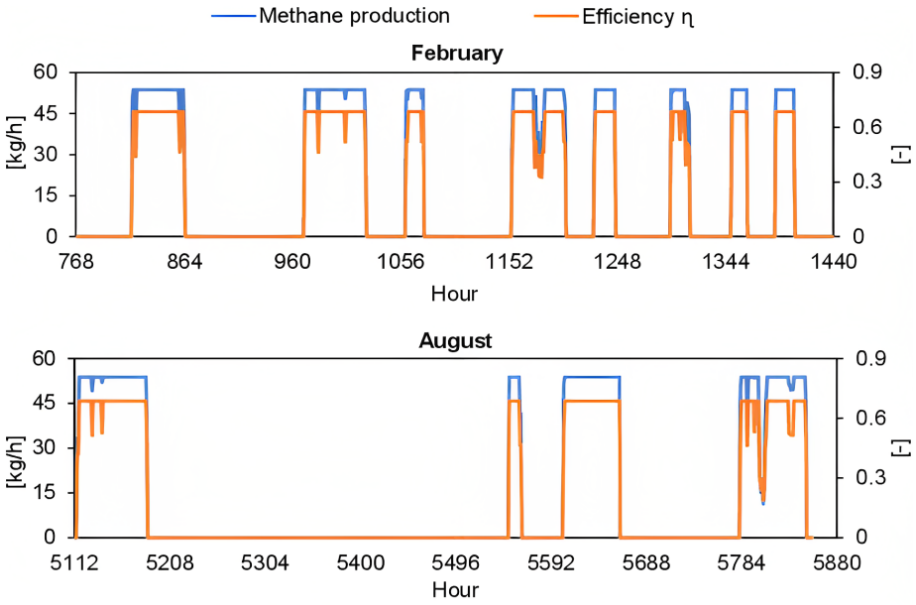

Figure 4.44: Methane production and efficiency for the month of February and August, considering the system linked to wind power.

The data collected allow for a comparison between process efficiency and power. Based on the results presented in Figure 4.45a, the two parameters have a proportional relationship. The process efficiency reaches its maximum value of 68% under nominal operation. However, reducing the power supply leads to a decrease in methane production and a significant decrease in process efficiency. This is because the energy required for the process does not decrease proportionally with the reduction in methane production. Moreover, when the power is lowered below the nominal value, the cell's state changes from exothermal into endothermal, as shown in Figure 4.45b, thus impacting the process efficiency.

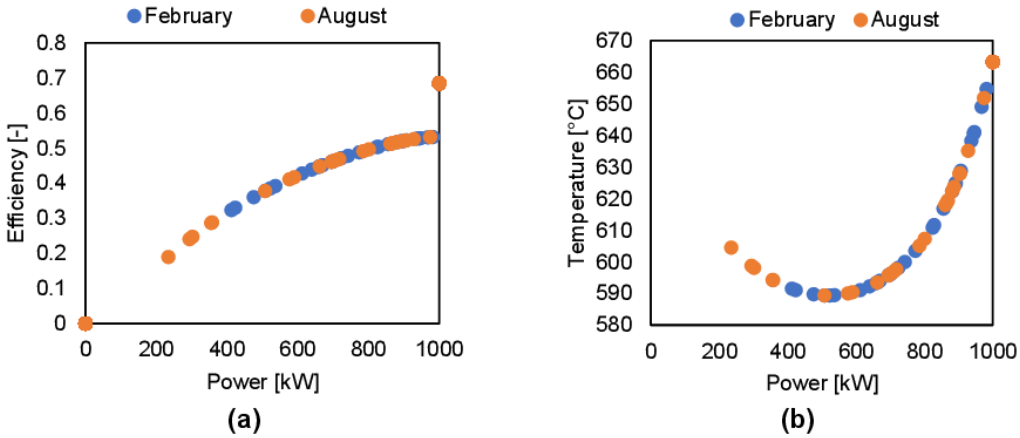

Figure 4.45: **(a)** Efficiency of the process and **(b)** outlet temperature as a function of the power supplied to the electrolyzer.

To ensure the overall quality of the process, it was essential to analyze parameters related to the syngas and final substitute natural gas (SNG), a mixture of methane and other secondary gases, produced. Since syngas is produced by the electrolyzer, it is affected by the power load, thus affecting methane synthesis. Figure 4.46a displays the syngas composition (in dotted lines) along with the power, with the August period chosen due to its high variability. The hydrogen content decreases, and the CO_2 content increases significantly when the load is reduced, implying that some CO_2 entering the electrolyzer does not react. This situation may result in low-quality syngas, adversely affecting the methanation process. Furthermore, producing syngas with such high CO_2 and CO concentrations would not be beneficial for an independent electrolysis step, as a purification process would be necessary.

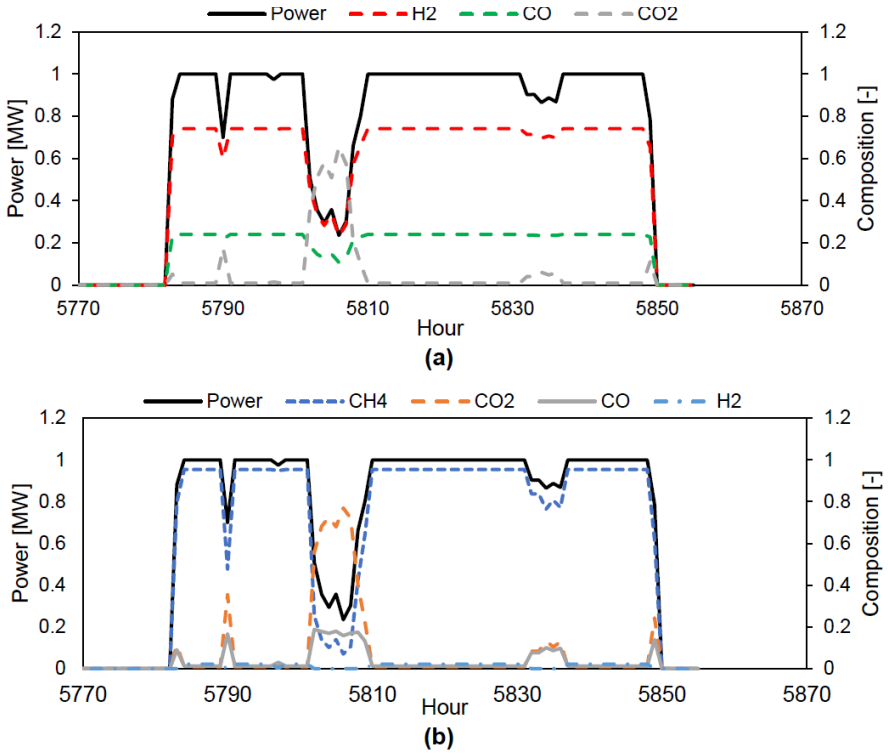

Figure 4.46: **(a)** Syngas and **(b)** SNG during a period of high variability (August).

The final SNG composition is presented in Figure 4.47. As expected, the CO_2 concentration increases when the power is reduced due to the low CO_2 utilization during the electrolysis process. Consequently, lower-quality SNG is produced, which requires a repurification procedure since, according to the French grid's standard for natural gas quality, the CO, H_2, and CO_2 secondary gas concentrations in the SNG cannot exceed 2%, 6%, and 2.5%, respectively [23]. The composition of the major gases in the SNG produced is shown in Figure 4.47, where H_2 is not presented due to its low concentration, making them unnoticeable. However, to couple the system with a changing load source, the gas must be purified, or a secondary system must be implemented to reduce the CO_2 inlet flow before the methanation reactor. Therefore, Figure 4.47 illustrates how changing just a few load parameters makes SNG unsuitable for injection into the natural gas grid.

The dynamic behavior has been analyzed, but it was essential to consider an overall perspective. Table 4.12 presents the methane production results for all months and the wind energy required by the

electrolyzer. The total amount of methane produced during the year is also estimated. If the operation hours in this case are compared to those obtained in Section 4.1.2.1, they increase by 30%, and methane production increases by 27%. Therefore, allowing more flexibility in the system leads to more methane production.

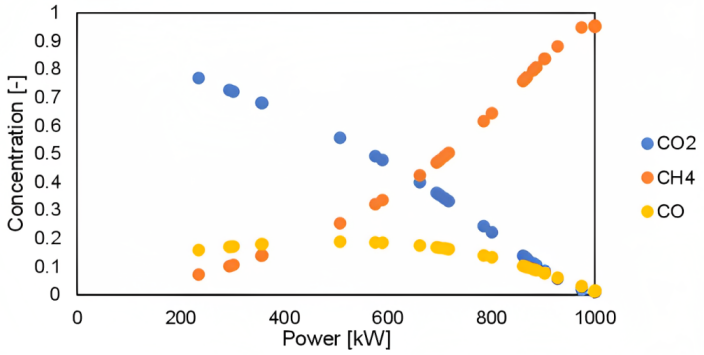

Figure 4.47: Final SNG composition as a function of the power.

	Methane production [kg]	Hours of operation	Wind energy [MWh]
February	13,897	233	225.2
August	12,548	208	200.3
Total year estimation	158,670	2,646	2,553

Table 4.12: Results for dynamic operation of one module coupled to a wind energy source.

It should be noted that the methane production values presented in Table 4.12 only consider the amount of pure methane produced. The outlet gas (SNG) from the methanation reactor is a mixture of gases, and considering that it will be stored for the entire month, it is possible to estimate its composition over the entire variability period. Therefore, using mass balance, the SNG composition for the summer and winter periods was estimated and is shown in Figure 4.48. As seen during both periods, the SNG contains CO_2 and CO concentrations that exceed the limitations for injection into the gas network.

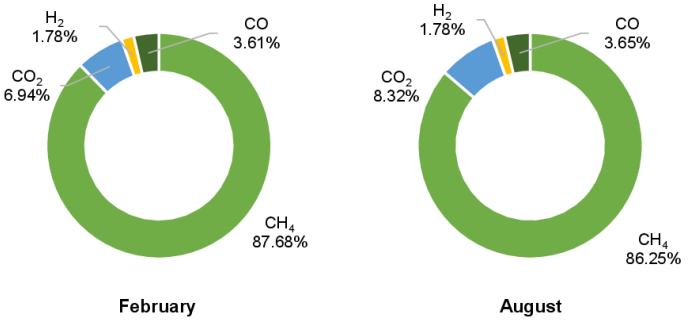

Figure 4.48: Final SNG composition along each month.

Although the system often operates close to the nominal power values, the allowed degree of variability produces SNG that requires a purification process. So, it is impossible to estimate the actual cost of SNG since including the cost of the purification process is not feasible.

4.2 Solar Power

Solar photovoltaic (PV) is a well-established and commercially feasible technology. In France, the installed capacity of photovoltaic solar parks reached 13.2 GW by the end of September 2021, with more than half corresponding to facilities with capacities greater than 250 kW [227]. Since this generation became viable, the installed capacity has continued to grow. New connections have increased yearly since 2016, indicating that solar photovoltaic energy has gained interest in the country.

The photovoltaic potential of France is lower than some other regions in the world. However, the southern part of the country has significant potential, particularly in regions close to the Mediterranean Sea and the border with Italy, where the photovoltaic potential exceeds 1,400 kWh/kWp (see Figure 4.49). Therefore, this study aims to investigate the energy output of a plant located in this region.

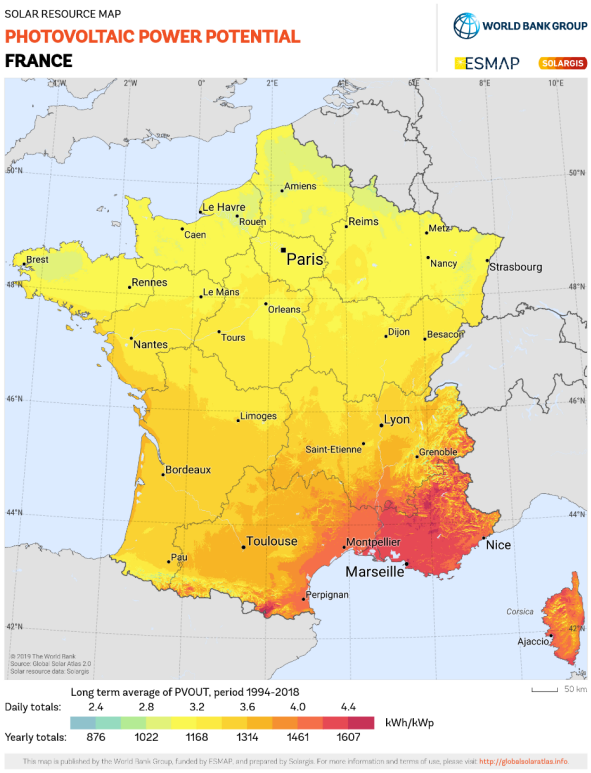

Figure 4.49: Photovoltaic power potential in France. Picture taken from © 2020 The World Bank, Source: Global Solar Atlas 2.0, Solar resource data: Solargis.

4.2.1 Solar Energy Data

To conduct this investigation, the Fabrègues solar power plant, situated in the Hérault department of Montpellier at coordinates 43.532, 3.756, was selected. This plant has an installed capacity of 1.3 MW and generates 1.5 GWh of electricity [228]. As not all the plant's characteristics are available, some assumptions are made to estimate the energy production. According to the satellite view, it was assumed that the solar panels are fixed and facing south and that their tilt angle corresponds to the area's latitude, which is 43.532°.

Initially, the total Annual Energy Production (AEP) was estimated to be approximately 2 GWh, notably different from the reported value of 1.5 GWh. However, it is important to note that the simulation assumed a brand-new system in SAM and did not account for shading effects. Therefore, the same assumptions as the first simulation were used in the second, but a degradation coefficient of 8% was considered. This value was determined based on the assumption that the plant had been in operation since 2010 and that the annual degradation coefficient is 0.8%/year, as proposed by Jordan and Kurtz [229]. As a result, the new value for the AEP is 1.56 GWh, which is quite similar to the reported value. Therefore, this configuration performs similarly to the actual plant.

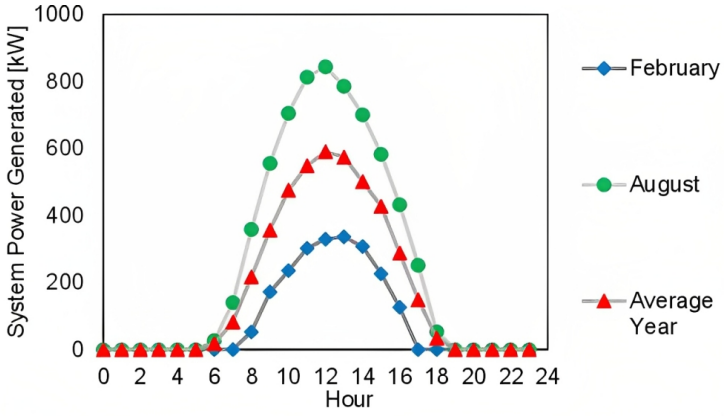

Figure 4.50: Average hourly solar power generated by PV system per day in February, August, and over the year.

Figure 4.50 displays the average hourly patterns of solar power generated by a photovoltaic system in February, August, and throughout the year. Noticeably, the system's power output varies from zero during the night to its maximum value around noon. Moreover, the figure reveals that the energy produced at noon in August is more than twice that produced in February. Additionally, the number of sun hours received in February is lower than in August, with February receiving 10 hours and August receiving 14 hours. This behavior highlights the seasonal impact on solar energy production, as Figure 4.51 demonstrates a significant decrease in energy production during winter.

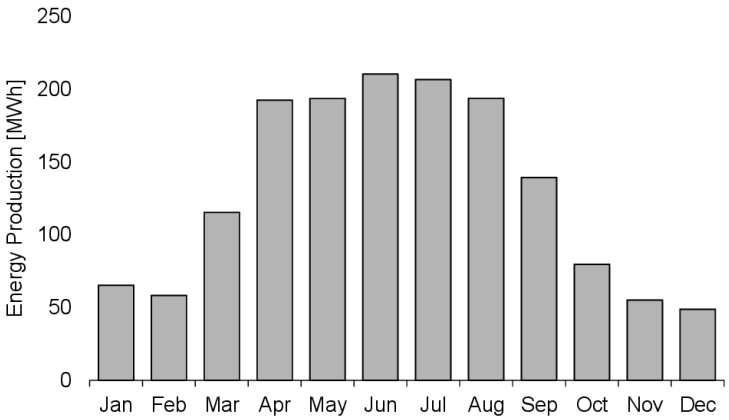

Figure 4.51: Monthly energy production in MWh by the solar farm.

4.2.2 Case Study

This case study focused solely on the dynamic mode operation, which examined the Power-to-SNG system's dynamic operation using solar power. The system's primary function is to produce high-quality SNG for the natural gas grid while maintaining high energy efficiency. Therefore, examining how solar power affects methane production and the system's energy efficiency was crucial.

Figure 4.52 displays the variations of methane production in kg/h and process efficiency η with solar power during February and August. As anticipated, solar power is more efficient in summer than in winter. The figure highlights that methane production and process efficiency vary significantly with solar power, as the electrolyzer is subjected to intermittent hourly or no power. This situation is more pronounced during winter (February) than in summer (August). During the summer, the electrolyzer operates around its nominal capacity for most days, whereas during the winter, some days have very low or even zero PV production. Despite this, high methane production and process efficiency are only achievable during peak hours, indicating that the electrolyzer must be well-controlled to respond effectively to these significant load changes.

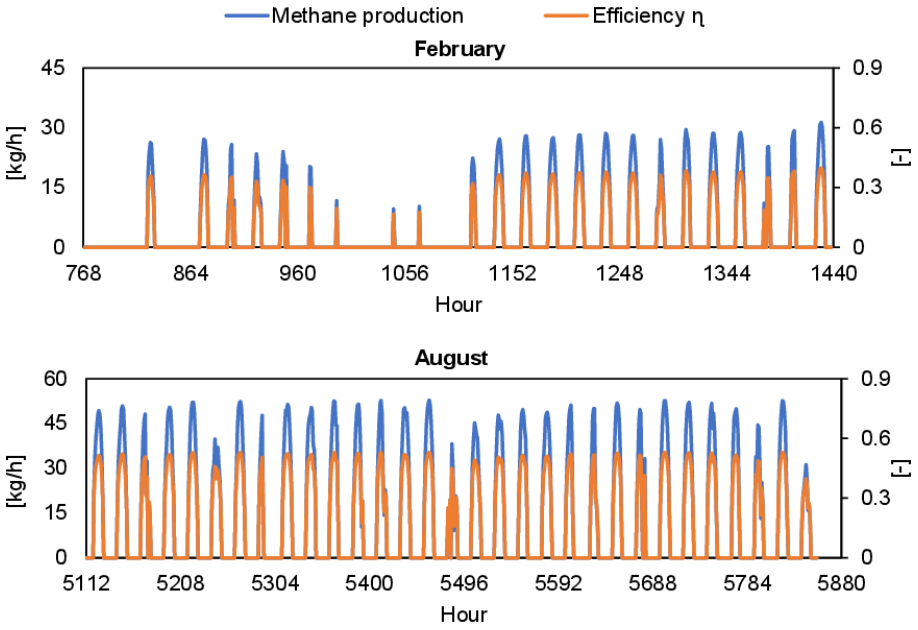

Figure 4.52: Methane production and efficiency for February and August, considering the system linked to solar power.

As process efficiency is crucial, the impact of solar power on efficiency is highlighted in Figure 4.53a. According to the findings, it is evident that efficiency decreases with power. Therefore, a solar power load between 80% and 100% of the nominal capacity of 1 MW is necessary to achieve an energy efficiency above 50%. Additionally, it was essential to examine the electrolyzer's operation mode (endothermic or exothermic) with changes in power load. Hence, Figure 4.53b depicts the outlet temperature of the electrolyzer as the power load changes. It was observed that the cell operates in endothermic mode at a power load below the nominal load (1 MW), meaning that the cell requires further heating to compensate for the heat absorbed by the electrolysis process.

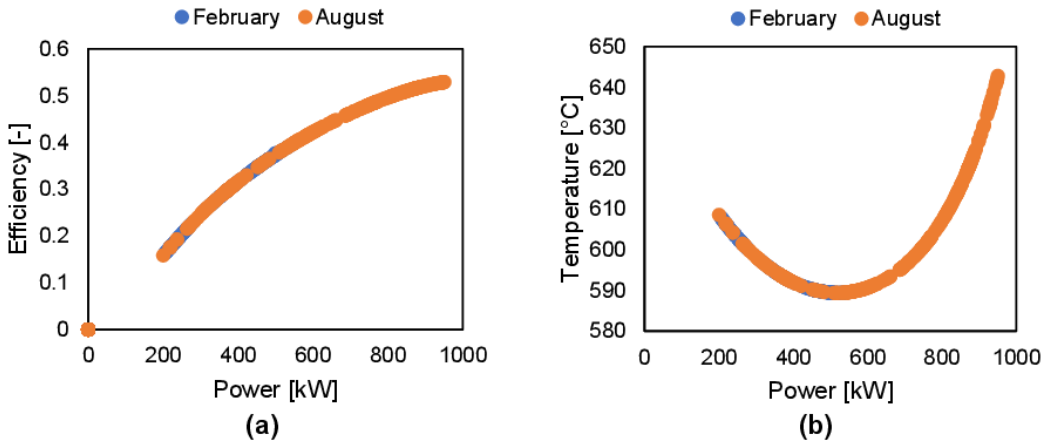

Figure 4.53: **(a)** Efficiency of the process and **(b)** outlet temperature as a function of the power supplied to the electrolyzer.

After evaluating the performance of the Power-to-SNG system in terms of methane production and process efficiency, the quality of both the syngas and the substitute natural gas (SNG) is a crucial aspect to consider. The syngas composition consists mainly of H_2, CO, and CO_2 and must follow a ratio of about 3 for methane synthesis to ensure high-quality SNG production. As shown in Figure 4.54a, the syngas quality is high when the power load is around the nominal capacity but deteriorates with the power load, resulting in a higher CO_2 content than H_2 and CO.

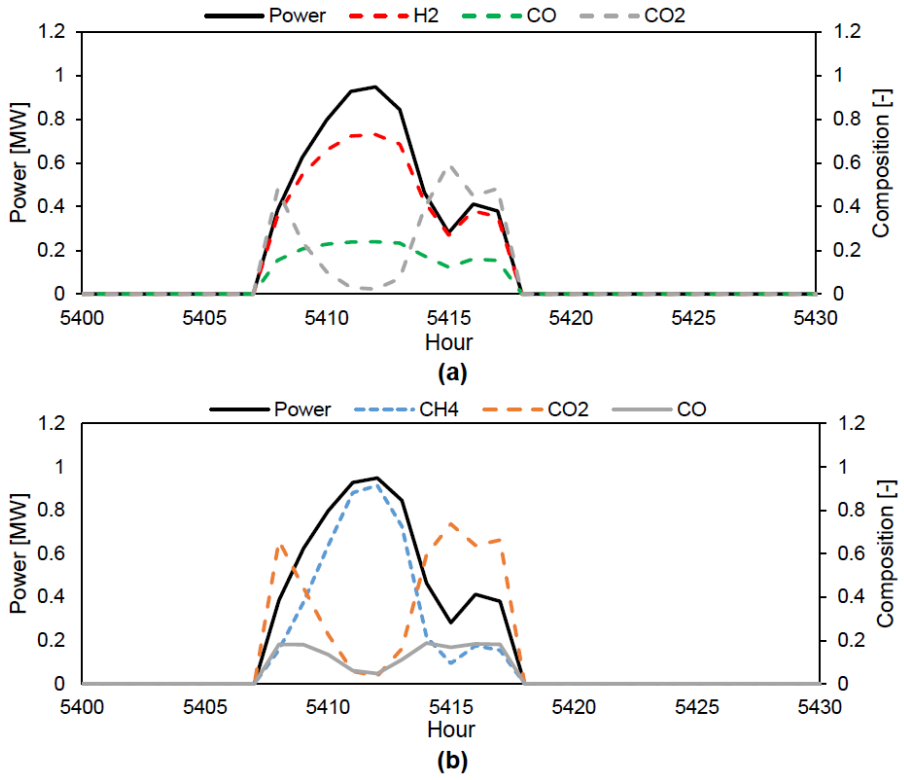

Figure 4.54: **(a)** Syngas and **(b)** SNG composition during a period of high variability (August).

The SNG composition, shown in Figure 4.54b, must comply with the natural gas grid requirements for direct injection into the grid. However, the SNG quality decreases with decreasing power, and it contains more CO_2 and CO, which exceeds the natural gas grid's 2.5% and 2% limit, respectively. This implies that it is difficult to control the SNG quality for direct injection into the grid due to the highly intermittent nature of solar power. Therefore, the substitute natural gas will require purification to remove excess CO_2 and CO, or it may need to be diluted with a natural gas portion to lower the CO_2 and CO concentrations.

Additionally, while the natural gas grid sets a maximum 6% limit for H_2 content, there are no issues with H_2 content fluctuating with changes in power load since it is consumed, thus remaining below this limit. However, the CO_2 and CO contents are more problematic, exceeding the limit with decreasing power. Consequently, the SNG composition, mainly CH_4, CO_2 and CO composition, are plotted against power load in Figure 4.56, revealing that it is difficult to have CO and CO_2 contents limit below nominal loads. While the power load between 70% and 100% had more CH_4 than CO_2 content, a purification process is still necessary to meet the 2.5% limit. Meanwhile, power loads below 60% decreased CO_2 conversion and CH_4 yield, resulting in more unreacted CO_2 content than CH_4 product content.

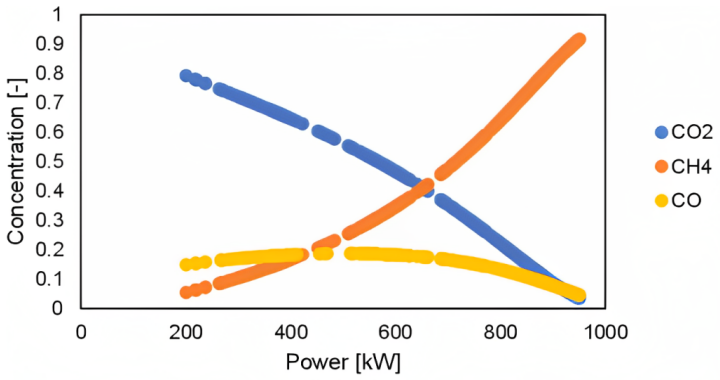

Figure 4.55: Final SNG composition as a function of the power.

Lastly, assuming the produced SNG may be stored before injection into the grid, its composition was analyzed over February and August. The results indicated that SNG contained a significant amount of CO_2, surpassing the CH_4 content, necessitating additional purification.

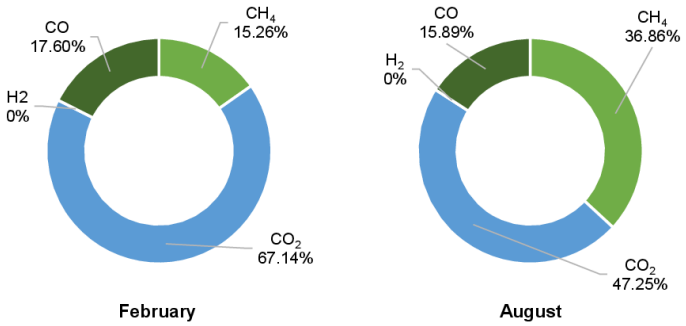

Figure 4.56: Final SNG composition along each month.

4.3 Power Coupling Case Studies Conclusion

The Power-to-SNG system's performance using wind and solar power was investigated, focusing on methane production, process efficiency, and gas quality. The results revealed that the solar power's intermittent nature significantly impacted the system's performance, with winter months experiencing more significant fluctuations in methane production and process efficiency than summer months. It was also observed that the electrolyzer operated in endothermic mode at power loads below the nominal load, requiring additional heating. Regarding gas quality, the syngas quality deteriorated with decreasing power load, with a higher CO_2 and CO contents than H_2, thus affecting the SNG quality, with a CO_2 and CO contents higher than the natural gas grid's limit of 2.5%, and 2%, respectively.

Comparing the results obtained from wind and PV, wind power was observed to be more consistent than solar power, leading to higher methane production and process efficiency. However, the syngas and SNG composition remained challenging for both sources, with power fluctuations impacting the gas quality, requiring additional purification or dilution with natural gas.

Overall, the Power-to-SNG system's performance using renewable energy sources highly depends on various factors such as weather conditions, power load, and control systems. Utilizing a single large electrolyzer that can handle the entire power production can be inefficient since it might require the electrolyzer to operate at low loads, leading to lower efficiency. Instead, a modular configuration consisting of multiple smaller electrolyzers, each capable of handling a portion of the renewable power production, could provide greater flexibility in power production management while ensuring optimal electrolyzer efficiency. Further research could explore developing more robust control strategies that can effectively manage the system's response to power fluctuations, thereby improving the system's overall efficiency and reliability.

5 Conclusion

This chapter comprehensively analyzes the dynamic behavior of a Power-to-SNG system consisting of a molten carbonate electrolyzer (MCEC) and a methanation reactor. It is divided into three main parts.

The first part focuses on the dynamic operation of the MCEC electrolyzer. Two cases are studied: electrode degradation and the response of the MCEC to unexpected changes in input variables. The results show that electrode degradation decreases cell potential and power due to the impact on the syngas' partial pressure. Maintaining the same syngas production requires increased applied current to enhance electrolysis. The significance of degradation issues in large-scale cells is highlighted. Furthermore, the MCEC exhibits proportional changes in the cell's power and voltage, H_2 and CO outlet composition, and outlet temperature in response to load and cell number variations. In contrast, they respond reversibly to changes in the inlet gas flow rate. Moreover, a five-day heating process with a specific profile is the most energy-efficient cold start-up procedure.

The second part analyzes the dynamic behavior of the methanation process under transient operation. A tubular-cooled fixed bed reactor design achieves high reactant conversion and produces a substitute natural gas (SNG) with a desired composition that meets natural gas grid requirements.

The final part investigates integrating the Power-to-SNG system with intermittent renewable power sources. Solar power shows significant fluctuations in methane production and process efficiency during winter, while wind power demonstrates a higher consistency. The variable source produces intermediate-stage syngas with a high content of CO_2 and CO when the power supplied to the electrolyzer is slightly below the nominal power. This gas with a high CO_2 and CO contents enters the methanation reactor, which generates a substitute natural gas that does not meet the minimum requirements for injection in the natural gas grid. This behavior occurs only during periods of low power; however, for the total gas obtained during the two periods of winter and summer, the CO_2 and CO contents are not satisfactory and are of the order of 8% for CO_2 and 4% for CO for wind source and of the order of 60% for CO_2 and 17% for CO for solar source. Maintaining desired syngas and SNG compositions becomes challenging due to power fluctuations, requiring additional purification or dilution with natural gas. The proposed options include a modular system with control strategies to mitigate variability or incorporating a purification process to the system when the desired gas quality cannot be achieved.

Résumé: Simulation dynamique

Ce chapitre examine le fonctionnement dynamique des différentes étapes impliquées dans le procédé Power-to-SNG. Un modèle dynamique a été développé à l'aide du logiciel « Aspen Custom Modeler (ACM) » pour étudier la dégradation de la cellule et sa réponse aux variations imprévues. L'unité de méthanation a été simulée en mode dynamique et les procédures de démarrage à froid de chaque unité ont été discutées. Enfin, la réponse du système Power-to-SNG aux sources d'énergie renouvelable variables telles que l'énergie éolienne et solaire a été examinée.

Modélisation dynamique du MCEC

La modélisation dynamique de l'électrolyseur MCEC couvre trois aspects : le développement d'un modèle dynamique dans ACM, la modification du modèle électrochimique pour étudier le fonctionnement dynamique du MCEC, et l'application du concept de réponse dynamique aux variations imprévues. Enfin, le procédé de chauffage de l'électrolyseur MCEC a été évalué et la meilleure procédure a été sélectionnée.

Développement du modèle dynamique de l'électrolyseur MCEC

Le modèle du MCEC a été mis à jour pour inclure l'opération transitoire de la cellule. Pour le bilan des matières, le taux d'accumulation avec le temps des composants a été ajoutée. Le bilan d'énergie a également été ajusté pour inclure le taux d'accumulation de l'énergie totale de la masse solide de la cellule. Le modèle électrochimique a été ajusté pour incorporer les coefficients de dégradation, qui affectent les matériaux des électrodes et de l'électrolyte. Pour prendre en compte la variation de la surface active de l'électrode dans le temps, une expression pour la variation de surface a été incluse dans le modèle. Ceci est important, car les matériaux des électrodes se détériorent avec le temps pendant l'opération d'électrolyse de la pile MCFC [73].

Le modèle dynamique MCEC a été validé en l'appliquant aux conditions expérimentales puis aux conditions de mise à l'échelle. Trois valeurs de taux de dégradation (d_A) ont été étudiées : 1%, 5% et 10% pour 1000 heures de fonctionnement. Selon Petipas et al. (2013) [208], la surface active de la cellule a diminué de 5% au cours d'une opération de 505 heures. Cela nous a permis d'étudier le taux de dégradation de 10% pour 1000 heures, étant donné que les électrolyseurs SOEC et MCEC fonctionnent à haute température. Ce taux de dégradation a été considéré comme le cas le plus défavorable, donc des valeurs plus faibles ont été examinées pour représenter les scénarios correspondant à l'état de la cellule.

Validation du modèle

Le modèle a été validé en étudiant les conditions expérimentales sur une période de 1630 h tout en tenant compte de la dégradation de la cellule avec le temps. Les données expérimentales correspondent à la courbe V-I obtenue après 1630 h. Pour valider le modèle, le potentiel de la cellule a été étudié au fil du temps à une densité de courant fixe de -75 mA/cm^2. Les résultats du modèle, présentés dans la Figure 4.57, sont comparés pour les trois taux de dégradation abordés dans l'étude.

Les données expérimentales ont montré une cellule à 1,39 V à 1630 h, et les résultats du modèle pour différents taux de dégradation sont comparables, avec une différence d'environ -1%. Le taux de

dégradation n'a pas eu d'effet significatif sur la tendance du potentiel de la cellule ou de la densité de puissance au fil du temps, probablement en raison du modèle basé sur la densité de courant fixe utilisée dans cette étude. De plus, l'augmentation de la densité de puissance de la cellule dans la Figure 4.58 a indiqué une consommation électrique plus élevée due à l'impact négatif de la dégradation. Les tendances de la densité de puissance de la cellule sont restées cohérentes indépendamment du taux de dégradation, tout comme les résultats du potentiel de la cellule.

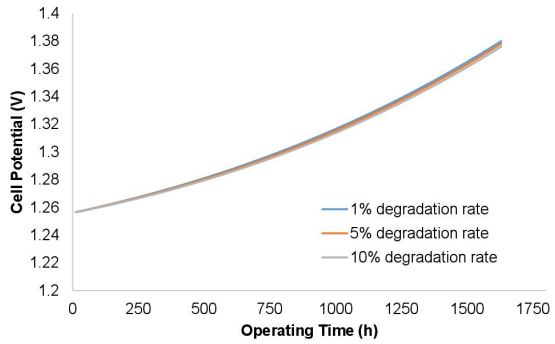

Figure 4.57: Potentiel de cellule (V) en fonction du temps à différents taux de dégradation dans les conditions expérimentales.

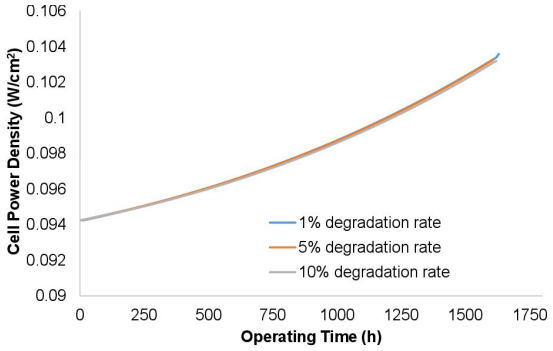

Figure 4.58: Densité de puissance de la cellule (W/cm^2) en fonction du temps pour différents taux de dégradation dans les conditions expérimentales.

Résultats dans les conditions de mise à l'échelle

Cette étude de cas a examiné le taux de dégradation lors de l'opération transitoire d'un module MCEC de 1 MW dans un procédé à l'échelle industrielle. Divers paramètres affectés par la dégradation ont été étudiés, notamment les débits de sortie de H_2 et CO, le courant de la cellule, la puissance, le potentiel et la température. La variation de surface active au fil du temps pour différents taux de dégradation était essentielle pour évaluer l'impact de la dégradation des électrodes sur les performances de la cellule. Le taux de dégradation détermine le taux de décroissance, comme le montre la Figure 4.59, ce qui affecte directement le courant appliqué (Figure 4.60).

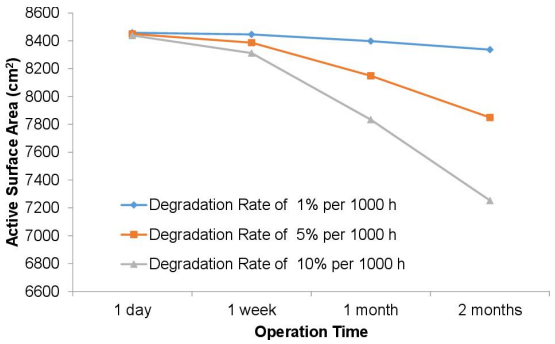

Figure 4.59: Surface active A (cm^2) en fonction du temps à différents taux de dégradation.

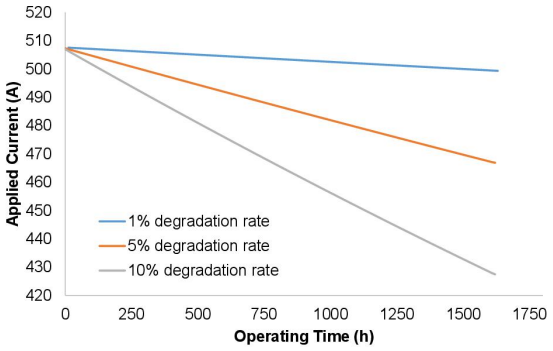

Figure 4.60: Courant de cellule (A) en fonction du temps à différents taux de dégradation.

L'analyse du potentiel de cellule (Figure 4.61) et de la densité de puissance (Figure 4.62) a révélé des tendances liées au taux de dégradation. À un taux de dégradation de 1%, le potentiel de cellule et la

densité de puissance augmentent avec le temps. Cependant, à des taux de dégradation de 5% et 10%, ils diminuent. Bien qu'ils finissent par augmenter après un certain temps, ils restent inférieurs à leur niveau initial. Cela pourrait être lié à l'impact significatif du taux de dégradation sur la pression partielle du gaz de synthèse, qui est directement liée au potentiel de Nernst.

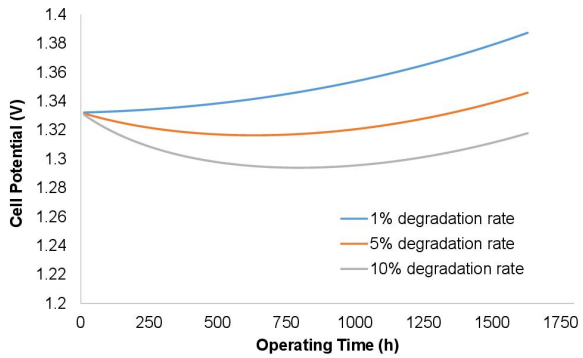

Figure 4.61: Potentiel de cellule (V) en fonction du temps à différents taux de dégradation dans les conditions de mise à l'échelle.

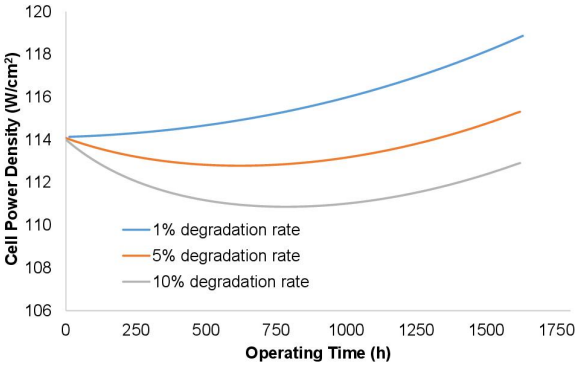

Figure 4.62: Densité de puissance de la cellule (W/cm^2) en fonction du temps pour différents taux de dégradation dans les conditions de mise à l'échelle.

La baisse du potentiel de la cellule et de la densité de puissance au fil du temps, en particulier en cas de forte dégradation, a été clarifiée en examinant la production de gaz de synthèse. Le taux de dégradation a influencé de manière significative les débits de sortie de H_2 et de CO au fil du temps, comme illustré dans la Figure 4.63 et la Figure 4.64. La diminution de la surface active a réduit la production d'hydrogène gazeux, et l'effet de la dégradation sur le débit de sortie de H_2 est devenu plus prononcé à des taux de dégradation plus élevés. Le débit de sortie de CO a également diminué au fil du temps, avec une baisse plus marquée à des taux de dégradation plus élevés. Les variations dans la composition de H_2 et de CO peuvent avoir un impact significatif sur la synthèse du méthane, qui nécessite des ratios spécifiques pour un rendement en CH_4 efficace et pour éviter le dépôt de carbone dû à des réactions indésirables.

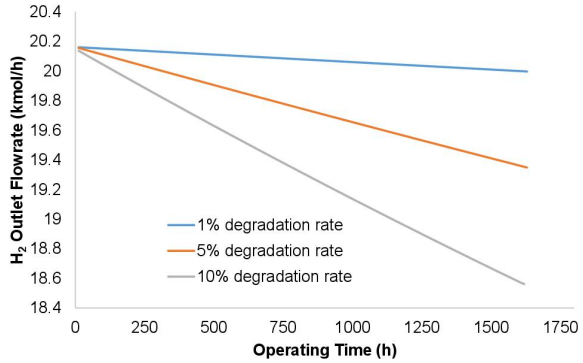

Figure 4.63: Débit de sortie de H_2 (kmol/h) en fonction du temps à différents taux de dégradation.

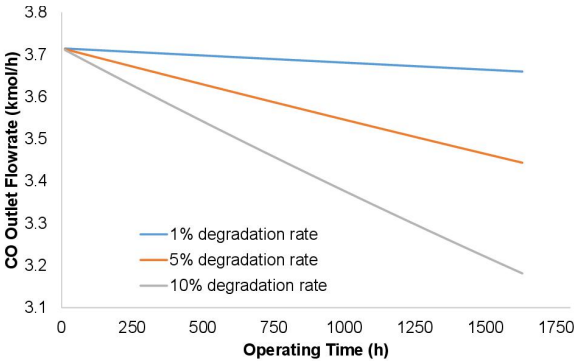

Figure 4.64: Débit de sortie du CO (kmol/h) en fonction du temps à différents taux de dégradation.

L'effet de la dégradation sur la température de la cellule au fil du temps a également été étudié. Les tendances de la température de sortie de la cellule, présentées dans la Figure 4.65, sont similaires

à celles observées pour le potentiel de la cellule et la densité de puissance, ce qui indique l'influence de la composition du gaz sur le bilan d'énergie du système. Ces résultats mettent en évidence l'impact significatif de la variation de la composition du gaz de synthèse sur le potentiel de la cellule en relation avec le taux de dégradation.

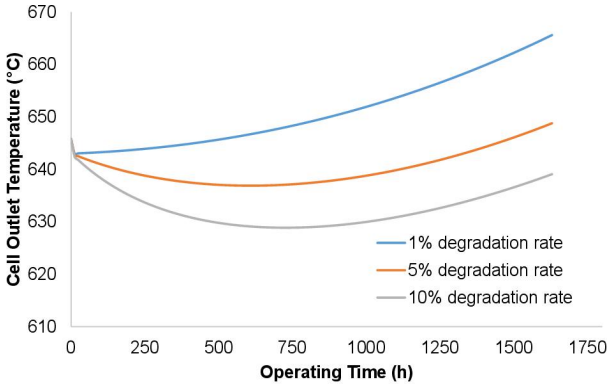

Figure 4.65: Température de sortie de la cellule en fonction du temps à différents taux de dégradation.

Toutefois, lorsque le courant total appliqué reste constant, la densité de courant augmente à mesure que la surface diminue. Bien que cela n'affecte pas le taux de production de gaz de synthèse en raison du courant constant, cela affecte de manière significative les performances de la cellule. Le potentiel de la cellule augmente en raison de l'augmentation de la densité de courant, directement liée à la réduction de la surface. Cela illustre clairement l'impact négatif de la dégradation sur les performances de la cellule. En outre, la dégradation de la cellule a des implications économiques pour le système. Elle réduit la durée de vie de la cellule, ce qui nécessite des remplacements plus fréquents. Cela entraîne également une augmentation des dépenses d'investissement, ce qui peut avoir une influence sur le coût-efficacité global du système.

Comparaison entre l'échelle expérimentale et l'échelle industrielle en termes d'impact sur la dégradation

La dégradation de la cellule est une préoccupation majeure pour les cellules à petite et grande échelle (échelle industrielle). Cette étude a examiné les paramètres critiques, tels que le potentiel et la température de la cellule, à un taux de dégradation de 1%. Les résultats du potentiel de la cellule et de la température de sortie pour les deux échelles augmentent avec le temps selon une pente similaire. Cependant, le potentiel et la température sont plus élevés à grande échelle par rapport à petite échelle aux mêmes conditions d'entrée. Ces résultats mettent en évidence l'importance accrue des problèmes de dégradation dans les opérations à grande échelle des cellules.

Réponse dynamique

Cette section examine la réponse dynamique d'un électrolyseur MCEC aux variations de la charge de puissance, du débit et du nombre de cellules en fonctionnement sur la puissance électrique, la tension, la composition du gaz de sortie et la température de la cellule.

Dans cette étude, les effets des variations de charge, impliquant des variations du courant d'entrée, ont été étudiés sur un électrolyseur MCEC. Il a été constaté une relation proportionnelle entre la charge et le potentiel de la cellule (Figure 4.13), la puissance de la cellule (Figure 4.14) et la température de sortie (Figure 4.15), indiquant qu'à mesure que la charge augmente, les paramètres de sortie de la cellule mentionnés ci-dessus augmentent, et vice versa. Les variations de charge ont un impact significatif sur l'état thermique de la cellule, provoquant des oscillations entre les états endothermique et exothermique. De plus, les débits d'entrée et de sortie des réactifs ont montré que les débits de sortie de H_2O et CO_2 diminuent lors de l'augmentation de la charge, tandis que les débits de H_2 et CO augmentent. La tendance inverse a été observée lorsque la charge diminue. Ces variations dans la production de gaz de synthèse peuvent affecter le rapport du gaz de synthèse pour la synthèse du méthane.

L'étude examine également les effets de la modification des débits d'entrée du gaz au niveau de la cathode et l'anode. Les résultats indiquent qu'une augmentation des débits d'entrée pour les deux électrodes entraîne une diminution du potentiel de la cellule et vice versa (Figure 4.18). Cependant, le potentiel de la cellule diminue avec une augmentation du débit d'entrée du gaz au niveau de la cathide et une diminution du débit d'entrée du mélange en oxygène et en CO_2 de l'anode. La même tendance est observée pour la puissance de la cellule (Figure 4.19) et la température de sortie (Figure 4.20). En effet, le débit d'entrée du gaz de la cathode a un impact plus significatif par rapport à celui de l'anode. Ces variations de débits affectent également la température de sortie de la cellule, qui diminue avec une augmentation du débit d'entrée du gaz de la cathode, et vice versa. Il est à noter que ces variations peuvent affecter les débits de sortie de H_2O, CO_2, H_2 et CO, car ces derniers sont consommés ou produits lors des réactions électrochimiques.

Le nombre de cellules dans la pile est un paramètre important qui affecte les performances globales de la pile. Un taux de désactivation de cellule de 0,1% par 1000 heures, équivalent à un dysfonctionnement de deux cellules, est retenu et analysé. Les résultats démontrent que lorsque le nombre de cellules diminue, à la fois le potentiel de la cellule et la puissance diminuent également (Figure 4.22 et Figure 4.23). Cette constatation peut s'expliquer par le fait que le potentiel de Nernst, influencé par les gaz, diminue avec la réduction du nombre de cellules. Les débits de sortie de H_2O, CO_2 (Figure 4.24) augmentent avec le dysfonctionnement des cellules, exprimé par une diminution du nombre de cellules en fonctionnement, tandis que les débits de sortie de H_2 et CO diminuent (Figure 4.25) lorsque le nombre de cellules en fonctionnement diminue. La diminution du nombre de cellules entraîne également une baisse de la température de sortie de la cellule (Figure 4.26), car le potentiel et la puissance de la cellule plus bas entraînent un effet de refroidissement. Ces analyses soulignent que moins de cellules en fonctionnement réduisent la production totale de H_2 et CO, ce qui entraîne une diminution du potentiel de la cellule et de sa puissance. Pour maintenir le même niveau de production avec des cellules défectueuses, le courant appliqué doit être augmenté pour améliorer la production, ce qui augmente le potentiel et la puissance de la cellule.

Démarrage à froid de l'électrolyseur MCEC

Le chauffage de la pile MCEC est similaire à celui du MCFC, deux scénarios de chauffage différents ont été élaborés. Le scénario A est présenté en détail dans le tableau 4.13, basé sur le brevet de chauffage de la pile MCFC [209]. Un autre scénario de chauffage a été appliqué par Zhou et al. (2006) [210], expliqué

dans le tableau 4.14. Les deux scénarios de chauffage proposés ont impliqué différentes étapes et durées de chauffage, de sorte qu'une analyse de la consommation d'énergie a été réalisée afin de déterminer la méthode de chauffage la plus économe en énergie. L'analyse énergétique a consisté à évaluer l'énergie consommée par l'empilement pour le chauffage et à compenser les pertes de chaleur pendant la période de maintien. Les pertes de chaleur se produisent en raison du transfert de chaleur entre l'empilement et l'environnement, qui est influencé par la différence de température.

Température (°C)	Temps (h)	Taux de chauffage (°C/h)
25 → 150	2	62
150 → 300	30	5
300 → HOLD	35	0
300 → 500	40	5
500 → 600	20	5
600→ 650	10	5
Total	137 h (≈ 5 jours)	

Table 4.13: Scénario (A) de chauffage de la MCFC [209].

Température (°C)	Temps (h)	Temps Moyen (h)
20→108	6-12	9
108→HOLD	6-12	9
108→210	32-42	37
210→HOLD	14-24	19
210→315	44-54	49
315→HOLD	25-35	29
315→375	32-42	37
375→HOLD	25-35	29
375→420	34-44	39
420→450	8-18	13
450→HOLD	2-6	4
450→530	12-20	16
530→600	7-13	10
600→650	4-9	6
Total	194 h (8 jours) - 289 h (12 jours)	

Table 4.14: Scénario (B) de chauffage de la MCFC [210].

Cependant, pour déterminer la quantité de transfert de chaleur, il faut connaître la géométrie de la pile. Le module MCFC présente deux géométries différentes : des collecteurs cylindriques et rectangulaires, chacun contenant quatre piles d'une capacité de 250 kW. Les deux géométries ont été évaluées en termes de consommation d'énergie pour le chauffage, en tenant compte des deux scénarios. Le collecteur du module cylindrique a un diamètre de 430 cm et une hauteur de 260 cm [143], avec une enveloppe externe en acier au carbone [143], et une enveloppe interne composée d'isolant en fibre céramique [212]. La consommation d'énergie a été évaluée pour les Scénarios de chauffage A et B avec deux épaisseurs d'isolation différentes (enveloppe interne), comme présenté dans la Figure 4.66. Le Scénario A est resté le plus économe en énergie, tandis que le Scénario B consommait 75% d'énergie de plus que le Scénario A lorsque l'épaisseur de l'isolation est de 25 mm, et 54% de plus lorsque l'épaisseur est de 50 mm.

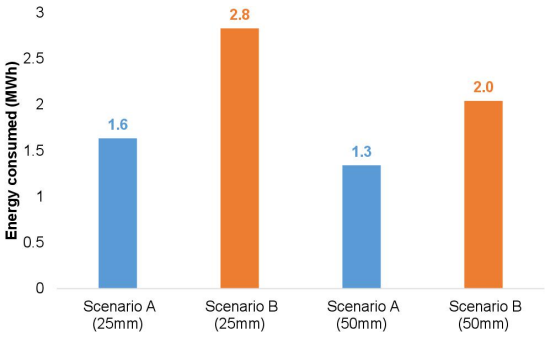

Figure 4.66: Consommation d'énergie lors du chauffage du module cylindrique du MCEC.

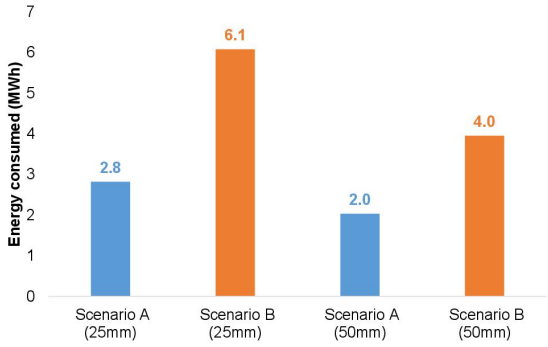

Figure 4.67: Consommation d'énergie lors du chauffage du module rectangulaire du MCEC.

Le collecteur rectangulaire a des dimensions de 6 m de longueur, 4 m de largeur et de hauteur [211], et la consommation d'énergie pour les procédés de chauffage du module rectangulaire (Figure 4.67) est plus élevée que celle du module cylindrique. Par conséquent, la forme cylindrique de l'enceinte du module s'est révélée plus adaptée pour minimiser les pertes de chaleur et la consommation d'énergie.

Modélisation dynamique de l'unité de méthanation

Cette section est dédiée à la modélisation des phénomènes dynamiques des réacteurs de méthanation à lit fixe. L'objectif principal est d'identifier le comportement du réacteur dans des conditions transitoires. Le modèle dynamique a été développé en prenant en compte la cinétique des réactions, et la procédure de démarrage à froid a été évaluée en termes de consommation d'énergie et de temps.

Développement du modèle dynamique de l'unité de méthanation

Les réactions impliquées dans le réacteur de méthanation sont la méthanation du CO_2, la réaction inverse du gaz à l'eau (RWGS) et la méthanation du CO. Le modèle dynamique utilisé dans cette étude repose sur la loi cinétique développée par Champon et al. (2019) [218] pour un catalyseur commercial dans un réacteur à lit fixe. Les expressions cinétiques pour ces réactions sont basées sur la formulation semi-empirique LHHW (Langmuir-Hinshelwood-Hougen-Watson) et sont intégrées dans Aspen Plus pour représenter les taux de conversion du CO et du CO_2, et sont représentées par les équations 4.24, 4.25 et 4.26.

$$r_{CO_2,\,meth} = \frac{k_{CO_2,\,meth} K_{H_2} K_{CO_2} p_{H_2} p_{CO_2} \left(1 - \frac{p_{CH_4} p_{H_2O}^2}{p_{H_2}^4 p_{CO_2} K_{eq,\,CO_2,\,meth}}\right)}{(1 + K_{CO_2} p_{CO_2} + K_{H_2} p_{H_2} + K_{H_2O} p_{H_2O} + K_{CO} p_{CO})^2} \tag{4.24}$$

$$r_{RWGS} = \frac{k_{RWGS} K_{CO_2} p_{CO_2} \left(1 - \frac{p_{CO} p_{H_2O}}{p_{H_2} p_{CO_2} K_{eq,\,RWGS}}\right)}{(1 + K_{CO_2} p_{CO_2} + K_{H_2} p_{H_2} + K_{H_2O} p_{H_2O} + K_{CO} p_{CO})} \tag{4.25}$$

$$r_{CO,\,meth} = \frac{k_{CO,\,meth} K_{H_2} K_{CO} p_{H_2} p_{CO} \left(1 - \frac{p_{CH_4} p_{H_2O}}{p_{H_2} p_{CO_2} K_{eq,\,CO,\,meth}}\right)}{(1 + K_{CO_2} p_{CO_2} + K_{H_2} p_{H_2} + K_{H_2O} p_{H_2O} + K_{CO} p_{CO})^2} \tag{4.26}$$

Validation du modèle

Le réacteur de méthanation a été modélisé en tant que réacteur à écoulement piston « *Plug Flow Reactor - PFR* » en utilisant Aspen Plus. Le modèle a supposé un transfert de masse et de chaleur uniforme dans la direction axiale, le simplifiant ainsi à une dimension. Les expressions cinétiques des réactions ont été implémentées et validées à partir de données industrielles présentées dans [219]. Celles-ci comprenaient la conception du réacteur et les spécifications d'alimentation en entrée. La simulation du procédé de méthanation avec ces données a produit des résultats correspondant aux données industrielles, confirmant la validité des cinétiques pour les trois réactions impliquées, comme présentées dans le tableau 4.9.

Espèces	Débit (kmol/h)	
	Simulation	Industrielle [219]
CO	0	0
CO_2	$2{,}54\times10^{-8}$	0
H_2	4111,6	4111,5
CH_4	50,0	50,1
H_2O	85,3	85,3
Inerte	16,6	16,6

Table 4.15: Résultats de la simulation et données industrielles du flux de sortie du réacteur.

Les expressions cinétiques de la méthanation ont été validées et appliquées à nos conditions de procédé. Pour la conception du réacteur, l'étude de Giglio et al. (2018) [205] a été utilisée pour déterminer les dimensions du réacteur. Pour prévenir les phénomènes de canaux dans le lit catalytique et réguler la température maximale, le rapport entre le diamètre du tube contenant le lit fixe et la particule de catalyseur a été supposé être d'au moins 10, comme recommandé par Giglio et al. (2018) [205]. La conception du réacteur comprend 15 tubes de 1,35 m de long et 60 mm de diamètre [205]. La masse totale de catalyseur m_c dans les tubes est de 39,9 kg [205], et la densité massique du catalyseur (ρ_c) est de 1270 kg/m^3 [203]. La fraction de vide du lit solide (ε) requise pour la simulation est déterminée en utilisant l'équation 4.30. Ainsi, avec les paramètres donnés, une fraction de vide du lit de 0,45 a été obtenue.

$$m_c = \rho_c.V_r.(1-\varepsilon) \tag{4.30}$$

Les paramètres de conception du réacteur ont été intégrés dans la simulation Aspen Plus. Au démarrage, l'alimentation en gaz de synthèse du réacteur est réalisé à 300°C et 20 bars. Elle est composée de 74,22% H_2, 24,04% CO, 0,89% CO_2 et 0,84% H_2O. Le temps de séjour, qui représente la durée totale pendant laquelle les gaz restent dans le réacteur, est un paramètre essentiel à déterminer. Il est calculé en divisant le volume du réacteur par le débit de gaz. La Figure 4.68 illustre l'augmentation du temps de séjour à mesure que les gaz progressent dans le réacteur. Un temps de séjour d'environ 0,0015 h est nécessaire pour atteindre une conversion de 97%. La composition molaire des gaz de sortie le long de la longueur du réacteur est donnée dans la Figure 4.69, la production de méthane augmente significativement dans la section initiale du réacteur, suivie d'une augmentation progressive le long de la longueur jusqu'à ce qu'elle se stabilise vers la fin du réacteur.

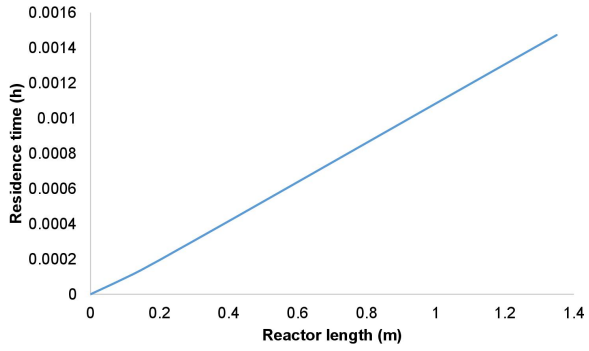

Figure 4.68: Le temps de séjour en fonction de la longueur du réacteur.

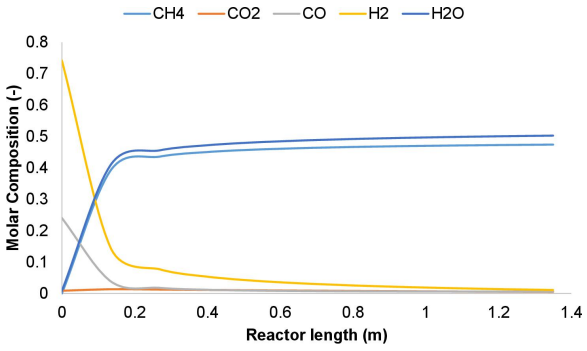

Figure 4.69: Les compositions des gaz de sortie en fonction de la longueur du réacteur.

En conclusion, la conception du réacteur a permis une conversion de 97% des réactifs, générant un produit de méthane avec une composition de 95,36% de CH_4, 1% de CO_2, 1,26% de CO, 2,2% de H_2, et 0,18% de H_2O. L'indice de Wobbe du méthane produit est de 51,52 MJ/m^3. Le débit de méthane atteint 53,389 kg/h, équivalent à 1,28 tonne par jour. En tenant compte de la cinétique de la réaction, la qualité du méthane répond de manière encore plus efficace aux exigences du réseau de gaz naturel. Cependant, la réponse dynamique du réacteur de méthanation est liée au fonctionnement de l'électrolyseur, qui est affecté par les variations de charge électrique. Cet aspect est abordé dans la section suivante qui étudie le couplage du système P2G avec une source d'énergie renouvelable intermittente.

Couplage du système de Power-to-Gas avec l'énergie renouvelable

Cette section examine la faisabilité de connecter le système de Power-to-SNG basé sur l'électrolyseur MCEC à une source d'énergie renouvelable variable (VRES), comme l'énergie éolienne et solaire. Pour cela, des données fiables sur la production d'énergie VRES ont été nécessaires, donc des parcs éoliens ou solaires réels en France ont été considérés. Le logiciel System Advisor Modeler (SAM), développé par le National Renewable Energy Laboratory (NREL) aux États-Unis [222], a été utilisé pour obtenir les données. Celles-ci couvrent deux mois : février pour représenter la saison hivernale et août pour représenter la saison estivale.

Énergie éolienne

Pour la source éolienne, une ferme située à Saint-Martin-de-Crau dans la région Provence-Alpes-Côte d'Azur (43,623, 4,765), a été choisie. Elle comprend neuf éoliennes Enercon E48/800 d'une puissance nominale de 800 kW, soit une puissance totale de 7,2 MW [224]. Après avoir collecté les données nécessaires, la connexion entre les sources d'énergie renouvelable et le procédé de Power-to-Gas a été explorée. L'électrolyseur nécessite un préchauffage progressif d'environ cinq jours qui consomme beaucoup d'énergie. Pour éviter de mettre l'électrolyseur en marche et à l'arrêt, un mode veille peut être utilisé, mais il nécessite une source de chauffage externe pour maintenir la température de fonctionnement et consomme de l'énergie supplémentaire. Cette section étudie le stockage saisonnier à l'aide de l'énergie éolienne, en se concentrant sur deux questions importantes :

- Question 1 : Quelle est la configuration optimale du système d'électrolyseur modulaire à mettre en œuvre, compte tenu de la production d'un parc éolien situé dans le sud de la France ?
- Question 2 : Comment l'électrolyseur MCEC réagit-il à l'alimentation électrique intermittente en ce qui concerne la production de gaz de synthèse et son impact sur le procédé de méthanation pour la synthèse du méthane et le rendement du procédé ?

Fonctionnement à puissance nominale avec appoint électrique

Une puissance de sortie fixe de 1 MW a été retenue pour chaque module, et un appoint de l'alimentation électrique externe a été utilisé lorsque la production d'énergie éolienne était insuffisante. Le stockage d'énergie était prévu pendant les périodes de forte production, tandis que l'électrolyseur fonctionnait en mode veille pendant les périodes de faible production. Un code Matlab a été développé pour identifier ces périodes de forte production, et les résultats, présentés dans le tableau 4.11, ont montré

que la production de méthane augmentait significativement d'un à deux modules, mais cette augmentation devenait négligeable pour plus de deux modules. Par conséquent, le nombre optimal de modules en termes de performance et d'efficacité a été déterminé entre un et deux. Une analyse économique a été réalisée (voir chapitre 5) pour déterminer la meilleure configuration modulaire entre un et deux modules en fonction du coût final de production de méthane. Les résultats ont montré que le coût de production de méthane pour un module était de 13,032 €/kg, tandis que pour deux modules, il augmentait à 14,074 €/kg. Bien que l'ajout d'un deuxième module augmente significativement la production de méthane, le coût de l'investissement l'emporte sur les avantages. Par conséquent, un seul module d'1 MW est le choix optimal pour le couplage avec des sources d'énergie renouvelable variables.

Nombre de modules	Nombre total d'heures de fonctionnement par an	Nombre total d'heures par an en mode veille	Énergie totale fournie par le réseau [MWh]	Énergie totale fournie par l'éolienne [MWh]	Production annuelle totale de méthane [kg]
1	2034	6462	196,96	1837	109475,98
2	1926	6570	712	3139,95	207326,20
3	1284	7212	679,65	3172,35	207326,20
4	1104	7392	833,56	3582,44	237682,37
5	528	7968	153,07	2486,93	142092,72
6	318	8178	106,69	1801,31	102694,28

Table 4.16: Résultats obtenus en utilisant différents nombres de modules couplés à une source éolienne au cours de l'année.

Fonctionnement en mode dynamique (100% d'énergie éolienne)

Cette partie a étudié l'impact de la variabilité de l'énergie éolienne sur les performances du système. Les périodes de stockage ont été déterminées en utilisant un code Matlab et ajustées manuellement pour les cas avec des courts intervalles. Les données ont ensuite été intégrées dans le modèle Aspen Plus pour analyser le comportement dynamique du système. Une stratégie de contrôle, basée sur celle d'Olivier et al. (2017) [226], a été appliquée pour déterminer les paramètres opérationnels en tenant compte de la charge variable. La puissance électrique consommée par l'électrolyseur a été ajustée en fonction de la densité de courant (j [A/cm^2]) jusqu'à ce qu'elle corresponde à la puissance fournie par la source d'énergie éolienne, comme présenté dans la Figure 4.70.

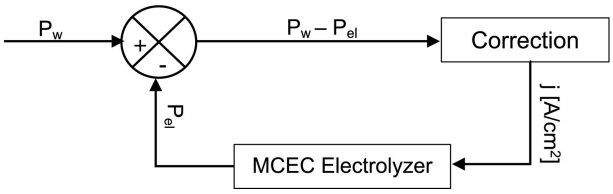

Figure 4.70: Stratégie de contrôle pour déterminer la valeur de la densité de courant de fonctionnement j, basée sur la puissance éolienne P_w et la puissance consommée par l'électrolyseur P_{el}.

D'abord, la production de méthane et le rendement du procédé ont été étudiés pour évaluer les performances globales. Ces paramètres suivent une tendance similaire à l'alimentation électrique, montrant l'impact direct de l'alimentation électrique sur le système. La relation entre le rendement du procédé et la puissance électrique, présentée dans la Figure 4.71a, montre une corrélation proportionnelle avec un rendement maximal de 68% en fonctionnement nominal. Une réduction de l'alimentation

électrique entraîne une diminution de la production de méthane et une baisse significative du rendement, car l'énergie requise pour le procédé ne diminue pas proportionnellement. De plus, à une puissance réduite, l'état de la cellule passe d'exothermique à endothermique (en dessous de 650 °C), comme illustré dans la Figure 4.71b, ce qui affecte davantage le rendement du procédé.

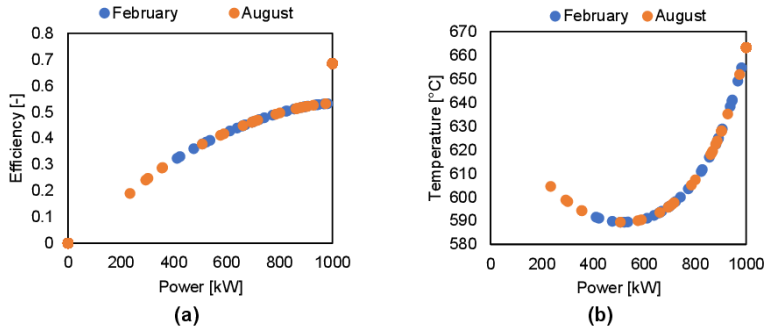

Figure 4.71: **(a)** Rendement du procédé et **(b)** température de sortie en fonction de la puissance fournie à l'électrolyseur.

Ensuite, les paramètres de production de gaz de synthèse et de substitut du gaz naturel (SNG), un mélange de méthane et d'autres gaz secondaires, ont été analysés pour assurer la qualité globale du procédé. La Figure 4.72a montre que la réduction de la charge entraîne une diminution de la teneur en H_2 et une augmentation de la teneur en CO_2, indiquant la présence de CO_2 non réagi dans l'électrolyseur. Cette situation pourrait affecter négativement la qualité du gaz de synthèse produit et la méthanation. De plus, des concentrations élevées de CO_2 et de CO dans le gaz de synthèse sont défavorables à l'électrolyse indépendante, nécessitant un procédé de purification.

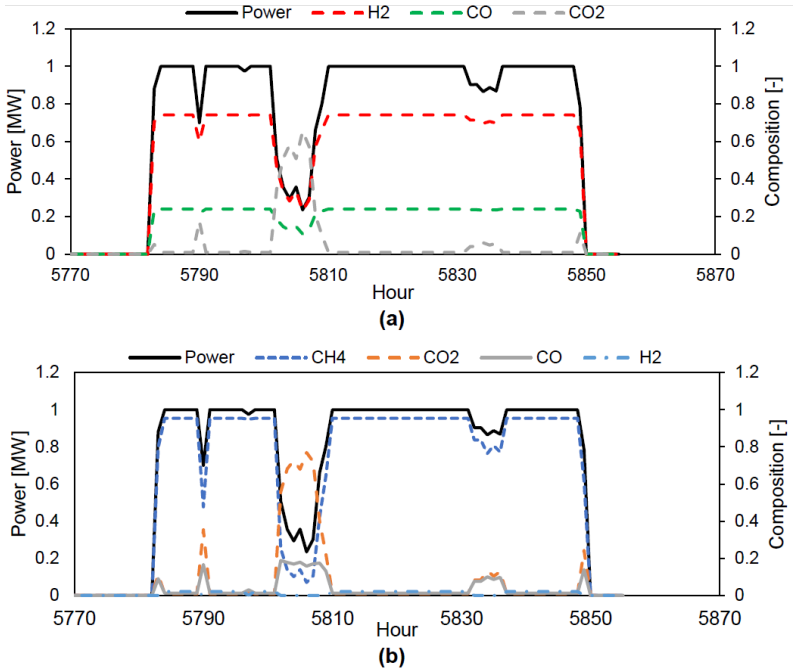

Figure 4.72: **(a)** Composition du gaz de synthèse et du SNG **(b)** pendant une période de forte variabilité (août).

En considérant le stockage du gaz pendant toute la durée du mois, la composition du gaz de sortie (SNG) du réacteur de méthanation peut être estimée. À l'aide d'un bilan de masse, la composition du SNG pour les périodes estivale et hivernale a été calculée (Figure 4.73). Malheureusement, les concentrations de CO_2 et de CO dépassent les limites acceptables pour l'injection dans le réseau de gaz. Par conséquent, le substitut de gaz naturel produit nécessite un procédé de purification, dont le coût réel ne peut pas être estimé.

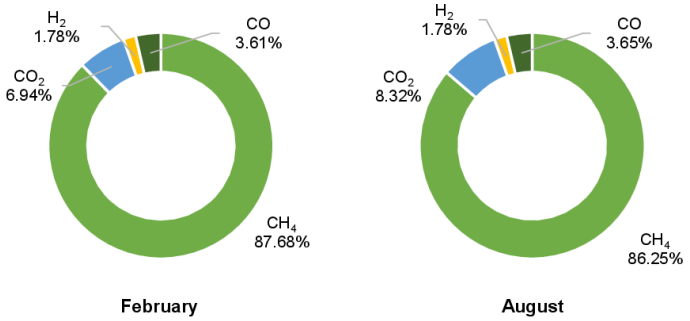

Figure 4.73: Composition finale du SNG le long de chaque mois.

Énergie solaire

La centrale solaire de Fabrègues, située dans le département de l'Hérault près de Montpellier, a été choisie comme source d'énergie solaire. Les hypothèses initiales pour estimer la production d'énergie ont été basées sur des panneaux solaires fixes orientés vers le sud avec un angle d'inclinaison correspondant à la latitude de la région, soit 43,532°[228]. Dans un premier temps, le résultat a donné une production d'énergie annuelle (AEP) de 2 GWh, mais sans prendre en compte les effets d'ombrage. Ensuite, un coefficient de dégradation de 8% [229] a été appliqué, ce qui a conduit à une nouvelle valeur de l'AEP de 1,56 GWh, en accord avec la valeur rapportée.

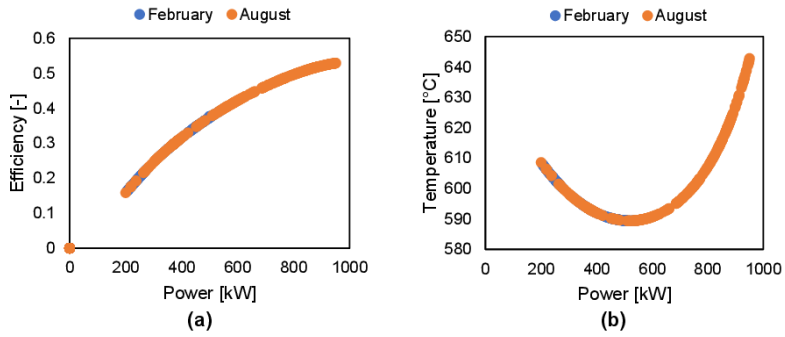

Figure 4.74: **(a)** Rendement du procédé et **(b)** température de sortie en fonction de la puissance fournie à l'électrolyseur.

L'étude s'est concentrée sur le fonctionnement en mode dynamique, analysant le fonctionnement dynamique d'un système Power-to-SNG utilisant l'énergie solaire. Les résultats ont montré que l'énergie solaire est plus efficace en été qu'en hiver. Pourtant, une production élevée de méthane et un rendement du procédé élevé ne sont réalisables que pendant les heures de pointe. Cela nécessite un bon contrôle de

l'électrolyseur pour répondre aux variations de charge. L'impact de l'énergie solaire sur le rendement du procédé est illustré dans la Figure 4.74a, où le rendement est supérieur à 50% pour une charge solaire entre 80% et 100% de la capacité nominale. De plus, le fonctionnement de l'électrolyseur avec une charge électrique variable est examiné dans la Figure 4.74b, montant que la cellule fonctionne en mode endothermique lorsque la charge électrique est inférieure à la charge nominale (1 MW), nécessitant un chauffage supplémentaire pour compenser la chaleur absorbée pendant l'électrolyse.

La qualité du gaz de synthèse et du SNG dans le système Power-to-SNG est cruciale. Le gaz de synthèse doit maintenir un rapport d'environ 3 pour une production de SNG de haute qualité, tandis que la composition du SNG doit répondre aux exigences pour une injection directe dans le réseau de gaz naturel. Cependant, comme le montre la Figure 4.75a, lorsque la puissance diminue, la qualité du SNG se détériore, avec des concentrations plus élevées de CO_2 et de CO dépassant les limites du réseau, fixées à 2,5% et 2% respectivement.

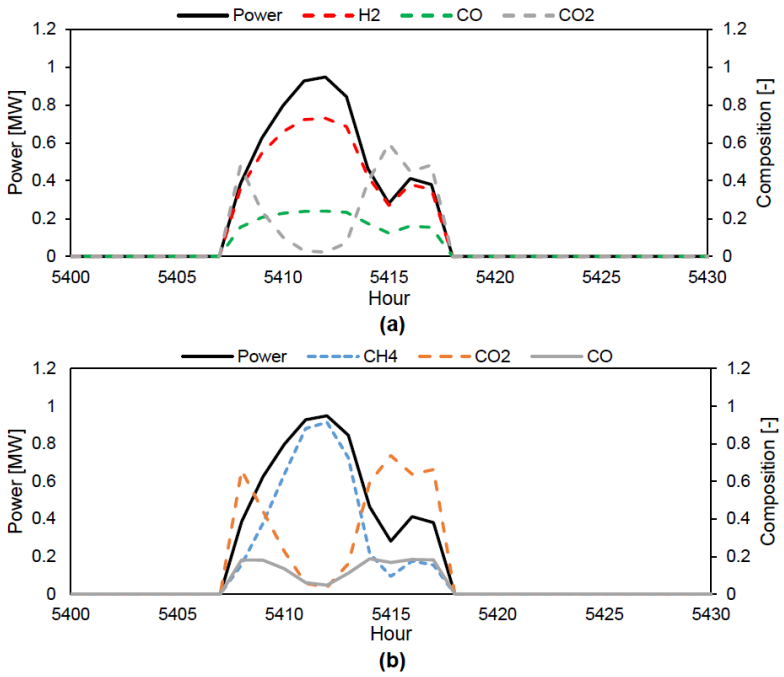

Figure 4.75: **(a)** Composition du gaz de synthèse et du SNG **(b)** pendant une période de forte variabilité (août).

Enfin, en supposant que le substitut de gaz naturel produit puisse être stocké avant l'injection dans le réseau, la composition du SNG a été analysée sur la période de février et août (Figure 4.76). Les résultats ont indiqué que le substitut de gaz naturel contenait une quantité importante de CO_2, dépassant la teneur en CH_4, ce qui nécessite une purification supplémentaire.

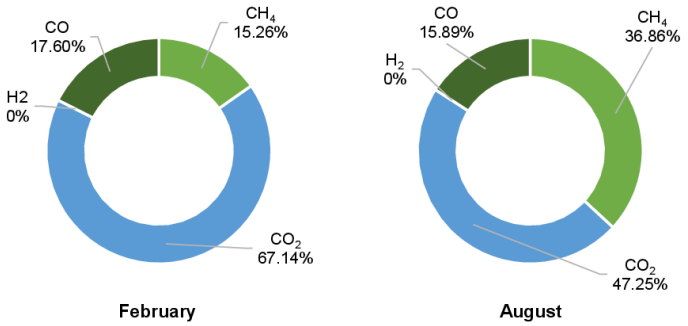

Figure 4.76: Composition finale du substitut de gaz naturel (SNG) le long de chaque mois.

Conclusion

Ce chapitre offre une analyse approfondie du comportement dynamique d'un système Power-to-SNG composé d'un électrolyseur à carbonates fondus (MCEC) et d'un réacteur de méthanation. Il est divisé en trois parties principales.

La première partie se concentre sur le fonctionnement dynamique de l'électrolyseur MCEC. Deux cas sont étudiés : la dégradation des électrodes et la réponse du MCEC aux variations inattendus des variables d'entrée. Les résultats montrent que la dégradation des électrodes entraîne une diminution du potentiel de la cellule et de la puissance en raison de son impact sur la pression partielle du gaz de synthèse. Maintenir la même production de gaz de synthèse nécessite une augmentation du courant appliqué pour améliorer l'électrolyse. L'importance des problèmes de dégradation dans les cellules à grande échelle est soulignée. Le MCEC présente des variations proportionnelles de la puissance et de la tension de la cellule, de la composition du gaz de sortie en H_2 et CO, ainsi que de la température de sortie en réponse aux variations de la charge et du nombre de cellules. En revanche, il réagit de manière réversible aux variations du débit d'entrée du gaz. De plus, un procédé de chauffage de cinq jours avec un profil spécifique est identifié comme la procédure de démarrage à froid la plus économe en énergie.

La deuxième partie analyse le comportement dynamique du procédé de méthanation en fonctionnement transitoire. Conception d'un réacteur tubulaire refroidi à lit fixe atteint une conversion élevée des réactifs et produit du substitut du gaz naturel (SNG) avec une composition souhaitée conforme aux exigences du réseau de gaz naturel.

La dernière partie examine l'intégration du système Power-to-SNG avec des sources d'énergie renouvelable intermittentes. L'énergie solaire présente des fluctuations significatives de la production de méthane et du rendement du procédé pendant l'hiver, tandis que l'énergie éolienne démontre une plus grande cohérence. La source variable produit un gaz de synthèse à une phase intermédiaire avec une teneur élevée en CO_2 et CO lorsque la puissance fournie à l'électrolyseur est légèrement inférieure à la puissance nominale. Ce gaz, contenant une quantité élevée de CO_2 et CO, entre dans le réacteur de méthanation, générant un substitut de gaz naturel qui ne satisfait pas aux exigences minimales pour être injecté dans le réseau de gaz naturel. Ce comportement se produit uniquement pendant les périodes de faible puissance ; cependant, pour la totalité du gaz obtenu au cours des deux périodes hivernales et estivales, les teneurs en CO_2 et CO ne sont pas satisfaisantes, et sont de l'ordre de 8% pour le CO_2 et 4% pour le CO pour la source éolienne, et de l'ordre de 60% pour le CO_2 et 17% pour le CO pour la source

solaire. Maintenir les compositions de gaz de synthèse et de SNG souhaitées devient difficile en raison des fluctuations de puissance, ce qui nécessite une purification supplémentaire ou une dilution avec du gaz naturel. Les options proposées comprennent un système modulaire avec des stratégies de contrôle pour atténuer la variabilité, ou l'incorporation d'un procédé de purification dans le système lorsque la qualité du gaz souhaitée ne peut pas être atteinte.

Chapter 5

Economic Study

Objective

This chapter presents an economic assessment of the Power-to-SNG system based on a molten carbonate electrolyzer. The analysis aims to evaluate the selling price of methane produced under actual conditions. Additionally, a sensitivity analysis of the CAPEX and OPEX parameters is conducted to identify the factors that impact the selling price of methane. Based on the findings of this study, a best-case scenario is selected and investigated to determine its potential for the future. Lastly, a roadmap is developed to assess the cost evolution of the MCFC technology with increasing installation capacity over time.

Table of Contents

1 Literature Review

Implementing Power-to-Gas (P2G) technology encounters economic challenges that necessitate further research. Several studies have been conducted to address this issue, focusing on different technologies such as AEL, PEM, and SOEC. For example, Götz et al. (2015) [87] examined the technical and economic requirements of existing electrolysis and methanation technologies in the Power-to-Gas chain. Peters et al. (2019) [230] analyzed the techno-economic features of this system utilizing the three existing technologies and evaluated the ecological aspects of using methane as a transport fuel. Gorre et al. (2019) [231] evaluated the production costs of synthetic methane in 2030 and 2050 for a Power-to-Gas plant with intermediate hydrogen storage.

Additionally, Szima and Cormos (2021) [232] assessed the techno-economic aspects of synthetic methane production from renewable hydrogen obtained from various renewable resources and captured CO_2. More recently, Fambri et al. (2022) [233] analyzed the potential of Power-to-Gas technology using PEM electrolyzer at the distribution network level to optimize the utilization of the renewable energy sources and increase energy system flexibility. They also evaluated the economic potential by calculating the levelized cost of substitute natural gas (SNG) for cost scenarios in 2030 and 2050. All studies concluded that SNG produced from renewables is not yet competitive with conventional natural gas.

On the other hand, molten carbonate electrolyzers for Power-to-Gas systems have not yet been extensively researched in terms of their economic viability. This technology is still in the research and development phase, so studies have mainly focused on technical aspects rather than economic considerations. However, the commercial implementation of this carbon-neutral process depends on its economic competitiveness. Therefore, this study aims to evaluate the economic feasibility of using molten carbonate electrolyzers for Power-to-SNG systems, identify factors that impact the selling price of methane, and provide insight into how this technology can become competitive with conventional and other SNG production methods.

2 Cost Assumption and Calculation

After the Power-to-SNG system simulation was completed, an economic assessment was conducted to evaluate the capital investment and operating expenses of the process plant. These expenses were combined using Eq. 5.1, as stated in [4], to estimate the actualized cost per unit of methane.

$$CTA_i = \frac{\sum_{t=0}^{T}(C_{invest_t} + C_{electrolyzer_t} + C_{energy_t} + C_{feedstock_t} + C_{replace_t} + C_{maintenance_t}) \times (1+\tau)^{-t}}{\sum[m_{i_t} \times (1+\tau)^{-t}]} \tag{5.1}$$

where:
CTA_i = Actualized total cost (€/kg)
C_{invest} = Investment cost excluding electrolyzer (€)
$C_{electrolyser}$ = Investment cost of electrolyzer (€)
C_{energy} = operating cost related to energy consumption (€)
$C_{feedstock}$ = Annual feedstock cost (water, CO_2) (€)
$C_{replace}$ = Investment cost of replacement of equipment and electrolyzer (€)
$C_{maintenance}$ = Maintenance expenses, excluding replacement expenses, as a % of energy costs (€)
m_i = Annual production of component i (methane) (kg)
t = Year in which expenses are executed
T = Lifespan of production unit (years)
τ = Actualisation rate

The assessment estimated the capital investment cost (CAPEX) by considering the cost of the cell and all necessary balance of plant (BoP) equipment costs. It also calculated a replacement cost based on the lifespan of each piece of equipment, the operating hours, and the assumed 15-year lifetime of the plant. Maintenance cost was assumed to be 3% of operating costs, and the actualization rate is 10%. The operating cost (OPEX) was calculated per kg of feedstock required and per kW of electrical power consumed. The costs of the principal equipment were collected from literature data and industrial sources for this analysis. It is important to note that the investment cost, the lifetime of BoP equipment, water cost, maintenance cost, and actualization rate were kept constant throughout the study.

2.1 Electrolyzer

The investment cost of the molten carbonate electrolyzer (MCEC) was assumed to be the same as the molten carbonate fuel cell (MCFC) because they use the same materials and catalyst. According to data from 2010, the installed cost for a MCFC unit was about 4,200 $/kW, broken down as approximately 2,400 $/kW for the fuel cell module, 1,100 $/kW for the balance of plant, and 700 $/kW for conditioning, installation, and commissioning [234]. From this data, the installed cost of MCFC was estimated to be 3,100 $/kW$_{2010}$ based on the cost of the fuel cell module and the cost of commissioning and installation. This installed cost was updated to 2022 in €/kW by applying the inflation rate and performing the dollar-euro conversion. As a result, the updated installed cost for MCEC was chosen to be 3,500 €/kW$_{2022}$, assuming a lifetime of 10,000 h.

2.2 Other Equipment

The investment cost and the lifespan of the balance of plant equipment are summarized in Table 5.1.

Equipment	Cost	Lifespan(h)
Condensers/Evaporators	12 €/kW	100,000
Small Heat Exchangers	12 €/kW	100,000
Large Heat Exchangers	400 €/kW	100,000
Condenser and Evaporator HX	16.5 €/kW	100,000
Heater	600 €/kW	100,000
Cooler	400 €/kW	100,000
Fan	2,000 €	20,000
Compressor	400 €/kW	50,000
Pump	391 €	40,000
Valve	10,000 €	50,000
Methanator Reactor	100,000 €	80,000
Separator	2,440 €	100,000

Table 5.1: Investment costs and the lifespans of the main components.

2.3 Feedstocks and Utilities

The MCEC system requires water and CO_2 as feedstocks. The cost of water was fixed at 3 €/t [4]. Since the simulation did not include a water treatment plant, it was assumed that half of the water was used for the process while the remaining half was treated as wastewater. Consequently, twice the quantity of water required for the process was considered in the economic assessment. On the other hand, the cost of CO_2 can fluctuate based on the capture technology used. For instance, if a carbon capture unit was integrated with the Power-to-SNG unit, the cost of CO_2 would be zero, as it would be directly supplied from the capture unit.

As for the utilities, the operation of the system necessitates electrical power. The cost of electricity is linked to the levelized cost of renewable energy since the Power-to-Gas system stores excess renewable energy. However, for this study, the cost of electricity was based on the French grid electricity cost of 140 €/MWh for 2022, which has low carbon emissions. It is important to acknowledge that the cost of electricity can vary depending on the source of electricity and the country of installation. Additionally, the isothermal methanation reactor requires cooling water, and its cost was assumed to be 30 €/MWh [4].

3 Economic Evaluation of the Power-to-SNG System

An economic assessment of the Power-to-SNG system was conducted, focusing on installing the system units and assuming the purchase of CO_2 feedstock from suppliers. The economic analysis started by evaluating the process under current conditions. For this evaluation, the cost and lifespan of the cell stack were fixed at 3,500 €/kW and 10,000 h, respectively. The cost of CO_2 feedstock was assumed to be 50 €/t [235]. Furthermore, the electricity cost was set at 140 €/MWh.

Based on the pricing database, the Power-to-SNG system provides a methane price of 13.851 €/kg (1,057 €/MWh), assuming 8,000 hours of operation per year. However, this value is significantly higher than the actual market price of natural gas, even after the gas shortage crisis provoked by the Ukrainian war. In 2022, the market prices for household applications were 126 €/MWh in France and 340 €/MWh in the Netherlands [236]. The cost breakdown scenario presented in Figure 5.1 reveals that approximately

60% of the total cost is attributed to CAPEX, including the initial investment and replacement costs. The high replacement cost is primarily due to the short lifetime of the cell and its high capital cost. These findings provide valuable insights into the parameters that need attention to reduce costs.

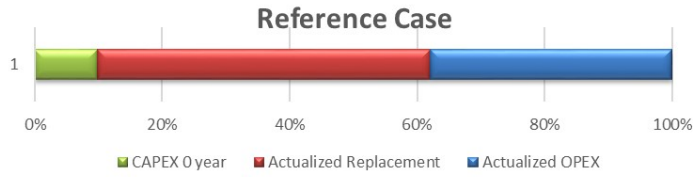

Figure 5.1: Methane cost breakdown based on CAPEX, OPEX, and replacement cost of equipment.

It is worth emphasizing that achieving cost reduction in the Power-to-SNG system is crucial for its widespread adoption and commercial viability. Therefore, efforts should prioritize reducing investment costs, particularly those associated with the MCEC electrolyzer cost, since it constitutes a significant proportion of the overall cost. Additionally, exploring other areas, such as enhancing system efficiency and reducing operating costs, would be beneficial.

The primary objective of the Power-to-Gas system is to address the challenge of renewable energy storage. Nonetheless, due to the intermittent nature of the energy source, the plant cannot operate for 8,000 hours annually. As a result, a study was conducted to investigate how the plant's operating hours impact the methane price produced. The trend of the actualized methane price with the plant's operating hours is presented in Figure 5.2. The methane cost is found to be extremely high for low operating hours below 500 h, gradually dropping to around 1,500 €/MWh within the range of 500-1,000 operating hours. After 1,000 hours, an increase in operating hours leads to a progressive decline in the methane price, reaching its lowest point at 6,600 h. This breakeven point is linked to the replacement cost of the cell, which varies with the operating hours.

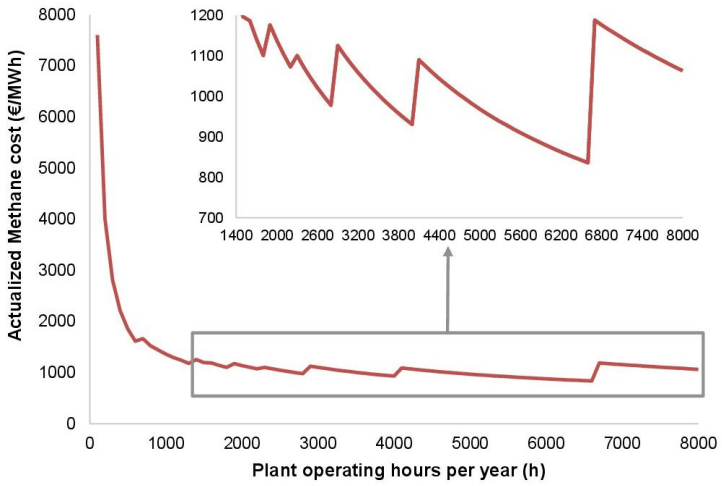

Figure 5.2: Methane price variation with the plant's yearly operation hours.

By reducing the operating hours of the Power-to-SNG plant from 8,000 to 6,600 hours, the total CAPEX has decreased from 60% to 50%, resulting in a drop in the methane price from 13.851 €/kg (1,057 €/MWh) to 10.95 €/kg (836 €/MWh). This decrease in the methane price implies that operating

the plant at lower hours can induce cost savings. Hence, it is crucial to consider the operating hours when designing and operating Power-to-Gas systems.

It is worth noting that the study does not account for the potential profit that can be obtained by valorizing the oxygen produced by the anode side of the electrolyzer when separated from carbon dioxide. Incorporating this aspect into the analysis can further decrease the methane price.

4 Economic Sensitivity Analysis

This study aims to enhance the understanding of the cost drivers and identify potential areas for cost reduction in the Power-to-Gas system. The economic analysis focused on two key costs: capital investment (CAPEX) and operating cost (OPEX). The reference case demonstrated that CAPEX has a greater influence on the overall cost than OPEX. Thus, this study investigated four parameters that impact the CAPEX and OPEX within an acceptable range. These parameters include the lifetime and cost of the electrolyzer (CAPEX), the cost of captured CO_2, and the expenses associated with electricity (OPEX). The study evaluated the methane cost while varying these parameters, and a summary of all the studied parameters along with their respective margins is presented in Figure 5.3.

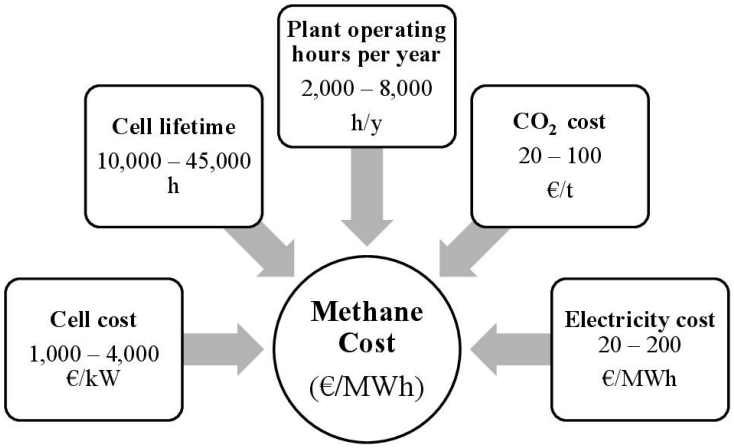

Figure 5.3: Schematic representation of the study's margin of the different sensitivity analysis parameters.

4.1 Impact of Sensitivity Parameters on the Production Cost of Synthetic Methane

The sensitivity analysis was conducted based on the assumption that the plant operates for 6,600 hours per year. Firstly, the impact of the cell cost and lifetime, corresponding to the CAPEX, was examined. Secondly, the CO_2 cost variation was studied with the variable CAPEX. In this category, the cost of the CO_2 is varied while keeping the electricity cost fixed at its minimum and maximum values. Finally, the electricity cost was varied with the CAPEX parameters while the CO_2 is fixed at its minimum and maximum values.

4.1.1 Cell Cost and Lifetime

The impact of varying the CAPEX parameters, specifically the cell cost and lifetime, is shown in Figure 5.4, with cell cost ranging from 1,000 €/kW to 4,000 €/kW and lifetime ranging from 10,000 h to 45,000 h. It

can be observed that as the cell cost decreases, the methane production cost also decreases since the cell contributes to the larger share of the plant's CAPEX.

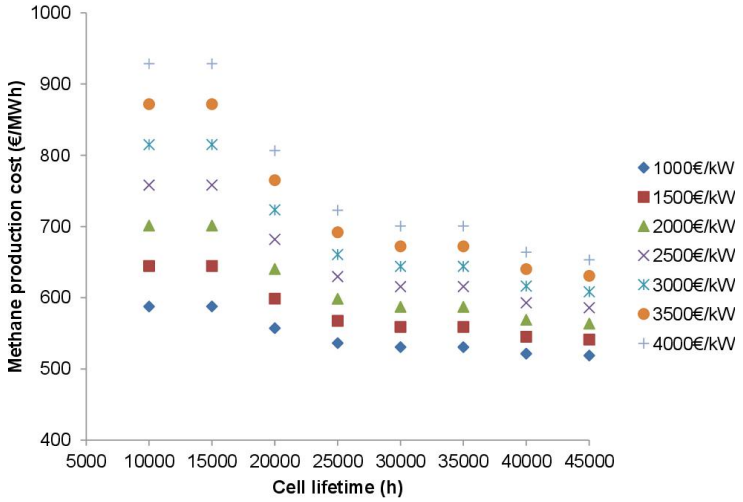

Figure 5.4: Impact of cell lifetime (h) and cost (€/kW) on the final methane cost (€/MWh).

On the contrary, the methane cost decreases with the enhancement in the cell's lifetime. However, no reduction in the methane cost is observed at specific lifetimes since the cell's lifetime is influenced by the frequency of periodic replacements occurring throughout the plant's lifetime. For example, improving the cell's lifetime time from 10,000 h to 15,000 h does not affect the methane cost since, for both lifetimes, the cell requires replacement every two years.

Based on the findings, the impact of the OPEX parameters, namely CO_2 and electricity costs, was evaluated while considering cell cost and lifetime variations. However, for the cell lifetime, only two values were selected: a low value of 10,000 h and a high value of 40,000 h. The high lifetime of 40,000 h is particularly important because previous studies have demonstrated that the MCFC can achieve this lifetime [237], making it essential to assess the economic implications of this extended lifespan.

4.1.2 CO_2 Cost

The study focused on varying the CO_2 cost (€/t) while keeping the electricity cost fixed. First, the analysis was conducted at the maximum electricity cost of 140 €/MWh, examining the impact of CO_2 feed cost and cell capital cost on the methane cost for two different cell lifetimes, as depicted in Figure 5.5. The x-axis of the figure represents the variation in CO_2 cost, while the colored curves represent the cell cost. At a cell lifetime of 10,000 h (Figure 5.5a), it was observed that the methane cost increases with the increase in the CO_2 cost, regardless of the cell cost. Besides, increasing the cell cost by 500 €/kW increased the methane cost by approximately 100 €/MWh. The lowest methane cost achieved under these conditions was 450 €/MWh, obtained at a CO_2 cost of 20 €/t and a cell cost of 1,000 €/kW. Nevertheless, at a cell lifetime of 40,000 h, the methane cost further decreased to 350 €/MWh under the same condition. To achieve a methane cost of 450 €/MWh at this lifetime, various combinations of CO_2 cost and cell cost were possible. For example, a CO_2 cost of 20 €/t and a cell cost of 4,000 €/kW, or a CO_2 cost of 30 €/t and a cell cost of 3,000 €/kW, or a CO_2 cost of 40 €/t and a cell cost of 2,500 €/kW, or a CO_2 cost of 50 €/t and a cell cost of 1,000 €/kW.

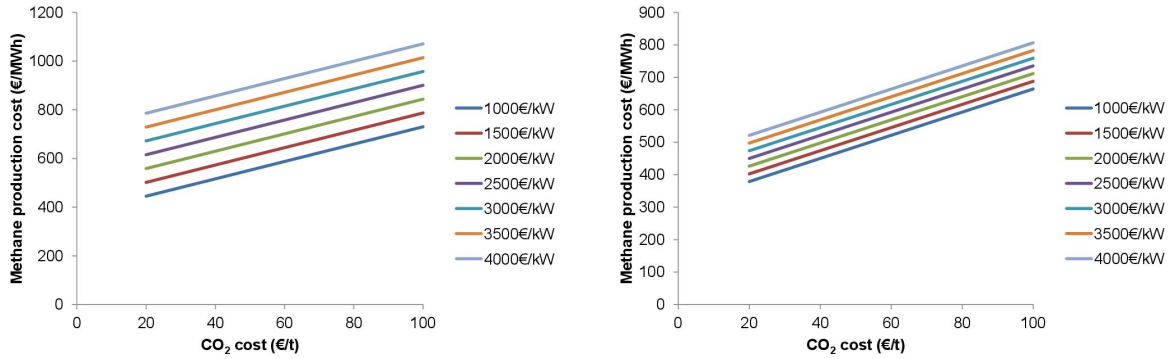

(a) (b)

Figure 5.5: Impact of CO_2 feed cost (€/t) and the cell capital cost (€/kW) on the final methane cost (€/MWh) at a fixed maximum electricity cost of 140 €/MWh, and two different cell lifetimes: 10,000 h **(a)**, and 40,000 h **(b)**.

Upon comparing the two figures representing different lifetimes, it becomes evident that the curves for a high cell lifetime of 40,000 h are remarkably close. This suggests that the cell cost has a negligible influence on the methane cost when the cell lifetime is high. This finding aligns with the fact that a longer lifetime implies fewer replacements and, thus, a minimal impact on the cell cost. For instance, assuming a plant lifetime of 15 years, a cell lifetime of 40,000 h with an annual operation of 6,600 h results in two cell replacements (every five years) within the 15-year plant lifetime. On the other hand, a cell lifetime of 10,000 h necessitates approximately one cell replacement per year, totaling 14 replacements throughout the plant's lifetime. Furthermore, beyond reaching 40,000 h, any additional improvement in the cell's lifetime has an insignificant effect on the methane selling price when the plant's lifetime is 15 years. However, it does slightly impact the methane cost for plant lifetimes exceeding 15 years. Therefore, based on the approach taken in this study, it can be deduced that achieving a cell lifetime of 40,000 h is crucial to attain a competitive cost for substitute natural gas.

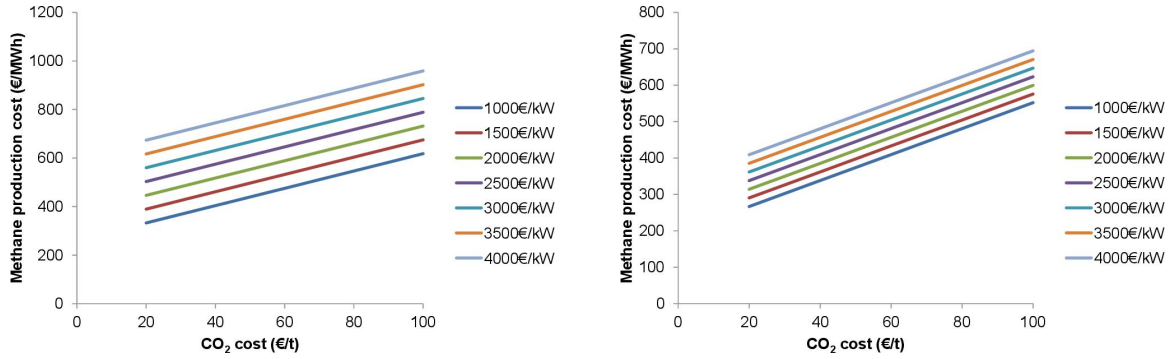

(a) (b)

Figure 5.6: Impact of CO_2 feed cost (€/t) and the cell capital cost (€/kW) on the final methane cost (€/MWh) at a fixed minimum electricity cost of 70 €/MWh, and two different cell lifetimes: 10,000 h **(a)**, and 40,000 h **(b)**.

On the other hand, the impact of the CO_2 cost was also examined at a fixed minimum value of 70 €/MWh. The results of this study are presented in Figure 5.6. Compared to the maximum value

case, the methane cost is reduced by 100 €/MWh, regardless of the cell cost, cell lifetime, and CO_2 cost. Consequently, a methane cost below 350 €/MWh can be achieved. For instance, at a lifetime of 10,000 h (Figure 5.6a), a methane cost of 350 €/MWh is obtained with a low CO_2 cost of 20 €/t and a cell cost of 1,000 €/kW. In contrast, at a lifetime of 40,000 h (Figure 5.6b), a methane cost of 350 €/MWh can be attained with a cell cost of 3,000 €/kW and a low CO_2 cost of 20 €/t, or with a cell cost of 1,500 €/kW and a CO_2 cost of 40 €/t.

The analysis conducted revealed that when the electricity cost is high, reaching 140 €/MWh, the methane price can only be reduced to 350 €/MWh if the CO_2 cost is low (20 €/t) and the cell cost is 1,000 €/kW, along with a long cell lifetime of 40,000 h. However, a lower electricity cost of 70 €/MWh could lead to a methane cost of 300 €/MWh, which is competitive with the conventional natural gas market price, under two conditions. The first condition is a cell lifetime of 10,000 h with a low cell cost of 1,000 €/kW and a CO_2 cost of 20 €/t. The second condition is a cell lifetime of 40,000 h with a cell cost ranging from 1,000 to 2,000 €/kW and a CO_2 cost ranging from 20 to 40 €/t.

4.1.3 Electricity Cost

This study focuses on the variation of electricity cost while maintaining a fixed maximum CO_2 cost of 100 €/t. The impact of electricity and cell costs on methane production costs at two different lifetimes is depicted in Figure 5.7. As expected, higher electricity cost results in higher methane cost. At a lifetime of 10,000 h (Figure 5.7a), the increase in cell cost has a consistent effect on methane cost, with a growth rate of approximately 50 €/MWh per 500 €/kW increase in cell cost. The minimum methane cost achievable with a CO_2 price of 100 €/t is 550 €/MWh at a lifetime of 10,000 h and 470 €/MWh at a lifetime of 40,000 h when the electricity cost is low at 20 €/MWh and the cell cost is 1,000 €/kW.

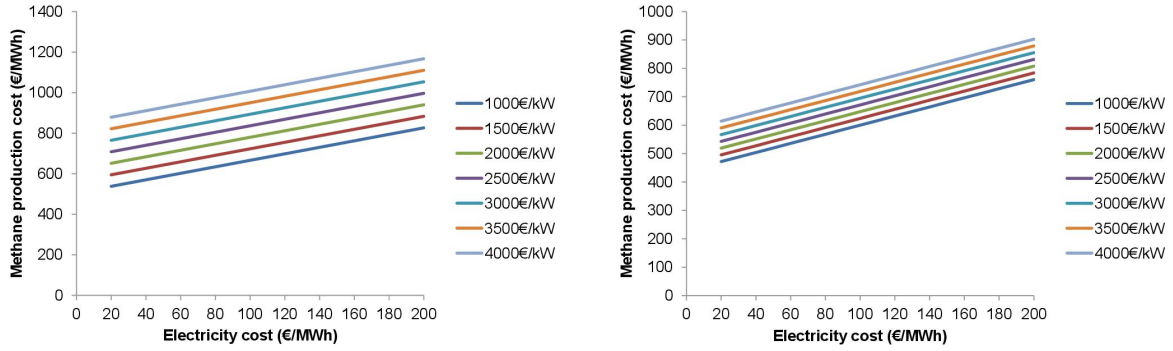

(a) (b)

Figure 5.7: Impact of electricity cost (€/MWh) and the cell capital cost (€/kW) on the final methane cost (€/MWh) at a fixed maximum CO_2 cost of 100 €/t, and two different cell lifetimes: 10,000 h **(a)**, and 40,000 h **(b)**.

The study was repeated with a minimum CO_2 cost of 20 €/t, and the results are depicted in Figure 5.8. The main difference between the two categories lies in the range of methane costs observed at both lifetimes. At a lifetime of 10,000 h (Figure 5.8a), the lowest methane cost reached is 300 €/MWh, compared to 550 €/MWh at the maximum CO_2 cost. On the other hand, at a 40,000 h lifetime (Figure 5.8b), the methane cost range of 470 €/MWh to 620 €/MWh at the maximum CO_2 cost shifts

to a range of 190 to 350 €/MWh at the minimum CO_2 cost when the electricity cost is low at 30 €/MWh.

Nevertheless, when considering a 40,000 h lifetime (Figure 5.8b), the methane cost exhibits a more optimistic outlook, varying between 190 and approximately 600 €/MWh with the changes in electricity and cell costs. Therefore, the minimum methane cost of 190 €/MWh can be deemed competitive with the actual natural gas prices of 126 €/MWh in France and 340 €/MWh in the Netherlands in 2022 [236]. These findings emphasize the importance of a cell lifetime of 40,000 h and indicate that a cell cost below 3,500 €/kW, along with an electricity cost range of 20 to 90 €/MWh and a low CO_2 feed cost of 20 €/MWh, represents an appealing target for achieving a competitive SNG price.

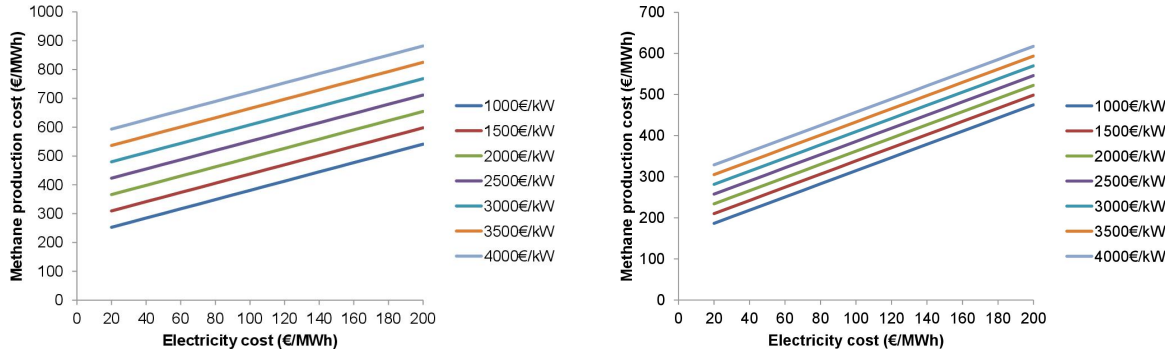

(a) (b)

Figure 5.8: Impact of electricity cost (€/MWh) and the cell capital cost (€/kW) on the final methane cost (€/MWh) at a fixed minimum CO_2 cost of 20 €/t, and two different cell lifetimes: 10,000 h **(a)**, and 40,000 h **(b)**.

In conclusion, this analysis category highlights that to attain a competitive methane price, a combination of factors including low CO_2 cost, low electricity price, and low capital cost is crucial. Specifically, an electricity price range of 20-90 €/MWh and a low capital cost can contribute to achieving a competitive methane price, but only when the CO_2 cost is also low. Conversely, if the CO_2 cost is high, the lowest methane price that can be achieved is 470 €/MWh, even with low electricity prices and a low capital cost. Therefore, it is essential to consider all these factors carefully when designing and operating a Power-to-Gas plant to ensure that the methane produced remains cost-competitive with conventional natural gas.

4.1.4 Plant's Operating Hours

The methane cost was subject to variation with the plant's operating hours per year, making it another crucial parameter to consider. In this study, the cell, electricity, and CO_2 cost were fixed at 3,500 €/kW, 100 €/MWh, and 60 €/t, respectively. The methane costs, expressed in €/MWh, are presented in Table 5.2, where the plant's operating hours per year range from 2,000 h/y to 8,000 h/y, and the cell's lifetime is also considered.

		Cell lifetime						
		10,000	**15,000**	**20,000**	**25,000**	**30,000**	**35,000**	**40,000**
Plant's operating hours per year	**2,000**	1,110	883.23	859.67	831.76	747.45	747.45	747.45
	3,000	1,073.59	869.45	778.37	718.22	702.51	689.53	683.91
	4,000	902.53	781.78	749.43	696.64	636	629.84	624.23
	5,000	940.60	799.73	703.13	677.25	635	622.60	586.51
	6,000	849.42	732	732	651.52	629.95	594.76	584.41
	7,000	1,127.10	786.30	685.68	616.67	616.67	598.19	568.02
	8,000	1,035	736.87	648.82	648.82	588.44	588.44	572.27

Table 5.2: Methane cost in €/MWh with different plant's operating hour per hour and cell lifetime.

The analysis revealed a decreasing trend in the methane cost with an increase in the plant's operating hours; however, there are instances where the methane cost exhibited turning points and started to increase. This trend is attributed to the cell's lifetime, thus directly impacting the replacement cost. As a result, it can be extrapolated that the impact of the plant's operating hours on the methane selling price is highly dependent on the cell's lifetime and vice versa. Additionally, it was found that the methane cost could approach 300 €/MWh if the costs of the cell, electricity, and CO_2 are lowered and the plant operates between 5,000 h/y and 7,000 h/y.

4.2 Best Case Scenario

Through the parametric study, valuable recommendations can be derived to attain a competitive selling price for methane compared to the current market price. The most significant factor influencing this price is the lifetime of the electrolyzer. Therefore, improving the durability and lifespan of the electrolyzer should be a top priority. The investment cost of the electrolyzer is another critical factor affecting the methane price. Since the OPEX parameters, such as CO_2 and electricity expenses, have a minor impact on the methane cost, they are positioned as the final considerations for potential economic improvements after the CAPEX parameters.

The cost of methane production is heavily influenced by the capital cost and the cell lifetime, but reducing the operating cost is an essential complementary route to make it competitive with conventional prices. To achieve a competitive synthetic methane selling price, its production cost must fall below 300 €/MWh. This price target offers a promising opportunity for establishing an eco-friendly SNG production plant, which can be directly used in the region where it is located, unlike the current natural gas spot price, which requires transportation and injection services. Several studies have proposed different price targets for the Power-to-Gas system by 2030, ranging from 200 to 350 €/MWh for a 1 MW PEM plant size [233], from 60 to 250 €/MWh for a 7 MW plant size [238], and from 40-313 €/MWh for a 10 MW plant size at an electricity cost of 0-25 €/MWh based on [231].

Therefore, to determine the optimal values for cost drivers, five variables (cell cost, lifetime, CO_2 cost, electricity cost, and plant operating hours per year) were evaluated, and only those that satisfy the methane selling price target (< 300 €/MWh) were selected. The results are presented in four figures, each corresponding to a specific cell cost. Each figure shows a scattered points plot with the x-axis representing

the minimum plant operation hours per year, the y-axis representing the cell lifetime, the size of the points representing a specific electricity cost, and their color corresponding to a particular CO_2 cost.

The graph shown in Figure 5.9 depicts the various conditions for an optimal methane selling price, assuming a cell cost of 1,000 €/kW. To achieve this price target, specific combinations of cell lifetime, electricity cost, CO_2 cost, and minimum plant operating hours are required. For instance, if the cell lifetime is 10,000 hours, the methane price can be below 300 €/MWh when the plant operates for 4,000 to 8,000 hours per year, with a CO_2 cost of 20 €/t, an electricity cost between 20 and 40 €/MWh, and a cell cost of 1,000 €/kW. However, this may be challenging to achieve due to the intermittency of renewable energy sources, which may not allow for such prolonged plant operation. Increasing the cell lifetime to 20,000 hours reduces the required minimum operating hours to 2,000 h/y, but low electricity and CO_2 costs and a low cell cost of 1,000 €/kW are still necessary to achieve the target methane price. Higher electricity and CO_2 costs necessitate longer operating hours to reach the price target, with electricity cost being limited to 90 €/MWh and CO_2 cost to 50 €/t.

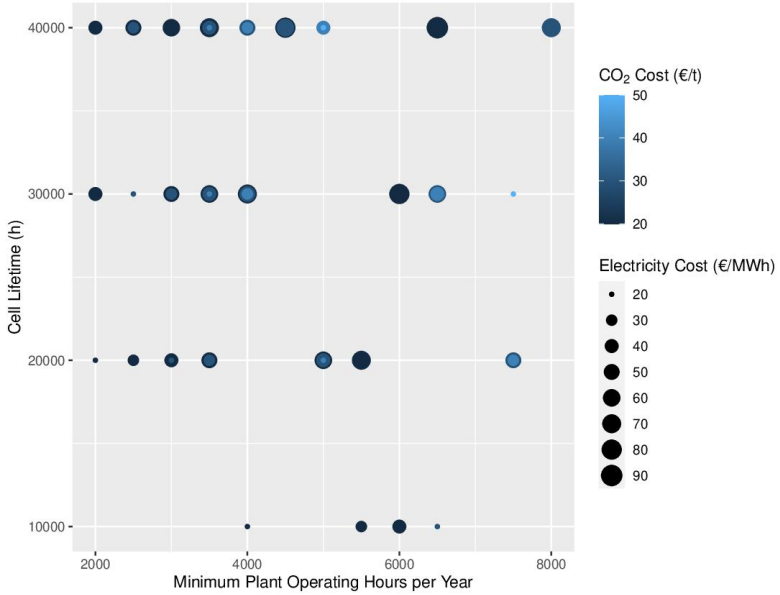

Figure 5.9: Optimal values of cell lifetime, plant operating hours, CO_2 cost, and electricity cost, at a cell cost of 1,000 €/kW.

Nevertheless, a longer cell lifetime can reduce the required operating hours even at higher operating costs. For example, a combination of a 40,000 h cell lifetime, a 20 €/t CO_2 cost, an electricity cost ranging from 20-40 €/MWh, and a minimum operating time of 2,000 hours per year can meet the target price. Other operating cost scenarios require a minimum operating time of 2,500 hours per year to reach the target price, which can be achieved with a 20 €/t CO_2 cost and an electricity cost of 50 €/MWh or a 30 €/t CO_2 cost and an electricity cost of 30 €/MWh. In summary, a low cell cost provides flexibility in other parameters, allowing the plant to operate between 2,000 and 8,000 hours per year, depending on the cell's lifetime. The CO_2 cost can range from 20 €/t to 50 €/t, while the electricity cost can vary from 20 €/MWh to 90 €/MWh.

If the cell cost reaches 1,500 €/kW, several conditions must be met to achieve the target methane price, as shown in Figure 5.10. Firstly, the cell lifetime must be equal to or greater than 20,000 h. Additionally, the minimum operating time for the plant would be 3,000 h/y for a cell lifetime of 20,000 h when operating costs are at their lowest value. The minimum operating time varies significantly based on the cell lifetime and operating costs.

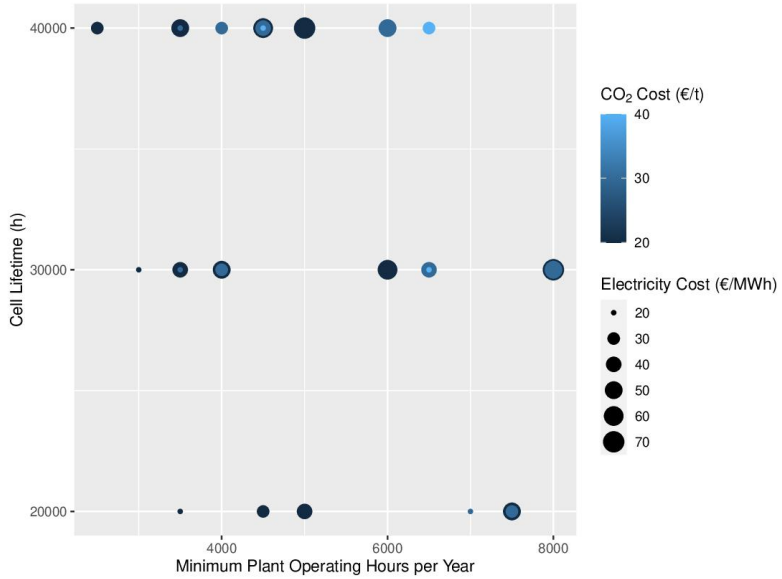

Figure 5.10: Optimal values of cell lifetime, plant operating hours, CO_2 cost, and electricity cost, at a cell cost of 1,500 €/kW.

However, at a cell cost of 1,500 €/kW, the plant can exclusively operate at a minimum of 2,500 h/y if the cell lifetime is 40,000 h, the CO_2 cost is 20 €/t, and the electricity cost is 30 €/MWh, while still maintaining a methane price below 300 €/MWh. Moreover, at this cell cost, the maximum allowable CO_2 and electricity costs are 40 €/t and 70 €/MWh, respectively. These values only lead to an optimal methane price when the cell lifetime equals or exceeds 30,000 h, and the plant operates for at least 5,000 h/y. Therefore, it can be inferred that, at a cell cost of 1,500 €/kW, the target methane price can be achieved under certain conditions, such as a cell lifetime of over 20,000 h, an electricity cost between 20-70 €/MWh, a CO_2 cost of 20-40 €/t, and a minimum operating time of at least 3,000 h.

When the cell cost is 2,000 €/kW, the range of optimal options is limited, as shown in Figure 5.11. In contrast to the six options available at a cell cost of 1,500 €/kW and 12 options at a cell cost of 1,000 €/kW, only two options are feasible for achieving a methane price below 300 €/MWh at a cell lifetime of 20,000 h. Specifically, at this cell lifetime, the CO_2 cost must be 20 €/t, the electricity cost must range between 20 and 30 €/MWh, and the plant must operate for more than 7,000 h/y to achieve the target methane price. Overall, to obtain a competitive methane price at a cell cost of 2,000 €/kW, the plant must operate for at least 3,500 h/y under specific conditions of electricity costs ranging from 20-60 €/MWh and CO_2 costs ranging from 20-30 €/t, and a cell lifetime above 30,000 h.

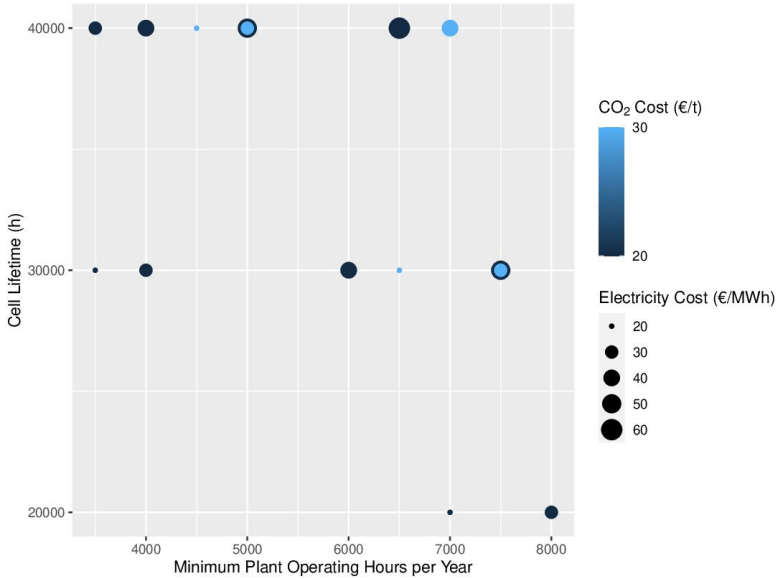

Figure 5.11: Optimal values of cell lifetime, plant operating hours, CO_2 cost, and electricity cost, at a cell cost of 2,000 €/kW.

At a cell cost of 2,500 €/kW, there are only seven possible cases for achieving a methane price below 300 €/MWh, as depicted in Figure 5.12. These cases require a cell lifetime of either 30,000 h or 40,000 h, a CO_2 cost of 20-30 €/t, an electricity cost of 20-50 €/MWh, and plant operating hours of at least 4,000 h/y. These conditions are interdependent, meaning that changing one condition will affect the others. For example, if the plant operates for 4,000 h/y, it must purchase CO_2 at 20 €/t, electricity at 20 €/MWh, and the cell must have a lifetime of 40,000 h. Conversely, at a fixed cell lifetime, an increase in electricity cost will increase the minimum allowed plant operating hours. At this cell cost, the CO_2 cost must always be 20 €/t, except for one option where the CO_2 cost can be up to 30 €/t. However, in this case, the electricity cost must be 20 €/MWh, the cell lifetime must be 40,000 h, and the plant must operate for at least 6,000 h/y. Therefore, achieving a competitive methane price at a cell cost of 2,500 €/kW requires meeting specific conditions, including a high cell lifetime, low CO_2 and electricity costs, and a minimum plant operating time of 4,000 h/y.

In conclusion, the analysis revealed that cell cost is a critical parameter in achieving a competitive methane price. At lower cell costs, a broader range of options was available to achieve a methane price below 300 €/MWh, while at higher cell costs, the options become more limited, and specific conditions must be satisfied, such as higher plant operating hours, lower CO_2 and electricity costs, and longer cell lifetimes. Additionally, the analysis highlighted the interdependence of the various parameters, such as cell lifetime, CO_2 cost, electricity cost, and plant operating hours, which must be considered when attempting to optimize the system to achieve the target methane price. Accordingly, to achieve this, it is necessary to select an optimal range of parameters, including a low CO_2 cost of 20-40 €/t, an electricity cost of 20-80 €/MWh, a cell cost below 2,000 €/kW, a cell lifetime of at least 30,000 h, and a plant operating duration longer than 3,000 h/y.

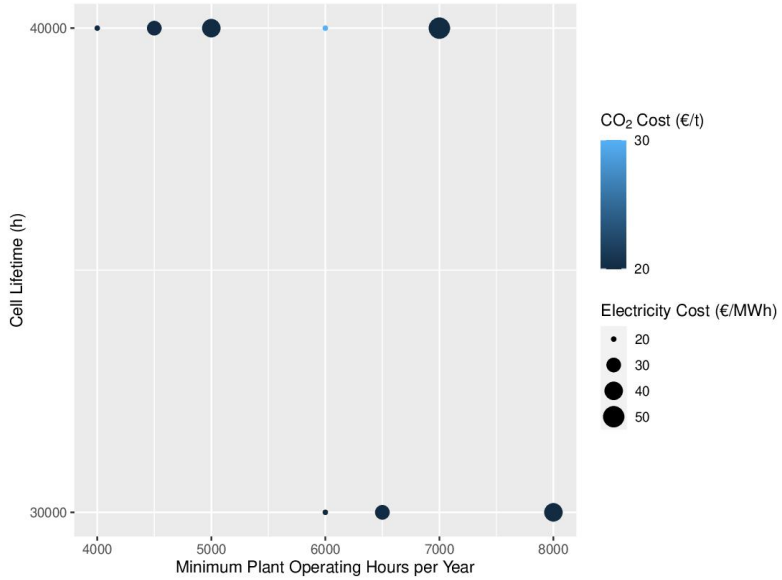

Figure 5.12: Optimal values of cell lifetime, plant operating hours, CO_2 cost, and electricity cost, at a cell cost of 2,500 €/kW.

5 Impact of CO_2 Penalty for the Methane Cost

An exciting advantage of the methane produced from Power-to-Gas is the CO_2 credits that can generate income. For instance, an income of 20 €/t of CO_2 instead of a conventional expense reduces the selling price of methane. Consequently, this produced SNG becomes economically competitive with natural gas. The results revealed that a CO_2 credit of 130 €/t of CO_2 could provide a methane selling price of 4.877 €/kg (372.23 €/MWh) under the reference conditions, which is comparable with the current market price. However, if the electrolyzer's cost is lowered to 1,500 €/kW and its lifetime is improved to 40,000 h, a CO_2 credit of 80 €/t results in a methane selling price of 2.937 €/kg (224.2 €/MWh). It can be typically perceived that the methane price would reduce with the CO_2 credit increase. This beneficial impact of CO_2 credits would encourage implementing Power-to-Gas plants in the future as a part of the energy transition and storage strategy.

6 Future Perspectives

The outcomes of the parametric study suggested a necessity for further research on changes in operating and capital costs over the past few years and future cost projections. This research will investigate the cost of electricity, including renewable energy costs and French grid electricity prices, and the cost of CO_2 capture from various technologies. Capital expenses will also be examined, including the lifetime and cost of the MCEC electrolyzer. Therefore, the current status of the MCEC's lifetime will be analyzed, and a roadmap study of the MCEC technology will be conducted to determine its learning curve.

6.1 Electricity Cost Evolution

The electricity cost mainly concerns the OPEX of the MCEC electrolyzer since it is the most electric energy-consuming equipment in the Power-to-Gas plant. This plant principally aims to store the surplus of renewable energy; thus, renewable power supplies the electrolyzer. Therefore, the electricity cost is driven by the cost of the renewable energy source. The International Renewable Energy Agency (IRENA) [225] has reported the decreasing trend of the levelized cost of the different renewable energy sources from 2010 to 2021, illustrated in Figure 5.13. In 2021, the cost of onshore wind turbine electricity was 33 $/MWh (≈ 30 €/MWh), and that of solar photovoltaic electricity was 48 $/MWh (≈ 45 €/MWh). These costs are expected to be very low in the coming years.

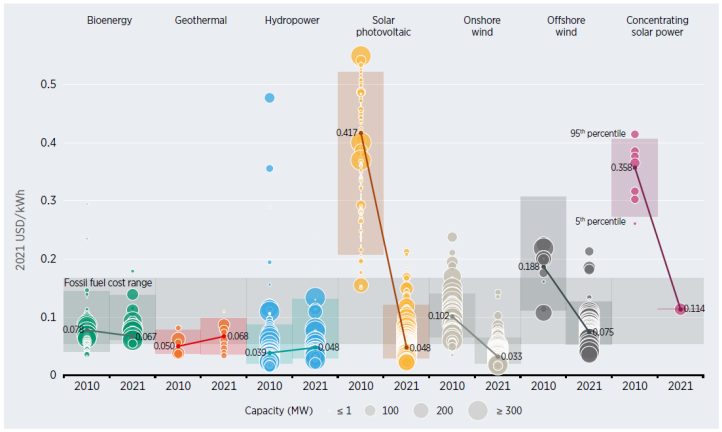

Source: IRENA Renewable Cost Database.

Figure 5.13: Global levelized cost of electricity of renewables, from 2010 to 2021, reprinted from [239].

The previous analysis has shown that the Power-to-Gas plant must operate for more than 3,000 h/y to be economically feasible. However, since renewable energy sources do not allow long operation duration, the plant needs support from the electricity grid. This means that the electricity cost should not only consider the levelized cost of electricity (LCOE) of renewables but also the price of electricity from the grid. The latter price is subject to change over time, depending on the energy mix and various geographical, political, and economic policies.

The electricity price in France has experienced significant changes since 2001 due to various circumstances, as shown in Figure 5.14. In the beginning of 2021, the price increased significantly due to the COVID-19 pandemic. This trend has continued due to the Ukrainian war crisis, which led to a gas shortage. Although most of the electricity in France is produced from nuclear power, the capacity was reduced in 2022 due to maintenance procedures, resulting in a higher demand for gas to meet energy needs. As a result, the Ukrainian crisis significantly impacted the price of electricity in France. The spot electricity price trend per month in France over the last three years, as shown in Figure 5.15, reveals that the cost began to rise at the end of 2021 and peaked in September 2022, exceeding 100 €/MWh during that period. However, in the first half of 2023, the cost began to decrease, with the latest cost in April 2023 approaching 100 €/MWh.

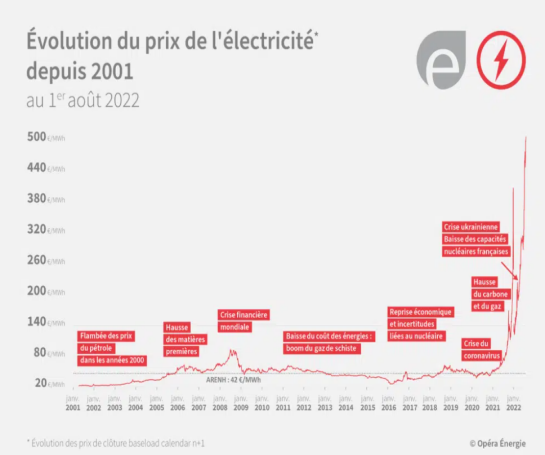

Figure 5.14: Electricity price evolution in France, from 2001 to august 2022 [240].

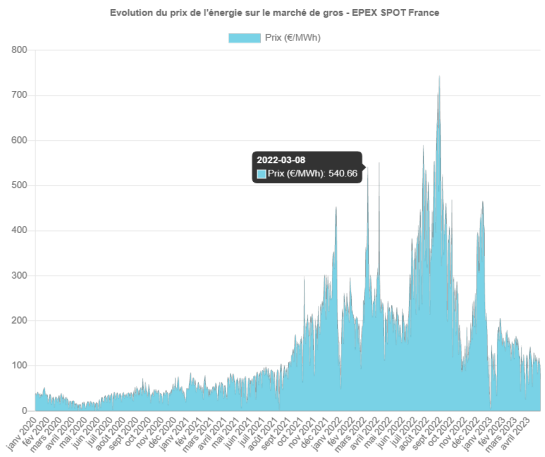

Figure 5.15: Spot electricity price evolution in France, from January 2020 to April 2023 [241].

6.2 Captured Carbon Dioxide Cost Evolution

The cost of CO_2 capture depends on the technology used, each having different investment and operating costs. Moreover, the cost of CO_2 capture can vary significantly depending on factors such as CO_2 concentration in the gas stream, plant location, energy and steam supply, and integration with the original facility, all of which can affect the selling price of the produced CO_2 [242]. The CO_2 cost from different carbon capture technologies is presented in Figure 5.16.

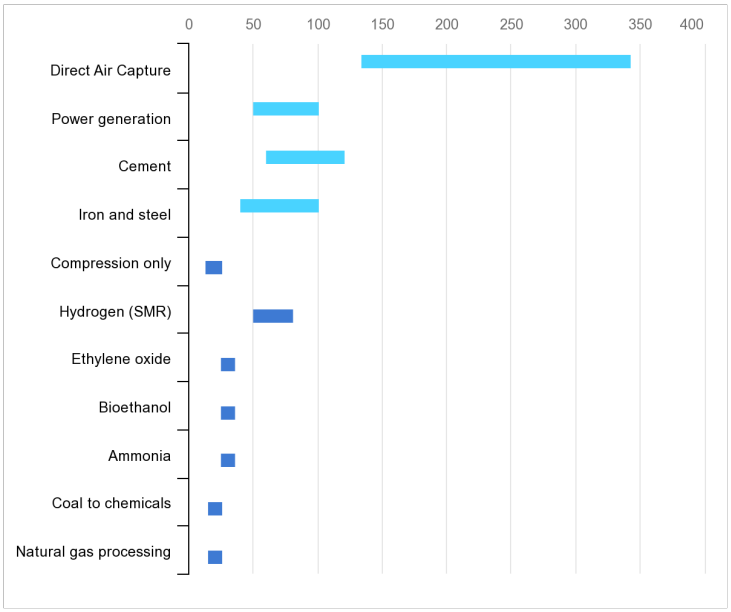

Figure 5.16: CO_2 capture cost in \$/MWh of different carbon capture technologies, [242].

In cases where CO_2 is already highly concentrated, such as in ethanol production or natural gas processing, the cost of CO_2 capture can be relatively low, with the separation of CO_2 from natural gas costing as little as 15-25 \$/t (approximately 13-23 €/t). However, for more diluted CO_2 streams, such as flue gas from power plants (3-14% CO_2 concentration) or a blast furnace in a steel plant (20-27%), the

cost of CO_2 capture can be much higher and can exceed 100 $/t (approximately 91 €/t) [242]. This cost accounts for around 75% of the total cost of carbon capture, utilization, and storage (CCUS), while the remaining 25% represents the cost of transport and storage. Therefore, it seems feasible to achieve a low cost of CO_2 of 20-40 €/t, especially for processes that capture CO_2 from highly concentrated streams, which can provide CO_2 at a cost lower than 50 $/t ($\approx$ 47 €/t).

6.3 MCEC Lifetime Evolution

The future perspective for having a 40,000 h lifetime of MCEC is anonymous. However, the lifetime of MCFC has reached over 40,000 h lifespan in fuel cell mode [237]. Besides, Hu et al. (2014) [58], in their study on a 3 cm^2 cell, proved that the cell exhibited better electrochemical performance in MCEC mode than in MCFC mode, which leads to a higher lifetime of the MCEC. However, a study carried out by Frangini et al. (2021) [73] on an 81 cm^2 cell revealed that there is a degradation of the cell during electrolysis mode due to electrolyte loss, increase in the chemical instability of the oxygen electrode NiO, reduction of the porosity of both electrodes and corrosion of the oxygen-current collector. According to this information, it can be deduced that there is no current certitude about the lifetime of MCEC. Based on the literature, some research strategies have been proposed to increase the stability of conventional electrodes and current collectors in the reverse mode of MCFC using advanced surface modification and coating technologies [73].

6.4 MCEC Cost Evolution

The MCEC cost is determined by the technology improvements and the manufacturing capacity, which will be reflected in an increase in the cell market, causing a reduction in the cell cost per installed capacity. In 2003, MTU (a former fuel cell manufacturing company in Germany that transferred its assets to FuelCell Solution GmbH in 2012, a subsidiary of FuelCell Energy USA) expected that the commercial MCFC cost would attain a value of < 1,250 €/kW once the production volume reaches 160 to 200 systems annually [243]. However, there is still no publicly available information on the current status of the MCEC cost; thus, a roadmap study on the MCFC technology was conducted, which will be presented in Section 6.5.

6.5 Roadmap Study of the MCEC

6.5.1 Technology Learning Curves

After creating the first learning curve for the aircraft industry in 1936 [244], various technologies have undergone learning curve analyses to determine the possible cost reductions that can be achieved by assessing progress made in the past. The learning curve of a technology is a graphical representation of the relationship between the cumulative production of a technology and the corresponding reduction in its unit cost over time. The power law equation is the primary tool to correlate cost and cumulative production values in this field, as shown in Eq. 5.2. When the cost and cumulative capacity data are represented in logarithmic form, the power law of a learning curve takes the form of a downward-sloping straight line. The slope of this line is referred to as the learning index (α) [245]. This index can be restated

as the learning rate (lr), as shown in Eq. 5.3. The learning rate is the percentage by which technology costs decrease, with each doubling of cumulative production (P_i).

$$C_t = C_0 \left(\frac{P_t}{P_0} \right)^{-\alpha} \tag{5.2}$$

$$lr = 1 - 2^{-\alpha} \tag{5.3}$$

The learning curve concept is based on the idea that as the technology is manufactured and installed more, its production costs decrease due to factors such as economies of scale, learning-by-doing, and improvements in production processes. The learning rate quantifies the speed at which this cost reduction occurs and can be used to forecast future cost reductions for the technology.

6.5.2 Learning Curves of MCFC/MCEC Technology

FuelCell Energy (FCE) developed the MCFC product and launched its first commercial product in 2003. Before launching, FCE conducted a "Product Design Improvement" program to improve stack performance and reduce costs. The program covered product definition, system design, manufacturing process development, packaging design development, and resolving technology and cost issues [143]. Findings from the study led to cost reduction initiatives at an early stage of product development. In the early program years (1995-2003), the cost reduction was achieved mainly through innovative new cell designs, cell area scale-up, manufacturing simplification, partial automation, and material cost reduction by developing multiple vendors, which resulted in a cell component cost reduction by a factor of 3. The nominal cell area was scaled up from 6,000 cm^2 to 9,000 cm^2 to reduce cell costs and achieve optimum packaging of stacks in the truck-transportable module. Furthermore, FCE undertook process optimization, increased productivity initiatives, and overall quality improvement programs, such as optimizing the anode tape casting and matrix tape cast processes to improve production rates and dimensional tolerances. These efforts successfully reduced tape slurry preparation time by a factor of 30 and casting time by a factor of three, resulting in 60% dimensional variation reduction, three-fold manufacturing rate enhancement, and an associated cost reduction.

To construct the learning curve of the MCFC technology, two different sets of data were collected: the cost per kW of MCFC from 2003 to 2019 and the installation capacity by year and project. Due to insufficient data between 2015 and 2019, the data was examined by making some assumptions. First, a cost installation capacity of 1,400 kW per project is assumed, given that the minimum FCE product capacity is 1.4 MW. Second, a linear decrease in price per project is estimated over these four years. This information generated a learning curve and is presented in Figure 5.17. The curve demonstrates the progress of the cost of MCFC per kW with the cumulative installation capacity since the first commercialization in 2003. The cost revealed a decrease with a learning rate of 11.24%. The cost reduction is divided into two stages: early commercialization and development and marketing.

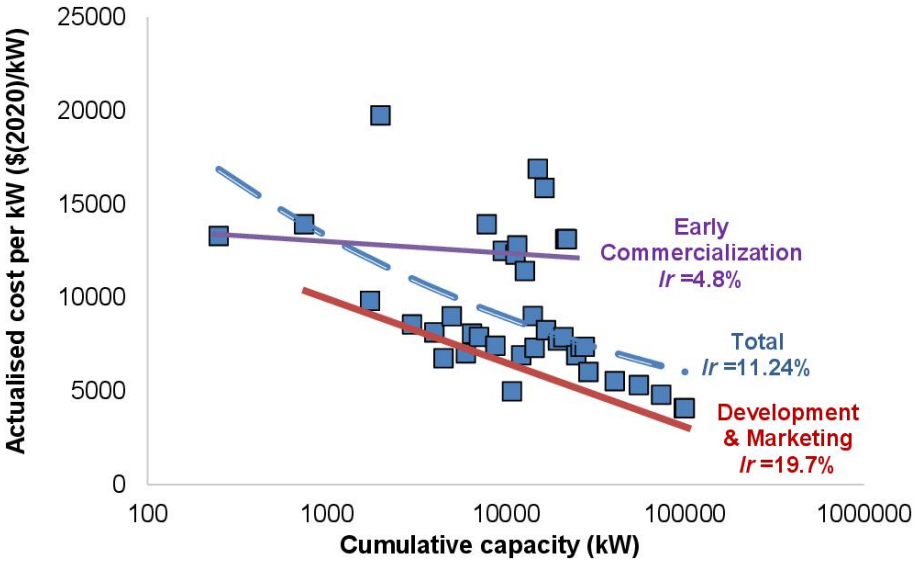

Figure 5.17: Learning curve of the MCFC.

Early Commercialization Stage

Several improvements were achieved during this phase, such as refining the cell and stack designs to enhance performance, reduce costs, and improve endurance capability. Performance improvements in the stack were accomplished through enhancements in cell conversion efficiency, thermal management, and high-power operation. High surface area cathodes were developed to offer lower cathode polarization loss and high-performance stability than baseline cathodes. The stack temperature distribution was optimized to enable 20% higher power operation of full-size stacks without penalty for thermal management. A new symmetric manifold retention system and gas-seal design were constructed, resulting in a two-fold improvement in gas-seal effectiveness, thus providing greater stack endurance capability. The performance decay rate was significantly reduced and met product market-entry life/stability goals in 2004, with a lifetime of 7,800 hours and a decay rate of 0.2%/1,000 hours. Materials were developed to extend the stack life to > 40,000 hours and reduce product cost. The bipolar plate design was optimized, and an advanced design eliminated several expensive vendor-processing operations. Additionally, a low-cost wet-seal corrosion protection process was developed and successfully demonstrated for full-size bipolar plates. Moreover, significant improvements were made in direct internal reforming (DIR) catalyst performance, stability, and cost. The balance of plant (BoP) equipment was developed, including an advanced pre-converter design for operation on alternate propane fuel and a load leveler development for stack operations. BoP equipment cost reduction achievements included a 50% cost reduction for the fuel humidifier and a 36% cost reduction for the DC-to-AC inverter resulting from alternate vendor qualifying [246].

Furthermore, in 2004, FCE initiated a concerted cost-out effort for the stack and the sub-megawatt power plant's BoP. The efforts included design simplification/optimization, eliminating unnecessary components, developing alternate vendors for key equipment, directly purchasing key equipment and drop-shipping it to the packager, eliminating the middleman's markup, and developing low-cost power plant packaging concepts. As a result of this concerted effort, FCE achieved a cost reduction of 25% for the sub-megawatt product on a per kW basis over the 2003 cost basis [246]. The

MCFC performance was further enhanced in 2007 by advancing the electrode and electrolyte designs to improve cell power output and to achieve the stack useful life of more than five years for power generation applications [247].

Development and Marketing Stage

Cost reductions were achieved during this period through design and manufacturing improvements, global sourcing, and economies of scale resulting from increased volume. The information on these aspects was obtained from press releases issued by FCE [248]. FCE has introduced three products: DFC300A (250 kW), DFC1500 (1,000 kW), and DFC3000 (2,000 kW), all using a standard full-size stack with a different balance of plant designs. The larger size plant has significantly lower BoP costs per-kW output basis.

Besides, FCE has developed a global supply chain for materials used in the module manufacturing process and balance of plant components, and manufacturing capacity has been increased by implementing lean manufacturing principles and expanding facilities. In 2015, the company expanded its North American facility from 65,000 ft^2 (6,000 m^2) to 155,000 ft^2 (14,400 m^2) and installed manufacturing equipment to increase annual capacity from 100 MW to at least 200 MW. Additionally, manufacturing in Asia was brought into function in 2015 by POSCO Energy at a facility in Pohang, South Korea, under a licensing agreement with FCE. Furthermore, a facility in Ottobrun, Germany, was installed to serve the European continent. In 2018, the company transitioned production from its five-year stack design to its seven-year stack design, reducing maintenance costs and improving smaller projects' economics. Therefore, the primary source of cost reductions comes from increased manufacturing volume and fuel cell endurance improvement.

In 2007, FuelCell Energy began its global expansion in the market sector by partnering with POSCO Energy to target Southeast Asian markets, specifically South Korea. However, in 2020, the partnership was terminated. The company established its European facility in 2012 through German-based FuelCell Energy Solutions GmbH and completed a joint venture with Fraunhofer IKTS while also acquiring Versa Power Systems, Inc. During the same year, FCE entered into a partnership with ExxonMobil, aiming to remove carbon dioxide from the exhaust of Exxon's power plants and sequester it in the ground through carbon capture and sequestration processes. In 2016, FCE made significant progress towards commercializing fuel cell carbon capture, beginning with its partnership with ExxonMobil to pursue it together. In 2019, the company made critical technological advances, including developing dual-fuel capability, fuel-blending capability, improved gas cleanup, and advanced gas monitoring. The dual-fuel capability allowed MCFC to operate on propane during biogas outages and any blend ratio of biogas and natural gas.

In addition, FCE developed an in-house, proprietary cleanup system to remove sulfur for gas cleanup, with the first SureSource Treatment system operating since September 2016. Further, FCE developed a proprietary approach to sulfur detection that is exponentially more sensitive than anything available on the market. In 2019, FCE declared that it was reintroducing the sub-MW distributed generation solution to the European market, utilizing the SureSource 250 and SureSource 400 fuel cell systems. In 2020, FCE began commercializing its multi-MW SureSource 4000 fuel cell project.

6.5.3 Future Perspective of the MCFC/MCEC Cost

The cost of the MCEC can become competitive, ranging between 2,000 $/kW (1,700 €/kW) and 3,000 $/kW (2,600 €/kW) when the total installed capacity exceeds 1,000 MW (1,000,000 kW), according to the range of the total learning curve shown in Figure 5.18. As of 2019, the total installed capacity was reported to have reached 100 MW. A market study by "Inkwood Research", a US-based market research reports company [249], predicts that a cost range of 2,500 $/kW to 4,500 $/kW will be achieved in 2028 with a total capacity of 500 MW. Therefore, the MCFC cost of 1,500-2,000 €/kW could be reached in 2030 if there is a ramp-up increase in the installed capacity of MCFC in the coming years, as depicted in Figure 5.19.

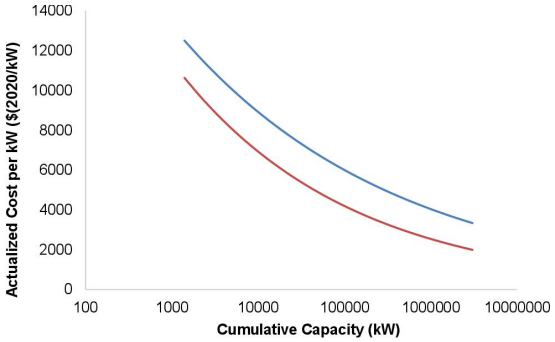

Figure 5.18: Total learning curve range of MCFC.

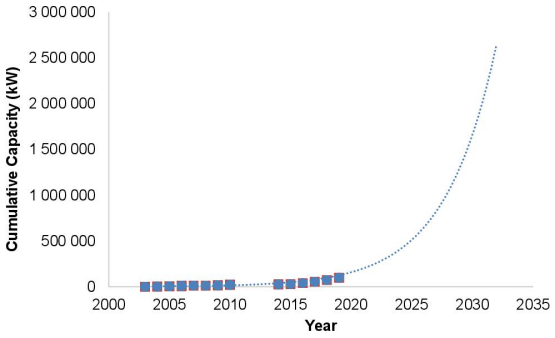

Figure 5.19: Cumulative installed capacity in kW over the years.

Although the MCFC has achieved technical success in fuel cell mode, further research is needed to enhance the electrode materials for its reverse operation in MCEC and MCFC. However, as the sensitivity study has demonstrated, the cost of MCEC has little effect on the price of methane without improving its lifetime. Therefore, the primary objective is to achieve a 40,000-hour lifetime for MCEC. If the improvement of electrode materials can achieve this lifetime while maintaining the current price of MCFC per kW, MCEC would be an attractive electrolysis technology for renewable energy storage and CO_2 valorization in the future.

6.6 Natural Gas Price Evolution

Several factors can influence the price of natural gas, including supply and demand, economic growth, and geopolitical circumstances. Production levels, transportation and infrastructure, and natural disasters can also impact the availability of natural gas. Additionally, the price of natural gas can be affected by geopolitical events such as wars, sanctions, and political instability in major producing or consuming countries. As shown in Figure 5.20, various economic and geopolitical circumstances have influenced the natural gas price trend since 2014. The price of natural gas remained relatively stable below 40 €/MWh until the beginning of 2021. Then, it gradually increased due to the impact of the COVID-19 pandemic on production, transportation, and economic levels. In 2022, the price continued to increase due to global political instability, particularly the war in Ukraine. This conflict caused Russia to reduce its natural gas supplies, forcing Europe to turn to liquified natural gas (LNG), which led to a significant increase in the natural gas price. As a result, in 2022, the price of natural gas reached 300 €/MWh.

While the price of natural gas from fossil fuels fluctuates due to various economic and geopolitical factors and often remains lower than green substitute natural gas, its production contradicts the goal of achieving zero carbon emissions and combating climate change. Additionally, countries that rely on natural gas production may face geopolitical challenges and increased price fluctuations. Therefore, investing in green substitute natural gas production with low carbon emissions can reduce dependency on fossil fuels and promote local production. This shift can help countries meet ecological targets while improving energy security and reducing economic vulnerability to global price fluctuations.

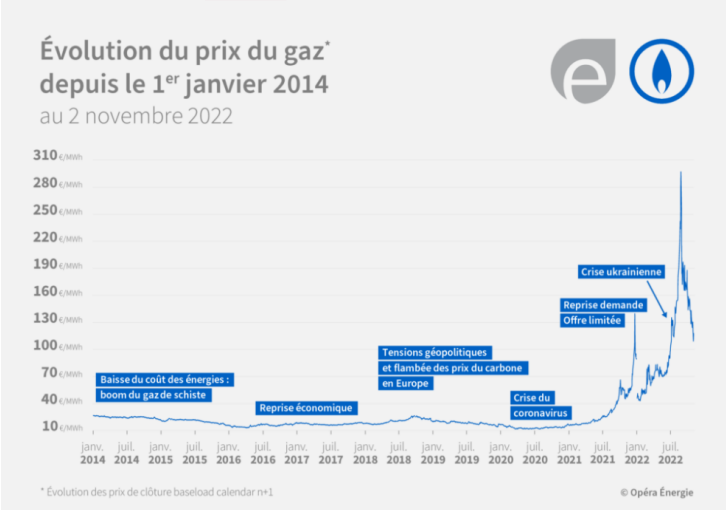

Figure 5.20: Natural Gas evolution in France since 2014, [250].

7 Conclusion

An economic assessment of the Power-to-SNG process using a high-temperature molten carbonate electrolyzer (MCEC) was conducted. The study evaluated the methane production costs under current conditions and performed a sensitivity analysis to assess economic feasibility. The findings revealed that the electrolyzer's lifespan and cost were the main contributors to production costs, while utility expenses had a negligible impact. Optimal cost drivers were determined, enabling competitive pricing below 300 €/MWh. However, the process is currently not economically competitive compared to conventional methods. Operational expenses need to be low, with CO_2 costs of 20-40 €/t and electricity costs of 20-80 €/MWh, while the electrolyzer cost should be below 2,000 €/kW, its lifetime must exceed 30,000 h, and the plant should operate for more than 3,000 hours per year. Furthermore, the study of the impact of CO_2 penalty showed that methane production cost would decrease with an increase in CO_2 credits.

The future perspective for achieving competitive substitute natural gas (SNG) production costs was also evaluated. Electricity costs are expected to decrease significantly, but a minimum of 3,000 hours of annual electricity supply is necessary for economic advantage. Grid support may be required if renewable capacity is insufficient. Despite high grid electricity costs in France due to geopolitical issues, a decrease is projected after nuclear reactor maintenance. CO_2 capture costs are low for various technologies, making CO_2 cost targets achievable. However, capital expenses remain a challenge, as the lifetime

and cost of the MCEC electrolyzer are unknown, and several tests must be conducted to determine its lifetime. In contrast, MCFC technology learning curves revealed potential cost reductions by 2030 with a 1,500-2,000 €/kW cost range. Improvements in the lifespan and cost of the electrolyzer are essential for achieving competitive SNG production costs. While operating costs are promising, addressing capital expenditures, including electrolyzer lifespan and cost, is crucial for economically viable substitute natural gas production.

Résumé: Étude économique

Ce chapitre présente une évaluation économique du système Power-to-Gas (P2G) basé sur un électrolyseur à carbonates fondus. L'analyse vise à évaluer le prix de vente du méthane produit dans des conditions réelles. Une analyse de sensibilité des paramètres CAPEX et OPEX est réalisée pour identifier les facteurs qui influencent le prix de vente du méthane. Sur la base des résultats de cette étude, un scénario favorable est sélectionné et étudié pour déterminer son potentiel futur. Enfin, une feuille de route est élaborée pour évaluer l'évolution des coûts de la technologie MCFC avec l'augmentation de la capacité d'installation au fil du temps.

État de l'art

La mise en œuvre de la technologie Power-to-Gas rencontre des défis économiques qui nécessitent des recherches complémentaires. Plusieurs études ont été menées pour aborder cette problématique, en se concentrant sur différentes technologies telles que l'électrolyse alcaline, la PEM et la SOEC. La plupart des études : Götz et al. (2015) [87], Peters et al. (2019) [230], Szima et Cormos (2021) [232], Fambri et al. (2022) [233] ont examiné les exigences techniques et économiques des technologies d'électrolyse et de méthanation existantes, et ont analysé les caractéristiques technico-économiques des systèmes P2G. Ces études ont évalué les coûts de production de méthane synthétique et examiné les aspects technico-économiques de la production de méthane de synthèse à partir de l'hydrogène renouvelable et de CO_2 capté. Cependant, toutes ces études concluent que le substitut de gaz naturel (SNG) produit à partir de sources renouvelables n'est actuellement pas compétitif par rapport au gaz naturel conventionnel.

Les électrolyseurs à carbonates fondus pour les systèmes Power-to-Gas n'ont pas encore été largement étudiés en termes de viabilité économique. La plupart des études se sont concentrées sur les aspects techniques plutôt que sur les considérations économiques. Cependant, la mise en œuvre commerciale de ce procédé neutre en carbone dépend de sa compétitivité économique. Par conséquent, cette étude vise à évaluer la faisabilité économique de l'utilisation d'électrolyseurs à carbonates fondus pour les systèmes Power-to-Gas, à identifier les facteurs influençant le prix de vente du méthane et à fournir des perspectives sur la manière dont cette technologie peut devenir compétitive par rapport aux méthodes conventionnelles et autres méthodes de production de substitut de gaz naturel.

Évaluation économique du cas de réference

Après avoir étudié le système Power-to-SNG, une évaluation économique a été réalisée pour évaluer l'investissement en capital et les frais de fonctionnement de l'usine. L'évaluation a permis d'estimer le coût réel par unité de méthane en combinant l'investissement en capital et les frais de fonctionnement, en utilisant l'équation 5.1. Le coût d'investissement (CAPEX) a été calculé en tenant compte du coût de la cellule et des autres équipements nécessaires, et un coût de remplacement a été calculé en fonction de la durée de vie des équipements et de la durée fonctionnement. Le coût de maintenance a été estimé à 3% des coûts de fonctionnement, et un taux d'actualisation de 10% a été utilisé. Le coût de fonctionnement (OPEX) a été calculé par kg de matière première requise et par kW de puissance électrique consommée. Les coûts des principaux équipements ont été obtenus à partir de la littérature et de sources industrielles. Il est important de noter que certains facteurs tels que le coût d'investissement, la durée de vie des

équipements, le coût de l'eau, le coût de maintenance et le taux d'actualisation sont restés constants tout au long de l'étude.

$$CTA_i = \frac{\sum_{t=0}^{T}(C_{invest_t} + C_{electrolyzer_t} + C_{energy_t} + C_{feedstock_t} + C_{replace_t} + C_{maintenance_t}) \times (1+\tau)^{-t}}{\sum[m_{i_t} \times (1+\tau)^{-t}]} \tag{5.1}$$

L'évaluation économique s'est concentrée sur le système Power-to-SNG, plus précisément sur l'installation des unités du système et l'achat de matières premières CO_2 auprès des fournisseurs. L'analyse a supposé des coûts fixes et une durée de vie fixe pour la cellule, respectivement de 3500 €/kW et de 10000 h, ainsi que des coûts fixes pour les matières premières CO_2 à 50 €/t [235] et l'électricité à 140 €/MWh.

Le prix calculé du méthane pour le système Power-to-SNG s'est avéré être de 13,851 €/kg (1057 €/MWh), en supposant 8000 heures de fonctionnement par an, ce qui est significativement plus élevé que le prix réel du gaz naturel sur le marché, même après la crise de la penurie de gaz liee à la guerre en ukraine, qui est de l'ordre de 126 €/MWh en France et 340 €/MWh aux Pays-Bas en 2022 [236]. La répartition des coûts dans la Figure 5.21 a montré qu'une grande partie du coût total (environ 60%) était attribuée aux investissements en capital et aux coûts de remplacement. Cela est principalement dû à la durée de vie courte et au coût élevé de la cellule. Ces résultats fournissent des informations importantes sur les facteurs à prendre en compte afin d'améliorer la faisabilité économique du système.

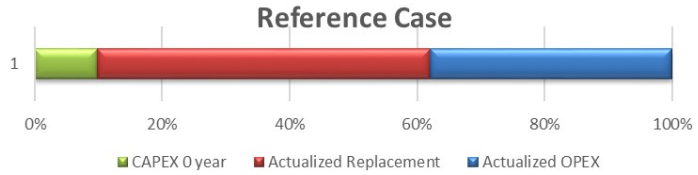

Figure 5.21: Répartition du coût du méthane sur la base des CAPEX, OPEX et du remplacement de l'équipement.

Le système Power-to-Gas vise à relever le défi du stockage de l'énergie renouvelable. Cependant, en raison de la nature intermittente de la source d'énergie, l'installation ne peut pas fonctionner pendant les 8000 heures annuelles complètes. Par conséquent, une étude a été réalisée pour examiner l'impact de la durée de fonctionnement sur le prix du méthane produit. Il a été constaté que de faibles durées de fonctionnement, inférieures à 500 h, entraînent un coût élevé du méthane. Cependant, en augmentant la durée de fonctionnement, le prix du méthane diminue progressivement, atteignant son point le plus bas à 6600 heures. Ce point d'équilibre est lié au coût de remplacement de la cellule, qui varie avec la durée de fonctionnement. En réduisant la durée de fonctionnement de l'installation de 8000 heures à 6600 heures, l'investissement en capital total (CAPEX) est passé de 60% à 50%, ce qui a entraîné une baisse du prix du méthane de 13,851 €/kg (1057 €/MWh) à 10,95 €/kg (836 €/MWh). Cette réduction des coûts met en évidence l'importance de prendre en compte la durée de fonctionnement dans la conception et l'exploitation des systèmes P2G. Il convient de noter que l'étude n'a pas pris en compte le potentiel de bénéfice découlant de l'utilisation de l'oxygène produit du côté anode de l'électrolyseur lorsqu'il est séparé du CO_2. L'intégration de cet aspect a le potentiel de réduire davantage le prix du méthane.

Étude de la sensitivité

L'objectif de cette étude est de mieux comprendre les facteurs de coût et d'identifier les domaines potentiels de réduction des coûts dans le système Power-to-Gas. L'analyse économique s'est concentrée sur deux coûts clés : l'investissement en capital (CAPEX) et les coûts d'exploitation (OPEX). Le cas de référence a démontré que le CAPEX a une plus grande influence sur le coût global par rapport à l'OPEX. Ainsi, cette étude a examiné quatre paramètres qui influent sur le CAPEX et l'OPEX dans une plage acceptable. Ces paramètres comprennent la durée de vie et le coût de l'électrolyseur (CAPEX), le coût du CO_2 capté et les dépenses liées à l'électricité (OPEX). L'étude a évalué le coût du méthane en faisant varier ces paramètres, et un résumé de tous les paramètres étudiés ainsi que leurs plages respectives est présenté dans la Figure 5.22.

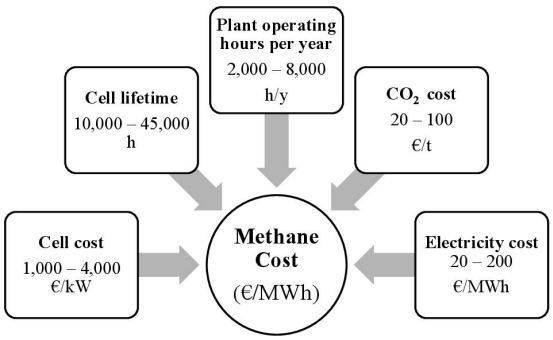

Figure 5.22: Représentation schématique des plages de l'étude des différents paramètres de l'analyse de sensibilité.

L'analyse de sensibilité a été réalisée en supposant que l'usine fonctionne pendant 6600 heures par an. Tout d'abord, l'impact du coût et de la durée de vie de la cellule, qui correspond au CAPEX, a été examiné. Ensuite, la variation du coût du CO_2 a été étudiée en relation avec le CAPEX variable. Dans cette catégorie, le coût du CO_2 est modifié tout en maintenant le coût de l'électricité fixe à ses valeurs minimale et maximale. Enfin, le coût de l'électricité a été modifié avec les paramètres du CAPEX tandis que le CO_2 est fixé à sa valeur minimale et maximale.

Impact du coût et de la durée de vie de la cellule sur le coût de production du méthane de synthèse

Les résultats, présentés dans la Figure 5.23, ont montré que la diminution du coût de la cellule entraînait une réduction du coût de production de méthane, étant donné que la cellule constituait une part importante des dépenses totales en investissement. En revanche, l'augmentation de la durée de vie de la cellule se traduisait par un coût de méthane plus faible. Cependant, il existait des durées de vie spécifiques où aucune réduction du coût de méthane n'était observée, car la durée de vie de la cellule déterminait la fréquence des remplacements au cours de la vie de l'usine. Par exemple, améliorer la durée de vie de la cellule de 10000 h à 15000 h n'affectait pas le coût de méthane, car les deux durées de vie nécessitaient un remplacement tous les deux ans. Ces résultats soulignent l'importance de prendre soigneusement en compte les paramètres de coût et de durée de vie de la cellule afin d'optimiser la faisabilité économique du système Power-to-Gas.

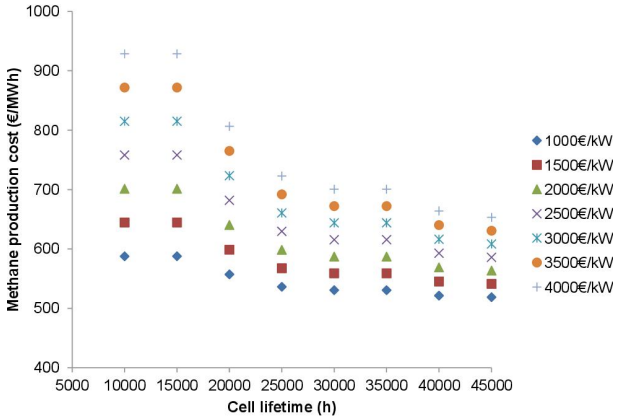

Figure 5.23: Impact de la durée de vie de la cellule (h) et de son coût (€/kW) sur le coût final du méthane (€/MWh).

À partir des résultats, l'impact des paramètres OPEX (coûts du CO_2 et de l'électricité) a été évalué en tenant compte de la variation du coût et de la durée de vie de la cellule. Cependant, pour la durée de vie de la cellule, seules deux valeurs ont été sélectionnées : la valeur basse à 10000 heures et la valeur élevée à 40000 heures. La durée de vie élevée de 40000 heures est d'un intérêt particulier car des études antérieures ont démontré que la MCFC peut atteindre cette durée de vie [237], il est donc essentiel d'évaluer l'aspect économique de cette durée de vie prolongée.

Impact du coût du CO_2 sur le coût de production du méthane de synthèse

Tout d'abord, l'analyse a été réalisée avec un coût maximum de l'électricité fixé à 140 €/MWh, et les résultats sont présentés dans la Figure 5.24.

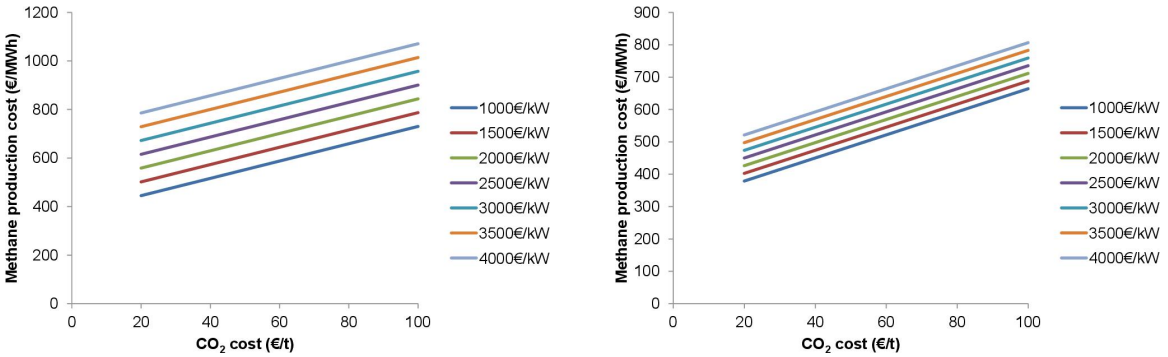

(a) (b)

Figure 5.24: Impact du coût d'alimentation en CO_2 (€/t) et du coût d'investissement de la cellule (€/kW) sur le coût final du méthane (€/MWh) pour un coût maximum fixe de l'électricité de 140 €/MWh, et deux durées de vie différentes de la cellule : 10000 h **(a)**, et 40000 h **(b)**.

Les résultats ont montré que le coût du méthane augmentait avec un coût de CO_2 plus élevé, indépendamment du coût de la cellule. Le coût du méthane le plus bas atteint était de 450 €/MWh pour un coût de CO_2 de 20 €/t et un coût de cellule de 1000 €/kW. Cependant, pour une durée de vie de la cellule de 40000 h, le coût du méthane diminuait encore pour atteindre 350 €/MWh dans les mêmes conditions.

Il a été conclu que la durée de vie de la cellule de 40000 h était essentielle pour obtenir un coût acceptable de production de substitute de gaz naturel. Cependant, une fois que la durée de vie de la cellule atteignait 40000 h, l'impact du coût de la cellule sur le coût du méthane devenait négligeable. Les améliorations ultérieures de la durée de vie de la cellule avaient un impact minimal sur le prix de vente du méthane pour une durée de vie de l'installation de 15 ans.

L'étude a également examiné l'impact du coût du CO_2 pour un coût de l'électricité minimal de 70 €/MWh. Les résultats, présentés dans la Figure 5.25, ont révélé que par rapport au cas avec un coût maximum de l'électricité, le coût du méthane diminuait de 100 €/MWh, indépendamment du coût de la cellule, de la durée de vie de la cellule et du coût du CO_2. Cette réduction a permis d'atteindre un coût du méthane inférieur à 350 €/MWh. Pour un coût de l'électricité de 140 €/MWh, un coût du méthane de 350 €/MWh nécessite un faible coût du CO_2 à 20 €/t, un coût de la cellule à 1000 €/kW et une durée de vie de la cellule de 40000 h. Avec un coût de l'électricité de 70 €/MWh, un coût du méthane de 300 €/MWh peut être atteint avec une durée de vie de la cellule de 10000 h et un coût de la cellule de 1000 €/kW, ou avec une durée de vie de la cellule de 40000 h et un coût de la cellule variant entre 1000 et 2000 €/kW et un coût du CO_2 variant entre 20 et 40 €/t.

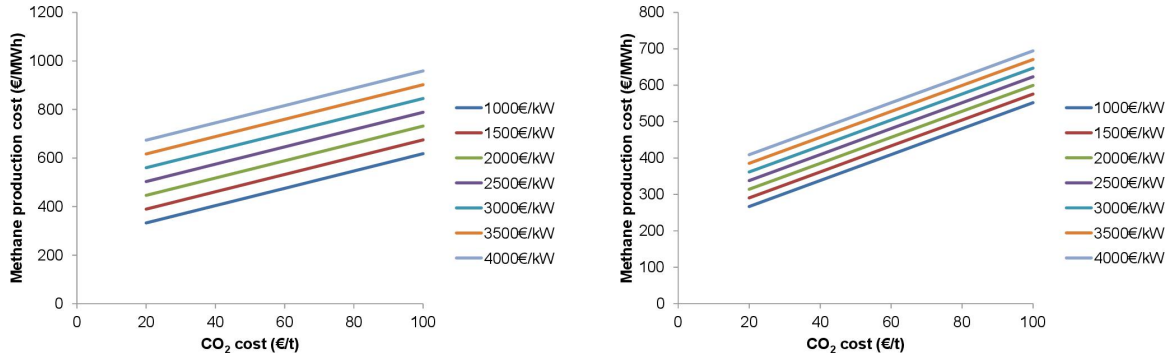

(a) (b)

Figure 5.25: Impact du coût d'alimentation en CO_2 (€/t) et du coût d'investissement de la cellule (€/kW) sur le coût final du méthane (€/MWh) pour un coût minimum fixe de l'électricité de 70 €/MWh et deux durées de vie différentes de la cellule : 10000 h **(a)**, et 40000 h **(b)**.

Impact du coût de l'électricité sur le coût de production du méthane de synthèse

L'étude a examiné l'impact de la variation du coût de l'électricité tout en maintenant le coût du CO_2 dans des valeurs minimales et maximales fixes. Lorsque le coût maximal du CO_2 était fixé à 100 €/t, il a été observé que le coût du méthane augmentait avec le coût croissant de l'électricité. Pour une durée de vie de 10000 h (Figure 5.26a), le coût minimal du méthane était de 550 €/MWh avec un prix du CO_2 de 100 €/t, un faible coût de l'électricité de 20 €/MWh et un coût de la cellule de 1000 €/kW, tandis qu'à 40000 h, il diminuait à 470 €/MWh.

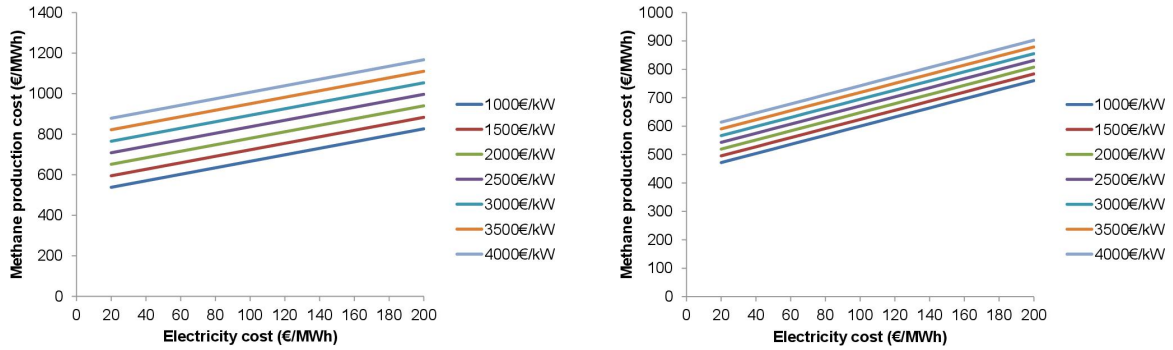

(a) (b)

Figure 5.26: Impact du coût de l'électricité (€/MWh) et du coût d'investissement de la cellule (€/kW) sur le coût final du méthane (€/MWh) pour un coût maximum fixe du CO_2 de 100 €/t, et deux durées de vie différentes de la cellule : 10000 h **(a)**, et 40000 h **(b)**.

L'étude a aussi considéré l'analyse avec un coût minimal à CO_2 de 20 €/t. Les résultats, représentés dans la Figure 5.27, ont montré que pour une durée de vie de 10000 h, le coût minimal du méthane était de 300 €/MWh, nettement inférieur aux 550 €/MWh du coût maximal du CO_2. Pour une durée de vie de 40000 h (Figure 5.27b), le coût du méthane variait entre 190 et environ 600 €/MWh en fonction des variations du coût de l'électricité et du coût de la cellule. Un coût minimal du méthane de 190 €/MWh peut être considéré comme compétitif par rapport aux prix réels du gaz naturel. Ces résultats soulignent l'importance d'une durée de vie de la cellule de 40000 h, d'un coût de cellule inférieur à 3500 €/kW, d'un faible coût d'alimentation en CO_2 et d'une plage de coût de l'électricité variant de 20 à 90 €/MWh pour atteindre un prix compétitif pour le substitut de gaz naturel. Il est essentiel de prendre en compte ces facteurs lors de la conception et de l'exploitation d'une centrale Power-to-Gas pour garantir la compétitivité du substitut de gaz naturel produit par rapport au gaz naturel conventionnel.

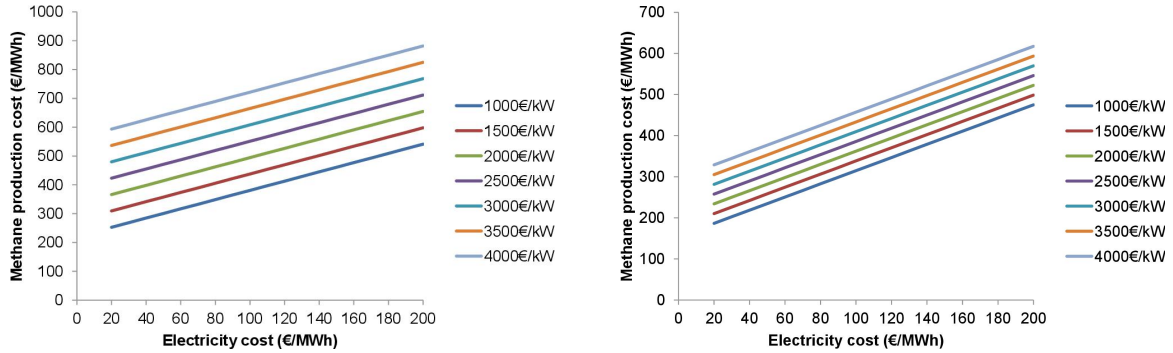

(a) (b)

Figure 5.27: Impact du coût de l'électricité (€/MWh) et du coût d'investissement de la cellule (€/kW) sur le coût final du méthane (€/MWh) pour un coût minimum fixe du CO_2 de 20 €/t, et deux durées de vie différentes de la cellule : 10000 h **(a)**, et 40000 h **(b)**.

Impact de la durée de fonctionnement de l'usine sur le coût de production du méthane de synthèse

Le coût du méthane était soumis à des variations en fonction de la durée de fonctionnement annuelle de l'installation, ce qui en fait un autre paramètre crucial à prendre en compte. Dans cette étude, le

coût de la cellule, de l'électricité et du CO_2 était fixé respectivement à 3500 €/kW, 100 €/MWh et 60 €/t. Les coûts du méthane, exprimés en €/MWh, sont présentés dans le tableau 5.2, où le nombre d'heures de fonctionnement annuel de l'installation varie de 2000 h/an à 8000 h/an, et la durée de vie de la cellule est également prise en compte.

L'analyse a révélé une tendance à la baisse du coût du méthane avec une augmentation du nombre d'heures de fonctionnement de l'installation, cependant, il existe des points de retournement où le coût du méthane commence à augmenter. Cette tendance est attribuée à la durée de vie de la cellule, ce qui a un impact direct sur le coût de remplacement. Ainsi, l'impact de la durée de fonctionnement de l'installation sur le prix de vente du méthane dépend fortement de la durée de vie de la cellule et vice versa. De plus, il a été constaté que le coût du méthane pourrait approcher les 300 €/MWh si les coûts de la cellule, de l'électricité et du CO_2 sont réduits, et si l'installation fonctionne entre 5000 h/an et 7000 h/an.

Le meilleur scénario

L'étude paramétrique permet de proposer des recommandations pour atteindre un ordre de prix de vente compétitif du méthane par rapport au prix actuel du marché. Le facteur le plus significatif influençant ce prix est la durée de vie de l'électrolyseur. Par conséquent, améliorer la durabilité et la durée de vie de l'électrolyseur devrait être une priorité absolue. Le coût d'investissement de l'électrolyseur est un autre facteur critique qui affecte le prix du méthane. Étant donné que les paramètres des dépenses opérationnelles (OPEX), tels que les dépenses en CO_2 et en électricité, ont un impact mineur sur le coût du méthane, ils sont considérés comme les derniers éléments à prendre en compte pour les améliorations économiques potentielles, après les paramètres CAPEX.

Ainsi, afin d'atteindre un prix de vente compétitif du méthane de synthèse, le coût de production du méthane doit être inférieur à 300 €/MWh. Cet objectif de prix offre une opportunité prometteuse pour établir une installation de production de substitut de gaz naturel respectueuse de l'environnement, pouvant être directement utilisée dans la région où elle est implantée, contrairement au prix courant du gaz naturel qui nécessite des services de transport et d'injection.

Pour déterminer les valeurs optimales des facteurs de coût, cinq variables (coût de la cellule, durée de vie, coût du CO_2, coût de l'électricité et durée de fonctionnement de l'installation par an) ont été évaluées, et seules celles qui fournissent le prix cible du méthane (< 300 €/MWh) ont été retenues. L'analyse a révélé que le coût de la cellule est un paramètre critique pour atteindre un prix compétitif du méthane. À des coûts de cellule plus bas, une gamme plus large d'options était disponible, tandis qu'à des coûts de cellule plus élevés, les options sont plus limitées et des conditions spécifiques doivent être remplies, telles qu'une durée de fonctionnement de l'installation plus élevée, des coûts de CO_2 et d'électricité plus bas, et une durée de vie de la cellule plus longue. De plus, l'analyse a mis en évidence l'interdépendance des différents paramètres, tels que la durée de vie de la cellule, le coût du CO_2, le coût de l'électricité et la durée de fonctionnement de l'installation, qui doivent être pris en compte lors de l'optimisation du système pour atteindre le prix cible du méthane. Par conséquent, pour ce faire, il est nécessaire de sélectionner une plage optimale de paramètres, comprenant un faible coût du CO_2 de 20 à 40 €/t, un coût de l'électricité de 20 à 80 €/MWh, un coût de la cellule inférieur à 2000 €/kW, une durée de vie de la cellule d'au moins 30000 h et une durée de fonctionnement de l'installation supérieure à 3000 h/an.

Impact de la pénalité sur le CO_2 pour le coût du méthane

Un avantage appréciable du méthane produit par la technologie Power-to-Gas est ses crédits CO_2 qui génèrent des revenus. Par exemple, un revenu de 20 €/t de CO_2 au lieu d'une dépense conventionnelle réduit le prix de vente du méthane. Ainsi, ce méthane devient économiquement compétitif par rapport au gaz naturel. Les résultats ont révélé qu'un crédit CO_2 de 130 €/t de CO_2 pourrait permettre un prix du méthane de 4,877 €/kg (372,23 €/MWh) dans les conditions de référence, ce qui est comparable au prix actuel du gaz. Cependant, si le coût de l'électrolyseur est réduit à 1500 €/kW et sa durée de vie est améliorée à 40000 heures, un crédit CO_2 de 80 €/t entraîne un prix de vente du méthane de 2,937 €/kg (224,2 €/MWh). En général, le prix du méthane diminuerait avec l'augmentation du crédit CO_2. Cet impact bénéfique des crédits CO_2 encouragerait la mise en place future de système P2G dans le cadre de la transition énergétique et de la stratégie de stockage.

Perspectives

L'étude paramétrique suggère la nécessité de poursuivre la recherche sur les variations des coûts d'exploitation et d'investissement, ainsi que sur les projections futures des coûts. Cela implique une analyse approfondie des coûts de l'électricité, y compris les énergies renouvelables et l'électricité du réseau français, ainsi que le coût du captage du CO_2 à partir de différentes technologies. Les dépenses en investissement, telles que la durée de vie et le coût de l'électrolyseur MCEC, doivent également être examinées. L'état actuel de la durée de vie du MCEC sera analysé, et une étude de planification de la technologie MCEC sera réalisée pour déterminer ses courbes d'apprentissage.

Concernant les coûts de l'électricité, la principale préoccupation réside dans les OPEX de l'électrolyseur MCEC, qui consomme le plus d'énergie électrique dans l'usine Power-to-Gas. Le coût de l'électricité dépend du coût de la source d'énergie renouvelable. Selon l'Agence internationale des énergies renouvelables (IRENA) [225], les coûts actualisés de différentes sources d'énergie renouvelable ont diminué entre 2010 et 2021. Par exemple, le coût de l'électricité produite par des éoliennes terrestres était d'environ 30 €/MWh en 2021, tandis que celui de l'électricité photovoltaïque solaire était d'environ 45 €/MWh. Cependant, l'électrolyseur MCEC devrait s'appuyer sur l'électricité du réseau pendant plus de 3000 heures par an si l'énergie renouvelable est utilisée de manière intermittente pour le stockage. Par conséquent, le coût de l'électricité doit prendre en compte à la fois le coût actualisé des énergies renouvelables et le prix de l'électricité du réseau, qui peut varier en fonction de facteurs tels que le mix énergétique et les politiques. En France, le prix de l'électricité sur le marché spot a connu des variations importantes, atteignant plus de 100 €/MWh en septembre 2022, mais a baissé pour atteindre environ 100 €/MWh en avril 2023.

Le coût du captage du CO_2 dépend de la technologie utilisée et de divers facteurs tels que la concentration en CO_2, l'emplacement de l'usine, l'approvisionnement énergétique et l'intégration avec l'installation [242]. Le coût peut varier de 13 à 23 €/t pour les flux de CO_2 hautement concentrés à plus de 91 €/t pour les flux plus dilués [242]. Atteindre un faible coût de CO_2 de 20 à 40 €/t semble réalisable, notamment pour les procédés captant le CO_2 à partir de sources hautement concentrées.

La durée de vie de la MCEC reste incertaine, bien que les MCFC aient dépassé les 40000 heures en mode pile à combustible. Les études menées par Hu et al. (2014) [58] ont montré que la MCEC

présente de meilleures performances électrochimiques en mode MCEC. Cependant, des problèmes de dégradation peuvent survenir pendant le mode d'électrolyse en raison de divers facteurs, tels que la perte d'électrolyte, l'instabilité chimique de l'électrode d'oxygène NiO, la réduction de la porosité des électrodes et la corrosion du collecteur de courant d'oxygène [73]. Des stratégies telles que des technologies avancées de modification de surface et de revêtement ont été proposées pour augmenter la stabilité des électrodes conventionnelles et des collecteurs de courant en mode inverse des MCFC.

Le coût de la MCEC dépend des améliorations technologiques et la capacité de production, entraînant une réduction du coût par capacité installée. Toutefois, l'état actuel du coût de la MCEC n'est pas disponible publiquement, c'est pourquoi une feuille de route sur la technologie MCFC a été réalisée. La courbe d'apprentissage de la technologie MCFC (Figure 5.28) montre l'évolution du coût par kW en fonction de la capacité installée cumulée depuis sa commercialisation en 2003.

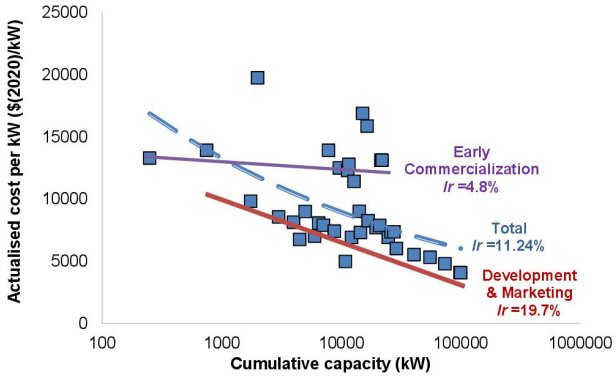

Figure 5.28: Courbe d'apprentissage du MCFC.

Le coût a révélé une diminution avec un taux d'apprentissage de 11,24%. La réduction des coûts est divisée en deux étapes : la phase de commercialisation précoce et la phase de développement et de marketing. Le coût de la MCEC peut devenir compétitif, se situant entre 1700 €/kW et 2600 €/kW, lorsque la capacité installée totale dépasse 1000 MW (1000000 kW), selon la plage de la courbe d'apprentissage totale présentée dans la Figure 5.29. En 2019, la capacité installée totale avait atteint 100 MW. Selon une étude de marché réalisée par "Inkwood Research", une société américaine de recherche sur le marché [249], on prévoit qu'une fourchette de coût de 2500 $/kW à 4500 $/kW sera atteinte en 2028 avec une capacité totale de 500 MW. Par conséquent, le coût des MCFC pourrait atteindre 1500-2000 €/kW en 2030 s'il y a une augmentation rapide de la capacité installée de MCFC au cours des prochaines années, comme le montre la Figure 5.30.

Bien que les MCFC aient connu un succès technique en mode pile à combustible, des recherches complémentaires sont nécessaires pour améliorer les matériaux d'électrode pour leur fonctionnement inversé en MCEC et MCFC. Cependant, comme l'étude de sensibilité l'a démontré, le coût du MCEC a peu d'effet sur le prix du méthane sans l'amélioration de sa durée de vie. Par conséquent, l'objectif principal est d'atteindre une durée de vie de 40000 h pour le MCEC. Si l'amélioration des matériaux d'électrode peut permettre d'atteindre cette durée de vie tout en maintenant le prix actuel des MCFC par kW, le MCEC serait une technologie d'électrolyse attrayante pour le stockage d'énergie renouvelable et la valorisation du CO_2 à l'avenir.

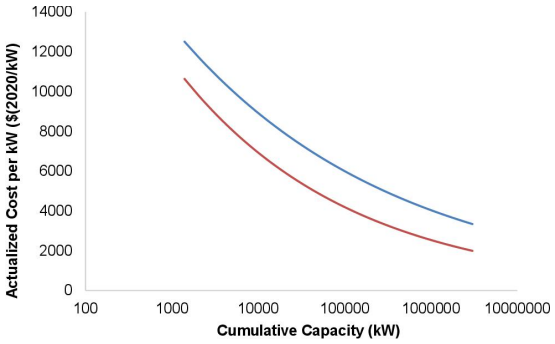

Figure 5.29: Courbe d'apprentissage totale du MCFC.

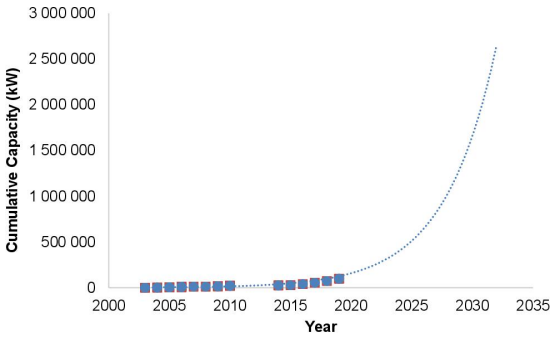

Figure 5.30: Capacité installée cumulée en kW au fil des ans.

Conclusion

Une évaluation économique du procédé Power-to-SNG utilisant un électrolyseur à haute température à carbonates fondus (MCEC) a été réalisée. L'étude a évalué le coût actuel de production de méthane et a effectué une analyse de sensibilité pour évaluer la faisabilité économique. Les résultats ont révélé que la durée de vie et le coût de l'électrolyseur étaient les principaux contributeurs aux coûts de production, tandis que les dépenses de fonctionnement avaient un impact négligeable. Les facteurs de coût optimaux ont été identifiés, permettant une tarification compétitive inférieure à 300 €/MWh. Cependant, le procédé n'est actuellement pas économiquement compétitif par rapport aux méthodes conventionnelles. Les dépenses opérationnelles doivent être faibles, avec des coûts de CO_2 de 20 à 40 €/t et des coûts d'électricité de 20 à 80 €/MWh, tandis que le coût de l'électrolyseur doit être inférieur à 2000 €/kW, sa durée de vie supérieure à 30000 h et que l'installation doit fonctionner pendant plus de 3000 heures par an. De plus, l'étude de l'impact de la pénalité CO_2 a montré que le coût de production du méthane diminuerait avec une augmentation des crédits CO_2.

La perspective future pour atteindre des coûts de production compétitifs de substitut de gaz naturel (SNG) a également été évaluée. Les coûts de l'électricité devraient diminuer de manière significative, mais un minimum de 3000 heures d'approvisionnement en électricité par an est nécessaire pour bénéficier d'un avantage économique. Un soutien du réseau peut être nécessaire en cas de capacité renouvelable insuffisante. Malgré les coûts élevés de l'électricité du réseau en France en raison de problèmes géopolitiques, une diminution est prévue après la maintenance des réacteurs nucléaires. Les coûts de captage du CO_2 sont faibles pour diverses technologies, ce qui rend les objectifs de coût du CO_2 réalisables. Cependant, les dépenses en investissement restent un défi, car la durée de vie et le coût de l'électrolyseur MCEC sont inconnus, et plusieurs tests doivent être effectués pour déterminer sa durée de vie. En revanche, les courbes d'apprentissage de la technologie MCFC ont révélé des réductions potentielles de coûts d'ici 2030 avec une fourchette de coûts de 1500 à 2000 €/kW. Des améliorations de la durée de vie et du coût de l'électrolyseur sont essentielles pour atteindre des coûts de production compétitifs de SNG. Bien que les coûts d'exploitation montrent des perspectives prometteuses, il est essentiel de s'attaquer aux dépenses en investissement, y compris la durée de vie et le coût de l'électrolyseur, pour une production économiquement viable substitut de gaz naturel.

Conclusion and Perspectives

Conclusions of the study

Power-to-Gas system serves as a way out for two main issues. On the one hand, it fulfills the growing necessity for energy storage related to integrating renewable energy into the power grid. On the other hand, it can provide an effective route for the sequestration and the re-use of the captured CO_2 in the form of synthetic fuels. This work's main objective is to demonstrate this system's capability using molten carbonate electrolysis cells from technical and economic standpoints.

The first part of the study provided a global overview to explain the rationale behind the focus on Power-to-Gas systems. The urgent global warming and climate change issue has led to adopting energy transition and decarbonization strategies to achieve a zero-carbon future. These strategies involve the widespread integration of renewable energy sources to replace polluting fossil fuels. However, the intermittent nature of renewable sources necessitates using energy storage systems to balance the supply and demand of energy. Among the various storage systems studied, chemical storage through Power-to-Gas systems has emerged as a leading solution due to its high storage capacity and long-term duration. The Power-to-Gas system comprises two main processes: electrolysis and methanation. The electrolysis process converts electrical power into hydrogen through water electrolysis. There are different electrolyzers, including well-established low-temperature ones (AEL and PEM) and high-temperature ones, focusing on SOEC electrolyzers. The methanation process aims to valorize captured CO_2 by converting it into substitute natural gas (SNG), which has become increasingly attractive given the recent rise in natural gas prices. Methanation is typically carried out in a series of adiabatic fixed-bed reactors with inter-cooling stages; however, isothermal reactors using structured reactor designs have proven to be more effective for Power-to-Gas applications. Indeed, Power-to-Gas technology is being implemented worldwide, with approximately 153 projects already implemented across 22 countries.

In the second part, two models were developed, the H_2O electrolysis model (Scenario I) and the co-electrolysis of CO_2 and H_2O model (Scenario II). Based on mass and energy balances and electrochemical approaches, the developed one-dimensional steady-state model provided satisfactory results that align with experimental studies and literature. Both models' results are comparable until a certain point, beyond which the co-electrolysis outputs diverge. These deviations were caused by the chemical extent of the CO_2 electrolysis reaction with the reverse water gas shift reaction. According to the obtained results, it can be concluded that CO_2 electrolysis imposes certain constraints on the applied current density for safe cell operation. This constraint is due to the massive consumption of CO_2 during the

co-electrolysis process, where the limiting current density is rapidly reached. Furthermore, the sensitivity analysis revealed the contradictory effects of H_2O, CO_2, and H_2 inlet flow rates on cell performance and syngas production. Therefore, optimal feed compositions are required for specific syngas ratios in methane synthesis. The study emphasized the need for further research and experimental investigation into co-electrolysis and its influence on cell performance and degradation. Considering co-electrolysis is critical for ensuring safe cell operation.

In the third part, a simulation of a 1 MW scale Power-to-SNG process using a co-electrolysis model of MCEC was performed and optimized via a profound sensitivity analysis, where the optimal conditions were selected. The simulation covers the electrolysis and the methane synthesis processes, starting from the raw material preparation for the syngas production, which undergoes further purification and compression to reach the methanation feed specifications, and ending by producing the substitute natural gas. In addition to the process optimization, a pinch analysis study was carried out to improve the process's energy efficiency by acting on the energy recovery and reuse possibilities. Thus, in the resulting process, the steam required for electrolysis was generated using the system's internal heat without needing any external energy for heating. The elimination of the external energy supply for heating showed an improvement in the system's overall performance, with an efficiency of 68.7%. Besides, the process demonstrated a methane production capacity of 1.3 t/day, ready for injection into the natural gas network.

The fourth part investigated the dynamic behavior of a Power-to-SNG system using a molten carbonate electrolyzer. The study includes developing and validating a dynamic model for the electrolyzer, analyzing its degradation over time, examining the system's response to changes in input variables, and evaluating cold start-up procedures. It also analyzed the dynamic behavior of the methanation process, considering reactor design and operating conditions. The findings revealed that the electrode's surface area degradation leads to decreased syngas production, requiring an increase in current to maintain the same production. The MCEC system showed a proportional response to changes in load and the number of cells, while the inlet flow rate caused reversible changes. Moreover, the study identified the most energy-efficient heating process for a cold start-up of the MCEC electrolyzer. The methanation process achieved high conversion and produced methane with desired quality.

Furthermore, coupling the Power-to-SNG system with intermittent renewable power was investigated, highlighting the system's sensitivity to power fluctuations. The variable power source was found to generate intermediate-stage syngas with high CO_2 and CO content. This gas enters the methanation reactor, producing SNG that fails to meet the minimum requirements for injection into the natural gas grid. It was also observed that wind power exhibited greater consistency than solar power. The total gas obtained in both winter and summer remains above the minimum CO_2 and CO levels: approximately 8% for CO_2 and 4% for CO in the case of wind power, and approximately 60% for CO_2 and 17% for CO in the case of solar power. Therefore, maintaining the desired compositions of SNG becomes challenging, necessitating additional purification or dilution with natural gas. Finally, possible enhancements were proposed, such as implementing a modular system with a control strategy to mitigate variability and considering a purification process if the desired gas quality cannot be achieved.

In the fifth part, an economic study was accomplished to comprehend the feasibility of such a process and identify the cost-driver parameter of the production cost of methane. The initial evaluation of methane production cost under current conditions revealed that the process is not economically competitive compared to conventional methane synthesis methods. A sensitivity analysis was then performed to identify the main cost drivers of methane production. The analysis showed that the electrolyzer's lifespan and cost significantly contributed to the production cost while operating expenses had a negligible impact. Optimizing the cost drivers could achieve competitive synthetic methane pricing below 300 €/MWh. The study concluded that the process could be economically feasible if the capital and operational expenses meet specific criteria, including a CO_2 cost of 20-40 €/t, an electricity cost of 20-80 €/MWh, a cell cost below 2,000 €/kW, a cell lifetime above 30,000 h, and the operating duration of the plant is more extended than 3,000 h/y. Additionally, the study explored the future perspective of achieving competitive production costs, considering factors such as the expected decrease in electricity cost from renewable sources and the low CO_2 capture cost. However, capital expenses, particularly the lifetime and cost of the molten carbonate electrolyzer, remained a significant obstacle that must be overcome to achieve competitive substitute natural gas production costs. While there is promise in operating cost reduction, there is a need to focus on improving capital expenses and optimizing the electrolyzer's lifetime and cost.

This process based on a molten carbonate electrolyzer can be intriguing for storing energy and reusing CO_2. However, significant advances in terms of technical and cost feasibility are required. From the technical viewpoint, it is recommended that the electrolyzer structure and electrolyte environment conditions be improved to enhance CO_2 and H_2O co-electrolysis and expand the operating current density range while avoiding the limiting state. In this manner, higher current densities could be applied, thus increasing syngas and methane production. Also, this process may be economically competitive with other technologies if the cell's lifetime is improved and the cost is reduced, in addition to a further increase in the carbon tax imposed on the CO_2 emissions.

Opening and Perspectives

This study's findings open up further exploration in modeling methodologies and experimental investigations. In modeling, there is an opportunity to dig into more complex aspects of the electrolyzer's functioning. More particularly, investigating the kinetics of the reactions involved in the co-electrolysis of H_2O and CO_2, as well as other potential chemical reactions occurring at the electrode interface, would be a valuable approach to consider. Additionally, enhancing the model by incorporating a detailed analysis of the three overpotential terms, which depend on the electrode's material and physical properties, could lead to further improvements. Regarding the experimental approach, further testing needs to be performed to comprehend the co-electrolysis process in the molten carbonate electrolysis cell and determine the lifetime of this cell during electrolysis mode.

Furthermore, the coupling of renewable energy with such technology revealed that it is highly sensitive to intermittent power load since it directly produces syngas with different hydrogen-to-carbon ratios, thus impacting the methane quality produced. Consequently, a well-controlled strategy must be developed to allow more flexibility for the system when integrated with renewable energy, thus producing the desired syngas ratio for the methanation process.

Lastly, considering that the Power-to-Gas system represents a means of reducing carbon emissions, it would be intriguing to initiate a preliminary study on the environmental implications of an integrated system incorporating MCEC technology compared to other technologies. Such a study could shed light on several important aspects, including the CO_2 impacts arising from roundtrip utilization and energy restitution, the water footprint associated with large-scale electrolysis, and an assessment of the environmental risks associated with the use of underground large-scale gas storage. Examining these elements would provide a comprehensive understanding of the environmental impact of this technology.

Conclusions et perspectives

Conclusions de l'étude

Le Power-to-Gas est un système qui constitue une solution à deux problèmes majeurs. D'une part, il répond à la nécessité croissante de stockage d'énergie liée à l'intégration des énergies renouvelables dans le réseau électrique. D'autre part, il offre une voie efficace pour la séquestration et la réutilisation du CO_2 capté sous forme de carburants synthétiques. L'objectif principal de ce travail est de démontrer les capacités de ce système en utilisant des cellules d'électrolyse à carbonates fondus d'un point de vue technique et économique.

La première partie de l'étude fournit un aperçu global pour expliquer les raisons qui motivent l'attention portée aux systèmes Power-to-Gas. L'urgence du problème du changement climatique a conduit à adopter des stratégies de transition énergétique et de décarbonisation visant à atteindre un avenir sans carbone. Ces stratégies impliquent l'intégration généralisée des sources d'énergie renouvelables pour remplacer les combustibles fossiles polluants. Cependant, la nature intermittente des sources renouvelables nécessite l'utilisation de systèmes de stockage d'énergie pour équilibrer l'offre et la demande d'énergie. Parmi les différents systèmes de stockage étudiés, le stockage chimique par le biais des systèmes Power-to-Gas s'est imposé comme une solution de premier plan en raison de sa grande capacité de stockage et de sa durée de stockage à long terme. Le système Power-to-Gas comprend deux procédés principaux : l'électrolyse et la méthanation. Le procédé d'électrolyse convertit l'énergie électrique en hydrogène par électrolyse de l'eau. Il existe différents types d'électrolyseurs: les électrolyseurs à basse température bien établis (AEL et PEM) et les électrolyseurs à haute température, axés sur les électrolyseurs SOEC. Le procédé de méthanation vise à valoriser le CO_2 capté en le convertissant en substitut de gaz naturel (SNG), ce qui est devenu de plus en plus attrayant compte tenu de la récente hausse des prix du gaz naturel. La méthanation est généralement réalisée dans une série de réacteurs adiabatiques à lit fixe avec des étapes d'inter-refroidissement ; cependant, des réacteurs isothermes utilisant des conceptions de réacteurs structurés se sont révélés plus efficaces pour les applications Power-to-Gas. En effet, la technologie Power-to-Gas est mise en œuvre dans le monde entier, avec environ 153 projets déjà réalisés dans 22 pays.

Dans la deuxième partie, deux modèles ont été développés : le modèle d'électrolyse de H_2O (scénario I) et le modèle de co-électrolyse de CO_2 et H_2O (scénario II). Basés sur des bilans de masse et d'énergie ainsi que des approches électrochimiques, les modèles unidimensionnels en régime permanent développés ont fourni des résultats satisfaisants qui concordent avec les études expérimentales et la littérature. Les

résultats des deux modèles sont comparables jusqu'à un certain point, au-delà duquel les sorties de co-électrolyse divergent. Ces écarts sont dus à l'extension chimique de la réaction d'électrolyse du CO_2 avec la réaction inverse de gaz à l'eau. Selon les résultats obtenus, on peut conclure que l'électrolyse du CO_2 impose certaines contraintes sur la densité de courant appliquée pour un fonctionnement sûr de la cellule. Cette contrainte est due à la consommation massive de CO_2 pendant le procédé de co-électrolyse, où la densité de courant limite est atteinte rapidement. De plus, l'analyse de sensibilité a révélé les effets contradictoires des débits d'entrée de H_2O, CO_2 et H_2 sur les performances de la cellule et la production de gaz de synthèse. Par conséquent, des compositions d'alimentation optimales sont nécessaires pour obtenir des ratios de gaz de synthèse spécifiques dans la synthèse du méthane. L'étude a donc souligné la nécessité de poursuivre les recherches et les investigations expérimentales sur la co-électrolyse et son influence sur les performances et la dégradation de la cellule. La prise en compte de la co-électrolyse est essentielle pour garantir un fonctionnement sûr de la cellule.

Dans la troisième partie, une simulation d'un procédé Power-to-SNG à l'échelle de 1 MW utilisant le modèle de co-électrolyse de MCEC a été réalisée et optimisée grâce à une analyse de sensibilité approfondie, permettant de sélectionner les conditions optimales. La simulation couvre à la fois les procédés d'électrolyse et de synthèse du méthane, en commençant par la préparation des matières premières pour la production du gaz de synthèse, qui subit ensuite une purification et une compression supplémentaires pour atteindre les spécifications d'alimentation de la méthanation, et se termine par la production du substitut de gaz naturel. En plus de l'optimisation du procédé, une étude d'analyse de pincement a été réalisée pour améliorer davantage l'efficacité énergétique du procédé en agissant sur les possibilités de récupération et de réutilisation de l'énergie. Ainsi, dans le procédé obtenu, la vapeur nécessaire à l'électrolyse était générée à l'aide de la chaleur interne du système, sans nécessiter d'énergie externe pour le chauffage. L'élimination de l'apport d'énergie externe pour le chauffage a permis d'améliorer les performances globales du système, avec un rendement de 68,7%. De plus, le procédé a démontré une capacité de production de méthane de 1,3 t/jour, prêt à être injecté dans le réseau de gaz naturel.

La quatrième partie s'est penchée sur le comportement dynamique d'un système Power-to-SNG utilisant un électrolyseur à carbonates fondus. L'étude comprend le développement et la validation d'un modèle dynamique pour l'électrolyseur, l'analyse de sa dégradation au fil du temps, l'examen de la réponse du système aux variations des variables d'entrée et l'évaluation des procédures de démarrage à froid. Elle a également analysé le comportement dynamique du procédé de méthanation, en tenant compte de la conception du réacteur et des conditions de fonctionnement. Les résultats ont révélé que la dégradation de la surface de l'électrode entraîne une diminution de la production de gaz de synthèse, nécessitant une augmentation du courant pour maintenir la même production. Le système MCEC a montré une réponse proportionnelle aux variations de charge et du nombre de cellules, tandis que le débit d'entrée a provoqué des variations réversibles. De plus, l'étude a identifié le procédé de chauffage le plus économe en énergie pour un démarrage à froid de l'électrolyseur MCEC. Le procédé de méthanation a atteint une conversion élevée et a produit du méthane de qualité souhaitée.

De plus, le couplage du système Power-to-SNG avec une alimentation intermittente d'énergie renouvelable a été étudié, mettant en évidence la sensibilité du système aux fluctuations de puissance. Il a été constaté que la source d'énergie variable génère un gaz de synthèse à une phase intermédiaire avec

une teneur élevée en CO_2 et CO. Ce gaz entre dans le réacteur de méthanation, produisant un substitut de gaz naturel qui ne répond pas aux exigences minimales pour être injecté dans le réseau de gaz naturel. Il a également été observé que l'énergie éolienne présente une plus grande cohérence que l'énergie solaire. La quantité totale de gaz obtenue en hiver et en été reste supérieure aux niveaux minimaux de CO_2 et CO : environ 8% pour le CO_2 et 4% pour le CO dans le cas de l'énergie éolienne, et environ 60% pour le CO_2 et 17% pour le CO dans le cas de l'énergie solaire. Par conséquent, maintenir les compositions souhaitées de substitut de gaz naturel devient un défi, ce qui nécessite une purification supplémentaire ou une dilution avec du gaz naturel. Enfin, des améliorations possibles ont été proposées, telles que la mise en œuvre d'un système modulaire avec une stratégie de contrôle pour atténuer la variabilité et la prise en compte d'un procédé de purification si la qualité du gaz souhaitée ne peut pas être atteinte.

La cinquième partie a consisté en une étude économique visant à comprendre la faisabilité d'un tel procédé et à identifier le paramètre déterminant pour le coût de production du méthane. L'évaluation initiale du coût de production du méthane dans les conditions actuelles a révélé que le procédé n'est pas économiquement compétitif par rapport aux méthodes conventionnelles de synthèse du méthane. Une analyse de sensibilité a ensuite été réalisée pour identifier les principaux facteurs de coût de production du méthane. L'analyse a montré que la durée de vie et le coût de l'électrolyseur contribuaient de manière significative au coût de production, tandis que les dépenses de fonctionnement avaient un impact négligeable. L'optimisation des facteurs de coût permettrait d'atteindre un prix compétitif du substitut de gaz naturel inférieur à 300 €/MWh. L'étude a conclu que le procédé pourrait être économiquement viable si les dépenses en capital et les dépenses opérationnelles répondaient à des critères spécifiques, notamment un coût du CO_2 compris entre 20 et 40 €/t, un coût de l'électricité compris entre 20 et 80 €/MWh, un coût de la cellule inférieur à 2000 €/kW, une durée de vie de la cellule supérieure à 30 000 h et une durée de fonctionnement de l'installation supérieure à 3 000 h/an. De plus, l'étude a exploré les perspectives futures de réduction des coûts de production compétitifs, en tenant compte de facteurs tels que la baisse attendue du coût de l'électricité provenant de sources renouvelables et du faible coût de captage du CO_2. Cependant, les dépenses en capital, en particulier la durée de vie et le coût de l'électrolyseur à carbonates fondus, demeurent un obstacle important qui doit être surmonté pour atteindre des coûts de production compétitifs du substitut de gaz naturel. Bien qu'il y ait des perspectives de réduction des coûts d'exploitation, il est nécessaire de se concentrer sur l'amélioration des dépenses en capital et sur l'optimisation de la durée de vie et du coût de l'électrolyseur.

Cette technologie basée sur un électrolyseur à carbonates fondus peut être un concept fascinant de stockage d'énergie et de réutilisation du CO_2. Cependant, des avancées significatives en termes de faisabilité technique et économique sont nécessaires. Du point de vue technique, il est recommandé d'améliorer la structure de l'électrolyseur et les conditions environnementales de l'électrolyte afin d'améliorer la co-électrolyse du CO_2 et de H_2O et d'élargir la plage de densité de courant de fonctionnement tout en évitant l'état limite. De cette manière, des densités de courant plus élevées pourraient être appliquées, ce qui se traduirait par une augmentation de la production de gaz de synthèse et de méthane. De plus, ce procédé peut être économiquement compétitif par rapport à d'autres technologies si la durée de vie de la cellule est améliorée et que le coût est réduit, en plus d'une augmentation supplémentaire de la taxe carbone imposée aux émissions de CO_2.

Ouverture et perspectives

Les résultats de cette étude ouvrent sur de nouvelles perspectives pour l'exploration des méthodologies de modélisation et les investigations expérimentales. Du point de vue de la modélisation, il existe une opportunité d'approfondir les aspects complexes du fonctionnement de l'électrolyseur. Plus particulièrement, l'étude de la cinétique des réactions impliquées dans la co-électrolyse de H_2O et CO_2, ainsi que d'autres réactions chimiques potentielles se produisant à l'interface de l'électrode, serait une approche précieuse à considérer. De plus, améliorer le modèle en intégrant une analyse détaillée des trois termes de surtension, qui dépendent du matériau de l'électrode et de ses propriétés physiques, pourrait conduire à des améliorations supplémentaires. En ce qui concerne l'approche expérimentale, des tests supplémentaires doivent être réalisés pour bien comprendre le procédé de co-électrolyse dans la cellule d'électrolyse à carbonates fondus et déterminer la durée de vie de cette cellule en mode électrolyse.

De plus, le couplage de l'énergie renouvelable avec une telle technologie a révélé qu'elle est très sensible aux charges d'énergie intermittentes, car elle produit directement du gaz de synthèse avec différents ratios hydrogène-carbone, ce qui impacte la qualité du méthane produit. Par conséquent, il est nécessaire de développer une stratégie de contrôle adéquate pour permettre une plus grande flexibilité du système lorsqu'il est intégré à l'énergie renouvelable, produisant ainsi le rapport de gaz de synthèse souhaité pour le procédé de méthanation.

Enfin, étant donné que le système Power-to-Gas représente un moyen de réduire les émissions de carbone, il serait intéressant d'initier une étude préliminaire sur les implications environnementales d'un système intégré incorporant la technologie MCEC par rapport à d'autres technologies. Une telle étude pourrait éclairer plusieurs aspects importants, notamment les impacts de CO_2 résultant de l'utilisation circulaire et de la restitution d'énergie, l'empreinte hydrique associée à l'électrolyse à grande échelle, et une évaluation des risques environnementaux liés à l'utilisation d'un stockage de gaz souterrain à grande échelle. L'examen de ces éléments permettrait de mieux comprendre l'impact environnemental de cette technologie.

Appendix A

Thermodynamic Properties

1 Free Energy

The free energy is calculated using data and equations from NIST Webbook [135], as a function of temperature t, equivalent to T in Kelvin K divided by 1,000 as reported in NIST Webbook. The free energy equation used in this work is given in Eq. A.1, where its coefficients are determined according to the reaction. The coefficients for the reverse water gas shift reaction "RWGS" are presented in Table A.1. The coefficients used for H_2O electrolysis free energy and CO_2 electrolysis free energy are illustrated in Table A.2 and Table A.3, respectively.

$$\Delta G^0 = A + Bt\ln t + Ct + Dt^2 + Et^3 + Ft^4 + \frac{G}{t} \tag{A.1}$$

Coefficients	Value	Unit
A	44.689	kJ/mol
B	2.404	kJ/mol.K
C	-52.206	kJ/mol.K
D	15.522	kJ/mol·K^2
E	-5.518	kJ/mol·K^3
F	0.865	kJ/mol·K^4
G	-0.254	kJ.K/mol

Table A.1: Coefficients of the RWGS free energy.

Coefficients	Value	Unit
A	235.24	kJ/mol
B	-17.99	kJ/mol.K
C	-49.414	kJ/mol.K
D	6.83	kJ/mol·K^2
E	-0.441	kJ/mol·K^3
F	-0.013	kJ/mol·K^4
G	0.306	kJ.K/mol

Table A.2: Coefficients of the H_2O electrolysis free energy.

Coefficients	Value	Unit
A	279.92	kJ/mol
B	-15.586	kJ/mol.K
C	-101.62	kJ/mol.K
D	22.352	kJ/mol·K^2
E	-5.959	kJ/mol·K^3
F	0.852	kJ/mol·K^4
G	0.052	kJ.K/mol

Table A.3: Coefficients of the CO_2 Electrolysis free energy.

2 Heat Enthalpy

$$\Delta H = A't + \frac{B'}{2}t^2 + \frac{C'}{3}t^3 + \frac{D'}{4}t^4 - \frac{E'}{t} + F' \tag{A.2}$$

Coefficients	Value	Unit
A'	-2.4039	kJ/mol.K
B'	-31.044	kJ/mol·K^2
C'	33.107	kJ/mol·K^3
D'	-10.381	kJ/mol·K^4
E'	0.508	kJ.K/mol
F'	44.698	kJ/mol

Table A.4: Coefficients of the RWGS Heat Enthalpy.

Coefficients	Value	Unit
A'	17.99	kJ/mol.K
B'	-13.66	kJ/mol·K^2
C'	2.645	kJ/mol·K^3
D'	0.156	kJ/mol·K^4
E'	-0.612	kJ.K/mol
F'	235.24	kJ/mol

Table A.5: Coefficients of the H_2O electrolysis Heat Enthalpy

Coefficients	Value	Unit
A'	15.586	kJ/mol.K
B'	-44.704	kJ/mol·K^2
C'	35.752	kJ/mol·K^3
D'	-10.226	kJ/mol·K^4
E'	-0.103	kJ.K/mol
F'	279.94	kJ/mol

Table A.6: Coefficients of the CO_2 Electrolysis Heat Enthalpy.

3 Heat Capacity

$$C_p^i = A_i + B_i t + C_i t^2 + D_i t^3 - \frac{E_i}{t^2} \tag{A.3}$$

	i						
Coefficients	**H_2O**	**H_2**	**O_2**	**CO_2**	**CO**	**N_2**	**Unit**
A_i	30.092	33.066	30.032	24.997	25.568	19.506	kJ/mol.K
B_i	6.683	-11.363	8.773	55.187	6.096	19.887	kJ/mol·K^2
C_i	6.793	11.433	-3.988	-33.691	4.055	-8.599	kJ/mol·K^3
D_i	-2.534	-2.773	0.788	7.948	-2.671	1.370	kJ/mol·K^4
E_i	0.082	-0.159	-0.742	-0.137	0.131	0.528	kJ.K/mol

Table A.7: Coefficients of the Heat Capacity of each component i.

4 Entropy

$$S = \alpha T^2 + \beta T + \gamma \tag{A.4}$$

$$\alpha = constant \tag{A.5}$$

$$\beta = a + bP + cP^2 + dP^3 + eP^4 + fP^5 \tag{A.6}$$

$$\gamma = a' + b'P + c'P^2 + d'P^3 + e'P^4 + f'ln(P/P_{ref}) \tag{A.7}$$

where:

$\boldsymbol{S}$	kJ/kmol.K
$\boldsymbol{P}$	bar
$\boldsymbol{T}$	°C

the conversion is within the equation

Coefficients	**H_2O**	**CO_2**	**CH_4**	**O_2**	**H_2**	**CO**	**N_2**
$\boldsymbol{\alpha}$	-2×10^{-5}	-3×10^{-5}	-2×10^{-5}	-2×10^{-5}	-2×10^{-5}	-2×10^{-5}	-2×10^{-5}
$\boldsymbol{\beta}$	$a + bP + cP^2 + dP^3 + eP^4 + fP^5$						
a	0.734	0.0961	0.0968	0.0669	0.0605	0.0622	0.0614
b	-7.13×10^{-4}	-2.08×10^{-3}	3.05×10^{-3}	-2.06×10^{-3}	0	0	0
c	4.48×10^{-4}	1.66×10^{-3}	-2.15×10^{-3}	1.44×10^{-3}	0	0	0
d	-9.03×10^{-5}	-5.67×10^{-4}	6.96×10^{-4}	-4.42×10^{-4}	0	0	0
e	6.25×10^{-6}	8.75×10^{-5}	-1.04×10^{-4}	6.25×10^{-5}	0	0	0
f	0	-5×10^{-6}	5.83×10^{-6}	-3.33×10^{-6}	0	0	0
$\boldsymbol{\gamma}$	$a' + b'P + c'P^2 + d'P^3 + e'P^4 + f'ln(P/P_{ref})$						
a'	-32.972	15.076	-8.362	1.3724	2.3552	91.706	2.7917
b'	-12.35	-12.971	1.3724	0	0	0	0
c'	3.012	3.342	0	0	0	0	0
d'	-0.403	-0.465	0	0	0	0	0
e'	0.021	0.025	0	0	0	0	0
f'	0	0	0	-8.362	-8.315	-8.35	-8.335

Table A.8: Coefficients of the Heat Entropy of each component.

Coefficients	RWGS	H_2O Electrolysis	CO_2 Electrolysis
α	1×10^{-5}	-1×10^{-5}	0
β			
a	-0.021	0.021	-4.5×10^{-4}
b	1.37×10^{-3}	-3.15×10^{-4}	1.05×10^{-3}
c	-1.21×10^{-3}	2.71×10^{-4}	-9.44×10^{-4}
d	4.76×10^{-4}	-1.31×10^{-4}	3.46×10^{-4}
e	-8.13×10^{-5}	2.5×10^{-5}	-5.63×10^{-5}
f	5×10^{-6}	-1.67×10^{-6}	3.33×10^{-6}
γ			
a'	41.303	36.013	77.316
b'	0.621	12.35	12.971
c'	-0.33	-3.012	-3.342
d'	0.062	0.403	0.465
e'	-0.004	-0.021	-0.025
f'	0.035	-12.496	-12.531

Table A.9: Coefficients of the Heat Entropy of the three reactions: RWGS, H_2O Electrolysis, and CO_2 Electrolysis.

To supply the specific amount of heat absorbed from the reactor, an energy balance on the reactor is conducted, and the cooling water molar flow rate required is calculated, after assuming the value of the temperature change of the water. In this balance, the heat removed from the reactor to remain isothermal, represented by the syn gas molar flow rate $\dot{n}_{syngas}$ multiplied by the methane synthesis reaction's enthalpy $\Delta H_{CH_4\ reaction}$, is equal to the heat supplied to the cooling water, as shown in Eq. A.8. The heat absorbed by the cooling water is composed of two terms, the heat required to increase the water temperature which is determined by multiplying the molar flow rate of the cooling water $\dot{n}_{Cooling\ Water}$, the heat capacity of water $C_{p,\ water}$ (kJ/kmol.K), and the water's temperature change ΔT ($\dot{n}_{Cooling\ Water} \times C_{p,water}\Delta T$), and the heat of evaporation of water ($\dot{n}_{Cooling\ Water} \times \Delta H_{evaporation}$), where $\Delta H_{evaporation}$ represents the heat of evaporation or latent heat of water (kJ/kmol).

$$\begin{aligned} \dot{n}_{syngas} \times \Delta H_{CH_4\ reaction} &= \dot{n}_{Cooling\ Water} \times (C_p^{H_2O}\Delta T + \Delta H_{evaporation}) \\ \dot{n}_{Cooling\ Water} &= \frac{\dot{n}_{syngas} \times \Delta H_{CH_4\ reaction}}{C_p^{H_2O}\Delta T + \Delta H_{evaporation}} \end{aligned} \tag{A.8}$$

Appendix B

Process Flow Diagram Stream Details

The operating condition (Temperature T, Pressure P, Vapor Fraction), flowrate F and composition (comp*) of the overall process streams from the Electrolysis to the Methane Synthesis are presented in the tables below. Table B.1 displays the streams' results of the electrolysis process in Figures 3.2 and 3.22. Table B.2 presents the streams' of the syngas purification and post-treatment process in Figures 3.3 and 3.22. Finally, Tables B.3 and B.4 include the streams' conditions for the methane synthesis using TREMP's process (Figure 3.4) and isothermal process (Figure 3.6), respectively.
($\sim$ *refers to a very small composition (traces)*) VF: Vapor Fraction

Stream Name in Figure 3.2	Stream Name in Figure 3.22	From	To	T (°C)	P (bar)	VF	F (kmol/h)	H_2O comp*	CO_2 comp*	H_2 comp*	CO comp*	O_2 comp*
CO2FEED												
CO2STORE	**1**	-	Valve	25	50	1	56.6868	-	1	-	-	-
EXPCO2	**2**	VALVE	HXs (HEATER1)	-39.42	1.203	1	56.6868	-	1	-	-	-
CO2FEED		HXs (HEATER1)	SPLIT	7.19	1.133	1	56.6868	-	1	-	-	-
Anode Loop												
CO2ANOD	**CO2ANODE**	SPLIT	RMIXER2	7.19	1.133	1	39.6808	-	1	-	-	-
TOANODE		RMIXER2	HXANODE (HEATER4)	50.57	1.12	1	54.6717	-	0.969	-	-	0.031
INANODE	**10**	HXANODE (HEATER4)	MCEC	650	1.133	1	54.6717	-	0.969	-	-	0.031
OUTANODE		MCEC	HXCATH (COOLER1)	663.25	1.12	1	74.9544	-	0.887	-	-	0.113
OUTANOD1		HXCATH (COOLER1)	SPLIT2	159.59	1.12	1	74.9544	-	0.887	-	-	0.113
RECYCLE2		SPLIT2	RMIXER2	159.59	1.12	1	14.9909	-	0.887	-	-	0.113
OUTANOD2	**12**	SPLIT2	HX (COOLER2)	159.59	1.12	1	59.5935	-	0.887	-	-	0.113
OUTANOD3	**13**	HX (COOLER2)	SEP	103	1.12	1	59.5935	-	0.887	-	-	0.113
H2OFEED												
H2O	**5**	-	PUMP	25	1.013	0	31.4927	1	-	-	-	-
H2OPUMP		PUMP	MIXER1	25	1.133	0	31.4927	1	-	-	-	-
Cathode Loop												
CO2CATH	**CO2CATH**	SPLIT	MIXER1	7.19	1.133	1	17.006	-	1	-	-	-
FUELMIX	**FUELMIX**	MIXER1	STEAM GENERATION (HEATER2)	18.58	1.133	0.35	49.3805	0.6556	0.3444	-	-	-
FUELMIX1		STEAM GENERATION (HEATER2)	RMIXER1	96	1.133	1	49.3805	0.6556	0.3444	-	-	-
TOCATH	**7**	RMIXER1	HXCATH (HEATER3)	92.25	1.013	1	83.475	0.6323	0.2057	0.1222	0.0397	-
INCATH	**INCATH**	HXCATH (HEATER3)	MCEC	650	1.013	1	83.475	0.6323	0.2057	0.1222	0.0397	-
OUTCATH	**OUTCATH**	MCEC	HXANODE (COOLER3)	663.25	1.013	1	69.9527	0.6087	0.0047	0.2917	0.0945	-
OUTCATH1		HXANODE (COOLER3)	SPLIT1	86.14	1.013	0.975	69.9527	0.6087	0.0047	0.2917	0.0945	-
RECYCLE1		SPLIT1	RMIXER1	86.14	1.013	1	34.0945	0.5985	0.0048	0.2993	0.0973	-
OUTCATH2	**14**	SPLIT1	Process 2	86.14	1.013	0.975	34.9763	0.6087	0.0047	0.2917	0.0945	-

Table B.1: Results of the streams involved in the Electrolysis process, Figures 3.2 and 3.22.

Stream Name in Figure 3.3	Stream Name in Figure 3.22	From	To	T (°C)	P (bar)	VF	F (kmol/h)	H_2O comp*	CO_2 comp*	H_2 comp*	CO comp*
OUTCATH2	**14**	SPLIT1	HX (COOLER4)	86.14	1.013	0.975	34.9763	0.6087	0.0047	0.2917	0.0945
OUTCATH3	**15**	HX + FAN (COOLER4)	DRUM1	25	0.99	0.4	34.9763	0.6087	0.0047	0.2917	0.0945
GAS		DRUM1	HX (COOLER5)	25	0.99	1	14.091	0.0322	0.0092	0.724	0.235
WATER		DRUM1		86.14	1.013	0.975	34.9763	0.6087	0.0047	0.2917	0.0945
GAS1		HX (COOLER5)	DRUM2	5	0.97	0.977	14.091	0.0322	0.0092	0.724	0.235
WATER1		DRUM2		5.61	0.97	0	0.33	0.985	0.0144	∼	∼
INCOMP1		DRUM2	COMP1	5.61	1	0.977	13.761	0.0093	0.009	0.7415	0.24
GASCOMP1		COMP1	HX(COOLER6)	116.73	2.43	1	13.761	0.0093	0.009	0.7415	0.24
INCOMP2		HX (COOLER6)	COMP2	30	2.43	1	13.761	0.0093	0.009	0.7415	0.24
GASCOMP2		COMP2	HX (COOLER7)	118.24	4.854	1	13.761	0.0093	0.009	0.7415	0.24
INCOMP3		HX (COOLER7)	COMP3	30	4.854	1	13.761	0.0093	0.009	0.7415	0.24
GASCOMP3		COMP3	HEATER5	228.7	20	1	13.761	0.0093	0.009	0.7415	0.24
SYNGAS		HEATER5	Process 3	300	20	1	13.761	0.0093	0.009	0.7415	0.24

Table B.2: Results of the streams involved in the Syngas Purification and Post-treatment for methanation process, Figures 3.3 and 3.22.

Stream Name in Figure 3.4	From	To	T (°C)	P (bar)	VF	F (kmol/h)	H_2O comp*	CO_2 comp*	H_2 comp*	CO comp*	CH_4 comp*
SYNGAS	HEATER5	R1	300	20	1	13.761	0.0093	0.009	0.7415	0.24	-
S1	R1	COOL1	684.85	20	1	34.5415	0.2662	0.058	0.337	0.0423	0.2963
S2	COOL1	SPLIT	300	20	1	34.5415	0.2662	0.058	0.337	0.0423	0.2963
RECYCLE	SPLIT	R1	300	20	1	25.9061	0.2662	0.058	0.337	0.0423	0.2963
S3	SPLIT	R2	300	20	1	8.63538	0.2662	0.058	0.337	0.0423	0.2963
S4	R2	COOL2	562.54	20	1	7.74694	0.3714	0.0477	0.186	0.0072	0.3876
S5	COOL2	R3	300	20	1	7.74694	0.3714	0.0477	0.186	0.0072	0.3876
S6	R3	COOL3	406.87	20	1	7.2066	0.467	0.0212	0.0576	∼	0.454
S7	COOL3	DRUM1	120	20	0.57	7.2066	0.467	0.0212	0.0576	∼	0.454
WATER	DRUM1		120	20	0	3.118	0.945	∼	∼	∼	0.055
S8	DRUM1	HEATER	120	20	1	4.088	0.1022	0.037	0.1016	0.0004	0.7589
S9	HEATER	R4	250	20	1	4.088	0.1022	0.037	0.1016	0.0004	0.7589
S10	R4	COOL5	333.59	20	1	3.9104	0.152	0.0162	0.0155	∼	0.816
S11	COOL5	DRUM2	25	20	0.784	3.9104	0.152	0.0162	0.0155	∼	0.816
RESIDUE	DRUM2	-	25	20	0	0.845	0.6986	0.025	∼	∼	0.276
METHANE	DRUM2	NG grid	25	20	1	3.066	0.0013	0.014	0.02	∼	0.965

Table B.3: Results of the streams involved in the Methane Synthesis process, Figure 3.4.

Stream Name in Figure 3.6	From	To	T (°C)	P (bar)	Vapor Fraction	F (kmol/h)	H_2O comp*	CO_2 comp*	H_2 comp*	CO comp*	CH_4 comp*
SYNGAS	HEATER5	ISOREACT	300	20	1	13.761	0.0093	0.009	0.7415	0.24	-
CH4GAS	ISOREACT	HX +COOLER (COOLER8)	300	20	1	7.0618	0.4986	0.011	0.0158	∼	0.4743
CH4GAS1	HX +COOLER (COOLER8)	DRUM	25	19.6	0.5	7.0618	0.4986	0.011	0.0158	∼	0.4743
RESIDUE1	DRUM	-	25	19.6	0	3.5143	0.9999	∼	∼	∼	∼
METHANE	DRUM1	NG grid	25	19.6	1	3.54754	0.0019	0.022	0.031	∼	0.9441

Table B.4: Results of the streams involved in the Methane Synthesis process, Figure 3.6.

List of Publications

Published articles

Dayan Monzer, Rodrigo Rivera-Tinoco, Chakib Bouallou. "*Investigation of the Techno-Economical Feasibility of the Power-to-Methane Process Based on Molten Carbonate Electrolyzer*". Frontiers in Energy Research (2021).
DOI: 10.3389/fenrg.2021.650303

Dayan Monzer, Chakib Bouallou. "*CO_2 Capture and Purification for Use in the Molten Carbonate Electrolysis Cell*". Chemical Engineering Transactions (2022).
DOI: 10.3303/CET2294068

Erick Jair Reyes Rodriguez, **Dayan Monzer**, Chakib Bouallou. "*Study of interest for integrating wind energy with a power-to-methane system based on the Molten Carbonate Electrolyzer*". The Journal of Energy Storage (2023).
DOI: 10.1016/j.est.2023.107021

Dayan Monzer, Chakib Bouallou. "*Production of Synthetic Gas by the co-electrolysis of H_2O and CO_2 in the Molten Carbonate Electrolyzer* ". International Journal of Hydrogen Energy (2023).
DOI: 10.1016/j.ijhydene.2023.03.402

Dayan Monzer, Chakib Bouallou. "*Economic Analysis of the Power to Methane Process Using a High-Temperature Molten Carbonates Electrolyzer*". Chemical Engineering Transactions (2023).
DOI: 10.3303/CET23103099

International Conferences (First Author)

Dayan Monzer, Chakib Bouallou. "*Future Economic perspective of Power-to-gas system based on Molten Carbonate Electrolyzer*". 23rd World Hydrogen Energy Conference, Istanbul, Turkey, June 2022.

Dayan Monzer, Chakib Bouallou. "*Modeling of H_2O and CO_2 Electrolysis in a Molten Carbonate Electrolyzer*". 23rd World Hydrogen Energy Conference, Istanbul, Turkey, June 2022.

Dayan Monzer, Chakib Bouallou. "*CO_2 Capture and Purification for Use in the Molten Carbonate Electrolysis Cell*". 25th Conference on Process Integration for Energy Saving and Pollution Reduction - PRES22, Split, Croatia, Sep 2022.

Dayan Monzer, Chakib Bouallou. "*Economic Analysis of the Power to Methane Process Using a High-Temperature Molten Carbonates Electrolyzer*". 26th Conference on Process Integration for Energy Saving and Pollution Reduction - PRES23, Thessaloniki, Greece, Oct 2023.

Bibliography

[1] United Nation (2021). *Emissions Gap Report 2021: The Heat Is On, a world of climate promises not yet delivered*. Tech. rep. 78-92-807-3890-2. URL: http://www.unep.org/resources/emissions-gap-report-2021 (cit. on pp. 1, 3).

[2] IEA (2020a). *The role of CCUS in low-carbon power systems, IEA*. Technical Report. URL: https://www.iea.org/reports/the-role-of-ccus-in-low-carbon-power-systems (accessed 11/1/2023) (cit. on pp. 1, 3).

[3] BP (2023). *bp energy charting tool : Statistical Review of World Energy*. URL: https://www.bp.com/en/global/corporate/energy-economics/statistical-review-of-world-energy/energy-charting-tool-desktop.html (accessed 24/1/2023) (cit. on pp. 1, 3, 11, 39).

[4] R. Rivera-Tinoco, M. Farran, C. Bouallou, F. Auprêtre, S. Valentin, P. Millet, and J. R. Ngameni (2016). "Investigation of power-to-methanol processes coupling electrolytic hydrogen production and catalytic CO_2 reduction". *International Journal of Hydrogen Energy* 41.8, pp. 4546–4559. DOI: 10.1016/j.ijhydene.2016.01.059 (cit. on pp. 1, 4, 192, 194).

[5] Linda Barelli, Gianni Bidini, Giovanni Cinti, and Jaroslaw Milewski (2021). "High temperature electrolysis using Molten Carbonate Electrolyzer". *International Journal of Hydrogen Energy*. International Workshop of Molten Carbonates & Related Topics 2019 (IWMC2019) 46.28, pp. 14922–14931. DOI: 10.1016/j.ijhydene.2020.07.220 (cit. on pp. 2, 4, 24, 25, 51, 121, 128).

[6] Andrew A. Lacis, Gavin A. Schmidt, David Rind, and Reto A. Ruedy (2010). "Atmospheric CO_2: Principal Control Knob Governing Earth's Temperature". *Science* 330.6002, pp. 356–359. DOI: 10.1126/science.1190653 (cit. on pp. 8, 38).

[7] Hannah Ritchie, Max Roser, and Pablo Rosado (2020). "CO and Greenhouse Gas Emissions". *Our World in Data*. URL: https://ourworldindata.org/co2-and-greenhouse-gas-emissions (accessed 19/2/2023) (cit. on pp. 8, 38).

[8] Pablo Rosado, Hannah Ritchie, and Mathieu Edouard (2022). "Data update: We've just updated all of our global CO emissions data". *Our World in Data*. URL: https://ourworldindata.org/co2-data-update-2022 (accessed 19/2/2023) (cit. on pp. 8, 38).

[9] Corinne Le Quéré, Robert B. Jackson, Matthew W. Jones, Adam J. P. Smith, Sam Abernethy, Robbie M. Andrew, Anthony J. De-Gol, David R. Willis, et al. (2020). "Temporary reduction in daily global CO_2 emissions during the COVID-19 forced confinement". *Nature Climate Change* 10.7, pp. 647–653. DOI: 10.1038/s41558-020-0797-x (cit. on pp. 9, 10).

[10] V. V. Klimenko, A. V. Klimenko, and A. G. Tereshin (2019). "From Rio to Paris via Kyoto: How the Efforts to Protect the Global Climate Affect the World Energy Development". *Thermal Engineering* 66.11, pp. 769–778. DOI: 10.1134/S0040601519110028 (cit. on pp. 10, 38).

[11] IRENA (2021a). *World Energy Transitions Outlook 2021: 1.5°C Pathway*, Technical Report. Abu Dhabi: International Renewable Energy Agency. URL: https://www.irena.org/publications/2021/Jun/World-Energy-Transitions-Outlook (cit. on pp. 10, 11, 39).

[12] IRENA (2022a). *World Energy Transitions Outlook 2022: 1.5 °C Pathway*. Technical Report. Abu Dhabi: International Renewable Energy Agency. URL: https://www.irena.org/Publications/2022/Mar/World-Energy-Transitions-Outlook-2022 (accessed 17/1/2023) (cit. on pp. 10, 39).

[13] European Commission (2021). *Directive of the European Parliament and of the Council*. Technical Report. Brussels. URL: https://oeil.secure.europarl.europa.eu/oeil/popups/ficheprocedure.do?reference=2021/0218(COD)&l=fr (accessed 2/12/2022) (cit. on pp. 11, 102).

[14] RTE (2021). *RTE Bilan électrique 2021*. URL: https://bilan-electrique-2021.rte-france.com/production_totale/ (accessed 17/1/2023) (cit. on pp. 11, 39, 160).

[15] Leonhard Brandeis, David Sprake, Yuriy Vagapov, and Hein Tun (2016). "Analysis of electrical energy storage technologies for future electric grids". *2016 IEEE NW Russia Young Researchers in Electrical and Electronic Engineering Conference (EIConRusNW)*. Saint Petersburg, Russia, pp. 513–518. DOI: 10.1109/EIConRusNW.2016.7448235 (cit. on pp. 12–15, 39, 40).

[16] Francisco Díaz-González, Andreas Sumper, Oriol Gomis-Bellmunt, and Roberto Villafáfila-Robles (2012). "A review of energy storage technologies for wind power applications". *Renewable and Sustainable Energy Reviews* 16.4, pp. 2154–2171. DOI: 10.1016/j.rser.2012.01.029 (cit. on p. 12).

[17] Mathew Aneke and Meihong Wang (2016). "Energy storage technologies and real life applications – A state of the art review". *Applied Energy* 179, pp. 350–377. DOI: 10.1016/j.apenergy.2016.06.097 (cit. on p. 13).

[18] Md Mustafizur Rahman, Abayomi Olufemi Oni, Eskinder Gemechu, and Amit Kumar (2020). "Assessment of energy storage technologies: A review". *Energy Conversion and Management* 223, p. 113295. DOI: 10.1016/j.enconman.2020.113295 (cit. on p. 13).

[19] Pavlos Nikolaidis and Andreas Poullikkas (2017). "A comparative review of electrical energy storage systems for better sustainability". *Journal of Power Technologies* 97.3, pp. 220–245 (cit. on p. 14).

[20] Muhammed Y. Worku (2022). "Recent Advances in Energy Storage Systems for Renewable Source Grid Integration: A Comprehensive Review". *Sustainability* 14.10, p. 5985. DOI: 10.3390/su14105985 (cit. on pp. 15, 16).

[21] K Hashimoto, M Yamasaki, K Fujimura, T Matsui, K Izumiya, M Komori, A. A El-Moneim, E Akiyama, et al. (1999). "Global CO_2 recycling—novel materials and prospect for prevention of global warming and abundant energy supply". *Materials Science and Engineering: A* 267.2, pp. 200–206. DOI: 10.1016/S0921-5093(99)00092-1 (cit. on pp. 16, 40).

[22] Jonathan Reynolds, Muhammad Waseem Ahmad, and Yacine Rezgui (2018). "Holistic modelling techniques for the operational optimisation of multi-vector energy systems". *Energy and Buildings* 169, pp. 397–416. DOI: 10.1016/j.enbuild.2018.03.065 (cit. on pp. 17, 40).

[23] GRTgaz (2018). *Technical Requirements Applicable to GRTGAZ' Transmission Pipelines and to Gas Transmission, Distribution and Storage Installations Connected to the GRTGAZ Network*. Technical Report. URL: https://www.grtgaz.com/sites/default/files/2021-03/A2-2018-04-01-EN.pdf (cit. on pp. 17, 41, 96, 166).

[24] Michael Sterner and Michael Specht (2021). "Power-to-Gas and Power-to-X—The History and Results of Developing a New Storage Concept". *Energies* 14.20, p. 6594. DOI: 10.3390/en14206594 (cit. on pp. 17, 41).

[25] U.F. Vogt, M. Schlupp, D. Burnat, and A. Züttel (2014). "Novel Developments in Alkaline Water Electrolysis". *8th International Symposium Hydrogen & Energy*. Zhaoquing, China (cit. on p. 18).

[26] Diogo M. F. Santos, César A. C. Sequeira, and José L. Figueiredo (2013). "Hydrogen production by alkaline water electrolysis". *Química Nova* 36, pp. 1176–1193. DOI: 10.1590/S0100-40422013000800017 (cit. on p. 18).

[27] Mónica Sánchez, Ernesto Amores, David Abad, Lourdes Rodríguez, and Carmen Clemente-Jul (2020). "Aspen Plus model of an alkaline electrolysis system for hydrogen production". *International Journal of Hydrogen Energy* 45.7, pp. 3916–3929. DOI: 10.1016/j.ijhydene.2019.12.027 (cit. on p. 18).

[28] Siniša Zorica, Marko Vukšić, and Ivan Zulim (2014). "Evaluation of DC-DC Resonant Converters for Solar Hydrogen Production Based on Load Current Characteristics". *International Scientific and Professional Conference of Contemporary Issues in Economy and Technology*. Split, Croatia (cit. on pp. 18, 19, 41, 42).

[29] Kai Zeng and Dongke Zhang (2009). "Recent progress in alkaline water electrolysis for hydrogen production and applications". *Progress in Energy and Combustion Science* 36.3, pp. 307–326. DOI: 10.1016/j.pecs.2009.11.002 (cit. on pp. 18, 41).

[30] S. Shiva Kumar and V. Himabindu (2019). "Hydrogen production by PEM water electrolysis – A review". *Materials Science for Energy Technologies* 2.3, pp. 442–454. DOI: 10.1016/j.mset.2019.03.002 (cit. on pp. 19, 41).

[31] S. Shiva Kumar and Hankwon Lim (2022). "An overview of water electrolysis technologies for green hydrogen production". *Energy Reports* 8, pp. 13793–13813. DOI: 10.1016/j.egyr.2022.10.127 (cit. on p. 19).

[32] Ragnhild Hancke, Thomas Holm, and Øystein Ulleberg (2022). "The case for high-pressure PEM water electrolysis". *Energy Conversion and Management* 261, p. 115642. DOI: 10.1016/j.enconman.2022.115642 (cit. on p. 19).

[33] IRENA (2020). *Green hydrogen cost reduction: Scaling up electrolysers to meet the 1.5 °C climate global*. Technical Report. Abu Dhabi (cit. on pp. 19, 25, 42).

[34] Nel. (2018a). *Atmospheric Alkaline Electrolyser technical datasheet*. URL: https://nelhydrogen.com/product/atmospheric-alkaline-electrolyser-a-series/ (accessed 31/1/2023) (cit. on p. 20).

[35] Cummins (2021). *Alkaline Electroyzer (HyStat) technical datasheet*. URL: https://www.cummins.com/sites/default/files/2021-08/cummins-hystat-100-specsheet.pdf (accessed 31/1/2023) (cit. on p. 20).

[36] John Cockerill (2021). *Alkaline Electrolyzer (DQ500) technical datasheet*. URL: https://h2.johncockerill.com/wp-content/uploads/2022/02/DQ-500-def-hd.pdf (accessed 31/1/2023) (cit. on p. 20).

[37] McPhy (2023). *PEM Electrolyzer technical datasheet*. URL: https://mcphy.com/fr/equipements-et-services/electrolyseurs/ (accessed 31/1/2023) (cit. on p. 20).

[38] Sunfire (2022a). *Alkaline Electrolyzer (HyLink) technical datasheet*. URL: https://www.sunfire.de/files/sunfire/images/content/Sunfire.de%20(neu)/Sunfire-Factsheet-HyLink-Alkaline_20220520.pdf (accessed 30/1/2023) (cit. on p. 20).

[39] GreenHydrogen (2021). *Alkaline Electrolyzer (HyProvide A-Series) technical datasheet*. URL: https://greenhydrogen.dk/wp-content/uploads/2021/02/A-Series-brochure-120421.pdf (accessed 30/1/2023) (cit. on p. 20).

[40] Nel. (2018b). *PEM Electrolyser technical datasheet*. URL: https://nelhydrogen.com/product/m-series-3/ (accessed 31/1/2023) (cit. on p. 20).

[41] Cummins (2023). *PEM Electrolyzer (Hylyzer) technical datasheet*. URL: https://www.cummins.com/sites/default/files/2021-08/cummins-hylyzer-1000-specsheet.pdf (accessed 30/1/2023) (cit. on p. 20).

[42] Siemens energy (2020). *PEM Electroyzer (Silyzer 300) technical datasheet*. URL: https://assets.siemens-energy.com/siemens/assets/api/uuid:a193b68f-7ab4-4536-abe2-c23e01d0b526/datasheet-silyzer300.pdf (accessed 31/1/2023) (cit. on p. 20).

[43] Proton onsite (2017). *PEM Electrolyzer technical datasheet*. URL: https://www.protononsite.com/sites/default/files/2017-04/PD-0600-0119%20REV%20A.pdf (accessed 30/1/2023) (cit. on p. 20).

[44] ITM Power (2023a). *PEM electrolyzer technical datasheet*. URL: https://itm-power.com/products (accessed 31/1/2023) (cit. on p. 20).

[45] Plug Power (2023b). *PEM Electrolyzer technical datasheet*. URL: https://www.plugpower.com/hydrogen/electrolyzer-hydrogen/electrolyzer-products/ (accessed 31/1/2023) (cit. on p. 20).

[46] Elogen (2021). *PEM Electrolyzer technical datasheet*. URL: https://elogenh2.com/wp-content/uploads/2021/04/Elogen_Product_sheet-Elyte260.pdf (accessed 31/1/2023) (cit. on p. 20).

[47] Md Mamoon Rashid, Mohammed K Al Mesfer, Hamid Naseem, and Mohd Danish (2015). "Hydrogen Production by Water Electrolysis: A Review of Alkaline Water Electrolysis, PEM Water Electrolysis and High Temperature Water Electrolysis". *International Journal of Engineering and Advanced Technology* 4.3, pp. 2249–8958 (cit. on pp. 20, 42).

[48] Alexander Buttler and Hartmut Spliethoff (2018). "Current status of water electrolysis for energy storage, grid balancing and sector coupling via power-to-gas and power-to-liquids: A review". *Renewable and Sustainable Energy Reviews* 82, pp. 2440–2454. DOI: 10.1016/j.rser.2017.09.003 (cit. on p. 20).

[49] FuelCell Energy (2023). *Decarbonize Your Power: CHPs & Microgrids*. URL: https://www.fuelcellenergy.com/solutions/decarbonize-power (accessed 3/10/2023) (cit. on p. 21).

[50] W. Dönitz and E. Erdle (1985). "High-temperature electrolysis of water vapor-status of development and perspectives for application". *International Journal of Hydrogen Energy* 10.5, pp. 291–295. DOI: 10.1016/0360-3199(85)90181-8 (cit. on p. 21).

[51] Lei Bi, Samir Boulfrad, and Enrico Traversa (2014). "Steam electrolysis by solid oxide electrolysis cells (SOECs) with proton-conducting oxides". *Chemical Society Reviews* 43.24, pp. 8255–8270. DOI: 10.1039/C4CS00194J (cit. on pp. 21, 43).

[52] J. Udagawa, P. Aguiar, and N. P. Brandon (2007). "Hydrogen production through steam electrolysis: Model-based steady state performance of a cathode-supported intermediate temperature solid oxide electrolysis cell". *Journal of Power Sources* 166.1, pp. 127–136. DOI: 10.1016/j.jpowsour.2006.12.081 (cit. on pp. 21, 43).

[53] J E O Brien, J S Herring, C M Stoots, M G McKellar, E A Harvego, K G Condie, G K Housley, and J J Hartvigsen (2009). "Status of the INL High- Temperature Electrolysis Research Program – Experimental and Modeling Fourth Information Exchange Meeting on the Nuclear Production of Hydrogen". *4th Information Exchange Meeting on the Nuclear Production of Hydrogen*, pp. 1–13 (cit. on pp. 22, 43).

[54] J. E. O'Brien, M. G. McKellar, E. A. Harvego, and C. M. Stoots (2010). "High-temperature electrolysis for large-scale hydrogen and syngas production from nuclear energy - summary of system simulation and economic analyses". *International Journal of Hydrogen Energy* 35.10, pp. 4808–4819. DOI: 10.1016/j.ijhydene.2009.09.009 (cit. on pp. 22, 43, 63).

[55] Floriane Petipas, Annabelle Brisse, and Chakib Bouallou (2013a). "Model-based behaviour of a high temperature electrolyser system operated at various loads". *Journal of Power Sources* 239.3, pp. 584–595. DOI: 10.1016/j.jpowsour.2013.03.027 (cit. on pp. 22, 43, 63, 64).

[56] B Laoun (2007). "Thermodynamics aspect of high pressure hydrogen production by water electrolysis". *Revue des Energies Renouvelables* 10.3, pp. 435–444 (cit. on pp. 22, 43).

[57] Christopher H. Wendel, Pejman Kazempoor, and Robert J. Braun (2016). "A thermodynamic approach for selecting operating conditions in the design of reversible solid oxide cell energy systems". *Journal of Power Sources* 301, pp. 93–104. DOI: 10.1016/j.jpowsour.2015.09.093 (cit. on pp. 22, 43).

[58] Lan Hu, Ivan Rexed, Göran Lindbergh, and Carina Lagergren (2014). "Electrochemical performance of reversible molten carbonate fuel cells". *International Journal of Hydrogen Energy* 39.23, pp. 12323–12329. DOI: 10.1016/j.ijhydene.2014.02.144 (cit. on pp. 22, 24, 43, 44, 208, 222).

[59] Arunkumar Pandiyan, Aarthi Uthayakumar, Rengaraj Subrayan, Suk Won Cha, and Suresh Babu Krishna Moorthy (2019). "Review of solid oxide electrolysis cells: a clean energy strategy for hydrogen generation". *Nanomaterials and Energy* 8.1, pp. 2–22. DOI: 10.1680/jnaen.18.00009 (cit. on pp. 22, 43).

[60] Sunfire (2022b). *SOEC Electrolyzer (Hylink) technical datasheet*. URL: https://www.sunfire.de/files/sunfire/images/content/Sunfire.de%20(neu)/Sunfire-Factsheet-HyLink-SOEC-20210303.pdf (accessed 31/1/2023) (cit. on pp. 22, 44).

[61] TOPSOE (2021). *SOEC Technical datasheet*. URL: https://info.topsoe.com/green-hydrogen (accessed 3/2/2023) (cit. on pp. 22, 44).

[62] FuelCell Energy (2022). *SOEC technical datasheet*. URL: https://www.fuelcellenergy.com/platform/solid-oxide-electrolysis (accessed 3/2/2023) (cit. on pp. 22, 44).

[63] Déborah Chery, Virginie Lair, and Michel Cassir (2015a). "Overview on CO_2 valorization: Challenge of molten carbonates". *Frontiers in Energy Research* 3.43. DOI: 10.3389/fenrg.2015.00043 (cit. on pp. 22, 44).

[64] Andreas Bodén (2007). "The anode and the electrolyte in the MCFC". PhD thesis. KTH – Chemical Science and Engineering (cit. on pp. 22, 44).

[65] Xuehui An, Jinhui Cheng, Peng Zhang, Zhongfeng Tang, and Jianqiang Wang (2016). "Determination and evaluation of the thermophysical properties of an alkali carbonate eutectic molten salt". *Faraday Discussions* 190, pp. 327–338. DOI: 10.1039/c5fd00236b (cit. on p. 22).

[66] Lan Hu, Göran Lindbergh, and Carina Lagergren (2015a). "Electrode Kinetics of the Ni Porous Electrode for Hydrogen Production in a Molten Carbonate Electrolysis Cell (MCEC)". *Journal of The Electrochemical Society* 162.9, F1020. DOI: 10.1149/2.0491509jes (cit. on pp. 23, 44).

[67] Lan Hu, Göran Lindbergh, and Carina Lagergren (2015b). "Electrode kinetics of the NiO porous electrode for oxygen production in the molten carbonate electrolysis cell (MCEC)". *Faraday Discussions* 182.0, pp. 493–509. DOI: 10.1039/C5FD00011D (cit. on pp. 23, 44).

[68] Lan Hu, Göran Lindbergh, and Carina Lagergren (2016a). "Operating the nickel electrode with hydrogen-lean gases in the molten carbonate electrolysis cell (MCEC)". *International Journal of Hydrogen Energy* 41.41, pp. 18692–18698. DOI: 10.1016/j.ijhydene.2016.06.037 (cit. on pp. 23, 45, 73, 76, 77, 87, 89).

[69] Lan Hu, Göran Lindbergh, and Carina Lagergren (2016b). "Performance and Durability of the Molten Carbonate Electrolysis Cell and the Reversible Molten Carbonate Fuel Cell". *The Journal of Physical Chemistry C* 120.25, pp. 13427–13433. DOI: 10.1021/acs.jpcc.6b04417 (cit. on pp. 23, 45).

[70] Miguel A. Reyes-Belmonte, Alfonso Delgado, Elena Díaz, José González-Aguilar, and Manuel Romero (2017). "Molten carbonates electrolyzer model for hydrogen production coupled to medium/low temperature solar power plant". *ISES Solar World Congress 2017 - IEA SHC International Conference on Solar Heating and Cooling for Buildings and Industry 2017*, pp. 168–178. DOI: 10.18086/swc.2017.04.13 (cit. on pp. 23, 25, 45).

[71] Luca Mastropasqua, Francesca Baia, Luca Conti, and Stefano Campanari (2018). "Electrochemical Energy Storage and Synthetic Natural Gas". *ASME 2018 12th International Conference on Energy Sustainability*. FL,USA, pp. 1–13 (cit. on pp. 24, 25, 45, 51, 121, 128).

[72] Andrea Monforti Ferrario, Francesca Santoni, Massimiliano Della Pietra, Mosè Rossi, Nicola Piacente, Gabriele Comodi, and Luca Simonetti (2021). "A System Integration Analysis of a Molten Carbonate Electrolysis Cell as an Off-Gas Recovery System in a Steam-Reforming Process of an Oil Refinery". *Frontiers in Energy Research* 9. DOI: 10.3389/fenrg.2021.655915 (cit. on pp. 24, 25, 51).

[73] Stefano Frangini, Massimilano Della Pietra, Livia Della Seta, Claudia Paoletti, and Juan Pedro Pérez-Trujillo (2021). "Degradation of MCFC Materials in a 81 cm^2 Single Cell Operated Under Alternated Fuel Cell/Electrolysis Mode". *Frontiers in Energy Research* 9, pp. 1–10. DOI: 10.3389/fenrg.2021.653531 (cit. on pp. 24, 25, 45, 135, 139, 175, 208, 223).

[74] Emilio Audasso, Kab In Kim, Grazia Accardo, Han Sung Kim, and Sung Pil Yoon (2022). "Investigation of molten carbonate electrolysis cells performance for H_2 production and CO_2 capture". *Journal of Power Sources* 523.November 2021, p. 231039. DOI: 10.1016/j.jpowsour.2022.231039 (cit. on pp. 24, 25, 45).

[75] Samuel Koomson and Choong-Gon Lee (2022). "Comparison of gas phase transport effects between fuel cell and electrolysis cell modes of a 100 cm^2 class molten carbonate cell". *Journal of Electroanalytical Chemistry* 925, p. 116896. DOI: 10.1016/j.jelechem.2022.116896 (cit. on pp. 24, 45).

[76] Paul Sabatier and JB Senderens (1902). "Comptes Rendus Des Séances De L'Académie Des Sciences, Section VI–Chimie [Reports of the Meetings of the Academy of Sciences, Section VI–Chemistry]". *Paris: Imprimerie Gauthier-Villars* (accessed. 1/2/2023) (cit. on pp. 26, 45).

[77] Julien Ducamp, Alain Bengaouer, Pierre Baurens, Ioana Fechete, Philippe Turek, and François Garin (2018). "Statu quo sur la méthanation du dioxyde de carbone: une revue de la littérature [Status quo on carbon dioxide methanation: a review of the literature]". *Comptes Rendus Chimie* 21.3, pp. 427–469. DOI: 10.1016/j.crci.2017.07.005 (cit. on pp. 26, 32).

[78] Jiajian Gao, Yingli Wang, Yuan Ping, Dacheng Hu, Guangwen Xu, Fangna Gu, and Fabing Su (2012). "A thermodynamic analysis of methanation reactions of carbon oxides for the production of synthetic natural gas". *RSC Advances* 2.6, pp. 2358–2368. DOI: 10.1039/c2ra00632d (cit. on pp. 26, 46, 113).

[79] Daniel Schmider, Lubow Maier, and Olaf Deutschmann (2021). "Reaction Kinetics of CO and CO_2 Methanation over Nickel". *Industrial and Engineering Chemistry Research* 60.16, pp. 5792–5805. DOI: 10.1021/acs.iecr.1c00389 (cit. on pp. 26, 27).

[80] Ligang Wang, Megha Rao, Stefan Diethelm, Tzu En Lin, Hanfei Zhang, Anke Hagen, François Maréchal, and Jan Van herle (2019). "Power-to-methane via co-electrolysis of H_2O and CO_2: The effects of pressurized operation and internal methanation". *Applied Energy* 250.April, pp. 1432–1445. DOI: 10.1016/j.apenergy.2019.05.098 (cit. on pp. 26, 46, 50).

[81] Eigenberger Gerhart (1992). "Fixed-Bed Reactors". Vol. B4. Ullmann's Encyclopedia of Industnal Chemistry. VCH Publishers, Inc. URL: https://elib.uni-stuttgart.de/bitstream/11682/1848/1/eig16.pdf (cit. on pp. 27, 28).

[82] Jonathan Lefebvre, Manuel Götz, Siegfried Bajohr, Rainer Reimert, and Thomas Kolb (2015). "Improvement of three-phase methanation reactor performance for steady-state and transient operation". *Fuel Processing Technology* 132, pp. 83–90. DOI: 10.1016/j.fuproc.2014.10.040 (cit. on pp. 28, 29).

[83] *Fluidized bed reactor* (2021). URL: https://en.wikipedia.org/w/index.php?title=Fluidized_bed_reactor&oldid=1023962323 (accessed 31/5/2023) (cit. on p. 29).

[84] Stefan Rönsch, Jens Schneider, Steffi Matthischke, Michael Schlüter, Manuel Götz, Jonathan Lefebvre, Praseeth Prabhakaran, and Siegfried Bajohr (2016). "Review on methanation – From fundamentals to current projects". *Fuel* 166, pp. 276–296. DOI: 10.1016/j.fuel.2015.10.111 (cit. on pp. 28, 29, 33).

[85] Vassilis J. Inglezakis and Stavros G. Poulopoulos (2006). "3 - Heterogeneous Processes and Reactor Analysis". *Adsorption, Ion Exchange and Catalysis*. Ed. by Vassilis J. Inglezakis and Stavros G. Poulopoulos. Amsterdam: Elsevier, pp. 57–242. DOI: 10.1016/B978-044452783-7/50003-3 (cit. on p. 29).

[86] Nur Diyan Mohd Ridzuan, Maizatul Shima Shaharun, Mohd Azrizan Anawar, and Israf Ud-Din (2022). "Ni-Based Catalyst for Carbon Dioxide Methanation: A Review on Performance and Progress". *Catalysts* 12.5. DOI: 10.3390/catal12050469 (cit. on p. 29).

[87] Manuel Götz, Jonathan Lefebvre, Friedemann Mörs, Amy McDaniel Koch, Frank Graf, Siegfried Bajohr, Rainer Reimert, and Thomas Kolb (2015). "Renewable Power-to-Gas: A technological and economic review". *Renewable Energy* 85, pp. 1371–1390. DOI: 10.1016/j.renene.2015.07.066 (cit. on pp. 30, 192, 215).

[88] Philipp Biegger, Florian Kirchbacher, Ana Roza Medved, Martin Miltner, Markus Lehner, and Michael Harasek (2018). "Development of Honeycomb Methanation Catalyst and Its Application in Power to Gas Systems". *Energies* 11.7, p. 1679. DOI: 10.3390/en11071679 (cit. on p. 30).

[89] Steph Hazlegreaves (2018). *Renewable energy promotion: From wind to green gas*. URL: https://www.openaccessgovernment.org/renewable-energy-promotion/52337/ (accessed 10/2/2023) (cit. on p. 30).

[90] Zhihong Liu, Bozhao Chu, Xuli Zhai, Yong Jin, and Yi Cheng (2012). "Total methanation of syngas to synthetic natural gas over Ni catalyst in a micro-channel reactor". *Fuel* 95, pp. 599–605. DOI: 10.1016/j.fuel.2011.12.045 (cit. on pp. 30, 31).

[91] Ruth Schlautmann, Hans Böhm, Andreas Zauner, Friedemann Mörs, Robert Tichler, Frank Graf, and Thomas Kolb (2021). "Renewable Power-to-Gas: A Technical and Economic Evaluation of Three Demo Sites Within the STORE&GO Project". *Chemie Ingenieur Technik* 93.4, pp. 568–579. DOI: 10.1002/cite.202000187 (cit. on p. 30).

[92] ATMOSTAT (2017). *Power To Gas : Unité de méthanation compacte et modulaire [Power To Gas: modular and compact methanation unit]*. URL: https://atee.fr/system/files/2020-01/14.%20BRUNO%20LANGLOIS%20-%20ATMOSTAT.pdf (accessed 10/2/2023) (cit. on p. 31).

[93] Jürgen Karl, Michael Neubert, M. R. Riazi, and David Chiaramonti (2017). "Production of Substitute Natural Gas: Thermochemical Methods". *Biofuels Production and Processing Technology*. CRC Press (cit. on p. 31).

[94] Jan Kopyscinski, Tilman J. Schildhauer, and Serge M. A. Biollaz (2010). "Production of synthetic natural gas (SNG) from coal and dry biomass – A technology review from 1950 to 2009". *Fuel* 89.8, pp. 1763–1783. DOI: 10.1016/j.fuel.2010.01.027 (cit. on pp. 32, 34, 47).

[95] L. W. Zahnstecher (1984). *Coal gasification via the Lurgi process: Topical report: Volume 2, Production of IFG (industrial fuel gas)*. Technical Report. United States: Foster Wheeler Corp., Livingston, NJ (USA). URL: https://www.osti.gov/biblio/6747545 (accessed 13/2/2023) (cit. on p. 32).

[96] Haldor Topsoe (2009). *From solid fuels to substitute natural gas (SNG) using TREMP™*. URL: https://www.netl.doe.gov/sites/default/files/netl-file/tremp-2009.pdf (accessed 13/2/2023) (cit. on pp. 32, 33, 47).

[97] B. Höhlein, R. Menzer, and J. Range (1981). "High temperature methanation in the long-distance nuclear energy transport system". *Applied Catalysis* 1.3, pp. 125–139. DOI: 10.1016/0166-9834(81)80001-2 (cit. on p. 32).

[98] Haldor Topsoe (2023). URL: https://www.topsoe.com (accessed 13/2/2023) (cit. on p. 33).

[99] Jacques De Bucy (2016). *The Potential of Power-to-Gas*. Technical Report. ENEA (cit. on pp. 33, 46).

[100] Stefan Rönsch, Steffi Matthischke, Markus Müller, and Philipp Eichler (2014). "Dynamic Simulation of Fixed-Bed Methanation Reactors". *Chemie Ingenieur Technik* 86.8, pp. 1198–1204. DOI: 10.1002/cite.201300046 (cit. on pp. 33, 46).

[101] R. Lohmueller (1977). "Methansynthese mit kombinierten Isothermen und adiabaten Reaktoren [Methane synthesis with combined isotherms and adiabatic reactors]". *Berichte aus Technik und Wissenschaft* 44 (cit. on pp. 34, 47).

[102] M. Thema, F. Bauer, and M. Sterner (2019). "Power-to-Gas: Electrolysis and methanation status review". *Renewable and Sustainable Energy Reviews* 112, pp. 775–787. DOI: 10.1016/j.rser.2019.06.030 (cit. on pp. 35, 48).

[103] *Audi Technology Portal - Audi e-gas* (2023). URL: https://www.audi-technology-portal.de/en/mobility-for-the-future/audi-future-lab-mobility_en/audi-future-energies_en/audi-e-gas_en (accessed 10/3/2023) (cit. on p. 35).

[104] *Energiepark Mainz: Technical Data* (2017). URL: https://www.energiepark-mainz.de/en/technology/technical-data/ (accessed 14/3/2023) (cit. on p. 35).

[105] *STORE&GO* (2019). URL: https://www.storeandgo.info/ (accessed 28/2/2023) (cit. on p. 35).

[106] Reinhard Otten (2014). *The first industrial PtG plant Audi e-gas as driver for the energy turnaround*. URL: http://www.cedec.com/files/default/8-2014-05-27-cedec-gas-day-reinhard-otten-audi-ag.pdf (accessed 14/3/2023) (cit. on p. 35).

[107] *Jupiter1000: First industrial demonstrator of Power-to-gas in France* (2023). URL: https://www.jupiter1000.eu/english (accessed 28/2/2023) (cit. on p. 36).

[108] GRtgaz (2022). *Jupiter 1000 : Démonstrateur industriel de Power-to-Gas [Jupiter 1000: Power-to-Gas industrial demonstrator]*. Technical Report. URL: https://www.iesf.fr/offres/doc_inline_src/752/BRISSAUD%2BJNI%2B2022%2B-%2BJupiter%2B1000%2B-%2BGRTgaz%2B-%2B2022-03-04%2B-%2Bvdif.pdf (accessed 14/3/2023) (cit. on p. 36).

[109] ATEE (2020). *Des démonstrateurs de Power to Gas indispensables au développement d'une filière industrielle française [Essential Power to Gas demonstrators for the development of a French industrial sector]*. URL: https://atee.fr/actualite/des-demonstrateurs-de-power-gas-indispensables-au-developpement-dune-filiere-industrielle (accessed 15/3/2023) (cit. on p. 36).

[110] Charlotte De Lorgeril, Noel Courtemanche, Baptiste Guichard, and Lisa Miller (2018). *Le Power-to-Gas: Outil de flexibilité pour accompagner la transformation du système énergétique Solution de stockage de l'électricité renouvelable [Power-to-Gas: A flexibility tool to support the transformation of the energy system Renewable electricity storage solution]* (cit. on p. 37).

[111] Carl M. Stoots, James O E Rien, James Herring, Paul Lessing, Grant L. Hawkes, and J. Hartvigsen Joseph (2008). "High Temperature Electrolysis For Syngas Production". US7951283B2 (Idaho Falls, ID) (cit. on pp. 50, 82).

[112] Sune Dalgaard Ebbesen, Christopher Graves, and Mogens Mogensen (2009). "Production of synthetic fuels by co-electrolysis of steam and carbon dioxide". *International Journal of Green Energy* 6.6, pp. 646–660. DOI: 10.1080/15435070903372577 (cit. on pp. 50, 82).

[113] Meng Ni (2012a). "2D thermal modeling of a solid oxide electrolyzer cell (SOEC) for syngas production by H_2O/CO_2 co-electrolysis". *International Journal of Hydrogen Energy* 37.8, pp. 6389–6399. DOI: 10.1016/j.ijhydene.2012.01.072 (cit. on p. 50).

[114] Meng Ni (2012b). "An electrochemical model for syngas production by co-electrolysis of H_2O and CO_2". *Journal of Power Sources* 202, pp. 209–216. DOI: 10.1016/j.jpowsour.2011.11.080 (cit. on pp. 50, 54).

[115] Youssef Redissi and Chakib Bouallou (2013). "Valorization of carbon dioxide by co-electrolysis of CO_2/H_2O at high temperature for syngas production". *Energy Procedia* 37, pp. 6667–6678. DOI: 10.1016/j.egypro.2013.06.599 (cit. on p. 50).

[116] Hanaâ Er-rbib, Nouaamane Kezibri, and Chakib Bouallou (2018). "Performance assessment of a power-to-gas process based on reversible solid oxide cell". *Frontiers of Chemical Science and Engineering* 12.4, pp. 697–707. DOI: 10.1007/s11705-018-1774-z (cit. on p. 50).

[117] D. Chery, V. Liar, and M. Cassir (2015b). "CO_2 electrochemical reduction into CO or C in molten carbonates: a thermodynamic point of view". *Electrochimica Acta* 160, pp. 74–81. DOI: 10.1016/j.electacta.2015.01.216 (cit. on pp. 50, 51).

[118] P. K. Lorenz and G. J. Janz (1970). "Electrolysis of molten carbonates: anodic and cathodic gas-evolving reactions". *Electrochimica Acta* 15.6, pp. 1025–1035. DOI: 10.1016/0013-4686(70)80042-1 (cit. on pp. 50, 82).

[119] WHA. Peelen., K Hemmes, and JHW. de Wit. (1997). "CO_2 reduction in molten 62/38 mole% Li/K carbonate mixture". *Electrochimica Acta* 43.7, pp. 763–769. DOI: 10.1016/S0013-4686(97)00141-2 (cit. on pp. 50, 82).

[120] Valery Kaplan, Ellen Wachtel, Konstantin Gartsman, Yishay Feldman, and Igor Lubomirsky (2010). "Conversion of CO_2 to CO by Electrolysis of Molten Lithium Carbonate". *Journal of The Electrochemical Society* 157.4, B552–B556. DOI: 10.1149/1.3308596 (cit. on pp. 51, 82).

[121] Valery Kaplan, Ellen Wachtel, and Igor Lubomirsky (2012). "Titanium Carbide Coating of Titanium by Cathodic Deposition from a Carbonate Melt". *Journal of The Electrochemical Society* 159.11, E159–E161. DOI: 10.1149/2.016211jes (cit. on pp. 51, 82).

[122] D. Chery, V. Albin, V. Lair, and M. Cassir (2014). "Thermodynamic and experimental approach of electrochemical reduction of CO_2 in molten carbonates". *International Journal of Hydrogen Energy* 39.23, pp. 12330–12339. DOI: 10.1016/j.ijhydene.2014.03.113 (cit. on p. 51).

[123] Deqiang Ji, Zhida Li, Wei Li, Dandan Yuan, Yuhang Wang, Yanyan Yu, and Hongjun Wu (2019). "The optimization of electrolyte composition for CH_4 and H_2 generation via CO_2/H_2O co-electrolysis in eutectic molten salts". *International Journal of Hydrogen Energy*, pp. 5082–5089. DOI: 10.1016/j.ijhydene.2018.09.089 (cit. on p. 51).

[124] H. Meskine, E. Gürbüz, V. Albin, A. Meléndez-Ceballos, M. Cassir, A. Ringuedé, and V. Lair (2020). "CO_2 electrolysis in a reversible molten carbonate fuel cell: Online chromatographic detection of CO". *International Journal of Hydrogen Energy* 46.28, pp. 14913–14921. DOI: 10.1016/J.IJHYDENE.2020.08.028 (cit. on pp. 51, 63, 64, 66, 82, 111, 116, 139).

[125] Juan Pedro Perez-Trujillo, Francisco Elizalde-Blancas, Massimiliano Della Pietra, and Stephen J. McPhail (2018). "A numerical and experimental comparison of a single reversible molten carbonate cell operating in fuel cell mode and electrolysis mode". *Applied Energy* 226.May, pp. 1037–1055. DOI: 10.1016/j.apenergy.2018.05.121 (cit. on p. 51).

[126] Juan Pedro Pérez-Trujillo, Francisco Elizalde-Blancas, Stephen J. McPhail, Massimiliano Della Pietra, and Barbara Bosio (2020). "Preliminary theoretical and experimental analysis of a Molten Carbonate Fuel Cell operating in reversible mode". *Applied Energy* 263, p. 114630. DOI: 10.1016/j.apenergy.2020.114630 (cit. on pp. 51, 68, 84).

[127] Sune Dalgaard Ebbesen, Søren Højgaard Jensen, Anne Hauch, and Mogens Bjerg Mogensen (2014). "High Temperature Electrolysis in Alkaline Cells, Solid Proton Conducting Cells, and Solid Oxide Cells". *Chemical Reviews* 114, pp. 10697–10734. DOI: dx.doi.org/10.1021/cr5000865 (cit. on pp. 52–54).

[128] Ernesto Amores, Jesús Rodríguez, José Oviedo, and Antonio de Lucas-Consuegra (2017). "Development of an operation strategy for hydrogen production using solar PV energy based on fluid dynamic aspects". *Open Engineering* 7.1, pp. 141–152. DOI: 10.1515/eng-2017-0020 (cit. on p. 55).

[129] Qingxi Fu, Corentin Mabilat, Mohsine Zahid, Annabelle Brisse, and Ludmila Gautier (2010). "Syngas production via high-temperature steam/CO_2 co-electrolysis: An economic assessment". *Energy and Environmental Science* 3.10, pp. 1382–1397. DOI: 10.1039/c0ee00092b (cit. on pp. 55, 63).

[130] Bengt Sundén (2019). "Electrochemistry and thermodynamics". *Hydrogen, Batteries and Fuel Cells*. Ed. by Bengt Sundén. Academic Press, pp. 15–36. DOI: https://doi.org/10.1016/B978-0-12-816950-6.00002-6 (cit. on p. 55).

[131] Anne-Lise Gehin, Belkacem Ould-Bouamama, and Ibrahim Abdallah (2021). "Operating mode management of renewable energy systems using event-driven hybrid bond graphs". *Design, Analysis, and Applications of Renewable Energy Systems*. Ed. by Ahmad Taher Azar and Nashwa Ahmad Kamal. Advances in Nonlinear Dynamics and Chaos (ANDC). Academic Press, pp. 413–436. DOI: 10.1016/B978-0-12-824555-2.00010-1 (cit. on p. 56).

[132] Mitja Mori, Tilen Mrzljak, Boštjan Drobnič, and M. Sekavčnik (2013). "Integral Characteristics of Hydrogen Production in Alkaline Electrolysers". *Journal of Mechanical Engineering* 59.10, pp. 585–594. DOI: 10.5545/sv-jme.2012.858 (cit. on p. 57).

[133] Fiammetta Rita Bianchi and Barbara Bosio (2021). "Operating principles, performance and technology readiness level of reversible solid oxide cells". *Sustainability* 13.9, p. 4777. DOI: 10.3390/su13094777 (cit. on p. 56).

[134] D. Bove, E. Audasso, T. Barckholtz, G. Kiss, J. Rosen, and B. Bosio (2021). "Process analysis of molten carbonate fuel cells in carbon capture applications". *International Journal of Hydrogen Energy* 46.28, pp. 15032–15045. DOI: 10.1016/J.IJHYDENE.2020.08.020 (cit. on p. 57).

[135] NIST (2018). *National Institute of Standards and Technology Webbook*. URL: https://webbook.nist.gov/chemistry/ (cit. on pp. 60, 64, 115, 233).

[136] J. Aicart, J. Laurencin, M. Petitjean, and L. Dessemond (2014). "Experimental validation of two-dimensional H_2O and CO_2 Co-electrolysis modeling". *Fuel Cells* 14.3, pp. 430–447. DOI: 10.1002/fuce.201300214 (cit. on pp. 60, 61, 83).

[137] Jason K. Lee, Chung Hyuk Lee, Kieran F. Fahy, Benzhong Zhao, Jacob M. LaManna, Elias Baltic, David L. Jacobson, Daniel S. Hussey, et al. (2020). "Critical Current Density as a Performance Indicator for Gas-Evolving Electrochemical Devices". *Cell Reports Physical Science* 1.8, p. 100147. DOI: 10.1016/J.XCRP.2020.100147 (cit. on pp. 61, 62).

[138] Pegah Mottaghizadeh, Srikanth Santhanam, Marc P. Heddrich, K. Andreas Friedrich, and Fabio Rinaldi (2017). "Process modeling of a reversible solid oxide cell (r-SOC) energy storage system utilizing commercially available SOC reactor". *Energy Conversion and Management* 142.June, pp. 477–493. DOI: 10.1016/j.enconman.2017.03.010 (cit. on p. 63).

[139] Nouaamane Kezibri (2019). "Etude dynamique du procédé de production de méthane à partir d ' hydrogène électrolytique basse température (Study of Process Dynamics of Methane Production from Low Temperature Electrolytic Hydrogen)". PhD thesis (cit. on p. 64).

[140] Ersan Gürbüz (2021). "Analyse et mise en oeuvre de la co-électrolyse de CO_2 et de H_2O dans les carbonates fondus [Analysis and implementation of the co-electrolysis of CO_2 and H_2O in molten carbonates]". PhD thesis. Chimie ParisTech - PSL University (cit. on pp. 65–67, 76, 88).

[141] Grant L. Hawkes, James E. O'Brien, Carl M. Stoots, J. Stephen Herring, and Mehrdad Shahnam (2007). "Computational fluid dynamics model of a planar solid-oxide electrolysis cell for hydrogen production from nuclear energy". *Nuclear Technology* 158.2, pp. 132–144. DOI: 10.13182/NT07-A3831 (cit. on pp. 69, 85).

[142] Arkadiusz Szczęśniak, Jarosław Milewski, Łukasz Szabłowski, Wojciech Bujalski, and Olaf Dybiński (2020). "Dynamic model of a molten carbonate fuel cell 1 kW stack". *Energy* 200, p. 117442. DOI: 10.1016/j.energy.2020.117442 (cit. on pp. 76, 88, 135, 146).

[143] Fuel Cell Energy Inc. (2005). *Molten carbonate fuel cell - Product design improvement*. Technical Report. FuelCell Energy, Inc. URL: http://patft.uspto.gov/netacgi/nph-Parser?patentnumber=4%2C609%2C595 (cit. on pp. 92, 123, 150, 180, 209).

[144] Linde (2017). *Safety advice: Carbon Dioxide*. URL: https://www.linde-gas.com/en/images/LMB_Safety%20Advice_01_66881_tcm17-165650.pdf (cit. on p. 93).

[145] J. C. M. Pires, F. G. Martins, M. C. M. Alvim-Ferraz, and M. Simões (2011). "Recent developments on carbon capture and storage: An overview". *Chemical Engineering Research and Design* 89.9, pp. 1446–1460. DOI: 10.1016/j.cherd.2011.01.028 (cit. on p. 97).

[146] Monoj Kumar Mondal, Hemant Kumar Balsora, and Prachi Varshney (2012). "Progress and trends in CO_2 capture/separation technologies: A review". *Energy* 46.1, pp. 431–441. DOI: 10.1016/j.energy.2012.08.006 (cit. on p. 97).

[147] Dennis Y.C. Leung, Giorgio Caramanna, and M. Mercedes Maroto-Valer (2014). "An overview of current status of carbon dioxide capture and storage technologies". *Renewable and Sustainable Energy Reviews* 39, pp. 426–443. DOI: 10.1016/j.rser.2014.07.093 (cit. on p. 97).

[148] Najmus S. Sifat and Yousef Haseli (2019). "A critical review of CO_2 capture technologies and prospects for clean power generation". *Energies* 12.21, p. 4143. DOI: 10.3390/en12214143 (cit. on p. 97).

[149] Ahmed I. Osman, Mahmoud Hefny, M. I.A. Abdel Maksoud, Ahmed M. Elgarahy, and David W. Rooney (2020). "Recent advances in carbon capture storage and utilisation technologies: a review". *Environmental Chemistry Letters* 19, pp. 797–849. DOI: 10.1007/s10311-020-01133-3 (cit. on pp. 97, 98).

[150] Toby Lockwood (2017). "A Compararitive Review of Next-generation Carbon Capture Technologies for Coal-fired Power Plant". *Energy Procedia*. 13th International Conference on Greenhouse Gas Control Technologies, GHGT-13, 14-18 November 2016, Lausanne, Switzerland 114, pp. 2658–2670. DOI: 10.1016/j.egypro.2017.03.1850 (cit. on pp. 97, 98).

[151] Xinli Zhu, Trung Hoang, Lance L. Lobban, and Richard G. Mallinson (2010). "Low CO content hydrogen production from bio-ethanol using a combined plasma reforming–catalytic water gas shift reactor". *Applied Catalysis B: Environmental* 94, pp. 311–317. DOI: 10.1016/J.APCATB.2009.12.004 (cit. on p. 97).

[152] Ofélia de Queiroz Fernandes Araújo and José Luiz de Medeiros (2017). "Carbon capture and storage technologies: present scenario and drivers of innovation". *Current Opinion in Chemical Engineering* 17, pp. 22–34. DOI: 10.1016/j.coche.2017.05.004 (cit. on pp. 97, 99).

[153] A. Basile, A. Gugliuzza, A. Iulianelli, and P. Morrone (2011). "Membrane technology for carbon dioxide (CO_2) capture in power plants". *Advanced Membrane Science and Technology for Sustainable Energy and Environmental Applications*. Ed. by Angelo Basile and Suzana Pereira Nunes. Woodhead Publishing Series in Energy. Woodhead Publishing, pp. 113–159. DOI: 10.1533/9780857093790.2.113 (cit. on p. 97).

[154] José D. Figueroa, Timothy Fout, Sean Plasynski, Howard McIlvried, and Rameshwar D. Srivastava (2008). "Advances in CO_2 capture technology—The U.S. Department of Energy's Carbon Sequestration Program". *International Journal of Greenhouse Gas Control* 2.1, pp. 9–20. DOI: 10.1016/S1750-5836(07)00094-1 (cit. on pp. 98, 99).

[155] U.S Departement of Energy (2022). *Pre-Combustion Carbon Capture Research*. URL: https://www.energy.gov/fecm/science-innovation/carbon-capture-and-storage-research/carbon-capture-rd/pre-combustion-carbon (accessed 13/12/2022) (cit. on p. 98).

[156] Esmeralda Portillo, Bernabé Alonso-Fariñas, Fernando Vega, Mercedes Cano, and Benito Navarrete (2019). "Alternatives for oxygen-selective membrane systems and their integration into the oxy-fuel combustion process: A review". *Separation and Purification Technology* 229, p. 115708. DOI: 10.1016/j.seppur.2019.115708 (cit. on p. 99).

[157] Xiao Wu, Meihong Wang, Peizhi Liao, Jiong Shen, and Yiguo Li (2020). "Solvent-based post-combustion CO_2 capture for power plants: A critical review and perspective on dynamic modelling, system identification, process control and flexible operation". *Applied Energy* 257, p. 113941. DOI: 10.1016/j.apenergy.2019.113941 (cit. on p. 99).

[158] Fernando Vega, Mercedes Cano, Sara Camino, Luz M. Gallego Fernández, Esmeralda Portillo, and Benito Navarrete (2018). "Solvents for Carbon Dioxide Capture". *Carbon Dioxide Chemistry, Capture and Oil Recovery*. Ed. by Iyad Karamé, Janah Shaya, and Hassan Srour. IntechOpen. URL: https://www.intechopen.com/books/carbon-dioxide-chemistry-capture-and-oil-recovery/solvents-for-carbon-dioxide-capture (accessed 25/3/2021) (cit. on p. 99).

[159] Richard T.J. Porter, Michael Fairweather, Mohamed Pourkashanian, and Robert M. Woolley (2015). "The range and level of impurities in CO_2 streams from different carbon capture sources". *International Journal of Greenhouse Gas Control* 36, pp. 161–174. DOI: 10.1016/j.ijggc.2015.02.016 (cit. on pp. 100, 101).

[160] Joo Youp Lee, Tim C. Keener, and Y. Jeffery Yang (2009). "Potential flue gas impurities in carbon dioxide streams separated from coal-fired power plants". *Journal of the Air and Waste Management Association* 59.6, pp. 725–732. DOI: 10.3155/1047-3289.59.6.725 (cit. on pp. 100, 106, 129).

[161] Marie Anheden, Annika Andersson, Christian Bernstone, Sara Eriksson, Jinying Yan, Stefan Liljemark, and Caroline Wall (2005). "CO_2 quality requirement for a system with CO_2 capture, transport and storage". *Greenhouse Gas Control Technologies 7*. Ed. by E. S. Rubin, D. W. Keith, C. F. Gilboy, M. Wilson, T. Morris, J. Gale, and K. Thambimuthu. Oxford: Elsevier Science Ltd, pp. 2559–2564. DOI: 10.1016/B978-008044704-9/50373-6 (cit. on p. 101).

[162] IEAGHG (2011). *Effects of Impurities on Geological Storage of CO_2*. Technical Report. URL: https://ieaghg.org/docs/General_Docs/Reports/2011-04.pdf (accessed 8/3/2021) (cit. on p. 101).

[163] Zeina Abbas, Toufic Mezher, and Mohammad R.M. Abu-Zahr (2013). "Evaluation of CO_2 purification requirements and the selection of processes for impurities deep removal from the CO_2 product stream". *Energy Procedia* 37, pp. 2389–2396. DOI: 10.1016/j.egypro.2013.06.120 (cit. on p. 101).

[164] Filip Neele, Joris Koornneef, Jana Poplsteinova Jakobsen, Amy Brunsvold, and Charles Eickhoff (2017). "Toolbox of Effects of CO_2 Impurities on CO_2 Transport and Storage Systems". *Energy Procedia* 114, pp. 6536–6542. DOI: 10.1016/j.egypro.2017.03.1789 (cit. on pp. 101, 102).

[165] A. Prelioceanu, H.-P. Kaballo, and Keresteciogl (2007). "Linde Rectisol ® Wash Process 2". *2nd International Freiberg Conference on IGCC & XtL Technologies*. Freiberg, Germany (cit. on p. 102).

[166] S Walspurger and H.A.J. Van Dijk (2012). *EDGAR CO_2 purity: type and quantities of impurities related to CO_2 point source and capture technology: a Literature study*. Technical Report ECN-E-12-054. URL: https://www.osti.gov/etdeweb/servlets/purl/22110197 (cit. on p. 102).

[167] Gabriele Pipitone and Olav Bolland (2009). "Power generation with CO_2 capture: Technology for CO_2 purification". *International Journal of Greenhouse Gas Control* 3.5, pp. 528–534. DOI: 10.1016/j.ijggc.2009.03.001 (cit. on p. 102).

[168] Timothy Fout and Steve Herron (2013). *Quality guidelines for Energy System Guidelines, CO_2 Impurity design parameters*. Technical Report. URL: https://www.osti.gov/servlets/purl/1566771 (cit. on p. 103).

[169] O A Marina (2014). *Molten Carbonate Fuel Cell Interactions with Impurities in Synthetic Flue Gas*. Technical Report. Richland, Washington: Pacific Northwest National Laboratory. URL: http://www.ntis.gov/ordering.htm (cit. on pp. 104, 105, 129).

[170] Maria Turco, Angelo Ausiello, and Luca Micoli (2016). "The Effect of Sulfur Compounds on MCFC". *Treatment of Biogas for Feeding High Temperature Fuel Cells, Green Energy and Technology*. Springer International Publishing Switzerland, pp. 131–136. DOI: 10.1007/978-3-319-03215-3_5 (cit. on p. 104).

[171] Fabio Zaza, Claudia Paoletti, Roberto LoPresti, Elisabetta Simonetti, and Mauro Pasquali (2010). "Studies on sulfur poisoning and development of advanced anodic materials for waste-to-energy fuel cells applications". *Journal of Power Sources* 195.13, pp. 4043–4050. DOI: 10.1016/j.jpowsour.2010.01.034 (cit. on pp. 104, 105).

[172] N. Di Giulio, B. Bosio, V. Cigolotti, and S. W. Nam (2012). "Experimental and theoretical analysis of H_2S effects on MCFCs". *International Journal of Hydrogen Energy* 37.24, pp. 19329–19336. DOI: 10.1016/j.ijhydene.2012.03.086 (cit. on pp. 104, 106, 128, 129).

[173] Mohammad Songolzadeh, Mansooreh Soleimani, Maryam Takht Ravanchi, and Reza Songolzadeh (2014). "Carbon dioxide separation from flue gases: A technological review emphasizing reduction in greenhouse gas emissions". *The Scientific World Journal* 2014.Article ID 828131. DOI: 10.1155/2014/828131 (cit. on pp. 106, 129).

[174] Xueke Li, Jinru Han, Yan Liu, Zhihe Dou, and Ting-an Zhang (2022). "Summary of research progress on industrial flue gas desulfurization technology". *Separation and Purification Technology* 281, p. 119849. DOI: 10.1016/j.seppur.2021.119849 (cit. on pp. 106, 107, 129).

[175] Colin F Alie (2004). "CO_2 Capture With MEA: Integrating the Absorption Process and Steam Cycle of an Existing Coal-Fired Power Plant". PhD thesis (cit. on p. 107).

[176] F. J. Gutiérrez Ortiz, F. Vidal, P Ollero, L Salvador, V Cortés, A. Giménez, and and P. Otero (2006). "Pilot-Plant Technical Assessment of Wet Flue Gas Desulfurization Using Limestone." *Ind. Eng. Chem.* 45.4, pp. 1466–1477 (cit. on pp. 107, 129).

[177] Yuqiu Zhang, Yanxia Wang, Yongqi Liu, Haibo Gao, Yueyue Shi, Min Lu, and Huazhen Yang (2021). "Experiments and simulation of varying parameters in cryogenic flue gas desulfurization process based on Aspen plus". *Separation and Purification Technology* 259, p. 118223. DOI: 10.1016/j.seppur.2020.118223 (cit. on pp. 108, 130).

[178] Carol Toro Molina and Chakib Bouallou (2015). "Assessment of different methods of CO_2 capture in post-combustion using ammonia as solvent". *Journal of Cleaner Production* 103, pp. 463–468. DOI: 10.1016/j.jclepro.2014.03.024 (cit. on p. 108).

[179] Joao De Castro, Rodrigo Rivera-Tinoco, and Chakib Bouallou (2010). "Hydrogen production from natural gas: Auto-Thermal Reforming and CO_2 capture". *Chemical Engineering Transactions* 21.August, pp. 163–168. DOI: 10.3303/CET1021028 (cit. on pp. 108, 131).

[180] Rupu Yang (2021). "Methodology for developing flexible, controllable and cost-effective heat exchanger network". PhD thesis. Ecole des Mines de Paris - Paris Science and Lettre University. URL: https://pastel.archives-ouvertes.fr/tel-03214564 (cit. on pp. 117, 124).

[181] Rupu Yang, Cong Toan Tran, and Assaad Zoughaib (2020). "Iterative non linear programming method for the heat exchanger network design". *ECOS 2020 - 33rd International Conference on Efficiency, Cost, Optimization, Simulation and Environmental Impact of Energy Systems*. Osaka, Japan (cit. on pp. 117, 124).

[182] Jarosław Milewski and Janusz Lewandowski (2012). "Separating CO_2 from Flue Gases Using a Molten Carbonate Fuel Cell". *IERI Procedia* 1, pp. 232–237. DOI: 10.1016/j.ieri.2012.06.036 (cit. on p. 129).

[183] Akira Sasaki, Shuichi Matsumoto, and Toshihide Tanaka (1988). "Dynamic Characteristics of a Molten Carbonate fuel cell Stack" (cit. on p. 134).

[184] W. He (1998). "Dynamic model for molten carbonate fuel-cell power-generation systems". *Energy Conversion and Management* 39.8, pp. 775–783. DOI: 10.1016/s0196-8904(97)10022-x (cit. on p. 134).

[185] Michael D. Lukas, Kwang Y. Lee, and Hossein Ghezel-Ayagh (1999). "Development of a stack simulation model for control study on direct reforming molten carbonate fuel cell power plant". *IEEE Transactions on Energy Conversion* 14.4, pp. 1651–1657. DOI: 10.1109/60.815119 (cit. on p. 134).

[186] Michael D. Lukas, Kwang Y. Lee, and Hossein Ghezel-Ayagh (2001). "An explicit dynamic model for direct reforming carbonate fuel cell stack". *IEEE Transactions on Energy Conversion* 16.3, pp. 289–295. DOI: 10.1109/60.937210 (cit. on p. 134).

[187] Byoung Sam Kang, Joon Ho Koh, and Hee Chun Lim (2001). "Experimental study on the dynamic characteristics of kW-scale molten carbonate fuel cell systems". *Journal of Power Sources* 94.1, pp. 51–62. DOI: 10.1016/S0378-7753(00)00606-6 (cit. on p. 134).

[188] P. Heidebrecht and K. Sundmacher (2003). "Dynamic Modeling and Simulation of a Countercurrent Molten Carbonate Fuel Cell (MCFC) with Internal Reforming". *Fuel Cells* 2.34, pp. 166–180. DOI: 10.1002/fuce.200290016 (cit. on p. 134).

[189] M Fermeglia, A Cudicio, G Desimon, G Longo, S Pricl, and Area Science Park (2004). "Steady state and Dynamic simulation of molten carbonate fuel cells". *Chemical Engineering* 4.1, pp. 391–396 (cit. on p. 134).

[190] Sergio Bittanti, Silvia Canevese, Antonio De Marco, Gianluca Moretti, and Valter Prandoni (2005). "Molten carbonate fuel cell modelling". *IFAC Proceedings Volumes (IFAC-PapersOnline)* 16, pp. 392–399. DOI: 10.3182/20050703-6-cz-1902.01794 (cit. on p. 134).

[191] Jacob Brouwer, Faryar Jabbari, Elisângela Martins Leal, and Trevor Orr (2006). "Analysis of a molten carbonate fuel cell: Numerical modeling and experimental validation". *Journal of Power Sources* 158.1, pp. 213–224. DOI: 10.1016/j.jpowsour.2005.07.093 (cit. on p. 134).

[192] Fan Yang, Xin Jian Zhu, and Guang Yi Cao (2007). "Nonlinear fuzzy modeling of a MCFC stack by an identification method". *Journal of Power Sources* 166.2, pp. 354–361. DOI: 10.1016/j.jpowsour.2007.01.062 (cit. on p. 134).

[193] Sergio Bittanti, Silvia Canevese, Antonio De Marco, Giorgio Giuffrida, Antonio Errigo, and Valter Prandoni (2007). "Molten carbonate fuel cell dynamical modeling". *Journal of Fuel Cell Science and Technology* 4.3, pp. 283–293. DOI: 10.1115/1.2743074 (cit. on p. 134).

[194] Aiguo Liu and Yiwu Weng (2009). "Modeling of molten carbonate fuel cell based on the volume-resistance characteristics and experimental analysis". *Journal of Power Sources* 195.7, pp. 1872–1879. DOI: 10.1016/j.jpowsour.2009.10.040 (cit. on p. 135).

[195] E. Ovrum and G. Dimopoulos (2011). "A validated dynamic model of the first marine molten carbonate fuel cell". *Applied Thermal Engineering* 35.1, pp. 15–28. DOI: 10.1016/j.applthermaleng.2011.09.023 (cit. on p. 135).

[196] H. Kim, J. H. Cho, and K. S. Lee (2013). "Detailed dynamic modeling of a molten carbonate fuel cell stack with indirect internal reformers". *Fuel Cells* 13.2, pp. 259–269. DOI: 10.1002/fuce.201200068 (cit. on p. 135).

[197] M. C. Law, V. C.C. Lee, and C. L. Tay (2015). "Dynamic behaviors of a molten carbonate fuel cell under a sudden shut-down scenario: The effects on temperature gradients". *Applied Thermal Engineering* 82, pp. 98–109. DOI: 10.1016/j.applthermaleng.2014.11.083 (cit. on p. 135).

[198] Yu Luo, Yixiang Shi, Wenying Li, and Ningsheng Cai (2015). "Dynamic electro-thermal modeling of co-electrolysis of steam and carbon dioxide in a tubular solid oxide electrolysis cell". *Energy* 89, pp. 637–647. DOI: 10.1016/j.energy.2015.05.150 (cit. on p. 135).

[199] Bin Chen, Yashar S. Hajimolana, Vikrant Venkataraman, Meng Ni, and P. V. Aravind (2019). "Integration of reversible solid oxide cells with methane synthesis (ReSOC-MS) in grid stabilization: A dynamic investigation". *Applied Energy* 250, pp. 558–567. DOI: 10.1016/j.apenergy.2019.04.162 (cit. on p. 135).

[200] Yi Sun, Wenjin Zheng, Shiyu Ji, Anwei Sun, Wei Shuai, Nan Zheng, Yu Han, Gang Xiao, et al. (2022). "Dynamic behavior of high-temperature CO_2/H_2O co-electrolysis coupled with real fluctuating renewable power". *Sustainable Energy Technologies and Assessments* 52, p. 102344. DOI: 10.1016/j.seta.2022.102344 (cit. on p. 135).

[201] Xingxing Li, Bolun Yang, and Yong Zhang (2013). "Dynamics and control study on the low temperature methanation reactor with mass and heat recycle". *Journal of Process Control* 23.10, pp. 1360–1370. DOI: 10.1016/j.jprocont.2013.09.003 (cit. on p. 136).

[202] Julien Ducamp, Alain Bengaouer, and Pierre Baurens (2017). "Modelling and experimental validation of a CO_2 methanation annular cooled fixed-bed reactor exchanger". *The Canadian Journal of Chemical Engineering* 95. URL: https://onlinelibrary.wiley.com/doi/full/10.1002/cjce.22706 (accessed 26/4/2023) (cit. on p. 136).

[203] Rasmey Try, Alain Bengaouer, Pierre Baurens, and Christian Jallut (2018). "Dynamic modeling and simulations of the behavior of a fixed-bed reactor-exchanger used for CO_2 methanation". *AIChE Journal* 64.2, pp. 468–480. DOI: 10.1002/aic.15874 (cit. on pp. 136, 158, 182).

[204] Ali El Sibai, Liisa Rihko-Struckmann, and Kai Sundmacher (2015). "Synthetic Methane from CO_2: Dynamic Optimization of the Sabatier Process for Power-to-Gas Applications". *Computer Aided Chemical Engineering*. Ed. by Krist V. Gernaey, Jakob K. Huusom, and Rafiqul Gani. Vol. 37. 12 International Symposium on Process Systems Engineering and 25 European Symposium on Computer Aided Process Engineering. Elsevier, pp. 1157–1162. DOI: 10.1016/B978-0-444-63577-8.50038-3 (cit. on p. 136).

[205] Emanuele Giglio, Fabio Alessandro Deorsola, Manuel Gruber, Stefan Raphael Harth, Eduard Alexandru Morosanu, Dimosthenis Trimis, Samir Bensaid, and Raffaele Pirone (2018). "Power-to-Gas through High Temperature Electrolysis and Carbon Dioxide Methanation: Reactor Design and Process Modeling". *Industrial & Engineering Chemistry Research* 57.11, pp. 4007–4018. DOI: 10.1021/acs.iecr.8b00477 (cit. on pp. 136, 157, 158, 182).

[206] Emanuele Giglio, Raffaele Pirone, and Samir Bensaid (2021). "Dynamic modelling of methanation reactors during start-up and regulation in intermittent power-to-gas applications". *Renewable Energy* 170, pp. 1040–1051. DOI: 10.1016/j.renene.2021.01.153 (cit. on p. 137).

[207] Philippe Aubin, Ligang Wang, and Jan Van herle (2023). "Evaporating water-cooled methanation reactor for solid-oxide stack-based power-to-methane systems: Design, experiment and modeling". *Chemical Engineering Journal* 456, p. 140256. DOI: 10.1016/j.cej.2022.140256 (cit. on pp. 137, 159).

[208] Floriane Petipas, Qingxi Fu, Annabelle Brisse, and Chakib Bouallou (2013b). "Transient operation of a solid oxide electrolysis cell". *International Journal of Hydrogen Energy* 38.7, pp. 2957–2964. DOI: 10.1016/j.ijhydene.2012.12.086 (cit. on pp. 139, 175).

[209] Rafael A. Donado (1995). "Molten carbonate fuel cell start-up process." URL: https://www.unhcr.org/publications/manuals/4d9352319/unhcr-protection-training-manual-european-border-entry-officials-2-legal.html?query=excom%201989 (cit. on pp. 148, 149, 154, 179, 180).

[210] Li Zhou, Huaxin Lin, Baolian Yi, Huamin Zhang, Zhigang Shao, Pingwen Ming, and Mojie Cheng (2006). "A study on the start-up and performance of a kW-class molten carbonate fuel cell (MCFC) stack". *Electrochimica Acta* 51.26, pp. 5698–5702. DOI: 10.1016/J.ELECTACTA.2006.03.007 (cit. on pp. 149, 179, 180).

[211] Stephen Jolly (2017). *Pre-FEED Study of a MW-Class Molten Carbonate Fuel Cell System for Carbon Capture Demonstration at an Oil Sands Facility*. Technical Report. FuelCell Energy, Inc. URL: https://albertainnovates.ca/app/uploads/2020/10/FuelCell-Energy-Pre-FEED-Study-of-a-MW-Class-Molten-Carbonate-Fuel-Cell-System-for-Carbon-Capture-Demonstration-at-an-Oil-Sands-Facility.pdf (accessed 5/2/2022) (cit. on pp. 150, 153, 181).

[212] Gabriele Discepoli, Giovanni Cinti, Umberto Desideri, Daniele Penchini, and Stefania Proietti (2012). "Carbon capture with molten carbonate fuel cells: Experimental tests and fuel cell performance assessment". *International Journal of Greenhouse Gas Control* 9, pp. 372–384. DOI: 10.1016/j.ijggc.2012.05.002 (cit. on pp. 151, 180).

[213] Warren M. Rohsenow, James P. Hartnett, and Young I. Cho (1998). *Handbook of heat transfer*. Vol. 3. Mcgraw-hill New York (cit. on p. 151).

[214] Azur Insulation (2019). *Ceramic Fiber*. DOI: 10.1007/978-1-4419-6247-8_2160 (cit. on p. 151).

[215] Opexworks (2022). *Purpose of Insulation*. URL: www.opexworks.com/KBase/Energy_Management/Termal_Energy_Management/Insulation_and_Refractorises/Purpose_of_Insulation.htm (accessed 25/2/2022) (cit. on p. 151).

[216] P.E Mark Baker (2009). *The Basics of API 650: API Standard 650 Welded Tanks for Oil Storage*. URL: https://www.nistm.org/houstonSept2009/docs/2009_HoustonConf_Pres/Basic_API650.pdf (accessed 1/3/2022) (cit. on p. 151).

[217] "External Natural Convection" (2013). *Convection Heat Transfer*. John Wiley & Sons, Ltd, pp. 168–232. DOI: 10.1002/9781118671627.ch4 (cit. on p. 152).

[218] Isabelle Champon, Alain Bengaouer, Albin Chaise, Sébastien Thomas, and Anne-Cécile Roger (2019). "Carbon dioxide methanation kinetic model on a commercial Ni/Al_2O_3 catalyst". *Journal of CO_2 Utilization* 34, pp. 256–265. DOI: 10.1016/j.jcou.2019.05.030 (cit. on pp. 155, 156, 181).

[219] Kayvan Khorsand, Mehdi A. Marvast, Narges Pooladian, and Madjid Kakavand (2007). "Modeling and Simulation of Methanation Catalytic Reactor in Ammonia Unit". *Petroleum & coal* 49.1, pp. 46–53 (cit. on pp. 156, 157, 181, 182).

[220] Steffi Matthischke, Stefan Roensch, and Robert Güttel (2018). "Start-up Time and Load Range for the Methanation of Carbon Dioxide in a Fixed-Bed Recycle Reactor". *Industrial and Engineering Chemistry Research* 57, pp. 6391–6400. DOI: 10.1021/acs.iecr.8b00755 (cit. on p. 160).

[221] Jens Bremer, Karsten H. G. Rätze, and Kai Sundmacher (2017). "CO_2 methanation: Optimal start-up control of a fixed-bed reactor for power-to-gas applications". *AIChE Journal* 63.1, pp. 23–31. DOI: 10.1002/aic.15496 (cit. on p. 160).

[222] *SAM Open Source - System Advisor Model - SAM*. (2023). URL: https://sam.nrel.gov/about-sam/sam-open-source (accessed 27/3/2023) (cit. on pp. 160, 183).

[223] Service des données et études statistiques (SDES) (2022). *Tableau de bord: éolien Quatrième trimestre 2021*. URL: https://www.statistiques.developpement-durable.gouv.fr/publicationweb/435 (accessed 6/5/2022) (cit. on p. 161).

[224] *Mas de Leuze (France) - Parcs éoliens - The Wind Power* (2022). URL: https://www.thewindpower.net/windfarm_fr_444_mas-de-leuze.php (accessed 18/5/2022) (cit. on pp. 161, 183).

[225] IRENA (2021b). *Renewable Power Generation Costs in 2020*. Technical Report. Abu Dhabi, p. 160. URL: https://www.irena.org/publications/2021/Jun/Renewable-Power-Costs-in-2020 (accessed 2/5/2022) (cit. on pp. 163, 206, 222).

[226] Pierre Olivier, Cyril Bourasseau, and Belkacem Bouamama (2017). "Dynamic and multiphysic PEM electrolysis system modelling: A bond graph approach". *International Journal of Hydrogen Energy* 42.22, pp. 14872–14904. DOI: 10.1016/j.ijhydene.2017.03.002 (cit. on pp. 164, 184).

[227] *Statinfo - solaire photovoltaique* (2023). URL: https://www.statistiques.developpement-durable.gouv.fr/publicationweb/412 (accessed 28/3/2023) (cit. on p. 168).

[228] Albioma (2022). *Centrale solaire de Fabrègues*. URL: https://www.albioma.com/implantation/france-metropolitaine/fabregues (accessed 23/6/2022) (cit. on pp. 168, 186).

[229] D. C. Jordan and S. R. Kurtz (2013). "Photovoltaic Degradation Rates—an Analytical Review". *Progress in Photovoltaics: Research and Applications* 21.1, pp. 12–29. DOI: 10.1002/pip.1182 (cit. on pp. 169, 186).

[230] Ralf Peters, Maxana Baltruweit, Thomas Grube, Remzi Can Samsun, and Detlef Stolten (2019). "A techno economic analysis of the power to gas route". *Journal of CO_2 Utilization* 34, pp. 616–634. DOI: 10.1016/J.JCOU.2019.07.009 (cit. on pp. 192, 215).

[231] Jachin Gorre, Felix Ortloff, and Charlotte van Leeuwen (2019). "Production costs for synthetic methane in 2030 and 2050 of an optimized Power-to-Gas plant with intermediate hydrogen storage". *Applied Energy* 253.2019, p. 113594. DOI: https://doi.org/10.1016/j.apenergy.2019.113594 (cit. on pp. 192, 201).

[232] Szabolcs Szima and Calin Cristian Cormos (2021). "CO_2 utilization technologies: A techno-economic analysis for synthetic natural gas production". *Energies* 14.5. DOI: 10.3390/en14051258 (cit. on pp. 192, 215).

[233] Gabriele Fambri, Cesar Diaz-Londono, Andrea Mazza, Marco Badami, Teemu Sihvonen, and Robert Weiss (2022). "Techno-economic analysis of Power-to-Gas plants in a gas and electricity distribution network system with high renewable energy penetration". *Applied Energy* 312, p. 118743. DOI: 10.1016/j.apenergy.2022.118743 (cit. on pp. 192, 201, 215).

[234] Robert Remick and Douglas Wheeler (2010). *Molten Carbonate and Phosphoric Acid Stationary Fuel Cells : Overview and Gap Analysis*. Technical Report, pp. 1–51. URL: https://www.nrel.gov/docs/fy10osti/49072.pdf (accessed 1/10/2020) (cit. on p. 193).

[235] Christian Breyer, Eemeli Tsupari, Ville Tikka, and Pasi Vainikka (2015). "Power-to-Gas as an Emerging Profitable Business Through Creating an Integrated Value Chain". *Energy Procedia*. 9th International Renewable Energy Storage Conference, IRES 2015 73, pp. 182–189. DOI: 10.1016/j.egypro.2015.07.668 (cit. on pp. 194, 216).

[236] *Natural gas prices around the world, June 2022* (2022). URL: https://www.globalpetrolprices.com/natural_gas_prices/ (accessed 9/2/2023) (cit. on pp. 194, 200, 216).

[237] M. Cassir, S. J. McPhail, and A. Moreno (2012). "Strategies and new developments in the field of molten carbonates and high-temperature fuel cells in the carbon cycle". *International Journal of Hydrogen Energy* 37.24, pp. 19345–19350. DOI: 10.1016/j.ijhydene.2011.11.006 (cit. on pp. 197, 208, 218).

[238] Fabio Salomone, Emanuele Giglio, Domenico Ferrero, Massimo Santarelli, Raffaele Pirone, and Samir Bensaid (2019). "Techno-economic modelling of a Power-to-Gas system based on SOEC electrolysis and CO_2 methanation in a RES-based electric grid". *Chemical Engineering Journal*. ISCRE 25 Special Issue: Bridging Science and Technology 377, p. 120233. DOI: 10.1016/j.cej.2018.10.170 (cit. on p. 201).

[239] IRENA (2022b). *RENEWABLE POWER GENERATION COSTS IN 2021*. Technical Report. International Renewable Energy Agency. URL: https://www.irena.org/publications/2022/Jul/Renewable-Power-Generation-Costs-in-2021 (accessed 30/4/2023) (cit. on p. 206).

[240] Caroline Dusanter (2020). *Prix de l'électricité : prix du kWh en 2023 et évolutions*. URL: https://opera-energie.com/prix-electricite-prix-du-kwh/ (accessed 29/4/2023) (cit. on p. 207).

[241] *Évolution du prix de l'électricité en France et prévisions 2030* (2018). URL: https://selectra.info/energie/electricite/prix/evolution (accessed 29/4/2023) (cit. on p. 207).

[242] IEA (2020b). *Special Report on Carbon Capture Utilisation and Storage: CCUS in clean energy transitions*. Technical Report. URL: https://www.iea.org/reports/ccus-in-clean-energy-transitions (accessed 29/4/2023) (cit. on pp. 207, 208, 222).

[243] W Krewitt and S Schmid (2005). *Fuel Cell Technologies and Hydrogen Production/Distribution Options*. Technical Report. DLR Institute, pp. 1–113. URL: https://www.dlr.de/fk/Portaldata/40/Resources/dokumente/publikationen/2005-09-02_CASCADE_D1.1_fin.pdf (accessed 1/10/2020) (cit. on p. 208).

[244] Theodore P. Wright (1936). "Factors affecting the cost of airplanes". *Journal of the aeronautical sciences* 3.4, pp. 122–128 (cit. on p. 208).

[245] Rodrigo Rivera-Tinoco, Koen Schoots, and Bob Van Der Zwaan (2012). "Learning curves for solid oxide fuel cells". *Energy Conversion and Management* 57, pp. 86–96. DOI: 10.1016/j.enconman.2011.11.018 (cit. on p. 208).

[246] FuelCell Energy Inc. (2004). *Molten Carbonate Fuel Cell Product Design Improvement: semi-annual technical progress report for period December 21,2003 to June 20,2004*. Technical Report. URL: https://www.osti.gov/scitech/servlets/purl/833250 (accessed 2/5/2023) (cit. on p. 210).

[247] Roberto Bove, Angelo Moreno, and Stephen Mcphail (2008). *International Status of Molten Carbonate Fuel Cell (MCFC) Technology*. Technical Report. Petten,The Netherlands: Joint Research Centre – Institute for Energy. URL: https://publications.jrc.ec.europa.eu/repository/bitstream/JRC44203/mcfc_status.pdf (accessed 15/10/2020) (cit. on p. 211).

[248] *FuelCell Energy, Inc. - Press Releases* (2023). URL: https://investor.fce.com/press-releases/default.aspx (accessed 2/5/2023) (cit. on p. 211).

[249] Inkwood Research (2021). *Market Research Reports, Custom Research, Industry Analysis*. URL: https://inkwoodresearch.com/ (accessed 19/6/2021) (cit. on pp. 212, 223).

[250] Charlotte Martin (2023). *Prix du gaz naturel : évolutions et tendances*. URL: https://opera-energie.com/prix-gaz-naturel/ (accessed 3/5/2023) (cit. on p. 213).

RÉSUMÉ

Ce travail vise à évaluer la faisabilité technico-économique d'une technologie Power-to-SNG utilisant des cellules d'électrolyse à haute température à base de carbonates fondus (MCEC) pour la production de gaz de synthèse et le stockage d'électricité par co-électrolyse de H_2O et CO_2. À cette fin, un modèle stationnaire validé du MCEC a été développé, suivi d'une analyse de sensibilité pour déterminer les conditions de fonctionnement optimales. Ensuite, un procédé Power-to-SNG à l'échelle de 1 MW a été proposé et simulé à l'aide du logiciel Aspen Plus, en tenant compte de l'intégration thermique pour assurer des économies d'énergie. L'évaluation montre un rendement énergétique global de 68,7% et un taux de production de méthane de 1,3 tonne par jour. Le comportement dynamique du système, comprenant l'électrolyseur MCEC et le réacteur de méthanation, a été évalué. La réponse dynamique du procédé global aux variations de charge lorsqu'il est couplé à une source d'énergie renouvelable intermittente a été examinée, révélant sa sensibilité à ces sources avec une meilleure cohérence vis-à-vis de l'énergie éolienne par rapport à l'énergie solaire. Enfin, la faisabilité économique a été analysée, mettant en évidence la nécessité d'améliorer la durée de vie de l'électrolyseur, de réduire les coûts des cellules et le prix de l'électricité pour être compétitif sur le marché. Les perspectives d'avenir pour atteindre des coûts compétitifs de production de méthane synthétique sont encourageantes, avec des coûts attendus bas de l'électricité provenant de sources renouvelables et des coûts réalistes pour le captage du CO_2. Cependant, des défis subsistent en ce qui concerne les dépenses en investissement, en particulier par rapport à l'amélioration de la durée de vie et du coût de l'électrolyseur MCEC, même si des avancées dans la technologie MCFC montrent un potentiel de réduction des coûts d'ici 2030. Cette recherche approfondie offre un aperçu du potentiel envisagé du procédé en tant que solution écologique et viable pour la production de méthane de synthèse.

MOTS CLÉS

Power-to-Gas, stockage d'énergie renouvelable, co-électrolyse MCEC, méthanation du CO et CO_2, modélisation dynamique

ABSTRACT

This work aims to assess the techno-economic feasibility of a Power-to-SNG technology utilizing high-temperature molten carbonate electrolysis cells (MCEC) for syngas production and electricity storage through co-electrolysis of H_2O and CO_2. For this purpose, a validated steady-state model of the MCEC was developed, followed by a sensitivity analysis to determine optimal operating conditions. Subsequently, a 1 MW scale Power-to-SNG process was proposed and simulated in Aspen Plus software, considering heat integration for energy savings. The evaluation shows an overall energy efficiency of 68.7% and a 1.3 tonne/day methane production rate. The system's dynamic behavior for the MCEC electrolyzer and the methanation reactor was assessed. Following this, the dynamic response of the overall process with load changes when coupled with intermittent renewable power was examined, revealing its sensitivity to these sources, with wind power showing better consistency than solar power. Finally, the economic feasibility was analyzed, highlighting the need for improvements in electrolyzer lifespan, cell cost reduction, and lower electricity prices to compete with market prices. The future outlook for achieving competitive synthetic methane production costs is promising, with expected low electricity costs from renewable sources and achievable CO_2 capture costs. However, challenges remain in capital expenses, particularly improving the lifetime and cost of the MCEC electrolyzer, although advancements in MCFC technology show potential for cost reduction by 2030. This extensive research provides insight into the envisaged process's potential as an environmentally friendly and viable solution for synthetic methane production.

KEYWORDS

Power-to-Gas, renewable energy storage, MCEC co-electrolysis, CO and CO_2 methanation, dynamic modeling